Momentum, Heat and Mass Transfer Rates in Boundary Flows

R. Waters

PhD. thesis

1979

ProQuest LLC
789 East Eisenhower Parkway
P.O. Box 1346
Ann Arbor, MI 48106-1346

The work detailed in this thesis was completed before 1974. This thesis was presented for examination in 1979.

Contents

Chapter 1

Introduction

The purpose of this thesis is to describe, and then validate a modelling technique for simulating the time averaged momentum, mass and heat transfer rates in a variety of specified boundary flows.

This technique will be constructed so that it's arithmetic calculations can be quickly and accurately performed with a digital electronic computer. In the context of this thesis boundary flows are regarded as being either boundary layer or radial wall jets that flow in an irreversible manner over a surface. The specified flows have structures that are similar to those found in industry so that this project has some practical significance. In particular it is hoped to construct a modelling technique capable of simulating complex flame and plasma radial wall jet flows; which will provide a theoretical foundation for future studies of the turbulent transfer processess involved in the welding and cutting of materials.

Electronic computers have had a profound effect on the ways and means in which scientific problems are both examined and solved. In the sciences of both aero and thermo-dynamics their effect has been particularly noticeable in the area concerning flow modelling of momentum, and more latterly mass and heat, transfer rates in boundary flows. This rapid advance has been caused by the fact that the quick repetitive arithmetic power of electronic computers, can be used to full advantage when solving the second order partial differential conservation equations for boundary flows.
Descriptions of the categories into which the various modelling techniques can be divided are presented in section one.

Two varieties of boundary flows are modelled in this thesis. The first are boundary layer flows; these have been simulated so that the performance of certain modelling techniques specifically constructed for these flow situations can be assessed and compared. The second, and more important are radial wall jets; the simulated flows are chosen to both validate a recommended modelling technique in various industrially significant situations and to estimate it's ability to simulate complex flame and plasma flows . In section 2 the selected radial wall jet flows are detailed, after describing the type of industrial applications they are meant to represent.

In section 3 the layout of the work described in this thesis is presented.

1.1 Modelling Techniques

The available modelling techniques have been split into two categories. Those in the first category predict sufficient flow properties to describe momentum transfer by solving relationships derived from the time averaged equations representing conservation of momentum. Techniques from this category are used in this study for reasons that will be detailed later. The techniques in the second category solve the Reynolds stress transport equations that describe momentum transfer. In the remainder of this section these categories , including the turbulence information they require, are described; and then the reason for choosing the first category of techniques given.

Modelling techniques of the first category predict sufficient time averaged properties to broadly define the characteristics of the simulated flows. In many ways this is an excellent approach,

because engineers are invariably concerned with time averaged data. However, the averaging and manipulation of the conservation equations in the derivation of these techniques, does not remove all the dominant correlations of the fluctuating components of the velocity. Therefore, before a solution can be obtained information relating these correlations to the time averaged flow properties has to be provided. There are a variety of standard semi-empirical and phenomenological hypothesis that have been developed to provide this information. For example, when the unknown fluctuating velocity correlations are equivalent to the Reynolds stress, turbulence models based upon the mixing length hypothesis by Prandtl [1] can be used.

These turbulence models are discussed more fully in chapters 2 and 3.

The Reynolds stress transport equations solved in the second category of modelling techniques represent conservation of the Reynolds stresses in the boundary flow. The equations contain unknowns concerning the pressure fluctuations p', length scales of turbulent eddies, and products of the fluctuating velocities in three spatial dimensions - namely u', v' and w'. Before a solution can be obtained these unknowns either have to be neglected or supplied in a generalized form from experimentation. Modelling techniques based upon this approach have been successfully constructed - Bradshaw [3] has constructed one of the better known models. However, such techniques at present cannot easily simulate flows in which momentum, mass and heat transfer processes simultaneously occur, because the large amount of turbulence information they require has not been collected.

Modelling techniques from the first of the described categories are recommended as the most suitable with which to start this study. The two reasons for this choice are both influenced by the fact that the recommended technique must be capable of simulating time averaged momentum, mass and heat transfer rates in boundary flows commonly found in industry. The first reason stems from the fact that techniques from the first category have been widely and successfully used to simulate all three specified turbulent transfer processes, whereas those from the second category have not. Secondly, concise turbulence information for techniques of the second category when simulating all three transfer processes is not at present available. In fact Beér and Chigier[4] and Gaines[5] have reported that in certain complex flames and plasma flows this information cannot be accurately measured.

1.2 Selected Flows

The purpose of the specified radial wall jet simulations are in part to assess the performance, and hence validate, those portions of a recommended modelling technique that will be used for simulating momentum, mass and heat transfer rates. Where possible the selected flows also corresponded to situations commonly found in industry. The recommended technique uses an approximate mathematical procedure for solving the conservation equations for a radial wall jet, after suitable semi-empirical turbulence information has been supplied. To assess the validity of specified portions of the technique predicted results from the technique will be compared with experimental data. Of course, the experiments will be subject to discrepancies which will be allowed for in all comparisons.

As background information various industrially significant applications for radial wall jets are detailed in sub-section a. Then in sub-section b the selected flows are described. The portions of the recommended modelling technique these flows will validate, will also be specified.

1.2a Industrial Applications

Since the industrial revolution impinging flows, of which radial wall jets are an integral part, have been used to cool, heat, join and cut materials. For example, glass sheet is often cooled by impinging jets during it's production process. Also in most industrial situations materials are cut, heated and welded with impinging combustible flows. Increasing mechanization of the production procedures involving these applications has caused not only a raising of industrial standards, but also the need for more efficient means of both producing and controlling these flows.

To meet these requirements a series of sponsored studies concerned with examining the turbulent transfer processes within these flows have been undertaken. An excellent example of one such study is that by Kestin et al[6]. In a series of papers on impinging flows Kestin etal have detailed and discussed the correlations between the variation of local heat transfer coefficient at the surface and, firstly nozzle diameter and configuration, secondly distance between nozzle & surface, and thirdly turbulence within the flow.

Another major industrial application in which radial wall jets are involved is in the propulsion of vertical take off and landing (hereafter abbreviated to V.T.O.L) aircraft. Although the radial wall jet has nothing to do with the act of propulsion its effect on the aircraft has to be considered. For an example, theoretical studies have, and are being carried out, on the effect of the radial wall jet from the propulsion unit of a V.T.O.L aircraft upon the crafts stability and control when hovering near the ground.

1.2b Chosen flows

The four selected radial wall jets all moved with similar mean velocities, and were submerged in the atmosphere. The first flow contained air, and the second Nitrogen and Oxygen (at concentration levels different to the atmosphere); both flows were at the same temperature as the submerging air. The third flow contained Argon, Nitrogen and Oxygen at a temperature greater than the submerging fluid ; and the fourth involved chemically reacting Methane, Carbon Monoxide and Oxygen. These details are summarized in table 1.1.

As shown in table 1.1 the first three flows involve turbulent momentum, momentum and mass, and momentum, mass and heat transfer respectively. Therefore the simulations of these flows with a particular modelling technique will validate the momentum, mass and heat transfer portions of the technique. Simulation of the fourth flow assesses the effect of chemical reaction upon the modelling technique.

Table 1.1

Selected Flows

	Constituents	Temperature	Chemical reaction	Turbulent transfer processes involved	Industrial application
i	Air	Same as submerging air	None	Momentum	Cooling of glass sheet and metals
ii	Nitrogen and Oxygen	Same as submerging air	None	Momentum and mass	Simulation of V.T.O.L aircraft
iii	Argon, Nitrogen & Oxygen	Greater than submerging air	None	Momentum, mass and heat	Welding, cutting and heating of materials
iv	Methane, Oxygen Nitrogen, Carbon Monoxide and Carbon dioxide	Greater than submerging air	Yes	Momentum, mass and heat with chemical reaction	Welding, cutting and heating of materials. An introduction into the possibility of simulating various plasma flows.

1.3 Layout

Modelling techniques proposed by Spalding- Patankar[7] and Denny-Landis[8] are used to start this study. They were selected from those techniques in the first category, that is those which solve the time averaged momentum conservation equations. This selection procedure is detailed in chapter two.

In chapter three the performance of the selected modelling techniques are assessed when they are used to simulate specified boundary layer and wall jet flows. (These modelling techniques were, to a large extent, specifically constructed to simulate these type of flows). From the results of this investigation the framework for a new modelling technique, making use of an interactive scheme to minimize numerical errors, was postulated. The mathematical derivation of this technique from the conservation equations for momentum , mass and heat transfer is presented in chapter four. The performance of the recommended technique, when simulating the flows specified in chapter three, is declared in chapter five. Also presented are comparisons between the results from Spalding-, Patankar, Denny-Landis and the recommended modelling technique - these show the new technique to be the more accurate.

The remainder of the thesis is concerned with the simulation, and appreciation, of the turbulent transfer processes in a variety of radial wall jet situations. The dearth of suitable time averaged experimental data detailing the flow patterns within such jets necessitated studies of three flow situations, i to iv in

table 1.1, being undertaken. These experiments are detailed in the appendicies, and besides providing data for the simulations also gave a comprehensive view of the time averaged properties over the complete impinging flow. The radial wall jet simulations for experiments i to iv in table 1.1 are given in chapters 6 - 9 respectively. The results from these simulations are summed up in chapter 10, and recommendations for future work given. The significant advances that have occurred since the work detailed in chapters one to ten was completed are discussed in chapter eleven.

Chapter 2

Review of Modelling Techniques

This review has two purposes. Firstly, to illustrate the types of modelling techniques available for simulating boundary flows in which turbulent momentum transfer predominates. Secondly, to provide sufficient information for a rational explanation of why the techniques proposed by Spalding- Patankar [7] and Denny-Landis were used to start this study. All the modelling techniques discussed in this chapter are based upon the solution of the equation for mainstream momentum conservation 2.1.

$$\frac{\partial U}{\partial x} = \frac{\partial}{\partial \psi}(\tilde{\tau}) - \frac{1}{\rho U}\frac{dp}{dx} \qquad (2.1$$

This equation models momentum conservation in the boundary flow shown in figure 2.1; U represents the mainstream velocity, ψ the stream function, $\tilde{\tau}$ the local shear stress, ρ density and p pressure. The four ways of reducing and then solving equation 2.1 are described in sections one to four - included with these descriptions are details of sample modelling techniques. The four ways of solving equation 2.1 are called parametric, explicit, cross-stream and marching integral methods of solution, and these are described in sections 1 - 4 respectively. This method of categorizing modelling techniques closely adheres to that postulated by Spalding- Patankar in reference [7]. The reasons for selecting the techniques postulated by Spalding- Patankar and Denny-Landis are detailed in section 5.

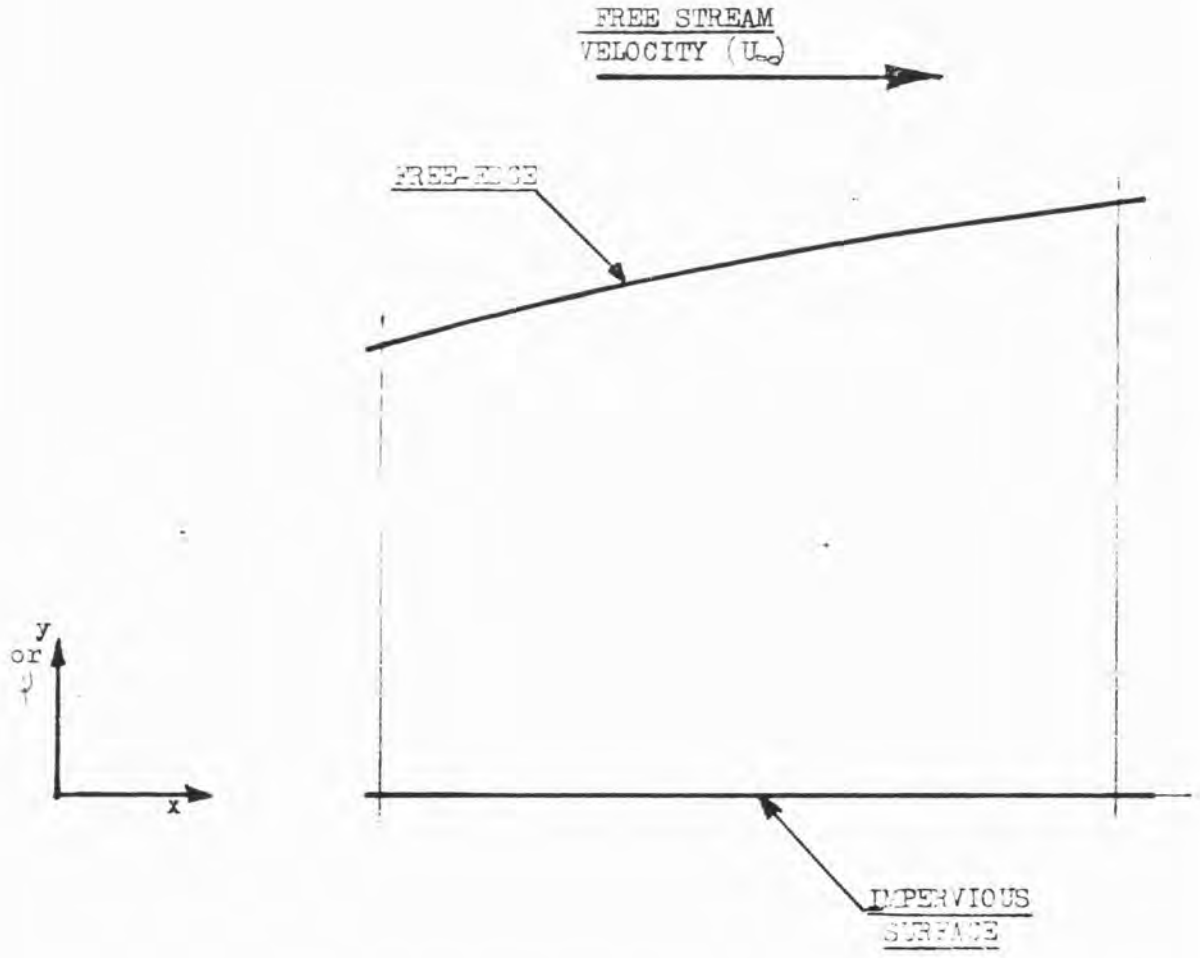

BOUNDARY LAYER

FIGURE 2.1

2.1 Parametric Integral

Modelling techniques that use this method predict momentum thickness δ_2, displacement thickness δ_1 and total skin friction C_f in turbulent boundary layer flows. These properties coarsely define the behaviour of the flow.

The parametric integral method is based upon the solution of the momentum integral equation 2.2 for the momentum thickness.

$$\frac{d\delta_2}{dx} + (H_{12} + 2)\frac{\delta_2}{U_\infty} \cdot \frac{dU}{dx} = \frac{\tau_o}{\rho U_\infty^2} \qquad (2.2$$

In this equation the shape factor H_{12} is defined by:

$$H_{12} = \frac{\delta_1}{\delta_2} \quad , \qquad (2.3$$

and τ_o representing the shear stress at the surface.

The momentum integral equation is derived from the equation representing momentum conservation 2.1 by the following procedure. Equation 2.1 is integrated across an incompressible boundary layer of the type shown in figure 2.1, after substituting for the cross-stream velocity V and rate of change of pressure $\frac{dp}{dx}$. The cross-stream velocity is derived from the continuity equation:

$$\frac{\partial V}{\partial y} = \frac{\partial U}{\partial x} \qquad (2.4$$

The rate of change of pressure $\frac{dp}{dx}$ is derived from the variation in velocity at the free-edge, by applying Bernoulli's relationship:

$$\frac{1}{\rho}\frac{dp}{dx} = \frac{-U_\infty dU_\infty}{dx} \qquad (2.5$$

The momentum integral equation 2.2 is solved for δ_2 using one of the many solution techniques for first order differential equations. After substituting semi-empirical information detailing the variation of τ_0 and f_{12} with various parameters in the flow. The remaining predicted properties δ_1 and C_f are determined from equation 2.3 and 6 respectively.

$$\tau_T = \int_{x=0}^{x=L} \frac{\tau_0}{\rho U_\infty^2} \, dx \qquad (2.5$$

Modelling techniques proposed by Gruschwitz [9], Garner[10] and von Doenhoff and Tetervin[11] all use this method, and provide accurate gross predictions for the behaviour of boundary layers. The major difference between these techniques is the formulation of the semi-empirical information they use. This information, together with references that detail it's origin, is presented in table 2.1.

2.2 Explicit Integral

Techniques using this mathematical method predict the momentum and displacement thickness, and total skin friction in incompressible boundary layer flows. The method is based upon the solution of the momentum integral 2.2, and or other additional integral equations, for the momentum thickness δ_2. The remaining predicted properties, the total skin friction C_f and boundary height δ_1, are normally determined from equation 2.6 and a relationship detailing the variation of a shape factor. Two types of additional equations are normally used. They are obtained by multiplying either the equation of motion 2.1 or continuity 2.4 with suitable weighing functions, and integrating the resulting relationship between the free-edge and impervious surface of the boundary flow.

Modelling Technique proposed by by	Empirical Relationship relating τ_o and δ_2	Proposer	Empirical Relationship to determine H_{12}	Proposer
Gruschwitz	$\frac{\tau_o}{\rho U^2} = \frac{0.128}{(U\delta_2/\nu)^{\frac{1}{4}}}$	Prandtl P32	$\delta_2 \frac{d\eta_1}{dx} = -2\eta_1 \frac{\delta_2}{U_\infty}\frac{dU_\infty}{dx} - 0.000894\eta_1 + 0.00461$ $\eta_1 = 1 - \left[\frac{H_{12}-1}{H_{12}(H_{12}+1)}\right]^{H_{12}-1}$	Gruschwitz G35 Pretsch P38
Garner	$\frac{\tau_o}{\rho U^2} = \frac{0.0065}{(U\delta_2/\nu)^{1/6}}$	Falkner F43	$\left[\frac{U_\infty \delta_2}{\nu}\right]^{\frac{1}{6}} \delta_2 \frac{dH_{12}}{dx} = \exp\left[5(H_{12}-1.4)\right]$ $\left[\left(\frac{U_\infty \delta_2}{\nu}\right)^{\frac{1}{6}} \frac{\delta_2}{U_\infty}\frac{dU_\infty}{dx} - 0.0185(H_{12}-1.4)\right]$	Garner G44
von Doenhoff and Tetervin	$\frac{\tau_o}{\rho U^2} = \frac{0.0288}{\left[\log\left[\frac{4.075\, U\delta_2}{\nu}\right]\right]^2}$	Squire and Young SY45	$\delta_2 H_{12} = \exp\left[4.08(H_{12}-2.975)\right]$ $\left[-\frac{\delta_2}{q}\frac{dq}{dx}\frac{2q}{\tau_o} - 2.035(H_{12}-1.286)\right]$	von Doenhoff and Tetervin DT45

Popular examples of modelling techniques that use this method are those proposed by Truckenbrodt [16] and Head [17].

Truckenbrodt's technique uses the mean energy relationship 2.7 as an additional equation. The energy equation is obtained by multiplying the momentum integral equation by U_∞ prior to integration.

$$\frac{1}{U_\infty^3}\left[\frac{d}{dx}\left(U_\infty^3 \delta_3\right)\right] = \frac{2\left(d_1 + t_1\right)}{\rho U_\infty^3} \qquad (2.7$$

In this equation δ_3 represents the energy thickness, d_1 is the proportion of the friction work in the boundary layer transformed into heat and t_1 the energy of turbulent motion. In general t_1 can be neglected with respect to d_1. Truckenbrodt solved this equation for the momentum thickness δ_2 ; after supplying semi-empirical information of the form of:

$$\frac{d_1}{\rho U_\infty^3} = \frac{0.56 \times 10^{-2}}{\left(U_\infty \delta_2 / \nu\right)^{1/6}}$$

and $\delta_2 = f(\delta_3)$

The momentum integral and energy equations have been combined to formulate a shape factor relationship used to estimate the onset of boundary layer separation.

Head modelling technique uses as the additional equation the continuity requirement:

$$\frac{d}{dx}\left(\int_0^{\delta_1} U\,dy\right) = \dot{m}''_{FE} \qquad (2.8$$

with $\dot{m}''_{FE}$ representing entrainment at the free-edge of the flow. The momentum integral and this equation have been solved for the momentum thickness, after supplying semi-empirical turbulence information relating the entrainment rate to properties of the mean flow field.

2.3 Cross-Stream

Modelling techniques making use of this mathematical method predict the mainstream velocity U at discrete points within incompressible boundary layer flows. The cross-stream method solves the Navier-Stokes equation 2.9, after substituting a phenomenological theory of turbulence for the Reynolds stress - $\overline{\rho u'v'}$.

$$U\frac{\partial U}{\partial x} + V\frac{\partial U}{\partial y} = -\frac{1}{\rho}\frac{dp}{dx} + \frac{\mu}{\rho}\frac{\partial^2 U}{\partial y^2} - \frac{\partial}{\partial y}\left(\overline{u'v'}\right) \qquad (2.9$$

This mathematical method, which was introduced by Hartree and Wormersley[18], reduces equation 2.9 to a first order differential equation in the velocity U, which can be integrated across the boundary layer to predict the velocity field. The steps used in this method are as follows. Firstly, one of the established phenomenological turbulence theories are used to represent Reynolds stress in equation 2.9. (Examples of such theories are those proposed by Van Driest[2] and Cebeci[19], which are based upon Prandtls' mixing length theory.) Secondly, a series of finite difference assumptions valid within a cross-stream strip through the flow, shown in figure 2.3, are substituted for the partial differentials in equation 2.9 to give a first order differential equation in $\frac{dU}{dy}$. It is this equation which is integrated across the boundary flow to predict the velocity.

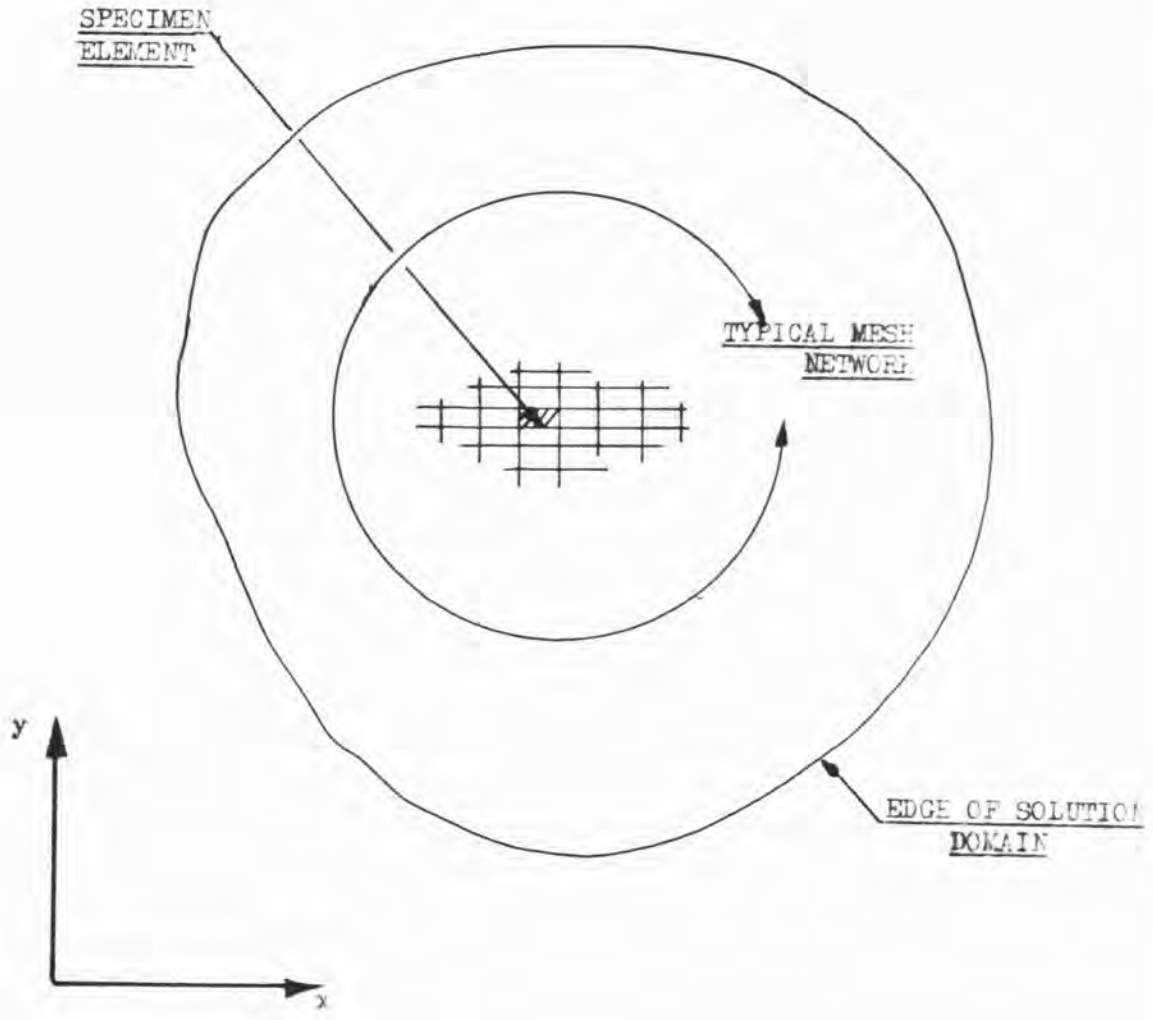

SOLUTION DOMAIN

FIGURE 2.1

Examples of modelling techniques that use this mathematical method to predict the velocity field in boundary layers are those proposed by Smith, Jaffe and Lind[20] and Mellor[21].

2.4 Marching Integration

Modelling techniques making use of this class of mathematical method predict the velocity field within a boundary flow from the Navier Stokes equation 2.9. The Reynolds stress is estimated from published turbulence models, which are not discussed in this section, because they do not form an essential part of the mathematical method. In fact most modern modelling techniques in this class can accept a wide variety of different turbulence models.

The purpose of the mathematical method is to solve equation 2.9 for the mainstream velocity U over a particular area of flow - often called the solution domain and shown in figure 2.2. This domain is sub-divided into a series of flow elements by the following procedure. Firstly, the domain is covered with a mesh network. Secondly, elements of a specified shape and size are positioned in the domain with reference to this network. As an example of this procedure the solution domain in figure 2.2 is covered with a cartesian xy mesh network, and rectangular flow elements are positioned so that their edges coincide with the lines of the mesh.

The mathematical method comprises two parts; firstly, a limited solution to equation 2.9 is derived within a

typical flow element. This solution takes the form of an algebraic relationship that relates the velocities at the corner of the element; and is obtained by substituting assumed rates of changes of velocity over the element for the partial differentials in equation 2.3. Secondly, overall predictions within the solution domain are obtained by applying the limited solution to each flow element, and solving the resultant set of simultaneous equations for the velocity.

Examples of modelling techniques that make use of this mathematical method are those proposed by Flugge-Lotz[22], Spalding- Patankar[7] and Denny-Landis[8]. The major differences between these techniques occur in the ways in which:

a) the co-ordinate system, the mesh network and finite difference assumptions are specified,

and b) information concerning the turbulent behaviour of the fluid is presented.

The co-ordinate systems, mesh networks and assumed velocity profiles used in the specimen modelling techniques are detailed in table 2.2. The mesh networks used by Spalding- Patankar and Denny-Landis are numerically the most efficient, because the networks grow with the flow. Turbulence information has been presented in the form of phenomenologically derived turbulence models that relate Reynolds stress to suitable flow properties. Examples of models that have been used in the named modelling techniques are those proposed by Prandtl[24], van Driest[2] and Cebeci[19]. These models will be discussed more fully in chapter three.

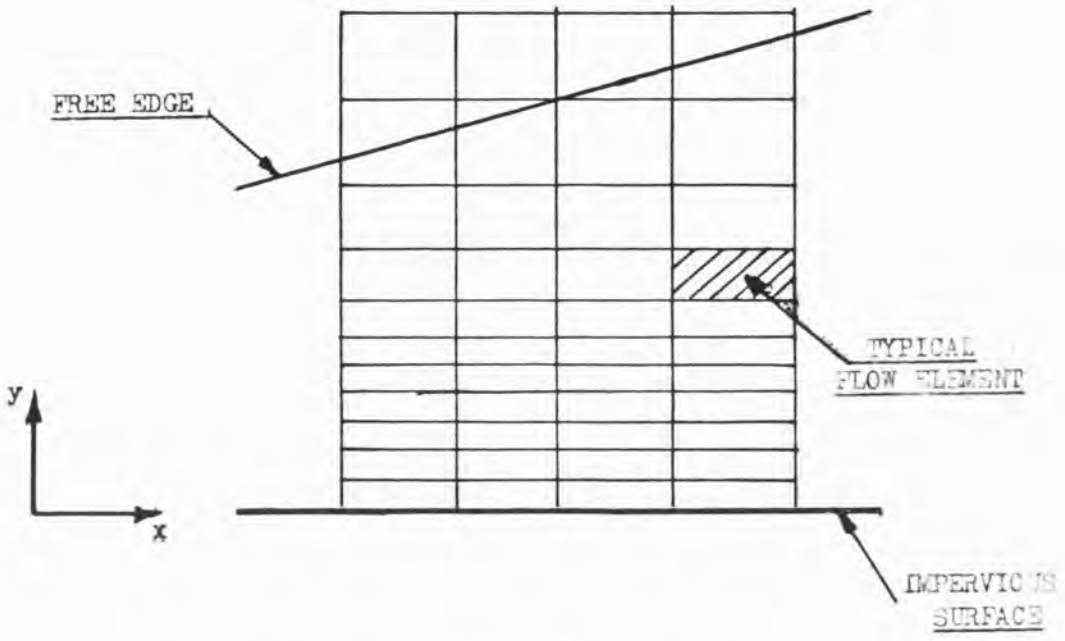

a. MESH NETWORK WITH CARTESIAN CO-ORDINATE SYSTEM

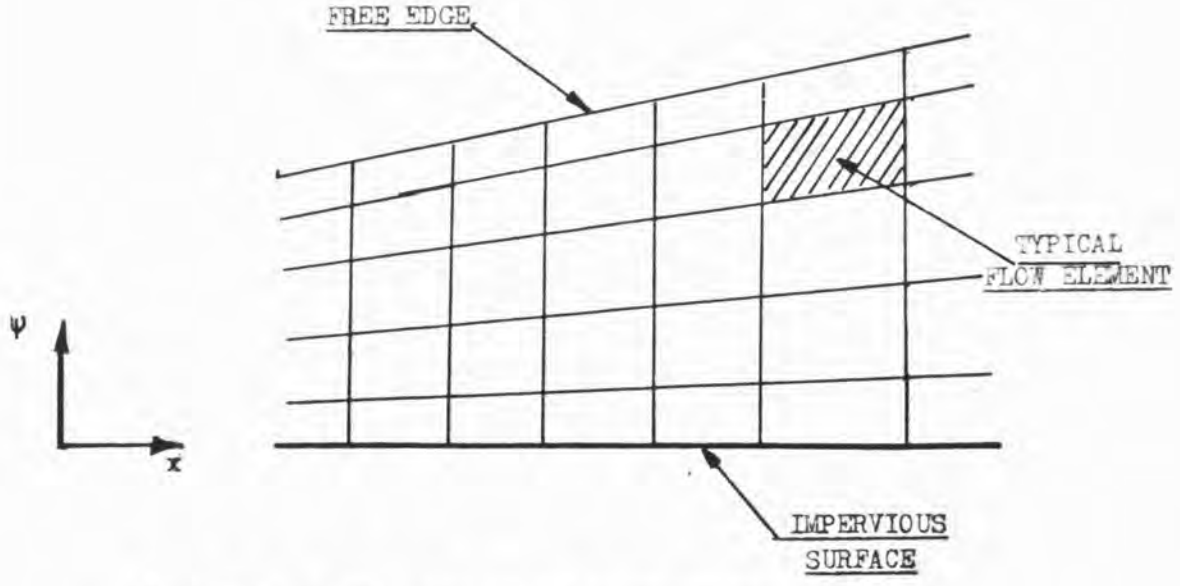

b. MESH NETWORK WITH CO-ORDINATE SYSTEM OF x AGAINST STREAMFUNCTION ψ.

FIGURE 2.3

Table 2.2

CO-ORDINATE SYSTEM & FINITE DIFFERENCE ASSUMPTIONS

Modelling Technique proposed by:	Co-ordinate systems	Velocity conditions around element	
		Streamwise direction	Cross-stream direction
Flugge-Lotz [22]	Cartesian as specified in figure 3.a	$U = a_1 y + b_1$ †	$U = a_3 x + b_3$ +
Spalding-Patankar and Denny-Landis [7] [8]	x against non-dimensional form of the stream function (see figure 3b)	$U = a_2 \Psi + b_2$ +	U = constant

+ The coefficients a_i b_i, i = 1.3 are constant over each element

2.5 Recommendations

The modelling techniques proposed by Spalding-Patankar and Denny-Landis have been selected as the most suitable with which to start this study. The selection process proceeds along the following lines. Firstly, the most suitable category of mathematical method with which to solve the equation of motion was chosen - this discussion is presented in sub-section a. Secondly, from those modelling techniques that use the selected mathematical method the most suitable techniques with which to start this study were chosen. This discussion is detailed in sub-section b.

2.5a Recommended Category

Modelling techniques making use of marching integration mathematical method were chosen as the most suitable with which to start this study. The reasons for this choice were as much to do with the unsuitability of the other mathematical methods, as with the advantages associated with the chosen one. In the discussion that follows, the reasons and causes for rejecting the parametric, explicit and cross-stream integral mathematical methods are explained; and then advantages of the chosen category expounded.

Both the parametric and explicit integral mathematical methods are unsuitable for the same two reasons. Firstly, the modelling techniques based upon these methods predict insufficient results to be of any serious use when examining flows involving momentum, mass and heat transfer. For example, when simulating momentum and heat transfer rates in boundary flows, only the momentum, energy and boundary thickness of the flow, and total skin friction, are

predicted. Secondly, in complex flows of the type described previously the turbulence information required is not readily available.

Modelling techniques making use of the cross-stream integration method have been used to simulate not only momentum, but also mass and heat transfer rates. The major problem associated with these techniques is that the numerical integration required for a solution becomes cumbersome and inefficient, because of the linking together of all the conservation equations through the physical properties of the flow — i.e the effective viscosity, Schmidt and Prandtl numbers.

Modelling techniques using the marching integration mathematical method avoid most of the problems encountered by other mathematical methods. These models can, and have, been used to predict velocity, temperature and species concentration fields within a boundary layer flow. And the turbulent information required can normally be derived from phenomenological theories, published and tested by other authors.

2.5b Chosen Technique

The modelling technique proposed by Spalding-Patankar and Denny-Landis were chosen as the most suitable with which to start this study for the following reasons. Firstly, the techniques have been widely used in industry to simulate turbulent momentum, and more recently mass and heat, transfer rates - and thus the work presented has some practical significance. Secondly, both techniques used efficient forms of mesh networks that grew with

the flow being simulated. Thirdly, and on a more practical level, the documentation concerning these techniques was well laid out, and this provided a good foundation for the presented work.

Chapter 3

Momentum Transfer Rates

The modelling techniques proposed by Spalding-Patankar [7] and Denny-Landis [8] are used to simulate momentum transfer rates in a two dimensional boundary layer and plane wall jet flow. Specimen results from these computational simulations are examined to determine the limitations of both modelling techniques.

Both techniques solve the equation of motion 3.1 by using the marching integration methematical method.

$$\frac{\partial U}{\partial x} = \frac{\partial}{\partial \psi}(\tilde{\tau}) - \frac{1}{\rho U}\frac{dp}{dx} \qquad (3.1$$

The Spalding-Patankar technique sub-divides the boundary layer into the wall, mainstream and free-edge regimes shown in figure 3.1, and solves different forms of the equation of motion in each regime. The co-ordinate system used consists of $\frac{\psi - \psi_1}{\psi_N - \psi_1}$ in the cross-stream, and x in the streamwise direction; with ψ representing the stream function, and the subscripts N and 1 designating the free-edge and surface respectively. (The derivation of the Spalding-Patankar technique is presented in appendix 1). The Denny-Landis technique solves the equation of motion over the complete boundary layer, and uses a mathematical method similar to that proposed by Spalding-Patankar. (The derivation of the Denny-Landis technique is detailed in appendix 2) The co-ordinate system used comprises $\sim = \frac{\psi - \psi_1}{\psi_N - \psi_1}^{\frac{1}{FN}}$ in the cross-stream, and x in the streamwise direction. FN is an integar which can have the values 1 or 2.

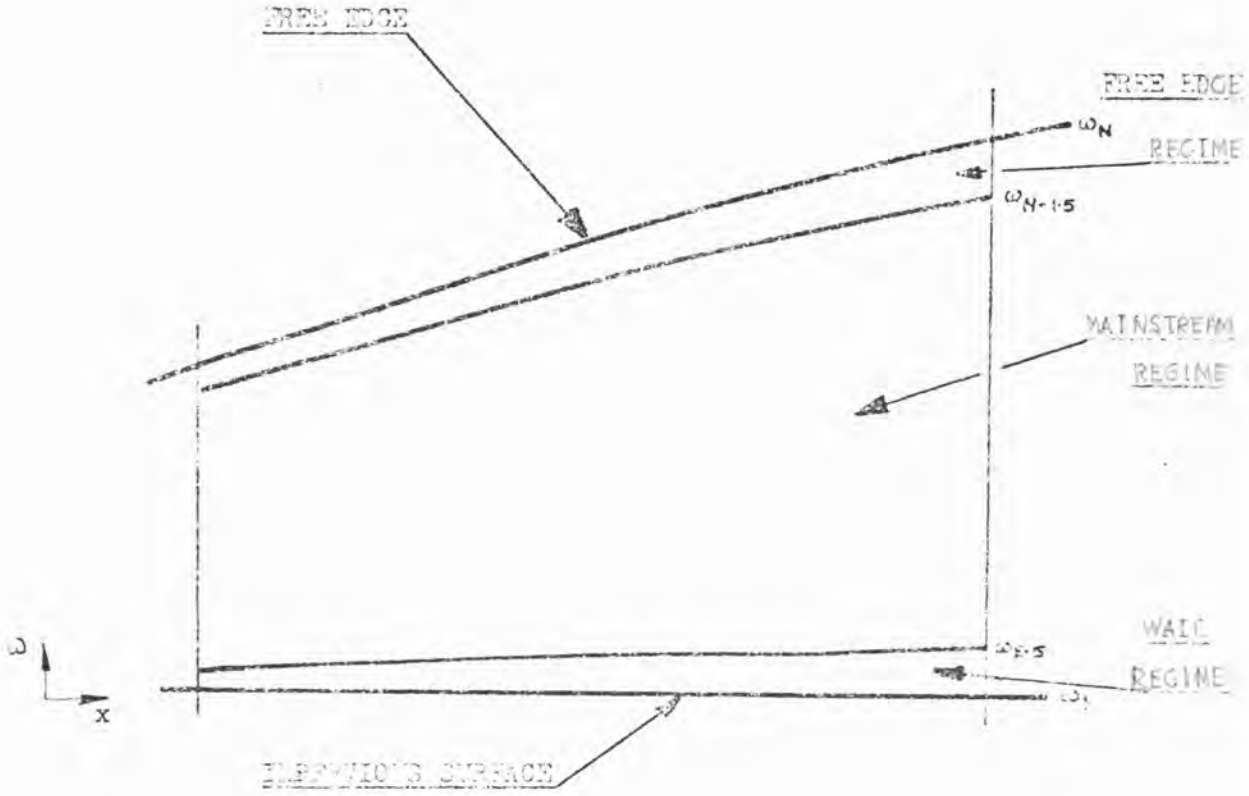

FLOW REGIMES

FIGURE 3.1

The methods used to define the physical properties required by both techniques, the density and effective viscosity, are derived from the works of other authors and are described in section 3.1. The errors generated in the computational simulations, represented by the discrepancies between the predicted velocity fields and experimental or theoretical results obtained elsewhere, are examined and discussed in section 3.2. In section 3.3 the limitations of both modelling techniques are assessed from the presented results. In section 3.4 the construction of a new type of technique recommended.

3.1. Physical Properties

To simulate momentum transfer rates with the specified modelling techniques information detailing the density and effective viscosity has to be supplied.

The density is determined from the equation for a perfect gas:

$$\rho = \frac{p}{\mathcal{R}T} \qquad (3.2$$

This equation accurately predicts the density of most common gases when they are not at high pressure (less than three atmospheres) and temperature (less than 2,000°K). If these conditions are not met the density can be calculated from semi-empirical relationships, as for example discussed by Hirshfelder, Curtis and Bird[23].

In this thesis the effective viscosity μ_{eff} has been used to represent both the molecular μ_l and turbulent (or eddy) μ_t viscosities by the communicative law:

$$\mu_{eff} = \mu_l + \mu_t$$

This nomenclature has been used, because it enables the specified modelling technique to deal with both laminar and turbulent flows.

The molecular viscosity of air has been given the value 1.84×10^{-5} kg/ms. Two categories of mathematical models of turbulence are compatible with the presented modelling techniques. In the first, the energy equation 3.3 is solved for the turbulent kinetic energy coefficient k; after assigning values to the constants C_D and σ_k, and prescribing the form taken by the length scale distribution. Turbulence models in this category have been developed by Prandtl[24], Kolmogroff[25], Glushko[26] and Nee - Kovasnay[27].

$$\frac{Dk}{Dt} = \frac{\partial}{\partial y}\left[\frac{\mu_t}{\sigma_k} \cdot \frac{\partial k}{\partial y}\right] + \mu_t\left[\frac{\partial U}{\partial y}\right]^2 - \frac{C_D \rho (k)^{\frac{3}{2}}}{l} \qquad (3.3$$

The turbulence models of the second category are based upon Prandtls mixing length hypothesis[1], represented by equation 3.4, but include suitable modifications to allow for the influence of the surface over which the flow is passing. (In equation 3.4 the mixing length l_m represents the cross-stream distance that must be covered by an agglomeration of fluid particles, before their momentum is changed by the new environmental conditions in which they find themselves.) Models of this sort have been developed by Van Driest[2], Cebeci[15] and Lauder-Spalding[28].

$$\mu_t = \rho l_m^2 \frac{\partial U}{\partial y} \qquad (3.4$$

In the present investigation, and for the reasons given below, the model by Lauder and Spalding is used. This employs Cebeci's model, represented by equations 3.5 and 6 to give a first estimate for the turbulent viscosity μ_t. In the presented equations, the constants k_m and A_+ are assigned the values 0.4 and 26.0 respectively, whilst the properties y_+ and p_+ are defined in the nomenclature.

$$\mu_t = (k_m y_+)^2 \left[1 - \exp\left[\frac{y_+}{A_1}\right]^2\right] \frac{dU}{dy} \qquad (3.5$$

$$A_1 = A_+ \left[\frac{p_+}{m_+}(1 - \exp(11.8m_+)) + \exp(11.8m_+)\right]^{-\frac{1}{2}} \qquad (3.6$$

Lauder and Spalding proposed that in the regions of the flow where Cebeci's model is unrealistic, that is where $\frac{dU}{dy}$ is approaching or equal to zero, a 'bridging technique' should be used to provide a second estimate for the turbulent viscosity. This bridging technique is most easily explained by referring it to a specific example, say a wall jet with a cross-stream velocity profile of the type shown in figure 3.2a. A schematic representation of the first estimate of the turbulent viscosity for the flow is detailed by the full line in figure 3.2b. Lauder and Spalding, note that this estimate for the turbulent viscosity is unrealistic in the region $y_A \leqslant y \leqslant y_C$. (The cross-stream ordinates y_A and y_C denote the values of y where $\frac{d\mu_t}{dy}$ is a maxima). They postulate that between the peaks at y_A and y_C the turbulent viscosity varies linearly with y

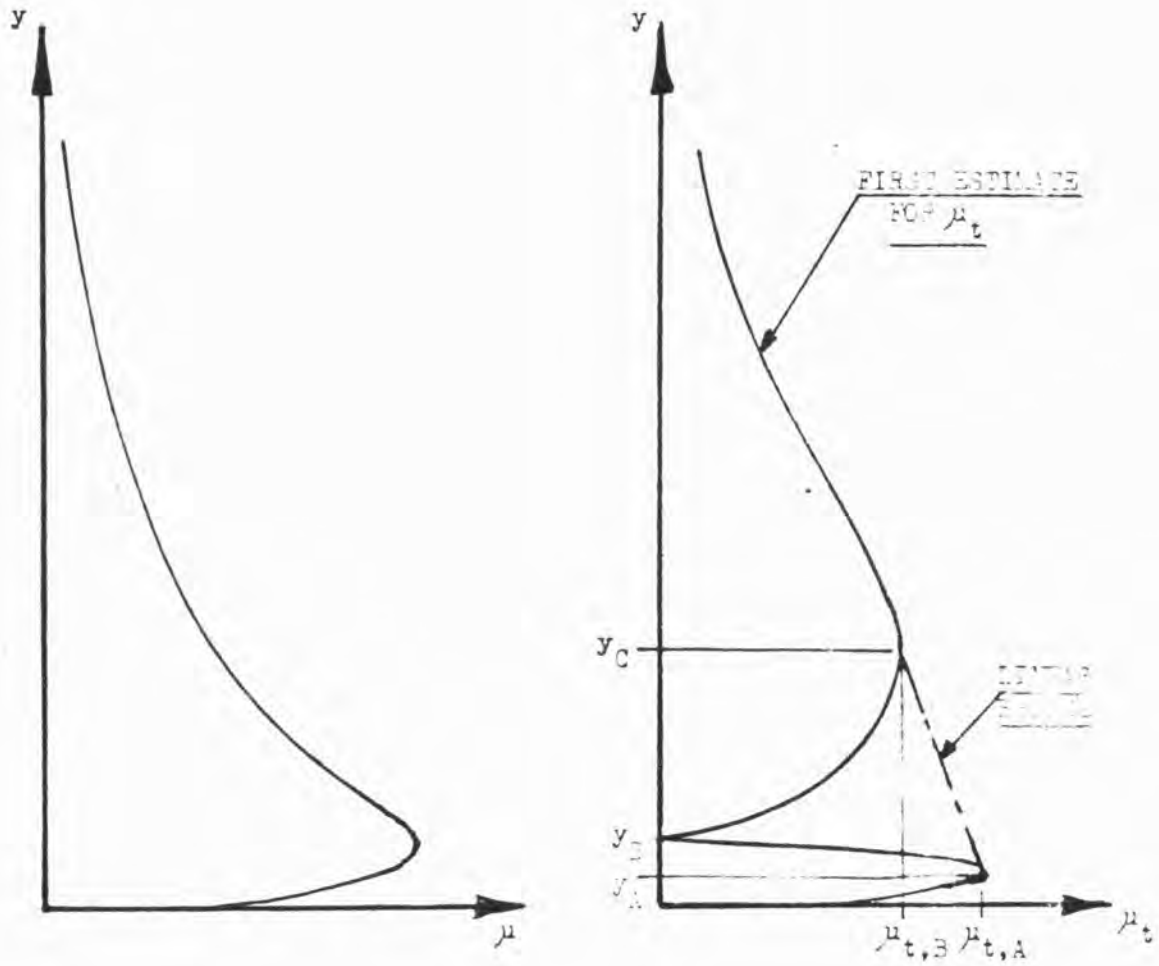

a. SPECIMEN VELOCITY PROFILE

b. ASSOCIATED TURBULENT VISCOSITY PROFILE

TURBULENCE MODEL

FIGURE 3.2

as shown by the dotted line in figure 3.2b - this relationship Lauder and Spalding call a 'linear bridge'. The mathematical representation of this model is:

$$\mu_t = y \left[\frac{\mu_{t,C} - \mu_{t,A}}{y_C - y_A} \right] + \frac{\mu_{t,C} - \mu_{t,A}}{y_C - y_A} \qquad (3.7$$

Mathematical models of turbulence based upon Prandtl's mixing length hypothesis are preferred to those derived from the turbulent energy equation, because they represent turbulence more simply and can consequently be easily and adequately adapted to simulate the more complex flows to be studied later. The model proposed by Lauder - Spalding has been selected, because it is the most advanced and general of those available.

3.2. Comparison of Results

The two situations chosen for simulation are:

a) a boundary layer,

and b) a plane wall jet;

both of which flow over flat impervious surfaces.

In these situations, and those to be described in chapters four to six, the grading of the mesh networks covering the flows are varied over a range of sizes typically employed in the modelling technique of other authors, so that comparison can be made. The two dimensional mesh networks used by both modelling techniques

are based upon co-ordinate system of the non-dimensional forms of the stream function ψ against distance along the impervious surface x. The mesh network have been defined by specifying streamwise lines along which the stream function is constant - these are henceforward called mesh stream lines - and cross-stream lines along which x is unchanged. The distance between consecutive mesh stream lines is dependent upon the cross-stream cartesian ordinate y and mainstream velocity U . These properties are related by the expression:

$$\partial\psi = \rho U \partial y.$$

The mesh spacing in the corss-stream direction has been defined by specifying the y grading and mainstream velocity profile along the starting cross-stream section of the simulation. The following relationship has been used to specify the intervals at which y is defined along the starting cross-stream section:

$$y_{1,j} = y_{1,j-1}(1 + Fr) \qquad (3.8$$

where $j = 3$, N and $y_{1,1}$, $y_{1,2}$ and Fr are prescribed constant. The distribution of the mainstream velocity along the starting cross-stream section is dependant upon the flow situation being simulated and is consequently described later. Along the impervious surface the mesh spacing $_{i-1}\Delta x_i$ is determined from:

$$_{i-1}\Delta x_i = 0.05\left[\frac{\psi_N - \psi_1}{\dot{m}''_{FE}}\right] \qquad (3.9$$

In this equation $\dot{m}''_{FE}$ represents entrainment rate at the free-edge of the cross-stream strip where $x_{i-1} \leq x \leq x_i$ shown in figure 3.3, and is determined from the expression:

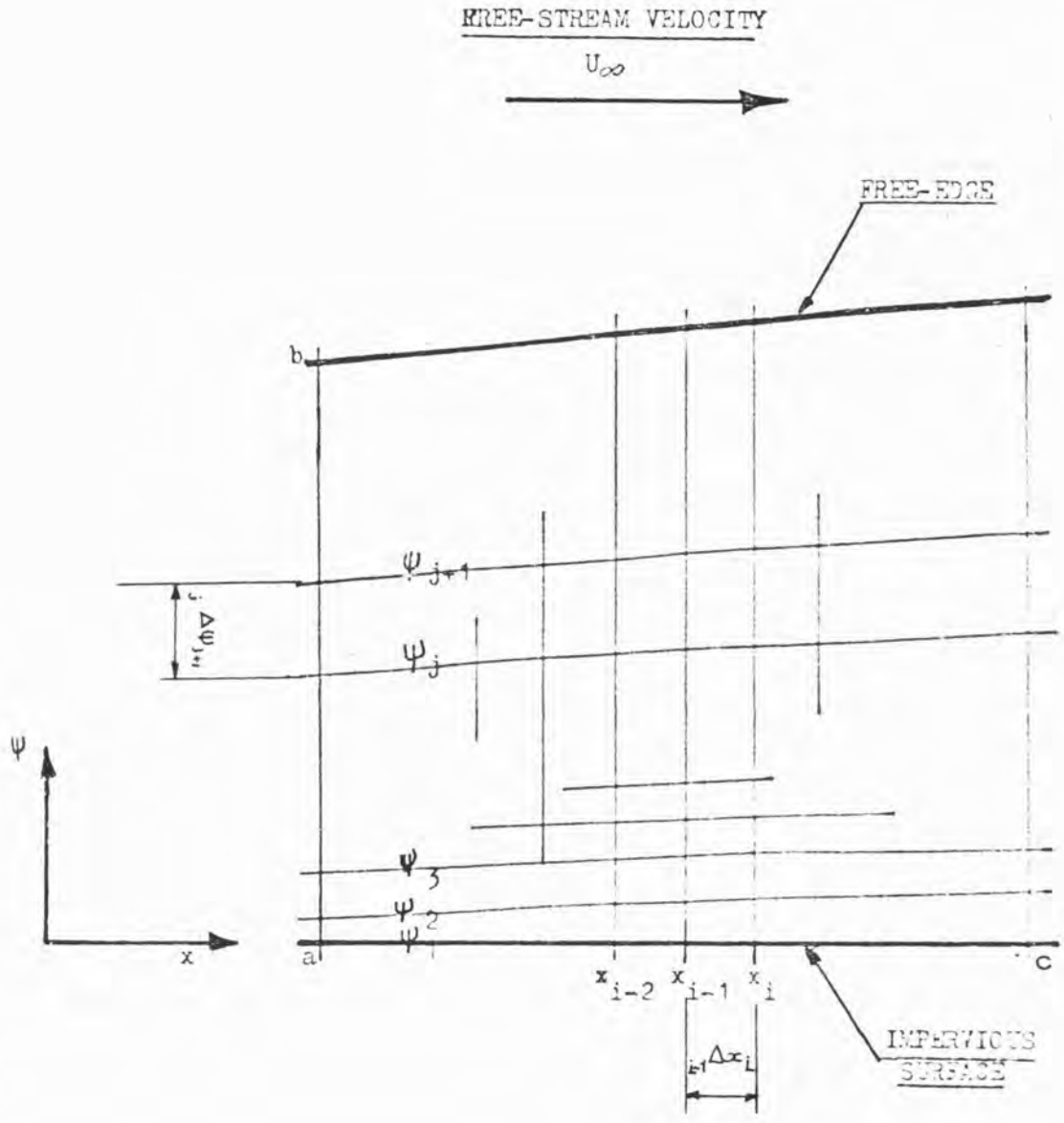

MESH GRADING

FIGURE 3.3

$$\dot{m}''_{FE} = \lim_{y \to \delta_1} \left[\frac{\frac{\partial}{\partial y}\left(\mu_{eff} \frac{\partial U}{\partial y}\right)}{\frac{\partial U}{\partial y}} \right] \qquad (3.10$$

3.2a. Boundary Layers

Formulae are used to describe the time averaged velocity field in a turbulent boundary layer adjacent to a flat impervious surface. They are used in preference to experimental results, because they have a similar order of accuracy and are more representative - being based upon the results of many experimental studies.

The chosen set of equations, which are valid over the required range of Reynolds numbers, are:

a) a non-dimensional cross-stream velocity profile relationship derived by Clauser[29]:

$$\frac{U - U_\infty}{U_\tau} = -2.44 \ln\left[\frac{y}{\delta_1}\right] + 2.5 \qquad (3.11$$

where U_τ is the skin friction velocity-which is equivalent to $\frac{2\tau_o}{\rho U_\infty^2}$

b) a wall resistance relationship by Schoenherr[30]:

$$C_f = \left(4.13 \ln (Re_x C_f)\right)^{-2} \qquad (3.12$$

where $Re_x = \frac{U_\infty x}{\nu}$

c) a growth rate relationship by Nikuradse[31]:

$$\delta_1 = 0.01738 \left[\frac{\nu}{U_\infty}(Re_x)^{0.861}\right] \qquad (3.13$$

Equations 3.12 and .13 are used to describe the velocity field within the outer region of the boundary layer, from van Driest[2] work this region occurs when $60\sqrt{\rho\nu^2/\tau_0} < y < \delta_1$. An indication of the flows behaviour close to the impervious surface has been supplied by the friction coefficient determined with equation 3.12.

The boundary layer chosen for the examination is one where the free-stream velocity U_∞ equals $30.5 ms^{-1}$ (or $100 ft\ s^{-1}$), and the kinematic viscosity ν is $1.6 \times 10^{-5} m^2 s^{-1}$. The flow has been simulated in the region $2.4 \leq x \leq 5.3m$ - as shown in figure 3.4. Plots of the cross-stream velocity profiles, from equation 3.11, at x = 2.5, 4.0 and 5.3m are shown by dotted lines in figures 3.5 to .7. The variation of the total skin friction (C_f) with Re_x, obtained from equation 3.12, is shown by the dotted line in figure 3.8. The thickness of the boundary layer is shown by the dotted line in figure 3.9, and is derived from equation 3.13.

The chosen boundary layer flow, has been simulated twice with the modelling techniques proposed by Spalding- Patankar, and four times with that by Denny-Landis. In each simulation the real mesh spacings along the starting cross-stream section and impervious surface, ab and ac respectively in figure 3.4, were derived from equations 3.8 and 3.9. The values prescribed to the constants $y_{1,2}$ and Fr in equation 3.8 are detailed in table 3.1. In the simulations with Denny-Landis's technique the power to which the non-dimensional mesh streamlines were raised FN was set at 2 and 1.

In each simulation the velocity profile at the starting cross-stream section was derived from equations 3.11 and .13; and the velocities at the free-edge and impervious surface set to U_∞ and zero respectively.

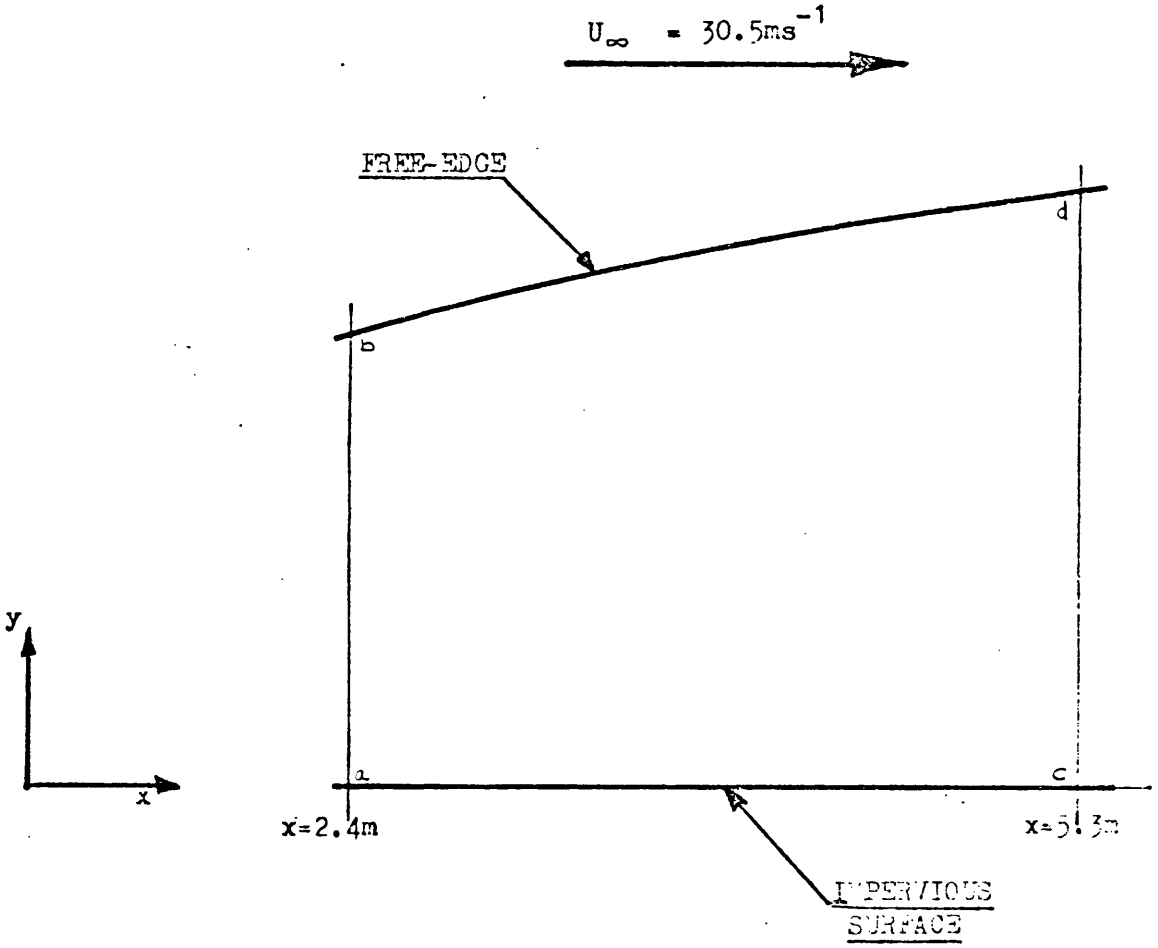

BOUNDARY LAYER FLOW

FIGURE 3.4

Table 3.1

Symbol	Modelling technique proposed by:	Dependent variables used in equation 3.8	
		$y_{1,2}$	Fr
□	Spalding - Patankar	$\delta_1/200$	1.10
◇	Spalding - Patankar	$\delta_1/50_3$	1.05
●	Denny-Landis with FN=2	$\delta_1/10^5$	1.12
▲	Denny-Landis with FN=2	$\delta_1/10_3$	1.19
○	Denny-Landis with FN=1	$\delta_1/10^5$	1.12
△	Denny-Landis with FN=1	$\delta_1/10^5$	1.19

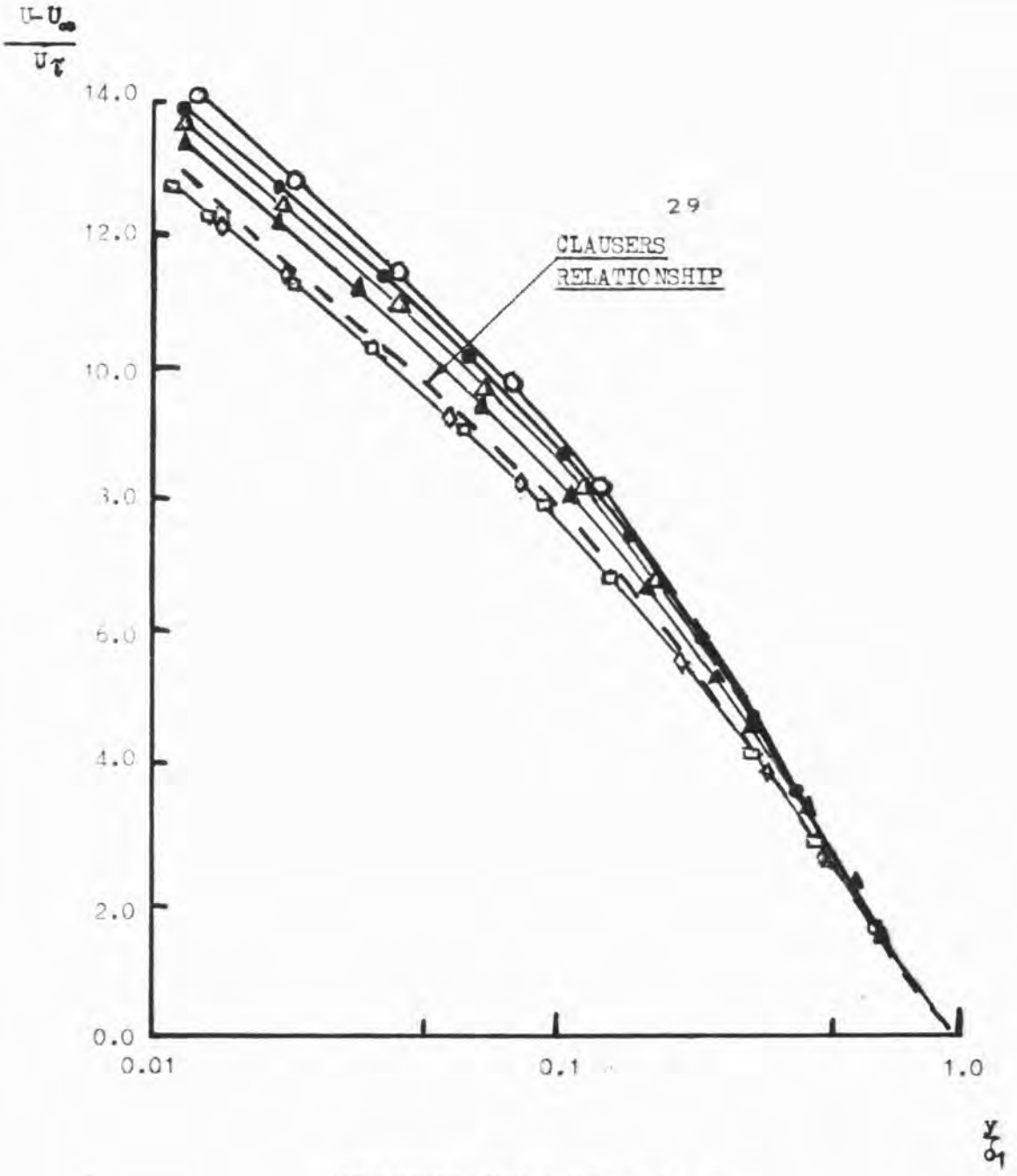

VELOCITY PROFILE AT x = 2.5m

FIGURE 3.5

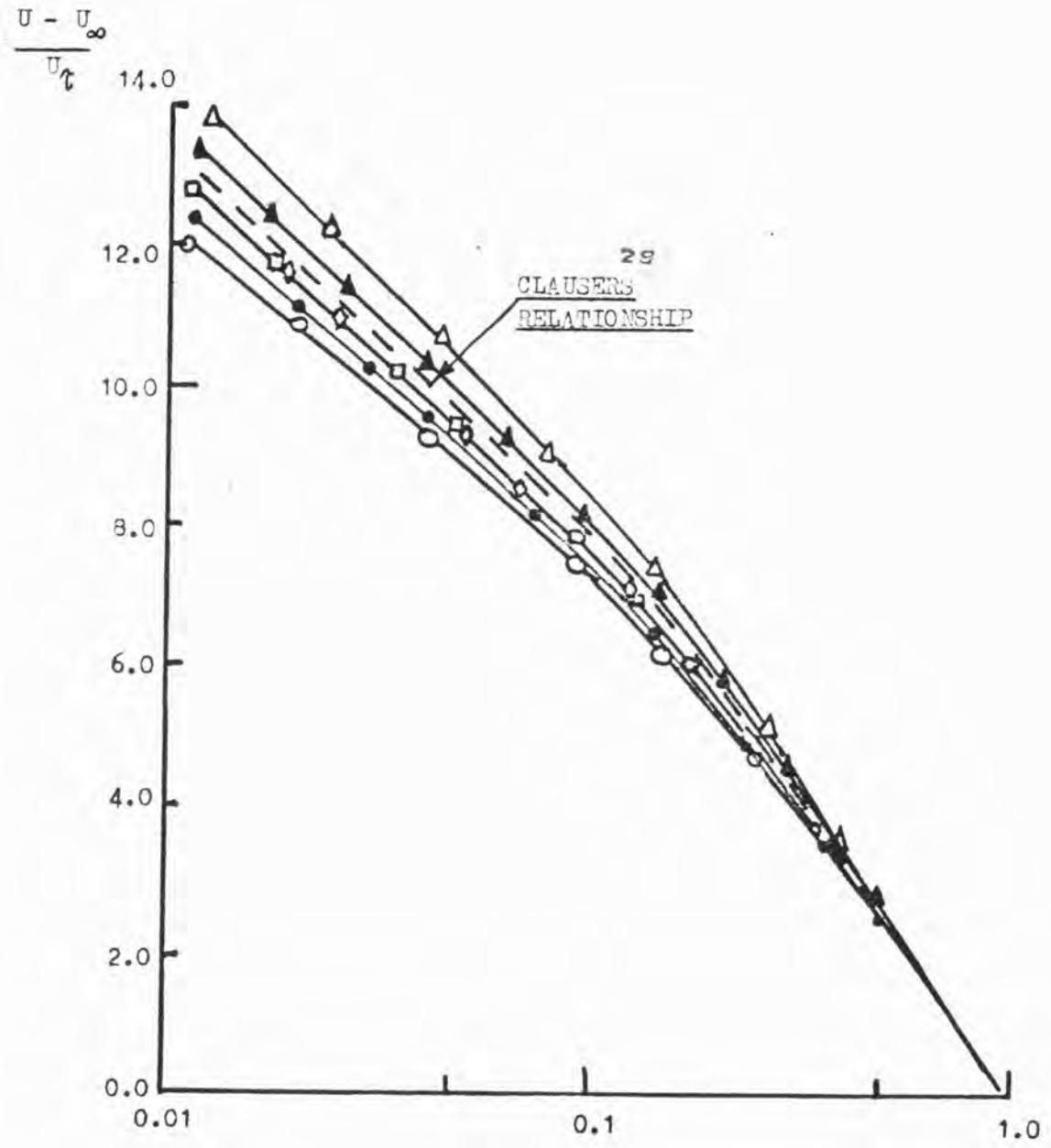

VELOCITY PROFILE AT x = 4.0m

FIGURE 3.6

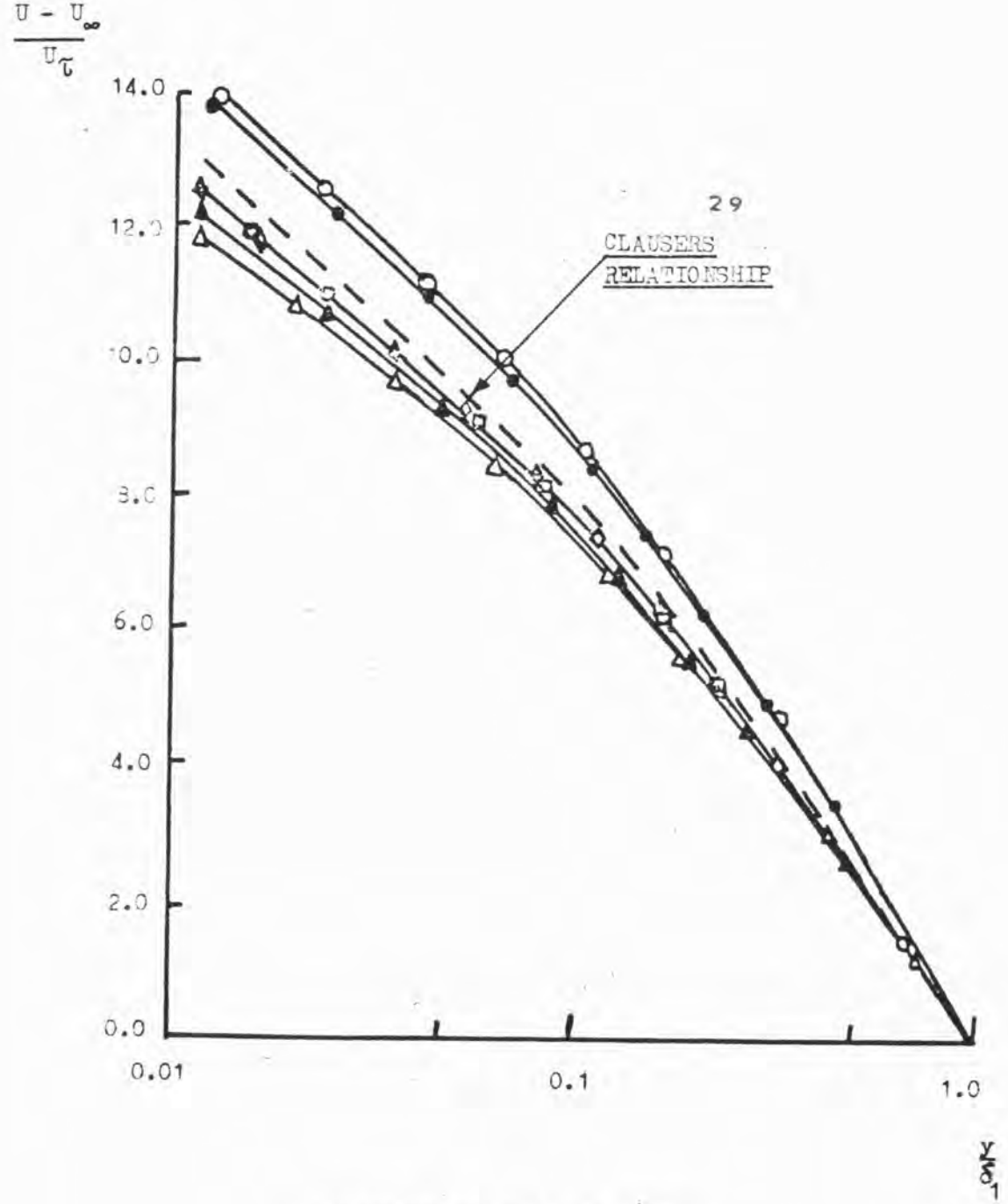

VELOCITY PROFILE AT x = 5.3m

FIGURE 3.7

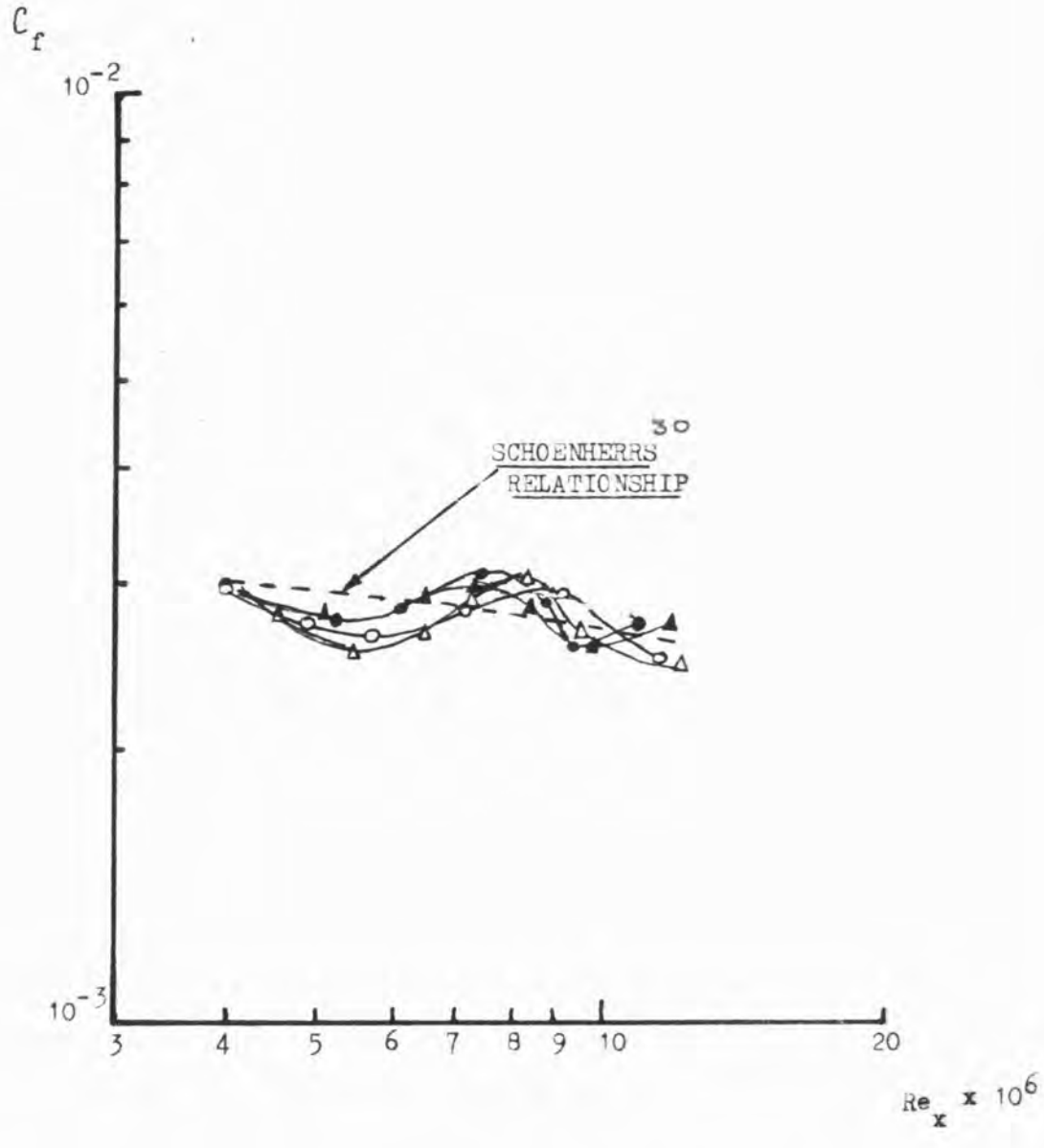

WALL RESISTANCE RELATIONSHIPS

FIGURE 3.8

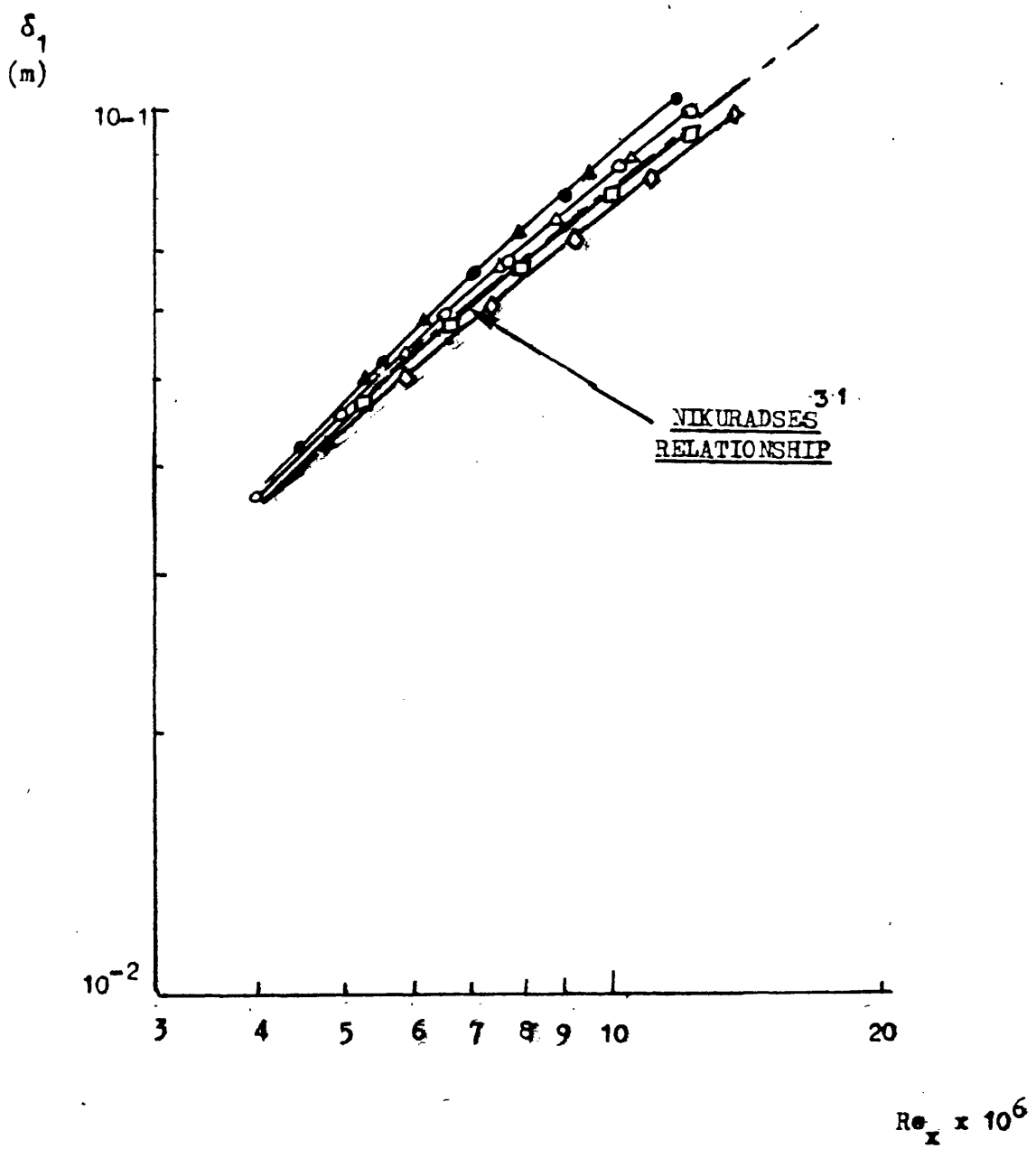

GROWTH RATE RELATIONSHIPS

FIGURE 3.9

Specimen results from the computational simulations are presented in figures 3.5 to 9, with table 3.1 detailing the symbols used. The maximum percentage differences between the specimen computational predictions and the results from equation 3.11 to 13 are detailed in tables 3.2 to 3.4 . In these tables, and those to be detailed in the remaining chapters, positive percentage differences are obtained when the computational predictions are greater than the experimental or accepted results.

The results from the modelling technique proposed by Spalding-Patankar are more accurate than those from Denny-Landis. As shown by the presented comparisons of results in figures 3.5 to .9 and more particularly the data in tables 3.2 to.4 detailing the percentage discrepancies in these results at the three specimen cross-stream sections.

The discrepancies in the predictions from the Spalding-Patankar technique are dependent upon the mesh gradings used. This dependency is particularly noticeable in the predictions of growth rate and total skin friction in figures 3.8 and .9. respectively - the percentage discrepancies of these results at three specimen sections are detailed in table 3.2.

The error in the results from the modelling technique of Denny-Landis are dependent upon both the spacing of the real ordinate y at the starting cross-stream section, and the value taken by FN - the power to which the non-dimensional streamlines are raised. For the same spacing of the real ordinate y, that is for the same values $y_{1,2}$ and Fr, the results are more accurate when FN = 2 than 1. As shown by the presented comparison of results in figures 3.5 to .9; and the percentage discrepancies at x = 2.6, 4.0 and 5.3m detailed in tables 3.2 to 4.

Table 3.2

Percentage Differences with the Modelling Technique Proposed by Spalding -Patankar

	Symbol	Maximum percentage differences between the results from the modelling technique and equations 3.11 to .13 for the properties:		
		$\frac{U - U_\infty}{\hat{U}}$	C_f	δ_1
(a) At x=2.5m				
	□	-2.0	6.3	6.7
	◇	-2.0	-3.3	3.6
(b) At x=4.0m				
	□	-4.8	5.3	3.2
	◇	-4.8	-3.5	4.5
(c) At x=5.3m				
	□	-5.4	4.9	8.9
	◇	-5.4	-3.1	4.1

Table 3.3

Percentage Differences from the Modelling Technique

Proposed by Denny-Landis with FN = 2

	Symbol	Maximum percentage differences between the results from the modelling technique and equations 3.11 to .13 for the properties:		
		$\frac{U - U_\infty}{U_\tau}$	C_f	δ_1
(a)At x=2.5m				
	●	9.6	-7.8	7.8
	▲	3.8	-5.1	
(b)At x=4.0m				
	●	-4.9	6.2	9.5
	▲	4.8	3.6	
(c)At x=5.3m				
	●	6.9	4.2	6.5
	▲	-5.8	3.8	

Table 3.4

Percentage Differences from the modelling technique

Proposed by Denny-Landis with FN = 1

	Symbol	Maximum percentage differences between the results from the modelling techniques and equation 3.11 to .13 for the properties:		
		$\frac{U - U_\infty}{U_\tau}$	C_f	δ_1
(a)At x=2.5m				
	o	9.8	-10.2	7.9
	Δ	5.3	-7.6	
(b)At x=4.0m				
	o	-7.6	7.3	11.1
	Δ	6.8	5.5	
(c)At x=5.3m				
	o	10.3	-5.9	7.5
	Δ	-8.4	-5.1	

3.2b Plane Wall Jet

Schwarz and Cosart [32] have experimentally studied the rate of change of momentum transfer in a series of plane wall jets, for various nozzle depths d_N and volumetric flowrates through the nozzle $\dot{V}_N$. The layout used is detailed schematically in figure 3.10a, and in figure 3.10b a typical velocity profile from the developed wall jet is detailed. The experimental results have been presented in the form of relationships that detail:

a) the variation of maximum velocity U_{max} over the wall jet,

b) the growth of the wall jet

and c) the non-dimensional velocity profiles, $\frac{U}{U_{max}}$ against the cross-stream height $\frac{y}{\delta_5}$, at x = 0.46, 1.0 and 1.83m.

In part c, δ_5 represents the height y at which the mainstream velocity equals $\frac{U_{max}}{2}$ – as shown in figure 3.10b.

The plane wall jet simulated has been selected from Schwarz and Cosart experimental study; and had a nozzle 0.025m wide through which air passed at a volumetric flowrate of 0.63 $m^2\ s^{-1}$ for every metre width of nozzle. Schwarz and Cosarts results for this wall jet - namely the maximum velocity and growth rate relationships, and the non-dimensional cross-stream velocity profiles at x = 0.46, 1.0 and 1.83m - are shown by the dotted lines in figures 3.11 to 3.15.

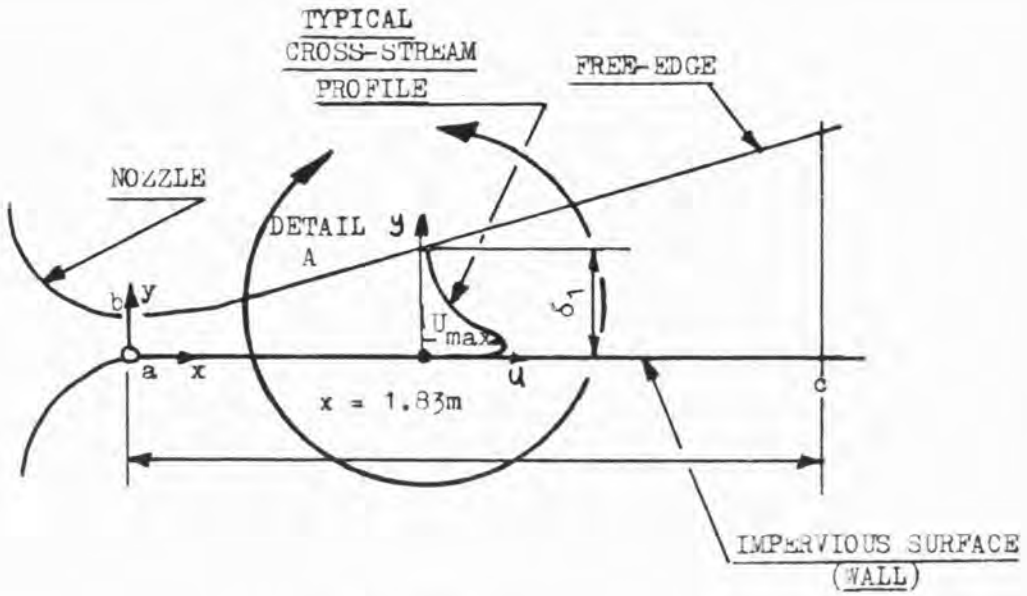

a. PLANE WALL JET

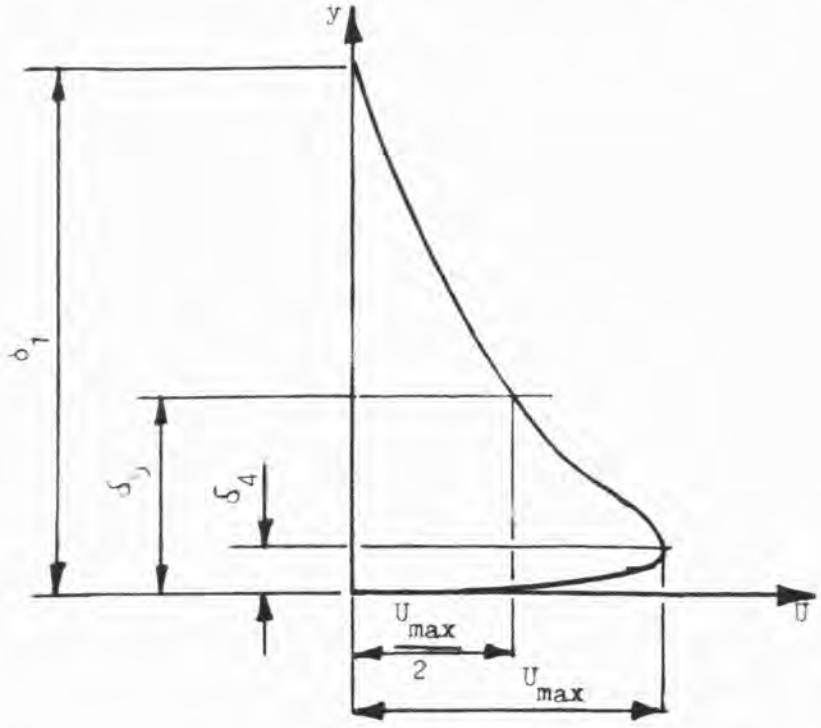

b. CROSS-STREAM VELOCITY PROFILE AT DETAIL A

FIGURE 3.10

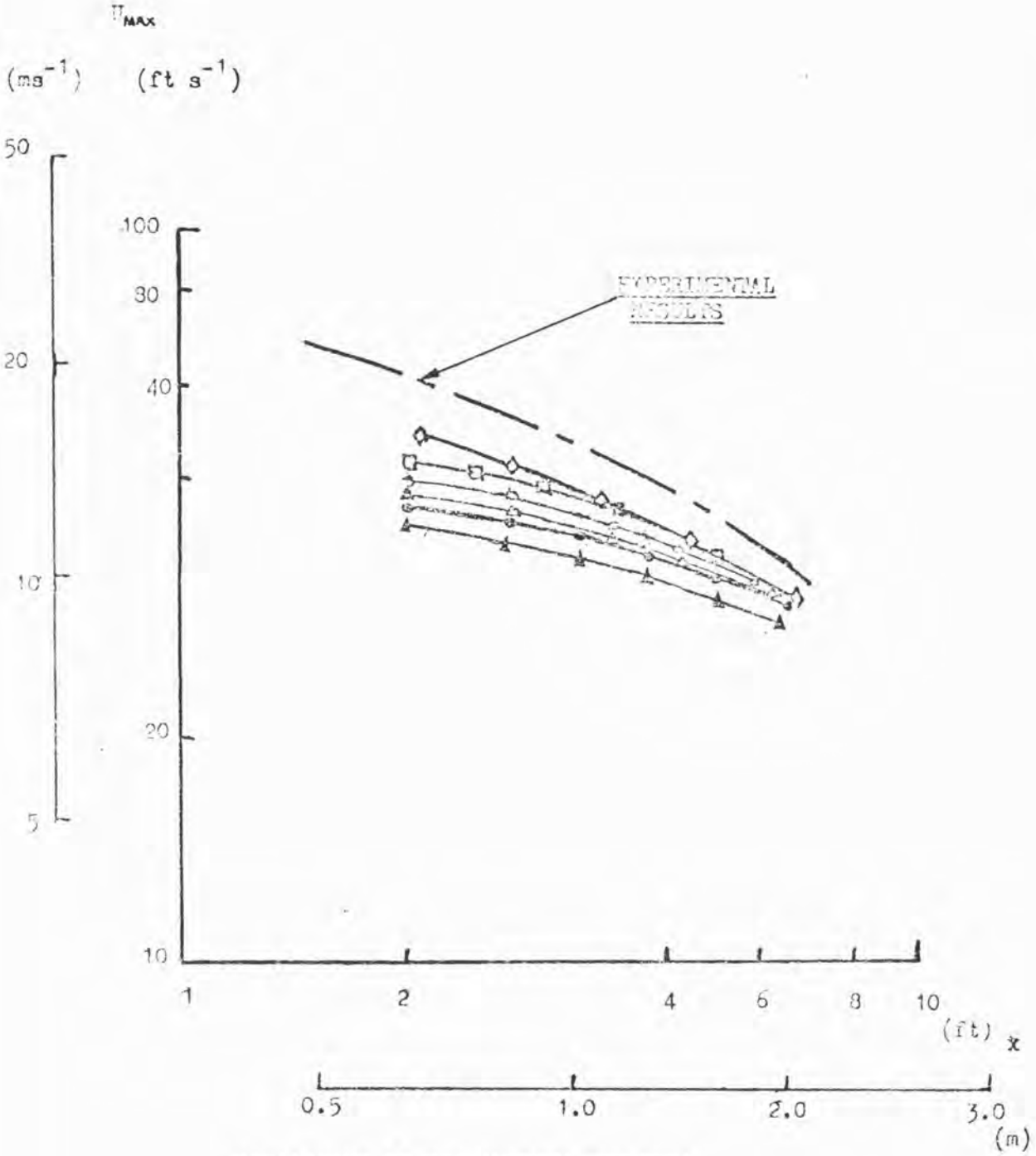

VARIATIONS IN THE MAXIMUM VELOCITY

FIGURE 3.11

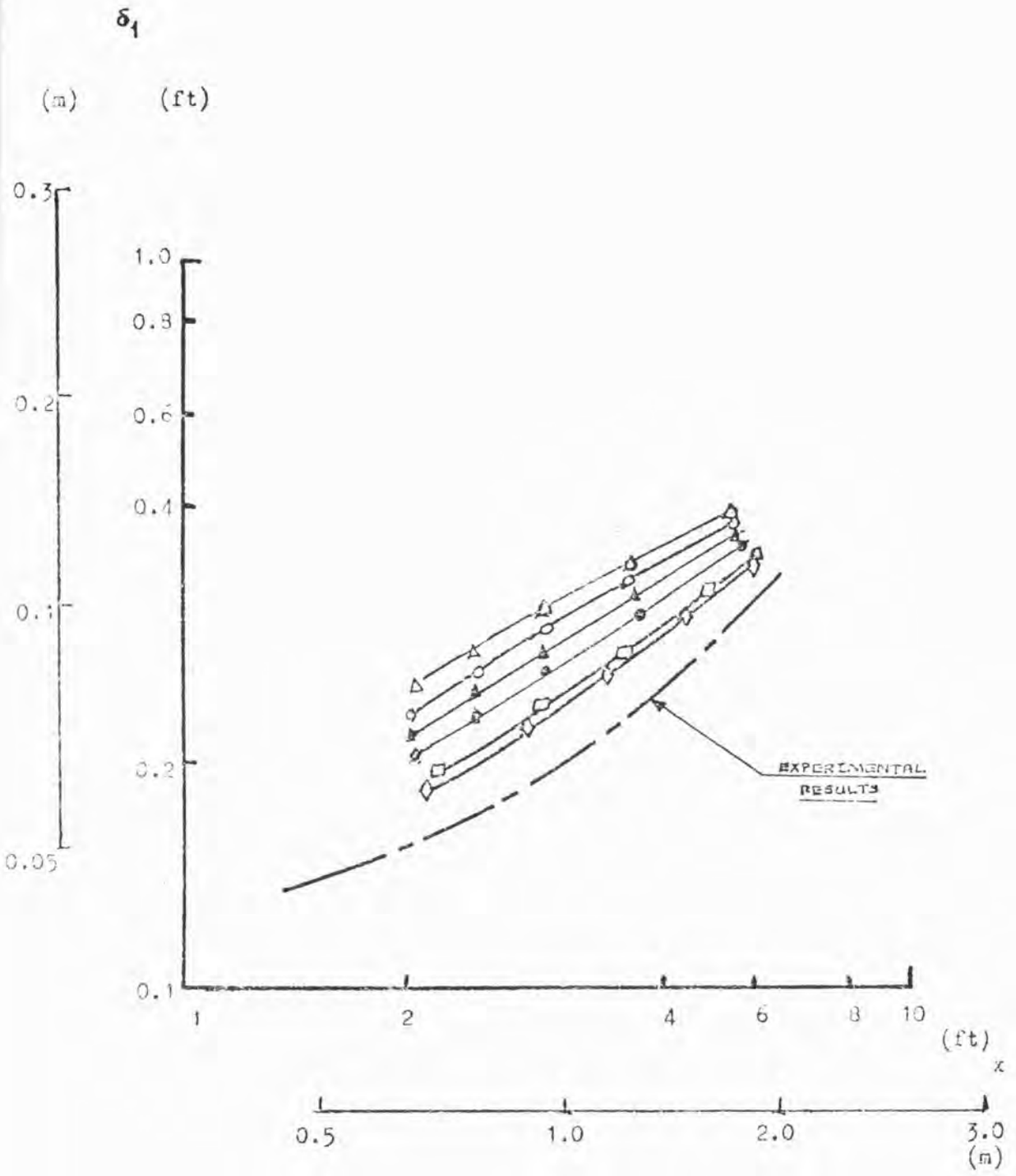

VARIATIONS IN THE GROWTH RATES

FIGURE 3.12

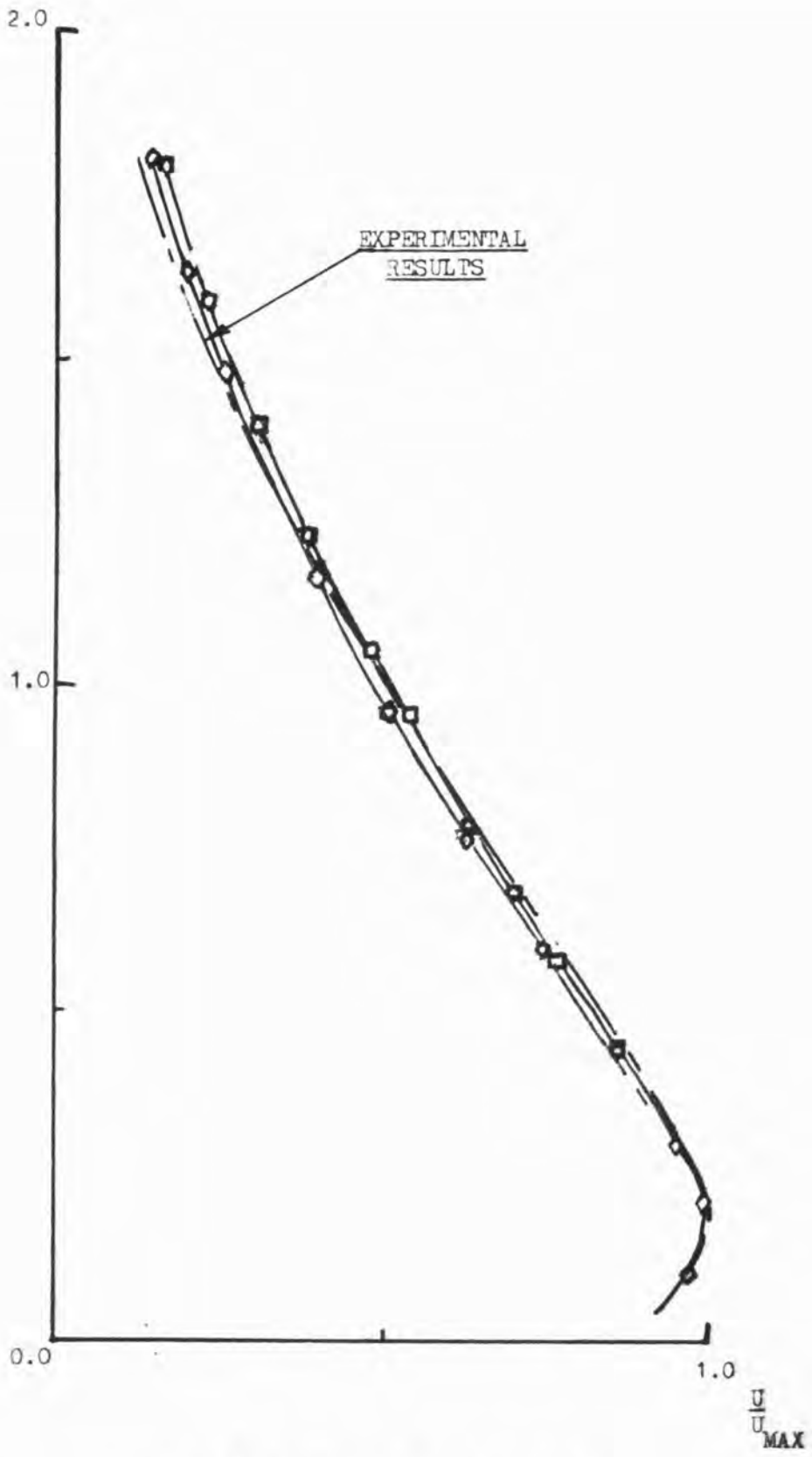

VELOCITY PROFILES AT x = 0.46m

FIGURE 3.13

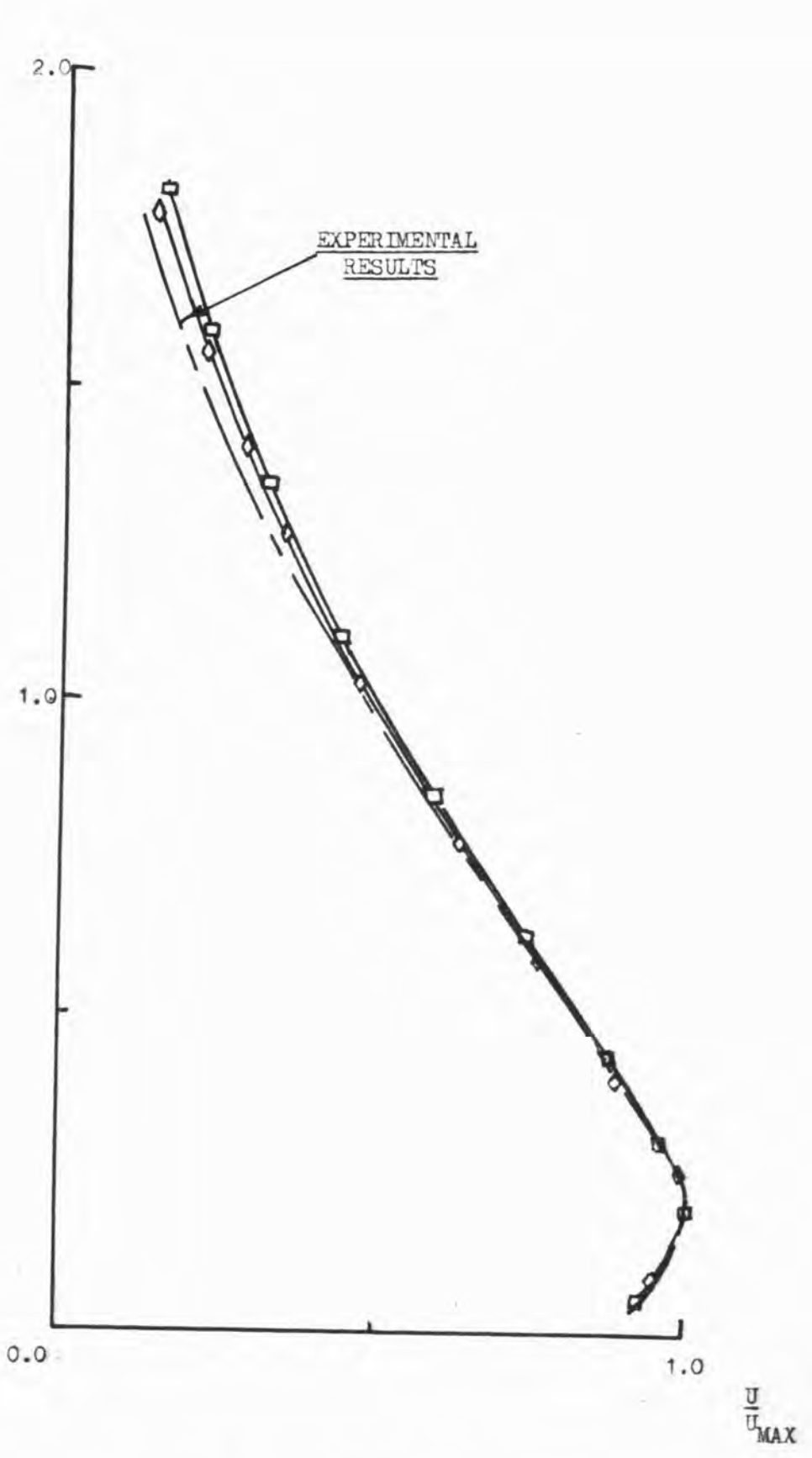

VELOCITY PROFILES AT x = 1.0m

FIGURE 3.14

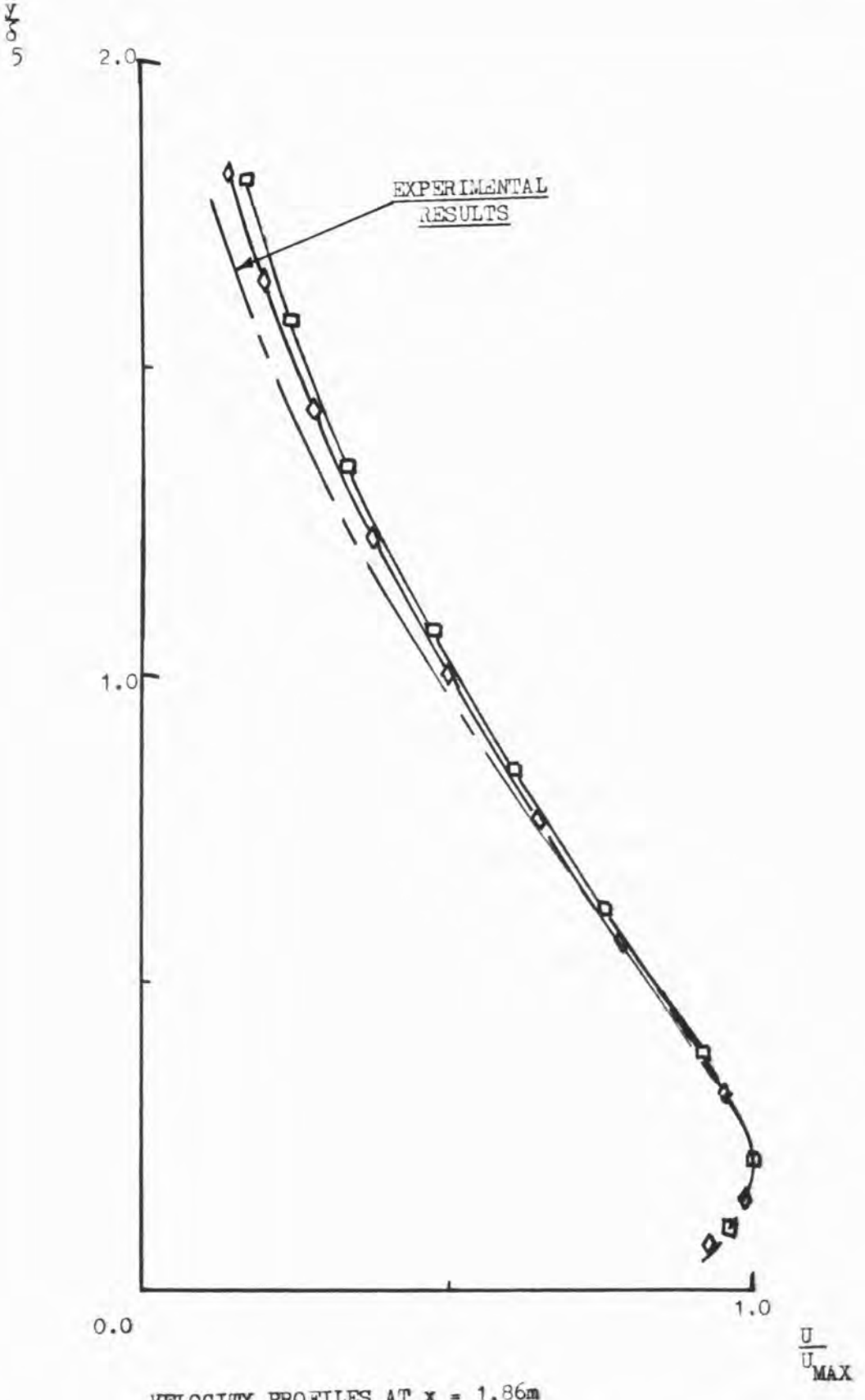

VELOCITY PROFILES AT x = 1.86m

FIGURE 3.15

The chosen wall jet has been simulated with the presented modelling techniques, for $0.0 \leq x \leq 1.83$m. In these simulations the real mesh spacings along the starting cross-stream section and impervious surface, ab and ac respectively in figure 3.10a, were derived from equations 3.8 and 9. The values taken by the constants $y_{1,2}$ and Fr of equation 3.8 being detailed in table 3.1. In each simulation the following boundary conditions were used:

a) along the impervious surface and free-edge the mainstream velocity was set at zero and $0.05 \times U_{max}$ respectively,

and b) At the starting cross stream section the velocity profile was assumed constant and equal to the average velocity.

The maximum velocity and growth rate relationships predicted by the modelling techniques are compared with Schwarz and Cosarts results in figures 3.11 and .12 respectively - the symbols used are detailed in table 3.1. The percentage discrepancies between the presented predicted and experimental results are detailed in tables 3.5 to 7.

The results from the Denny-Landis modelling technique, with FN set to 2 and 1, show extremely poor correspondence with the experimental data. As shown by the specimen comparisons of the maximum velocity and growth rate in figures 3.11 and 12 respectively. More concisely-the percentage variations in these properties at the three specimen sections are given in tables 3.5 and 6; and show discrepancies of the order twenty percent. In fact the presented correspondence between the predicted and experimental data is so poor that no further consideration is given to the results from this technique.

Table 3.5

Percentage Differences with the Modelling Technique of Denny-Landis with FN=2

	Symbols	Percentage differences between the predicted and experimental properties:	
		U_{Max}	δ_1
(a) At x=0.46m			
	●	23.1	32.1
	▲	26.3	33.7
(b) At x=1.0m			
	●	24.6	39.1
	▲	27.2	41.6
(c) At x=1.83m			
	●	14.8	32.0
	▲	15.1	32.1

Table 3.6

Percentage Differences with the Modelling Techniques of Denny-Landis with FN=1

	Symbols	Percentage differences between the predicted and experimental properties:	
		U_{Max}	δ_1
(a)At x=0.46m			
	o	19.1	19.3
	Δ	22.4	22.1
(b)At x=1.0m			
	o	20.9	35.1
	Δ	23.1	36.3
(c)At x=1.86m			
	o	12.1	25.2
	Δ	14.3	26.4

Table 3.7

Percentage Differences with the

Spalding-Patankar Modelling Technique

	Symbols	Percentage differences between the predicted and experimental properties:	
		U_{max}	δ_1
(a)At x=0.46m			
	□	7.2	9.0
	◇	9.0	5.4
(b)At x=1.0m			
	□	5.2	9.5
	◇	8.9	9.8
(c)At x=1.83m			
	□	9.3	8.7
	◇		8.2

Table 3.8

Percentage Differences with the Modelling Technique Proposed by Spalding-Patankar

	Symbol	Percentage differences between the predicted and experimented values of $\frac{U}{U_{max}}$ for:		
		$\frac{y}{\delta_5}$ = 0.5	1.0	1.5
(a)At x=0.4cm				
	□	-1.5	-0.7	6.3
	◇	-4.71	-7.7	10.1
(b)At x=1.0m				
	□	0.5	2.1	9.3
	◇	1.1	4.3	9.7
(c)At x=1.36m				
	□	-0.1	4.2	7.8
	◇	-1.8	7.3	13.1

The results from the Spalding - Patankar modelling technique show far better agreement with the experimental data. As shown by the presented comparisons of the maximum velocity and growth rate in figures 3.11 and .12 respectively. Table 3.7 gives precise measurements of the discrepancies in these results.

Predictions of the cross-stream velocity profiles at x = 0.46, 1.0 and 1.86m are detailed in figures 3.13, .14 and .15 respectively - the symbols used are defined in table 3.1. The percentage discrepancies between the predicted and experimental results in these figures for $\frac{y}{\delta_5}$ = 0.5, 1.0 and 1.5, are given in table 3.8. The maximum errors in these results are acceptable, being of the order of ten percent and their magnitude is dependent upon the mesh grading used in the simulations - as shown by the comparisons figures 3.13 - .15 and table 3.8.

3.3 Discussion

The modelling technique proposed by Spalding - Patankar has been widely used in industry to simulate momentum transfer rates in a variety of boundary flows. In the presented simulations of a boundary layer and plane wall jet, the discrepancies between the predicted and experimental results were of the same order of magnitude as those obtained by other users.

These discrepancies predominately originate from two sources. The first source of error is from the finite difference representations of the partial differentials. The second source is from the estimates for the physical and turbulence properties.

The finite difference approximations used in the modelling technique proposed by Spalding - Patankar are defined in appendix

one. In boundary flows passing over flat surfaces, with no external pressure gradients, the cross-stream mainstream velocity gradients are far greater than those in the streamwise direction. Consequently in our discussion of the finite difference approximations streamwise effects will be neglected. The finite difference estimates of the partial differential in the cross-stream direction approximate to:

$$\left(\frac{\partial U}{\partial \omega}\right)_i = \left[\frac{U_{i+1}-U_{i-1}}{\Delta\omega}\right] - \left[U''' \frac{\Delta\omega^2}{6} + H.O.T_1\right]_i$$

and

$$\frac{\partial}{\partial \omega}\left(\frac{\partial U}{\partial \omega}\right) = \left(\frac{1}{\Delta\omega}\right)\left[\left(\frac{U_{i+1}-U_i}{\Delta\omega}\right) - \left(\frac{U_i-U_{i-1}}{\Delta\omega}\right)\right] - \left[U''' \frac{\Delta\omega^2}{12} + H.O.T_2\right]_i$$

These representations have been derived from an analysis of Taylors series. H.O.T stands for the higher order terms of the Taylor series which are not precisely detailed in the above representations. The magnitude of the error in the finite difference representations are of the order $\Delta\omega^2$. These errors are solely dependent upon the spacing between sequential mesh streamlines, $\Delta\omega_i$, and this must, in part, account for the noted correlation between the discrepancy in the predictions from the modelling technique and the type of mesh grading used in the simulation. It is interesting to note that both Spalding-Patankar[46], and later Nash[164], have produced predictions that show this correlation.

Considering the discrepancies in the modelling technique caused by errors in the values assigned to the turbulent and physical properties. The turbulent properties contributed most towards the discrepancy, because these have the greatest error. Launder and Spalding[28], among many others, mention this point in their book

on turbulence models. The turbulent viscosity, the only turbulent property used in the presented simulations, was calculated with a model proposed by Cebeci[49]. The uncertainty in the predicted viscosity was of the order of five percent. The values given to the physical properties, the density and kinematic viscosity, were read from the thermodynamics data published by Rogers and Mayhew[45] - they have a probable error of the order of one percent.

The Denny Landis technique has not been widely used for predicting turbulent flows. Consequently the results obtained contain far more original information than those previously discussed Two sets of simulations have been presented with this modelling technique . In the first set, the cross-stream co-ordinates of the mesh networks were set to $\left[\frac{\psi - \psi_1}{\psi_N - \psi_1}\right]$; and in the second $\left[\frac{\psi - \psi_1}{\psi_N - \psi_1}\right]^{\frac{1}{FN}}$, with FN equal to 2. (Throughout this section the different cross-stream co-ordinate used will be designated by the value taken by FN = 1 or 2). In the boundary layer simulations the discrepancies in the predictions were smaller with FN = 2 than =1 . However, in the plane wall jet simulations the reverse was the case. Verification of these findings are provided by the specimen percentage discrepancies of important flow parameters, from both the above flow situations, re-presented in table 3.9. These results are extracted from those presented in table 3.2. to .8 for FN equal to two and one. (The same boundary conditions were used in simulations of each flow situation).

able 3.9

Comparisons

	FN	Predictions with Denny-Landis technique		
(i) Boundary layer		Maximum percentage differences between the results from the modelling technique and equations 3.11 to .13 for the properties		
		$\frac{U - U_\infty}{U_\tau}$	c_f	δ_1
(a) at x = 2.5m				
	2	8.6	-7.8	7.8
	1	9.8	-10.2	7.9
(b) at x = 4.0m				
	2	-4.9	6.2	9.5
	1	-7.6	7.3	11.1
(c) at x = 5.3m				
	2	6.9	4.2	6.5
	1	10.3	-5.9	7.5
(ii) Wall jet		Percentage differences between the predicted and experimental properties		
		U_{max}	δ_1	
(a) x = 0.46				
	2	23.1	32.1	
	1	19.1	22.1	
(b) x = 1.0m				
	2	24.6	39.1	
	1	20.9	35.1	
(c) x = 1.83m				
	2	14.8	32.0	
	1	12.1	25.2	

The same techniques were used for simulating the turbulent and physical properties in the presented simulations, and therefore it is assumed that errors in these properties do not cause the above mentioned correlation between accuracy and flow situation. To understand the reason for this correlation it is necessary to understand the effect of setting FN equal to two and one upon the mesh network in each flow situation.

Considering the boundary layer flow situation, the real cross-stream velocity profile typically has the form:

$$U \propto y^{\beta} \tag{3.14}$$

or when $$\omega = \left[\frac{\psi - \psi_1}{\psi_N - \psi_1}\right]^{\frac{1}{FN}} \tag{3.15}$$

$$U \propto \omega^{\left[\frac{\beta}{FN(1+\beta)}\right]} \tag{3.16}$$

Differentiating this new velocity profile gives:

$$\frac{dU}{d\omega} = C\left[\frac{\beta}{FN(1+\beta)}\right] \omega^{\left[\frac{\beta}{FN(1+\beta)} - 1\right]} \tag{3.17}$$

where C is a constant. A schematic illustration of the variation of $\frac{dU}{d\omega}$ with ω, when $\beta \simeq \frac{1}{7}$ and FN = 2 and 1, is presented in figure 3.15. This plot shows that the effect of setting FN to 2 instead of 1 is to reduce the rate of change of velocity $\frac{dU}{d\omega}$. This in turn means that the difference between the real, $U \sim y^{\frac{1}{7}}$, and assumed linear variation of velocity over each flows element is smaller when FN = 2 than 1. Which, since the error in the predictions is in part proportional to this difference in velocity, leads to the conclusion that the overall discrepancies in the predictions should be smaller for FN = 2 than 1.

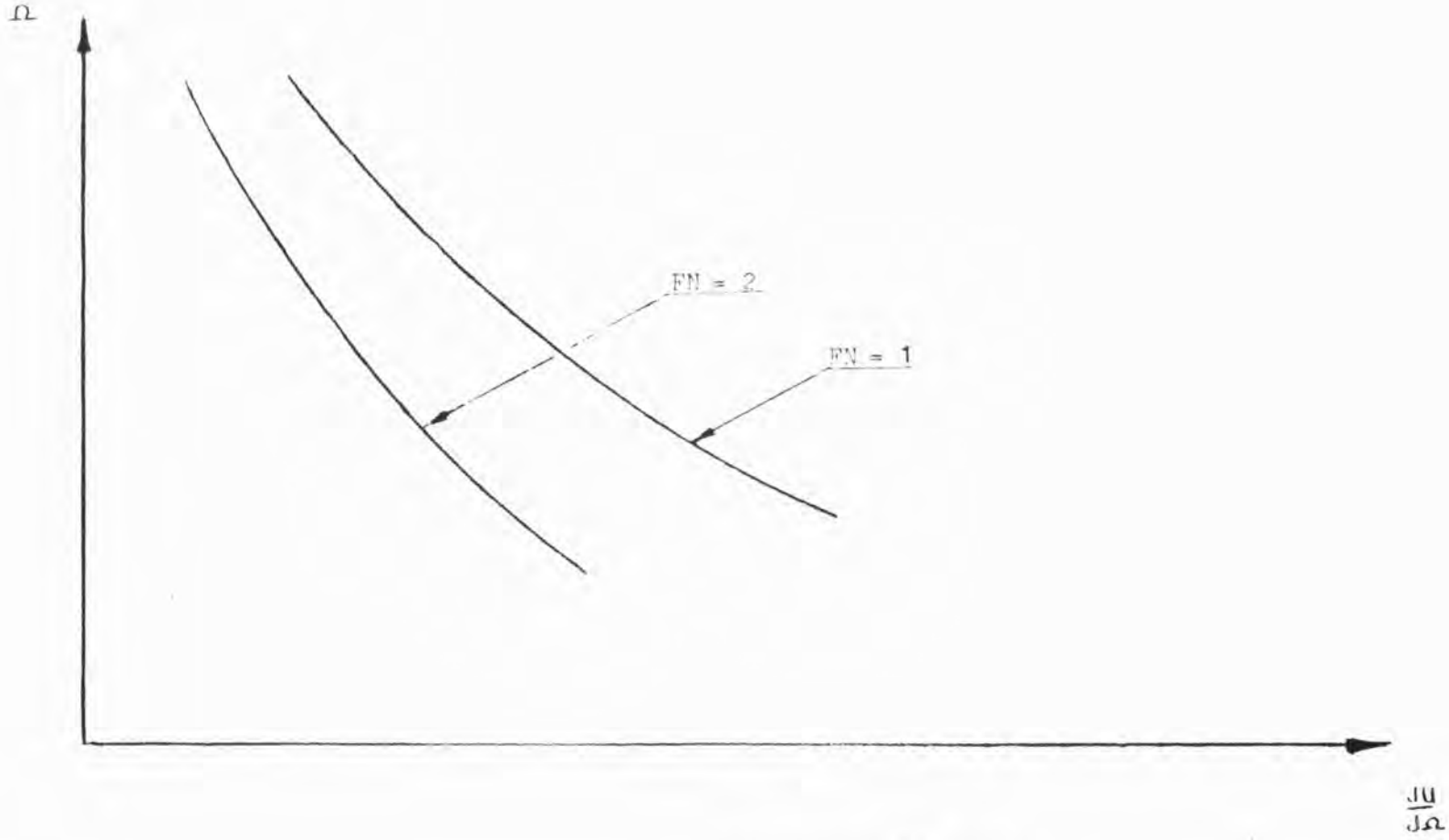

VARIATION OF $\frac{dU}{d\Omega}$ with Ω

FIGURE 3.1

In the plane wall jet situation the Denny-Landis technique with FN=1, gave more accurate predictions than the same technique with FN=2. In the remainder of this paragraph we shall consider why this result has occurred. The cross-stream velocity profile in a wall jet typically has the form specified in figure 5.16. This velocity profile has been divided into three regions-designated A to C. Region A, which is adjacent to the surface over which the flow is passing, contains that portion of the velocity profile that is similar to that obtained in a boundary layer flow close to a wall. The region where the velocity gradient approaches a change in sign is designated B. In this region the cross-stream rate of change in velocity is extremely small; in fact its absolute value is approximately the same as that obtained close to the edge of a boundary layer flow. As both modelling techniques accurately predicted boundary layer flows, it seems unlikely that errors in these regions could cause the noted change in the overall accuracy of the modelling technique. The remainder of the velocity profile is covered by region C. To understand why in this region the Denny-Landis technique with FN=2, is less accurate than the same technique using FN=1, the effect of the form of the non-dimensional mesh stream function on the velocity profile has to be assessed. The cross-stream profile in region C can be approximately represented by:

$$U = U_{max}\left(1 - \frac{y}{\delta}\right),$$

where U_{max} is the maximum mainstream velocity and δ the flow width at the section under consideration. This simple form of velocity profile has been assumed, because in this analysis we are attempting to approximately assess the effect of various mesh stream functions on the velocity profile. A more precise definition of the velocity

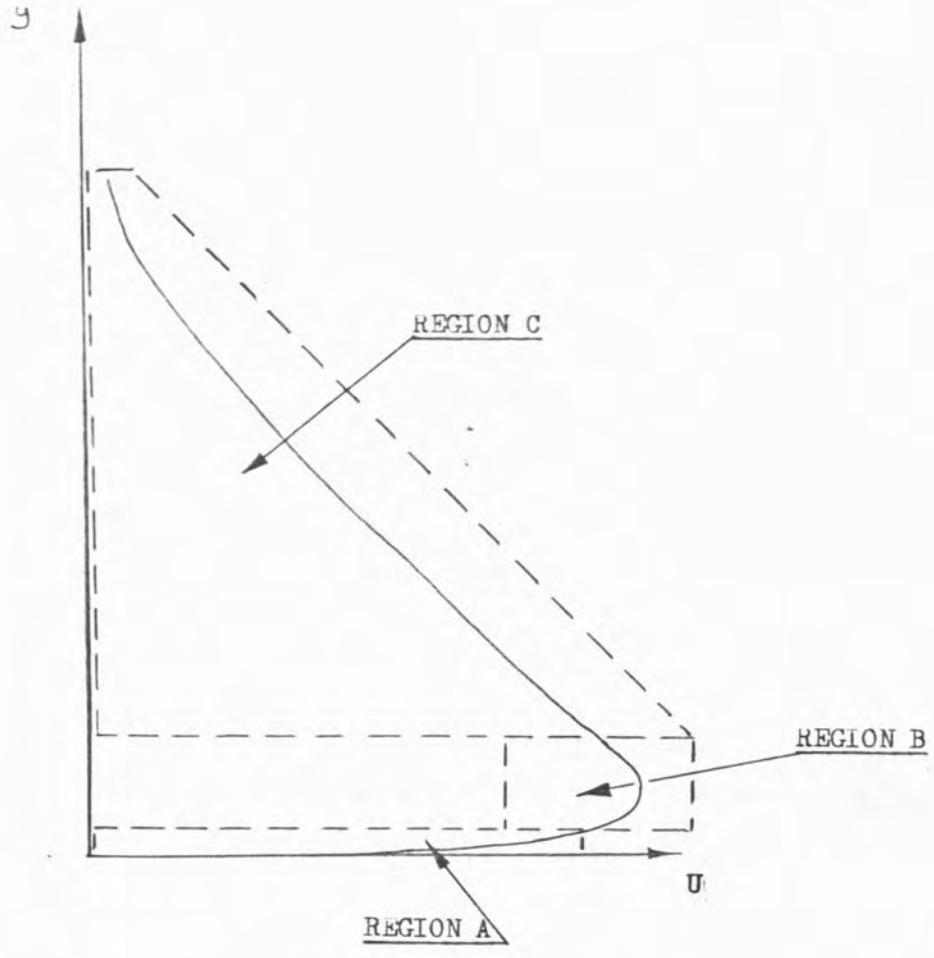

CROSS-STREAM VELOCITY PROFILE

FIGURE 3.16

profile leads to far more complex results from which the broad trends we are seeking to examine cannot be derived. The non-dimensional mesh stream function used in both modelling techniques can be represented by:

$$\omega^{\frac{1}{FN}} = \frac{\psi - \psi_I}{\psi_E - \psi_I}$$

The exponent FN can be set to either one or two. The mesh stream function, $\omega^{\frac{1}{FN}}$ and y are connected by the relationship:

$$\omega^{\frac{1}{FN}} = \left[\frac{\rho U_{max}}{\psi_E - \psi_I}\right]\left[y - \frac{y^2}{2s}\right]$$

Since $\omega = 1$ when $y = \delta$ then:

$$\frac{\delta}{2} \approx \left[\frac{\psi_E - \psi_I}{\rho U_{max}}\right]$$

and relationship between y and $\omega^{\frac{1}{FN}}$ becomes:

$$\omega^{\frac{1}{FN}} \simeq \frac{2y}{\delta}\left[1 - \frac{y}{2\delta}\right]$$

The variation of the velocity with the mesh stream function, with FN equal to one and two, and with discrete values of y is presented in table 5.11. These results are plotted in figure 5.17. In this plot it can be seen that near the edge of the flow, where $\omega^{\frac{1}{FN}}$ equals one,

Table 3.11

Values of Velocity and Non-Dimensional Stream Function for Different y^s.

y	U	Non-Dimensional Stream Function	
		Spalding-Pantankar technique (FN=1)	Denny-Landis technique (FN=2)
δ	0	1	1
$\frac{3\delta}{4}$	$\frac{U_{max}}{4}$	0.94	0.97
$\frac{\delta}{2}$	$\frac{U_{max}}{2}$	0.75	0.87
$\frac{\delta}{2}$	$\frac{3U_{max}}{4}$	0.44	0.66
$\frac{\delta}{10}$	$\frac{9U_{max}}{10}$	0.19	0.44

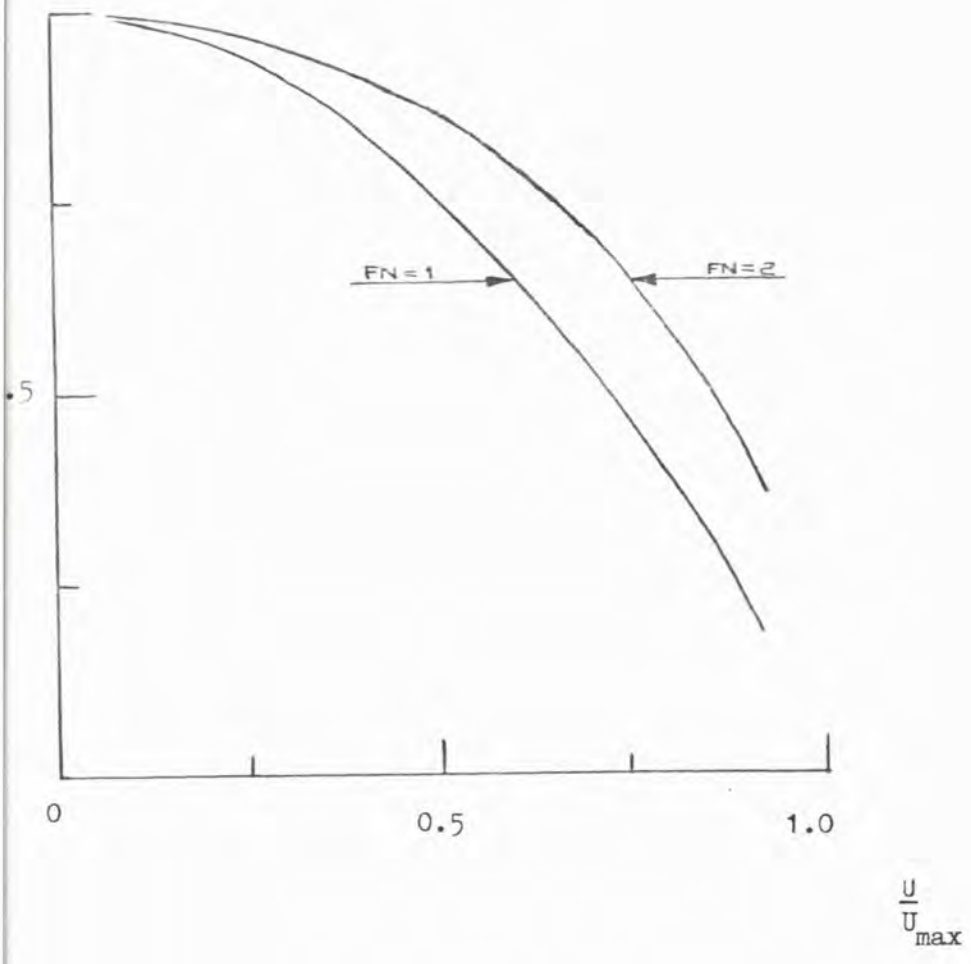

TYPICAL VELOCITY PROFILE

FIGURE 3.17

the rate of change of velocity in the cross-stream direction is far greater when FN equals two than one. The linear cross-stream finite difference assumptions used in each flow element in region C will be more accurate when the stream function is set with FN at one than when it is given the value of two. This is because the linear finite difference assumption is at its most accurate representation when the rate of change of velocity is constant, and at its least accurate when this rate of change is large. It is this effect which causes the modelling technique proposed by Denny-Landis, with FN=1, to be more accurate than the same technique, with FN=2 when simulating plane wall jets. (In all these simulations the same starting mesh networks, boundary conditions and models for the turbulent and physical properties were used).

The techniquesof Spalding-Patankar and Denny-Landis, with FN set to 1, differ in only one point. This is that Spalding-Patankar solve simplified forms of the conservation equation 2.1 in the wall and free-edge regimes, whereas Denny-Landis do not. The fact that the presented results from the Spalding-Patankar technique are more accurate than those from Denny-Landis's allows two conclusions to be drawn. Firstly, in the wall and free-edge regimes the numerical error associated with the solution of the full Navier Stokes equation is greater than the error associated with Spalding-Patankar's simplified modelling of these regimes. Secondly, when the areas occupied by the wall and free-edge regimes are specified with care only small errors are introduced into the prediction by Spalding-Patankar's modelling of these regimes.

The modelling technique proposed by Denny-Landis provided adequate predictions of the sample boundary layer, but not the wall jet flow. The Denny-Landis is the most suitable from which to develop a new technique, because it attempts to solve the Navier Stokes equation over the complete flow situation being simulated. This new technique will solve the equations of motion with the marching integration method of solution employed by Denny-Landis. However, the non-dimensional stream function $\omega^{1/n}$ will be replaced by a more general function so that a wider variety of flow situations can be adequately simulated.

The mathematical derivation of the new modelling technique is described in chapter four, together with a procedure for estimating the new non-dimensional stream function. In the remaining chapters of this thesis the ability of this modelling technique to simulate momentum, mass and heat transfer in a variety of radial wall jet flows is assessed.

Modelling Technique

In this chapter a new modelling technique for simulating the turbulent transfer processes in boundary flows is described. This technique has evolved from the Denny-Landis and Spalding - Patankar technique which were examined in chapter three.

The new modelling technique predicts the mainstream velocity U, total enthalpy h and species concentration m_k from equations that represent the conservation of momentum, heat and mass transfer within a boundary flow-equations 4.1 to 4.3 respectively.

$$\frac{\partial U}{\partial x} = \frac{\partial}{\partial \psi}(\ell) - \frac{1}{\rho U}\frac{dp}{dx} \qquad (4.1$$

$$\frac{\partial h}{\partial x} = -\frac{\partial}{\partial \psi}(J_h - U\tilde{\ell}) \qquad (4.2$$

$$\frac{\partial m_k}{\partial x} = -\frac{\partial}{\partial \psi}(J_k) + \frac{R_k}{\rho U} \qquad (4.3$$

In equation 4.3 m_k represents the concentration of the species k. The marching integration method described in chapter two, and used by Denny-Landis, is employed to solve these equations for the prescribed properties. The novel feature in the technique is that an interactive scheme is used to adjust the mesh network used in the simulation, so that the numerical errors associated with the solution are as small as practicable.

The co-ordinate system and mesh network used to cover the portion of the flow where predictions are sought are described in section 1. The mathematical method employed to solve the specified conservation equations is described in section 2; and the interactive scheme is specified in section 3.

4.1. Co-ordinate System

The mathematical method makes use of the following co-ordinate system:

a) in the streamwise direction, the distance along the impervious surface x - as shown in figure 4.1,

and b) in the cross-stream direction, a function of the non-

dimensional stream function $\Psi = f\left[\frac{\psi - \psi_1}{\psi_N - \psi_1}\right]$ (4.4

- where ψ represents the stream function, and the sub-scripts 1 and N refer to the impervious surface and free-edge of the flow.

The mesh network used to cover the portion of the simulated flow is detailed schematically in figure 4.2. In the stream-wise direction the network comprises a series of lines each representing unique values of $f\left[\frac{\psi - \psi_1}{\psi_N - \psi_1}\right]$ - these are henceforward called mesh-stream lines. In the cross-stream direction the flow is divided into strips of width $_{i-1}\Delta x_i$. The mesh stream lines are determined from two pieces of information. The first concerns the position and magnitude of the velocities specified at the starting cross-stream section of the network, ac in figure 4.2. The second concerns the functional relationship 'f' used in equation 4.4; this relationship is used to interactively adjust the mesh network, and is discussed in section 4.3. The width of any strip, say between the cross-stream lines x_{i-1} and x_i, is determined from:

$$_{i-1}\Delta x_i = F\left[\frac{\psi_i - \psi_1}{\dot{m}''_{FE}}\right]_i \qquad (4.5$$

where F is a constant that Spalding - Patankar recommend be assigned the value 0.05. The symbol $\dot{m}''_{FE}$ represents entrainment rate at the free edge between the cross stream lines at x_i and x_{i-1}, and is determined using the expression derived in the modelling technique by Spalding - Patankar - namely:

$$(\dot{m}''_{FE})_i = \lim_{y \to \delta} \left[\frac{\frac{\partial}{\partial y}\left(\mu_{eff}\frac{\partial U}{\partial y}\right)}{\frac{\partial U}{\partial y}}\right]_i \qquad (4.6$$

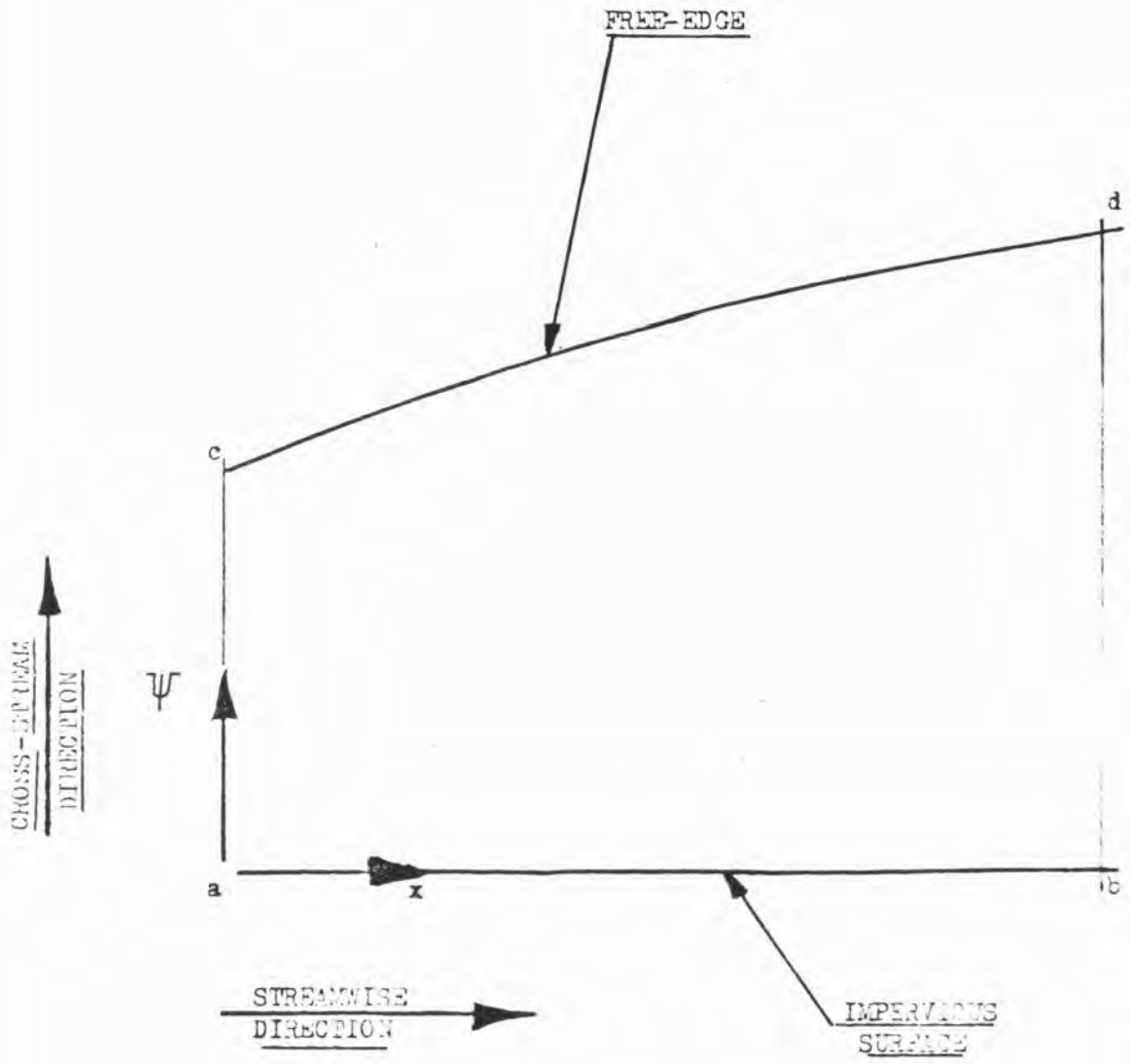

CO-ORDINATE SYSTEM

FIGURE 4.1

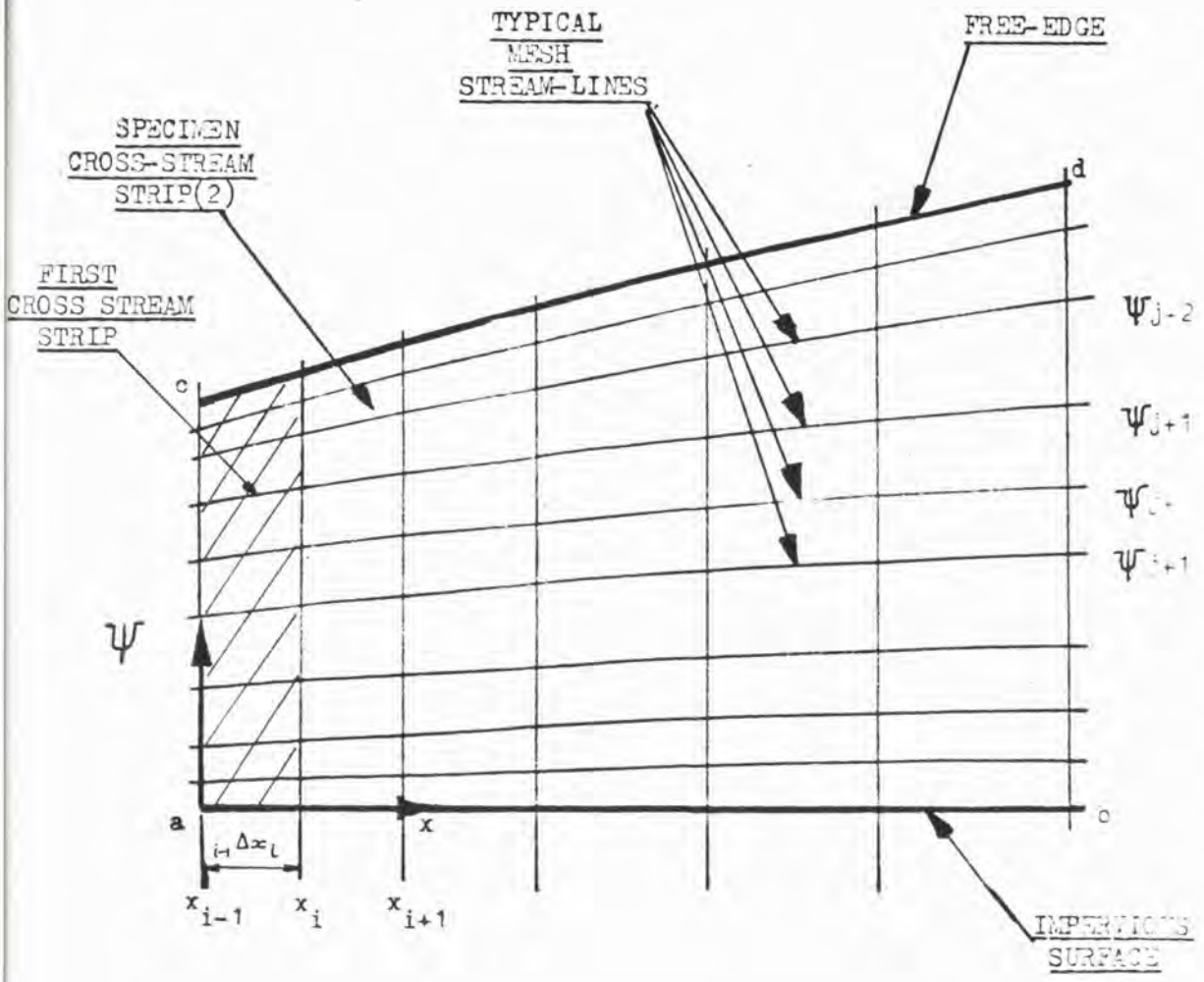

MESH NETWORK

FIGURE 4.2

4.2 Mathematical Method

The purpose of this method is to manipulate and transform the following equation:

$$\frac{\partial \bar{\Phi}}{\partial x} = \frac{\partial}{\partial \Psi}(G) - \bar{H} \quad , \qquad (4.7$$

so that it can be solved for the general property $\bar{\Phi}$. This equation represents the generalized form of the conservation equations 4.1 to .3 previously detailed - with table 4.1 specifying the meanings of $\bar{\Phi}$, G and H. The mathematical method makes use of the co-ordinate system and mesh network described in section 1.

The description of the mathematical method is presented in two inter-related parts. Firstly, details are given of an approximate limited solution of the generalized conservation equation within a trapezium shaped flow element. The positioning of the trapezium elements within the mesh network is detailed in sub-section a; and the approximate solution presented in sub-section b. Secondly, the manner in which this limited solution is used to provide predictions of the general property over a complete boundary flow is detailed in sub-section c.

Table 4.1

Transformations

General Property	G	H
U	$\tilde{U}$	$-\frac{1}{\rho U}\frac{dp}{dx}$
h	$-(J_h - U)$	-
m_k	$-J_k$	$\frac{R_k}{\rho U}$

4.2a Flow Elements

A typical flow element is shown positioned in the mesh network in figure 4.3. The two parallel boundaries of the element are coincident with the cross-stream mesh lines; the remaining boundaries are straight lines which bisect the non-dimensional stream tubes in which they are contained. (This description of the streamwise boundaries becomes clearer when referring to figure 4.3). In actual simulations it has been assumed that the element will be sufficiently small for discrepancies between the real stream functions $\Psi_{j-\frac{1}{2}}$ and $\Psi_{j+\frac{1}{2}}$, in figure 4.3, and their straight line approximations to be negligible.

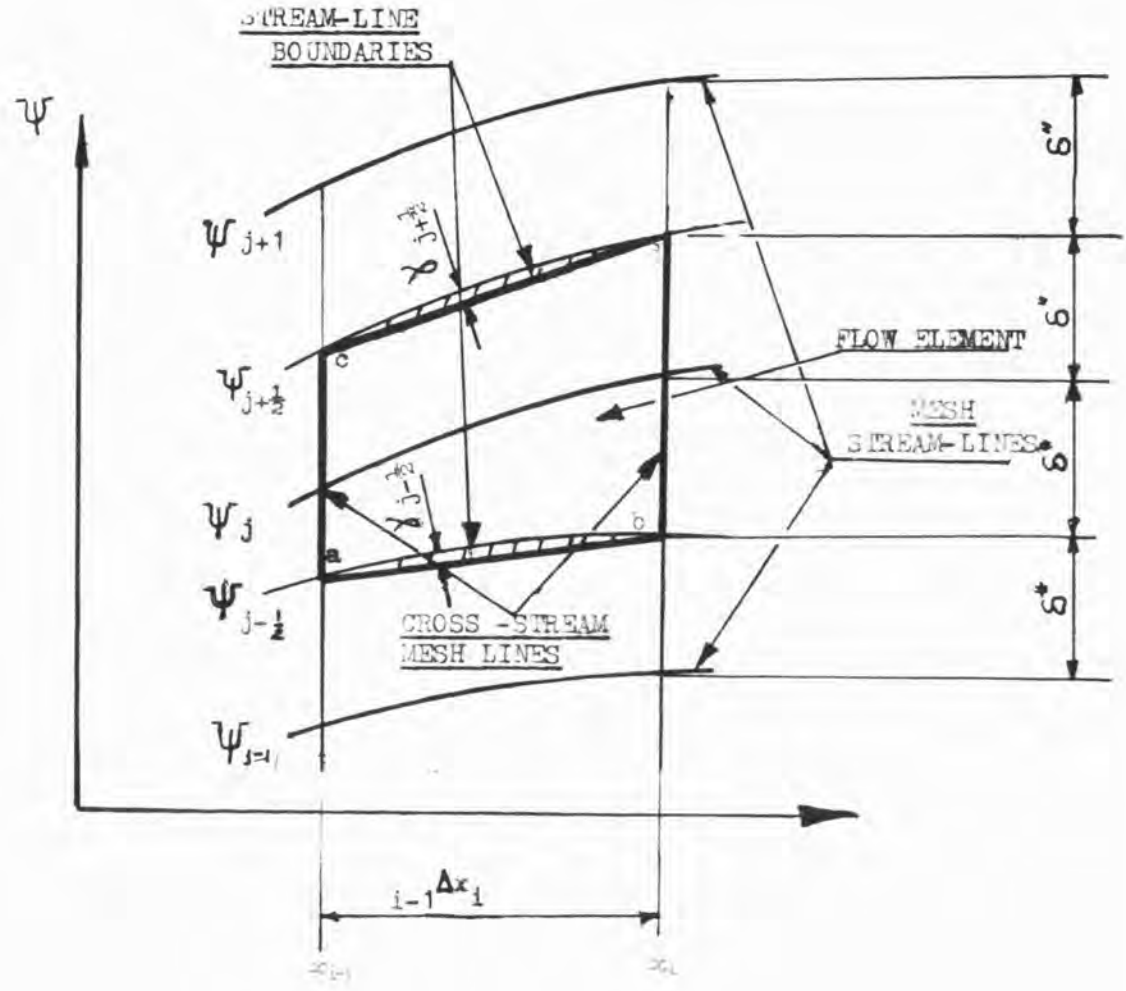

FLOW ELEMENT

FIGURE 4.3

4.2b Approximate Solution

The approximate solution of the generalized conservation equation within a typical trapezium shaped element, say abcd in figure 4.3, takes the form of:

$$\Phi_{i,j} = A''_{i,j}\,\Phi_{i,j-1} + B''_{i,j}\,\Phi_{i,j+1} + C''_{i,j} \qquad (4.8$$

The coefficients $A''_{i,j}$, $B''_{i,j}$ and $C''_{i,j}$ are dependent upon the flow properties at the inlet cross-stream boundary of the element, that is at x_{i-1} in figure 4.3, in the following way:

$$A''_{i,j} = \left[(P+G)\left(\overline{A2}-\frac{\overline{A1}}{\Delta_-}\right) + G\,\frac{\overline{A4}}{2} + (\psi_N-\psi_1)\,T_-\right] \Big/ A\varphi$$

$$B''_{i,j} = \left[(P+G)\,\frac{A1}{\Delta_+} - G\,\frac{A3}{2} - (\psi_N-\psi_-)\,T_+\right] \Big/ A\varphi$$

$$C''_{i,j} = \left\{-P\left[\Phi_{i-1,j+1}\left(\frac{A1}{\Delta_+}\right) + \Phi_{i,j}\left(A2-\frac{A1}{\Delta_+}+\frac{\overline{A1}}{\Delta_-}\right) + \Phi_{i-1,j-1}\left(\overline{A2}-\frac{\overline{A1}}{\Delta_-}\right)\right] - (\psi_N-\psi_1)\,S_{i,j}\right\}$$

$$A\varphi = -\left[(P+G)\left(A2-\frac{A1}{\Delta_+}+\frac{\overline{A1}}{\Delta_-}\right) - G\left(\frac{A3}{2}-A4+\overline{A3}-\frac{\overline{A4}}{2}\right) - (\psi_N-\psi_1)\left(T+S_{i,j}-T_+\right)\right]$$

$$A1 = \sum_{k=2}^{n}\left(\frac{k-1}{k}\right)a_k\left(\frac{\Delta_+}{2}\right)^k \qquad \overline{A1} = \sum_{k=2}^{n}\left(\frac{k-1}{k}\right)\left(1-\frac{1}{2^k}\right)\bar{a}_k\left(\Delta_-\right)^k$$

$$A2 = \sum_{k=2}^{n} a_k\left(\frac{\Delta_+}{2}\right)^{k-1} \qquad \overline{A2} = \sum_{k=2}^{n}\bar{a}_k\left(1-\frac{1}{2^k}\right)\left(\Delta_-\right)^{k-1}$$

$$A3 = \sum_{k=1}^{n} a_k\left(\frac{\Delta_+}{2}\right)^{k-1} \qquad \overline{A3} = \sum_{k=1}^{n}\bar{a}_k\left(\Delta_-\right)^{k-1}$$

$$A4 = a_1 \qquad \overline{A4} = \sum_{k=1}^{n}\bar{a}_k\left(\frac{\Delta_-}{2}\right)^{k-1}$$

$$\Delta_+ = \psi_{i,j+1} - \psi_{i,j} \qquad \Delta_- = \psi_{i,j} - \psi_{i,j-1}$$

$$T = \sum_{k=1}^{n} a_k\left(\frac{\Delta_+}{2}\right)^{k-1}\left(\frac{\Phi_{i,j+1}-\Phi_{i,j}}{\psi_{i,j+1}-\psi_{i,j}}\right) \qquad \overline{T} = \sum_{k=1}^{n}\bar{a}_k\left(\frac{\Delta_-}{2}\right)^{k-1}\left(\frac{\Phi_{i,j}-\Phi_{i,j-1}}{\psi_{i,j}-\psi_{i,j-1}}\right)$$

The algebraic equation 4.8 has been derived from the general conservation equation by using the following procedure Firstly, the variation of the general property $\bar{\Phi}$ is specified along the boundaries of the flow element. This has been achieved by detailing the variation of $\bar{\Phi}$ along the lines of the mesh network that encompass the element. (Or as an alternative explanation, finite difference approximations are made for the differentials $\frac{d\bar{\Phi}}{dx}$, $\frac{d\bar{\Phi}}{d\Psi}$ and $\frac{d^2\bar{\Phi}}{d\Psi^2}$). That is along the mesh stream lines $u_{j+1}\ d_{j+1}$, $u_j\ d_j$ and $u_{j-1}\ d_{j-1}$, and the cross-stream lines u_{j-1}, u_j, $u_j\ u_{j+1}$, $d_{j-1}\ d_j$ and $d_j\ d_{j+1}$ shown in figure 4.4a. Along the specified portion of the mesh stream lines the general property has been assumed constant, and equal to its value at the downstream cross-section -along u_{j-1} and u_{j+1} in figure 4.4a. Schematic representations of these profiles are presented in figure 4.4b. Along the detailed cross-stream lines the general property has been assumed to vary linearly with the cross-stream co-ordinate. Schematic representations of these profiles at the upstream and downstream cross-stream sections of the element are presented in figure 4.4c and d respectively. Secondly, it has been postulated that when the element is small:

a) $$\frac{\partial\bar{\Phi}}{\partial\Psi} = \frac{d\bar{\Phi}}{d\Psi}\ , \qquad (4.9$$

b) $$\frac{\partial\bar{\Phi}}{\partial x} = \frac{d\bar{\Phi}}{dx} \qquad (4.10$$

and c) $$\frac{\partial}{\partial\Psi}\left[Q\ \frac{\partial\bar{\Phi}}{\partial\Psi}\right] = \frac{\partial}{\partial\Psi}\left[Q\frac{\partial\bar{\Phi}}{\partial\Psi}\right]\ , \qquad (4.11$$

where Q represents various combinations of the effective viscosity and Schmidt or Prandtl numbers. Equation 4.8 was obtained by

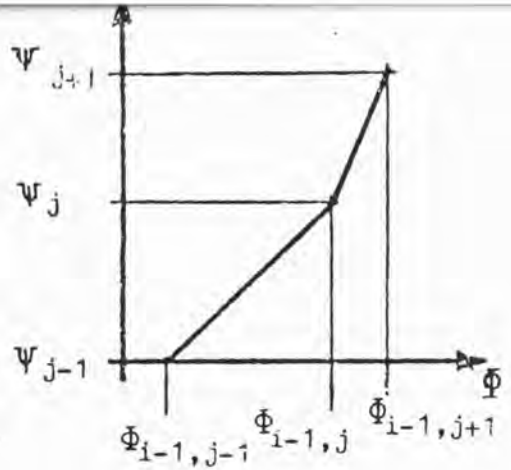

c. ASSUMED CROSS STREAM Φ PROFILE AT THE UPSTREAM BOUNDARY (x_{i-1})

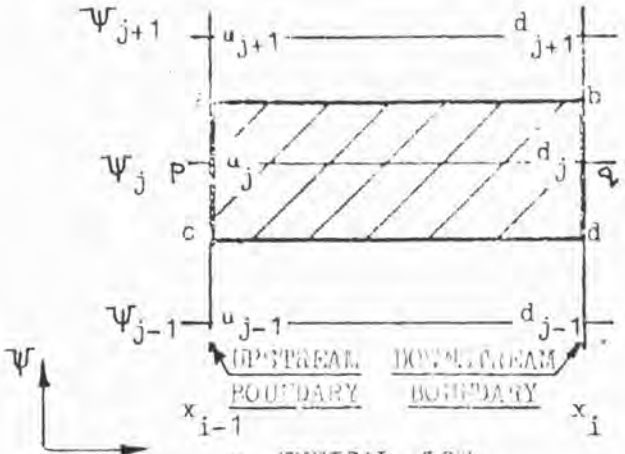

a. TYPICAL FLOW ELEMENT

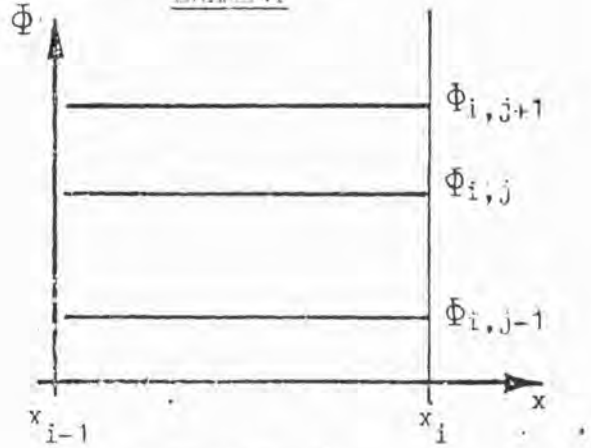

b. ASSUMED Φ PROFILE BETWEEN x_{i-1} AND x_i

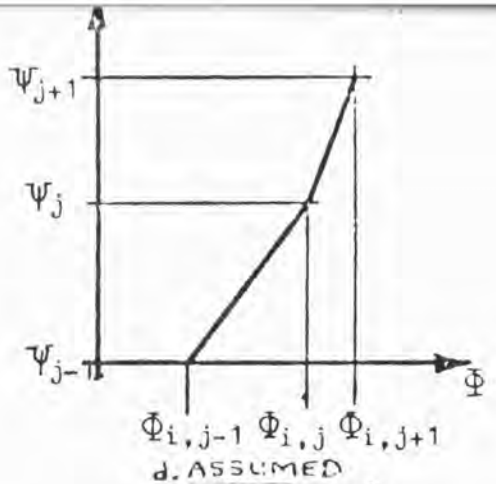

d. ASSUMED CROSS STREAM Φ PROFILE AT THE DOWNSTREAM BOUNDARY (x_i)

ASSUMED Φ PROFILES AROUND A SPECIMEN FLOW ELEMENT

FIGURE 4.4

substituting the equalities in 4.9 to .11 and assumed rates of change of Φ into the general conservation equation 4.7, and integrating the result over the specified flow element.

4.2c Overall Solution

The procedure used to solve the general conservation equation 4.7 for the property Φ over a particular flow situation involves the following steps . Firstly, the extent of the flow situation has to be mathematically specified. Secondly, the technique for extending the limited solution to equation 4.7 over the complete flow must be declared. These steps are detailed below.

The extent of the simulated boundary flow is defined by specifying:

a) the variation of Φ along the surface, free edge and starting cross-stream section - that is along ab, cd and ac respectively of the flow illustrated in figure 4.2

and b) the height of the flow $\delta_{1,1}$ at the starting cross-stream section.

The technique followed for an overall solution proceeds as follows. Equation 4.8, which represents a limited solution of the general conservation equation, is applied to each element of first the cross-stream strip in figure 4.2, leading to a set of equations of the form of:

$$\sum_{j=2}^{N-1} \left[-\Phi_{2,j} + A''_{2,j}\Phi_{2,j-1} + B''_{2,j}\Phi_{2,j+1} + C''_{2,j} \right] = 0. \quad (4.12$$

These equations can be solved for $\Phi_{2,j}$, where j=2, N-1; after substituting for $A''_{2,j}$, $B''_{2,j}$ and $C''_{2,j}$-which are determined

from the information specifying the flow situation. Equation 4.8 is then applied to all the flow elements in the next cross-stream strip, number 2 in figure 4.2, resulting in the following set of equations:

$$\sum_{j=2}^{N-1} \left[-\Phi_{3,j} + A''_{3,j}\,\Phi_{3,j-1} + B''_{3,j}\,\Phi_{3,j+1} + C''_{3,j} \right] = 0 \qquad (4.1$$

These equations are solved for $\Phi_{3,j}$, where $j = 2, N-1$, in the same way as previous cross-stream strips. This procedure is continued cross-stream strip by strip, until the boundary flow has been covered, and an overall solution achieved.

4.3 Interactive Scheme

The errors between the partial differentials, in the general conservation equation 4.7, and their finite difference representations have been estimated in appendix seven. The results obtained are summarized in table 4.1. In this table the symbols $U^n(q)$ represent $\frac{\partial^n(U)}{\partial q^n}$ at a particular nodal point of the mesh network - with 'q' designating x or y. The terms R_1, R_3, P_1 and P_3 have been defined in appendix seven. The coefficients a and b in the table act on the convective terms of the momentum equation and are specified in terms of known parameters in table 4.2. The coefficient c, which acts in the viscous diffusion term of equation 4.7 is also defined in table 4.2.

Error Terms

Partial Differential	Error	Leading Order Error Term
$aU'(\omega)$	$a\frac{\Delta\omega^2}{6}U'''(\omega) + a\frac{\Delta\omega^3}{24}U^{iv}(\omega) + HOT_1$	$\frac{a\Delta\omega^2}{6}.U'''(\omega)$
$U'.(cU'(\omega))$	$U'(\omega)(c_+ - \underline{c}) + \frac{\Delta\omega}{6}U'''(\underset{+}{c} - \underset{-}{c}) + \frac{\Delta\omega^2}{24}U^{iv}(\omega)(\underset{+}{c} + \underset{-}{c}) + HOT_2$	$\frac{\Delta\omega^2 c}{12}U^{iv}(\omega)$
$U'(x)$	$U''(x)\,\Delta x\Delta\omega(P_1-P_3) + U'''(x)\frac{\Delta x\Delta\omega^2}{2}(P_1+P_3) + HOT_3$	$\Delta x\Delta\omega(P_1-P_3)U''(x)$
$b\ U'(\omega)$	$U''(\omega)\frac{\Delta\omega^2}{2}(R_1+R_3) + U'''(\omega)\frac{\Delta\omega^3}{6}(R_1-R_3) + HOT_4$	$\frac{\Delta\omega^2}{2}(R_1+R_3)U''(\omega)$

Table 4.2

Definition of Coefficients

Coefficients	Meaning
a	$\dfrac{r_I \dot{m}''_I}{(\psi_E - \psi_I) \sum_{i=2}^{\infty} (i-1) a_i \Delta\omega^{i-2}}$
b	$\dfrac{r_E \dot{m}''_E - r_I \dot{m}''_I}{(\psi_E - \psi_I) \sum_{i=2}^{\infty} (i-1) a_i \Delta\omega^{i-2}}$
c	$\dfrac{\rho U r^2 \mu_{eff}}{(\psi_E - \psi_I)^2 \left[\sum_{i=2}^{\infty} (i-1) a_i \Delta\omega^{i-2}\right]^2}$

The error terms associated with the finite difference representations of the various partial differentials are presented in the second column of table 4.1. In the derivation of the error terms it has been assumed that the finite differentials were applied to the fluid element abcd in figure 4.4. The top and bottom halves of the fluid element were of equal area. In the derivation of the error terms it was assumed that the velocity profile between sequential nodal points conformed to Taylors series. The symbol H.O.T in the error represents the terms of Taylors series that are not precisely defined in table 4.1.

The leading order discretization error acting on each of the finite difference approximations is specified in the third column of table 4.1. The leading order error term for $U'(cU'(\omega))$ has been derived with the assumption that the value of the coefficient 'c' in the top and bottom halves of the fluid element, abcd in figure 4.4, are equal and represented by c. The leading order error terms are of the form one would expect from the finite difference profiles assumed over the fluid element. The velocity profile in the cross-stream direction was assumed linear over each half of the flow element, and in the stream-wise direction a constant value was assumed. (Specimen of these profiles are presented in figure 4.4). Thus the various forms of $U'(\omega)$ are represented in the interactive scheme by what is equivalent to a central order finite difference-which has a leading discretization error of the order of the square of the distance between successive streamwise mesh lines.

It is pertinent to highlight three points about the error terms. Firstly, their complex nature, especially through the terms R_1, R_2, R_3, P_1, P_2, and P_3, means that they cannot be manipulated so that the form of non-dimensional stream function, for minimum error from the modelling technique, can be derived. Secondly, for reasons detailed below, the errors from the finite difference

approximations are considerably greater than those caused by round off error from the computer. This point is of considerable importance, because if this condition is not met the error analysis described above serves no useful purpose. (Round off errors result from the approximate nature in which computers perform arithmetic manipulations.) On the I.C.L computer used in this study the round off error resulting from one arithmetic manipulation, with both numbers held in single precision form, caused an error on and beyond the eleventh digit of the answer. Thus the maximum round off error in the error terms detailed in table 4.1 will probably occur on and beyond the eigth digit. (This result was obtained by applying simple queueing theory to the error term involving the greatest number of arithmetic manipulations). Sample calculations for a boundary layer flow have been used to estimate the magnitude of the leading order discretization error for the differentials in table 4.1. In the sample calculation it was assumed that the mainstream velocity equalled $30.5 ms^{-1}$ with $2.5 \leq x \leq 5.3m$, and that the cross-stream velocity profile was of the form $U \propto y^{1/7}$ (This flow situation has been often simulated in this thesis). The non-dimensional stream function of Spalding-Patankar was assumed with cross- and streamwise distances between the respective mesh line of $10^{-5}\delta$. (The term δ represents the thickness of the boundary flow at the section under consideration). Calculations showed that the leading order error terms in table 4.1 cause errors which affect their differentials on the fourth to seventh digits. From these calculations it has been deduced that round off errors are negligible when compared with those from the leading order error terms - when the distances between mesh lines is kept at approximately $10^{-5}\delta$. Thirdly, numerical diffusion will occur in this technique. Roache[71], has defined numerical diffusion as

the summation of the error terms that contain the partial differential $U''(q)$ - where q represents x or ω. Numerical diffusion is important for two reasons. Firstly, because it can be extremely large in boundary flows. Secondly, errors from this source are difficult to separate from the predicted results, because real and numerical diffusion are computationally undistinguishable. However, before embarking on an examination of these effects the leading order error terms will be estimated.

The leading order error terms of the various partial differentials in the momentum equation have been specified in the third column of table 4.1. The first two terms, $aU'(\omega)$ and $U'(\rho U'(\omega))$, have leading order errors of the order $a\Delta\omega^2$ and $c\Delta\omega^2$ respectively. The third term, has an error of the order $\Delta x.\Delta\omega.(P_1-P_3)$ When the terms represented by P are in their basic form (i set to 2 in the definitions of P given in table two appendix seven) this term is approximately equal to $\Delta\omega$. The forth term, $b\omega U'(\omega)$, has an error of the order $\frac{\Delta\omega^2}{2}(R_1+R_3)$; when the terms represented by R are defined in their most basic form (i = 1 in the definition for R in table 2 appendix seven) this error term is approximately equivalent to $\Delta\omega$. It should be noted that the approximate error, $\Delta\omega$, from the third and fourth partial differentials in table 4.1 is the worst that could be obtained with this modelling technique. Judicious adjustment of the polynomial $\sum_{i=1}^{\infty} a_1 \Delta\omega^i$, and hence the coefficients P_1, P_2, P_3, R_1, R_2 and R_3, would reduce this error considerably.

The terms representing numerical diffusion are the error terms containing U". By referring to table 4.1 it can be deduced that numerical diffusion in this modelling technique is represented by:

$$U''(\omega).(R_1+R_3)\ \frac{\Delta\omega^2}{2} + U''(x)(P_1-P_3)\,\Delta x\,\Delta\omega\ ;$$

in this relationship

$$R_1 = \left[\frac{b}{\Delta\omega^2}\right]\left[\sum_{i=1}^{\infty}\frac{a_i\,\Delta\omega^i}{i}\right] ,$$

$$R_3 = \left[\frac{b}{\Delta\omega^2}\right]\left[\sum_{i=1}^{\infty}\frac{\bar{a}_i\,\Delta\omega^i}{i}\right] ,$$

$$P_1 = \left(\frac{1}{\Delta x}\right)\sum_{i=2}^{\infty}\frac{a_i\Delta\omega^{i-2}}{2^{i-1}} ,$$

and $$P_3 = \left(\frac{1}{\Delta x}\right)\sum_{i=2}^{\infty}\frac{\bar{a}_i\,\Delta\omega^{i-2}}{2^{i-1}}$$

In the above relationship the two error terms have leading errors of the order of $\Delta\omega$ with the non-dimensional stream function used in Spalding-Pantankars modelling technique. However, as detailed above judicious adjustment of this stream function will considerably reduce this error. From the proceeding discussion it can be seen that the magnitude of the numerical diffusion is dependent upon the mesh spacings, the form of the non-dimensional stream function (that is the values allocated a_i and $\bar{a}_i$) and the magnitude of 'b'. From table 4.2 'b' is

dependent upon the entrainment rates $\dot{m}''_I$ and $\dot{m}''_E$, a_i and $\bar{a}_i$, and the cross-stream mesh spacing. The most important point that can be deduced from this analysis is that the value of the numerical diffusion can be minimized through the user defined constants a_i and $\bar{a}_i$ for 'i' equals one to any other positive integer. Thus the magnitude of the error from this source cannot be precisely defined. As a supplementary point it is worthwhile noting that the second term in the expression for numerical diffusion is negligible when compared to the first term. This is because $U''(\omega)$ is considerably greater than $U''(x)$, at the same point in a boundary flow with no external pressure gradients, as detailed by Schlichting[22] Bradshaw etal[106] and Hinze[121].

4.3c Mesh Manipulation

The selected procedure for obtaining a small specified discrepancy between the real and assumed cross-stream velocity profiles over each element is to manipulate the grading of the non-dimensional mesh stream lines. This re-grading is accomplished by redefining the functional relationship 'f' in

the description of each mesh stream line, equation 4.4, at various points in the simulation.

To concisely manipulate the grading of the non-dimensional mesh stream lines so that the declared cross-stream velocity discrepancies are as small as possible, requires knowledge of the real cross-stream velocity profile, which in all but the most trivial or test cases, is not available. Two alternative and approximate forms of manipulation exist. The first, and chosen technique, is based upon a phenomenological approach. In this the grading of the mesh stream lines are modified at the starting section, so that the assumed cross-stream rate of change of velocity falls below a specified limit L - called the velocity gradient limit. The mathematical construction of such a scheme is discussed in the next paragraph. The value assigned the limit L, which is derived from observed results presented in chapter 3, is defined and discussed in sub-section d. The second manipulatory technique would be based upon a mathematically automated variation of the mesh stream lines at each cross-stream section, so that discrepancies between calculated and a previously declared cross-stream velocity profile, represented with a cubic spline, would be a minimum. This approach was rejected, because it's application would absorb a large amount of computational time.

The mathematical construction of the first manipulation technique is detailed below. A description of the ways in which this technique is monitored on an electric computer is also presented, because the techniques construction is dependent upon the man machine interfaces available on the computer - in this case an I.C.L. 4130. The velocity profile used by the modelling technique at the starting cross-stream section was outputted on to a calligraphic screen, connected to the computer, in co-ordinates of function of the

velocity $\tilde{U}$ against the mesh stream-function Ψ set to $\left[\frac{\Psi - \Psi_1}{\Psi_N - \Psi_1}\right]$.

The velocity profile was plotted in the following manner. Firstly, the co-ordinates axis $\tilde{U}$ and Ψ were drawn in specified units, (n.b. $\tilde{U}$ can be in metres/sec or non-dimensional). Secondly, the position of the end point of each velocity vector U was marked for each of the mesh stream lines. Finally, straight lines are drawn between successive points on the screen. An example of a typical plot for a boundary layer flow is presented in figure 4.5.

The grading between the mesh stream lines on the calligraphic screen was varied until $\frac{dU}{d\Psi}$, as detailed on the screen, fell below a specified limit L. Re-positioning of the mesh stream-lines was achieved with a light pen; which was first used to indicate which mesh stream line was to be moved and then identify it's new position.

After successfully positioning the non-dimensional mesh stream-lines, the relationship between Ψ and the original stream function ψ had to be defined, before the modelling technique could be used to solve the conservation equation 4.1 to .3. In this thesis this relationship has been defined mathematically with a cubic spline. The spline forms a smooth curve that passes through all the points defining the Ψ against ψ relationship. The mathematical formulation of the spline used is as follows:

a) between successive points, say $\Psi_{i,1}$ $\psi_{i,1}$ and $\Psi_{i+1,1}$ $\psi_{i+1,1}$ in figure 4.6, the relationship is assumed to be represented by a cubic equation,

b) the slope and curvature must be the same for the pair of cubics joining each point.

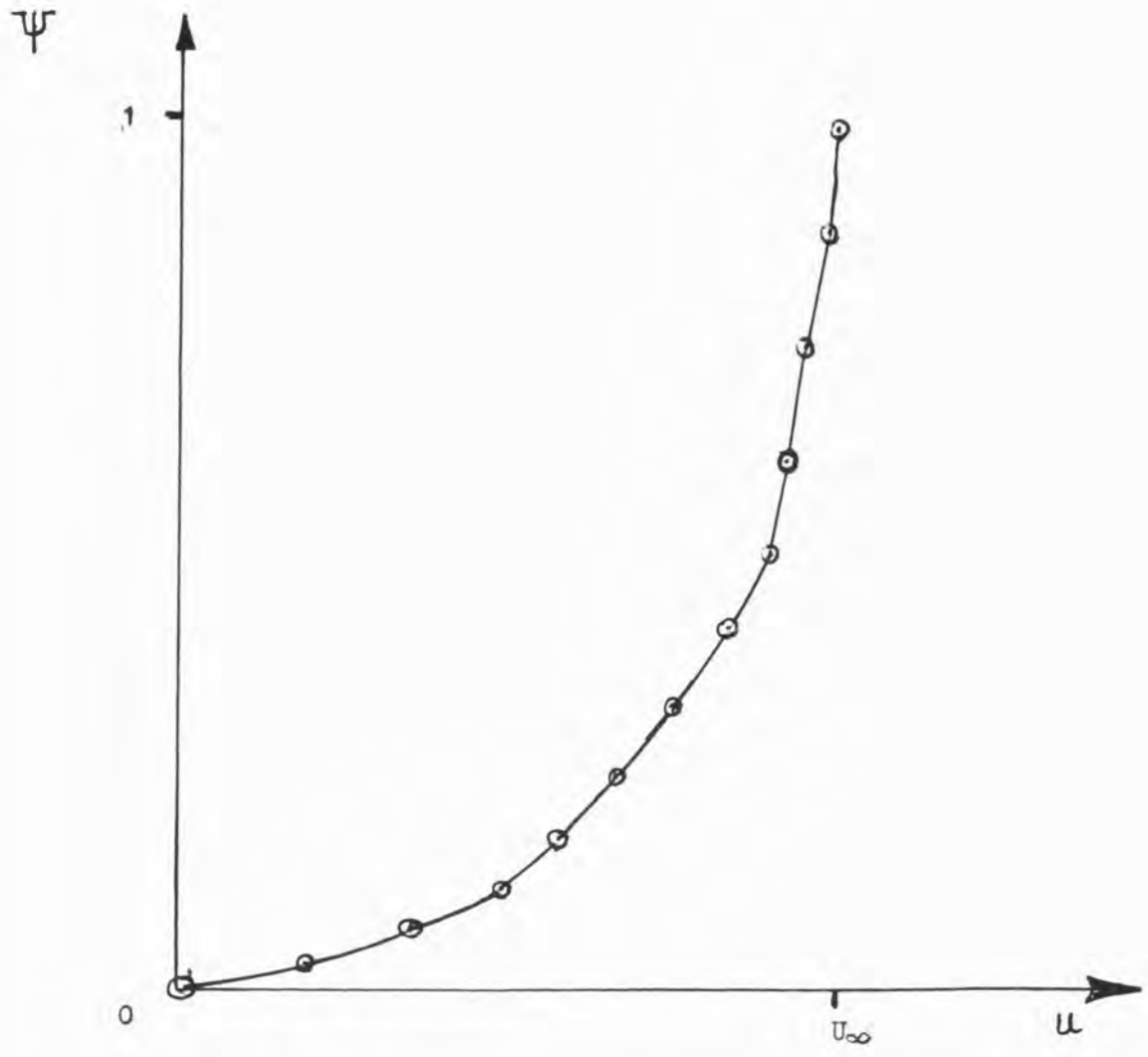

CROSS-STREAM VELOCITY PROFILE

IN BOUNDARY LAYER

FIGURE 4.5

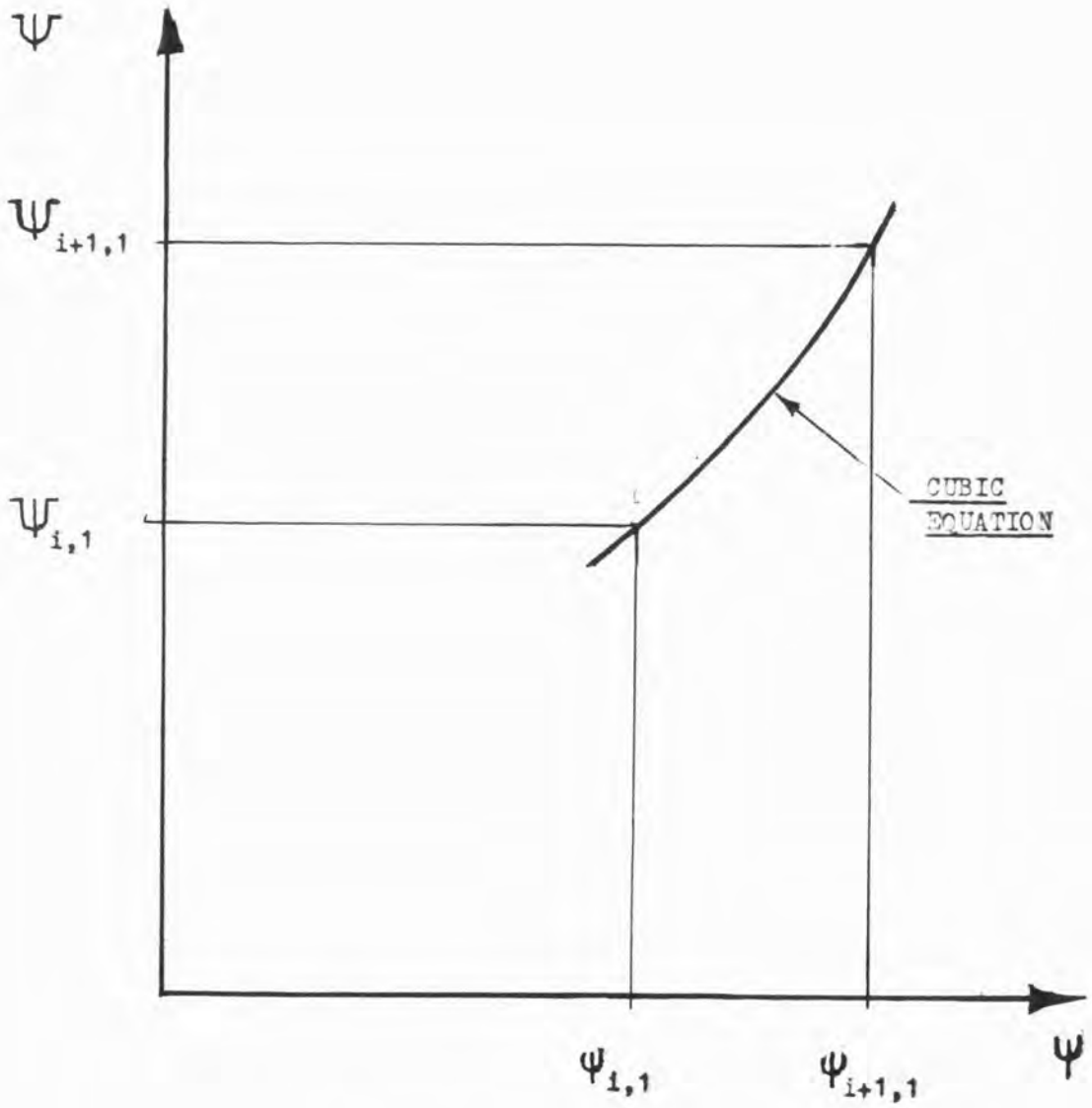

SPLINE

FIGURE 4.6

c) at the extreme points of the curve it has been assumed that $\frac{d^2\psi}{d\psi^2}$ is zero - this is called a relaxed end condition by South and Kelly[37].

Algebraic manipulation of these assumptions results in a set of simultaneous equations of the form:

$$[A]\ [s] = [C]$$

Where A is a tridiagonal array containing information on the distance in the ψ direction between successive points, s represents the second derivative of the spline, and C is an array holding information on the distance in the ψ direction between successive points. The equation was solved for s , and hence the coefficients of the spline, by using a relaxation method due to Serthwell. This method makes use of the Gauss-Seidel scheme for solving simultaneous equations, after selecting a suitable a pivotal equation for maximum accuracy. Allen[38] gives an excellent review of the method.

4.5 Velocity gradient limit

The intent of the work detailed in this sub-section is to estimate realistic values for the velocity gradient limit L. This limit was specified in sub-section 4.3b, and defines the value of $\frac{dU}{d\psi}$ above which errors resulting from the discrepancy between the real and assumed cross-stream velocity profiles become noticeable. As already discussed in sections 4.3b and c, there is no theoretical way of estimating L. Instead a phenomenological approach, based upon the results and discussions in chapter three, has been

used to estimate two probable values for the limit .

In chapter 3 it was shown that, if for a typical boundary layer flow:

$$U \propto y^{\beta},$$

then

$$\frac{dU}{d\Omega} = \frac{U}{\Omega}\left[\frac{\beta}{FN\,(1+\beta)}\right] \qquad (4.14$$

and

$$\Omega = \left[\frac{y}{\delta_1}\right]^{(\beta+1)}$$

It is postulated that a reasonable estimate for the velocity gradient L will be the value of $\frac{dU}{d\Omega}$ at the mesh point closest to the impervious surface, in the successful simulations of a boundary layer flow with the Denny-Landis's modelling technique, using $FN = 1$, in chapter 3. Assuming $y_{1,2}$, the first point above the surface at the starting cross-stream section, to be the specified point and letting $\beta = 1/7$; then from equation 4.14 $\left[\frac{dU}{d\Omega}\right]_{1,2}$ can be estimated. The values of $y_{1,2}$, and the calculated estimates for $\Omega_{1,2}$ and $\left[\frac{dU}{d\Omega}\right]_{1,2}$ are presented in table 4.2. The values given the velocity gradient limit L are 10^3 and 10^5, which are approximately equal to the two calculated of $\left[\frac{dU}{d\Omega}\right]_{1,2}$ in table 4.2.

Table 4.2

Velocity Gradient Calculations

$\frac{y_{1,2}}{\delta_{1,1}}$	$\Omega_{1,2}$	$\left[\frac{dU}{d\zeta}\right]_{1,2}$
10^{-3}	3.73×10^{-4}	2.813×10^{3}
10^{-5}	1.931×10^{-6}	2.813×10^{5}

Momentum Transfer Rates

The objective of this chapter is to assess whether the modelling technique incorporating a variable mesh network and making use of an interactive scheme, can accurately predict the momentum transfer rates in two 2-dimensional incompressible air boundary layers and a plane wall jet. To simulate momentum transfer processes the modelling technique requires additional information concerning the values taken by the density and effective viscosity. These properties are determined with the general gas law and turbulence model of Lauder-Spalding respectively - previously described in chapter 3. As the manner in which this information is presented to the modelling technique is as previously specified, no further discussion of these properties will be given.

Estimates of the errors generated in the computational simulations of the specified flows are obtained by comparing the predicted results with theoretical or experimental data obtained elsewhere. The results from this study are presented in section 5.1. In section 5.2 the overall performance of the modelling technique is discussed and assessed, and in section 5.3 the conclusions and recommendations presented.

5.1 Comparison of results

The flows chosen for examination are a:

a) boundary laver flowing over a flat impervious surface,

b) boundary layer with tangential air injection at the flat impervious surface

and c) plane wall jet,

The comparison of results are presented in sub-section a to c respectively.

Two mesh network gradings are used for the computational simulations of the chosen flows. As described in chapter 4 the network consists of lines representing constant values of x, the distance along the impervious surface, and Ψ, a non-dimensional form of the stream function ψ. The grading of the real ordinate y and specified velocity profile along the starting cross-stream section of the flow, enable the stream function ψ - and hence the basis of non-dimensional mesh stream function-to be established. The grading for the spatial ordinate y is estimated from equation 3.8 with:

a) $y_{1,1} = 0, y_{1,2} = \delta_{1,1}/10^3$ and Fr = 1.121

b) $y_{1,1} = 0, y_{1,2} = \delta_{1,1}/10^5$ and Fr = 1.196

$\delta_{1,1}$ is the width of the flow at the starting cross-stream section The velocity profiles at this section are specified in the description and comparisons for each of the chosen flow situations. The size of the steps along the x axis were estimated with equation 4.5 - this technique has been discussed in chapter four.

The purpose of the interactive scheme is to enhance the accuracy of the numerical approximations for the cross-stream partial differential $\frac{\partial U}{\partial \Psi}$ used in the modelling technique. This enhancement is achieved by manipulating the grading of the non-dimensional mesh stream lines, at the starting cross-section of the simulation, so that the numerical approximation for $\frac{\partial U}{\partial \Psi}$ are less than a pre-defined value - called the velocity gradient limit L. Two different values are used for L in the presented simulations:

i) $L = 10^3$

ii) $L = 10^5$

5.1a Boundary Layer

The formulae detailed in chapter 3, and designated by 3.11 to 3.13, are again used to describe the time averaged velocity field within the turbulent boundary layer flow shown in figure 5.1.

The flow chosen for examination is one where the free-stream velocity U_∞ is 30.5 ms^{-1} (100 ft s^{-1}) and the kinematic viscosity is 1.6 x 10^{-5} m^2s^{-1}. Plots of the cross-stream velocity profiles have been obtained from equation 3.11; specimen results at x = 2.5, 4.0 and 5.3m are shown by the dotted lines in figure 5.2 to 5.4 respectively. The variation of the total skin friction C_f with Reynolds number Re_x (based upon the distance along the impervious surface) is obtained from equation 3.12; and is shown by the dotted line in figure 5.5. The dependence of the boundary layer thickness δ_1 upon the Reynolds number Re_x has been derived from equation 3.13; and is designated by the dotted line in figure 5.6.

Four different computational simulations of the boundary layer, for $2.4 \leqslant x \leqslant 5.3$m, are presented. They correspond to the two forms of mesh a and b and two velocity gradient limits i and ii described in the introduction of this section. In each simulation the following boundary conditions have been specified:

a) along the starting cross-stream section, ab in figure 5.1, the velocity was described by equations 3.11 and .13.

and b) at the free edge and impervious surface the velocity was set to 30.5 and 0.0 ms^{-1} respectively.

Specimen results from these computations are shown in figures 5.2 to 5.6. Table 5.1 details the symbols used throughout this section for the presentation of results. Table 5.2 details the maximum discrepancies between the results from the computational simulations and those from equations 3.11 to .13 at the three specimen cross-stream section.

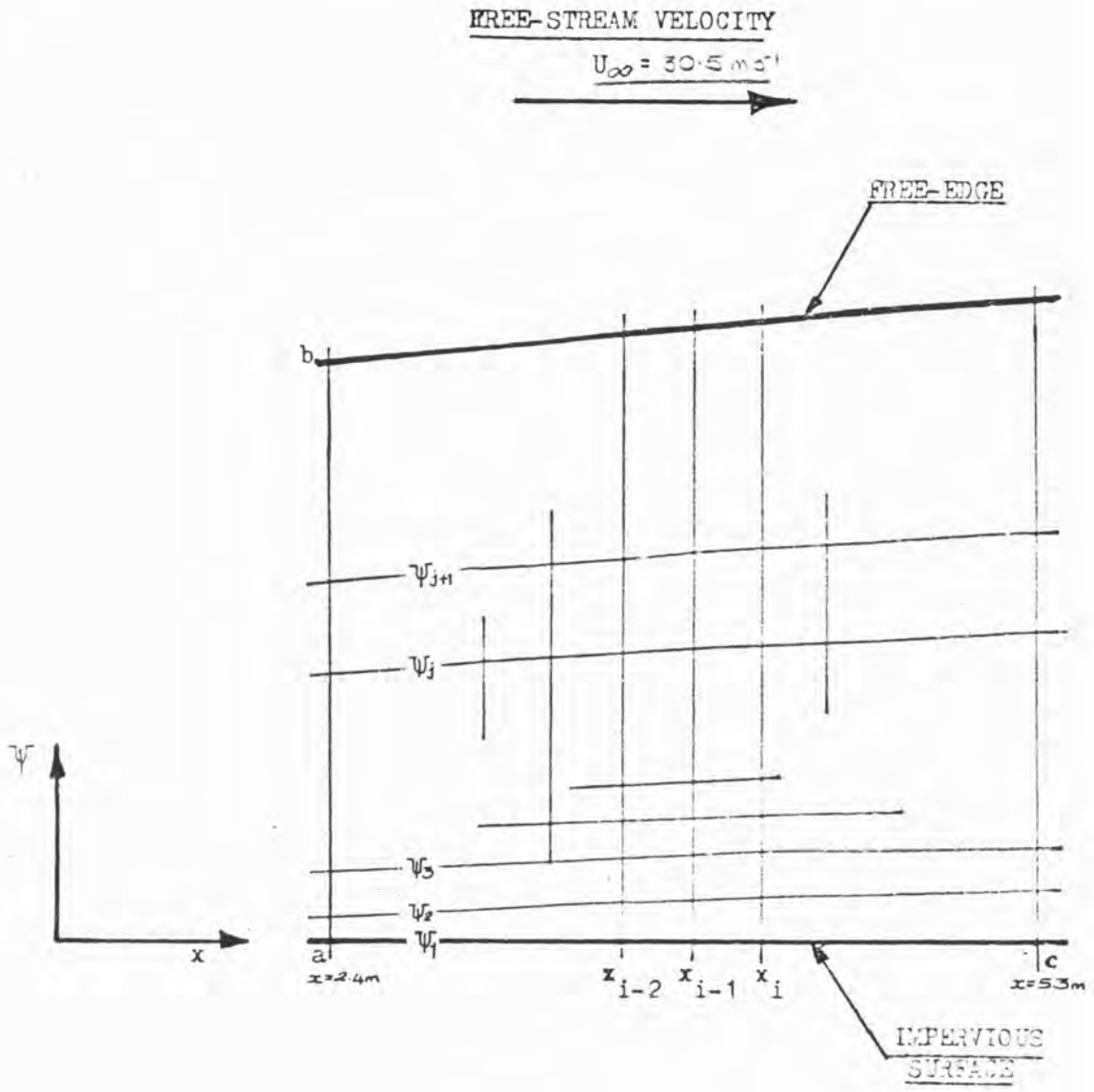

MESH GRADING

FIGURE 5.1

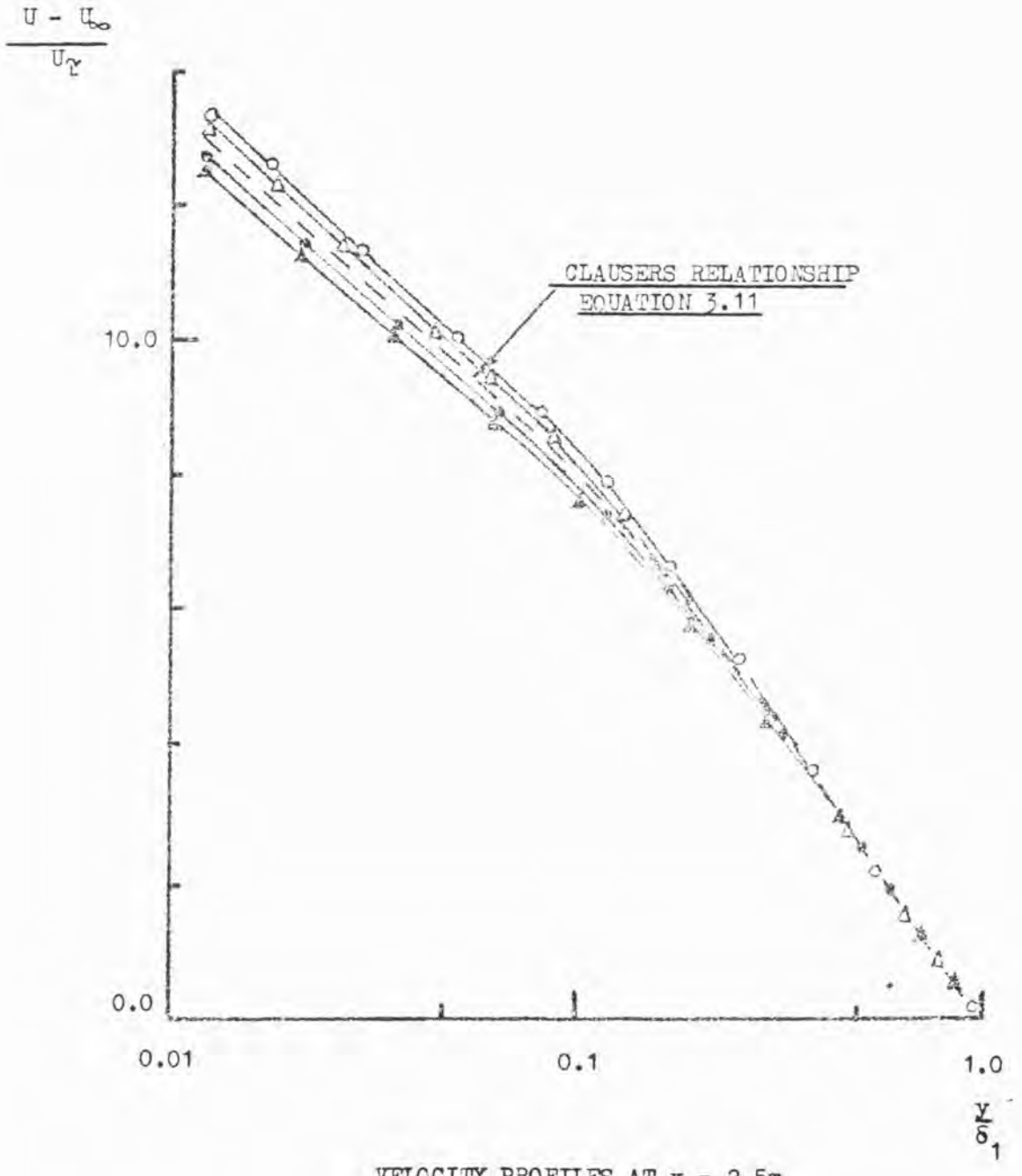

VELOCITY PROFILES AT x = 2.5m

FIGURE 5.2

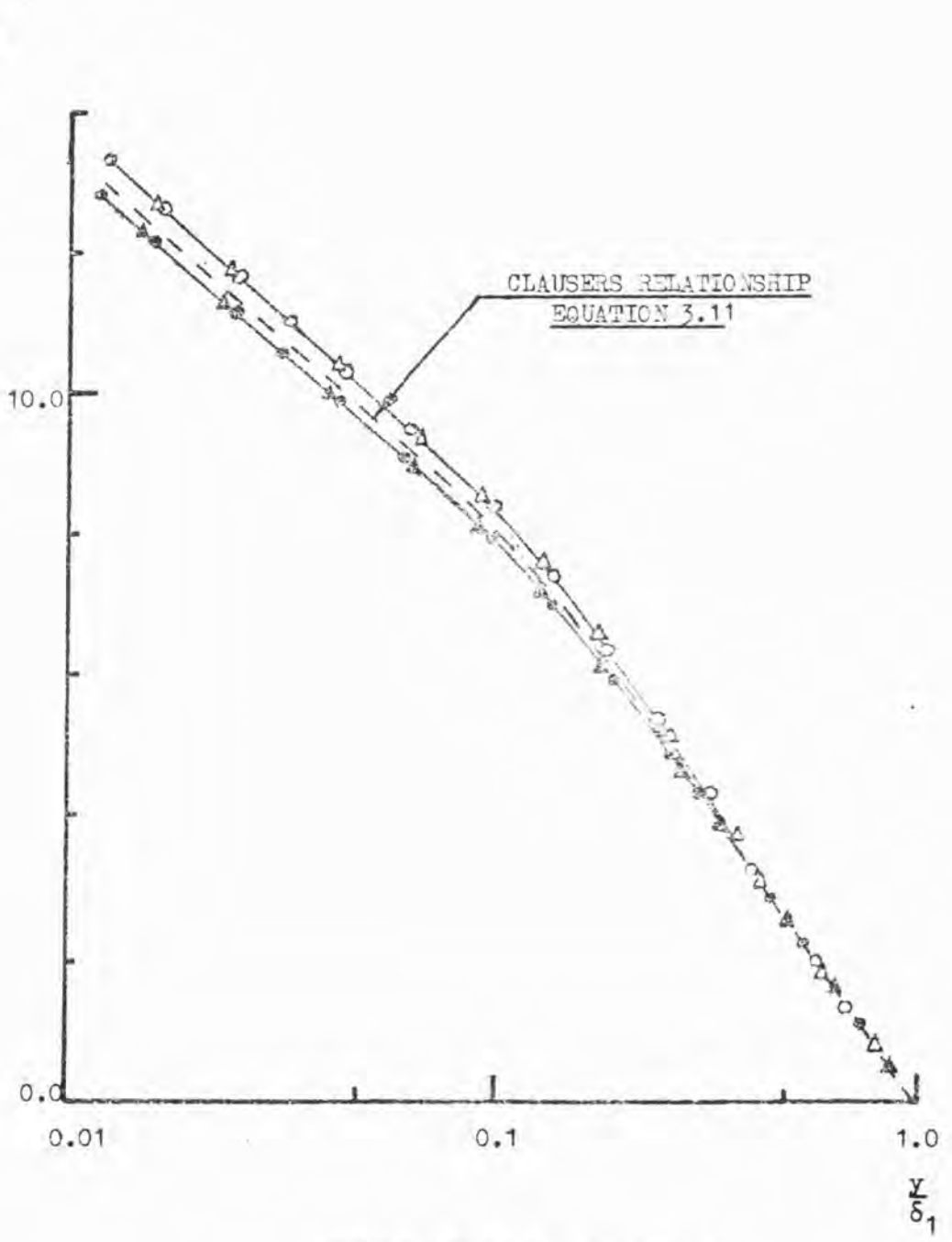

VELOCITY PROFILES AT x = 4.0m

FIGURE 5.3

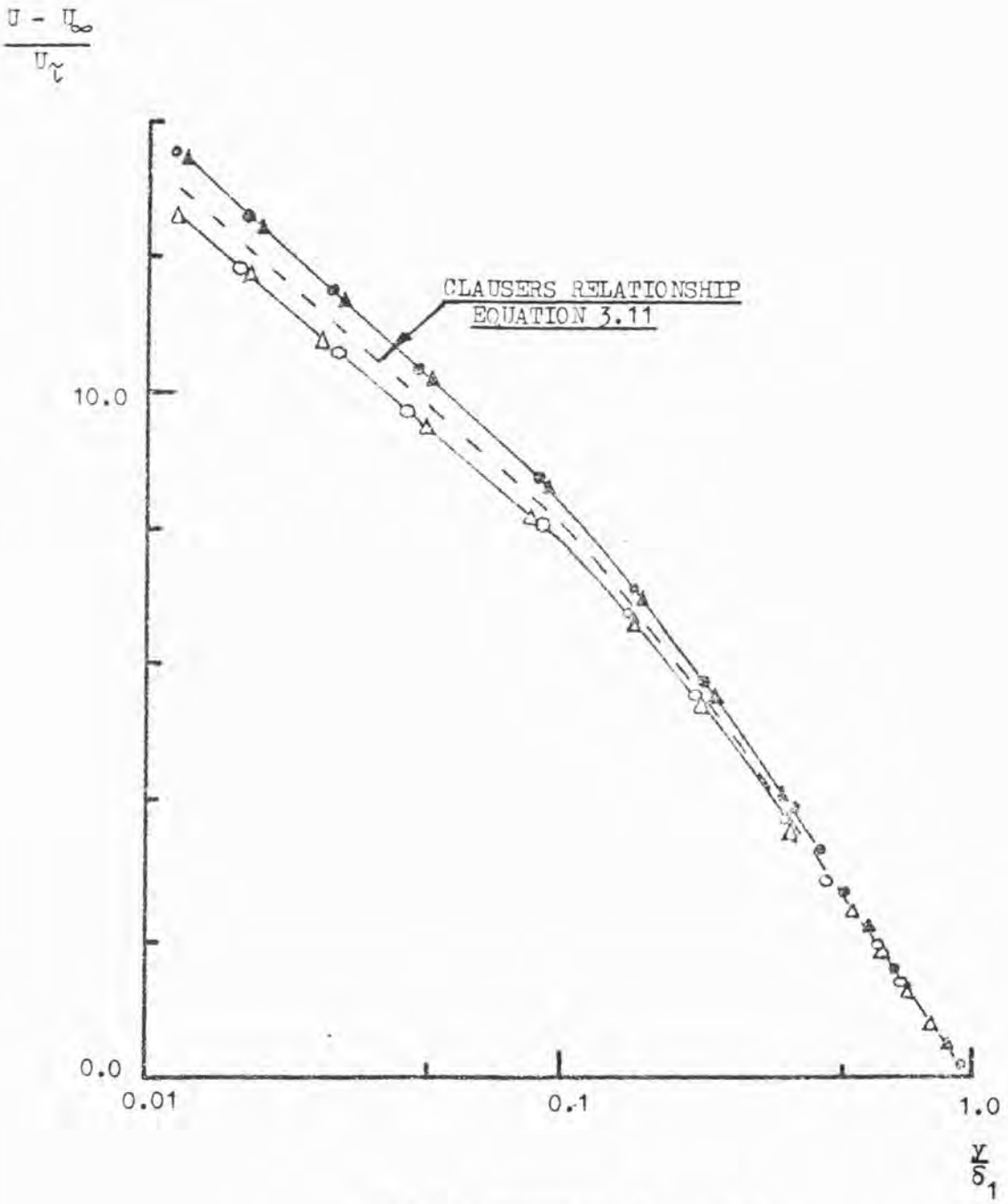

VELOCITY PROFILES AT x = 5.3m

FIGURE 5.4

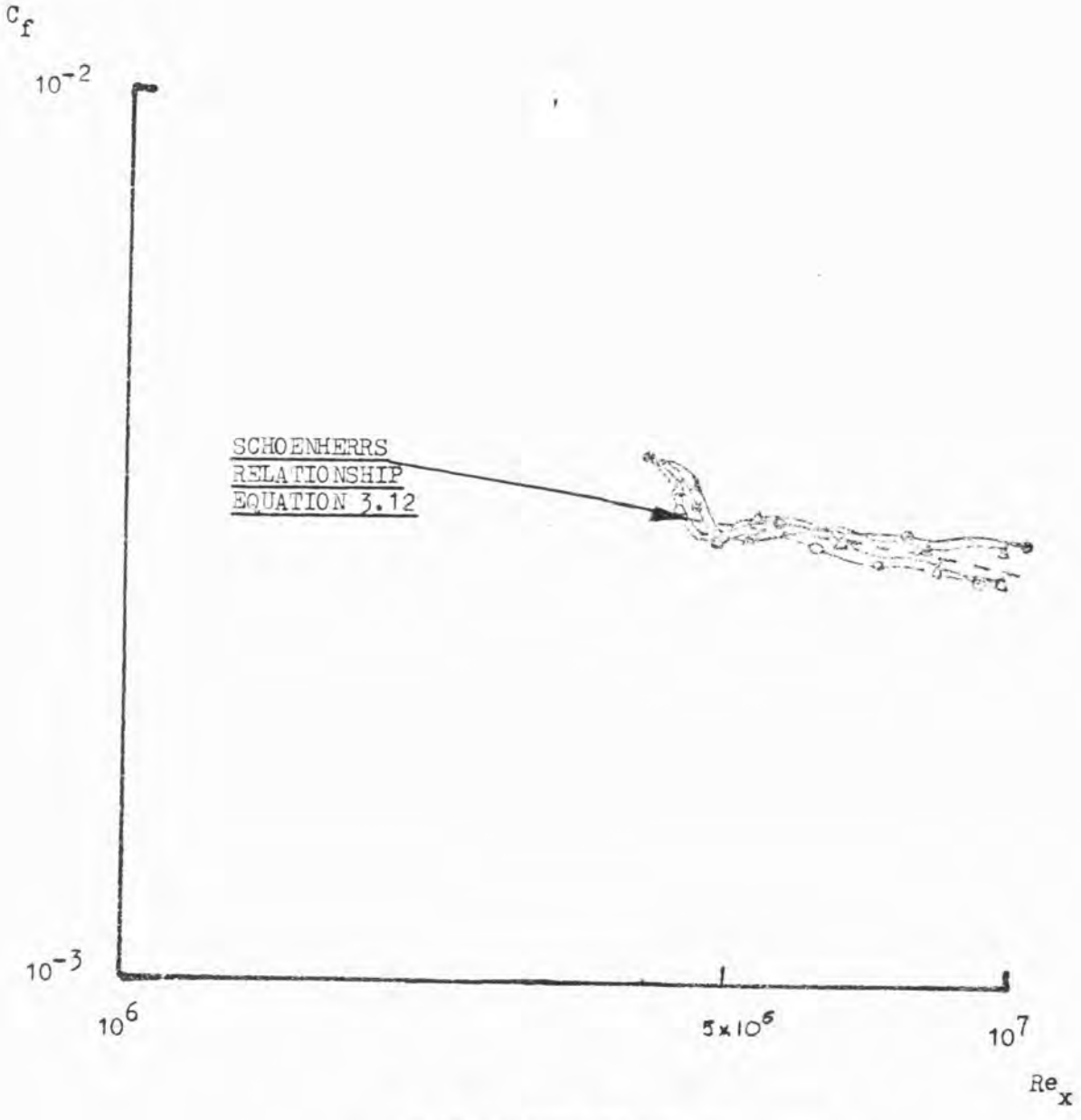

WALL RESISTANCE RELATIONSHIPS

FIGURE 5.5

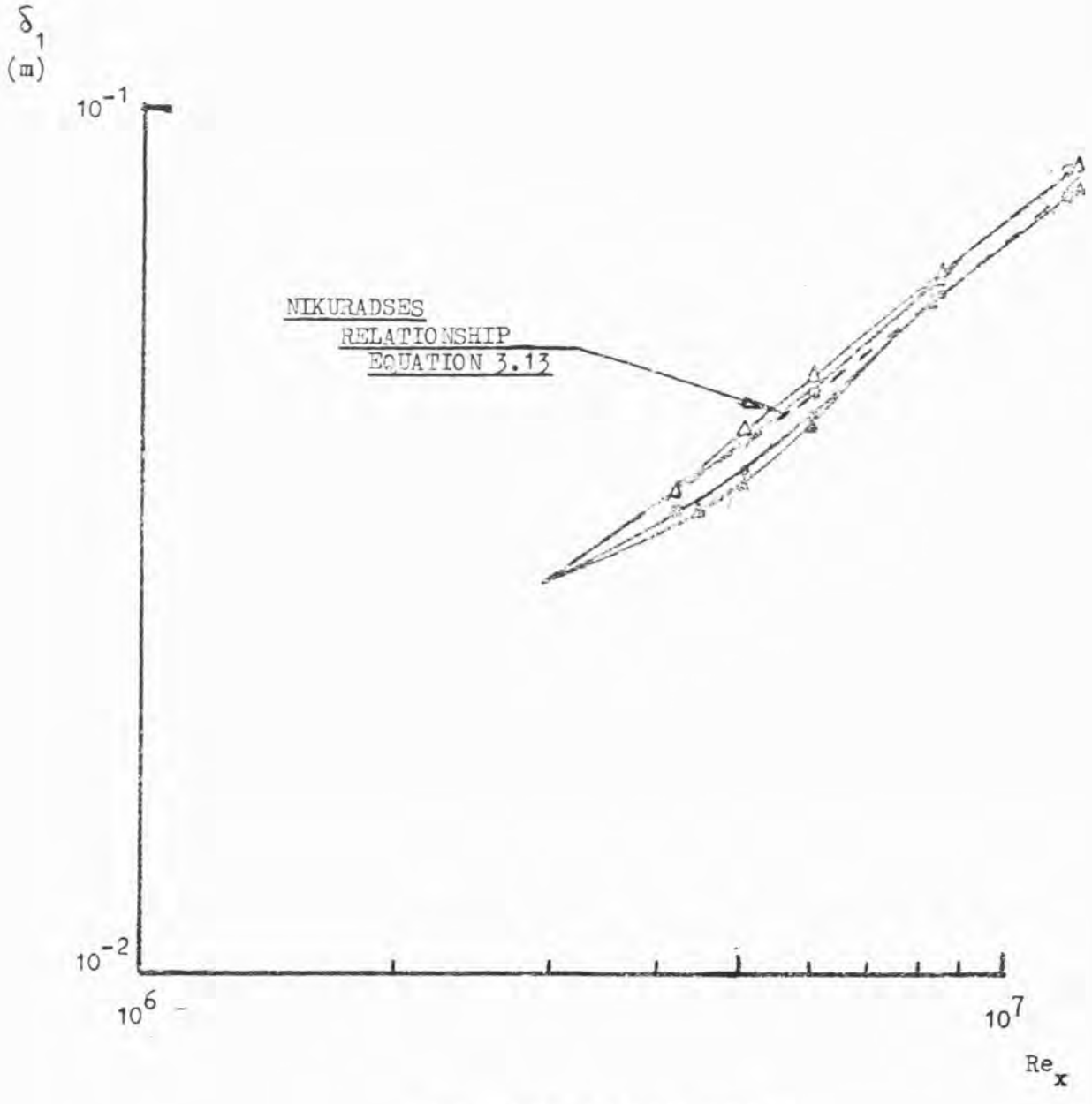

GROWTH RATE RELATIONSHIPS

FIGURE 5.6

Table 5.1

Symbols Used in the Computational Simulations

Symbol	$y_{1,2}$	Fr	L
Δ	$\delta_{1,1}/10^3$	1.121	10^3
o			10^5
▲	$\delta_{1,1}/10^5$	1.196	10^3
●			10^5

$\delta_{1,1}$ Thickness of boundary flow at the starting cross-stream section.

Table 5.2

Percentage Differences

	Symbol	Maximum percentage differences between the results from the modelling technique and equation 3.11 - .13, for the properties: $\frac{U - U_\infty}{U_\tau}$	C_f	δ_1
(a) at x = 2.5m				
	△	1.9	3.7	5.8
	○	5.9	-3.4	1.9
	▲	-4.5	3.1	-3.4
	●	-2.5	3.5	-6.5
(b) at x = 4.0m				
	△	5.3	-2.0	5.6
	○	5.3	-6.4	
	▲	-2.4	1.6	-1.4
	●	-2.4	3.9	
(c) at x = 5.3m				
	△	-5.0	-2.7	7.3
	○	-5.0	-3.4	
	▲	5.5	4.4	-1.2
	●	5.5	7.1	

In the region where $2.5 \leqslant x \leqslant 4.0$m the discrepancies in the predictions from the modelling technique are dependent upon the mesh gradings and velocity gradient limit used in the simulations. A measure of this correlation is provided by the comparisons involving the:

a) cross-stream velocity profiles at x = 2.5 and 4.0m,

and b) total skin friction and boundary layer thickness relationships for $2.5 \leqslant x \leqslant 4.0$m

presented in figures 5.2, 5.3, 5.5 and 5.6 respectively. More particularly the maximum percentage discrepancies at x = 2.5m in table 5.2 clearly show the specified dependence

The discrepancies in the computational results over the remainder of the flow, where $4.0 \leqslant x \leqslant 5.3$m, are again dependent upon the mesh gradings and velocity gradient limits. Close to the surface this correlation is marked - as shown by the presented comparisons concerning the total skin friction for $8 \times 10^6 \leqslant Re_x \leqslant 10^7$ $(4.0 \leqslant x \leqslant 5.3m)$ in figure 5.6. However over the remainder of the flow the discrepancy is almost totally dependent upon the velocity gradient limit used. As shown in the presented comparisons of:

a) the cross-stream velocity profiles at x = 4.0 and 5.3m

and b) the growth rate relationship at, and between, x = 4.0 and 5.3m

in figures 5.3-5.6, and table 5.2 b and c.

5.1b Boundary Layer with Tangential Air Injection Along the Impervious Surface

Seban and Back [39] have measured momentum and heat transfer rates in a series of boundary layer flows. These flows were produced by injecting air at the impervious surface of an established boundary layer - as shown by the schematic representation of the flow in figure 5.7 . The injected air was introduced parallel to the surface through a nozzle of specified width δ_N . The flow produced consisted of:

a) the mixing region - where the injected air and established boundary layer mixed

and b) a new boundary layer.

When studying momentum transfer rates Seban and Back characterized the flow in the boundary layer by plotting:

a) several cross-stream velocity profiles, of the form non-dimensional velocity against momentum thickness,

and b) the variation of the total skin friction with distance along the impervious surface.

The flow situation chosen for simulation is one where the free-stream velocity of the established boundary layer is $25ms^{-1}$. The depth of the injection nozzle δ_N is 0.00635m, and the volumetric flowrate of air passing through it is 0.128 m^2/s per metre width of the nozzle. The results from this flow situation comprise, three cross-stream velocity profiles - at x/δ_N = 18.2, 30.6 and 62.4 - and the total skin friction relationship , and are shown by dotted lines in figure 5.8 and 5.11 respectively.

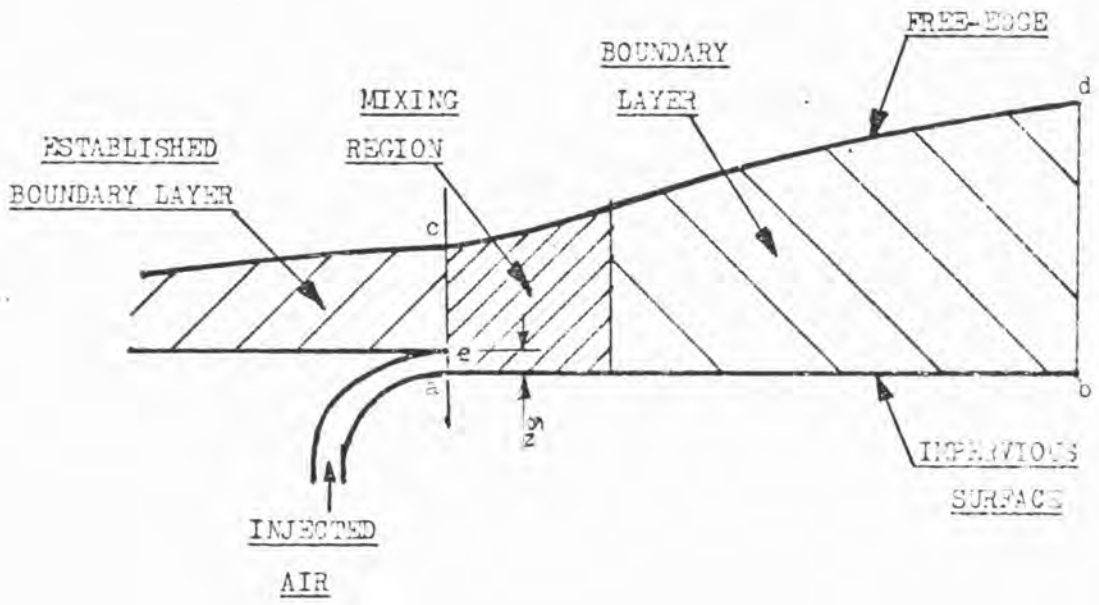

EXPERIMENTAL ARRANGEMENT

FIGURE 5.7

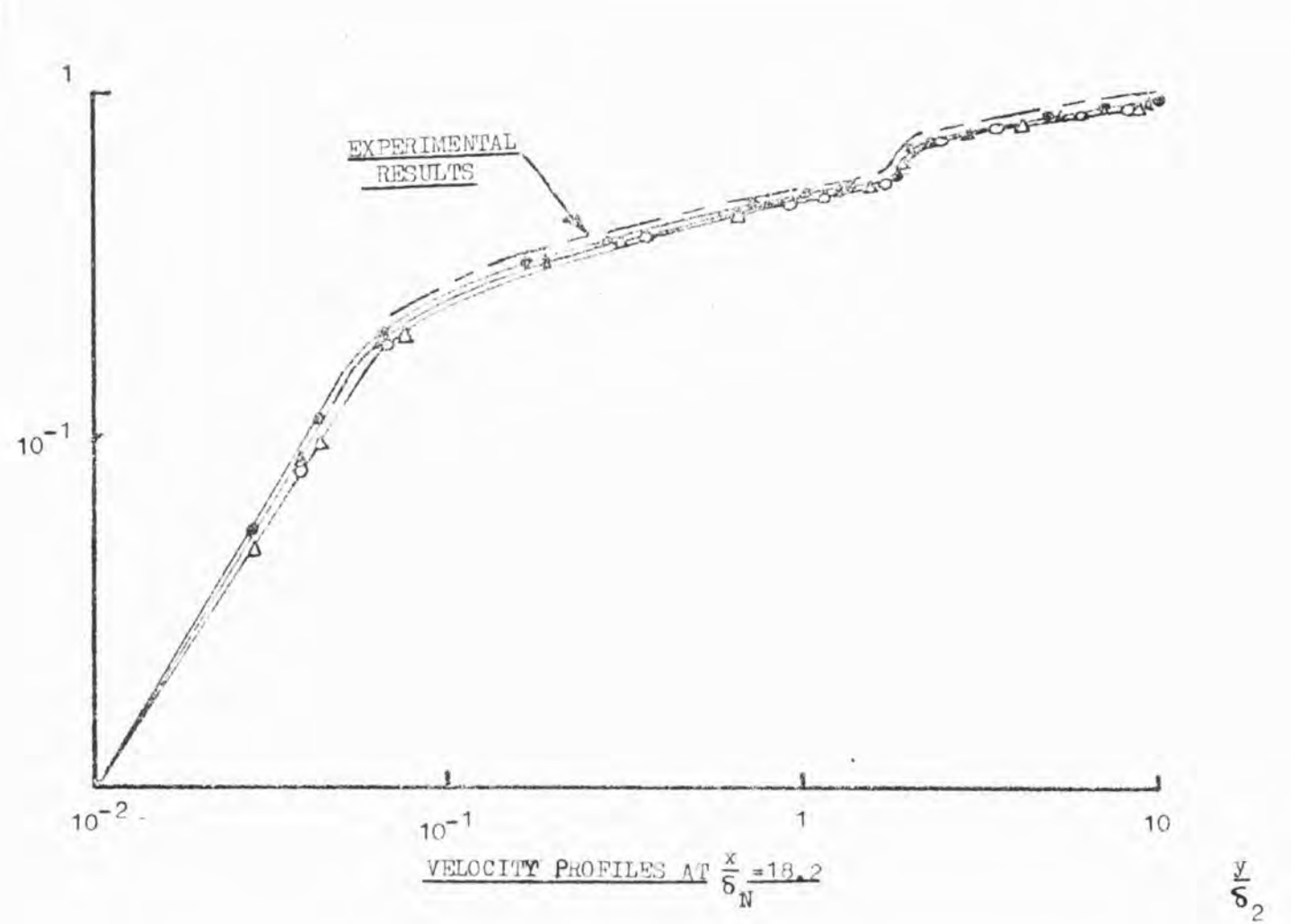

VELOCITY PROFILES AT $\frac{x}{\delta_N} = 18.2$

FIGURE 5.8

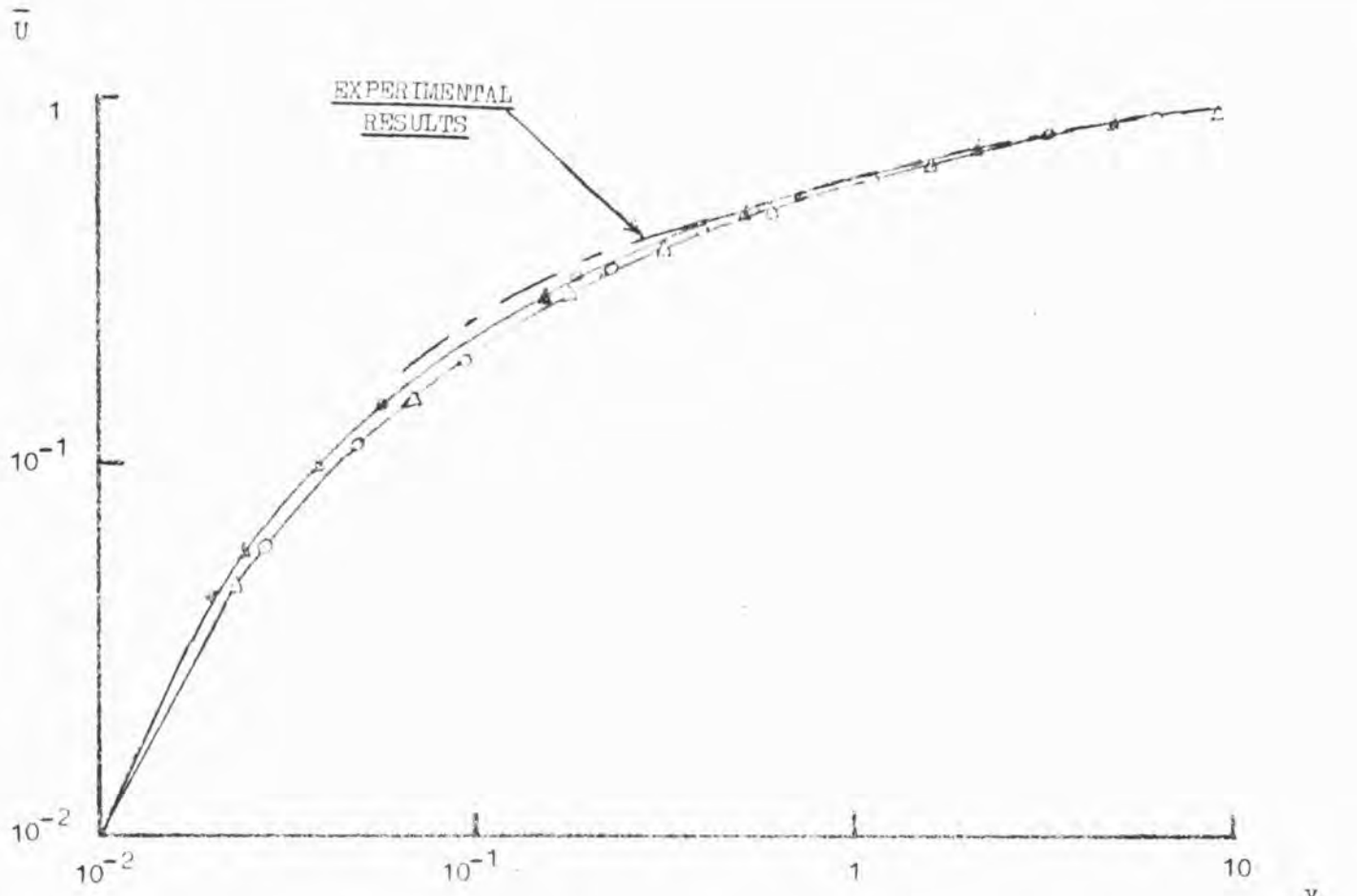

VELOCITY PROFILES AT $\frac{x}{\delta_N} = 30.6$

FIGURE 5.9

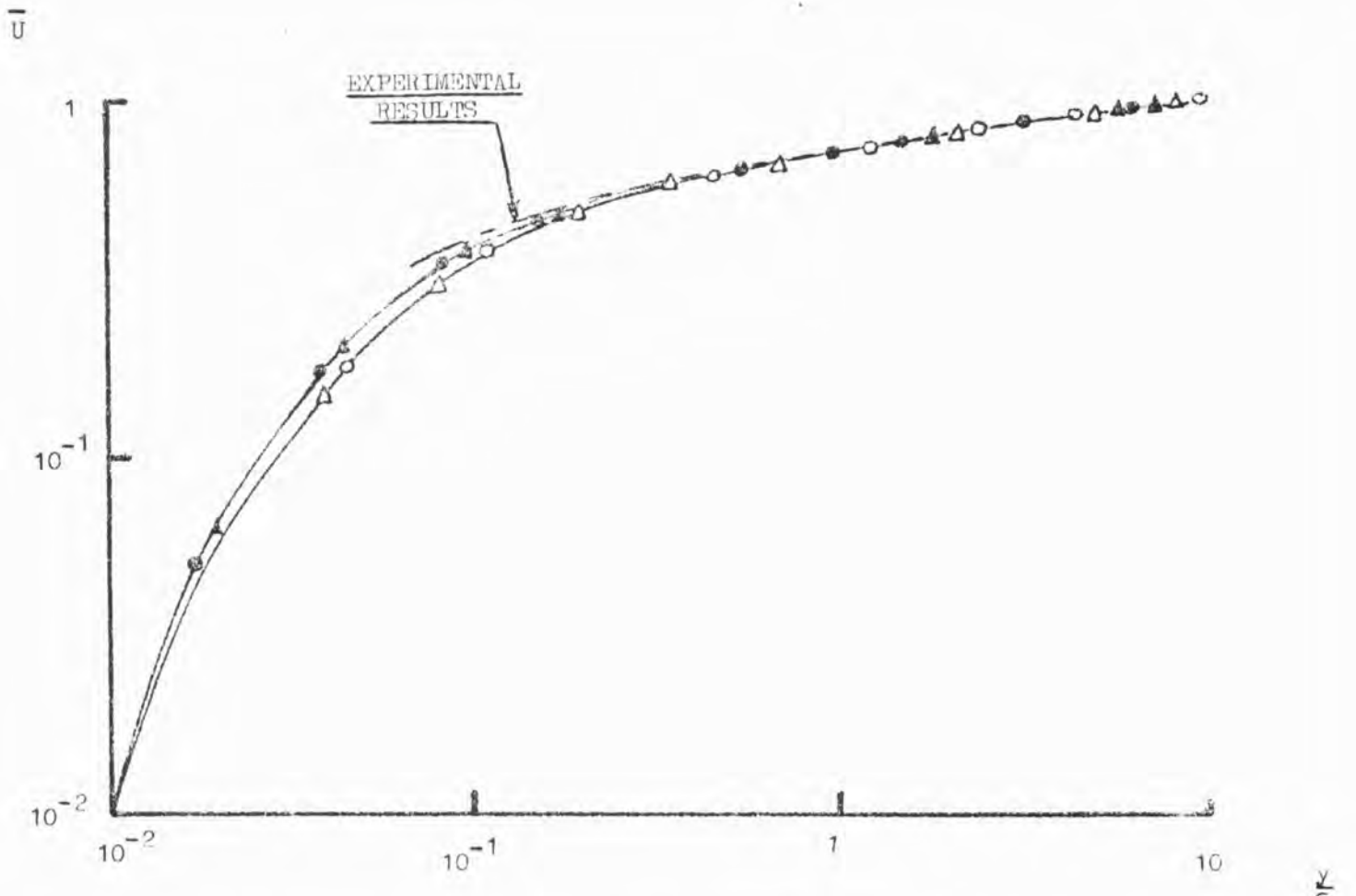

VELOCITY PROFILES AT $\frac{x}{\delta_N}$ =62.4

FIGURE 5.10

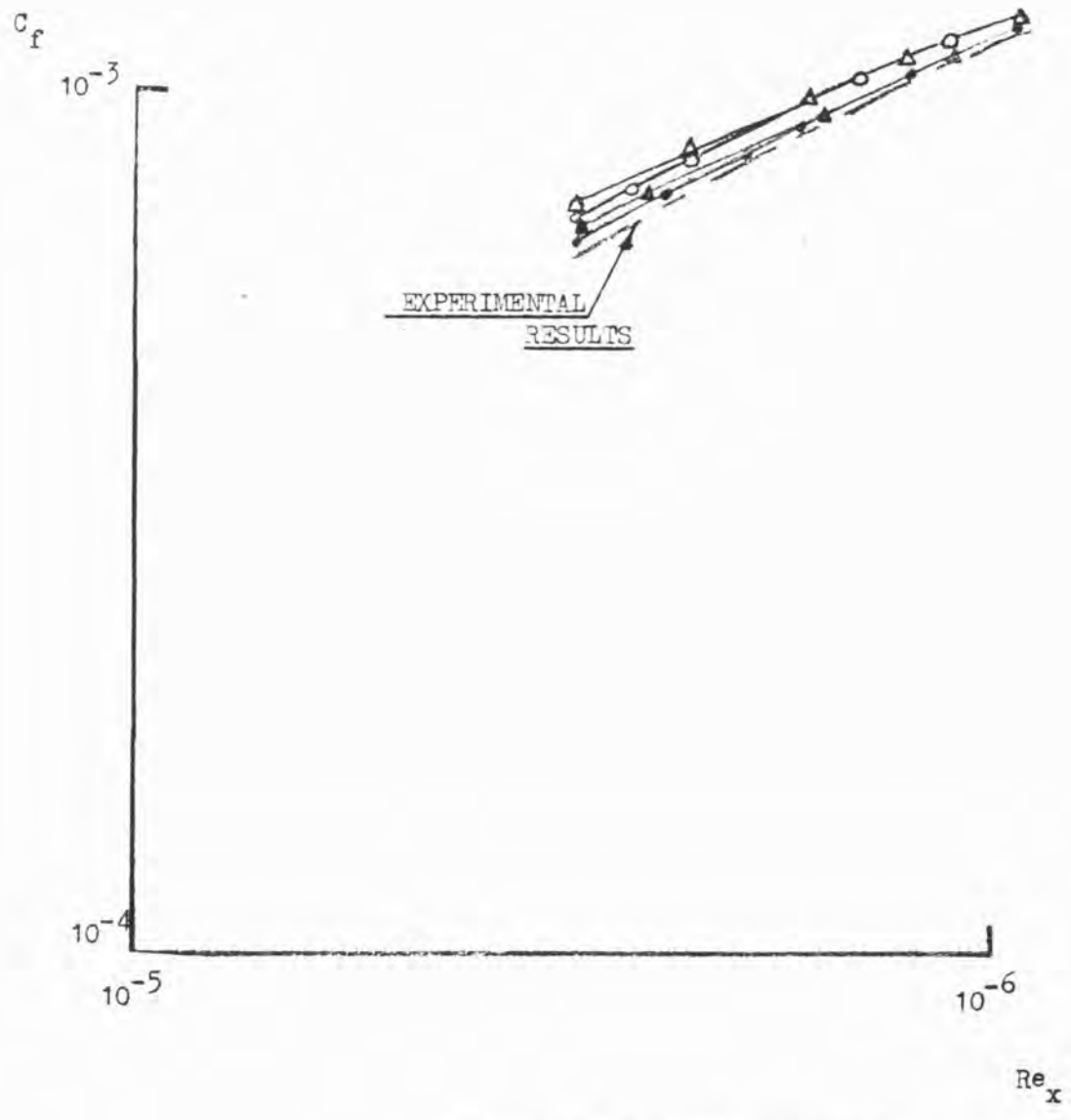

WALL RESISTANCE RELATIONSHIP

FIGURE 5.11

Four different computational simulations of the mixing region and boundary layer are presented. They correspond to the two forms of mesh 'a' and 'b', and two different velocity gradient limits 'i' and 'ii' described in the introduction of this section. The following boundary conditions have been used in each simulations:

a) along that portion of the starting cross-stream section occupied by the injected air, ae in figure 5.7, the velocity was assumed constant and equal to it's average value,

b) along the remainder of this section, ec in figure 5.7, the velocity profile of the established boundary layer was derived from Clausers relationship 3.11.

and c) at the impervious surface and free edge, ab and bc respectively, the velocity was set to zero and the free-stream value

Specimen results from the computational simulation are presented in figures 5.8 to .11. The symbols used in these figures are detailed in table 5.1.

The maximum discrepancies between the specimen results from the computational simulations and Seban-Zacks experimental study, for x/δ_N = 18.2, 30.6 and 62.4, are detailed in table 5.3.

In that portion of the simulation where $18.2 \leqslant y/\delta_N \leqslant 30.6$ the discrepancies in the predictions are dependent upon the the mesh grading and velocity gradient limit. An indication of this correlation is provided by the comparisons of the:

a) cross-stream velocity profiles at x/δ_N = 18.2 and 30.6,

and b) total skin friction relationship

Table 5.3

Percentage Differences

	Symbol	Maximum percentage discrepancies between the predicted and experimental values of: $\overline{U}$	C_f
(a) at $x/\delta_N = 18.2$			
	△	-10.4	12.3
	○	-10.4	9.7
	▲	-7.2	10.1
	●	-4.2	6.9
(b) at $x/\delta_N = 30.6$			
	△	-11.3	9.0
	○	-11.3	9.0
	▲	-7.9	3.2
	●	-7.9	3.2
(c) at $x/\delta_N = 62.4$			
	△	-10.8	7.1
	○	-10.8	7.1
	▲	-5.2	2.9
	●	-5.2	2.9

in figures 5.8, .9 and .11 respectively. Further evidence of the correlation is provided by the data concerning the percentage discrepancy at x/δ_N = 18.2 and 30.6 detailed in table 5.3a and b.

Over the remainder of the boundary layer, where $30.6 \leqslant x/\delta_N \leqslant 62.4$, the discrepancies in the predictions are largely dependent upon the velocity gradient limit. As shown by the comparisons concerning the:

a) cross-stream velocity profiles at x/δ_N = 30.6 and 62.4

and b) total skin friction between x/δ_N = 30.6 and 62.4

detailed in figures 5.9, .10 and .11 and table 5.3.

The presented computational results show that the modelling techniques can accurately simulate momentum transfer rates within the specified boundary flow. However, both the mesh grading and velocity gradient limit used in the simulations affect the accuracy of the predictions.

5.1c Plane Wall Jet

The experimental study of plane wall jets by Schwarz and Cosart[32] detailed in chapter 3 is again simulated. A schematic representation of the flow has been detailed in figure 3.9.

The experimental results are re-presented, with chain dotted lines, in figures 5.12 to .19 and comprise:

a) the variation of maximum velocity and jet thickness with distance along the impervious surface x

and b) three cross-stream velocity profiles at x = 0.46, 1.0 and 1.83m.

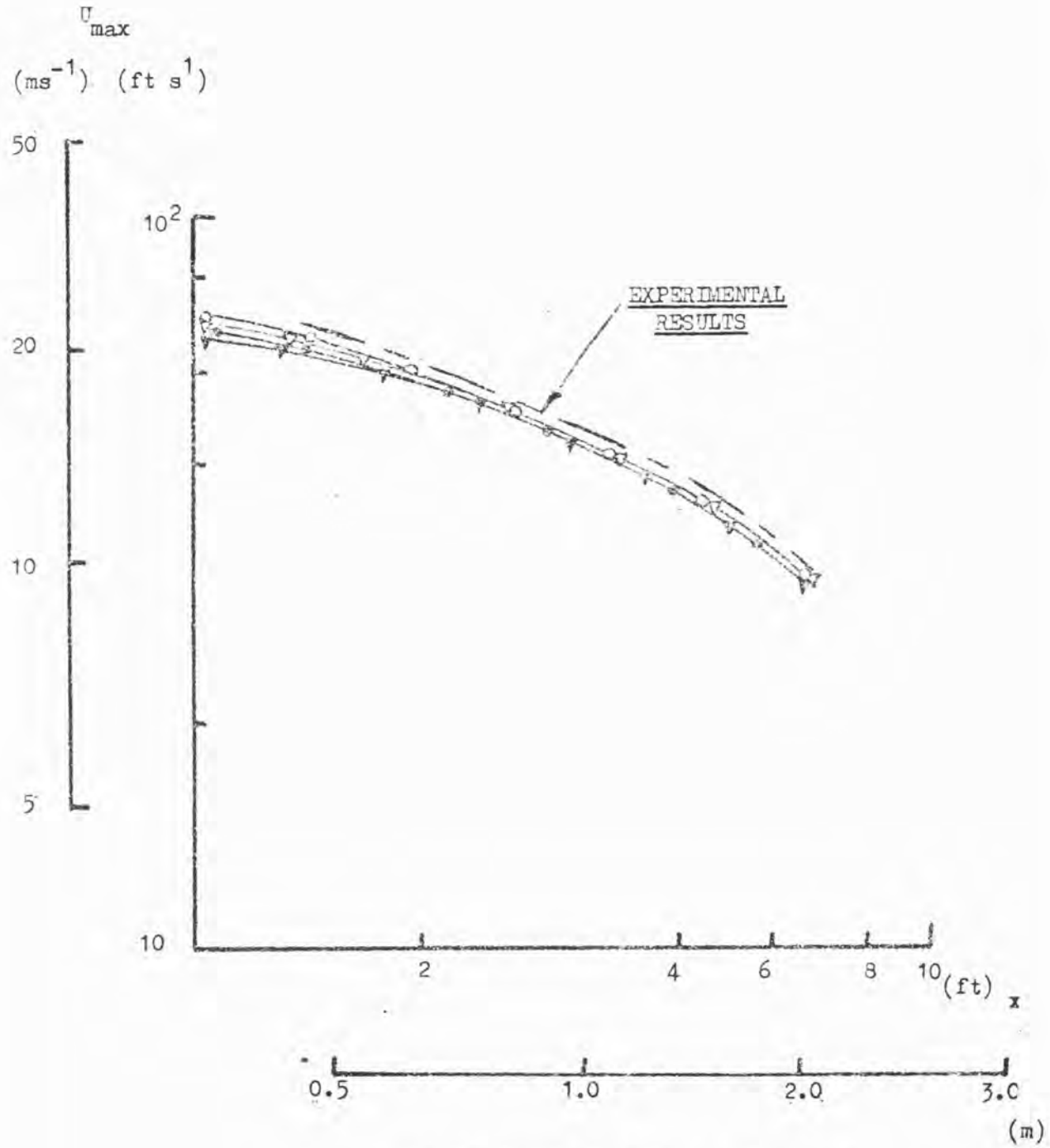

VARIATIONS IN THE MAXIMUM VELOCITY

FIGURE 5.12

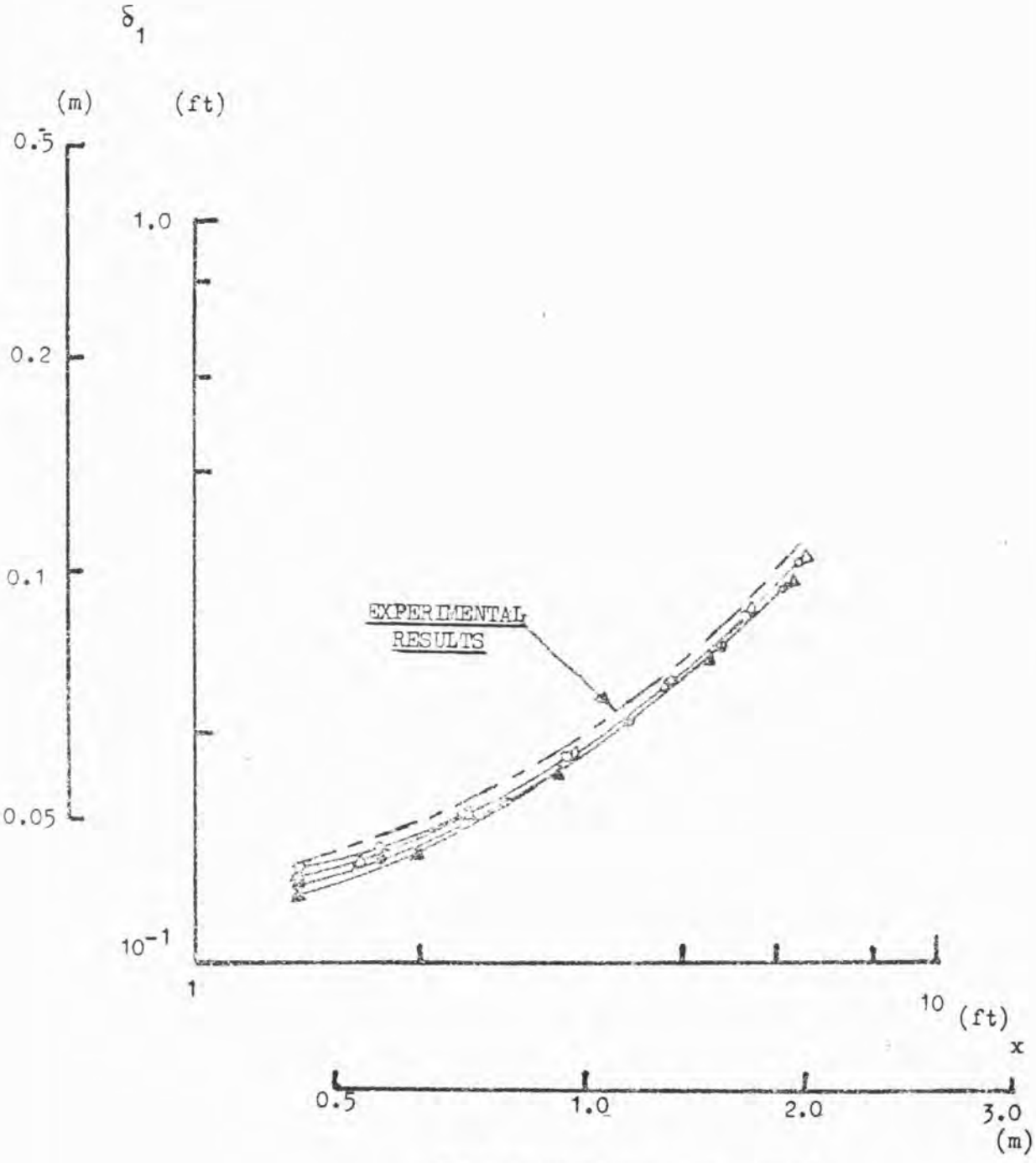

VARIATIONS IN THE GROWTH RATE

FIGURE 5.13

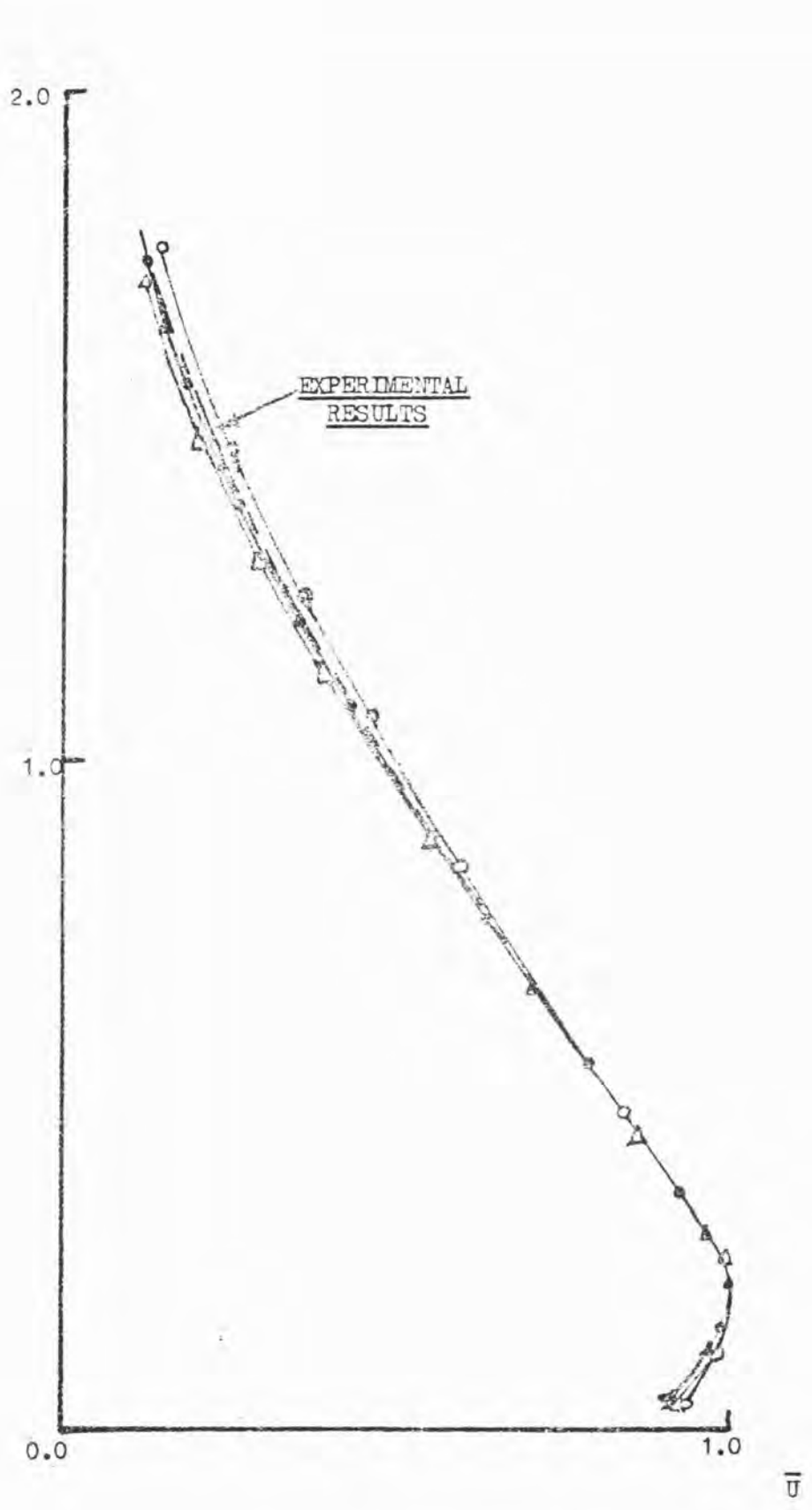

VELOCITY PROFILES AT x = 0.46m

FIGURE 5.14

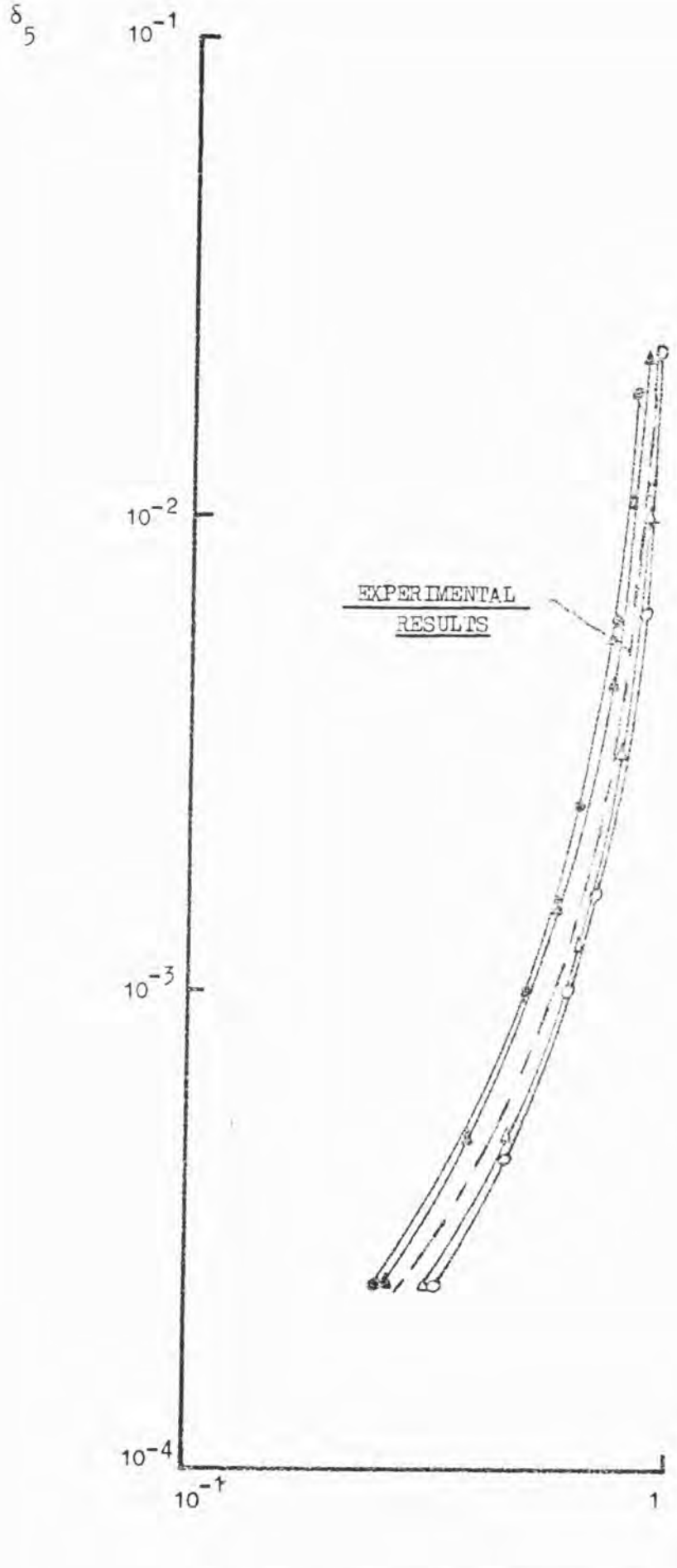

VELOCITY PROFILES AT x = 0.46m

FIGURE 5.15

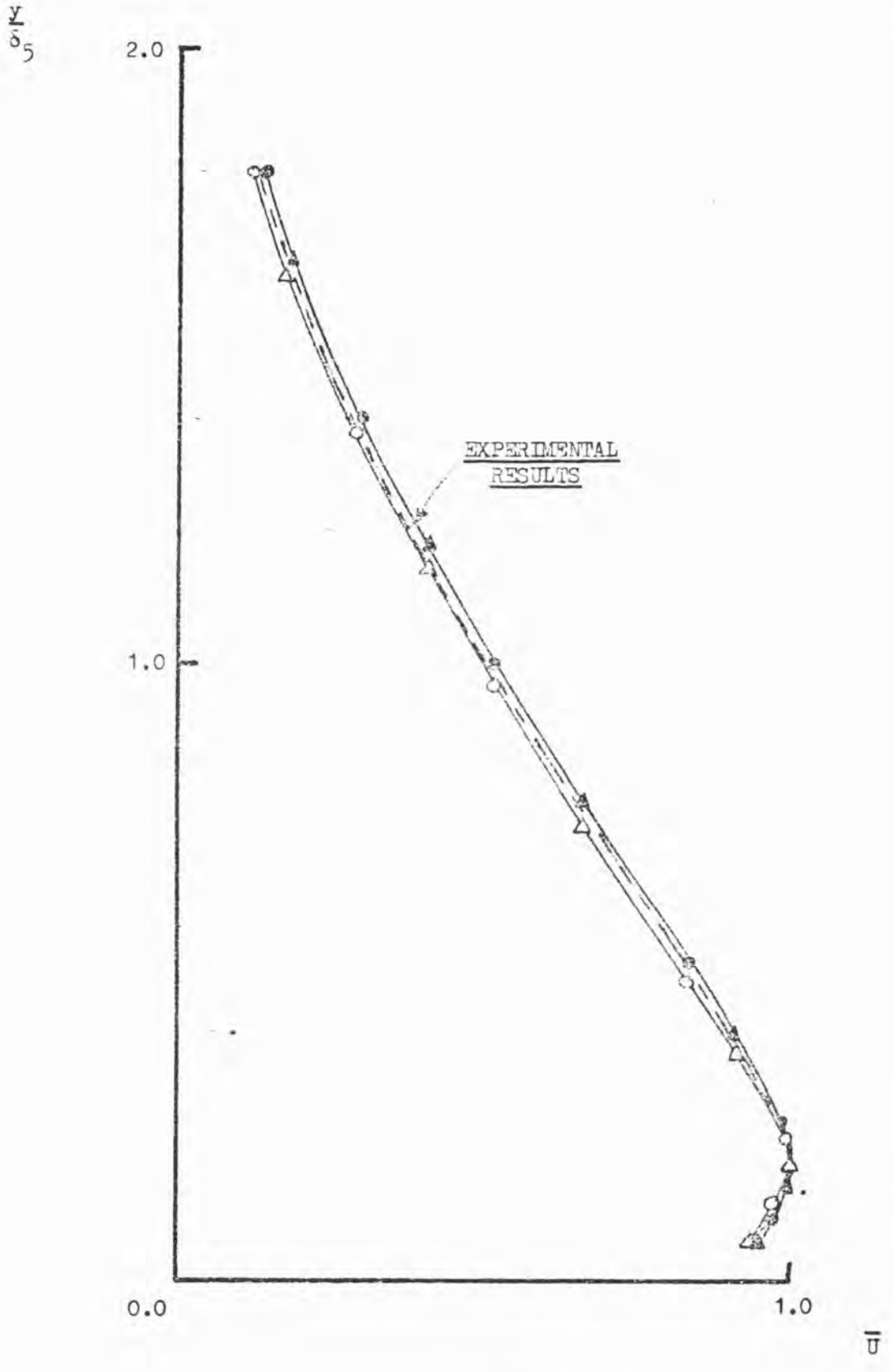

VELOCITY PROFILES AT x = 1.0m

FIGURE 5.16

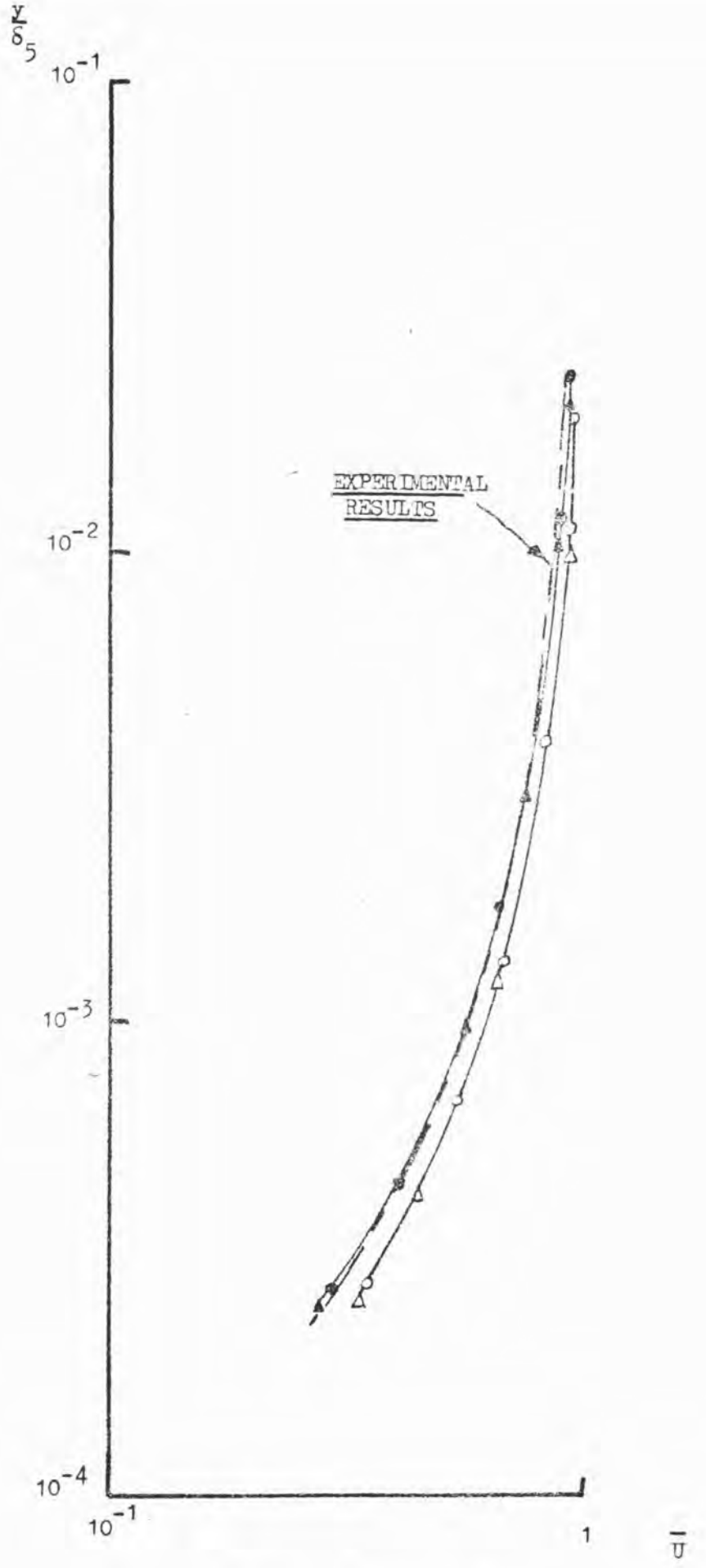

VELOCITY PROFILES AT x = 1.0m

FIGURE 5.17

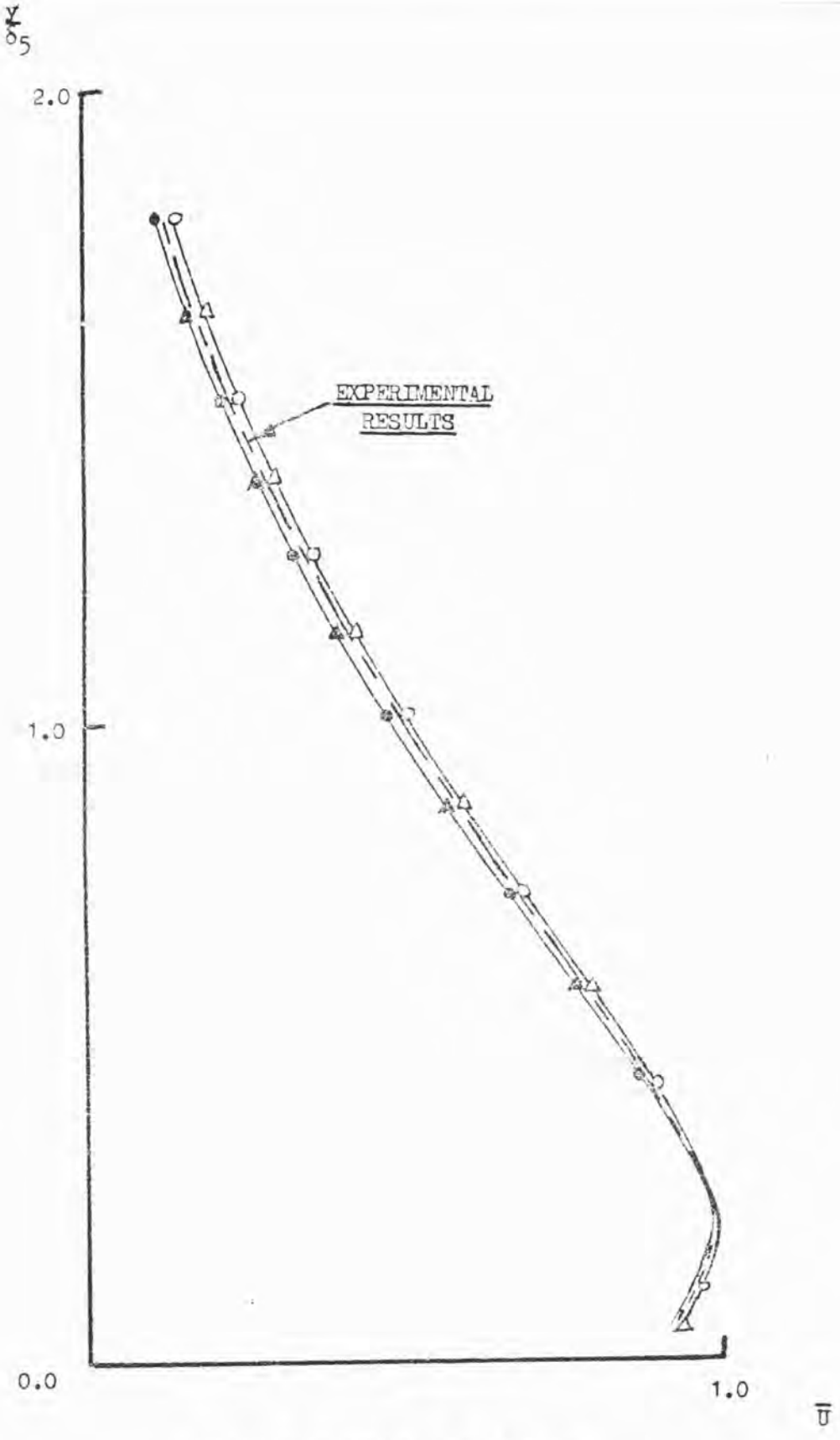

VELOCITY PROFILES AT x = 1.86m

FIGURE 5.18

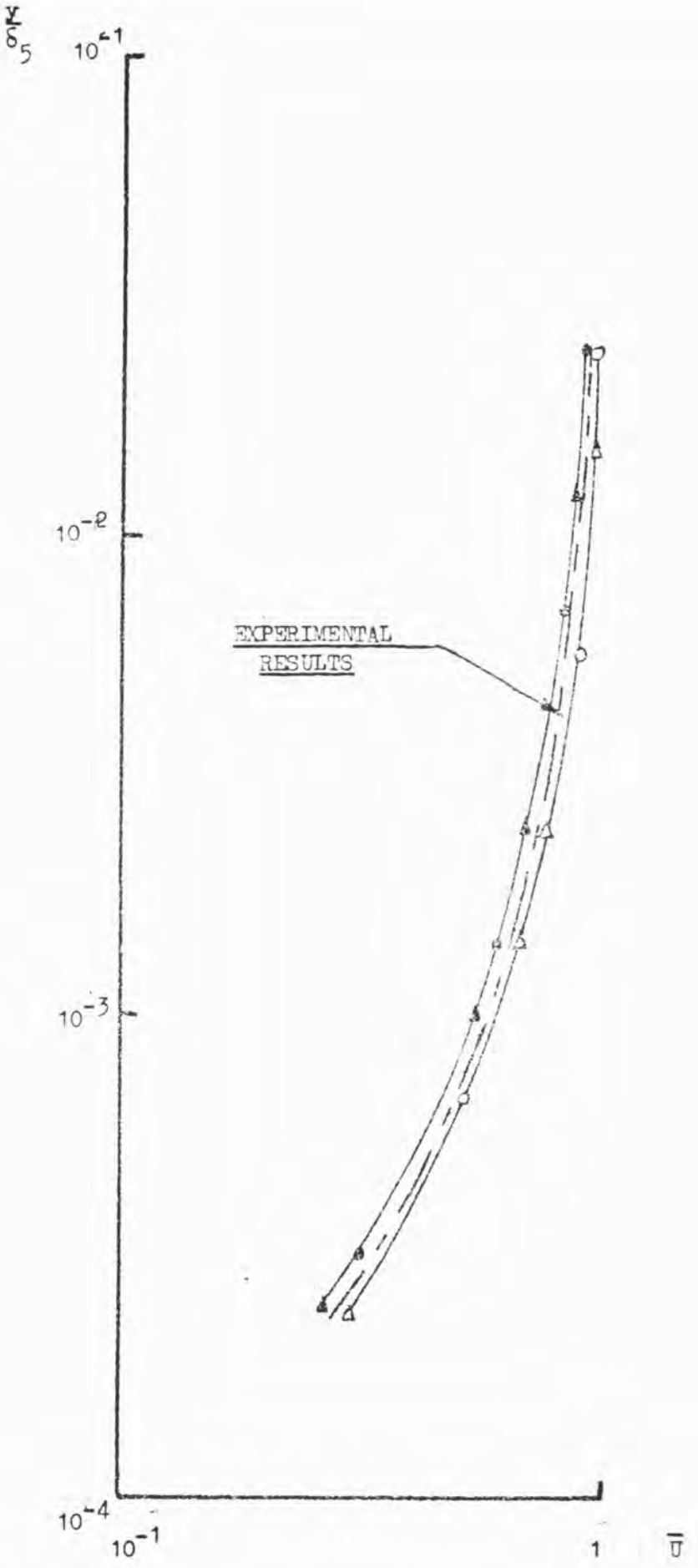

VELOCITY PROFILES AT x = 1.86m

FIGURE 5.19

The specified wall jet has been simulated four times between x = 0.0 and 1.83m. The four simulations correspond to the two forms of mesh 'a' and 'b' and two velocity gradient limits 'i' and 'ii' previously described. In each simulation the following boundary conditions were used:

a) along the starting cross-stream section, ab in figure 3.9, the velocity profile was set at the average velocity

and b) along the impervious surface and free-edge, ac and cd respectively in figure 3.9, the velocity was set to 0.0 and $U_{max}/10$ (U_{max} is the maximum velocity at a particular cross-stream section)

Selected results from each computational simulation are presented in figures 5.12 to .19 - the symbols used are detailed in table 5.1. The maximum discrepancies between the predicted and experimental results at x = 0.46, 1.0 and 1.83m are detailed in table 5.4.

At every cross-stream section within the wall jet the discrepancy between the predicted and experimental results increased as the impervious surface was approached. As shown by the specimen comparisons in figures 5.14 to .19; and more concisely by the maximum percentage discrepancies in table 5.4 for $y/\delta_5 < 10^{-1}$ and $y/\delta_5 - 1$, at x = 0.46, 1.0 and 1.83m. The term δ_5 represents the cross-stream height at which the mainstream velocity equals half it's maximum value at that section.

Table 5.4

Percentage Differences

	Symbol	Maximum percentage difference between the predicted and experimental values of $\overline{U}$ for:		Maximum percentage difference between the predicted and experimental values of:	
		$\frac{y}{\delta_5} < 10^{-2}$	$\frac{y}{\delta_5} = 1$	U_{max}	δ_1
(a) at x = 0.46m					
	△	13.4	-2.3	-5.7	-5.1
	○	14.4	4.1	-3.9	-2.2
	▲	-4.4	-1.3	-7.8	-7.3
	●	-9.4	-0.5	-9.4	-11.0
(b) at x = 1.0m					
	△	12.4	-0.5	-3.9	-5.3
	○	12.4	-0.5		
	▲	1.1	4.3	-5.9	-7.3
	●	1.1	4.3		
(c) at x = 1.83m					
	△	7.6	2.1	-2.7	-4.8
	○	7.6	2.1		
	▲	-5.8	-4.7	-4.3	-9.4
	●	-5.8	-4.7		

In two regions of the simulation the discrepancies in the predictions are dependent upon the mesh grading and velocity gradient limit. The two regions occupy the following parts of the wall jet:

a) $0.46 < x < 1.0$m for all y

and b) $10 < x < 1.83$ for $y < 10^{-2}$m

A measure of this correlation is provided by the comparisons concerning the:

a) velocity profiles at x = 0.46 and 1.0m in figures 5.14 to .17

and b) variation of the maximum velocity and wall thickness in figure 5.12 and .13 respectively.

Specific measurements of the discrepancy in the presented results, and thus of the described correlation, is given by the data detailed in table 5.4.

Over the remainder of the wall jet, where $1.0 \leq x \leq 1.83$m for $y < 10^{-2}$m, the discrepancies are dependent upon the value of the velocity gradient limit. As shown by the velocity profiles at x = 1.0 and 1.83m in figures 5.16 to .19, and the maximum velocity, and wall jet thickness relationships shown in figures 5.12 and .13 respectively. Again the maximum percentage discrepancies presented in table 5.4 provide evidence of this dependency.

Narasimha, Narayan and Parthasarathy[40] have postulated relationships that characterize the flow within a wide variety of wall jet situations. These relationships are of the form:

$$\frac{U_{max}\nu}{M_J} = f_1\left[\frac{xM_J}{\nu^2}\right] \quad (5.1$$

$$\frac{\delta_1 M_J}{\nu^2} = f\left[\frac{xM_J}{\nu^2}\right] \quad (5.2$$

$$\frac{\delta_5 M_J}{\nu^2} = f_3\left[\frac{xM_J}{\nu^2}\right] \quad (5.3$$

and

$$\frac{U_o \nu^2}{M_J} = f_4\left[\frac{xM_J}{\nu^2}\right] \quad (5.4$$

With M_J representing the jet momentum flux, which is discussed later, δ_5 representing the height at which the velocity is half the maximum at any cross-stream section - as shown in figure 3.9 and ν the kinematic viscosity at each station x. Narasimha, Narayan and Parthasarathys recommendations for these relationships are shown by the chain dotted lines in figure 5.20 to .23. These recommendations were obtained from a review of vast amounts of published experimental data, including Schwarz & Cosarts[3.2] study, concerning momentum transfer rates in wall jets. The extent of the scatter in the reviewed data about the recommended lines is shown in the presented figures by cross-hatching.

The relationships presented by Narasimha et al, 5.1 to .4, were derived from a dimensional analysis of the wall jet after applying the hypothesis of selective flow memory. This hypothesis is not new, and has often been tacitly or explicitly used for wake and jet studies - as detailed by Schlichting[22] and Townsend[41]. The hypothesis postulates that sufficiently far downstream in a flow the details of the initial conditions are not relevant; but rather certain combinations of parameters, which are dynamically equivalent,

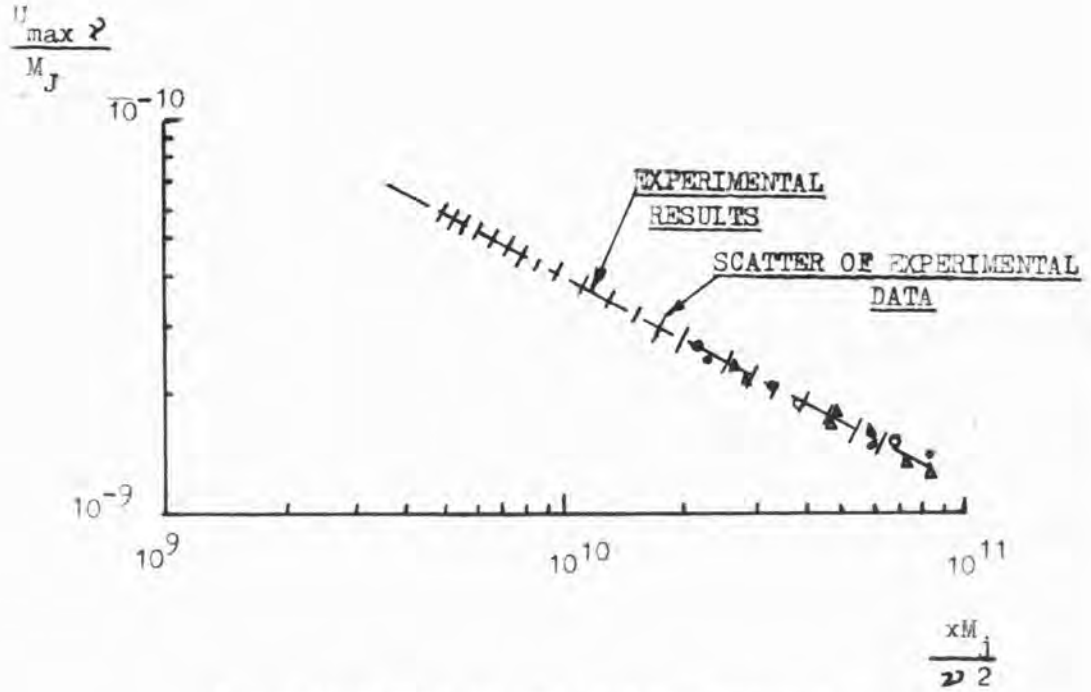

a THE VARIATION IN THE MAXIMUM VELOCITY

FIGURE 5.20

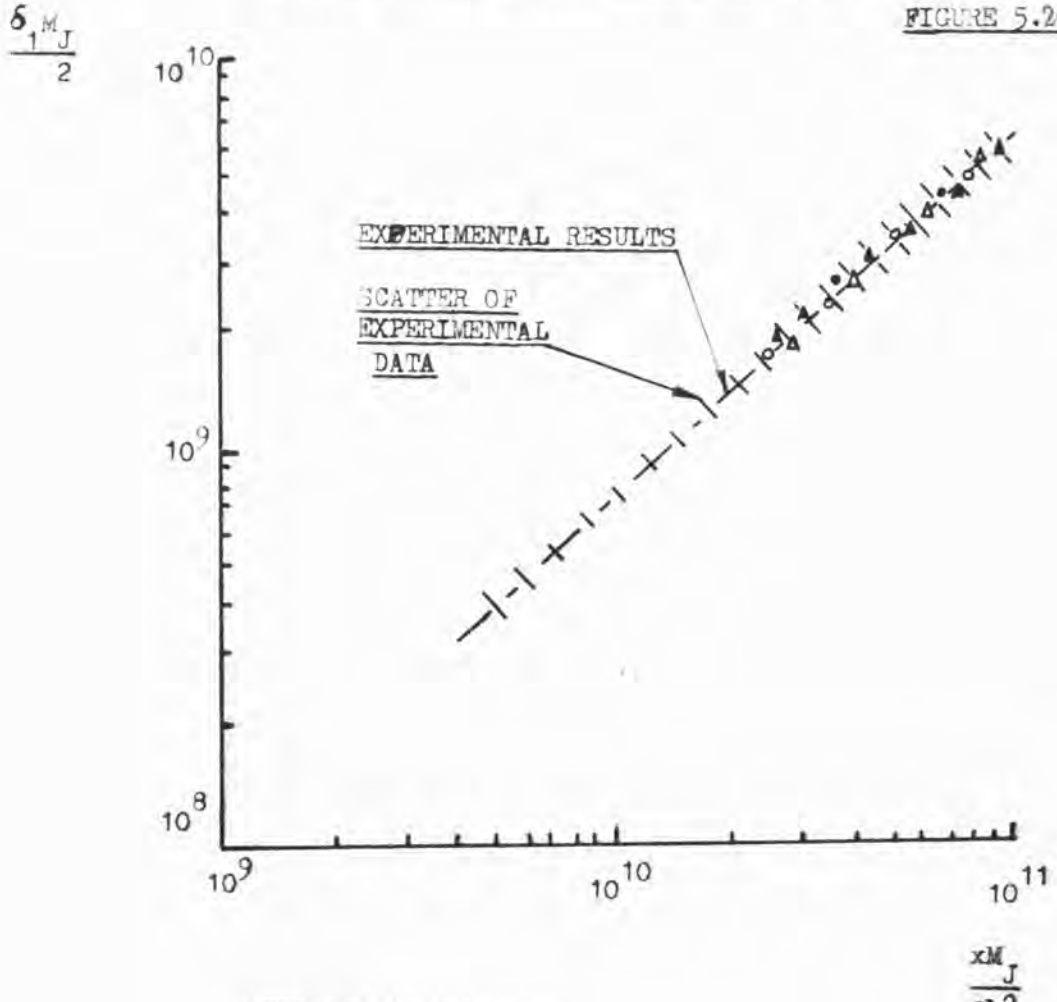

THE VARIATION IN THE TOTAL THICKNESS OF THE PLANE WALL JET

FIGURE 5.21

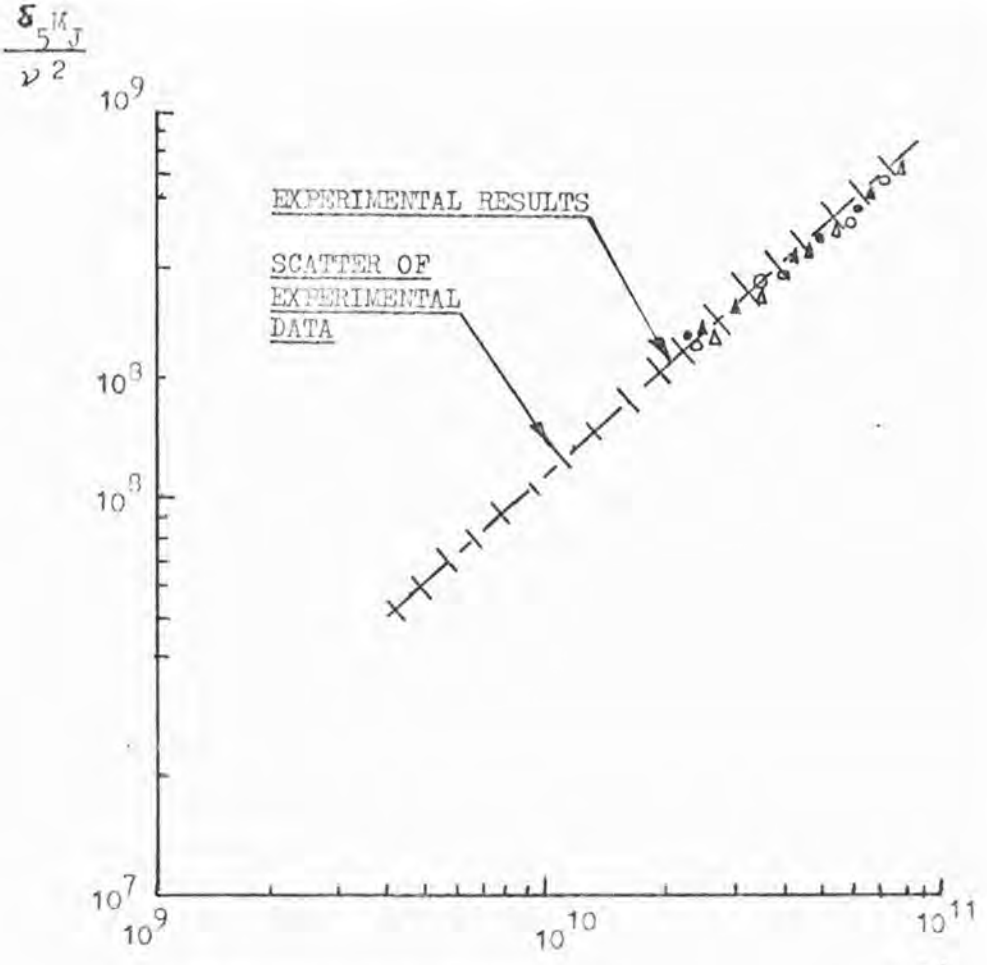

STREAMWISE VARIATIONS OF δ_5

FIGURE 5.22

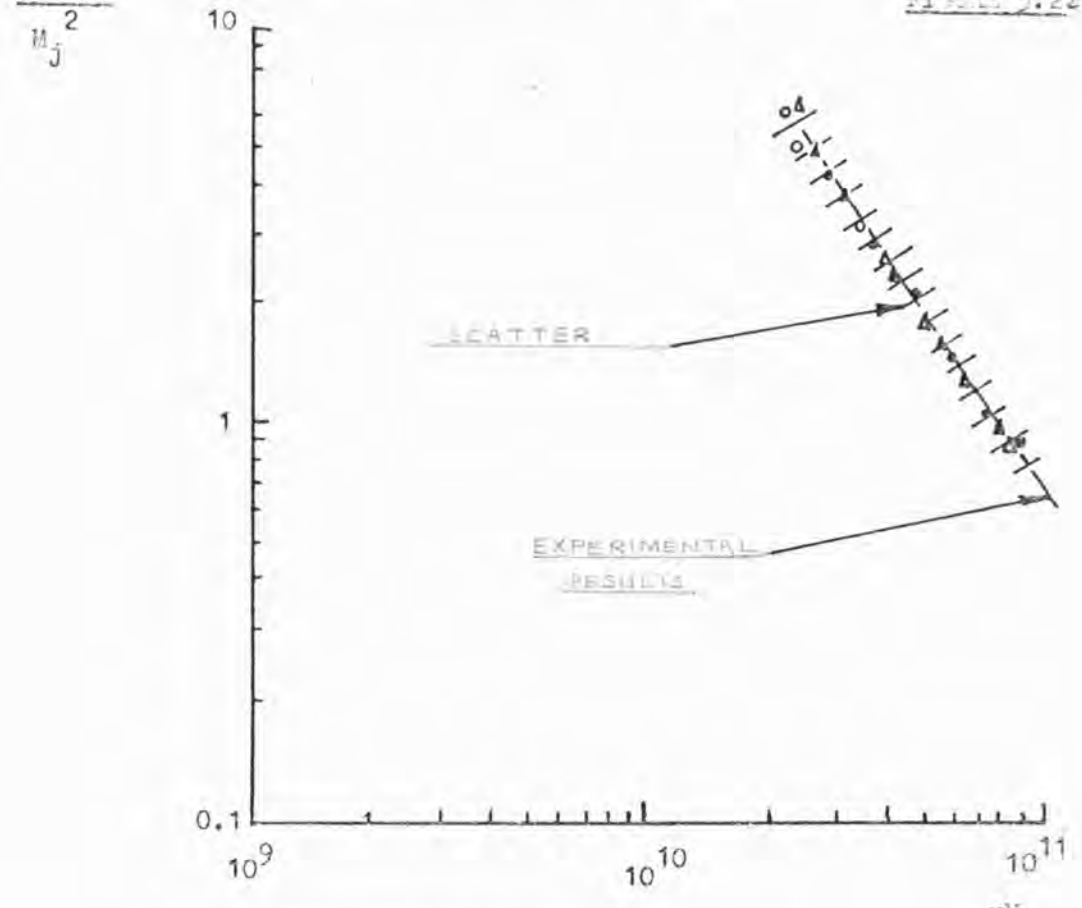

STREAMWISE VARIATION IN THE WALL SHEAR STRESS τ_0

FIGURE 5.23

are pertinent. Narashima et al proposed that these parameters could be expressed as the jet momentum flux $M_J = U_N^2 \delta_N$ - where U_N is equivalent to the average velocity of the air at the nozzle.

The results from the computational simulations of Schwarz and Cosarts experiment, are transformed into the form prescribed by Narasimha et al, and plotted in figures 5.20 to .23. The discrepancies between the predicted results and the recommended relationships fall within the quoted scatter of the experimental data.

The presented comparisons have shown that the modelling technique can accurately simulate momentum transfer rates in any wall jet that conforms to the relationships of Narasimha et al. With the descrepancy between predicted and experimental results slightly dependent upon the mesh grading and velocity gradient limit used.

5.2 Discussion

The major purpose of this discussion is to assess to what extent the finite difference approximations in the new modelling technique are superior to those used in the techniques proposed by Spalding - Patankar and Denny-Landis. The latter techniques were defined, used and discussed in chapter three . To achieve this assessment representative results from the three modelling techniques, for the same flow situations, are compared. In the simulations of each flow situation only the effects of the different finite difference assumptions are compared. This has been achieved by keeping the other variables - the turbulence models, physical properties, starting grading of the cartesian mesh network and starting velocity profiles - constant in each flow situation.

The flow situations chosen for comparison are the boundary layer detailed in figure 5.1, and the plane wall jet shown in figure 3.9. These situations have been simulated with the new modelling technique, as well as those proposed by Spalding-Pantankar and Denny-Landis. Data concerning the discrepancy between predicted and experimental results has been extracted from the specimen data presented in chapters three and five. The data relating to the boundary layer flow is detailed in table 5.5, and the results from the plane wall jet shown in table 5.7. The source of the presented data is also declared in these tables. Before comparing these results the variables held constant during the simulation are detailed. The results from the new and Denny-Landis techniques come from simulations that used the same starting mesh grading.

Table 5.5

Discrepancies in Boundary Layer

Predictions at x = 4.0m

Modelling Technique	Reported percentage discrepancies for the following flow properties: $\frac{U - U_\infty}{U_\infty}$	C_f	δ_1	Source of data
Spalding Patankar	-4.8	5.3	9.2	Table 3.2
FN = 1	-4.9	6.2		Table 3.4
Denny Landis			9.5	
FN = 2	4.8	3.6		Table 3.3
$L = 10^3$	4.2	-2.0		
New Technique			5.6	Table 5.2
$L = 10^5$	4.2	-6.4		

Table 5.6

Discrepancies in Wall Jets

Predictions at x = 1.0m

Modelling Technique	Reported percentage discrepancies for the following flow properties			Source of data
	$\bar{U}$ at $\frac{y}{\delta_5} = 1$	U_{max}	δ_1	
Spalding Patankar	0.5	7.2	9.0	Table 3.2
FN = 1 Denny	10.1	24.6	39.1	Table 3.6
Landis FN = 2	12.1	20.9	35.1	Table 3.5
$L = 10^3$ New Technique	-0.3	-3.9	-5.3	Table 5.4
$L = 10^5$	-0.5			

The grading along the starting 'y' ordinate was derived from equation 3.8, with $y_{1,2} = \delta_{1,1}/10^3$ and Fr = 1.121 ($\delta_{1,1}$ represents the width of the boundary flow at the starting cross-stream section). The grading used with the Spalding - Patankar technique is slightly different from that declared above, because the grading had to be modified to conform to the wall regime assumptions discussed in chapter three. In this case the grading along the starting 'y' ordinate was derived from equation 3.8 with $y_{1,2} = \delta_{1,1}/200$ and Fr - 1.12. In each flow situation the same velocity profiles were used as the starting boundary conditions. The boundary conditions for the boundary layer and wall jet situations are declared in sections 5.1a and c respectively. The same turbulence model and physical properties were used in all the simulations, they are defined in both sections 3.1 and 5.1.

In table 5.5 and 5.6 two sets of results are presented from both the Denny-Landis and new modelling technique. The results from the Denny-Landis technique are distinguished by the value of the variable FN, which can be either one or two. FN is the power to which the non-dimensional stream function was raised in the simulation - the use of the variable FN is discussed in chapter three. The two sets of results from the new modelling technique are distinguished by the value of the velocity gradient limit L. As will be remembered from chapter four, the grading of the mesh stream lines are modified at the starting section, so that the assumed cross-stream rate of change of velocity fell below the velocity gradient limit.

The predictions from the new modelling technique, including the samples in tables 5.5 and .6, are more accurate than those from the techniques proposed by Spalding-Patankar & Denny-Landis. From this it can be deduced that the finite difference approximations of the new modelling technique are the most accurate of those considered for $10^3 \leqslant L \leqslant 10^5$. (It will be remembered that the other variables of the modelling technique have, as far as is practical, been kept constant in the simulation of each flow situation).

In these specific flow situations estimates can be made of the contribution of numerical diffusion to the overall error from the finite difference approximations. As stated in chapter four the numerical diffusion is represented by:

$$U''(\omega).(R_1 + R_3)\ \frac{\Delta\omega^2}{2} + U''(x)(P_1 - P_3)_t \Delta x \Delta\omega$$

where the R^s and P^s are dependent upon the form of non-dimensional stream function. In both specimen flow situations $U''(\omega) \rangle\rangle U''(x)$, and thus in this examination it has been assumed that numerical diffusion is represented by:

$$U''(\omega)(R_1 + R_3)\ \frac{\Delta\omega}{2}^2$$

In both flow situations the numerical diffusion will be largest in the region where $U''(\omega)$ is greatest; that is in the area close to the wall. In this area the stream function was modified so that the rate of change of the cross-stream velocity profile did not exceed a specified limit-the velocity gradient limit. As will be remembered in the derivation of this limit the form of the cross-stream transform set in these regions is at least

equivalent to the transform used in the Penny-Landis technique. Under these circumstances the numerical diffusion conservatively becomes equivalent to:

$$U''(\omega)\ \frac{b\Delta\omega^3}{2}$$

From table 4.1 in chapter four the remaining finite difference error terms amount to:

$$c\ \frac{\Delta\omega^2}{12}\ U^{iv}(\omega)\ +\ \frac{a\Delta\omega^2}{6}.\ U'''(\omega)$$

The term '$\frac{a\Delta\omega^2}{6}U''(\omega)$' will be neglected, because 'a' is zero ('a' is proportional to the entrainment through the boundary surface at y equals zero - which in these examples is zero). From this work it can be deduced that the ratio of numerical diffusion errors to the remaining finite difference error is approximately equivalent to:

$$\frac{6b\ U''(\omega)\ \Delta\omega}{c\ U^{iv}(\omega)}$$

The first point to note about the ratio is that the spacing between sequential mesh stream lines, for $\Delta\omega < 1$, suppresses the effect of numerical diffusion.

Another important point to take note of is that in this modelling technique the above ratio is dependent upon the various properties of the flow through the terms 'b' and 'c'. This means that a simple value cannot be assigned to the ratio numerical diffusion to total finite difference error.

The best predictions, with the new modelling technique, occur with the velocity gradient limit set at 10^3 - as detailed in table 5.5 and 5.6. The discrepancy between the predicted and experimental results in these situations is caused by errors in the finite difference representations of the partial differentials in the general continuity equation 4.7, discrepancies in the turbulence properties, and uncertainty in the experimental data used for the comparisons. For the purpose of this discussion the last source of error is assumed negligible. No technique exists for theoretically estimating what proportion of the discrepancy in the predicted results is caused by the remaining two sources of error. The author is of the opinion that the model for turbulent viscosity, μ_{eff}, contributes most towards the total error in the prediction.

5.3 Conclusions and Recommendations

The results presented in this chapter show that the modelling technique with an interactive scheme can accurately simulate the time averaged velocity fields in three specified flow situations. However, this does not mean that the technique can accurately simulate all boundary flows in which momentum transfer processes predominate, because the situations examined are not a representative sample. It is consequently recommended that before this technique is used to simulate any other type of boundary flow some reappraisal of it's suitability be under taken. In chapter 6 one such reappraisal is conducted to show that the technique can simulate radial wall jet flows.

The successful simulation of a boundary layer flow with tangential air injection along the surface, as illustrated in figure 5.7, demonstrated the new techniques ability to predict results within a flow in which the cross-stream velocity profile were not self-similar. In the presented simulations the non-dimensional stream function of the mesh network was only modified at the starting section of the situation, ac in figure 5.7. It is likely that more accurate predictions could be obtained by re-defining the mesh stream lines at appropriate cross-stream sections in the flow.

Chapter 6

Momentum Transfer Rates in Radial Wall Jets

The purpose of this chapter is to illustrate that the modelling technique described and tested in chapter 4 and 5 can be modified to simulate momentum transfer rates in an air radial wall jet. In these simulations estimates for the density and effective viscosity are obtained from the general gas law and turbulence model of Lauder and Spalding respectively. The turbulence model has been previously described in chapter three.

In section 1 are detailed the assumptions involved in modifying the equations representing conservation in a radial wall jet flow sufficiently for them to correspond to the conservation equation 3.1 solved by the modelling technique. The new mesh network used is described in section 2. The accuracy of the modelling technique, when simulating a radial wall jet, is assessed by comparing the computational results with experimental data obtained elsewhere. The results from a study of this type are presented in section 3. The performance of the modelling technique is dicussed in section 4, and recommendations given in section 5.

6.1 Conservation of Momentum

Equations 6.1 and .2 represent the conservation of momentum in the radial and vertical direction of a turbulent radial wall jet. In these equations r and z are the radial and vertical axes of the cylindrical co-ordinate system detailed in figure 6.1. The time averaged and fluctuating velocity components in the radial, vertical and circumferential directions are represented by U, u', V, v' and W, w' respectively; p is the pressure, ρ specific density and $\mathcal{D}$ the kinematic viscosity.

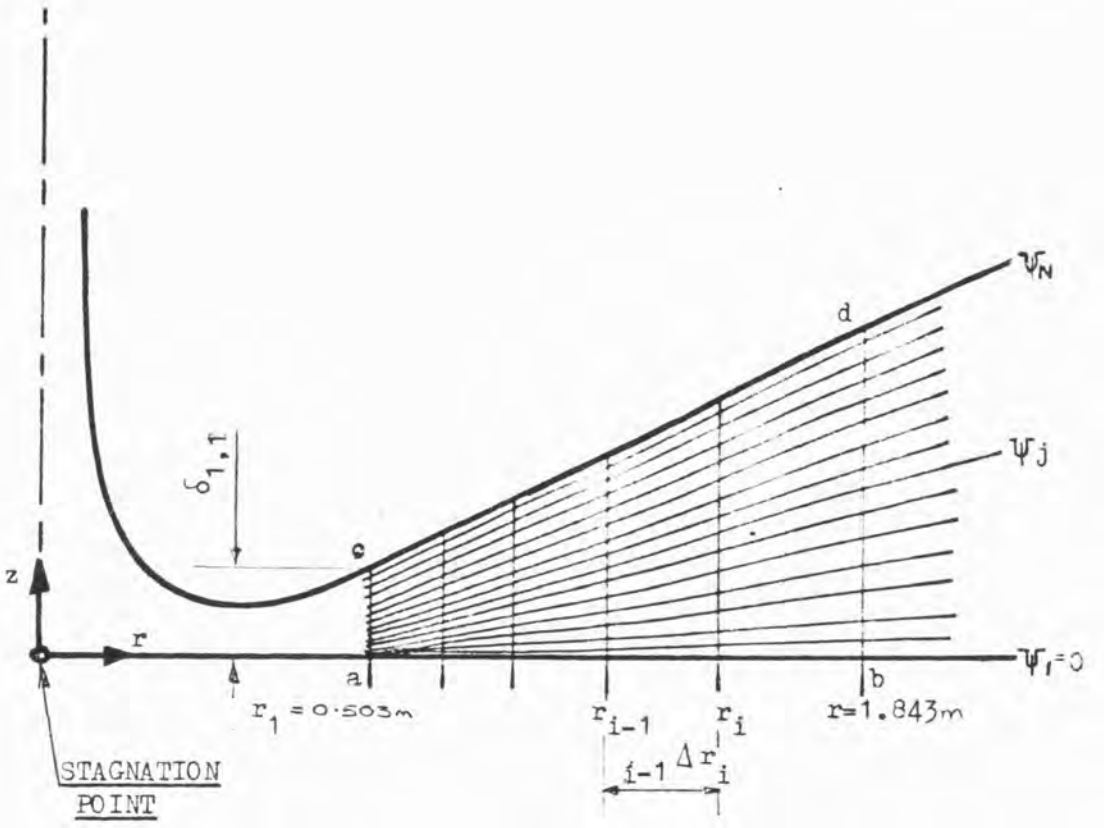

MESH NETWORK

FIGURE 6.1

$$U\frac{\partial U}{\partial z} + W\frac{\partial U}{\partial z} + \frac{\partial}{\partial r}\overline{u'^2} + \frac{1}{r}\left(\overline{u'^2} - \overline{v'^2}\right) + \frac{\partial}{\partial z}\overline{u'w'}$$

$$= -\frac{1}{\rho}\frac{\partial p}{\partial r} + \nu\left(\frac{\partial^2 U}{\partial r^2} + \frac{1}{r}\frac{\partial U}{\partial r} - \frac{U}{r^2} + \frac{\partial^2 U}{\partial z^2}\right) \qquad (6.1$$

$$U\frac{\partial W}{\partial r} + W\frac{\partial W}{\partial z} + \frac{\partial}{\partial r}\overline{u'w'} + \frac{\overline{u'w'}}{r} + \frac{\partial}{\partial z}\overline{w'^2}$$

$$= -\frac{1}{\rho}\frac{\partial p}{\partial z} + \nu\left(\frac{\partial^2 W}{\partial r^2} + \frac{1}{r}\frac{\partial W}{\partial r} + \frac{\partial^2 W}{\partial z^2}\right) \qquad (6.2$$

The continuity equation of the mean motion is represented by:

$$\frac{\partial}{\partial r}(Ur) + \frac{\partial}{\partial z}(Vr) = 0 \qquad (6.3$$

Various experimental studies of momentum transfer rates within air radial wall jets, of the types shown in figure 6.1, have shown that the flow properties change slowly in the radial but rapidly in the vertical direction. The more important of these studies are those by Bakke[42], Bradshaw and Lowe[43] and Porch, Tsuei and Germak[36]. Applying this result to the conservation equations 6.1 and .2 results in the following approximations:

$$\frac{U\partial U}{\partial r} + \frac{W\partial U}{\partial z} + \frac{\partial}{\partial z}(\overline{u'w'}) = \nu\frac{\partial^2 U}{\partial z^2} \qquad (6.4$$

and

$$\frac{\partial}{\partial z}(\overline{w'^2}) = -\frac{1}{\rho}\frac{\partial p}{\partial z} \qquad (6.5$$

Equation 6.5 affects the structure of the radial wall jet through w'; it has been assumed that this effect can be allowed for by

using suitable modified semi-empirical relationship for entrainment at the free-edge equation 6.6.

$$\dot{m}''_{FE} \propto r^{-1.2} \qquad (6.6$$

(Both Glauert [44] and Porch et al have produced accurate modelling techniques that, in a similar manner, neglect the effect of equation 6.5.) Re-arranging equation 6.4 results in:

$$\frac{U\partial U}{\partial r} + \frac{W\partial U}{\partial z} = \frac{\partial}{\partial z}\left[\mu_{eff}\ \frac{\partial U}{\partial z}\right], \qquad (6.7$$

which can be substituted for the general conservation equation 4.7 of the modelling technique.

6.2 Mesh Network

The mesh network used to cover the radial wall jet is detailed in figure 6.1. The co-ordinate system is one where z represents vertical distance from the impervious surface, and r the distance from the stagnation point. The mesh consists of cross-stream strips of width Δr, and lines along which the non-dimensional stream function Ψ, equal to $f\left[\frac{\Psi - \Psi_1}{\Psi_N - \Psi_1}\right]$, is constant. The subscripts 1 and N denote the surface and free-edge of the radial wall jet illustrated in figure 6.1.

The grading of the mesh networks used in each of the flow situations simulated in the remainder of this thesis are defined by two relationships. The first is the grading of real height z at which the starting cross-stream velocity profile is specified; the relationship used takes the form:

$$z_{1,i} = z_{1,\ i-1}(1 + Fr) \qquad (6.8$$

where $i = 3$, N and $z_{1,1}, z_{1,2}$ and Fr are constant which take the values:

a) $z_{1,1} = 0.0$, $z_{1,2} = \delta_{1,1}$ $/10^3$ and Fr = 1.121

b) $z_{1,1} = 0.0$, $z_{1,2} = \delta_{1,1}$ $/10^5$ and Fr = 1.196

$\delta_{1,1}$ is the width of the flow at this section. Secondly, the functional relationship between the non-dimensional mesh stream function Ψ and the stream function ψ has to be described. The interactive technique used to evaluate this relationship has been detailed in chapter four; and makes use of a velocity gradient L which has been set to either:

i) $L = 10^3$

or ii) $L = 10^5$

6.3 Radial Wall Jet

Porch, Tsuei and Germak [36] have studied the momentum transfer rates in air radial wall jets submerged in still air. The experimental arrangement used is shown schematically in figure 6.2; the center line of the nozzle aa is vertical, and the impervious surface horizontal. The flow in the radial wall jet has been characterized by plotting:

a) several cross-stream velocity profiles

b) the variation of the maximum velocity with distance along the impervious surface,

and c) the growth rate relationship.

The cross-stream velocity profiles appear self similar when presented in the form of $\frac{U}{U_{max}}$ against $\frac{z}{\delta_5}$.

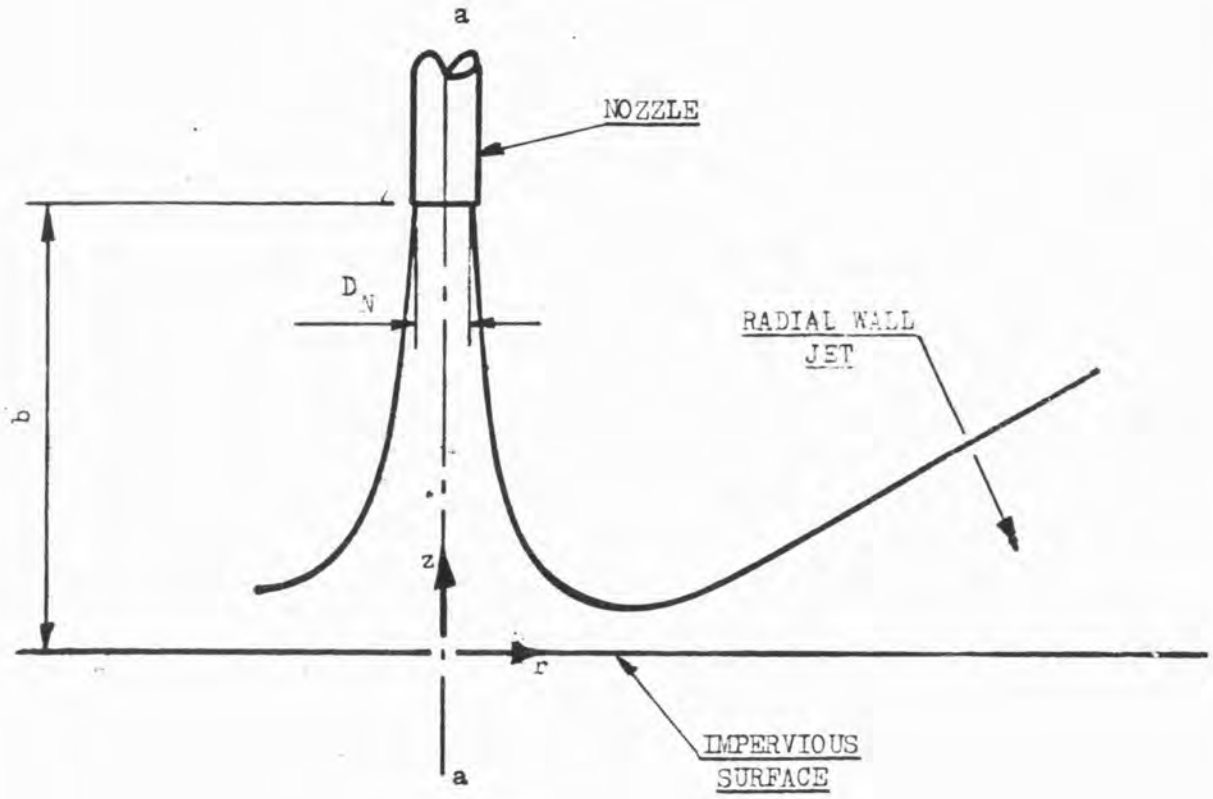

IMPINGEMENT FLOW

FIGURE 6.2

The flow situation chosen for examination is one where the nozzle diameter (D_N) is 0.0508m, the average exit jet velocity $U_{AV,N}$ 85.04ms^{-1} and the exit from the jet is at a height b = 0.67m above the impervious surface. Porch et al plots for the cross-stream velocity profiles at r/b = 0.75,2.0 and 2.75, and the maximum velocity and growth rate relationships are shown by chain dotted lines in figures 6.3 to.6 respectively.

Four different computational simulations of the specified radial wall jet are presented for $0.75 \leqslant r/b \leqslant 2.75$. They correspond to the two forms of mesh gradings 'a' and 'b', and the velocity gradient limits 'i' and 'ii' described in section 6.2. In each simulation the following boundary conditions were specified:

a) along the starting cross-stream section, ac in figure 6.1 , the velocity was determined from the theoretically derived relationship by Glauert.[4.4]

and b) at the impervious surface and free edge, ab and cd in figure 6.2 , the velocity has been set to zero and U_{max} / 10 respectively.

Specimen results from the computations are detailed in figures 6.3 to 6.6. The symbols used are detailed in table 6.1. The maximum discrepancies between the presented predicted and experimental results for r/b = 0.75, 2.0 and 2.5 are specified in table 6.2 ;with the discrepancies concerning the cross-stream velocity profiles presented at z = 0 (the impervious surface) and $\frac{z}{\delta_5}$ = 1.0.

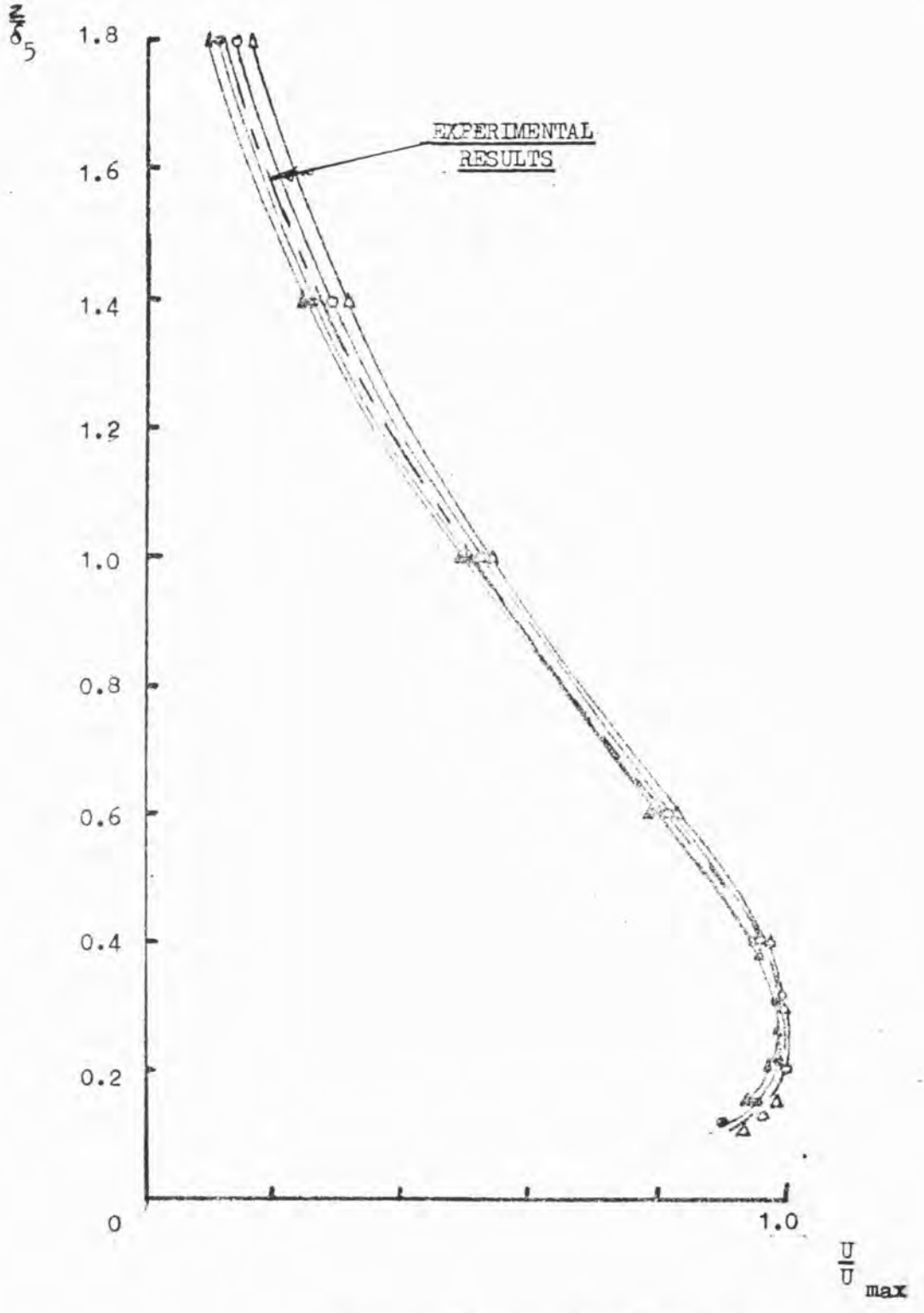

VELOCITY PROFILE AT r/b = 0.75

FIGURE 6.3

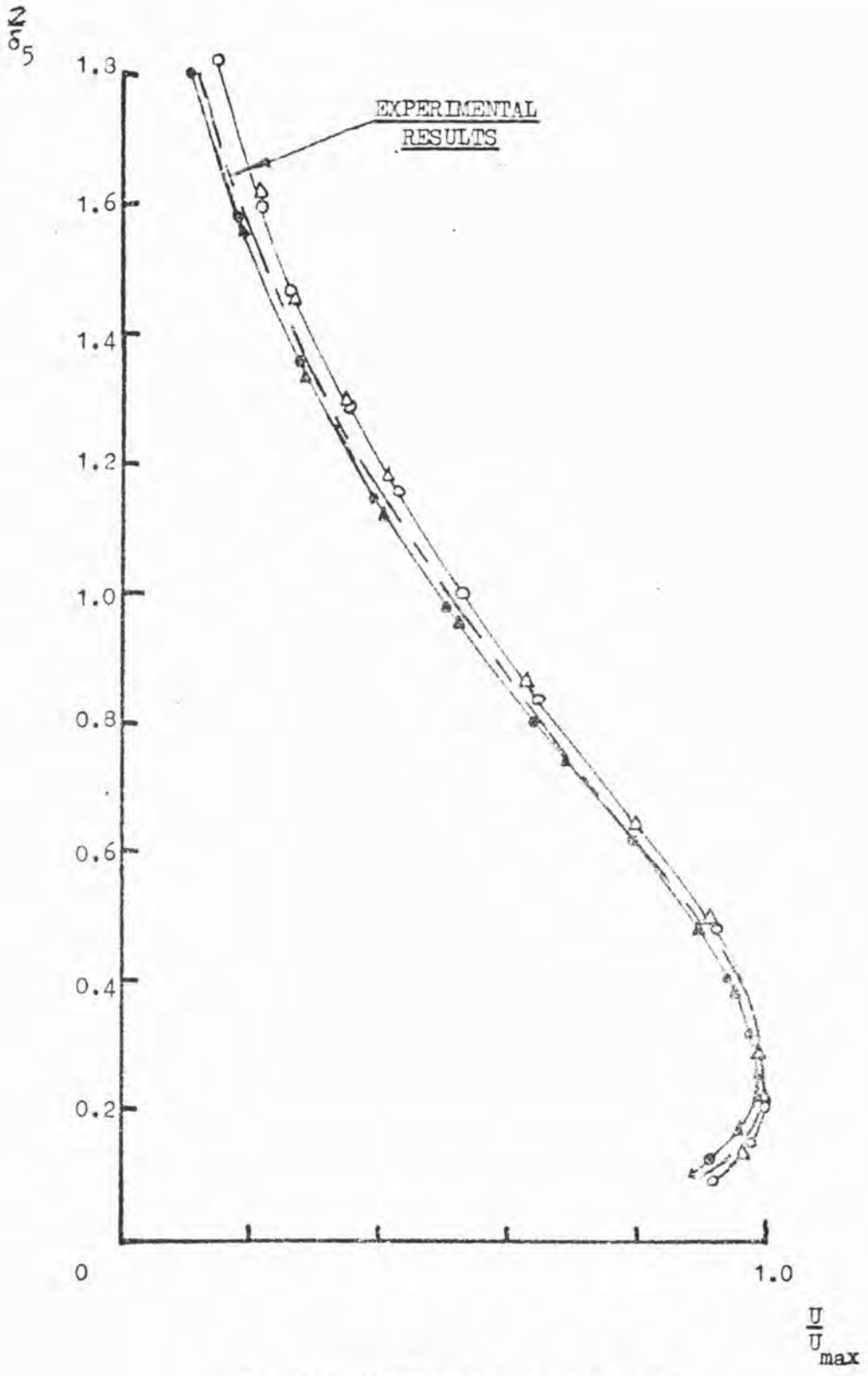

VELOCITY PROFILES AT r/b = 2.0

FIGURE 6.4

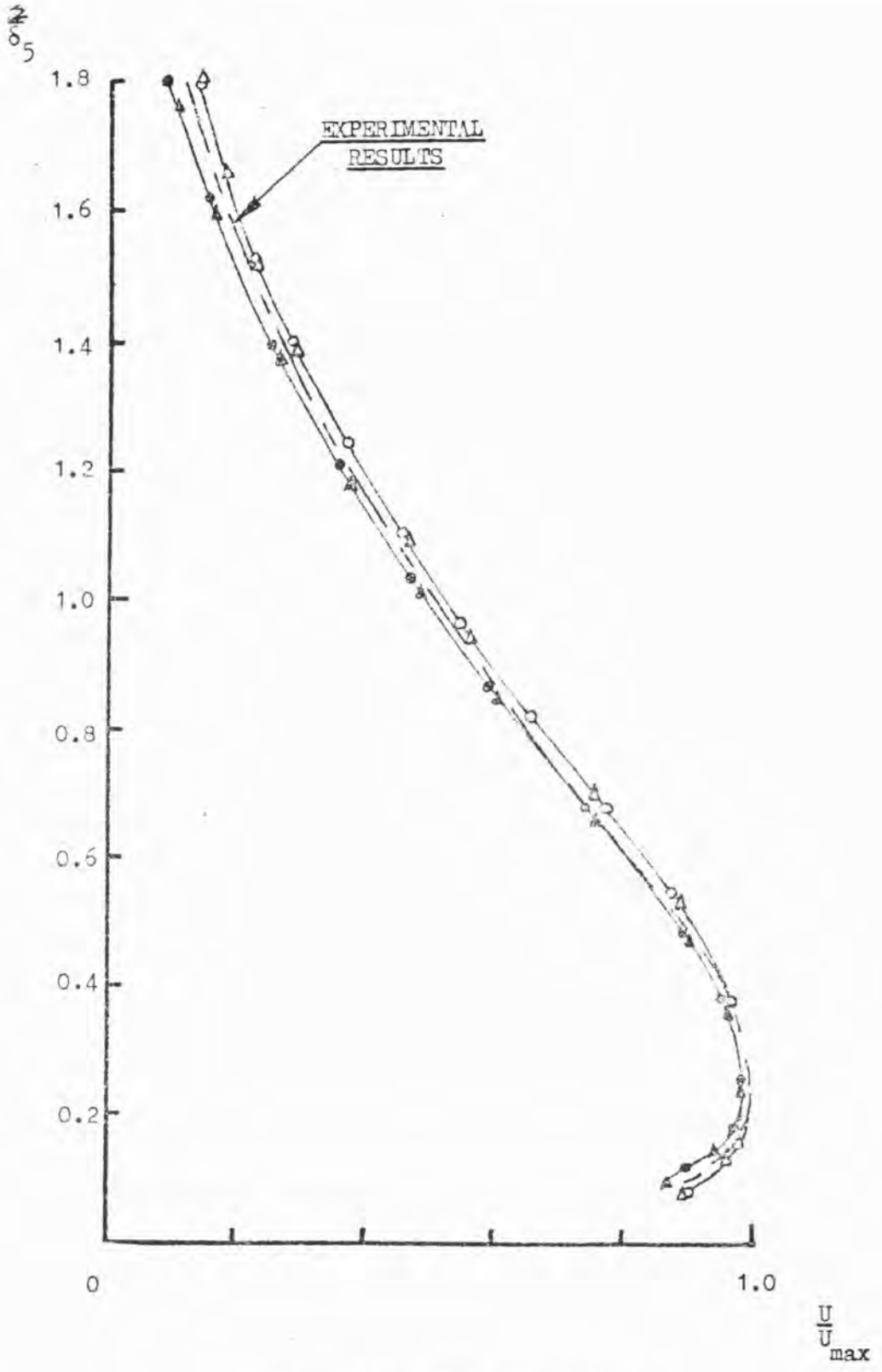

VELOCITY PROFILE AT r/b = 2.75

FIGURE 6.5

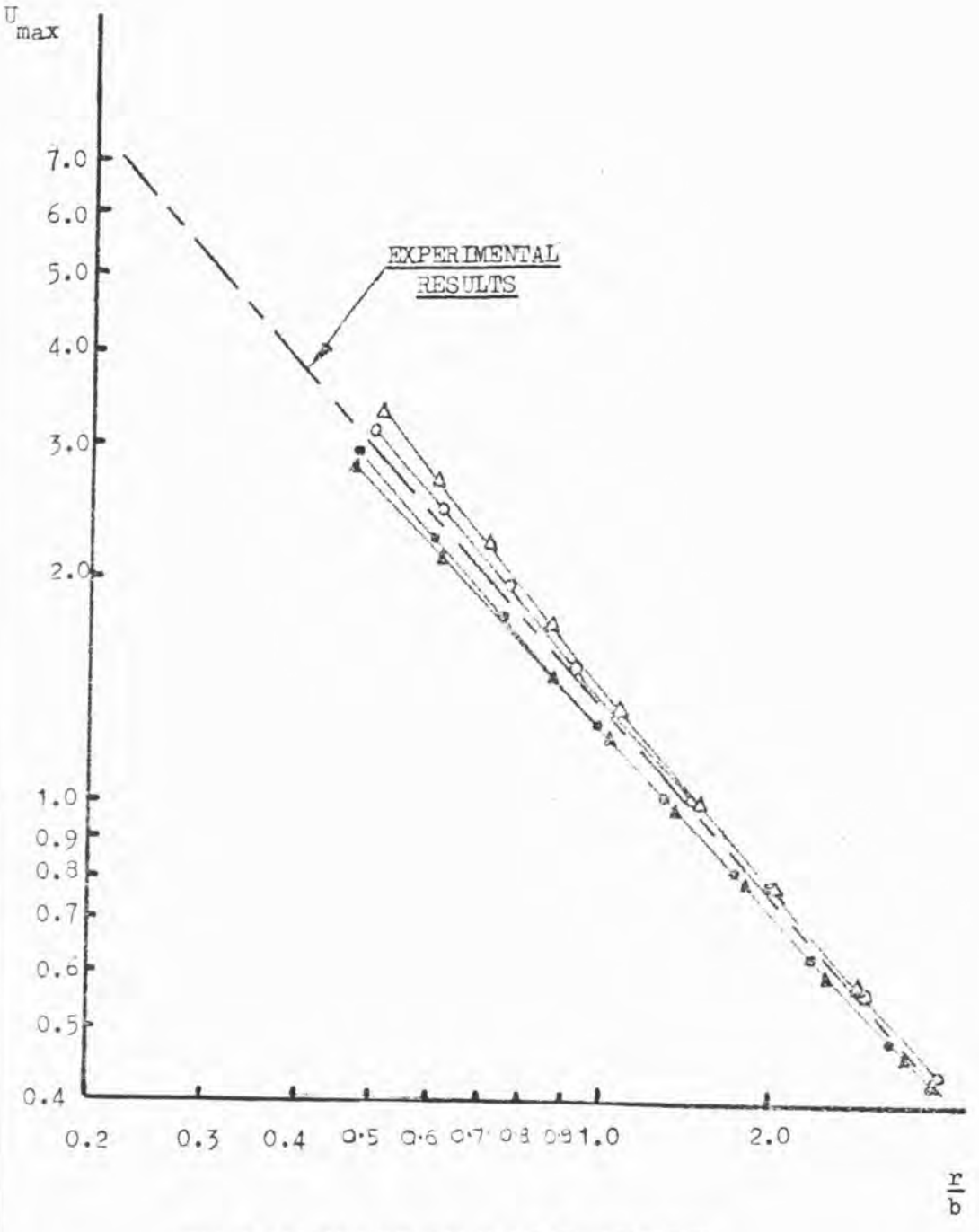

THE VARIATION OF THE MAXIMUM VELOCITY

FIGURE 6.6

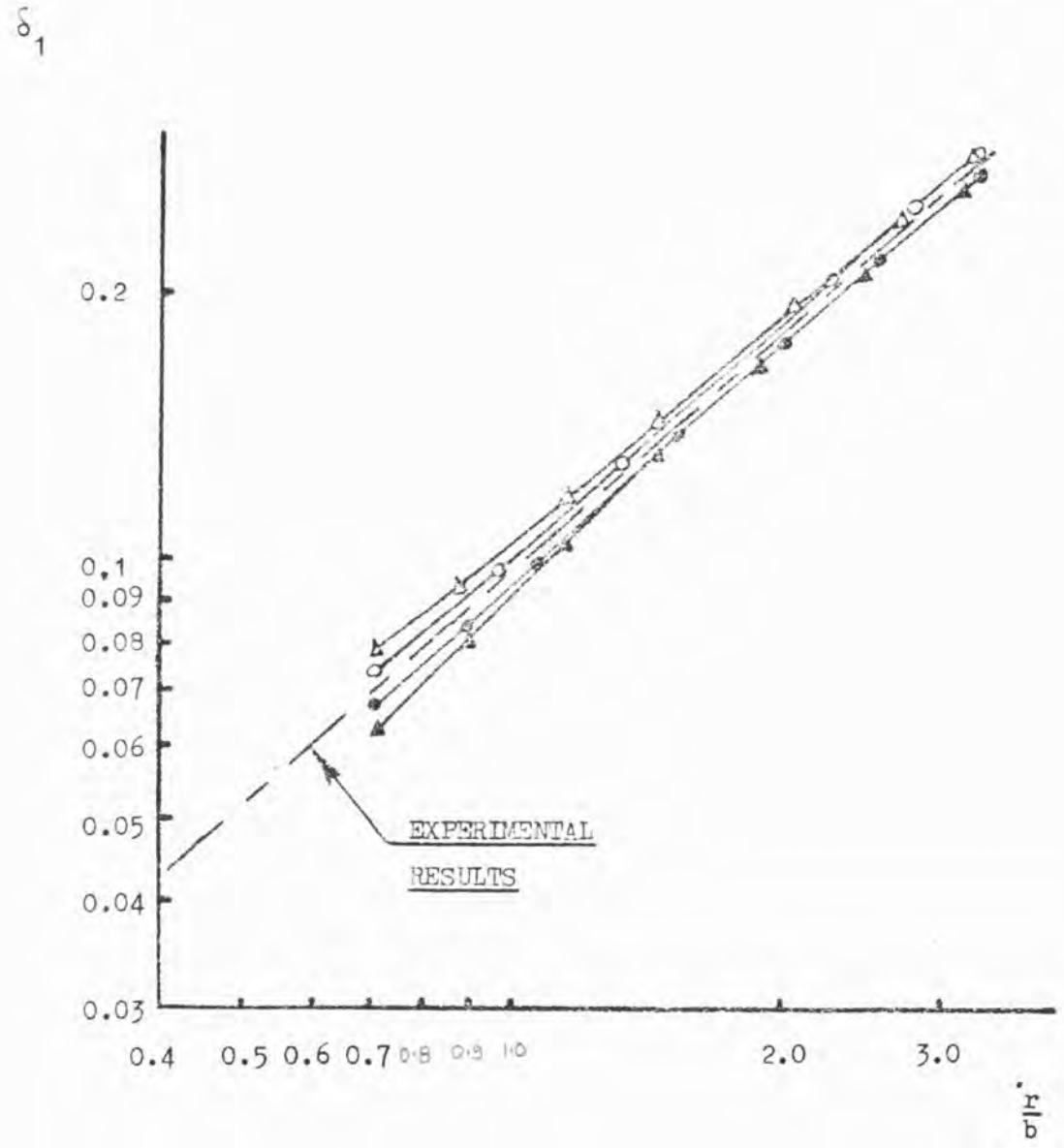

GROWTH RATE RELATIONSHIP

FIGURE 6.7

Table 6.2

Percentage Differences

Symbols	Percentage discrepancies between predicted and experimental values of: u at $\frac{z}{\delta_5} = 0$	u at $\frac{z}{\delta_5} = 1.0$	U_{max}	δ_1
a) at r/b=0.75				
Δ	2.8	6.0	5.1	10.0
○	0.9	2.9	2.5	4.3
▲	-2.9	-1.0	-10.0	-4.4
●	-4.6	-3.9	-9.2	-14.1
b) at r/b=2.0				
Δ				
○	-2.9	3.1	3.5	5.7
▲				
●	-2.1	-2.6	-7.7	-6.2
c) at r/b=2.5				
Δ				
○	3.5	3.2	2.1	3.9
▲				
●	-4.2	-3.0	-4.2	-4.8

The presented results show the modelling techniques ability to predict the velocity field within the radial wall jet with errors of the order ten percent.

The discrepancy in the predictions are dependent upon the mesh gradings used in the simulations. As previously reported the mesh grading is dependent upon the velocity gradient limit L, and z grading at the starting cross-stream section. And consequently an assessment of the correlation between the discrepancy and mesh network grading can be obtained, by comparing predicted results, from the two forms of starting cross-stream grading 'a' and 'b' and velocity gradient limit 'i' and 'ii' in section 6.1, with the presented experimental results. The percentage discrepancies shown in table 6.2 provide a quantitative assessment of effects of this correlation. It is interesting to note that for $2.0 \leq r/b \leq 2.5$m the discrepancies in the predictions are almost totally dependent upon the value taken by the velocity gradient limit. As shown by the specimen comparisons of the velocity profiles at r/b = 2 and 2.5, and the maximum velocity and jet width relationships shown in figures 6.3 and .7 respectively.

6.4 Discussions

The modelling technique accurately predicted the time averaged velocity field within the radial wall jet illustrated in figure 6.1, showing that use of the modified conservation equation 6.7 is valid in this particular flow situation. As previously reported the discrepancies in the predictions were slightly dependent upon the grading of the mesh network used in the simulations. The reasonable degree of accuracy obtained was not unexpected for two reasons. Firstly, several techniques based upon the simplified conservation equation 6.7 have accurately predicted the gross flow properties of radial wall jets. Two examples of such techniques are those proposed by Glauert[44] and Porch, Tsuei and Germak[36]. These use mathematical methods based upon the parametric integral method described in chapter two; and predict the variation of maximum velocity U_{max}, height to the maximum velocity δ_4, and the height of the half maximum velocity δ_5. Secondly, a semi-empirical relationship has been used with the recommended modelling technique to estimate the entrainment rate at the free edge as detailed in section 6.1. This relationship, designated equation 6.6, was derived and verified by Porch et al in their study of radial wall jets. Such a relationship supplements much of the information relating to the circumferential spread of the wall jet, that was lost in the derivation of the simplified conservation equation 6.7.

6.5 Recommendations

At this juncture in our investigations two vastly different courses of action were available. The first involved acceptance of the prescribed modelling technique; although validation of the calculation procedure for simulating heat and mass transfer in specific flow situations remained to be considered. This approach was adopted for reasons that will be detailed later. The second course involved the construction of a new technique for simulating momentum transfer, which would be based upon a more comprehensive set of equations, say 6.1 and .2, and use measured semi-empirical turbulence information to obtain a solution. There are three reasons for recommending the first course of action. Firstly, the described modelling technique seems capable of accurately simulating turbulent momentum transfer in radial wall jets. Secondly, the turbulence information required by this modelling technique, which relates to the effective viscosity Schmidt and Prandtl numbers, can be derived from readily available phenomenological theories; which may be adopted for use in more complex flows. Thirdly, the alternative course of action is at present unrealistic proposition, because of the vast amount of turbulent information that must be accumulated before a solution can be obtained.

Chapter 7

Mass Transfer Rates

The intent of this chapter is to show that the modelling technique using an interactive scheme can accurately simulate the turbulent mass transfer rates in an incompressible radial wall jet. As this flow was moving the momentum transfer rates were also simulated.

The accuracy of the modelling technique is assessed by comparing the computational results with those obtained from an experimental study of a Nitrogen Oxygen radial wall jet. Full details and results from this study are described in appendix 4; and a brief review is presented in section 1. The methods used to define the physical properties required in the computational simulations - the density, and effective viscosity and Schmidt number of the working fluid - are derived from the works of other authors, and are described in section 2. Specimen computational results are compared with the measured data in section 3. Finally, in section 4 the conclusions of this study are given.

7.1. Review of Experimental Study

The studied radial wall jet was part of a flow produced by the normal impingement of a Nitrogen jet, exposed to the atmosphere, onto a flat impervious surface. A schematic representation of the flow is presented in figure 7.1. The nozzle is 0.01m above the impervious surface and has an internal diameter of 0.02m. By adjustment of the flow rate the Reynolds number of the jet was maintained at 9×10^3 throughout the study.

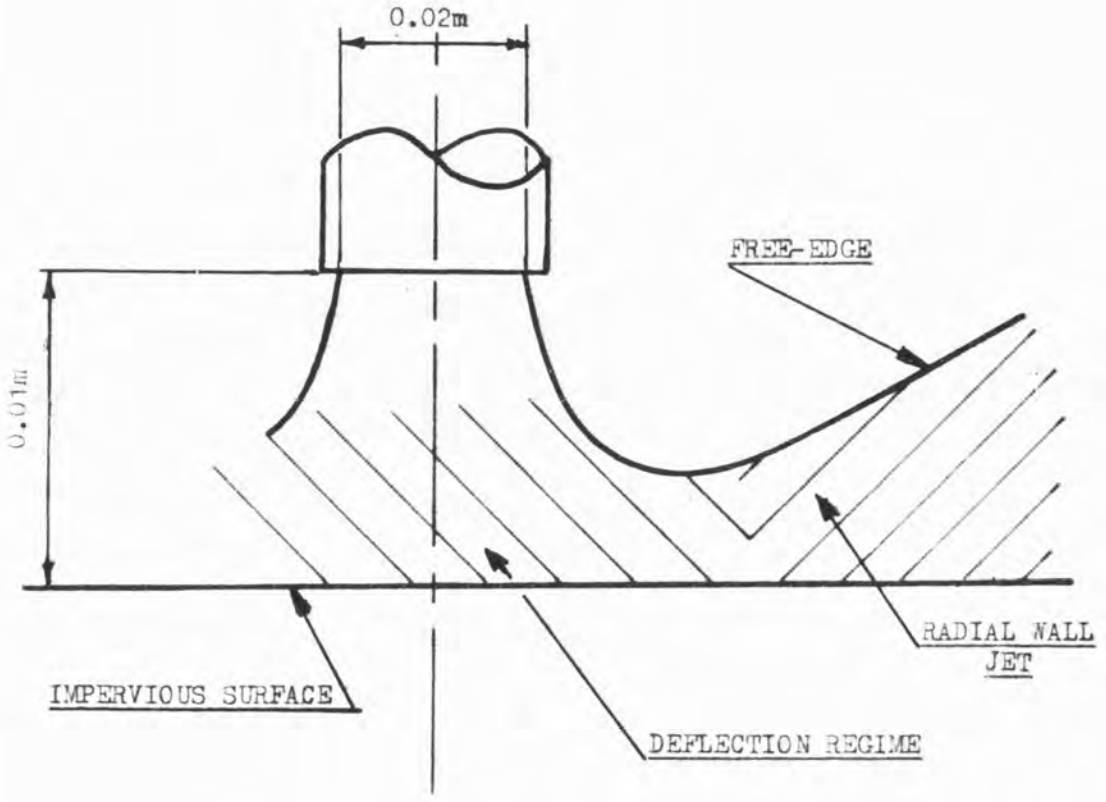

RADIAL WALL JET

FIGURE 7.1

The measured cross-stream variations of the time averaged radial velocity, and Oxygen and Nitrogen concentrations, at radii of 0.05 0.075 , 0.1, 0.125, 0.15, 0.175 and 0.2m are presented in figures 7.2 to .7 respectively. Table 7.1 details the symbols used in these figures. (The radial velocity was measured with the aid of hot wire anemometery and the species concentrations by mass-spectroscopy.)

Table 7.1

Symbol	Time Averaged Properties
Δ	U (radial velocity)
∇	m_{O_2} (gravimetric concentration of Oxygen)
○	m_{N_2} (gravimetric concentration of Nitrogen)

Table 7.2

Symbols for: U	m_{O_2}	m_{N_2}	$z_{1,2}$	Fr	L
⧩	⧨	♀	$\delta_{1,1}/10^3$	1.19	10^3
⧫	▼	●			10^5
⧩	⧨	♀	$\delta_{1,1}/10^5$	1.12	10^3
⧫	▼	●			10^5

$\delta_{1,1}$ the width of the radial wall jet at r = 0.047m

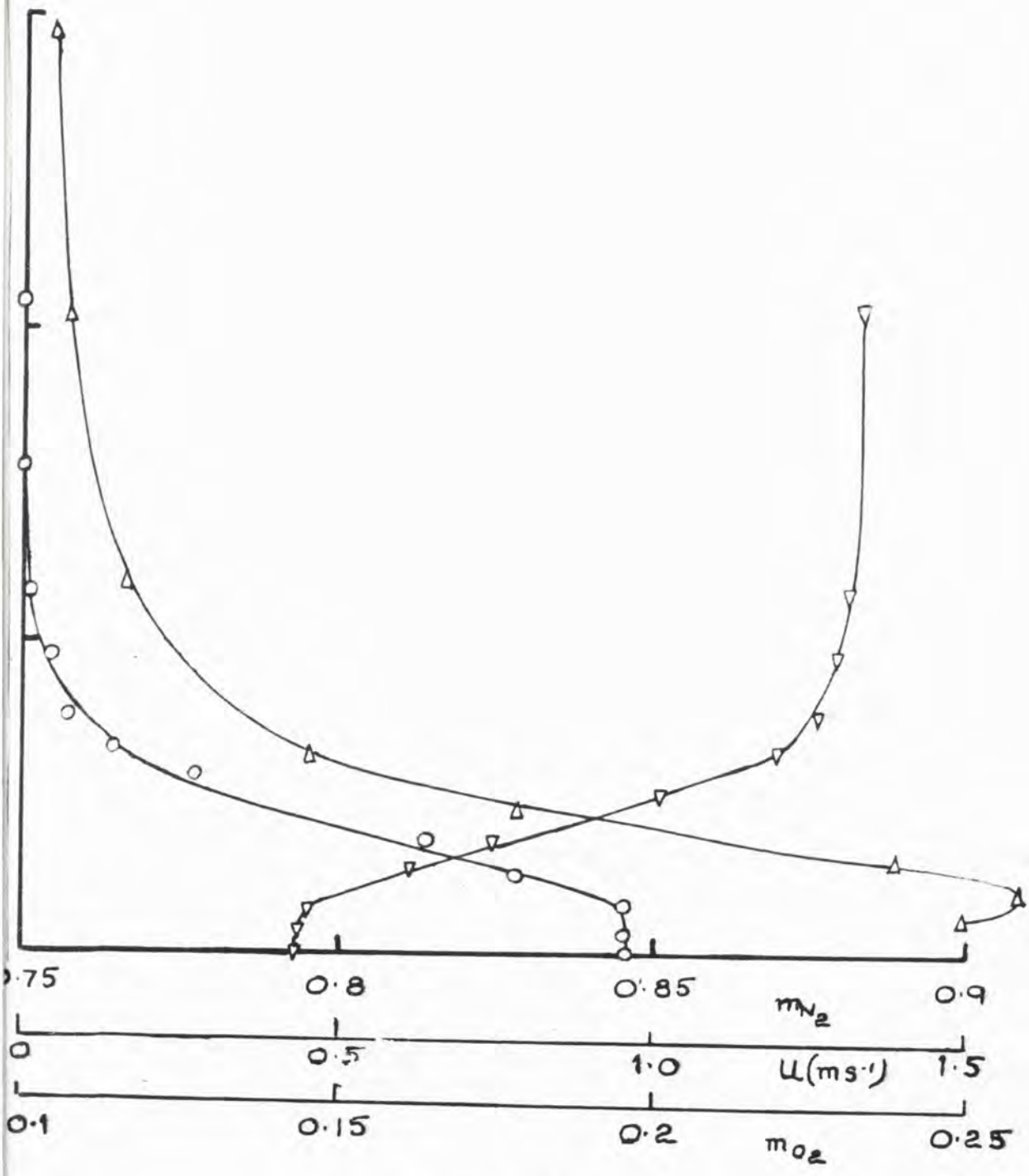

CROSS-STREAM FLOW PATTERN AT r = 0.05m

FIGURE 7.2

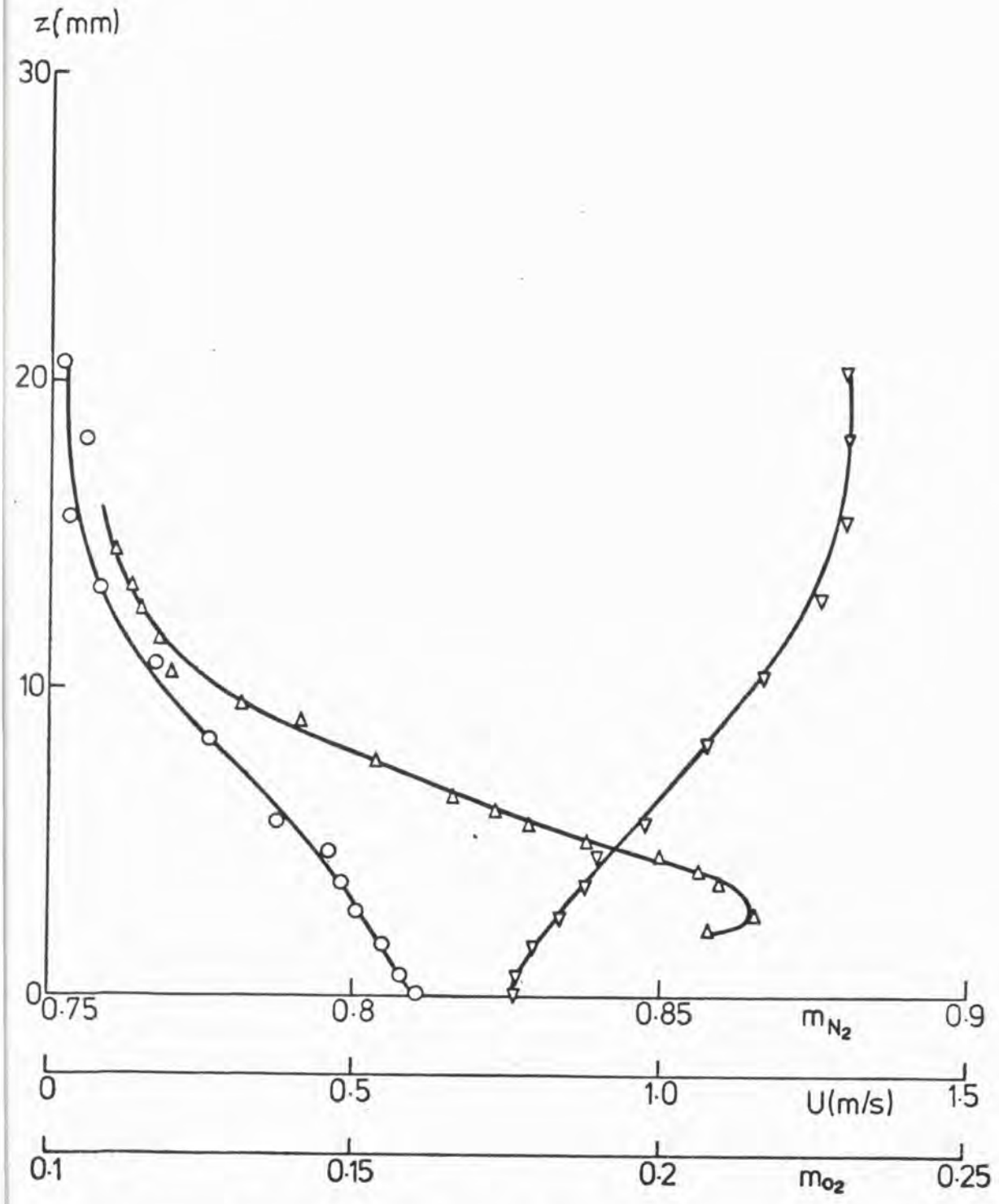

CROSS-STREAM FLOW PATTERN AT r = 0.075m

FIGURE 7.3

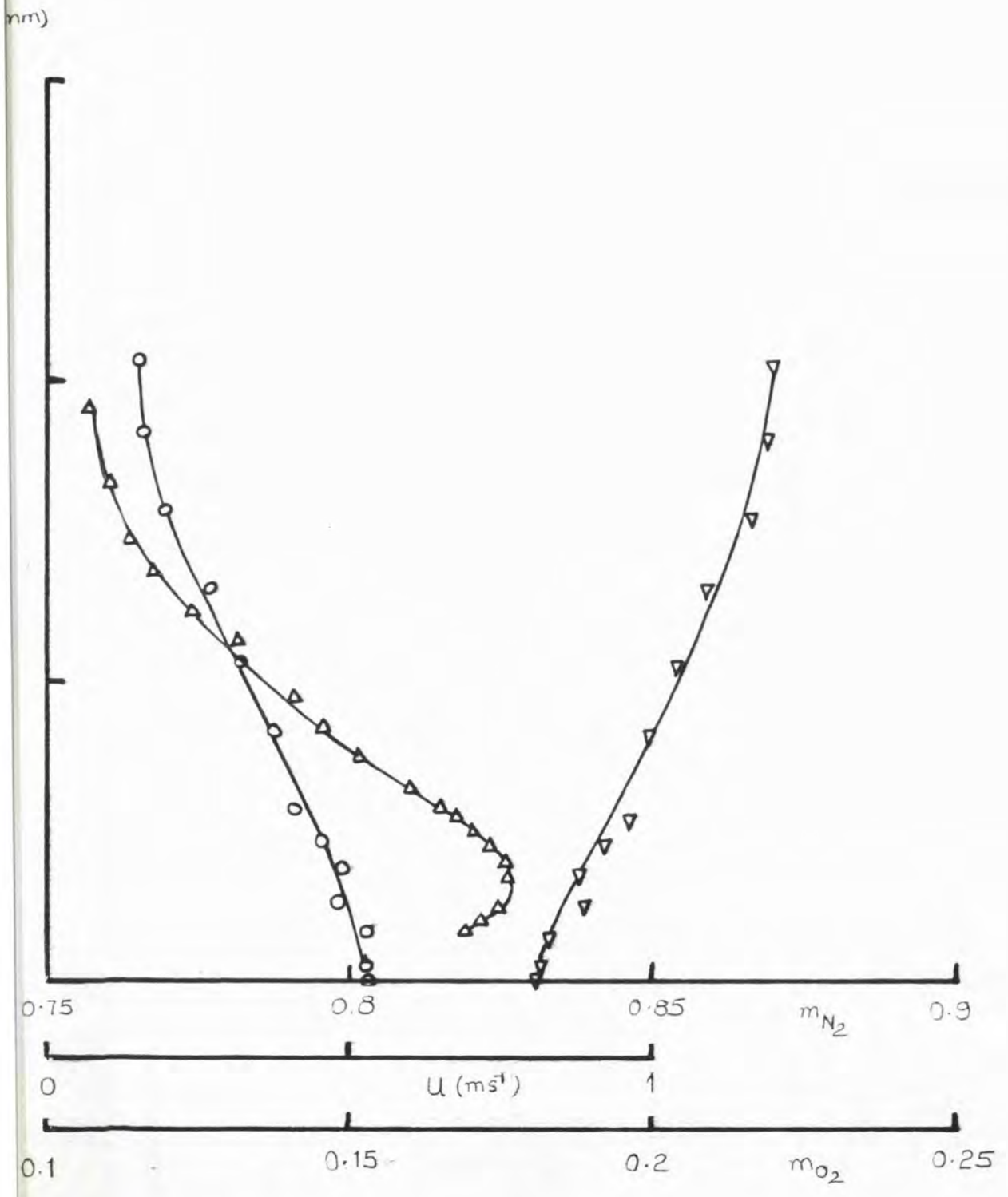

CROSS-STREAM FLOW PATTERN AT r.= 0.1m

FIGURE 7.4

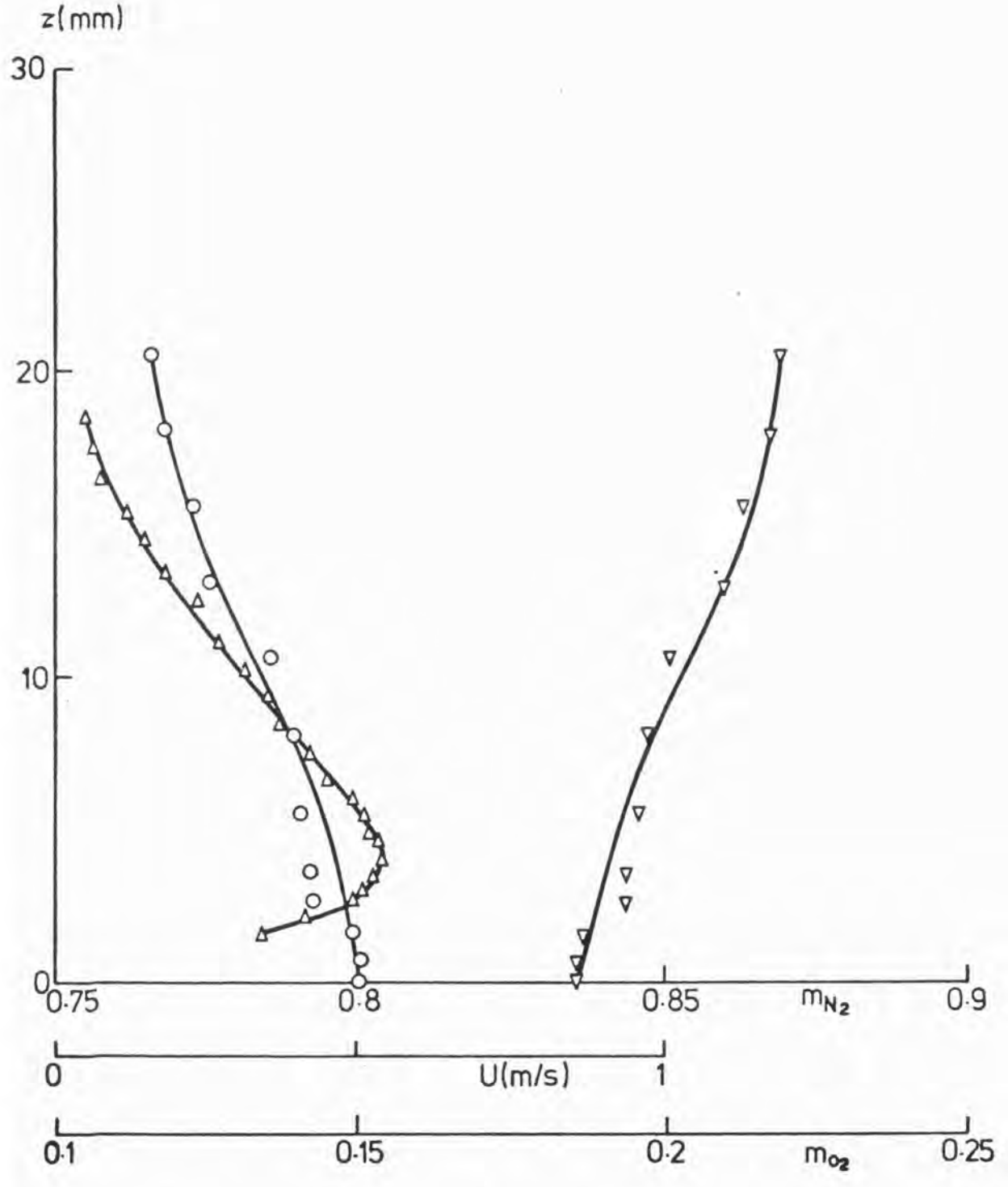

CROSS-STREAM FLOW PATTERN AT r = 0.125m

FIGURE 7.5

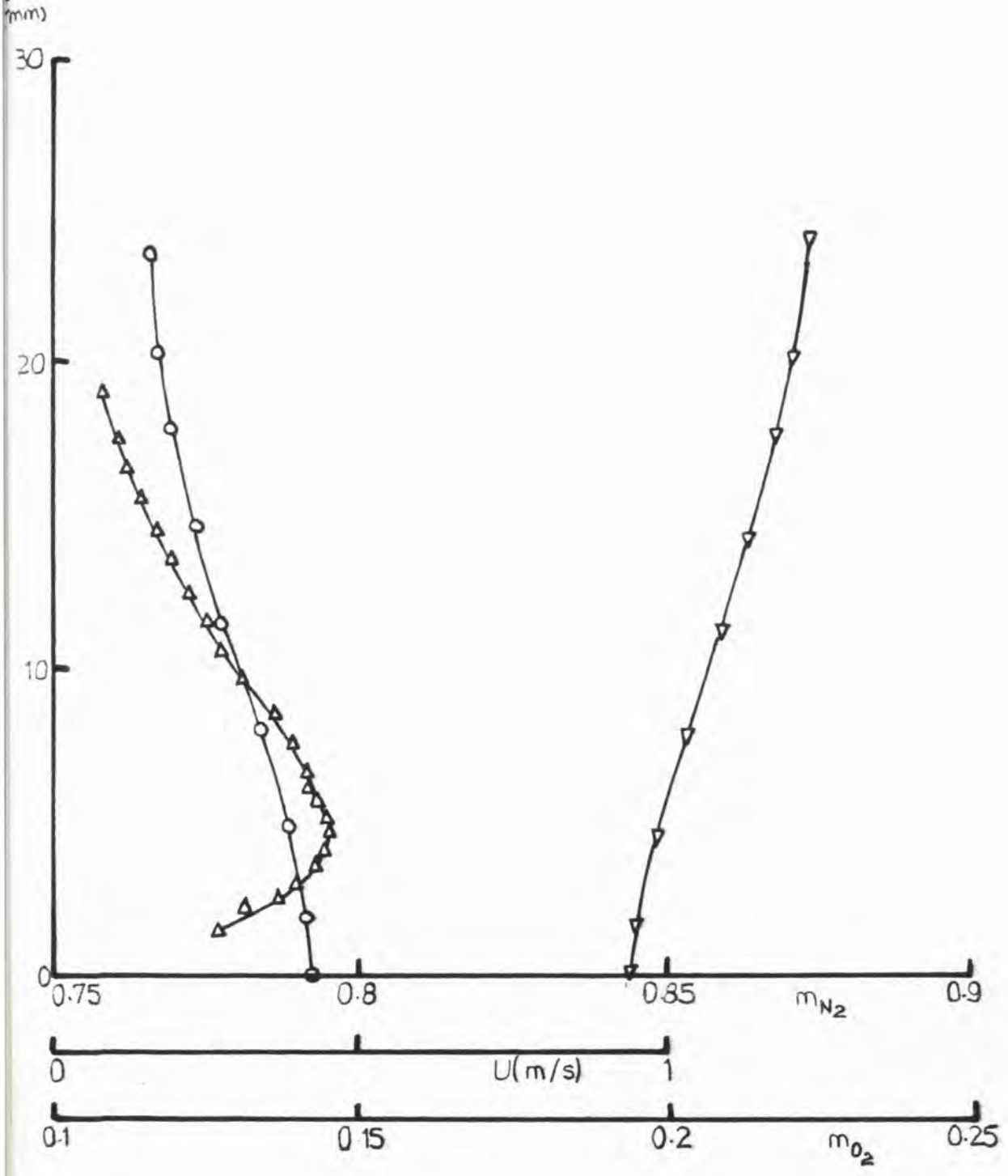

CROSS-STREAM FLOW PATTERN AT r = 0.15m

FIGURE 7.6

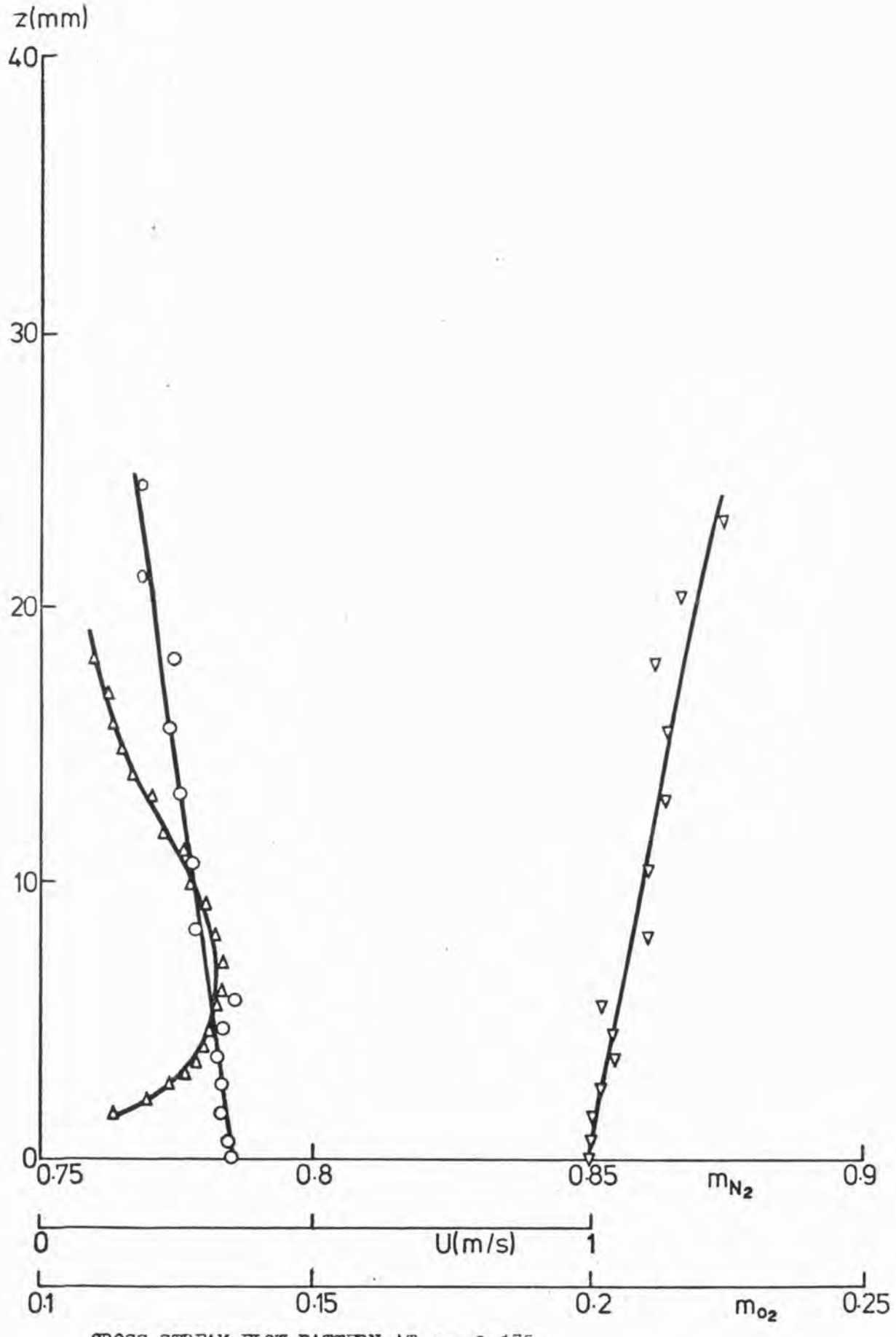

CROSS-STREAM FLOW PATTERN AT r = 0.175m

FIGURE 7.7

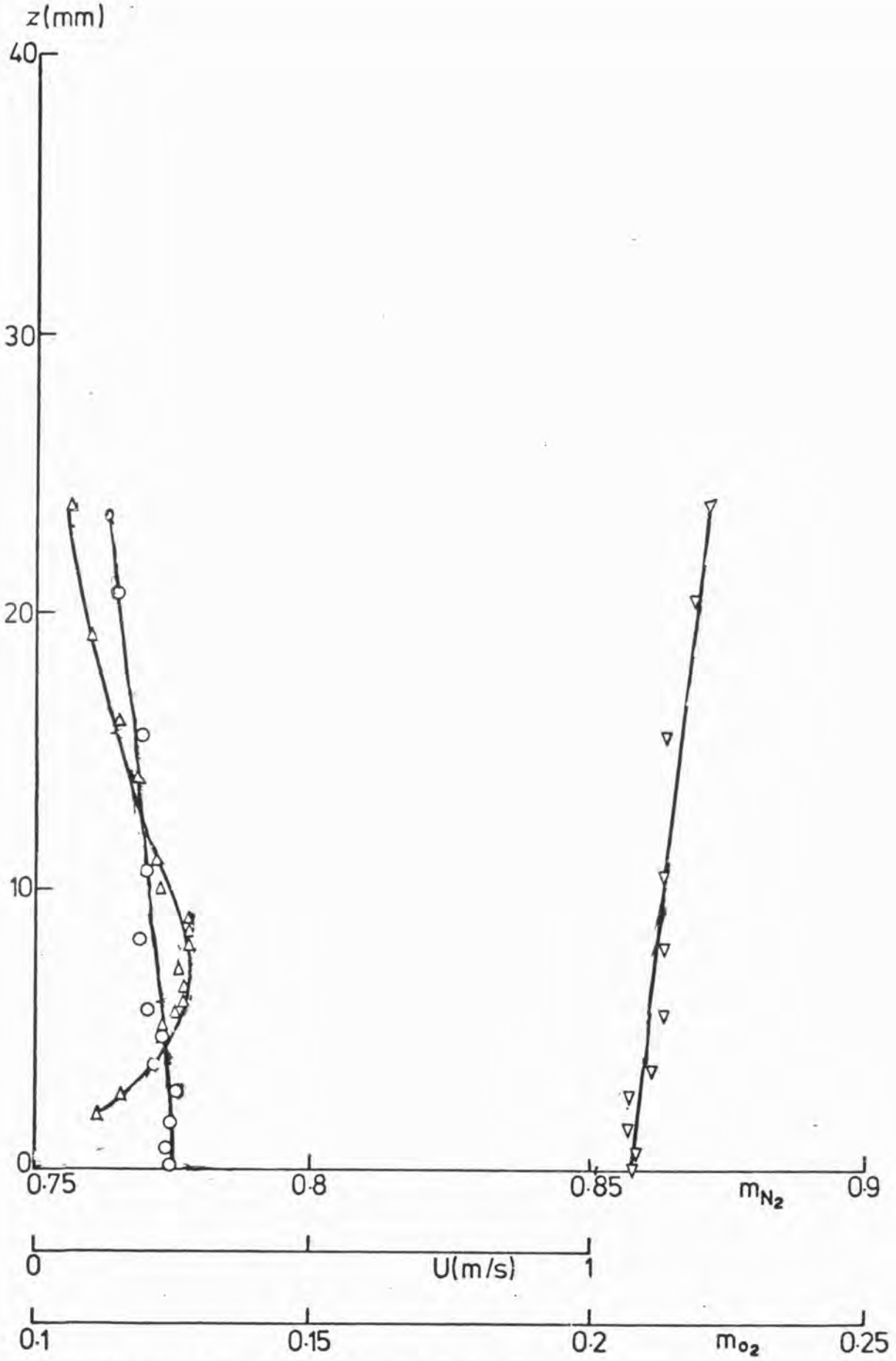

CROSS-STREAM FLOW PATTERNS AT r = 0.20m

FIGURE 7.8

7.2. Physical Properties

In the computational simulations of the specified radial wall jet the following properties have been supplied:

a) the density of the mixture,

b) effective viscosity of the mixture,

and c) the effective Schmidt number of the constituent gases.

The density of the mixture has been estimated from the equation of a perfect gas:

$$\rho = \frac{p}{\mathcal{R}T}\left[(mM)_{N_2} + (mM)_{O_2}\right] \qquad (7.1$$

; where the sub-scripts N_2 and O_2 refer to Nitrogen and Oxygen respectively.

The effective viscosity has again been determined using the communicative law:

$$\mu_{eff} = \mu_t + \mu_l \qquad (7.2$$

- previously detailed in chapter 3. With the turbulent viscosity μ_t determined from the model postulated by Lauder and Spalding - also described in chapter 3 . The molecular viscosity μ_l is determined from:

$$\mu_l = (\mu_l\, m)_{N_2} + (\mu_l\, m)_{O_2}\,, \qquad (7.3$$

with the molecular viscosities of Nitrogen and Oxygen read from tables published by Rogers and Mayhew[45] .

Near the impervious surface the effective Schmidt number Sc_{eff} has been estimated from the relationship:

$$Sc_{eff} = \frac{Sc_l \cdot Sc_t\,(\mu_t + \mu_l)}{\mu_l\, Sc_t + \mu_t\, Sc_l} \qquad (7.4$$

where Sc_l and Sc_t represent the molecular and turbulent Schmidt numbers. This relationship is based upon a hypothesis put forward by among others, Spalding-Patankar, that the turbulent and molecular

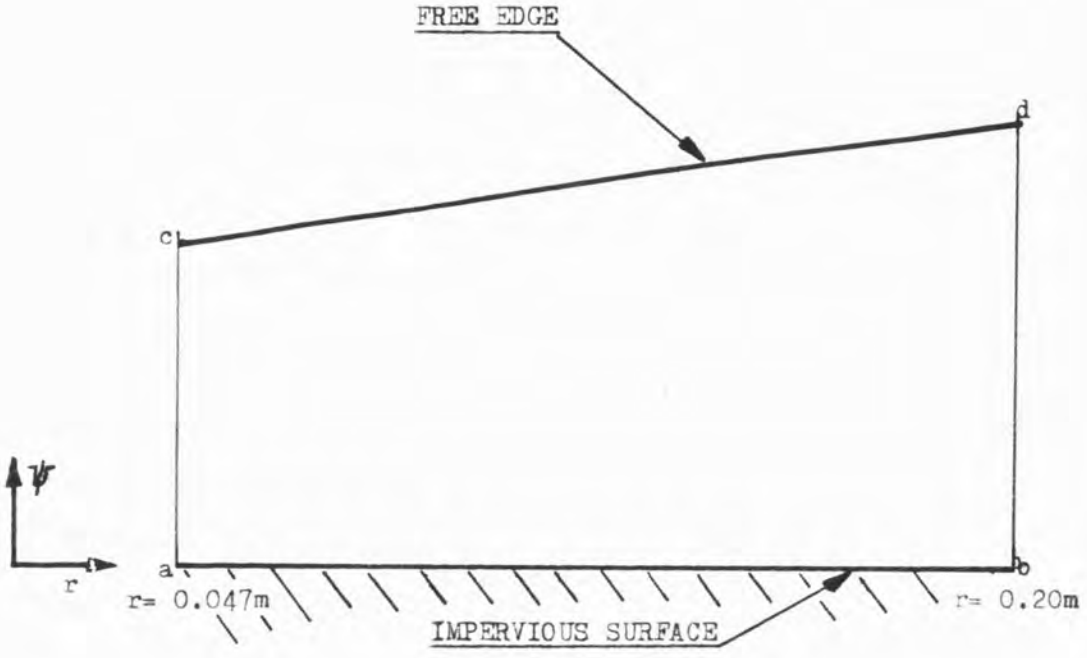

RADIAL WALL JET

FIGURE 7.9

contributions to the effective, or total, Schmidt number of the fluid are additive; and each has a prescribed constant value. Over the remainder of the flow, where $\mu_t >> \mu_l$, the Schmidt number of the fluid has been assumed equal to it's turbulent component Sc_t.

The turbulent Schmidt numbers for Nitrogen and Oxygen have been assumed constant throughout the radial wall jet. This assumption was used by Spalding-Patankar in references [46] and [47]; and conforms to the tentative experimental findings of Robertson and Old [48] in their studies of wake flows. The values prescribed these numbers are, from Robertson, $(Sc_t)_{N_2} = 0.7$ and $(Sc_t)_{O_2} = 0.71$. The molecular Schmidt numbers were looked up from tables presented by Roger and Mayhew [45].

7.3. Comparisons With Experimental Results

Four different computational simulations of the radial wall jet flow detailed in section 7.1 are presented. The specified flow has been simulated in the region where $0.047 \leq r \leq 0.2$m. Two gradings for z at the starting cross-stream section, and two values of the velocity gradient limit, have been used to provide the four simulations. At the starting cross-stream section of the radial wall jet, as in figure 7.9, the grading of the spacial ordinate z was established with equation 6.8 ; with the constants $z_{1,1}$, $z_{1,2}$ and Fr taking the following values:

a) $z_{1,1} = 0.0$, $z_{1,2} = \delta_{1,1}/10^3$ and Fr = 1.121

(7.5

b) $z_{1,1} = 0.0$, $z_{1,2} = \delta_{1,1}/10^5$ and Fr = 1.196

where $\delta_{1,1}$ is the width of the flow at this section. As before the velocity gradient limit L was set at values of 10^3 and 10^5 - as prescribed in chapter four.

In each simulation the following boundary conditions were used to specify the extent of the radial wall jet. The experimental results presented in figure 7.10 were used to obtain the properties along the starting cross-stream at r=0.047m. At the free-edge the radial velocity was set to 0.01 U_{max}, where U_{max} is the maximum velocity at that particular cross-stream section; and the gravimetric concentrations of Nitrogen and Oxygen set to 0.78 and 0.23 respectively. Along the impervious surface the radial velocity was set to zero, and the Nitrogen and Oxygen concentration prescribed values shown in figure 7.11. The two lines shown in this figure detail the measured variation of Nitrogen and Oxygen at the impervious surface; the symbols used are detailed in table 7.1.

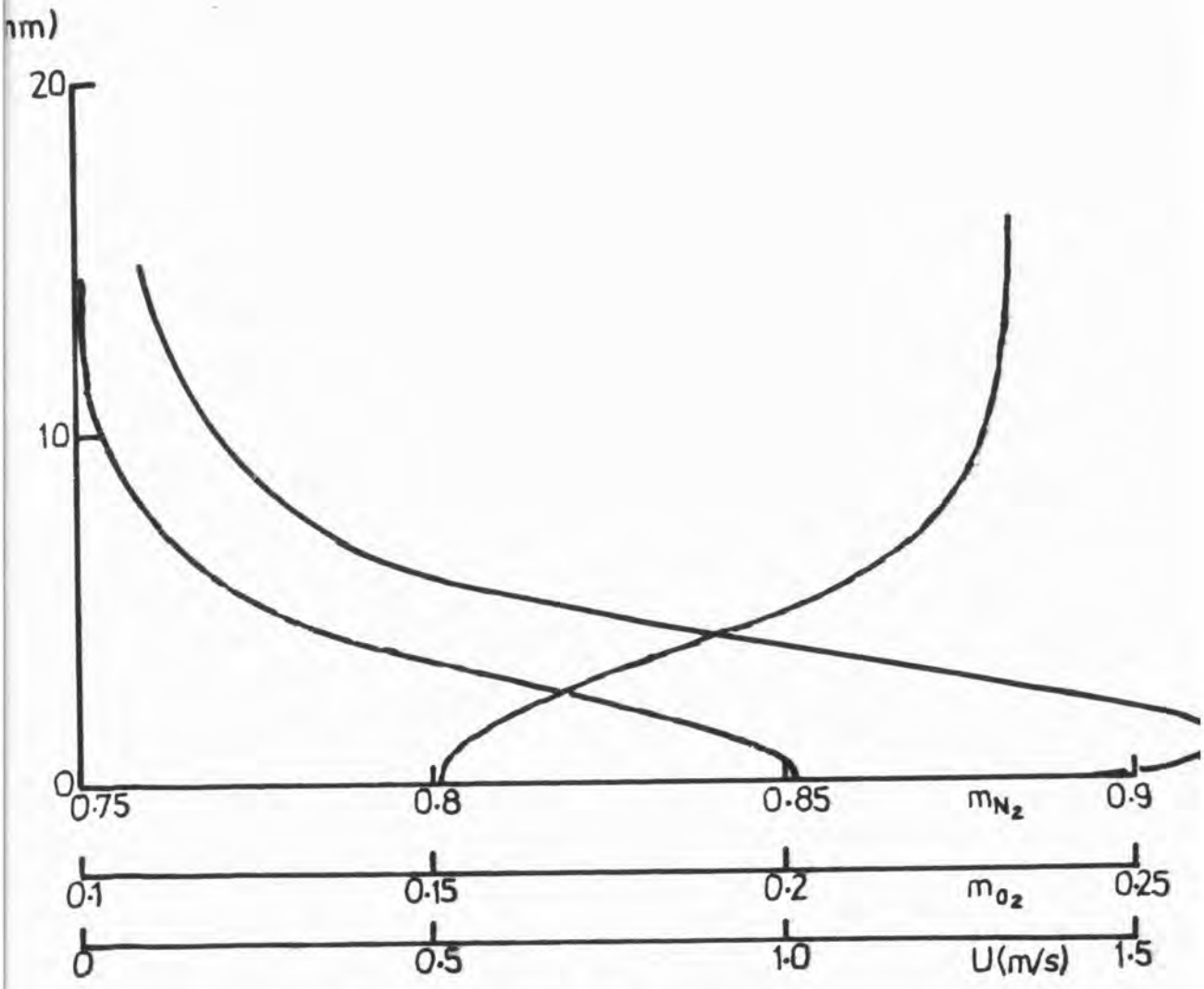

CROSS-STREAM FLOW PATTERN AT r = 0.047m

FIGURE 7.10

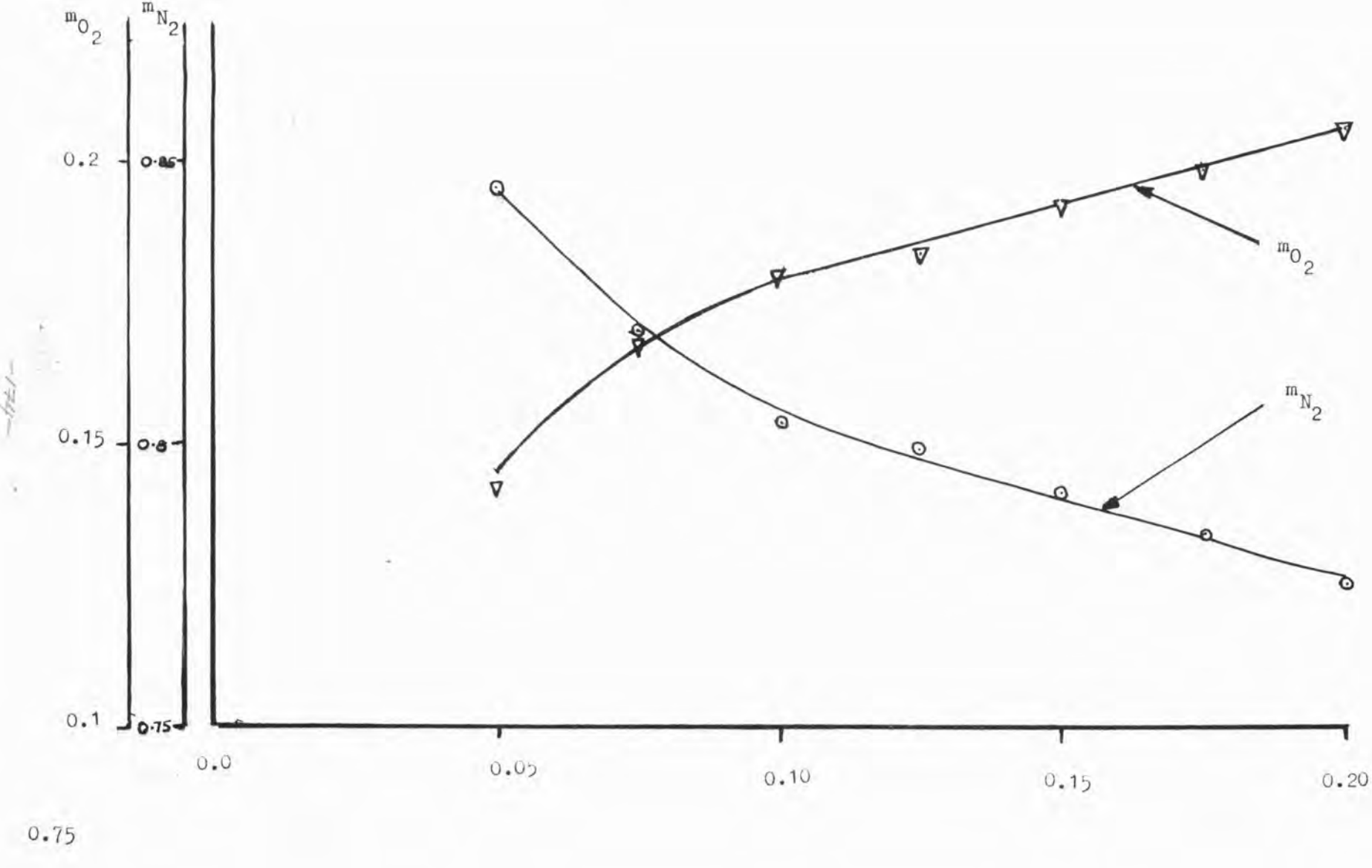

0.75

FIGURE 7.11

Specimen results from the computational simulations at radii of 0.05, 0.1, 0.15 and 0.2m are presented in figures 7.12 to .15 respectively. The symbols used in these figures are detailed in table 7.2. The percentage differences between the predicted and experimental results at z = 0, δ_4 and δ_5 are detailed in table 7.3. (In this table δ_4 represents the real height z at which the velocity is a maximum; and δ_5 is the height at which the velocity is $\frac{Umax}{2}$ with $\delta_5 > \delta_4$.)

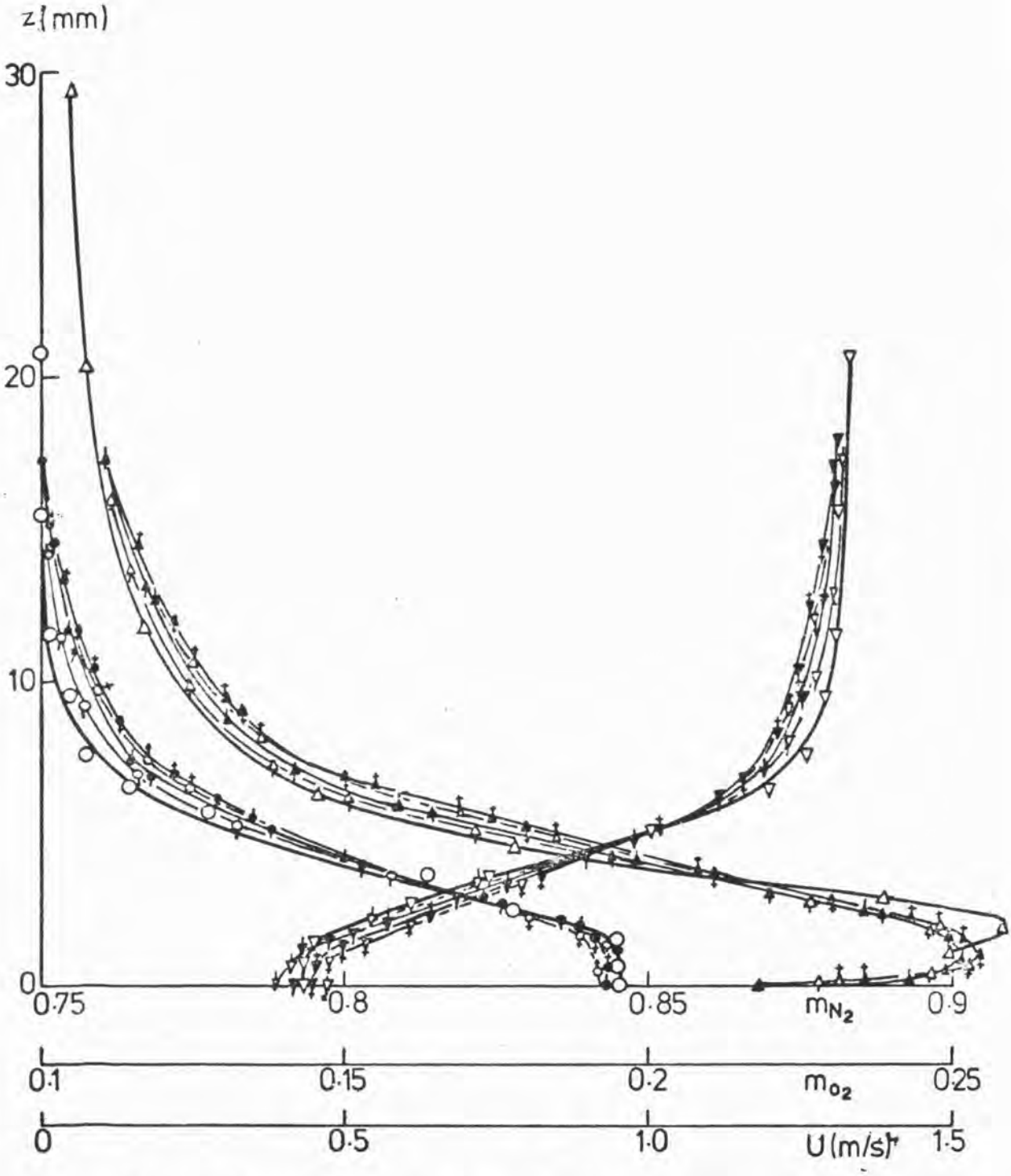

CROSS-STREAM FLOW PATTERNS AT r = 0.05m

FIGURE 7.12

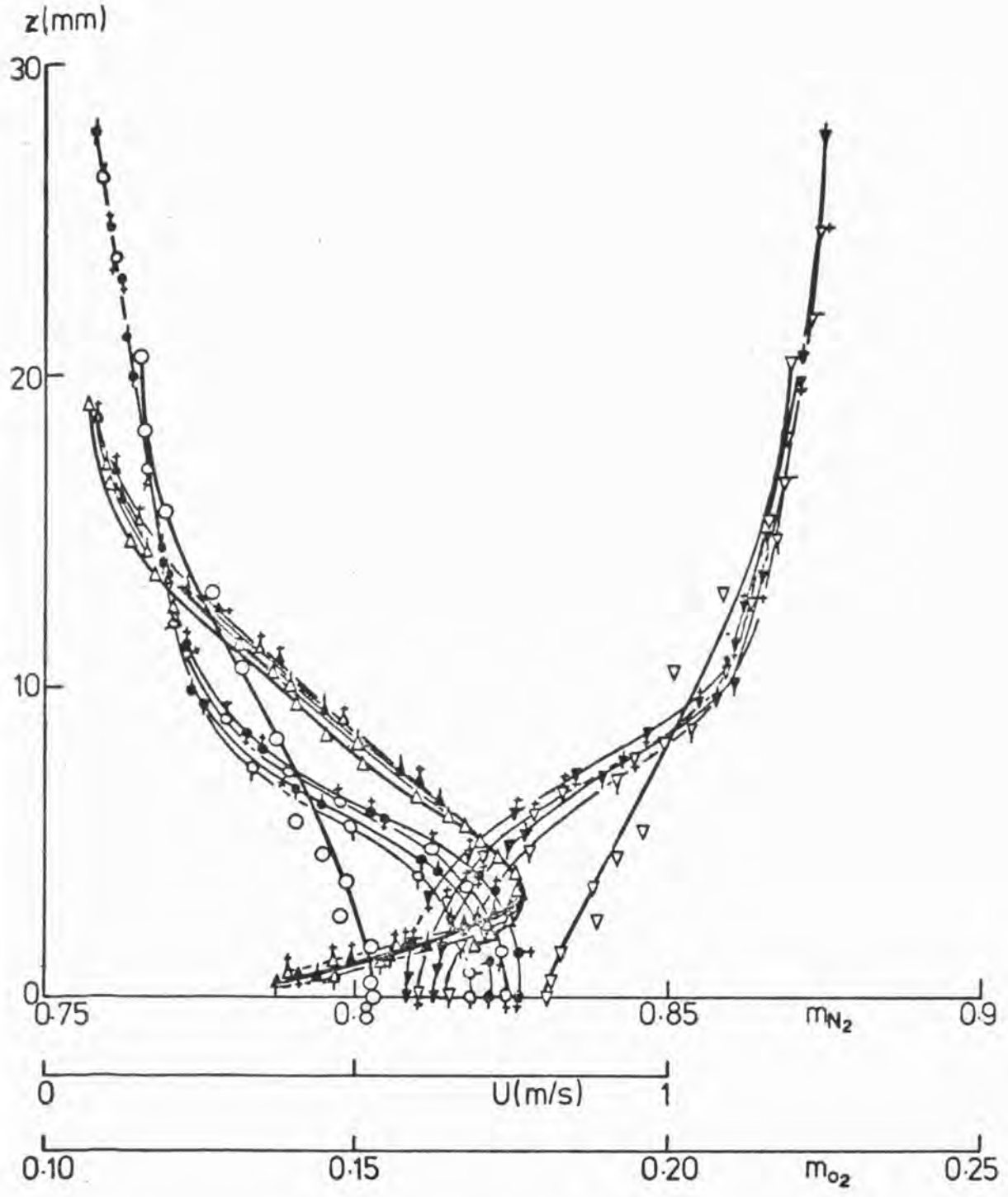

CROSS-STREAM FLOW PATTERNS AT r = 0.10m

FIGURE 7.13

CROSS-STREAM FLOW PATTERNS AT r = 0.15m

FIGURE 7.14

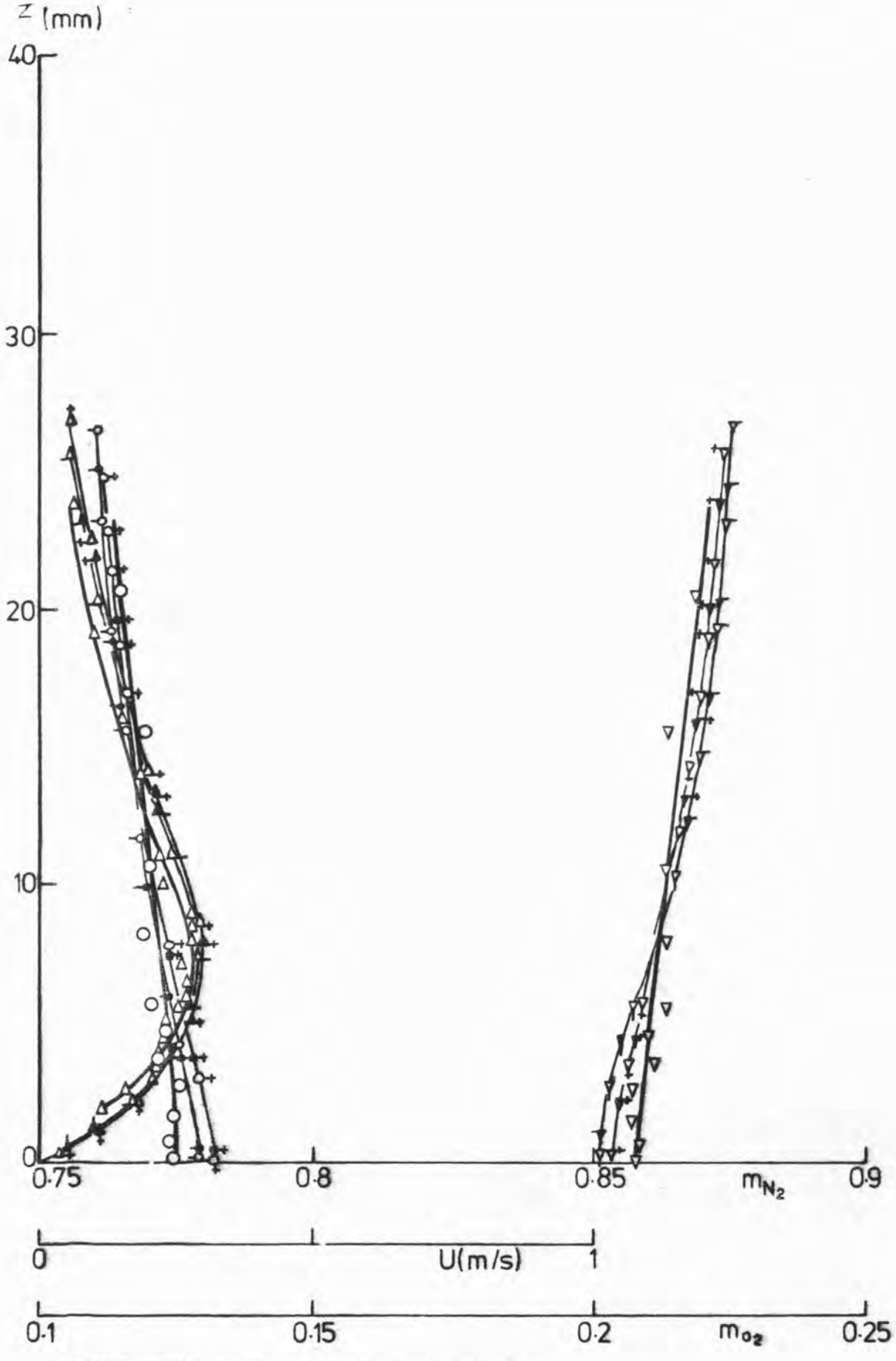

CROSS-STREAM FLOW PATTERNS AT r = 0.20m

FIGURE 7.15

	Mesh grading		Velocity gradient limit	Percentage difference between the predicted and experimental							
				Velocity		m_{O_2}			m_{N_2}		
	$\frac{\delta_{1,1}}{y_{1,2}}$	Fr	L	$z = \varepsilon_4$	$z = \varepsilon_5$	$z = 0$	$z = \varepsilon_4$	$z = \varepsilon_5$	$z = 0$	$z = S_5$	$z = S$
a) r = 0.05m	10^3	1.12	10^3	-6.0	12.0	3.0	-0.3	-0.5	-1.0	0.7	1.0
			10^5	-6.0	12.0	1.5	-0.3	-0.5	-0.5	1.0	1.0
	10^5	1.19	10^3	-8.5	8.0	-4.0	-0.3	-0.5	-1.0	0.5	0.5
			10^5	-8.5	11.0	-1.0	-0.3	-0.5	-0.5	0.8	0.5
b) r = 0.10m	10^3	1.12	10^3	2.9	8.9	2.7	2.6	-0.7	-1.7	-1.5	1.5
			10^5	2.1	10.1	2.9	3.0	-0.5	-2.1	-1.0	0.5
	10^5	1.19	10^3	2.6	3.8	2.0	1.8	-5.0	-2.0	-2.1	2.0
			10^5	2.6	6.3	2.3	2.3	-1.0	-1.3	-1.1	2.0
c) r = 0.15m	10^3	1.12	10^3	8.0	11.3	-4.0	0.0	1.5	1.9	1.0	0.0
			10^5	8.0	11.3	-4.9	-0.5	1.0	2.0	1.0	0.5
	10^5	1.19	10^3	6.0	8.0	-5.6	-0.8	1.0	1.5	0.4	-1.3
			10^5	6.0	8.0	-6.5	-2.1	0.3	1.7	0.7	0.3
d) r = 0.2m	10^3	1.12	10^3	7.0	9.0	-2.0	-0.5	1.0	1.5	0.3	-1.7
			10^5	7.0	9.0	-2.0	-0.5	1.0	1.5	0.3	-1.7
	10^5	1.19	10^3	4.0	8.0	-3.5	-0.5	2.0	1.0	0.0	-3.5
			10^5	4.0	8.0	-3.5	-0.5	2.0	1.0	0.0	-3.5

In the region of the radial wall jet where $0.05 \leq r \leq 0.15$m the discrepancies in the predicted properties are dependent upon the mesh grading of z, at the starting cross-stream section, and velocity gradient limit used. A measure of this correlation is provided by the comparisons of velocity and gravimetric concentrations of Nitrogen and Oxygen at r = 0.05, 0.1 and 0.15m shown in figures 7.12,.13 and .14 . Further evidence is provided by the percentage discrepancies presented in table 7.3 .

Over the remainder of the flow, where $0.15 < r \leq 0.20$m, the discrepancy is only relatively dependent upon the velocity gradient limit. As shown by the comparisons of the cross-stream velocity, and gravimetric Nitrogen and Oxygen profiles at x = 0.15 and 0.2m in figures 7.13 and .14. Again the percentage discrepancies in table 4.3 verify these findings.

7.4 Conclusions

The recommended modelling technique successfully simulated the measured time averaged velocity and concentration fields of the radial wall jet study detailed in appendix four . The discrepancy between the predicted and experimental results was less than twelve percent, which was considered sufficiently accurate for most engineering purposes. This result verifies that the portionsof the modelling technique used for simulating turbulent momentum and mass transfer were satisfactory in this particular flow situation.

Chapter Eight

Heat Transfer Rates

The purpose of the work detailed is to illustrate that the modelling technique presented in chapter four can accurately simulate heat transfer rates in a specified turbulent radial wall jet. As this flow is also moving at high speed, and contains more than one species of gas, momentum and mass transfer rates have also been simulated.

The accuracy of the modelling technique is assessed by comparing the computational results from the modelling technique with those from an experiment. A review of this experiment is presented in section 1; the full details and results obtained are give in appendix 5. The methods used to define the physical properties of the simulated flow are specified in section 2. The accuracy of presented computational predictions are discussed in section 3, and in section 4 the performance of the modelling technique is assessed.

8.1 Experiment

The studied impinging flow was produced by the normal impact of an Argon jet on to a flat impervious surface; the free edge of the flow was exposed to the atmosphere - as shown in figure 8.1. An appreciation of the momentum, mass and heat transfer rates within this flow were obtained by mapping the time averaged velocity, species concentration and temperature fields.

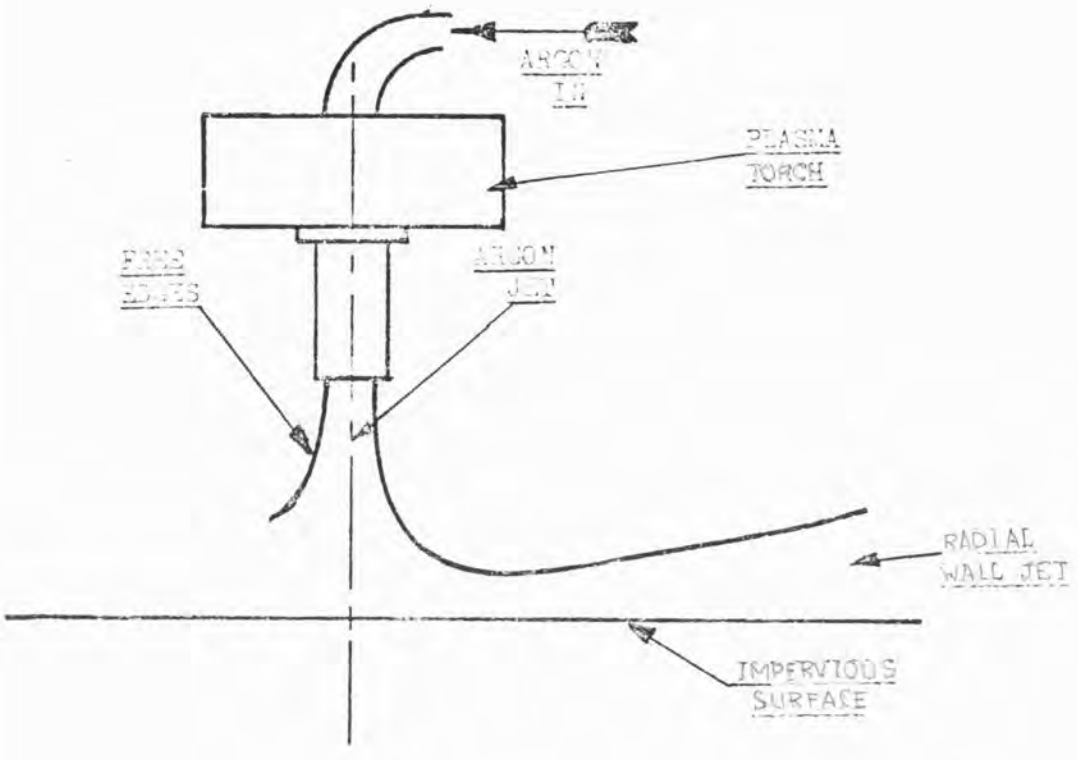

EXPERIMENTAL LAYOUT

FIGURE 8.1

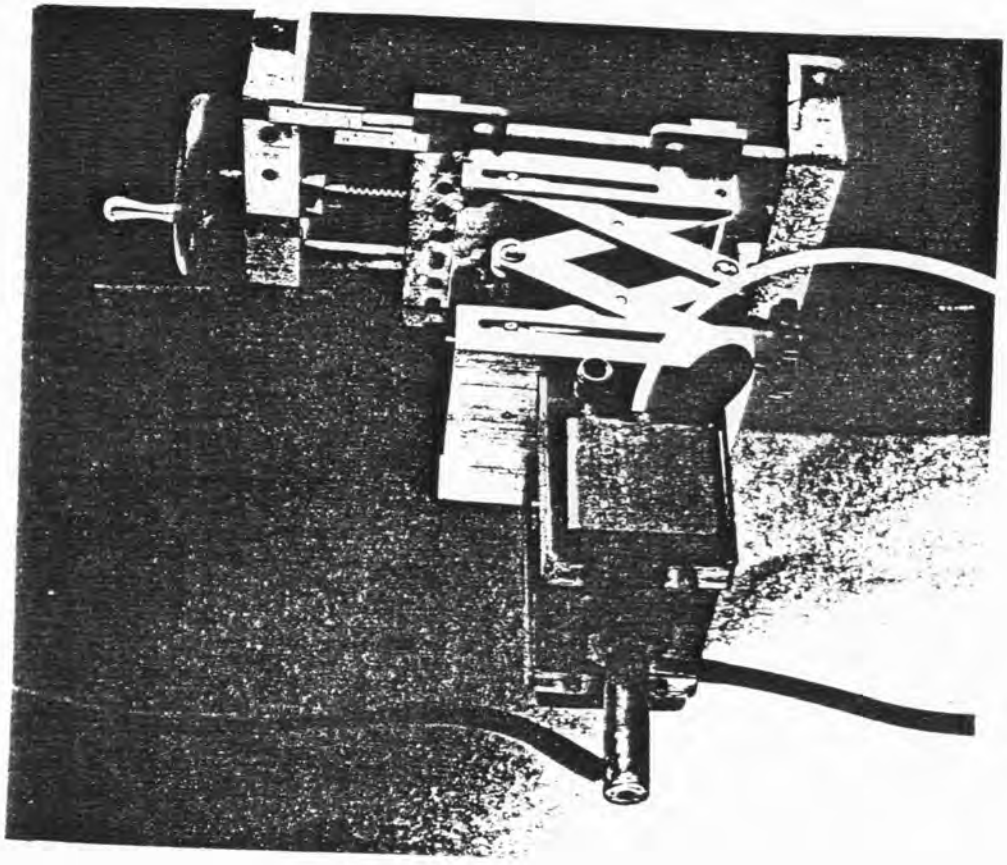

PLASMA TORCH

FIGURE 8.2

The argon jet was produced with a plasma torch of the type shown in figure 8.2; at the exit from the torch the plasma had a mean temperature of approximately 7.5×10^3 K. Throughout the experiment the flow rate of Argon into the torch was maintained at $7.1 \times 10^{-4} m^3 s^{-1}$. The nozzle had a diameter of 0.005m, and the distance between the surface and exit from the plasma torch was set at 0.04m. The jet impinged normally on to a circular impervious surface of 0.5m diameter, which had been ground flat to within $\pm$ 0.0002m.

The concentration of the gases within the impinging flow - that is of Argon, Nitrogen and Oxygen - were measured with a mass-spectrometer and suitable probe. The time averaged temperature was measured using thermocouple sensers made from Nickel Chromium and Nickel aluminium wires, &c. suitable measurement device. The radial U and vertical V velocities of the flow were deduced from the dynamic pressure P_D, which was measured with a pitot static tube that conformed to British Standard 1042 part 2a.

The measured variation of the time averaged velocity, species concentration of Argon, Nitrogen and Oxygen, and temperature are presented in this section. These results which are used to validate the recommended modelling technique, are explained and discussed in the experimental study detailed in appendix 5. The figure numbers and radi at which the experimental results were measured are given in table 8.1 the symbols used throughout are detailed in table 8.2.

Table 8.1

Radii (m)	Figure No.
0.0	8.3
0.0025	8.4
0.005	8.5
0.0075	8.6
0.01	8.7
0.015	8.8
0.02	8.9
0.03	8.10
0.04	8.11
0.05	8.12
0.06	8.13
0.07	8.14
0.08	8.15
0.09	8.16
0.10	8.17
0.11	8.18
0.12	8.19
0.13	8.20

Table 8.2

Symbol	Properties	
▷	V	(Vertical velocity)
◁	U	(Horizontal velocity)
⊙	T	(Temperature)
▽	m_{A_r}	(Gravimetric concentration) of Argon
⊡	m_{O_2}	(Gravimetric concentration) of Oxygen
△	m_{N_2}	(Gravimetric concentration) of Nitrogen

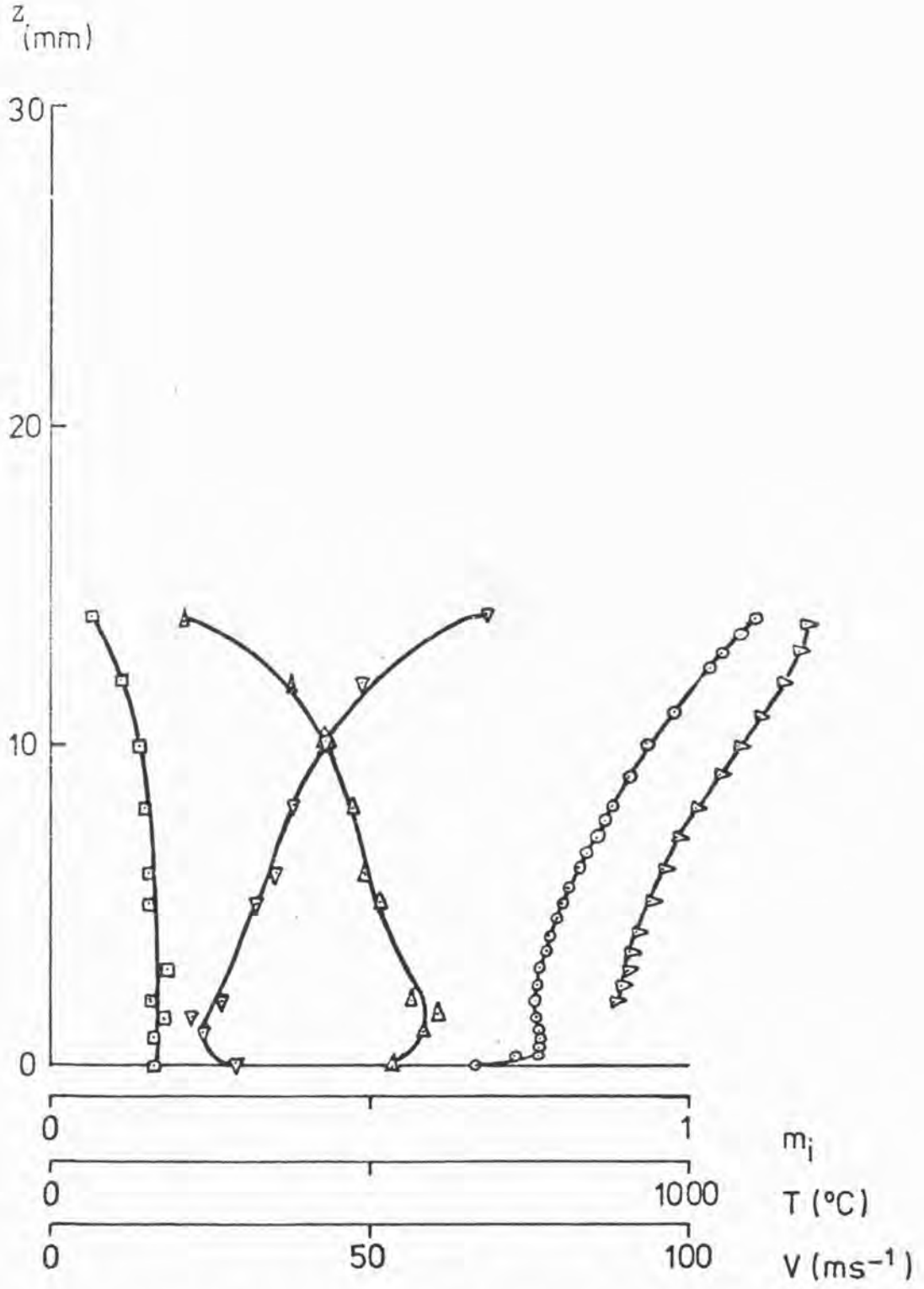

CROSS-STREAM FLOW PATTERN AT r = 0.0m

FIGURE 8.3

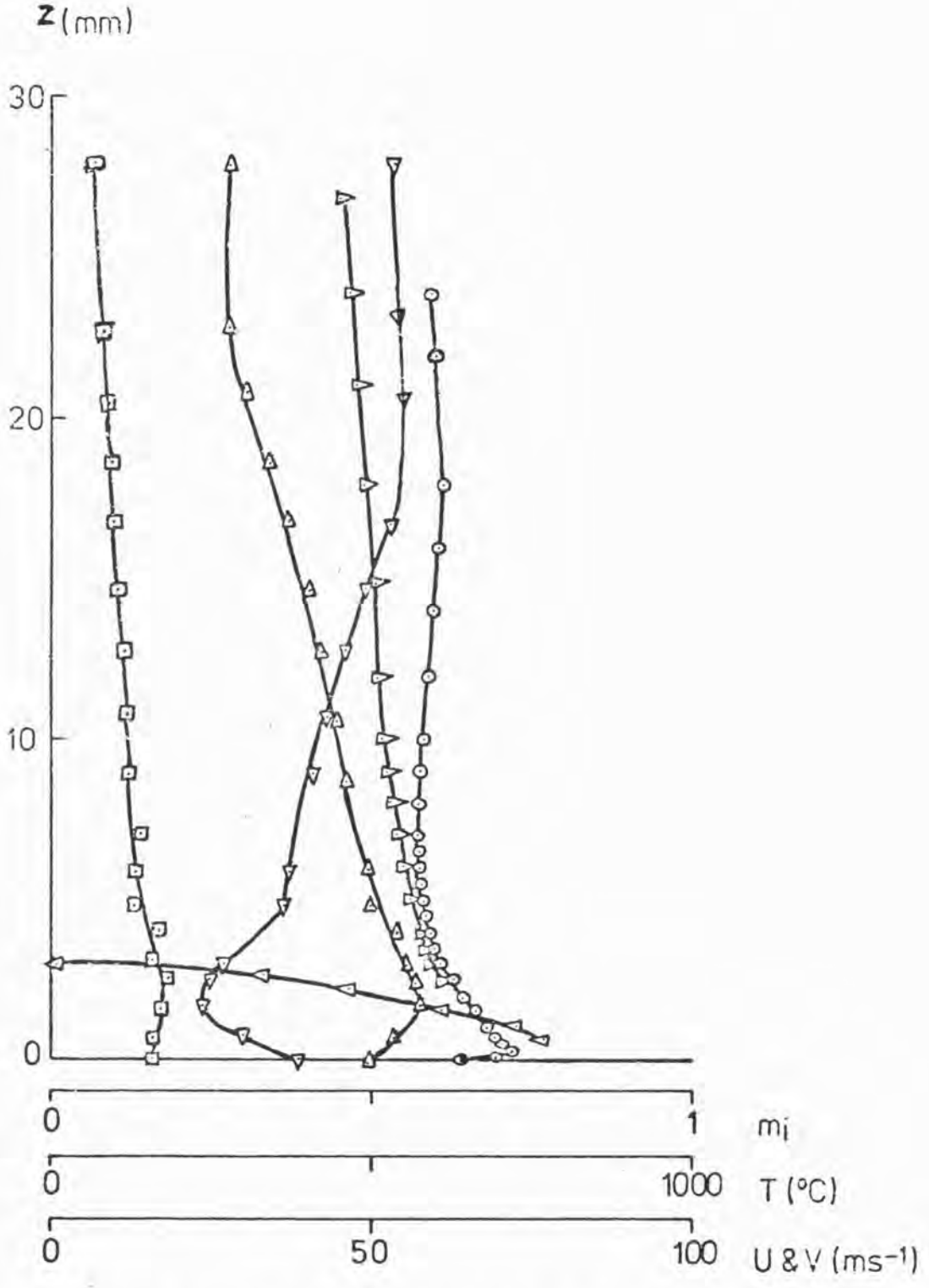

CROSS-STREAM FLOW PATTERN AT z = 0.0025m

FIGURE 72

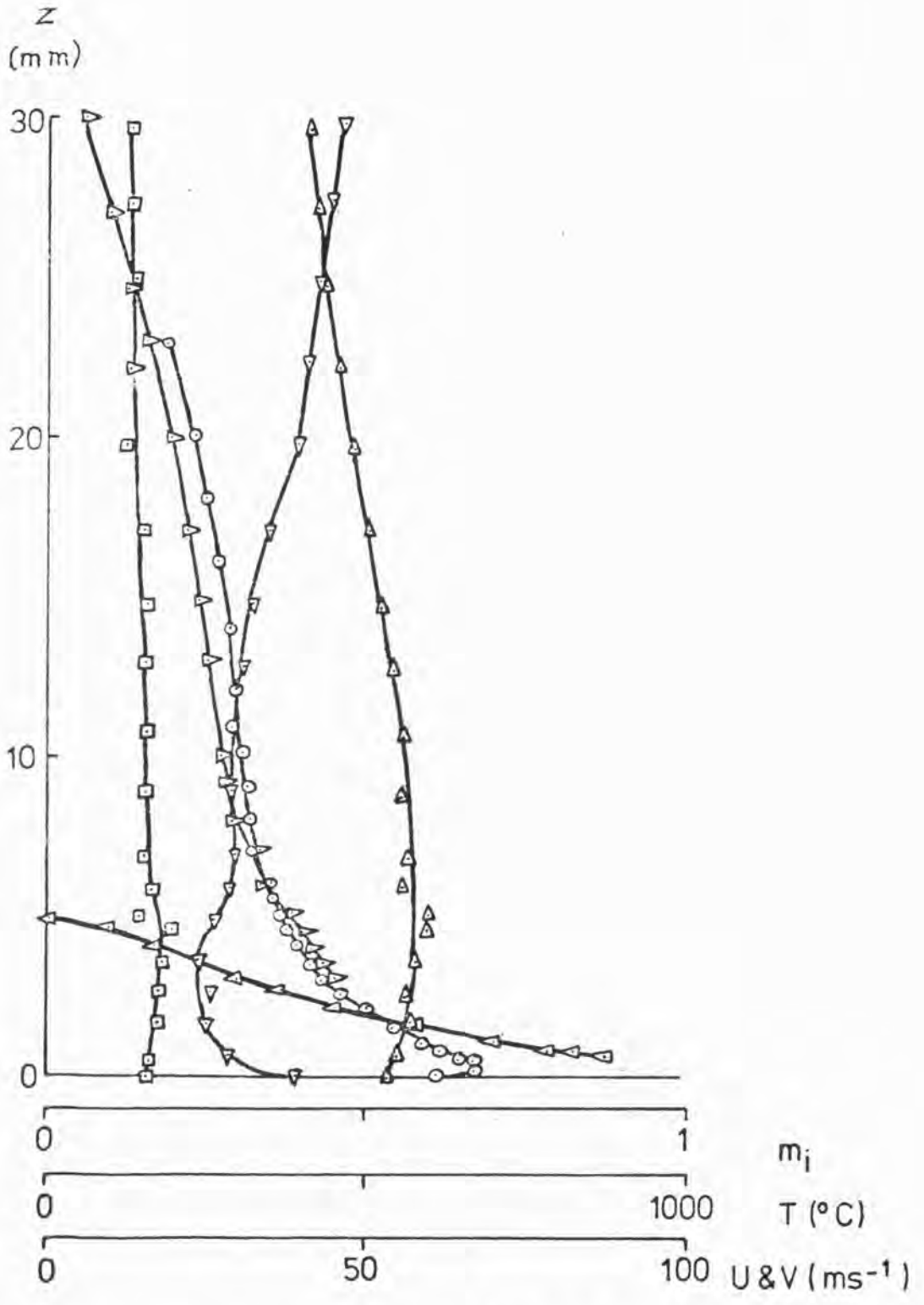

CROSS-STREAM FLOW PATTERN AT r =. 0.0050m

FIGURE 8.5

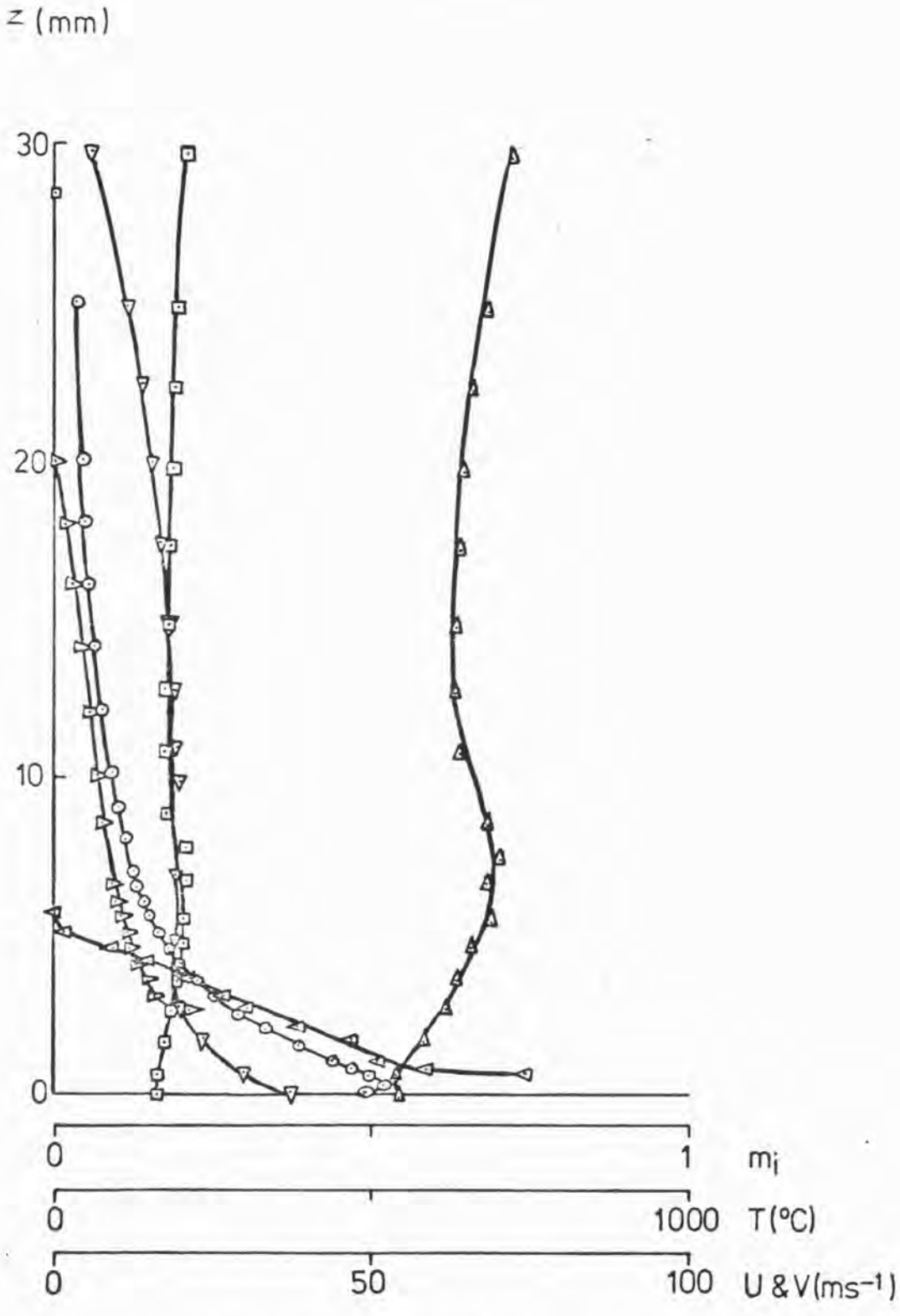

CROSS-STREAM FLOW PATTERN AT r = 0.0075m

FIGURE 8.6

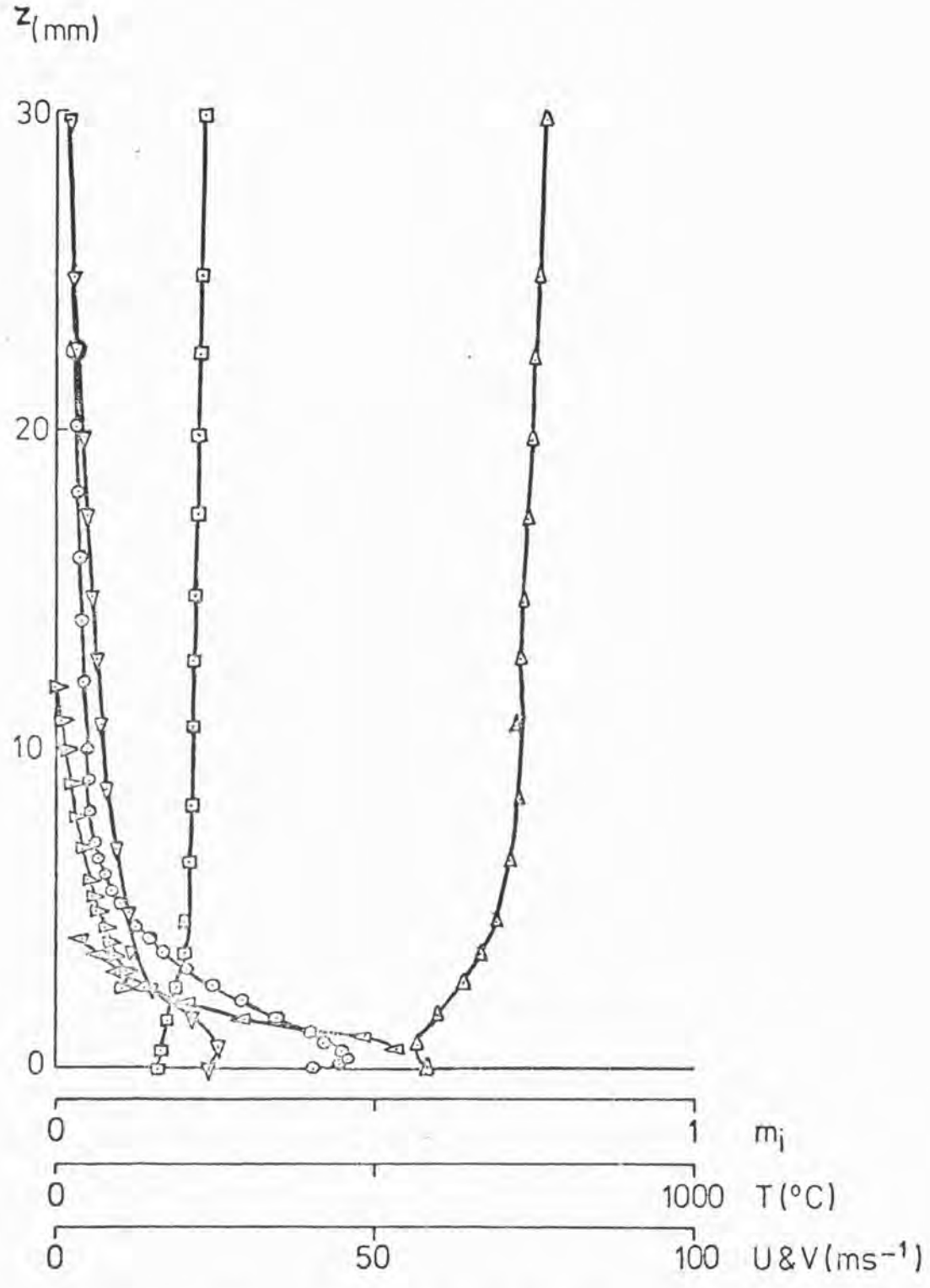

CROSS-STREAM FLOW PATTERN AT r = 0.010m

FIGURE 8.7

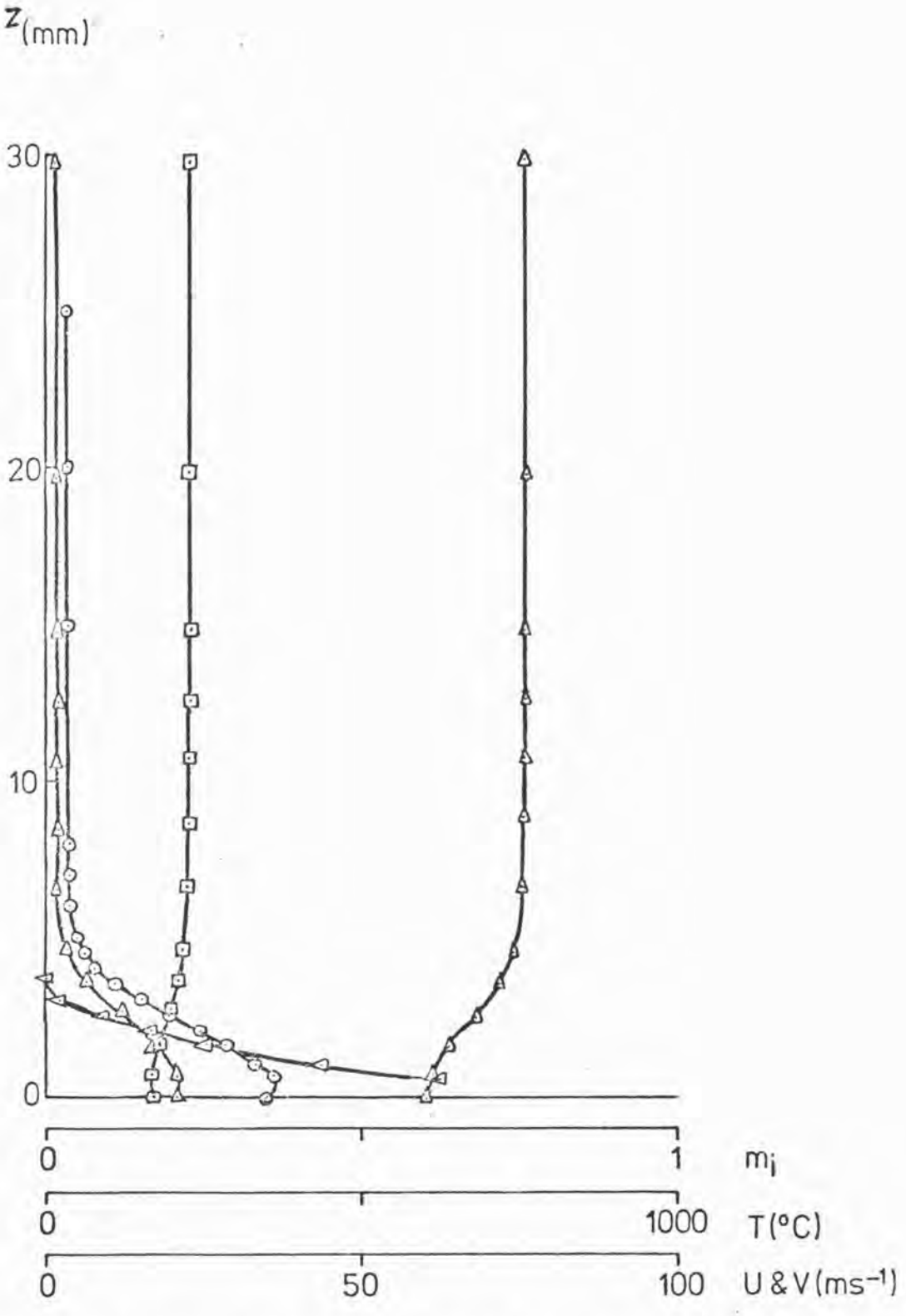

CROSS-STREAM FLOW PATTERN AT $r = 0.015m$

FIGURE 8.8

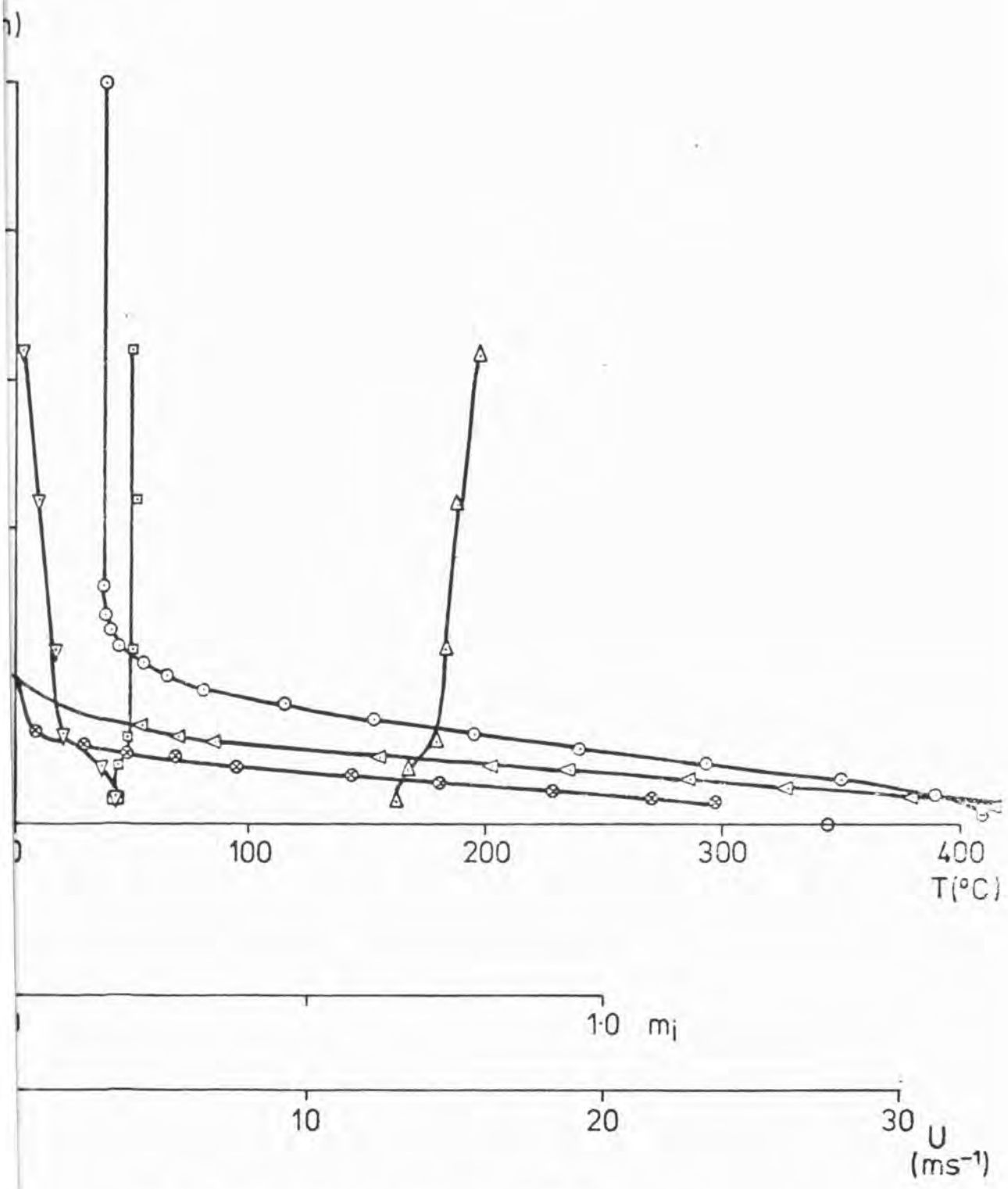

CROSS-STREAM FLOW PATTERN AT r = 0.02m

FIGURE 8.9

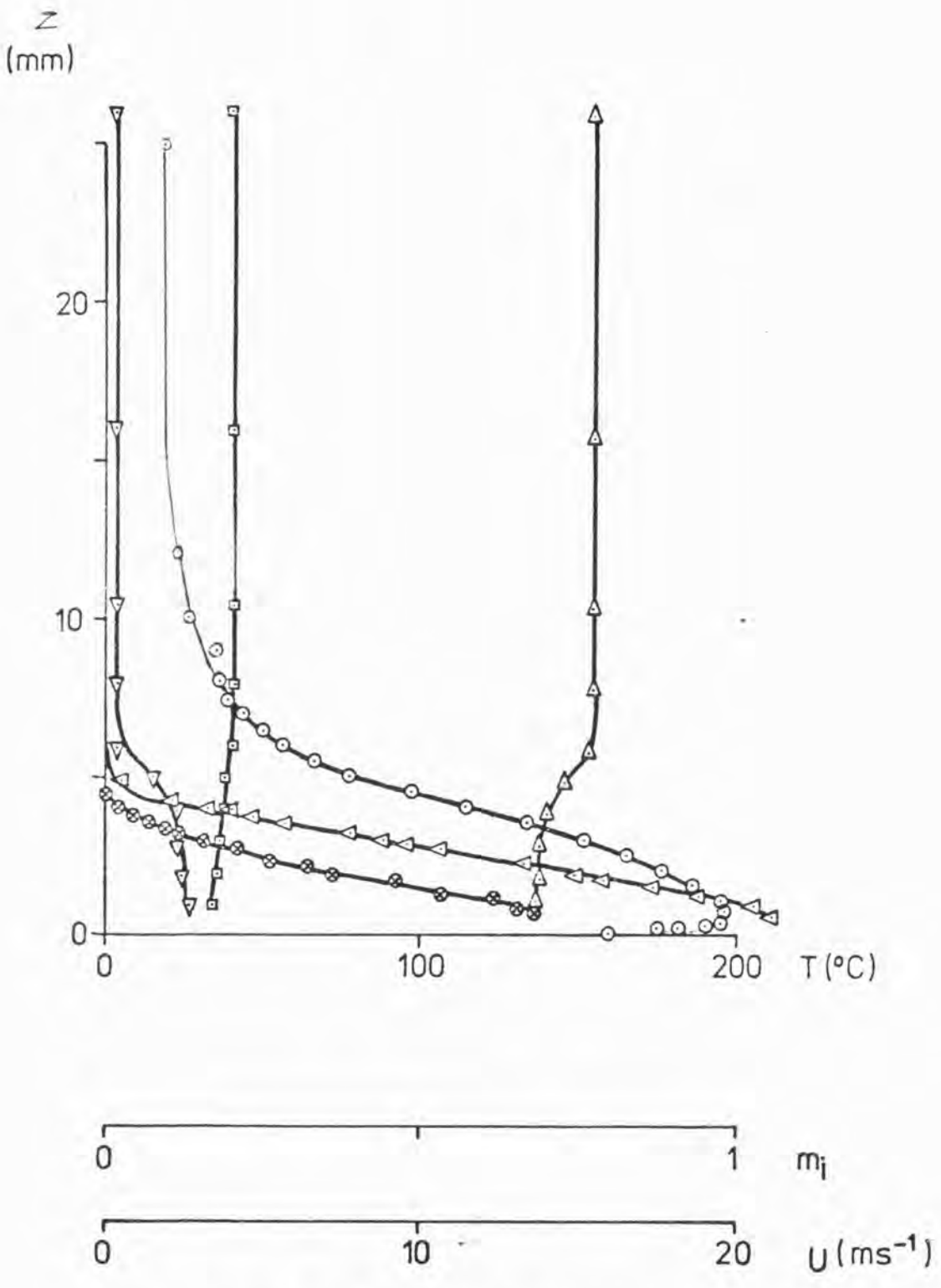

CROSS-STREAM FLOW PATTERN AT r = 0.03m

FIGURE 8.10

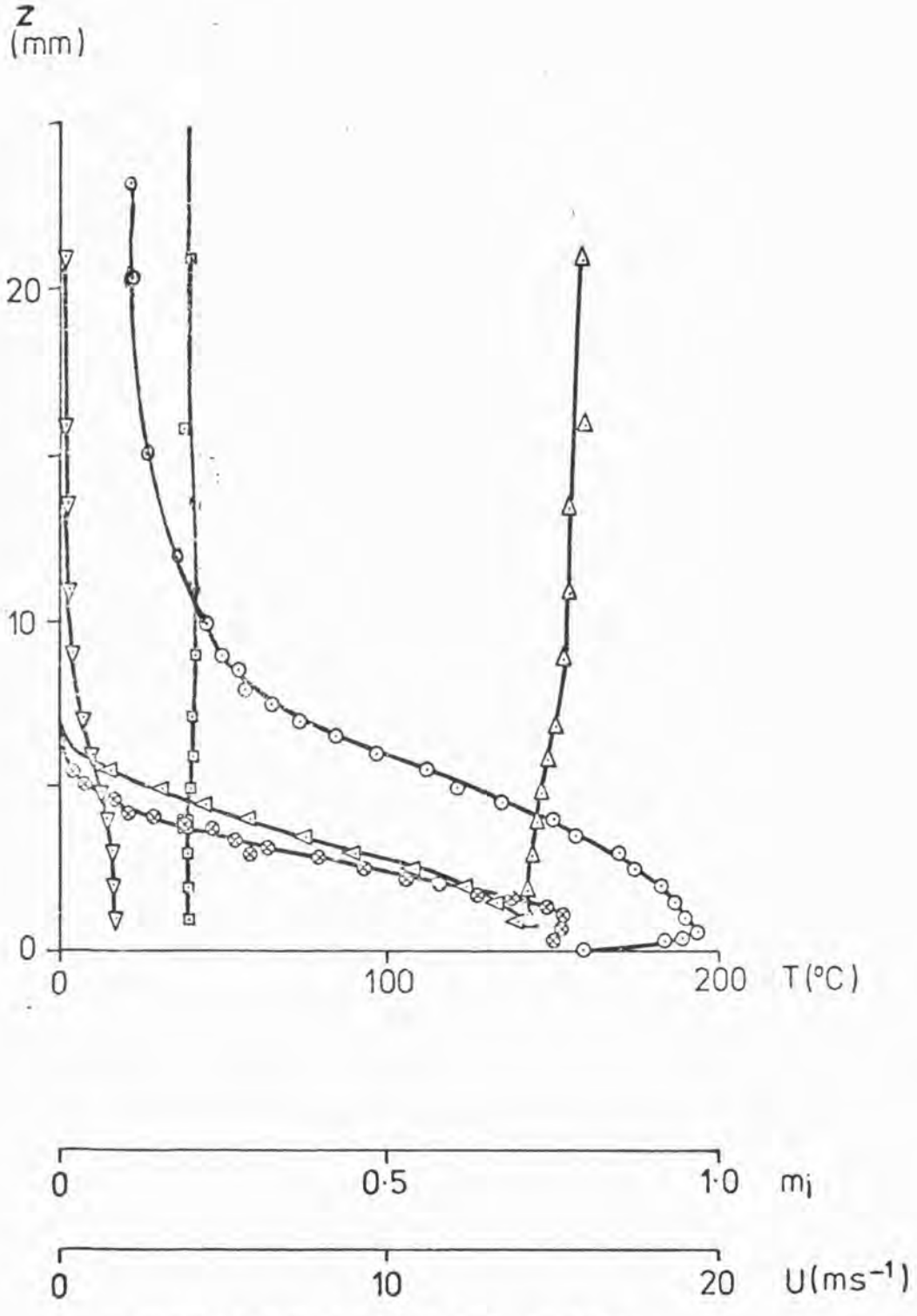

CROSS-STREAM FLOW PATTERN AT r = 0.04m

FIGURE 8.11

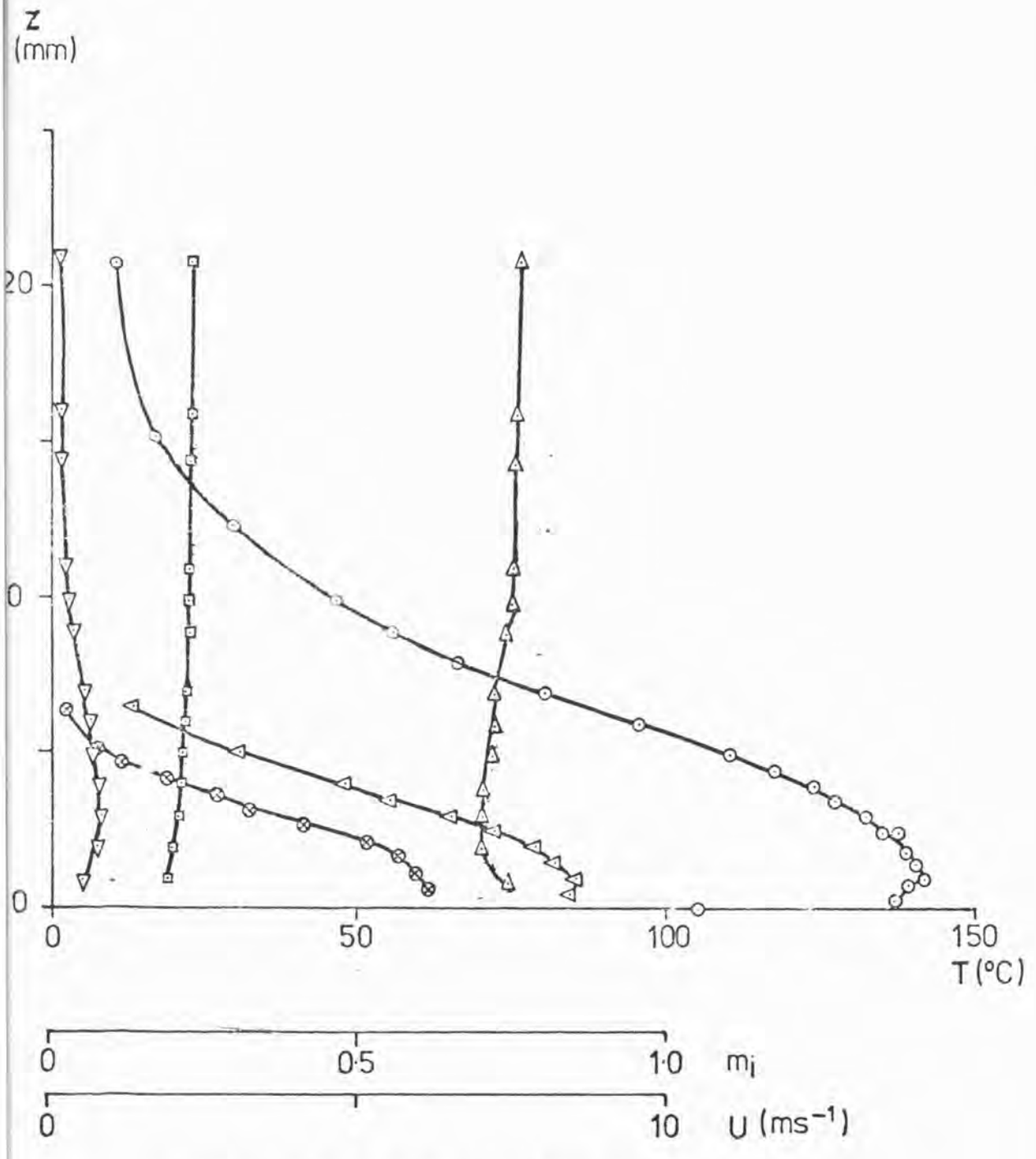

CROSS-STREAM FLOW PATTERN AT r = 0.05m

FIGURE 8.12

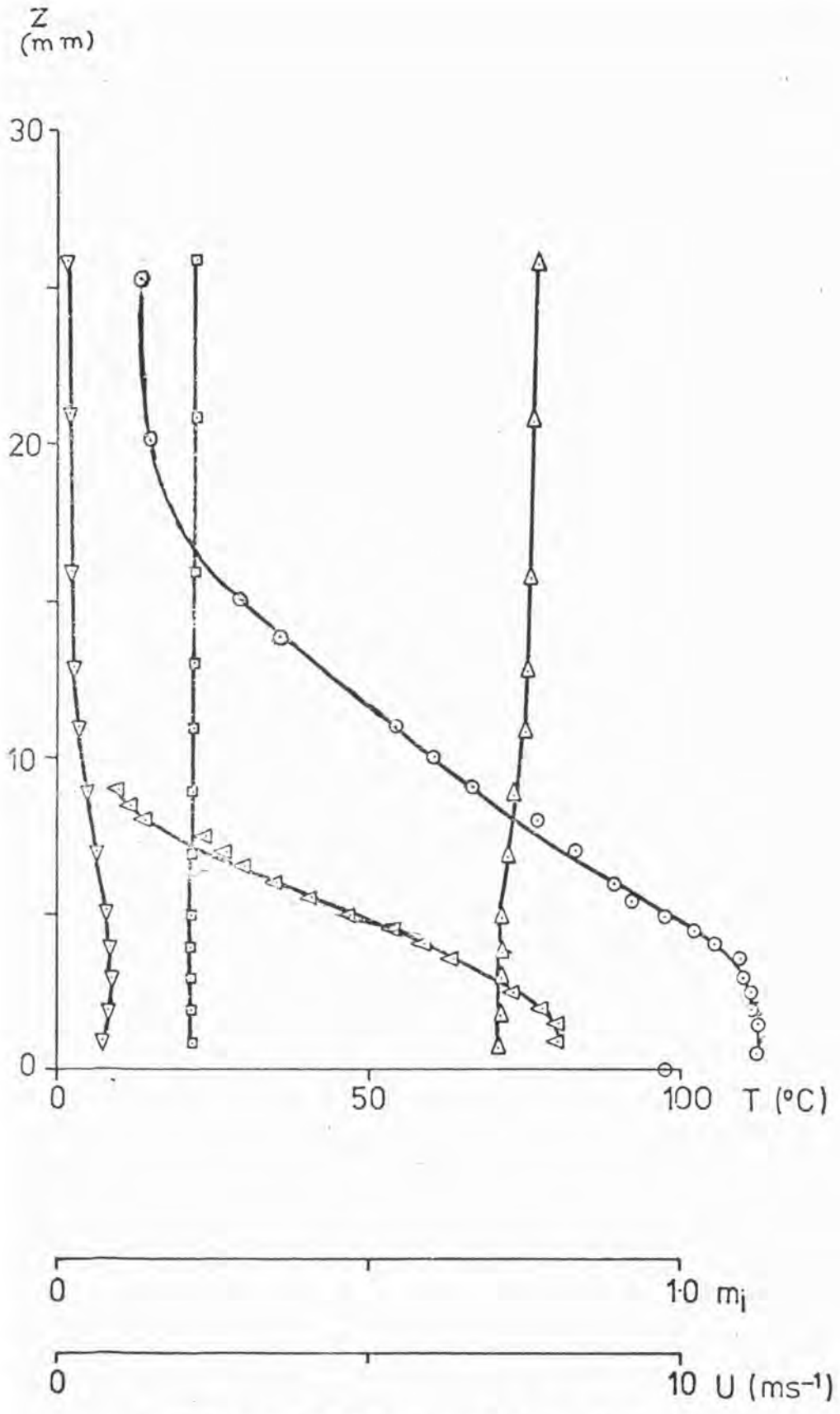

CROSS-STREAM FLOW PATTERN AT r = 0.06m

FIGURE 8.13

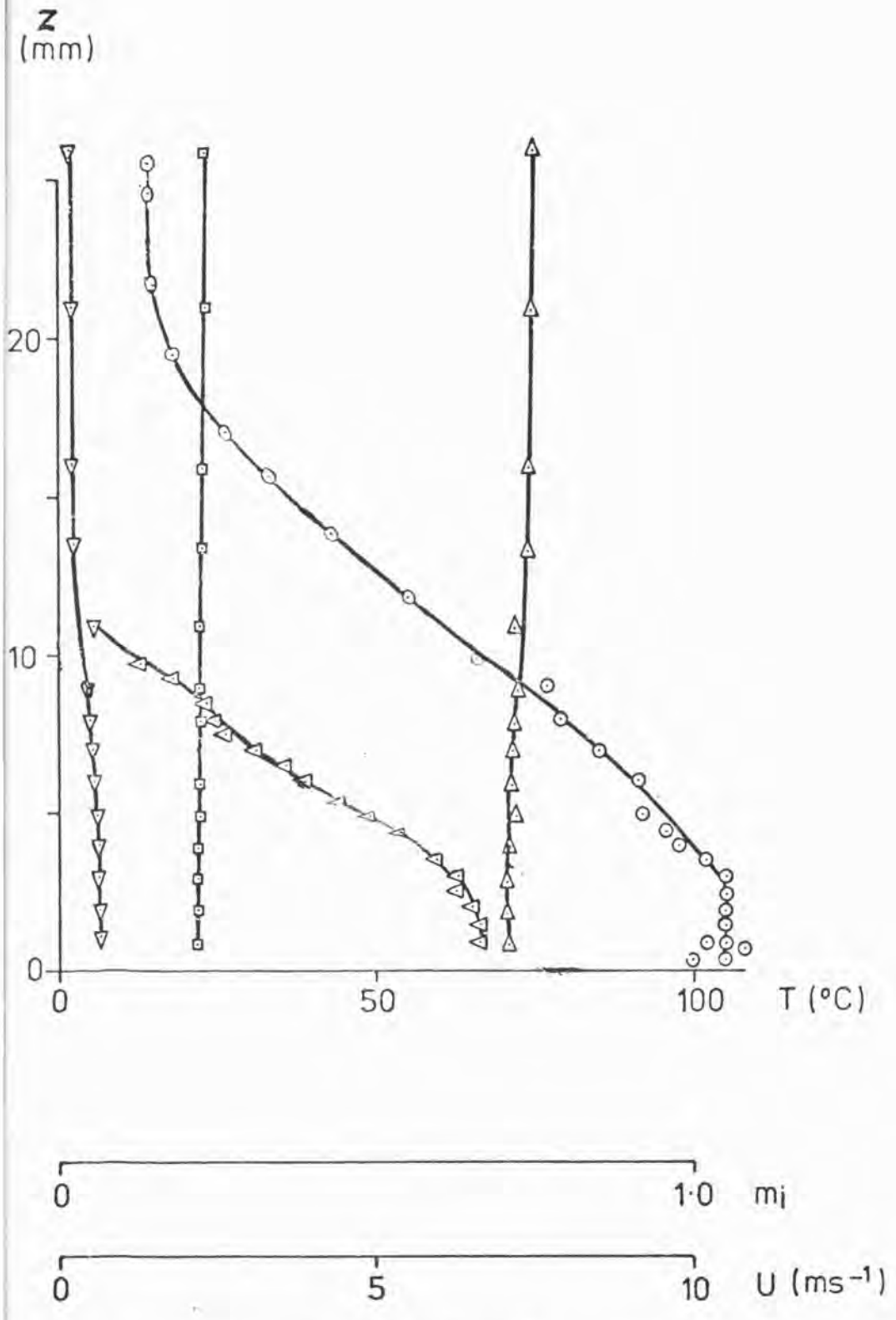

CROSS-STREAM FLOW PATTERN AT r = 0.07m

FIGURE 8.14

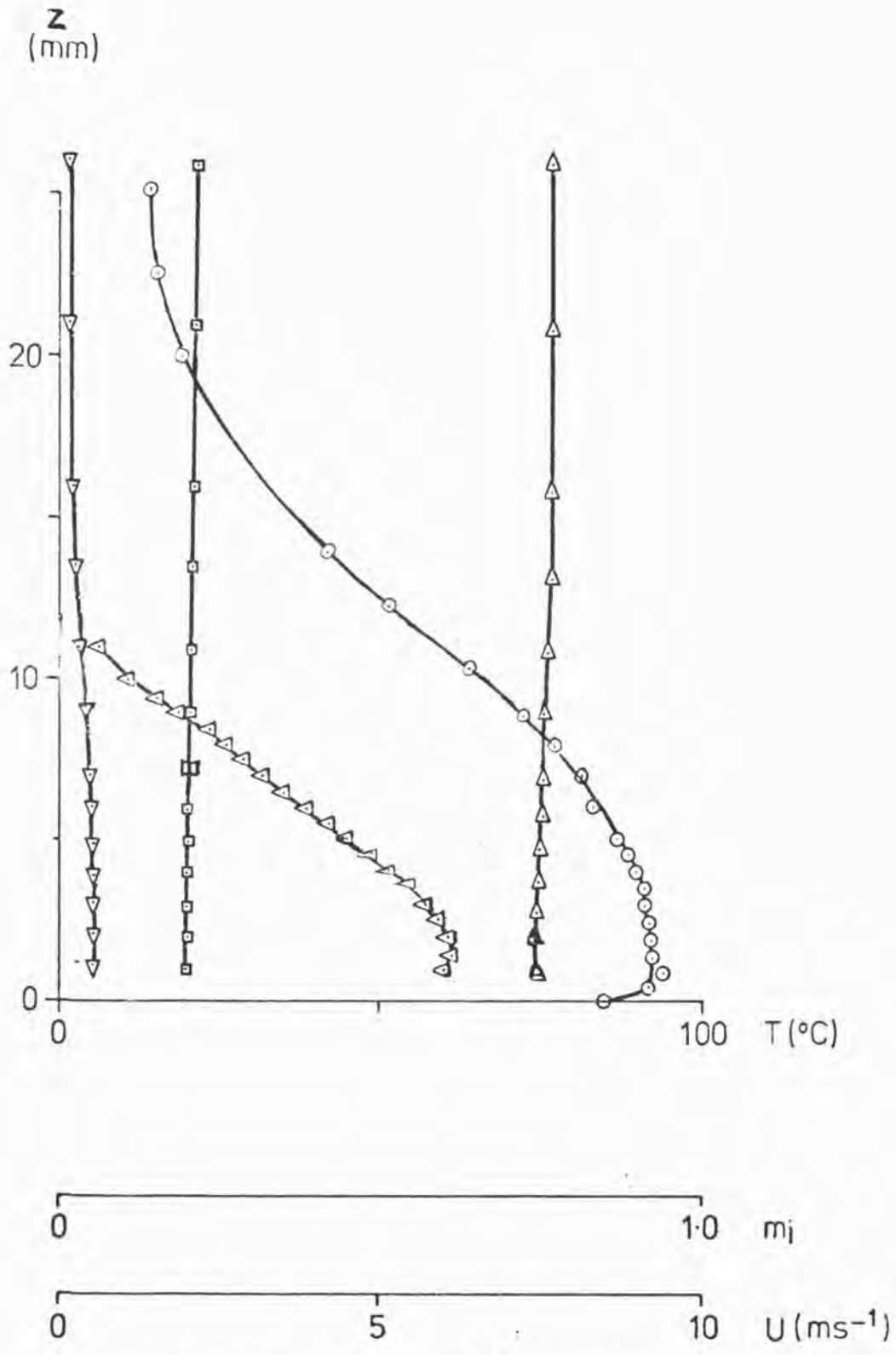

CROSS-STREAM FLOW PATTERN AT x = 0.08m

FIGURE 8.15

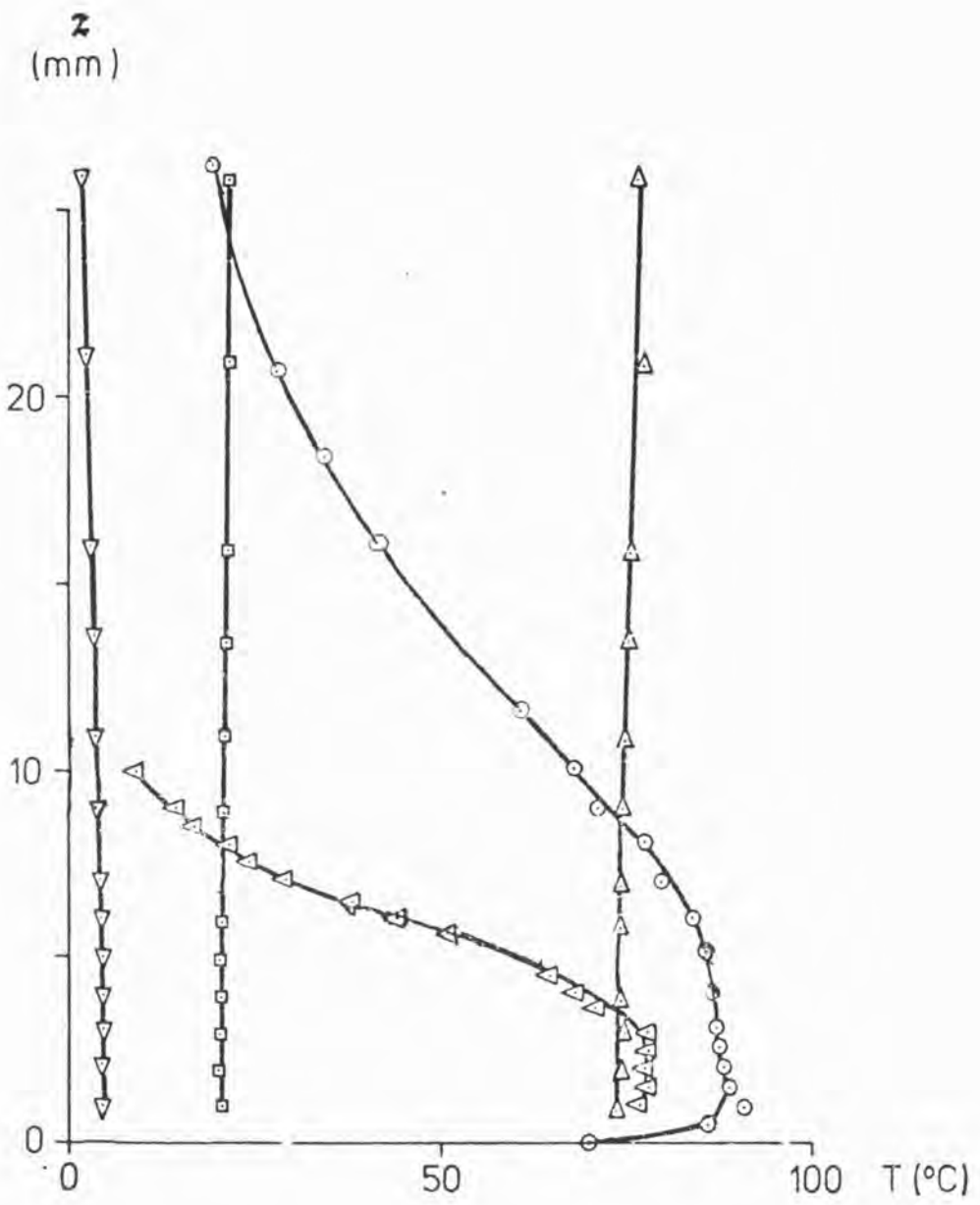

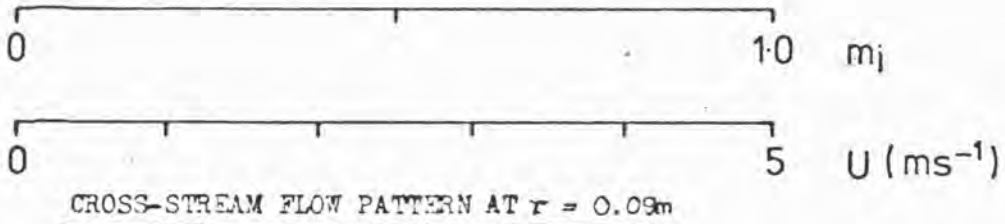

CROSS-STREAM FLOW PATTERN AT r = 0.09m

FIGURE 8.16

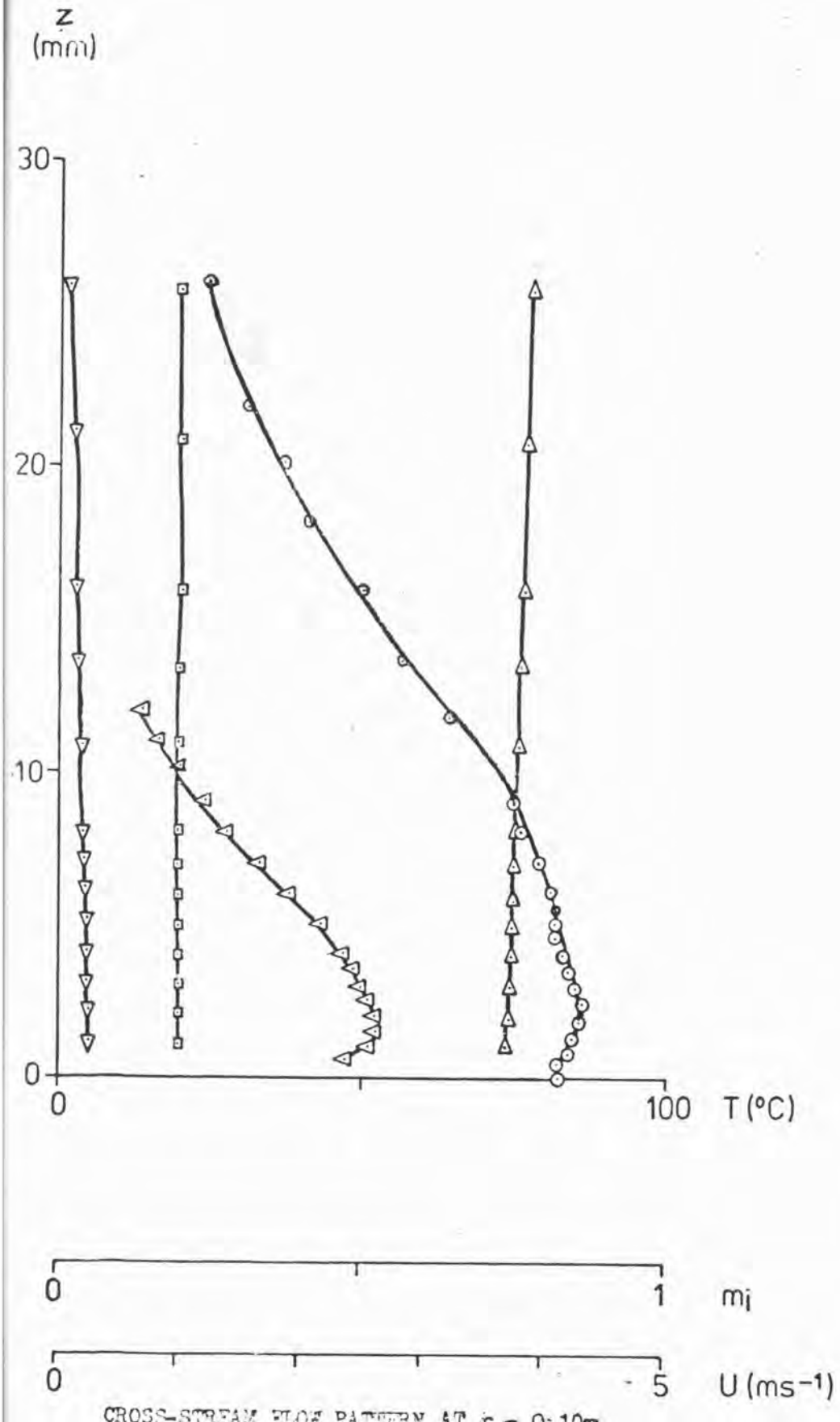

CROSS-STREAM FLOW PATTERN AT r = 0.10m

FIGURE 8.17

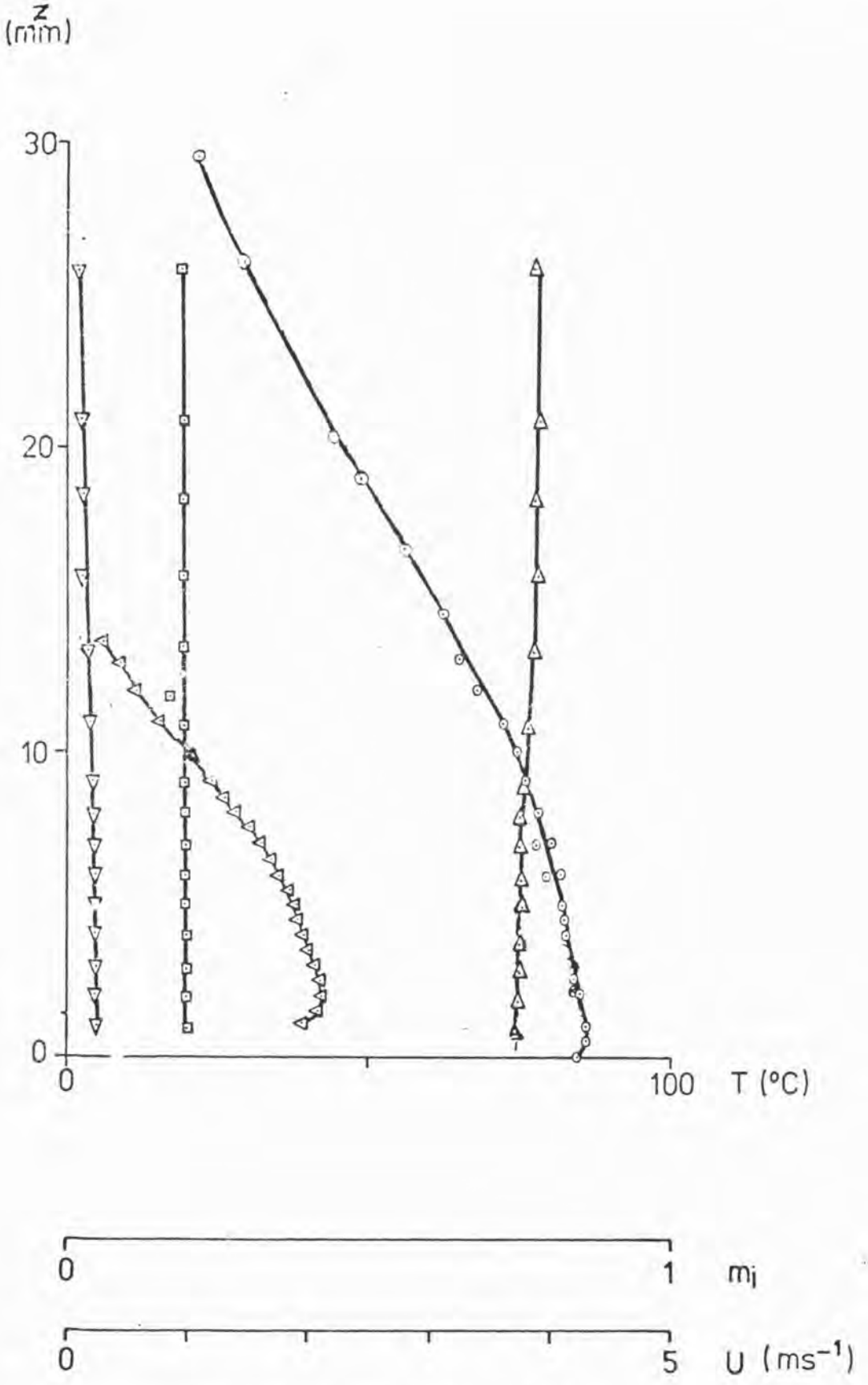

CROSS-STREAM FLOW PATTERN AT r = 0.11m

FIGURE 3.18

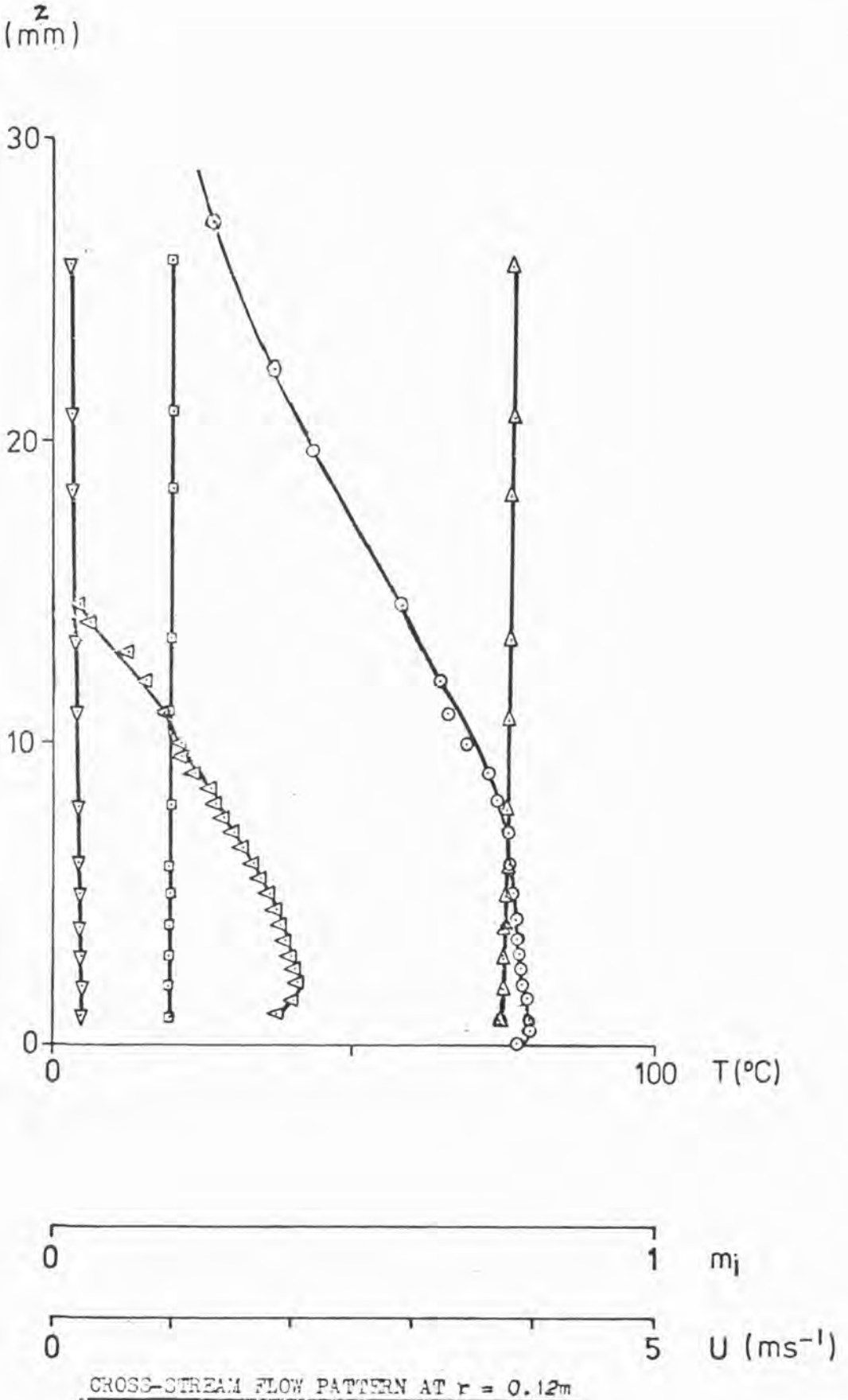

CROSS-STREAM FLOW PATTERN AT r = 0.12m

FIGURE 8.19

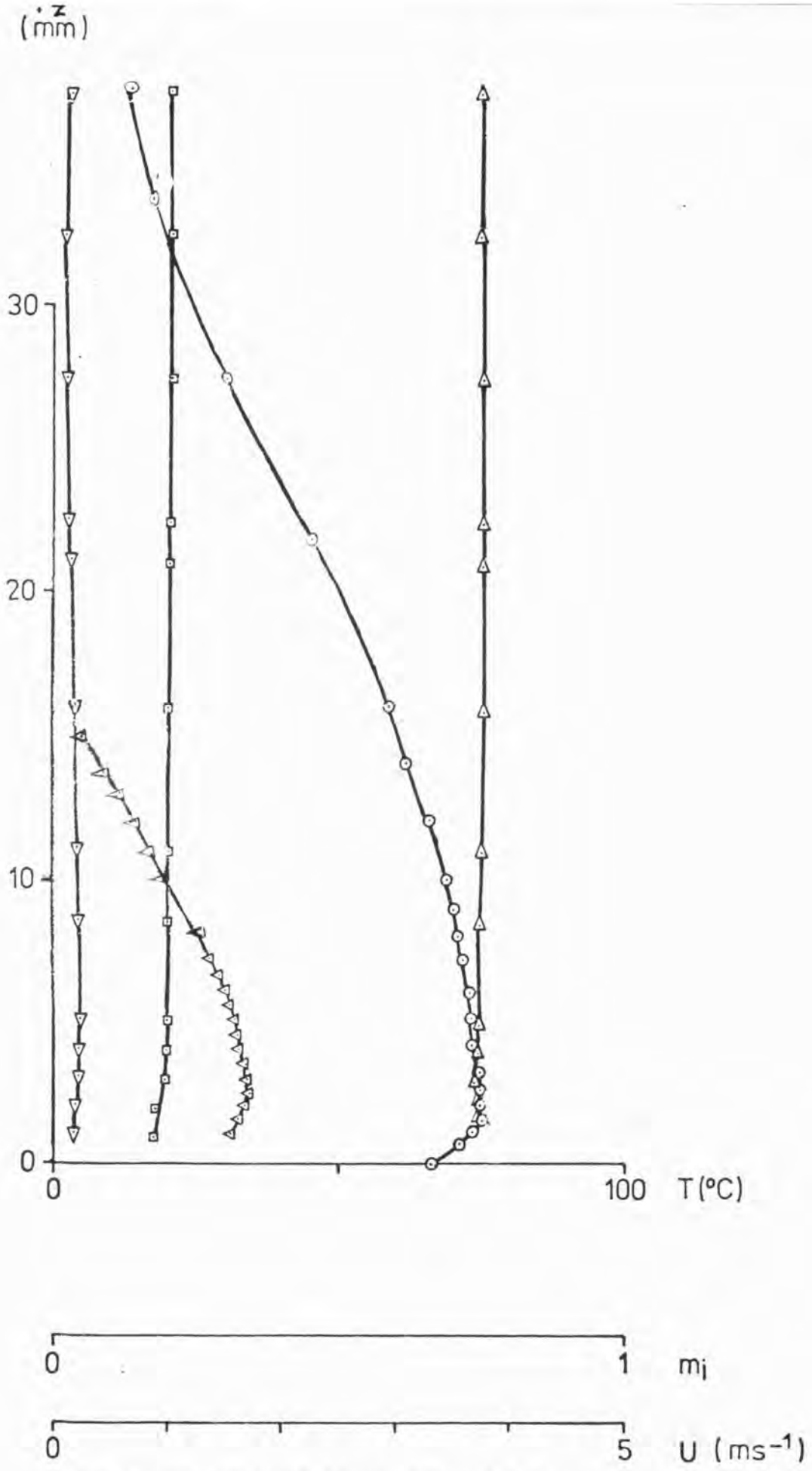

CROSS-STREAM FLOW PATTERN AT $r = 0.13m$

FIGURE 8.20

8.2 Physical Properties

To simulate the specified radial wall jet the following properties must be supplied to the modelling technique:

a) the density, effective viscosity and Prandtl number of the mixture,

and b) the effective Schmidt numbers for the constituent gas in the mixture.

In the computational simulations the density of the mixture is determined from the equation of a perfect gas:

$$\rho = \frac{P}{RT}\left((m\mathcal{M})_{Ar} + (m\mathcal{M})_{N_2} + (m\mathcal{M})_{O_2} \right) \qquad (8.1$$

In this equation the subscripts Ar, N_2 and O_2 refer to Argon, Nitrogen and Oxygen respectively.

The effective viscosity has been determined by the additive process described in chapter three - namely

$$\mu_{eff} = \mu_l + \mu_t \qquad (8.2$$

The molecular viscosity μ_l was determined from the viscosities of the constituent gases, as prescribed by Rogers and Mayhew[45], in the following manner:

$$\mu_l \quad (m\mu_l)_{Ar} + (m\mu_l)_{N_2} + (m\mu_l)_{O_2} \qquad (8.3$$

The turbulent viscosity μ_t has been estimated with the model proposed by Lauder - Spalding, and previously described in chapter 3. In this turbulence model the constant k_m and A_+ are, from Cebeci's work [20], prescribed the values 0.4 and 26.0 respectively.

Close to the impervious surface the effective Prandtl number of the mixture was assessed with the communicative law:

$$Pr_{eff} = \frac{Pr_l \cdot Pr_t \cdot \mu_{eff}}{\mu_{eff} \cdot Pr_t + \mu_t \cdot Pr} \qquad (8.4$$

where Pr_l and Pr_t represent the molecular and turbulent Prandtl numbers. This relationship is based upon a hypothesis, put forward by among others Spalding Patankar, that the turbulent and molecular contributions to the effective, or total, Prandtl number of the fluid are addative; and each has a prescribed constant value. Over the remainder of the flow the effective Prandtl number of the mixture was assumed equal to it's turbulent component Pr_t. The molecular Prandtl number for the mixture was determined by adding the products of the molecular-weight & Prandtl number of the individual components - this method was used by Spalding and Patankar[7]. The algebraic equation that results from the application of this method is:

$$Pr_l = (mPr_l)_{Ar} + P(mPr_l)_{N_2} + (mPr_l)_{O_2} \qquad (8.5$$

The turbulent Prandtl number of the mixture Pr_t was estimated from a mathematical model proposed by Cebeci[49], which postulates that:

$$Pr_t = \frac{km}{k_r} \left(\frac{1 - e^{-y/A_l}}{1 - e^{-y/B_l}} \right) \qquad (8.6$$

where $B_l = (Pr_t)_o \left(\frac{k_r A_l}{km} \right)$

From Cebeci's[49] work the constants have the following values:

$A_l = 26.0$

$k_m = 0.40$

$k_r = 0.44$

$(Pr_t)_o = 0.9$

Close to the impervious surface the effective Schmidt number for each individual gas in the mixture has been determined from the communicative law defined in chapter 7. That is close to the surface:

$$Sc_{eff} = \frac{Sc_l \cdot Sc_t (\mu_t + \mu_l)}{\mu_l Sc_t + \mu_t Sc_l} , \qquad (8.7$$

and over the remainder of the flow:

$$Sc_{eff} = Sc_t$$

Again the turbulent Schmidt number was assumed constant over the flow. The values prescribed the turbulent Schmidt numbers were as follows:

$$(Sc_t)_{N_2} = 0.7$$

$$(Sc_t)_{O_2} = 0.71$$

$$(Sc)_{Ar} = 0.7$$

This data was extracted from the work of Robertson[47] and Spalding-Patankar[7]. The molecular Schmidt numbers were looked up in tables by Roger and Mayhew[45].

8.3 Comparisons

Four different computational simulations are presented for the radial wall jet regime of the impinging flow detailed in section 1. The simulations are for $0.04 \leqslant r \leqslant 0.13$m - as shown in figure 8.21. Comparisons between predicted and measured properties are used to assess the adequacy and the accuracy of the modelling technique in this situation.

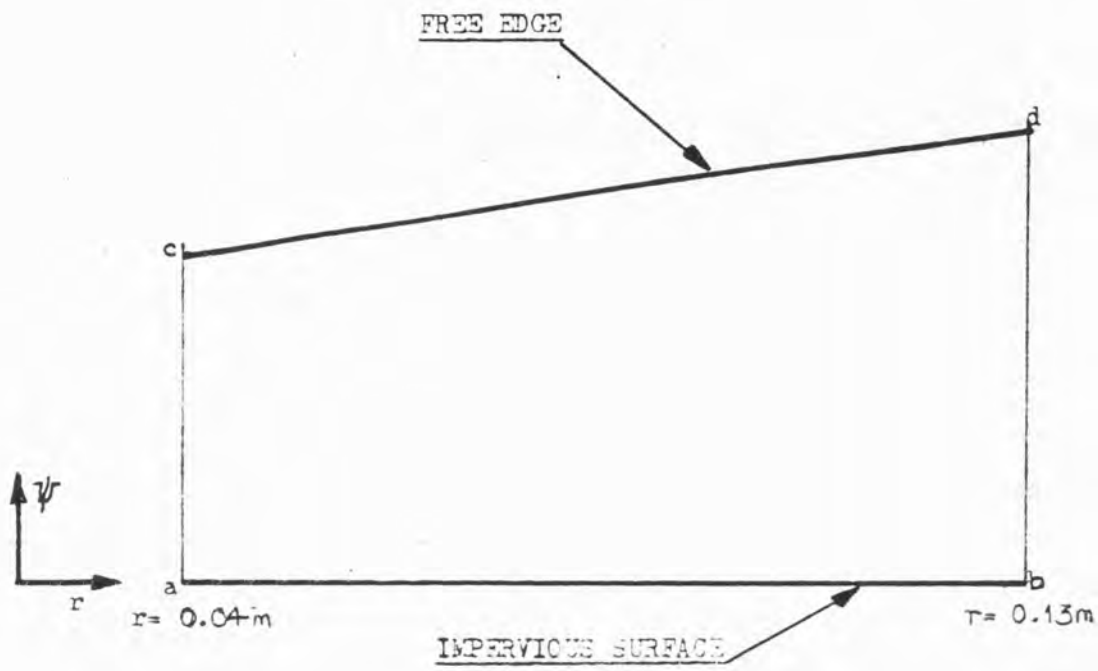

RADIAL WALL JET

FIGURE 8.2†

The four simulations differ in the following respects. Firstly, two different gradings were used for the spatial ordinate z at the starting cross-stream section. These gradings correspond to points a and b of equation 6.8 in chapter 6. Secondly, two values for the velocity gradient limit were used, these values were 10^3 and 10^5, and were prescribed in points i and ii of chapter 6.

In each simulation of the radial wall jet the boundary conditions for the predicted properties were defined along the:

a) starting cross-stream section, as specified by ac in figure 8.21 ,

b) free edge of the flow cd

and c) impervious surface ab.

Along the starting cross-stream section, at a radius of 0.04m, the variation of the radial velocity, Argon, Nitrogen and Oxygen concentrations and temperature were obtained from the experimental results presented in section 1. At the free edge the:

a) radial velocity was set at one percent of the maximum velocity at that cross-stream section,

b) gravimetric concentrations of Argon, Nitrogen and Oxygen were set to 0.0, 0.76 and 0.23 respectively

and c) temperature was prescribed the value 303K

Along the impervious surface:

a) the radial velocity was set to zero,

b) the gravimetric concentrations of Argon, Nitrogen and Oxygen were assumed equivalent to their measured values at z = 0.002m - as defined in figure 8.22, the symbols used are given in table 8.2

and c) the temperature was set at 303 K - for reasons detailed in the experiment.

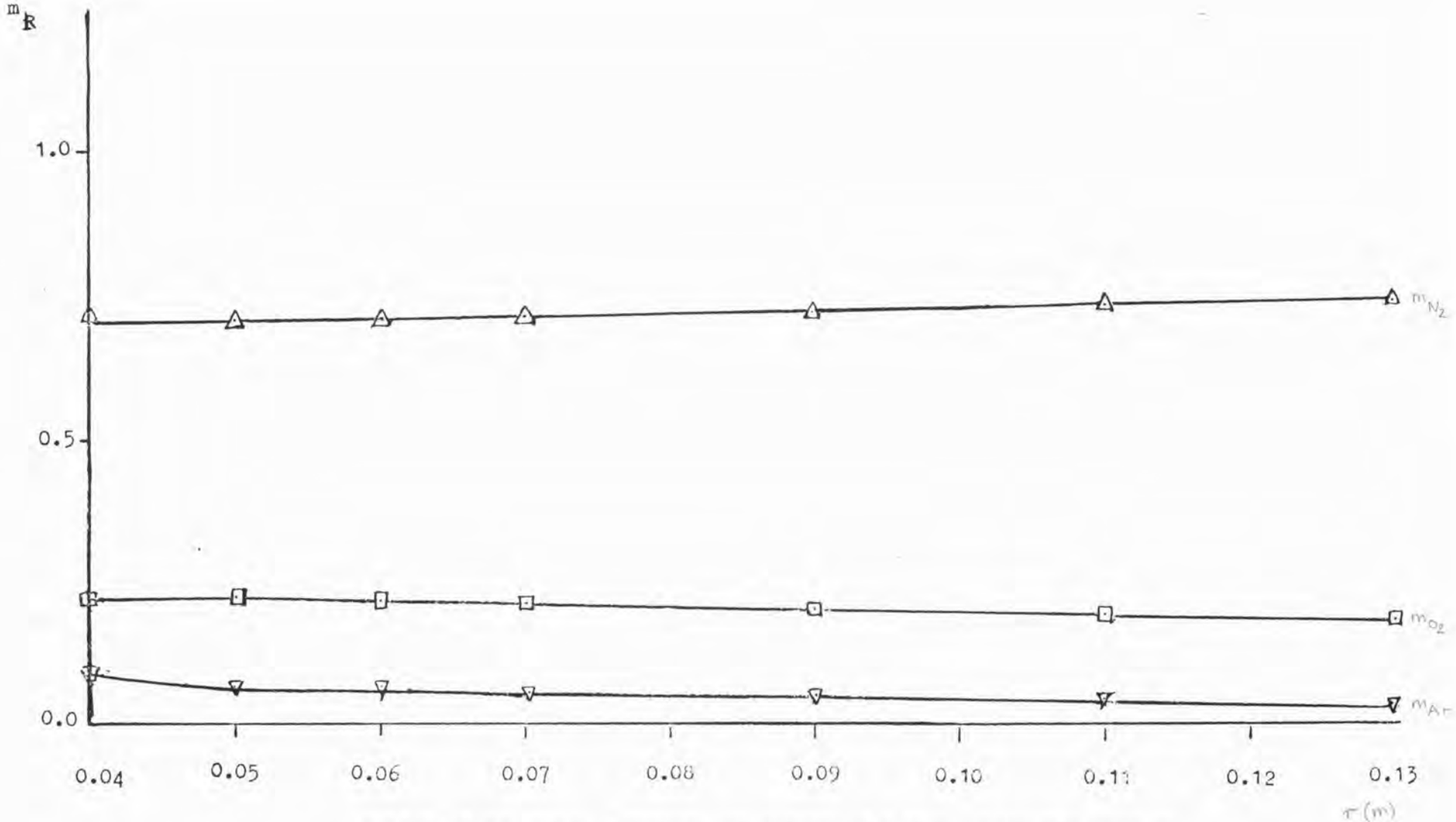

VARIATION OF ARGON, NITROGEN AND OXYGEN AT 0.002m ABOVE THE SURFACE

FIGURE 8.22

Specimen results from the computational simulations at radii of 0.05, 0.07, 0.1 and 0.13m are presented in figures 8.23 to .26 respectively. Table 8.3 details the symbols used to represent each simulation. The relevant experimental results are also re-presented in these figures, and are designated by dotted lines. Percentage differences between the predicted and experimental estimates of the flow properties at vertical heights $z = \delta_4$ and $z = \delta_5$ are given in table 8.4 at radii of 0.05, 0.07, 0.1 and 0.13m

Of the presented computational results those with a mesh grading set using $\delta/z_{1,2} = 10^5$, and Fr = 1.19, and a velocity gradient limit of 10^5 are the most accurate, the discrepancies between predicted and experimental results of less than twelve percent. An indication of the percentage discrepancies from the predictions can be obtained by referring to the data in table 8.4.

In the region where $0.05 \leqslant r \leqslant 0.07$m the discrepancy in the predictions are dependent upon both the starting mesh grading for z, and velocity gradient limit used in the computational simulation. As shown by the specimen cross-stream radial velocity, concentration and temperature profiles at r = 0.05 and 0.07m in figures 8.24 and .25. More precise evidence of this correlation is provided by the percentage discrepancies between predicted and experimental properties at $z = \delta_5$ and δ_4 in table 8.4.

Over the remainder of the flow, where $0.07 < r \leqslant 0.13$m, the discrepancy only dependent upon the velocity gradient limit. The specimen results at r = 0.07, 0.10 and 0.13m presented in figures 8.25, .26 and .27; and the associated data in table 8.4 corroborate this conclusion.

Table 8.3

Symbols for:					$z_{1,2}$	Fr	L
U	T	m_{A_r}	m_{O_2}	m_{N_2}			
							10^3
					$\delta_{1,1}/10^3$	1.19	
							10^5
							10^3
					$\delta_{1,1}/10^5$	1.12	
							10^5

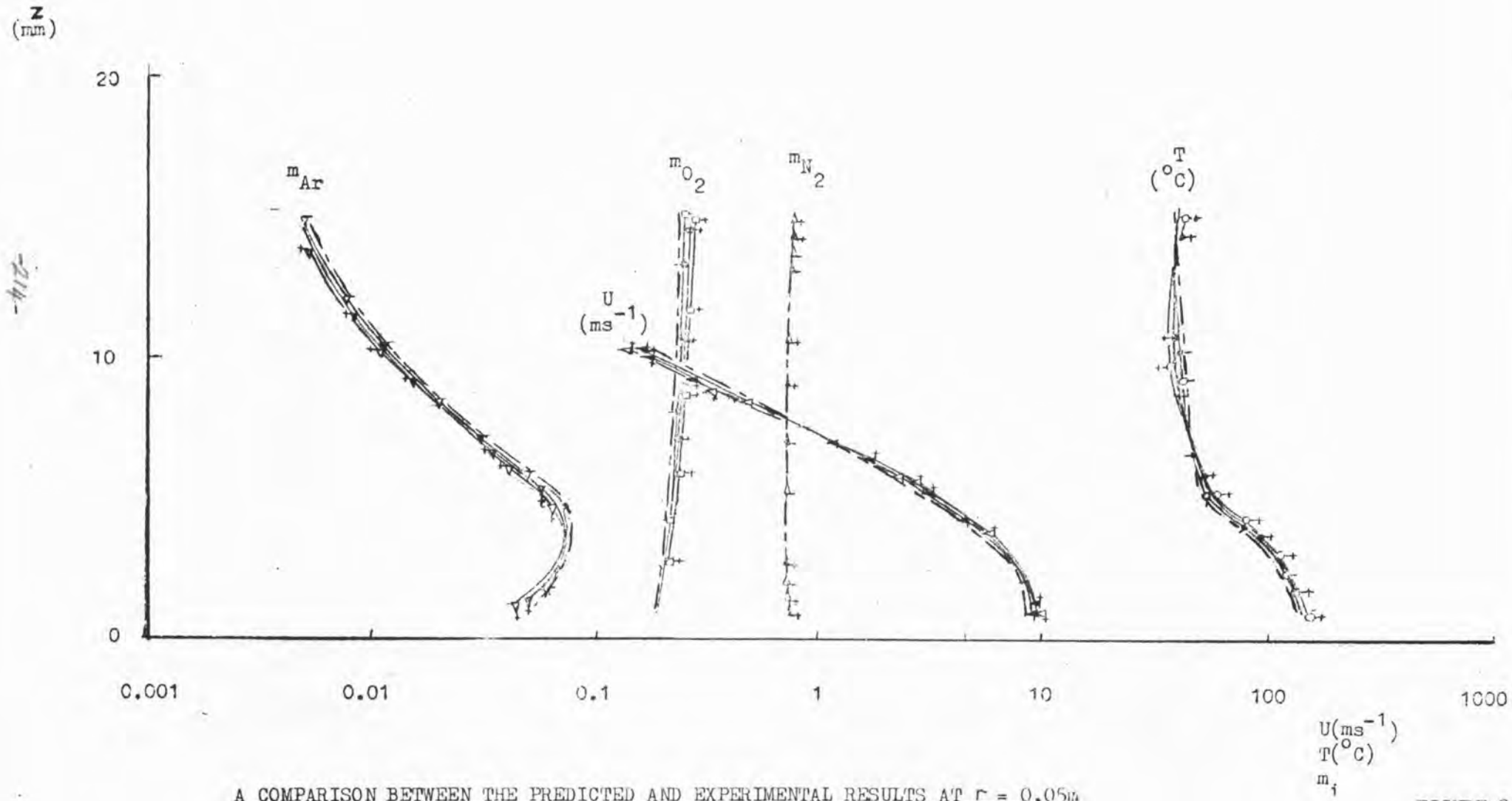

A COMPARISON BETWEEN THE PREDICTED AND EXPERIMENTAL RESULTS AT r = 0.05m

FIGURE 8.2

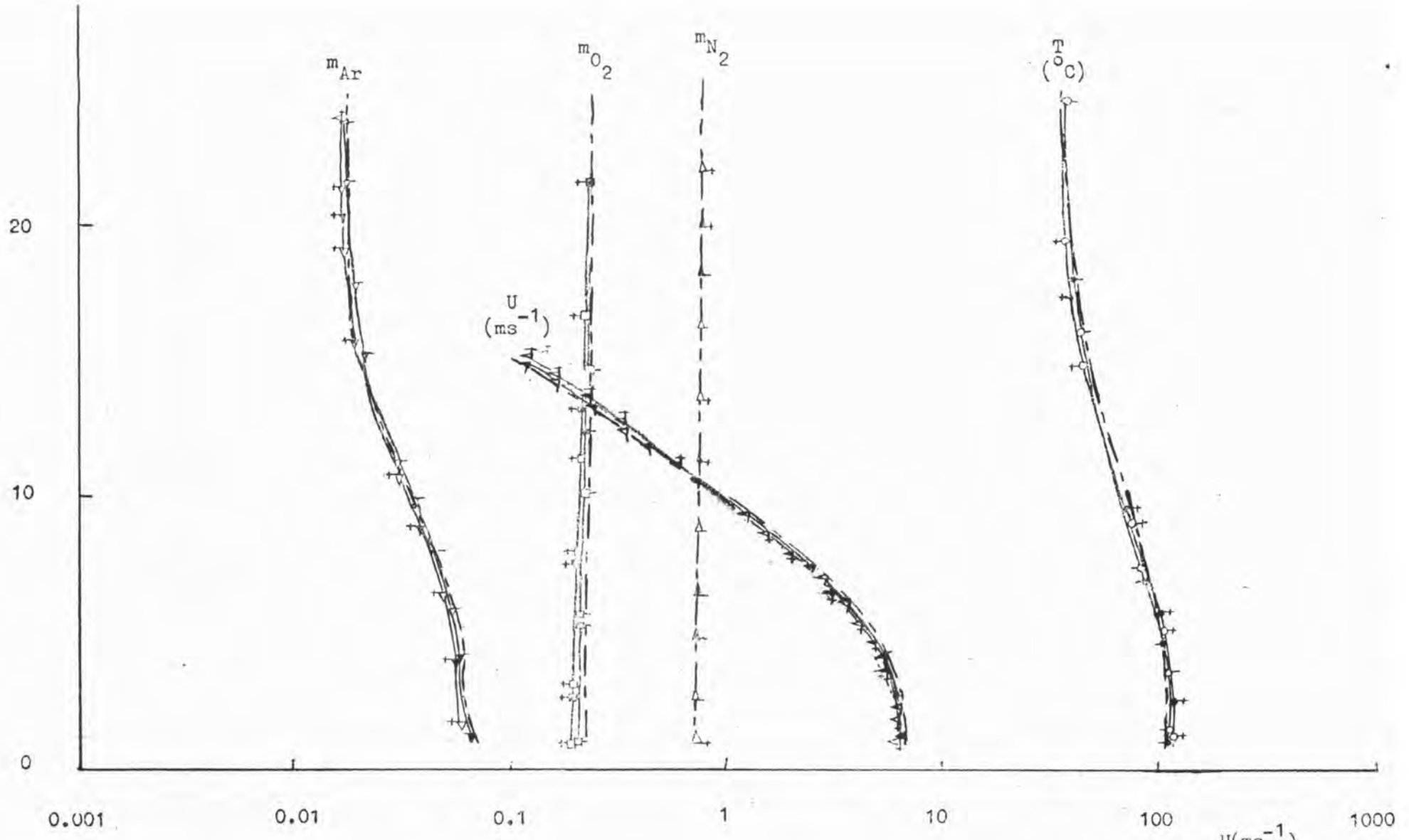

A COMPARISON BETWEEN THE PREDICTED AND EXPERIMENTAL RESULTS AT r = 0.07m

FIGURE 8.2

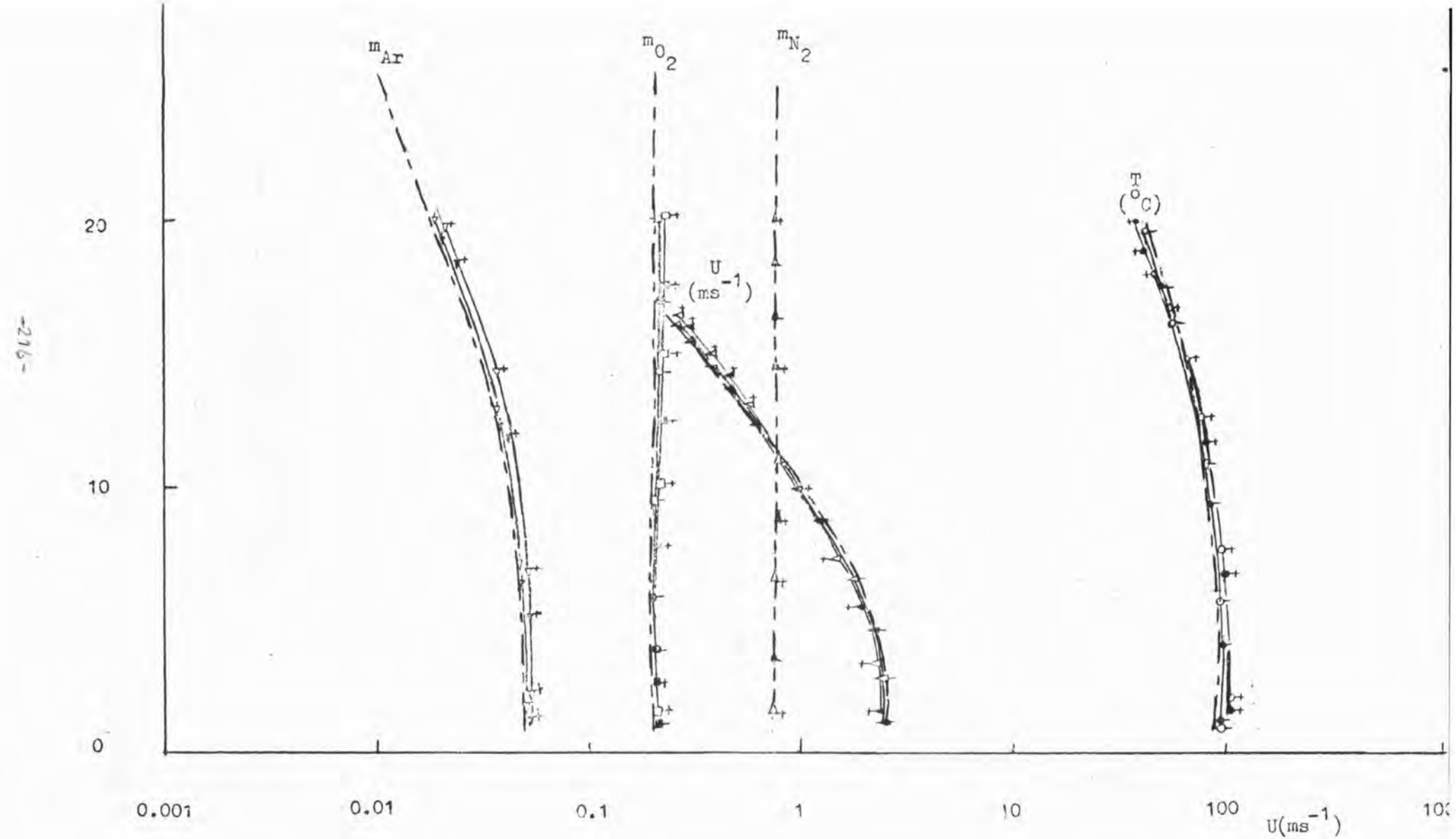

A COMPARISON BETWEEN THE PREDICTED AND EXPERIMENTAL RESULTS AT r = 0.1m

FIGURE

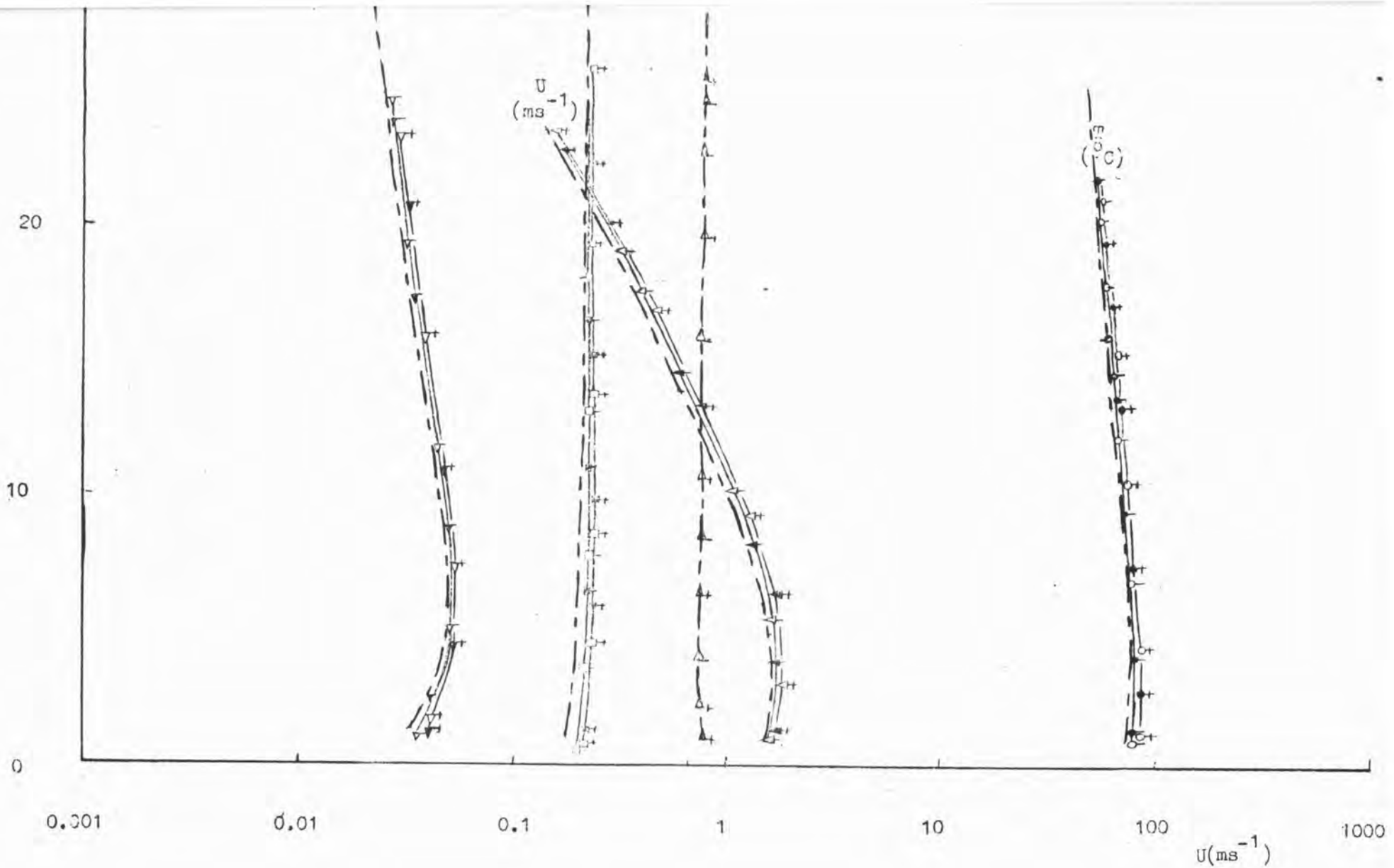

A COMPARISON BETWEEN THE PREDICTED AND EXPERIMENTAL RESULTS AT r = 0.13m

FIGURE 8.

Percentage difference between the predicted and experimental

	Mesh gradings $\frac{\delta_{1,1}}{z_{4,3}}$	Fr	gradient limit L	U $z=\delta_4$	U $z=\delta_5$	m_{Ar} $z=\delta_4$	m_{Ar} $z=\delta_5$	m_{O_2} $z=\delta_4$	m_{O_2} $z=\delta_5$	m_{N_2} $z=\delta_4$	m_{N_2} $z=\delta_5$	T $z=\delta_4$	T $z=\delta_5$
a) r = 0.05m	10^3	1.19	10^3	12.0	12.2	3.0	11.1	7.0	8.5	1.1	1.4	-12.0	-10.9
			10^5	12.0	10.9	9.0	8.4	7.0	8.5	1.3	1.5	- 6.0	- 7.2
	10^5	1.12	10^3	8.0	5.0	3.0	2.3	2.0	6.5	0.7	0.8	0.0	- 5.0
			10^5	3.0	5.0	3.0	2.3	2.0	6.5	1.1	0.3	0.0	- 5.0
b) r = 0.7m	10^3	1.19	10^3	-5.5	-12.0	9.0	0.0	-11.1	-8.0	0.4	1.0	- 7.7	- 5.6
			10^5	-5.5	-12.0	9.0	0.0	-13.0	-9.0	0.4	1.0	- 7.7	- 5.6
	10^5	1.12	10^3	-3.0	- 1.2	2.9	-5.6	- 7.0	-4.0	-0.1	-0.7	- 5.6	- 2.3
			10^5	-3.0	- 1.2	2.9	-5.6	- 7.0	-4.0	-0.1	-0.7	- 5.6	- 2.3
c) r = 0.10m	10^3	1.19	10^3	-8.1	- 1.2	8.2	5.3	5.6	4.5	-0.5	-0.3	+ 8.9	10.9
			10^5	-8.1	- 6.1	8.2	5.5	5.6	4.5	-0.5	-0.3	+ 8.9	10.9
	10^5	1.12	10^3	-5.4	- 3.6	3.1	4.1	5.1	4.7	1.0	1.0	+ 7.3	8.4
			10^5	-5.4	- 3.6	3.1	4.1	5.1	4.7	0.7	1.0	+ 7.3	8.4
d) r = 0.13m	10^5	1.19	10^3	8.3	10.8	10.5	10.3	11.0	10.1	-0.4	-0.9	10.9	10.9
			10^5	9.3	10.8	10.5	10.3	11.0	10.1	-0.4	-0.9	10.9	10.9
	10^3	1.12	10^3	4.1	7.2	5.9	4.7	1.0	5.0	-0.6	-0.5	5.9	5.7
			10^5	4.1	7.2	5.9	4.7	1.0	5.0	-0.6	-0.5	5.9	5.7

8.4 Conclusions

The recommended modelling technique successfully simulated the time averaged velocity, concentration and temperature fields of the radial wall jet study detailed in appendix five. The discrepancies between the predicted and experimental results were less than twelve percent, which was considered sufficiently accurate for most engineering purposes. This result verifies that those portions of the modelling technique used for simulating turbulent momentum, mass and heat transfer were satisfactory in this particular flow situation.

Chemical Reaction

The intent of the described work is to illustrate that the prescribed modelling technique cannot accurately simulate a specified turbulent radial wall jet flow in which chemical reactions occur. (As this flow is moving - the previously tested parts of the technique for predicting momentum, mass and heat transfer rates will also be used in the simulation).

The specified radial wall jet, and the measured time averaged flow pattern within it, are detailed and briefly discussed in section 1. The full experiment used to obtain these measured results is detailed in appendix 6. In section 2 the physical properties required by the modelling technique are specified, and the methods used to estimate them described. The model used to account for radiant energy transfer is not detailed in this section, because it is not involved in the simulation. However, for completeness the type of radiation model that could be used is briefly described. Typically, the model will allow radiant energy to travel in the streamwise and cross-stream directions, and could take account of local emission, absorption and scattering from grey bodies. Spalding-Patankar [7] and Whitelaw and Khalil [51] have used this type of technique, and called it the four flux model. Comparisons between predicted and experimental results are given in section 3; and in section 4 the conclusions of this investigation are presented.

9.1 Experiment

The specified flow was produced by the normal impingement of an air jet on to a porous surface through which a natural gas was passing. An illustration of the experimental layout is shown in figure9.1. The effective diameter of the porous surface is 0.25m, and it had a radius of curvature of 1.75m. The internal diameter of the nozzle is 0.004m; and the distance between the porous surface and nozzles exit is 0.02m. Natural gas contains Methane, Nitrogen and Oxygen in the following gravimetric concentration 0.81, 0.15 and

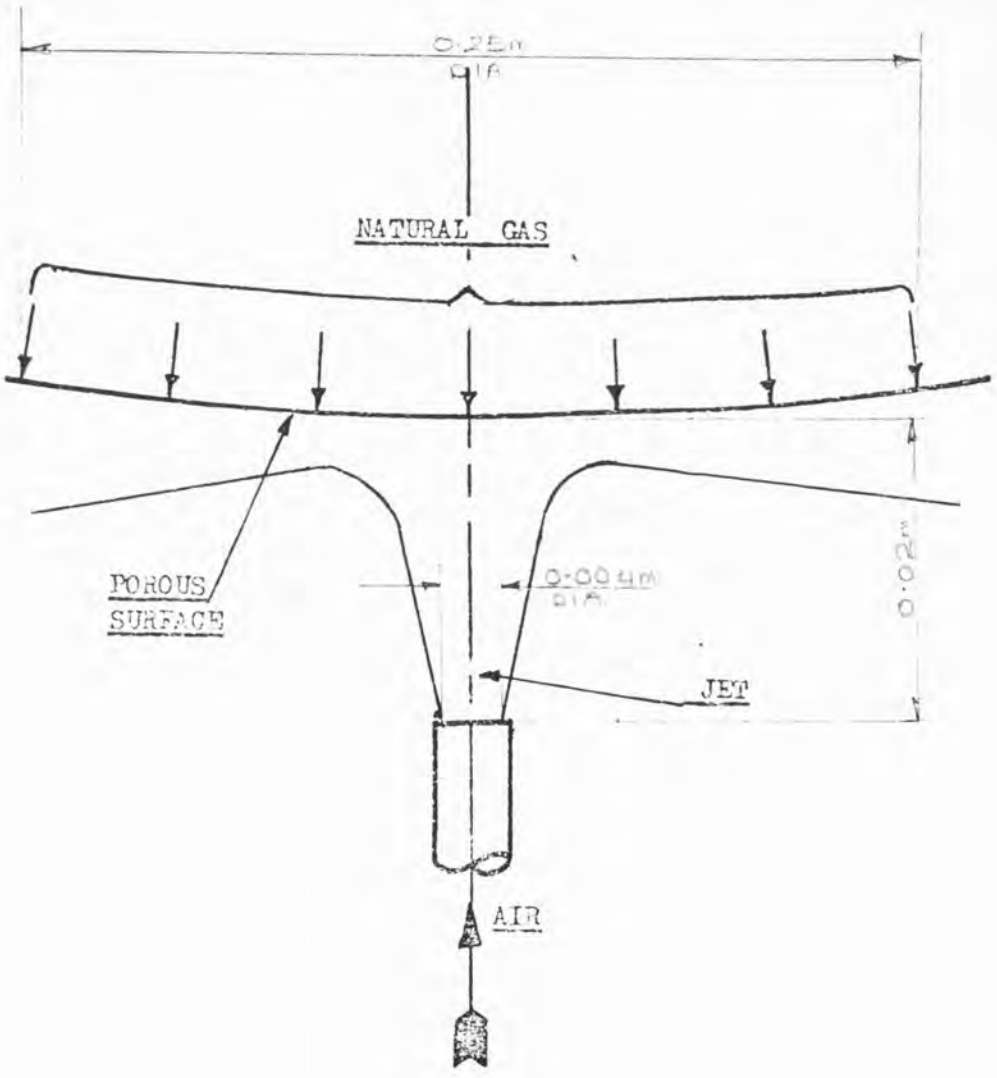

IMPINGEMENT FLOW

FIGURE 9.1

0.03. The volumetric flowrates of Air and Natural Gas were maintained at 8.1×10^{-2} and 3.65×10^{-2} $m^3 s^{-1}$ throughout the experiment.

The measured variation of the time averaged velocity, temperature and concentrations of Methane, Oxygen, Nitrogen, Carbon Dioxide, Carbon Monoxide and Water Vapour at radii of 0.0 to 0.11m are presented in figures 9.2 to .11. The symbols used in these figures are presented in table 9.1.

The accuracy of this data has been checked by repeating the experiment. The discrepancy between the two sets of data was greatest at a radius of 0.08m. The measured data at this section is shown in figure 9.28; the symbols used are detailed in table 9.1, with the filled in symbols representing one set of readings and the open symbols the other set.

The results from the experiment are re-presented in figures 9.12 to .19 to show the variation of the measured properties on a radial section through the flow. The temperature field is shown in the background of figures 9.13 to .19 with a dotted line, and provides a framework in which to discuss and examine the results.

The impingement flow contains the jet, deflection and radial wall jet regimes shown in figure 9.20 and in which different facets of the turbulent transfer processes predominate. In the summary of experimental results that follows the radial wall jet regime will be concentrated upon, because this is the part of the flow that has been simulated.

The wall jet extends from r = 0.03m to 0.11m; and contains that portion of the flow unaffected by direct contact with the impinging jet. It comprises the combustion and mixing regions shown in figure 9.20. The combustion region covered that portion of the flow where chemical reaction between Methane, Carbon Monoxide and Oxygen occurred. Experimental results in this region, for $0.065 \leqslant r \leqslant 0.13$m, are shown in figures 9.8 to .11. The most important feature of the presented results is that large amounts of excess Methane and Carbon Monoxide existed in this region - see figure 9.14 and .18, respectively. Indicating that the combustion process involved methane and Carbon Monoxide reacting with Oxygen to give Carbon

Table 9.1

Symbol	Meaning	
▷	mainstream velocity U	
◁	cross-stream " V	
○	temperature " T	
△	gravimetric concentration of Methane	m_{CH_4}
◇	" " " Oxygen	m_{O_2}
⊡	" " " Nitrogen	m_{N_2}
▽	" " " Carbon Dioxide	m_{CO_2}
◇	" " " Carbon Monoxide	m_{CO}
▽	" " " Water Vapour	m_{H_2O}

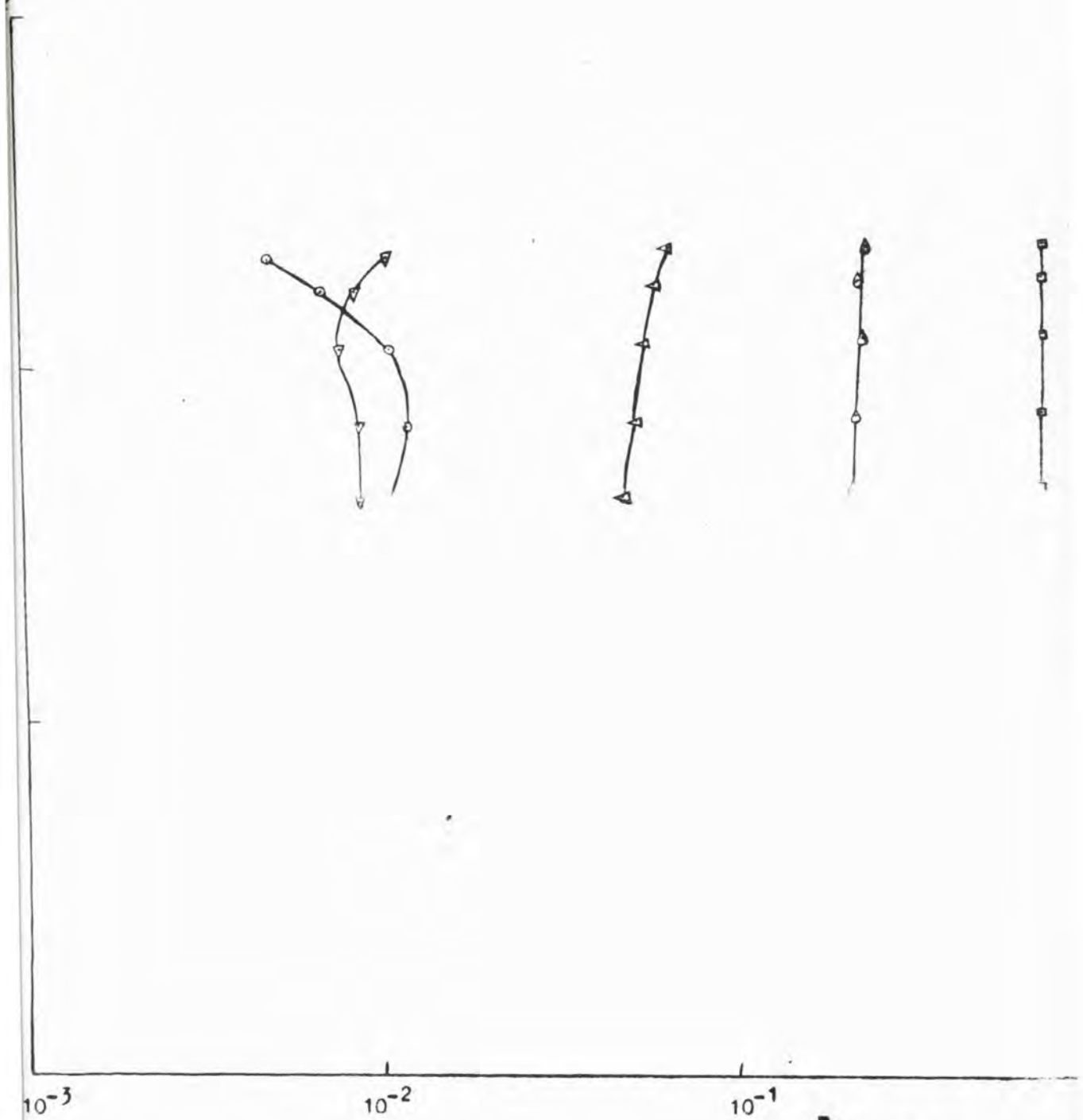

CROSS-STREAM FLOW PATTERN AT A RADIUS OF 0.0m

FIGURE 9.2

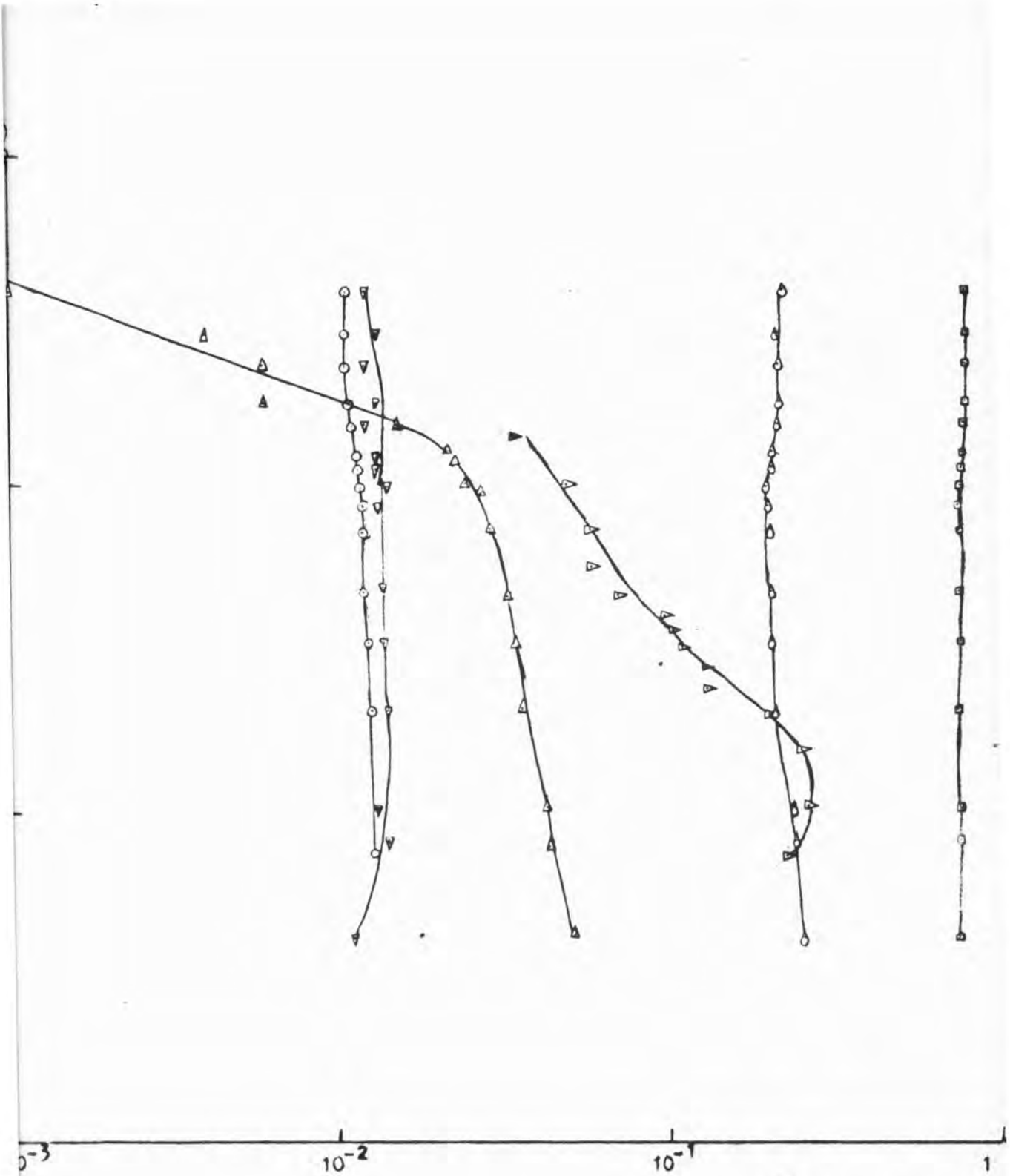

CROSS-STREAM FLOW PATTERN AT r = 0.005m

FIGURE 9.3

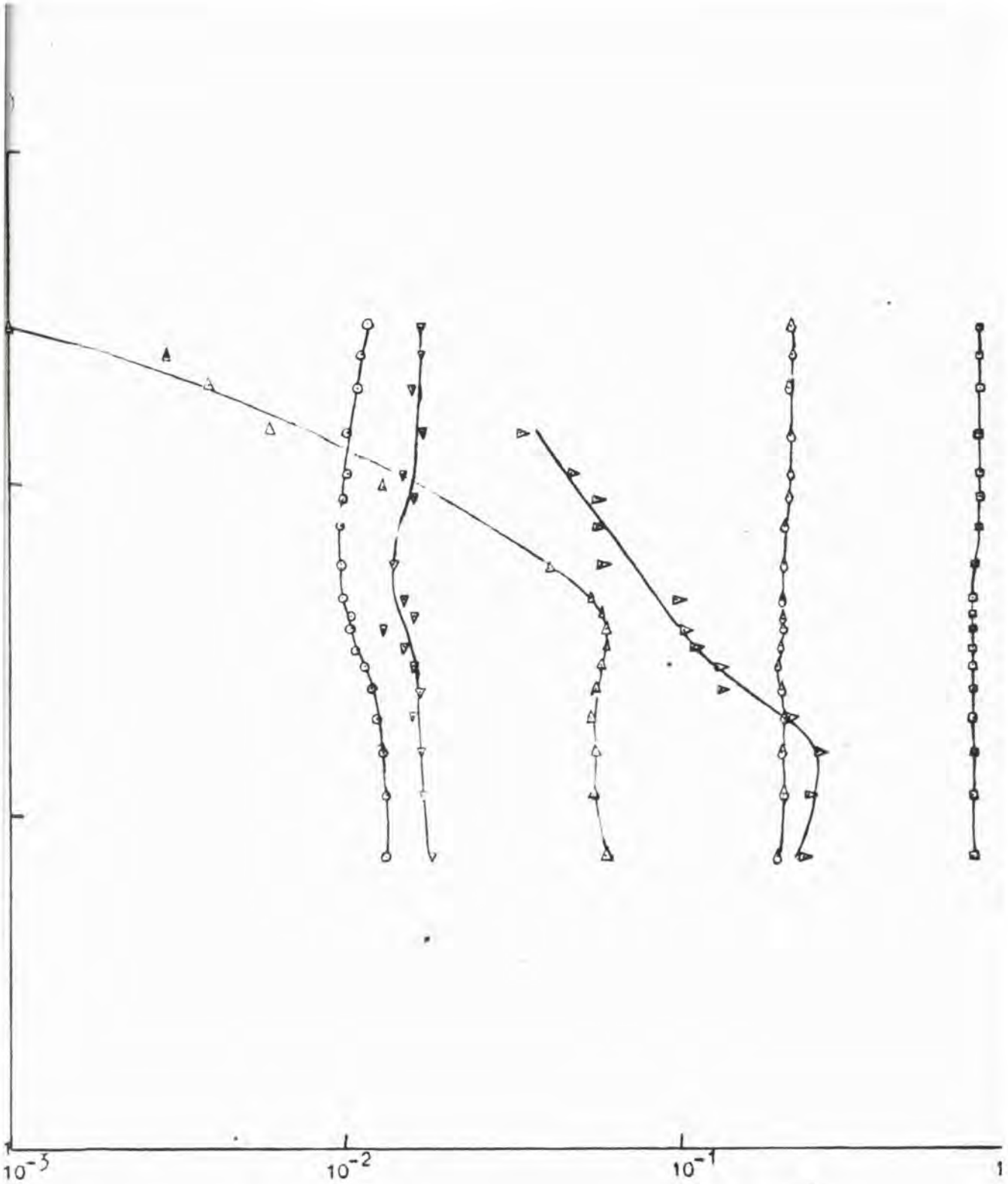

CROSS-STREAM FLOW PATTERN AT r = 0.010m

FIGURE 9.4

CROSS-STREAM FLOW PATTERN AT r = 0.015m

FIGURE 9.5

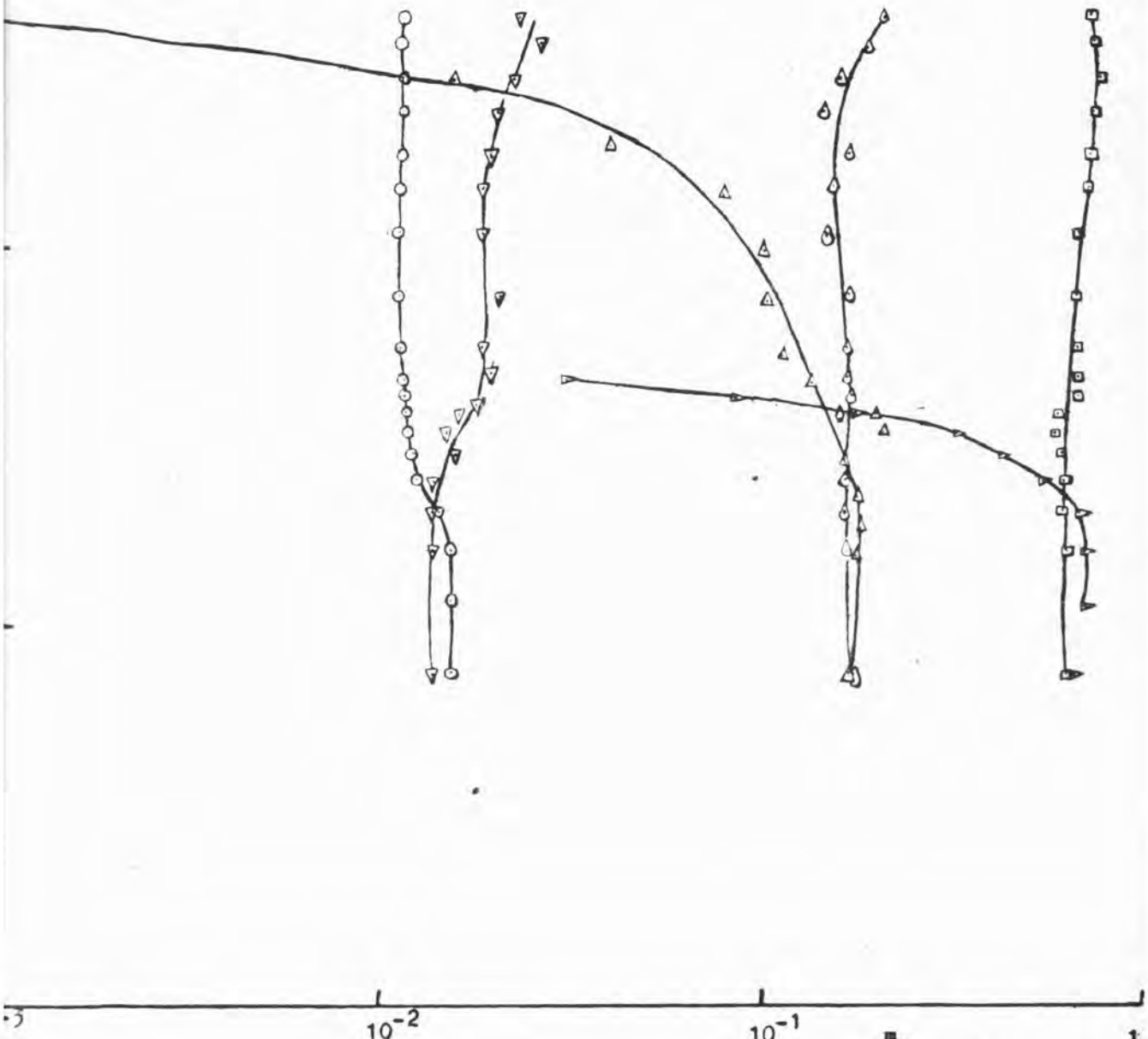

CROSS-STREAM FLOW PATTERN AT r = 0.020m

FIGURE 9.5

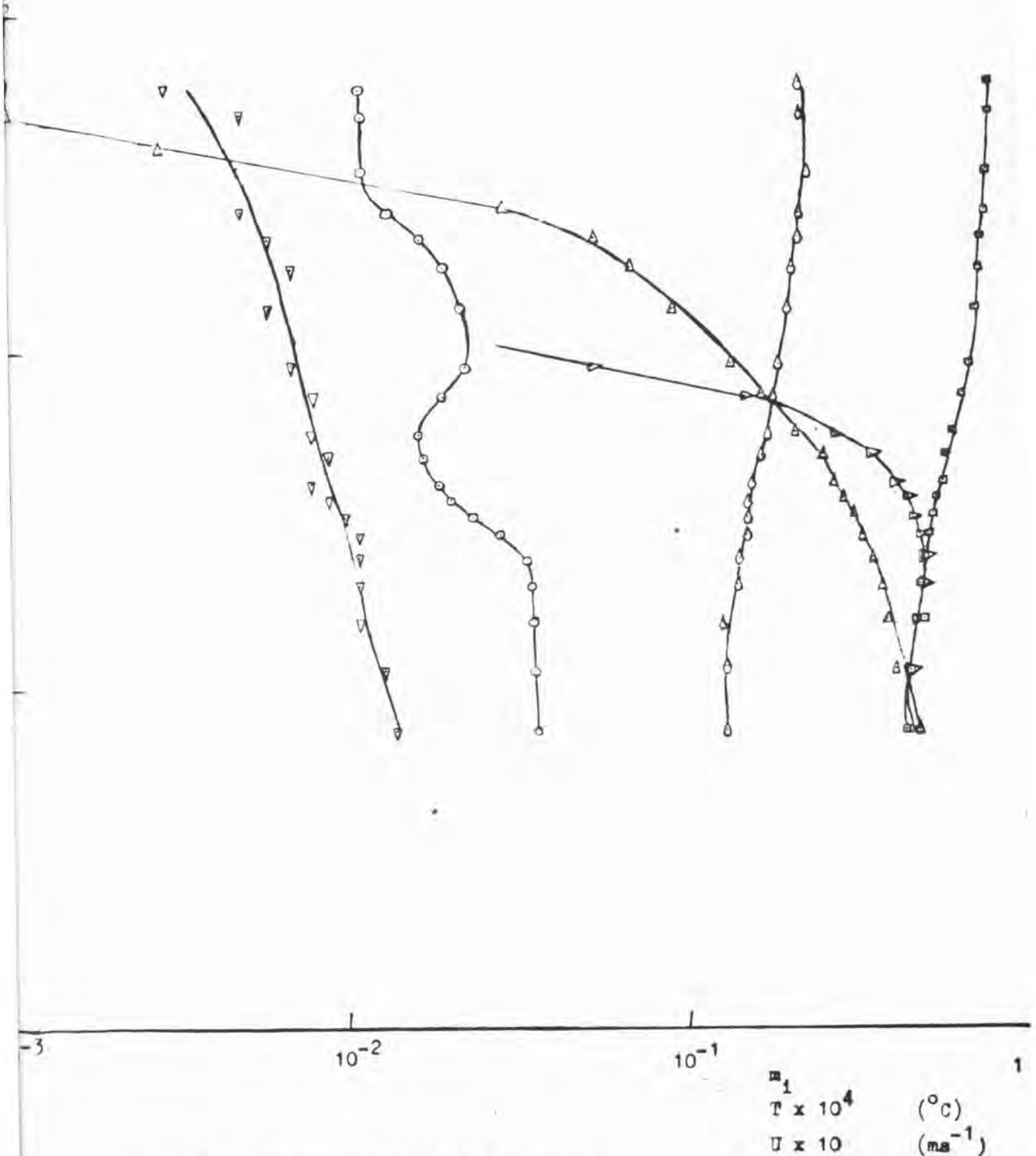

CROSS-STREAM FLOW PATTERN AT r = 0.040m

FIGURE 9.7

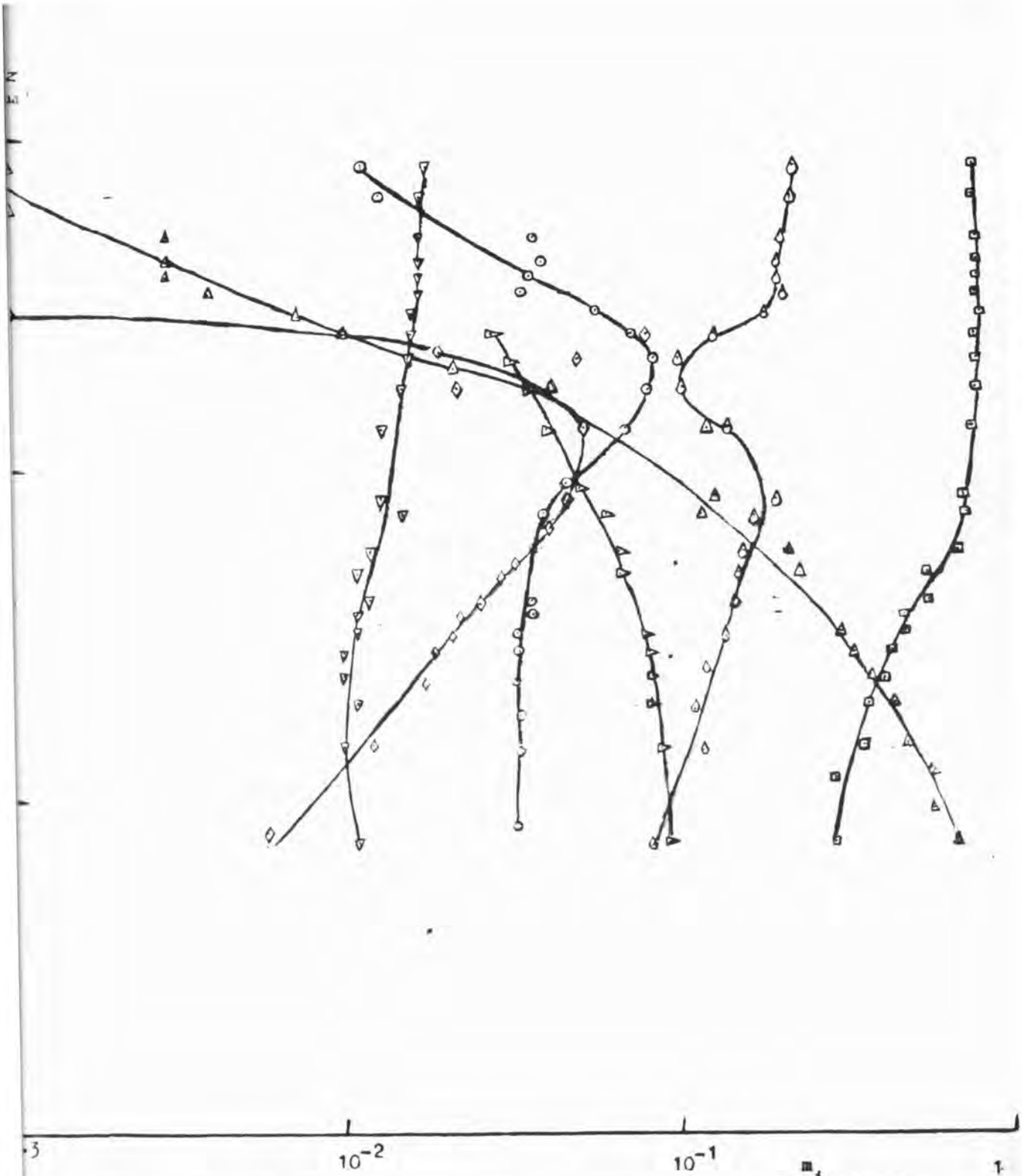

CROSS-STREAM FLOW PATTERN AT r = 0.065m

FIGURE 9.8

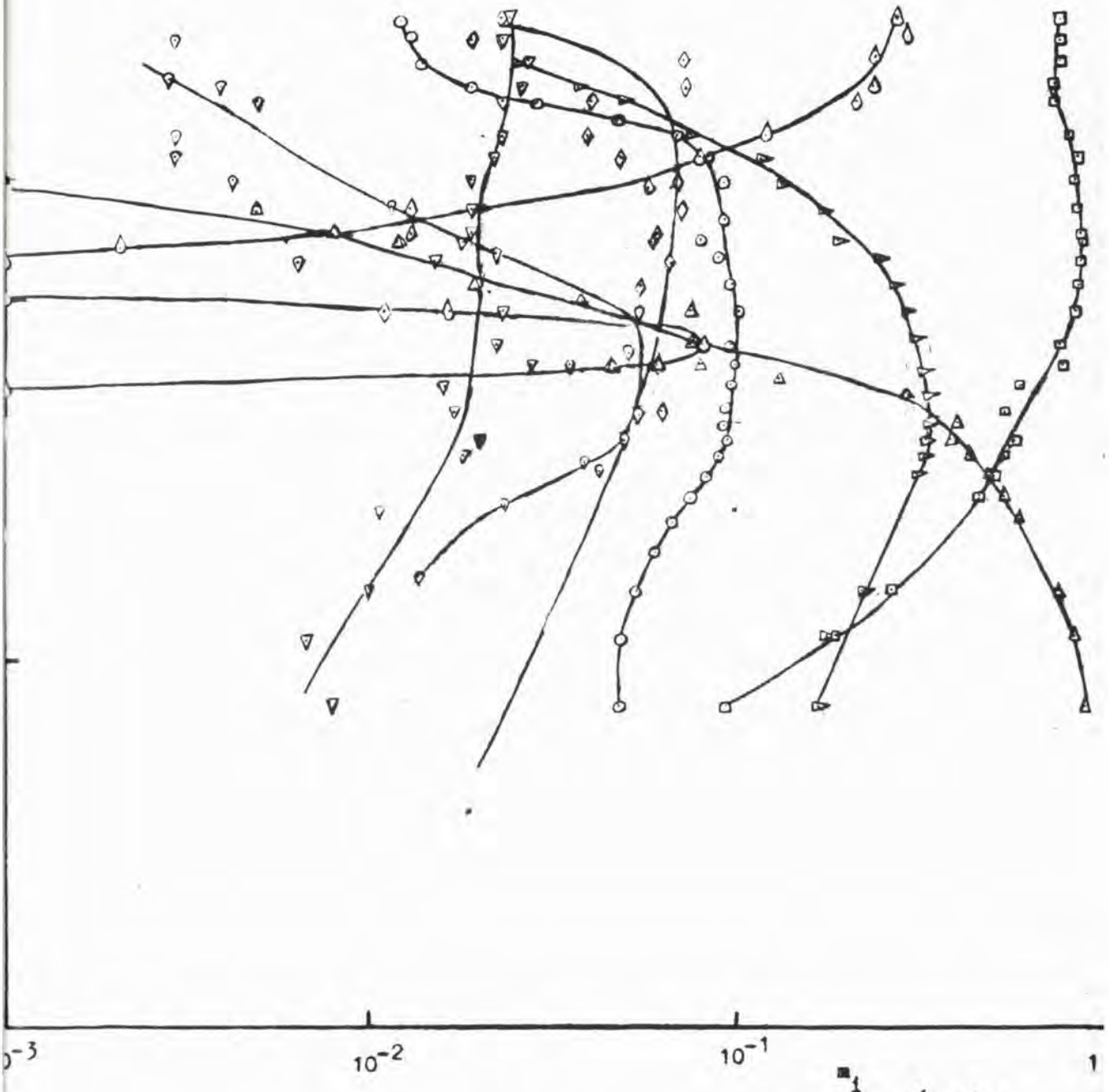

CROSS-STREAM FLOW PATTERN AT r = 0.080m

FIGURE 9.9

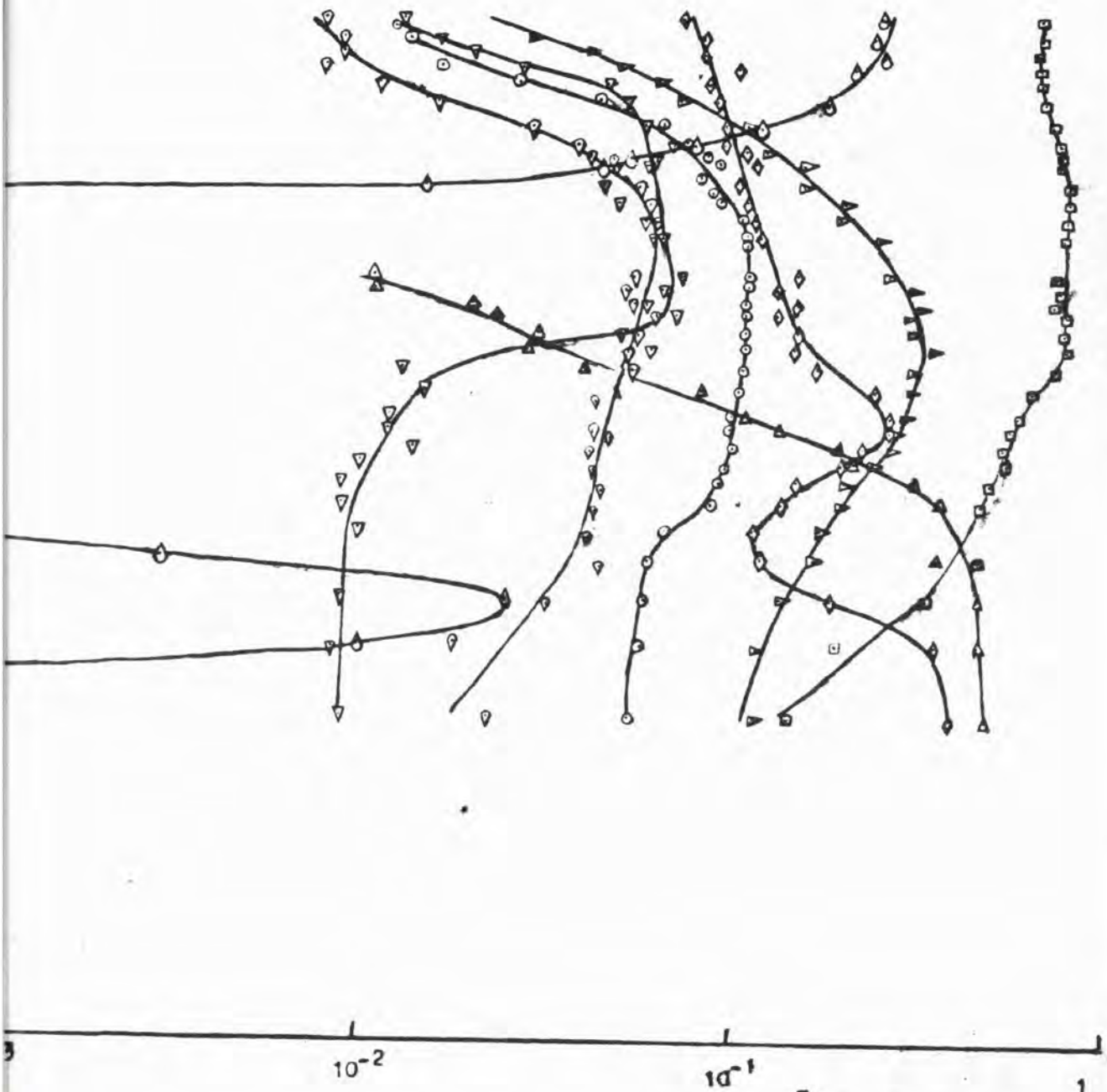

CROSS-STREAM FLOW PATTERN AT x = 0.095m

FIGURE 9.10

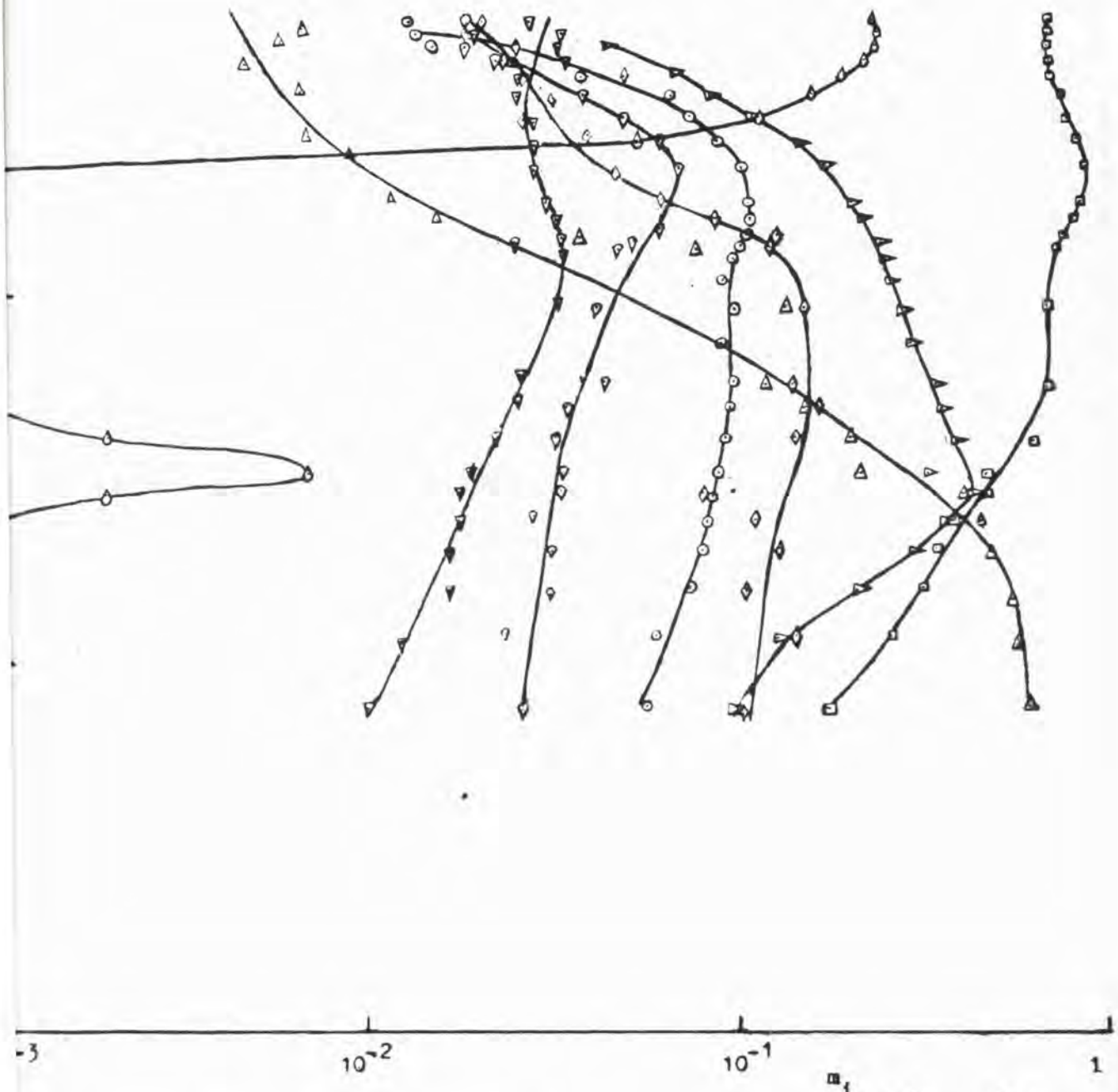

CROSS-STREAM FLOW PATTERN AT r = 0.11 m

FIGURE 3.11

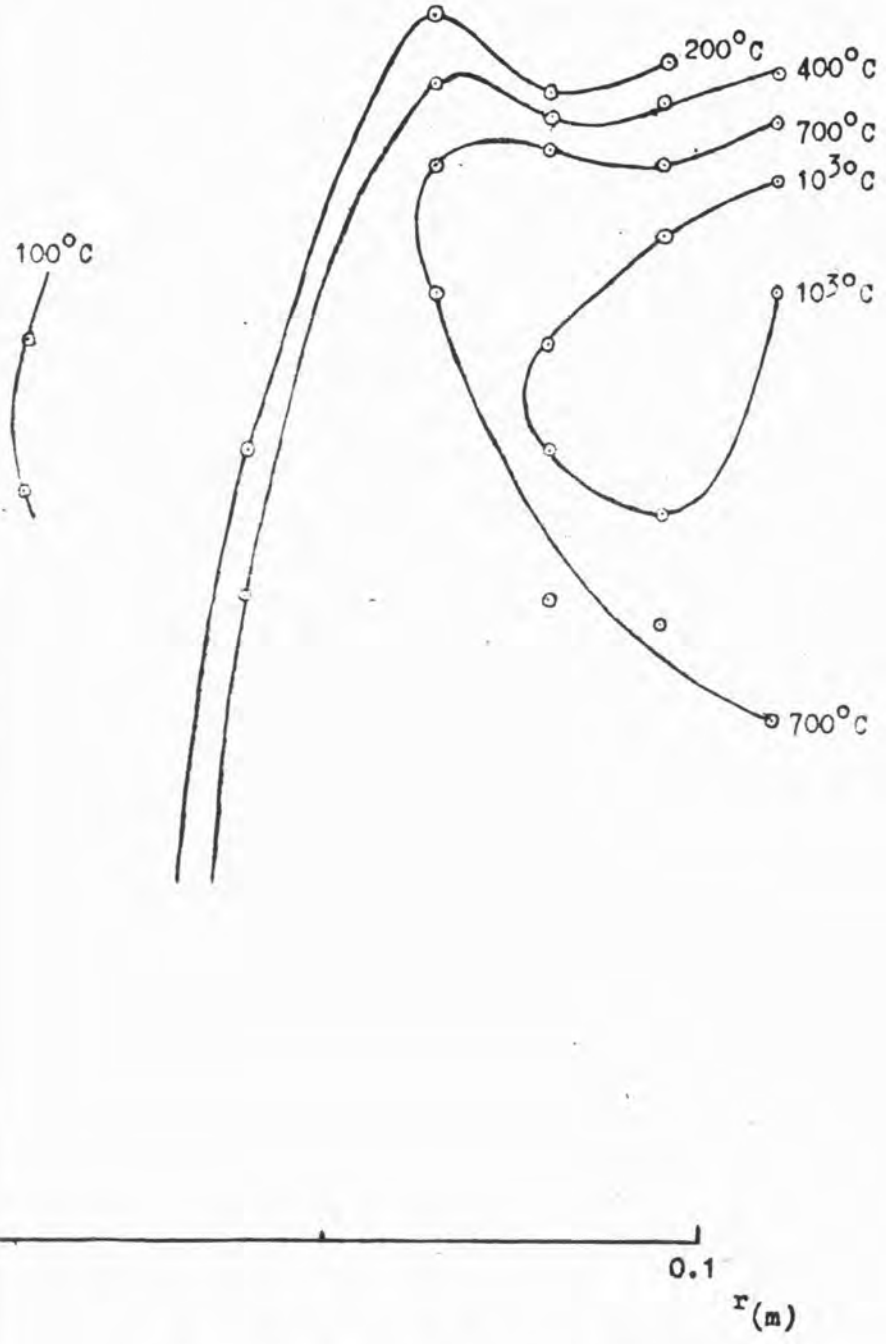

SPATIAL DISTRIBUTION OF TEMPERATURE

FIGURE 9.12

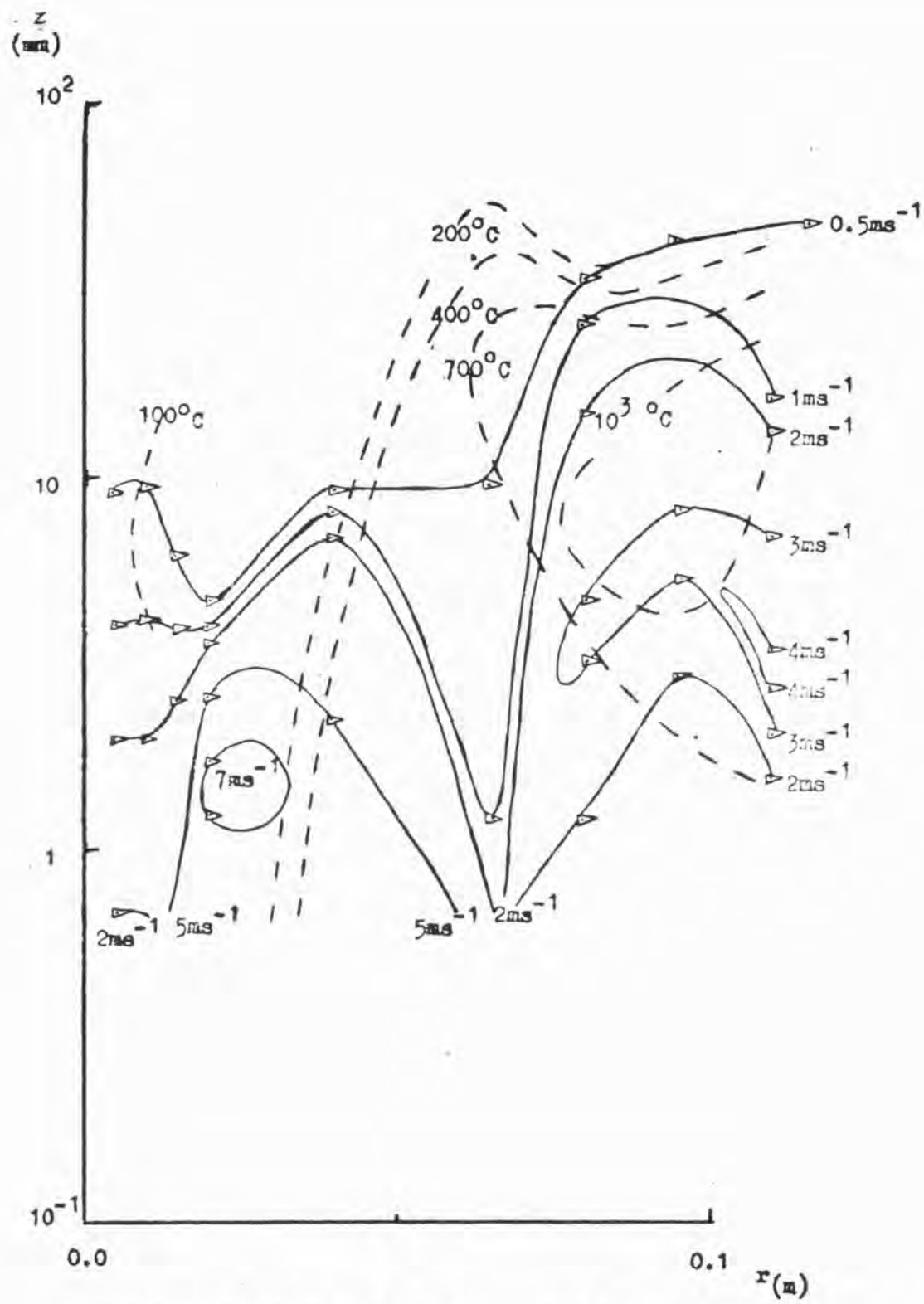

SPATIAL DISTRIBUTION OF THE MAINSTREAM VELOCITY

FIGURE 9.13

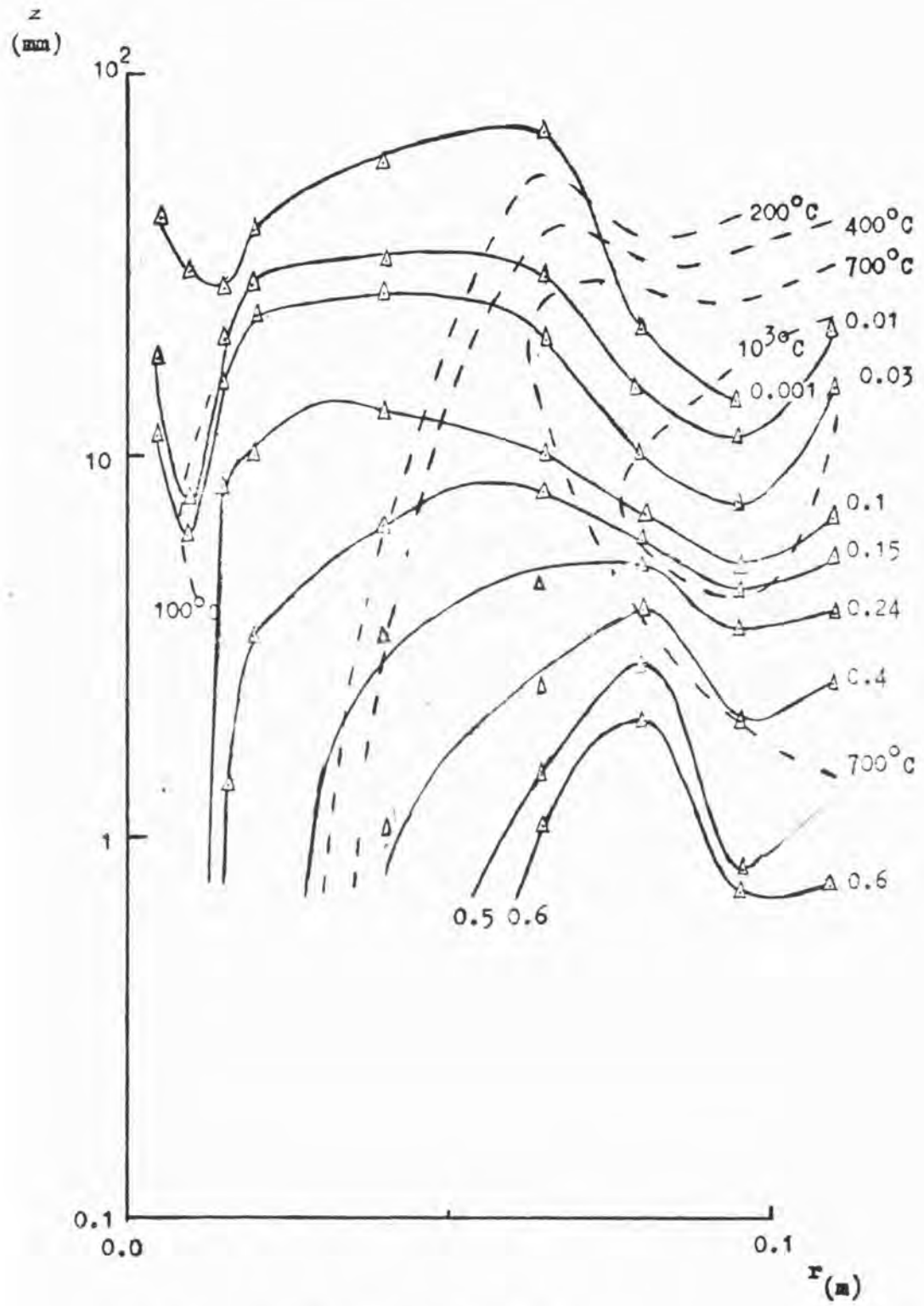

SPATIAL DISTRIBUTION OF METHANE

FIGURE 9.14

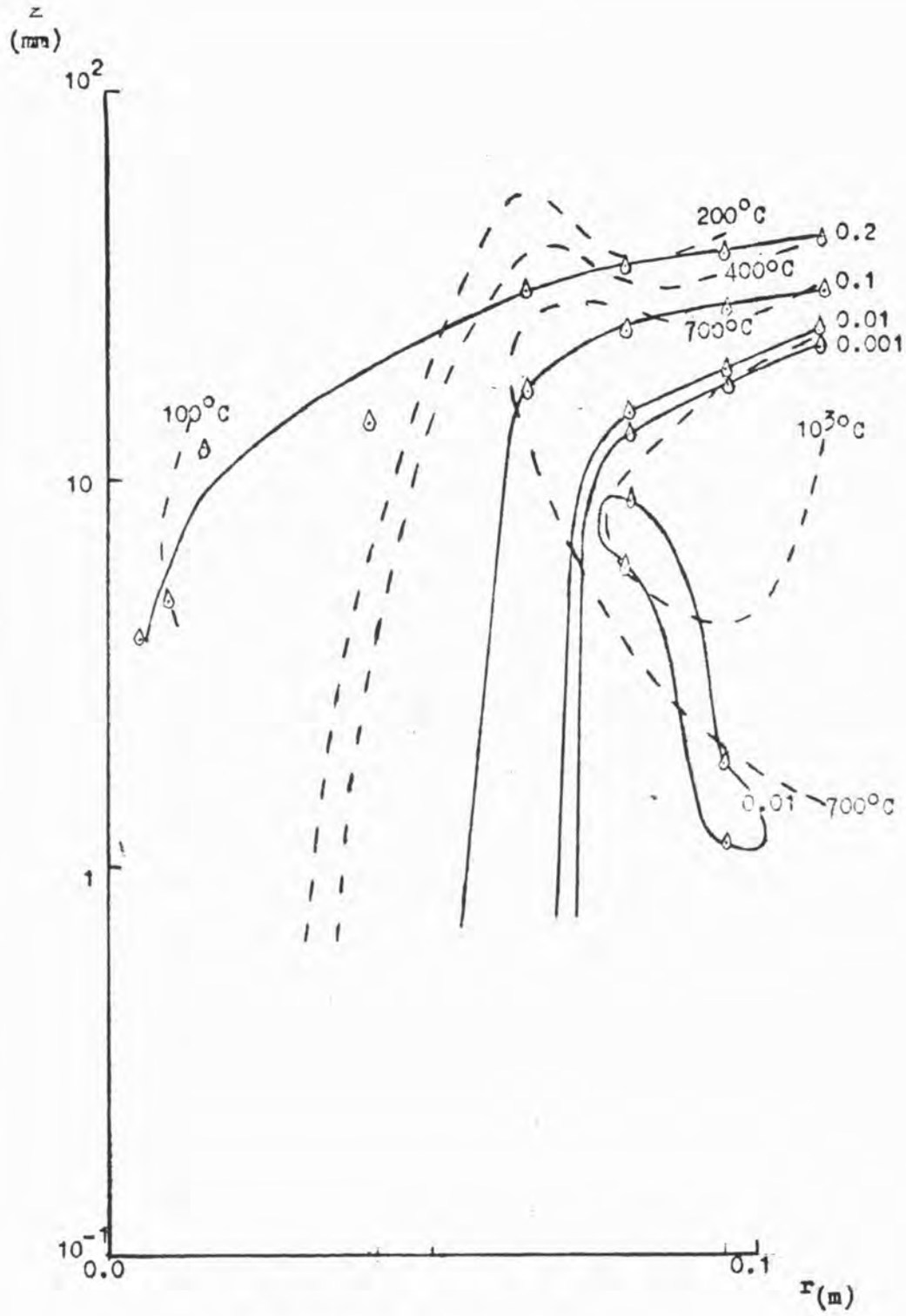

SPACIAL DISTRIBUTION OF OXYGEN

FIGURE 9.15

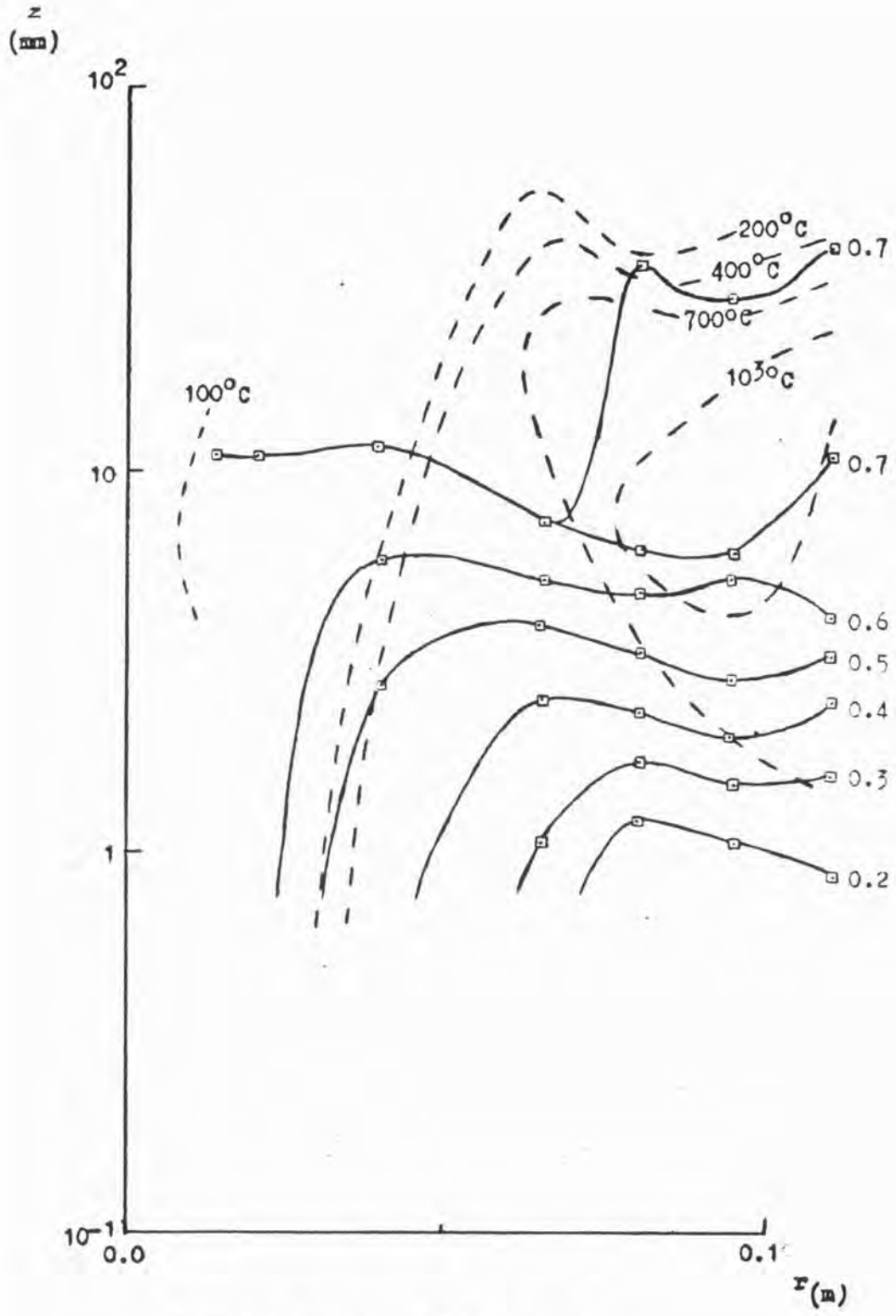

SPATIAL DISTRIBUTION OF NITROGEN

FIGURE 9.16

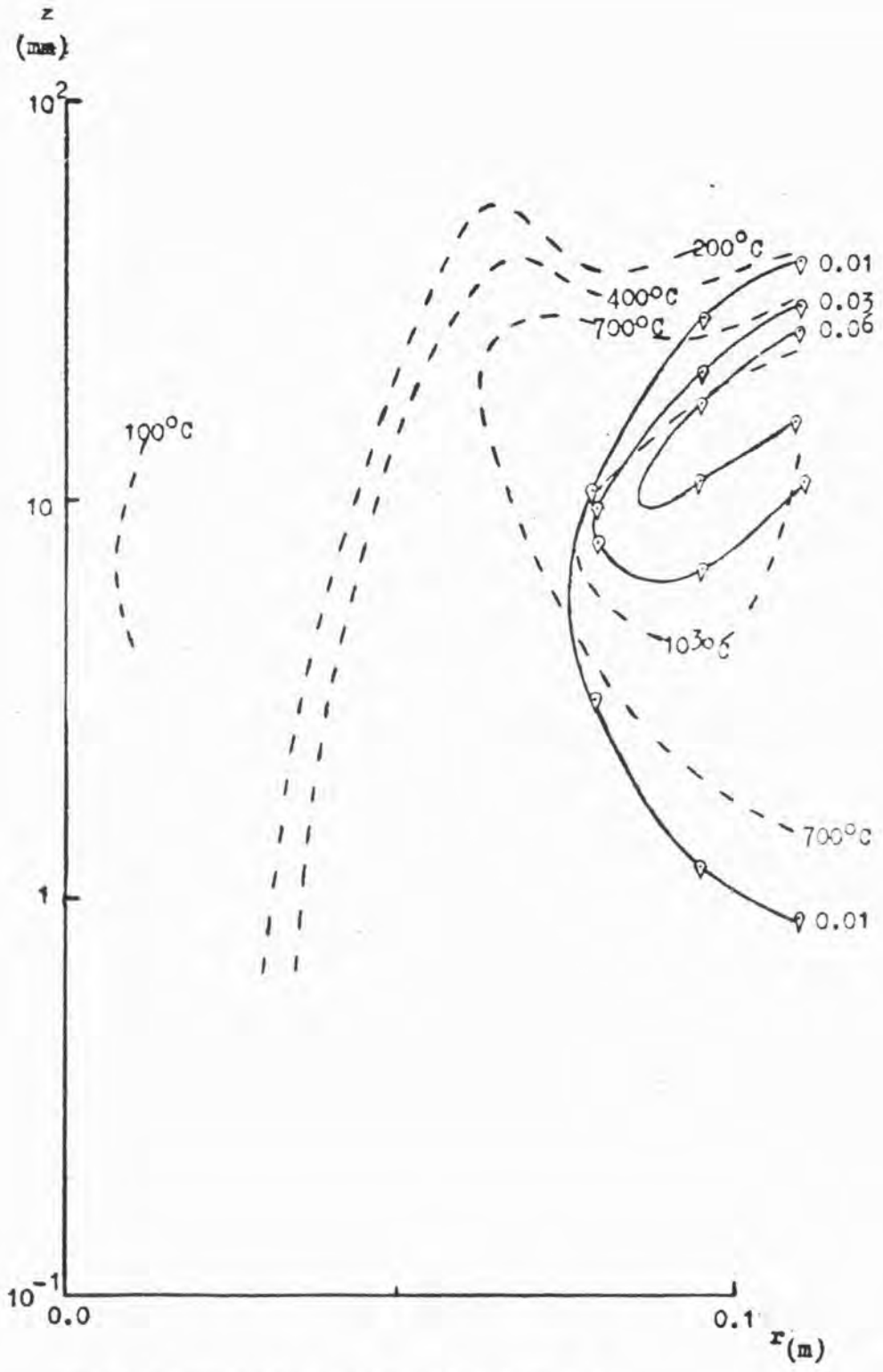

SPATIAL DISTRIBUTION OF CARBON DIOXIDE

FIGURE 9.17

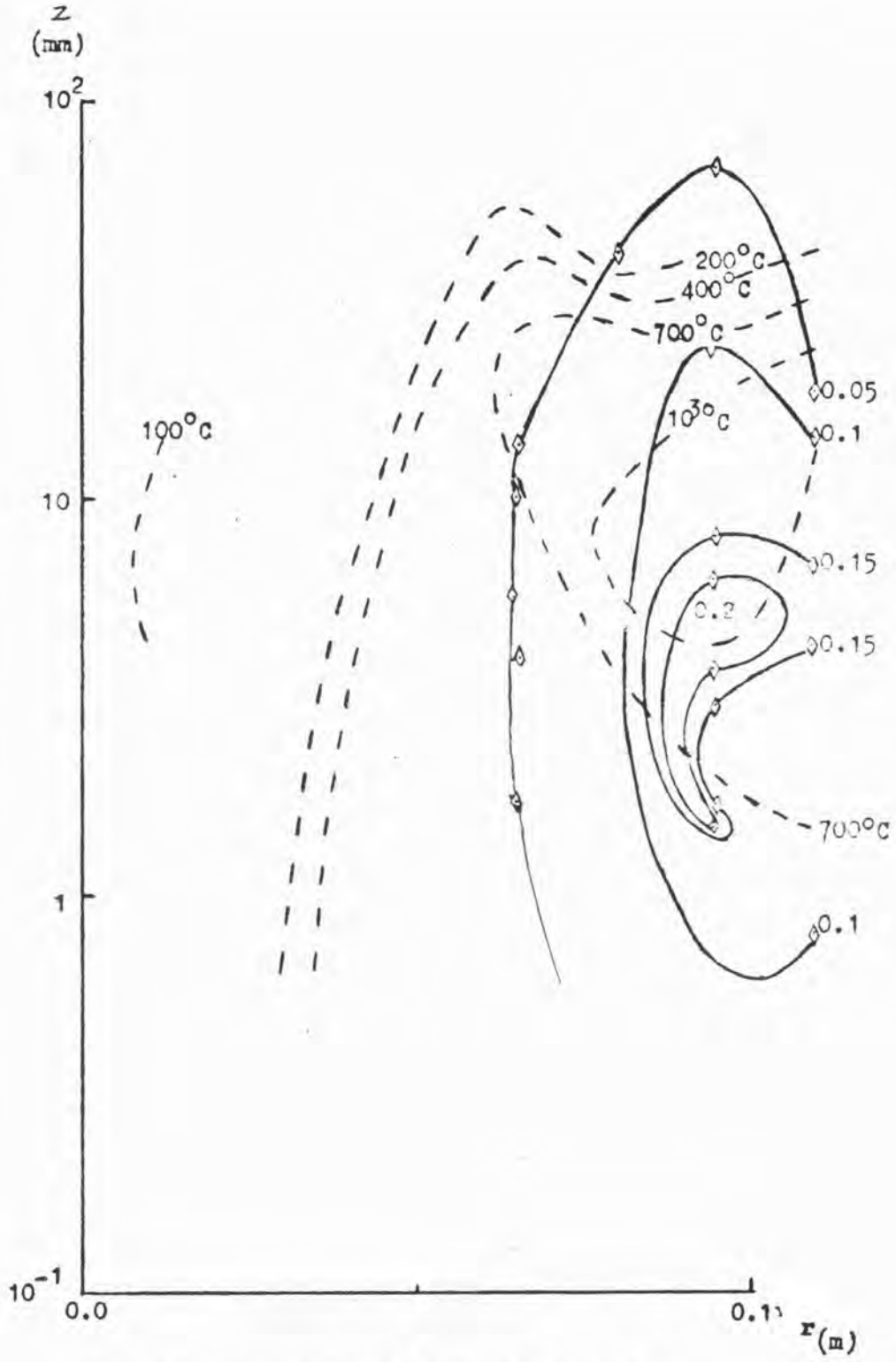

SPATIAL DISTRIBUTION OF CARBON MONOXIDE

FIGURE 9.18

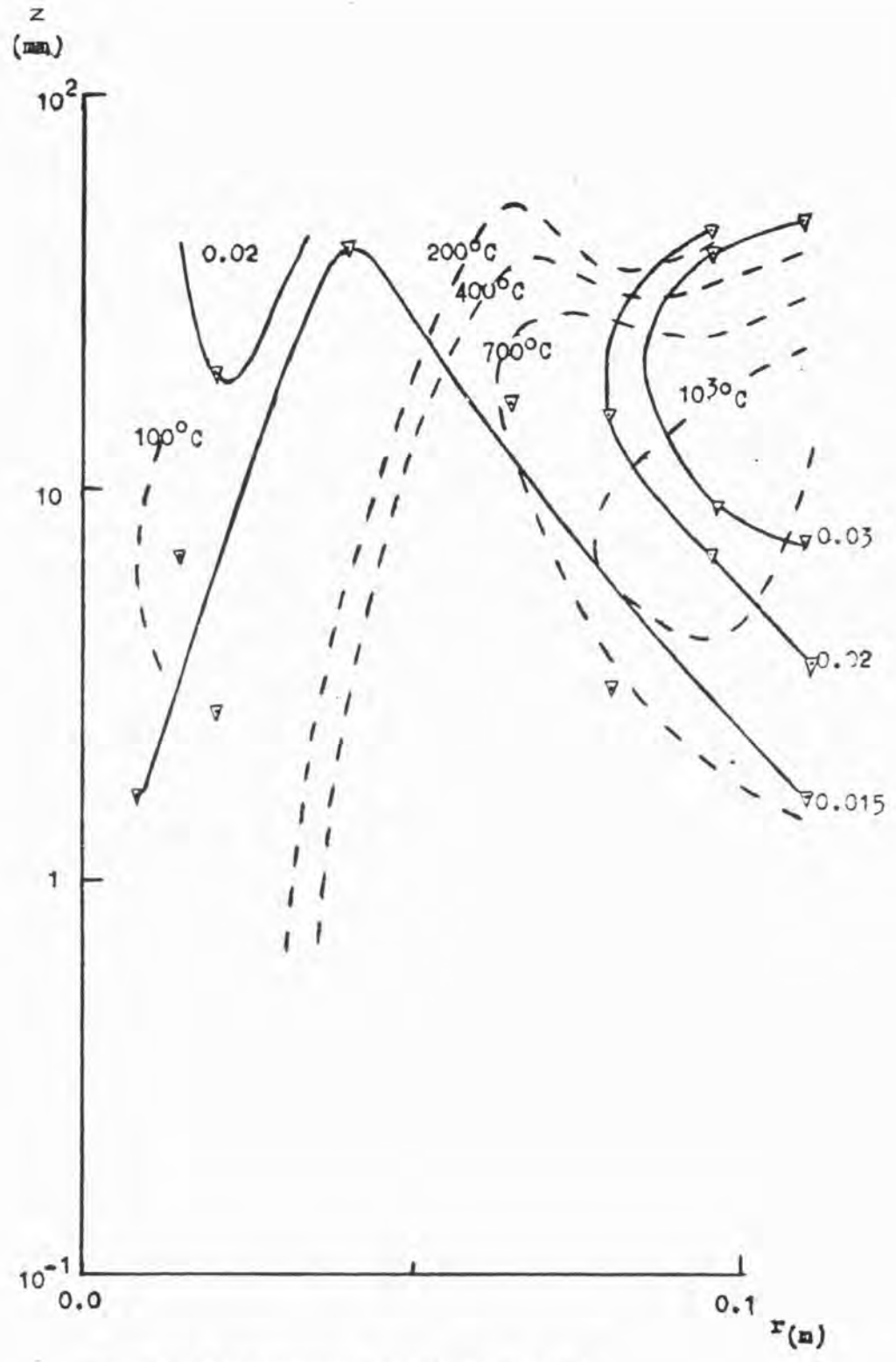

SPATIAL DISTRIBUTION OF WATER VAPOUR

FIGURE 9.19

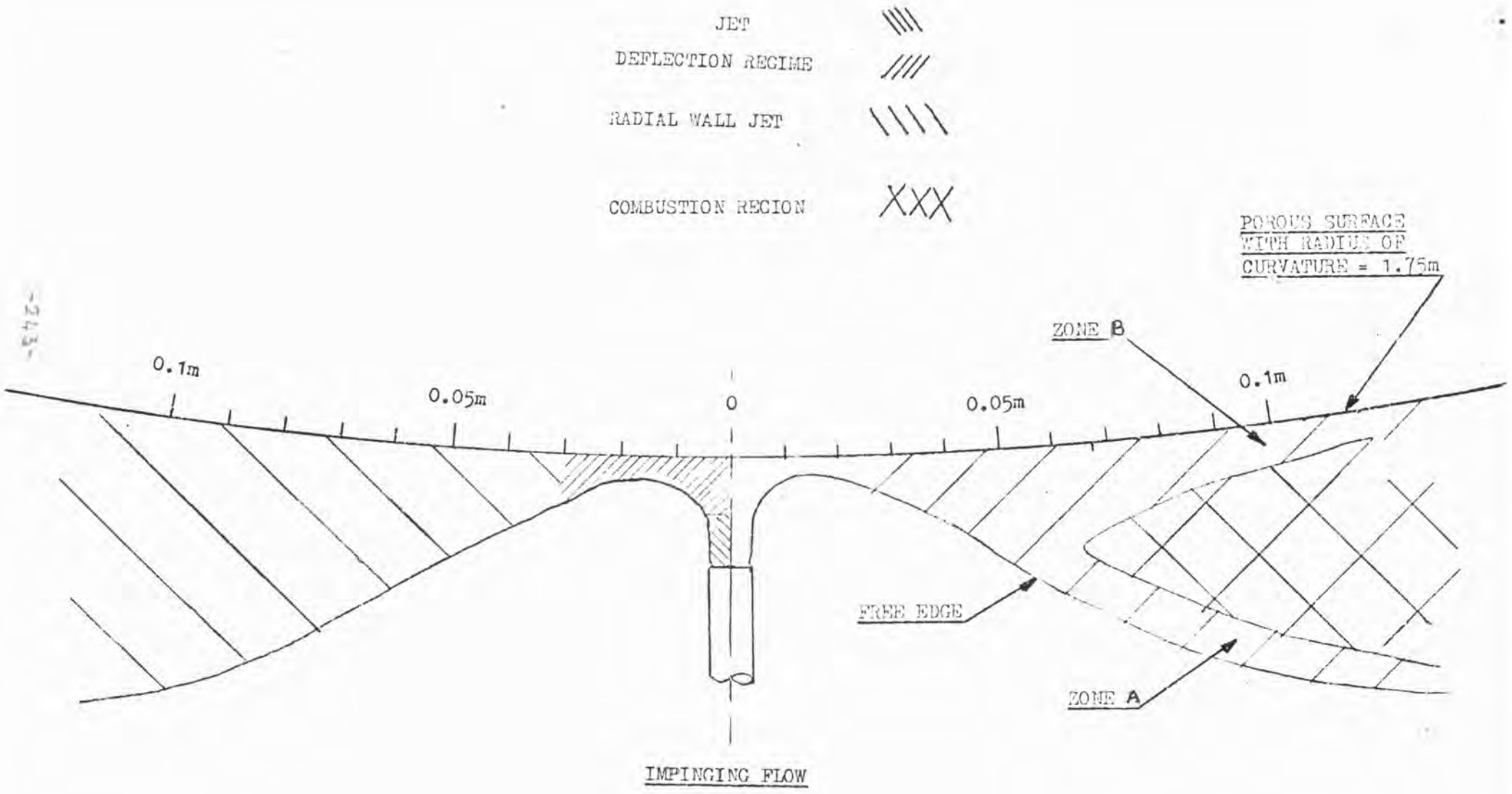
JET
DEFLECTION REGIME
RADIAL WALL JET
COMBUSTION REGION
POROUS SURFACE WITH RADIUS OF CURVATURE = 1.75m
ZONE B
0.1m
0.05m
0
0.05m
0.1m
FREE EDGE
ZONE A
IMPINGING FLOW

FIGURE 9.20

Dioxide, Carbon Monoxide and unburnt reactants.

The Mixing Region has been sub-divided into the two zones A and B specified in figure 9.20. Zone A separated the combustion region from the submerging air, and consequently Methane concentration decreased as the free-edge was approached - as shown in figure 9.14. Zone B occurred between the porous surface and lower streamwise boundary of the combustion region; this zone was rich in Methane, because Natural Gas was pumped through the porous surface. Both zones were heated by radiant energy transfer from the combustion region.

9.2 Physical Properties

To simulate momentum, mass and heat transfer rates with chemical reaction the following physical properties must be known:

a) the density, effective viscosity and effective Prandtl number of the mixture,

and b) effective Schmidt number and reaction rates of the constituent gases.

The expressions used to define these proprties are summarized in table 9.2b.

The density of the mixture is determined from the equation of a perfect gas, in this case:

$$\rho = \frac{p}{\mathcal{R}T}\left[(mM)_{CH_4} + (mM)_{N_2} + (mM)_{O_2} + (mM)_{CO} + (mM)_{CO_2} + (mM)_{H_2O}\right] \qquad (9.1$$

The subscripts CH_4, N_2, O_2, CO, CO_2 and H_2O refer to Methane, Nitrogen, Oxygen, Carbon Monoxide, Carbon Dioxide and Water Vapour respectively.

Constants used in the Turbulence and Chemical Reaction Models

Equations that are the basis of the model	Definition of Constants
i) Turbulence Models	
a) $\mu_t = (k_m y_+)^2 \left[1-\exp\left(\frac{y_+}{A_1}\right)^2\right] \frac{\partial U}{\partial y}$	$k_m = 0.4$
$A_1 = A_+ \left[\frac{p_+}{m_+}(1-\exp(11.8m_+)) + \exp(11.8m_+)\right]$	$A_+ = 26.0$
b) $(Pr)_t = \left(\frac{k_m}{k_r}\right)\left[\frac{1-\exp(-y/A_1)}{1-\exp(y/B_1)}\right]$	$k_m = 0.4$, $k_m = 0.44$
$A_1 = A_+ \left[\frac{p_+}{m_+}(1-\exp(11.8m_+)) + \exp(11.8m_+)\right]$	$A_+ = 26.0$ and $(Pr)_{to} = 0.89$
$B_1 = (Pr)_{to}\left[\frac{k_r A_1}{k_m}\right]$	
c) $(Sc)_{t_i} = (A_c)_i$ $i = CH_4, CO, CO_2$	$A = 0.8$
ii) Chemical Model	
d) $\dot{V}_{CH_4} = A \exp\left[\frac{-E}{RT}\right] (V_{CH_4})^{0.7} (V_{O_2})^{0.8}$ mole/cm^{3}s	$A = 10^{15.2}$ and $E = 48000$
e) $\dot{V}_{CO} = A \exp\left[\frac{-E}{RT}\right] (V_{CO})(V_{H_2O})^{0.5} (V_{O_2})^{0.25}$ mole/cm^{3}s	$A = 10^{14.75}$ and $E = 4500$

The effective viscosity has been determined from the communicative law:

$$\mu_{eff} = \mu_t + \mu_l \quad , \qquad (9.2$$

previously described in chapter three. Again the turbulent viscosity μ_t was determined with the model postulated by Lauder and Spalding, which has been described in chapter three. The molecular viscosity of the mixture μ_l was determined with the accumulative equation:

$$\mu = (m\mu_l)_{CH_4} + (m\mu_l)_{N_2} + (m\mu_l)_{O_2} + (m\mu_l)_{CO} + (m\mu_l)_{CO_2} + (m\mu_l)_{H_2O} \qquad (9.3$$

The molecular viscosities of the constituents were read off tables given in reference 45

Close to the impervious surface the effective Prandtl Number of the mixture was been determined from:

$$Pr_{\ell} = \frac{Pr_l \cdot Pr_t \cdot \mu_{eff}}{\mu_l \cdot Pr_t + \mu_t \cdot Pr_l} \qquad (9.4$$

described and used in chapter eight. Over the remainder of the flow the effective Prandtl number of the mixture was set to it's turbulent component. The molecular Prandtl number of the mixture, was determined from the values for each constituent, with:

$$Pr_{\ell} = (m.Pr_{\ell})_{CH_4} + (m.Pr_{\ell})_{N_2} + (m.Pr_{\ell})_{O_2} + (m.Pr_{\ell})_{CO} + (m.Pr_{\ell})_{CO_2} + (m.Pr_{\ell})_{H_2O} \qquad (9.5$$

where each Prandtl number was read from tables presented in reference RM6. The turbulent Prandtl number of the mixture Pr_t was estimated with the mathematical model postulated by

Cebeci which has been described and used in chapter eight.

Close to the impervious surface the effective Schmidt number for each individual gas has been determined from the communicative law 7.4, previously used and described in chapter seven. Again the molecular Schmidt number of each gas were looked up from tables by Rogers-Mayhew[45]

However, the dearth of suitable data relating to the turbulent Schmidt Number in chemically reacting flows, resulted in a value of 0.7 , which was loosely extrapolated from the work of Robertson[47] , being used throughout. Over the remainder of the flow the effective Schmidt number was set to the turbulent component.

In the simulations the following reactions has been allowed in each element:

$$a.\ CH_4 + b.CO + c.CO_2 + d.O_2 = e.CH_4 + f.CO + g.O_2 + h.CO_2,$$

the coefficients a to h represent the amount of each constituent involved. To achieve the simulation of this reaction the rates of change of Methane, Carbon Monoxide, and Carbon Dioxide must be supplied. In this case the rate of change of each species k, represented by R_k, is determined with an Arrhenius relationship of the type:

$$R_k = -F_k \exp \frac{-E_k}{RT} ,$$

with F_R and E_k being designated the frequency factor and activation energy coefficients respectively. In this work these coefficients are regarded as constants and determined from published data by Kondat'ev[52] . Two conditions have been used to control the implementation of the reaction equation within a flow element. Firstly, if the mixture temperature was less than 700°C, or the available oxygen less than three percent by weight, no chemical reaction was allowed. Secondly, if insufficient oxygen was available for complete reaction within a flow element, then Methane was allowed to react giving Carbon Monoxide, and if Oxygen was still available the Carbon Monoxide was allowed to react.

9.3 Comparisons

Four computational simulations of the radial wall jet described in section one were attempted with the new modelling technique. Estimates of the accuracy of the predictions were obtained by comparisons with measured data.

The radial wall jet was simulated where $0.065 \leq r \leq 0.11$m; this area of flow contains the combustion and mixing regions discussed in section one, and detailed in figure 9.20.

Along the cross-stream section at r = 0.065m the mainstream velocity, species concentrations and temperature were read from the measured results in figure 9.8. The porous surface was assumed isothermal at a temperature of 450°C. At the free edge air, at 87°C, was assumed with a mainstream velocity set to one percent of U_{max}.

Four simulations of the radial wall jet were attempted. In each simulation the grading of the mesh network used to cover the radial wall jet was varied. The grading of the mesh networks was varied in two ways. Firstly, the real distance was varied between the radial points at which the starting cross-stream velocity profile was specified. The relationship used to define this grading was of the form of:

$$z_{1,i} = z_{1,i-1}(1+Fr)$$

where $i = 3, N_j$, and $z_{1,1}, z_{1,2}$ and Fr are constants. $\delta_{1,1}$ is the width of the flow at this section. Two forms of this grading were tried, they corresponded to:

a) $z_{1,1} = 0.0$, $z_{1,2} = \delta_{1,1}/10^3$ and $Fr = 1.121$

b) $z_{1,1} = 0.0$, $z_{1,2} = \delta_{1,1}/10^5$ and $Fr = 1.196$

Secondly, the functional relationship between the non-dimensional mesh stream function and the stream function ψ was varied.

This relationship was defined with the interactive part of the modelling technique - as defined in chapter four. With this part of the model the relationship between the mesh stream function and "ψ" was adjusted until the rate of change of velocity with the non-dimensional mesh stream function was not greater than the velocity gradient limit. In the simulations two values for the velocity gradient limit were tried; these were:

$$\text{i) } L = 10^3$$

$$\text{or ii) } L = 10^5$$

These values for the velocity gradient limit were prescribed in chapter four.

Table 9.3

Boundary Conditions

Boundary	Gravimetric concentrations				
	m_{CH_4}	m_{CO}	m_{O_2}	m_{CO_2}	m_{N_2}
Impervious surface	0.81	-	0.03	-	0.15
Free-edge	-	-	0.23	-	0.76

Table 9.4

property

Property	Values at which predicted data is presented			
U	3.0	0.5		
T	1000°C	700°C		
m_{CH_4}	0.5	0.24	0.1	0.03
m_{O_2}	0.12	0.11		
m_{N_2}	0.6	0.3		
m_{CO_2}	0.03	0.01		
m_{CO}	0.1			

In each simulation the effects of radiant energy transfer were neglected. It had been envisaged that this facet of the energy transfer process could be allowed for by re-simulating the flow, and calculating the radiant energy with the four flux model based upon the previously predicted temperature field. For reasons defined in the next paragraph this technique of re-simulating the flow was not used.

The modelling technique did not accurately simulate the radial wall jet. In fact in each simulation many of the predictions oscillated over successive flow elements. To give some indication of these results, selected data from the simulation with the following mesh network restraints:

$$z_1 = 0, \quad z_{1,2} = \delta_{1,1}/10^5, \quad Fr = 1.12 \quad \text{and} \quad L = 10^5$$

has been presented. The selected data is shown in figures 9.21 to .26 and details the spatial position of lines of constant mainstream velocity, temperature, methane, oxygen, carbon monoxide and carbon dioxide concentrations; the associated measured data in this region is detailed with dotted lines. (The values of the constant property lines are detailed in table 9.4.) When the predicted results oscillated only the first centimetre of the trace is shown, for thereafter the results are meaningless.

There are three possible causes for the oscillation in the predicted results. The first, and most likely cause results from a deficiency in the model of the chemical reactions. This subject is discussed more fully in the next paragraph. The second and third possible causes of the reported oscillations are numerical errors generated by the modelling technique and deficiencies in the procedures used for estimating the turbulent and physical properties of the flow. The last two effects have been assumed not to cause the oscillations.

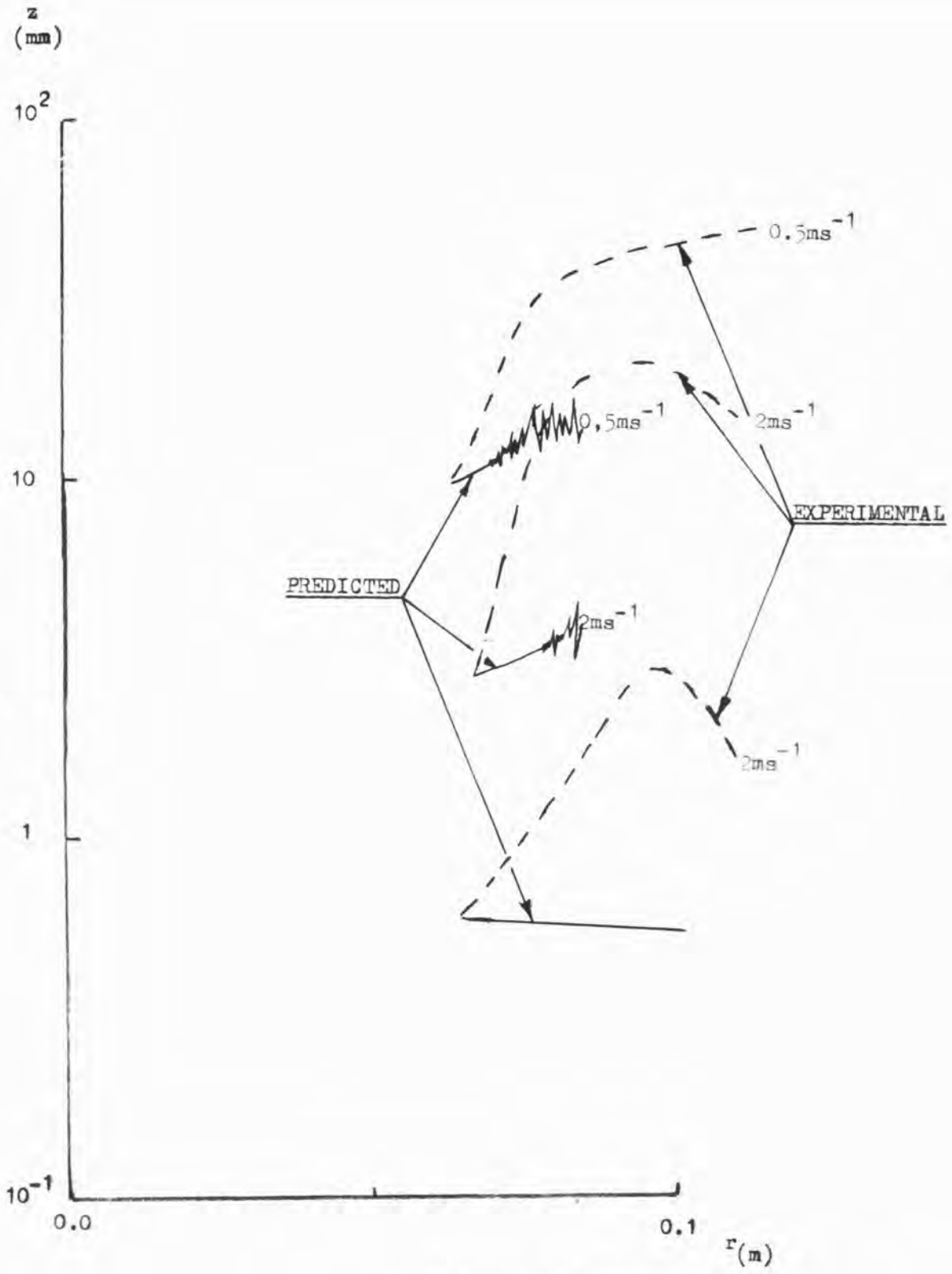

VELOCITY COMPARISONS

FIGURE 9.21

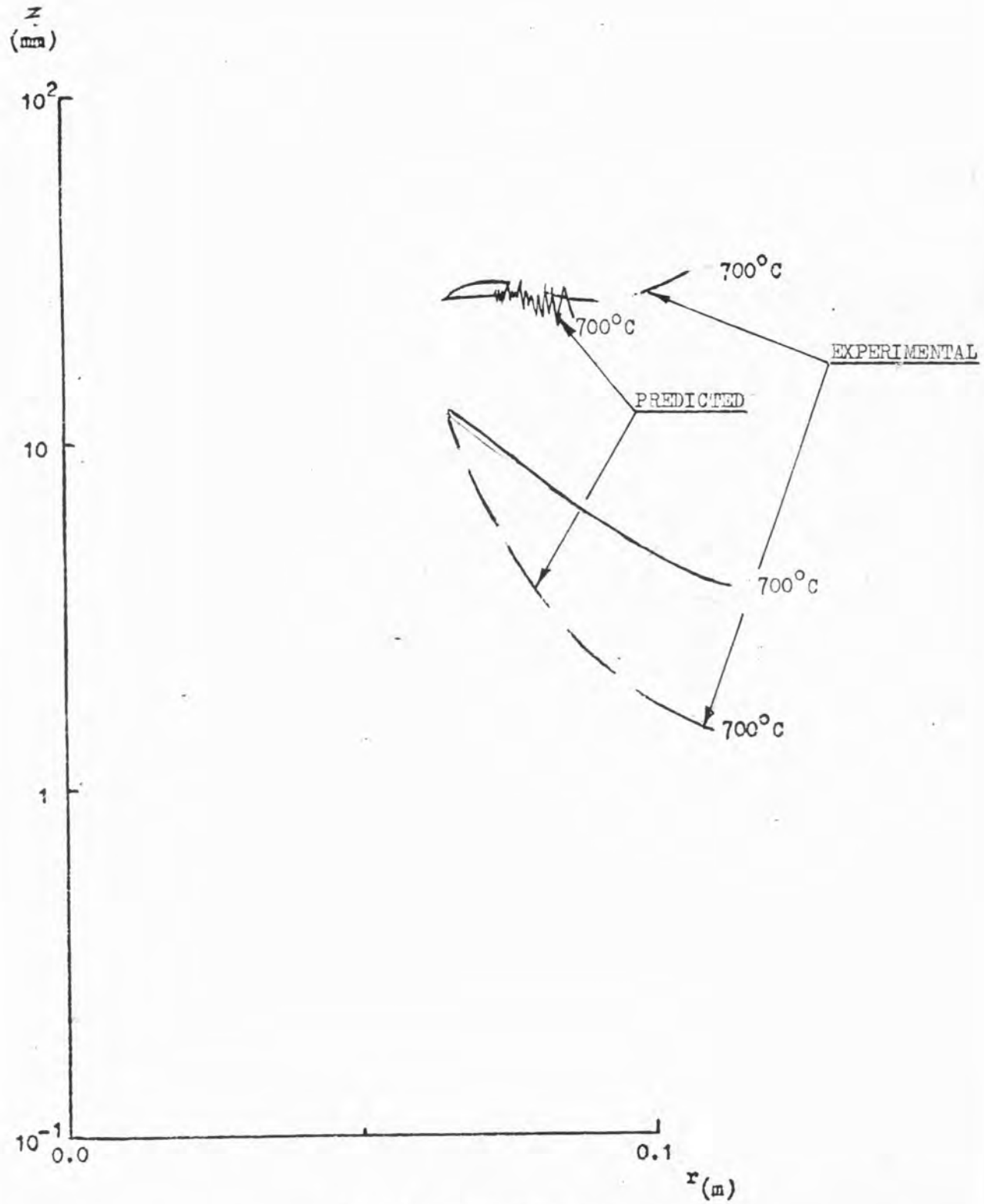

TEMPERATURE COMPARISONS

FIGURE 9.22

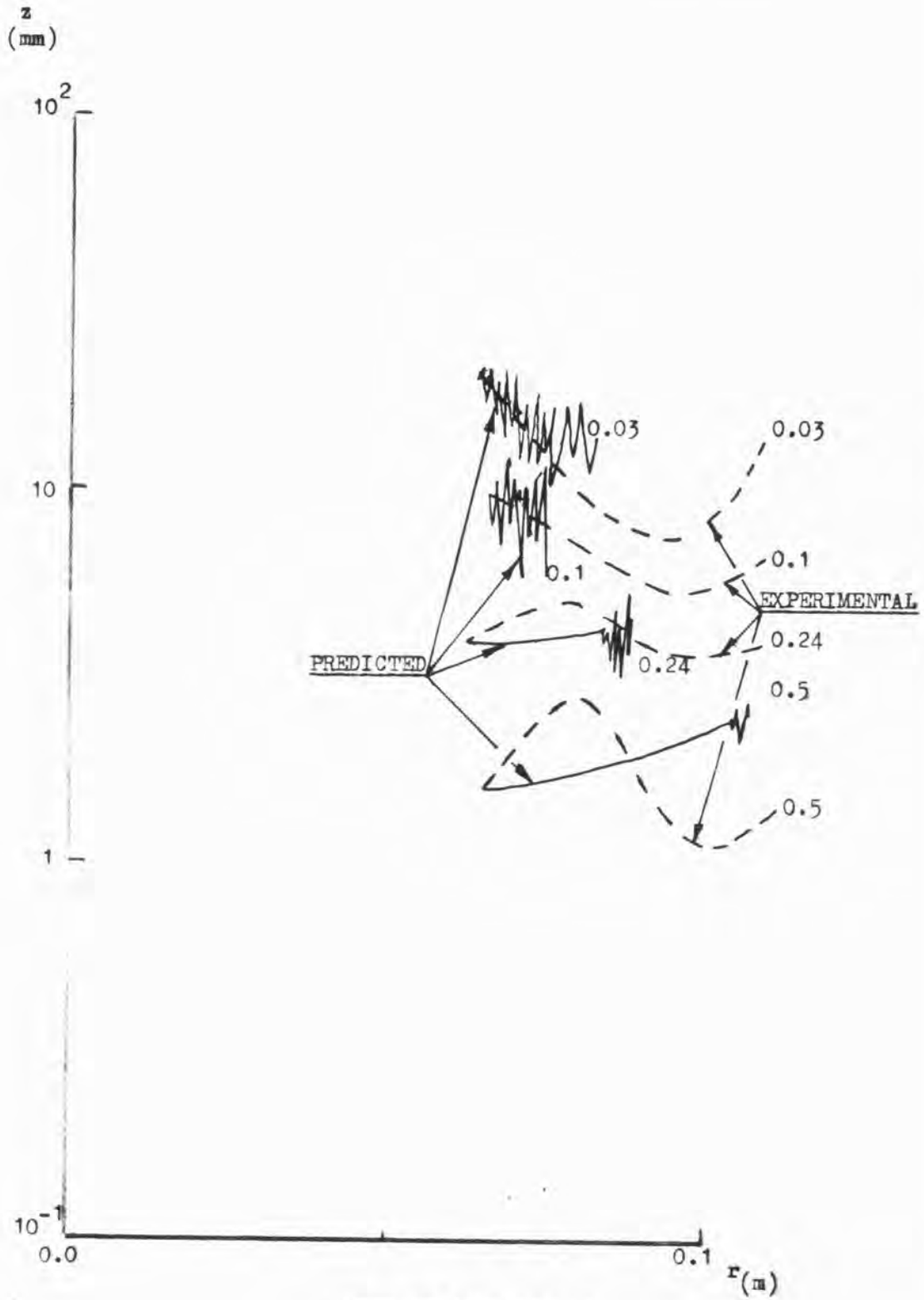

METHANE COMPARISONS

FIGURE 9.23

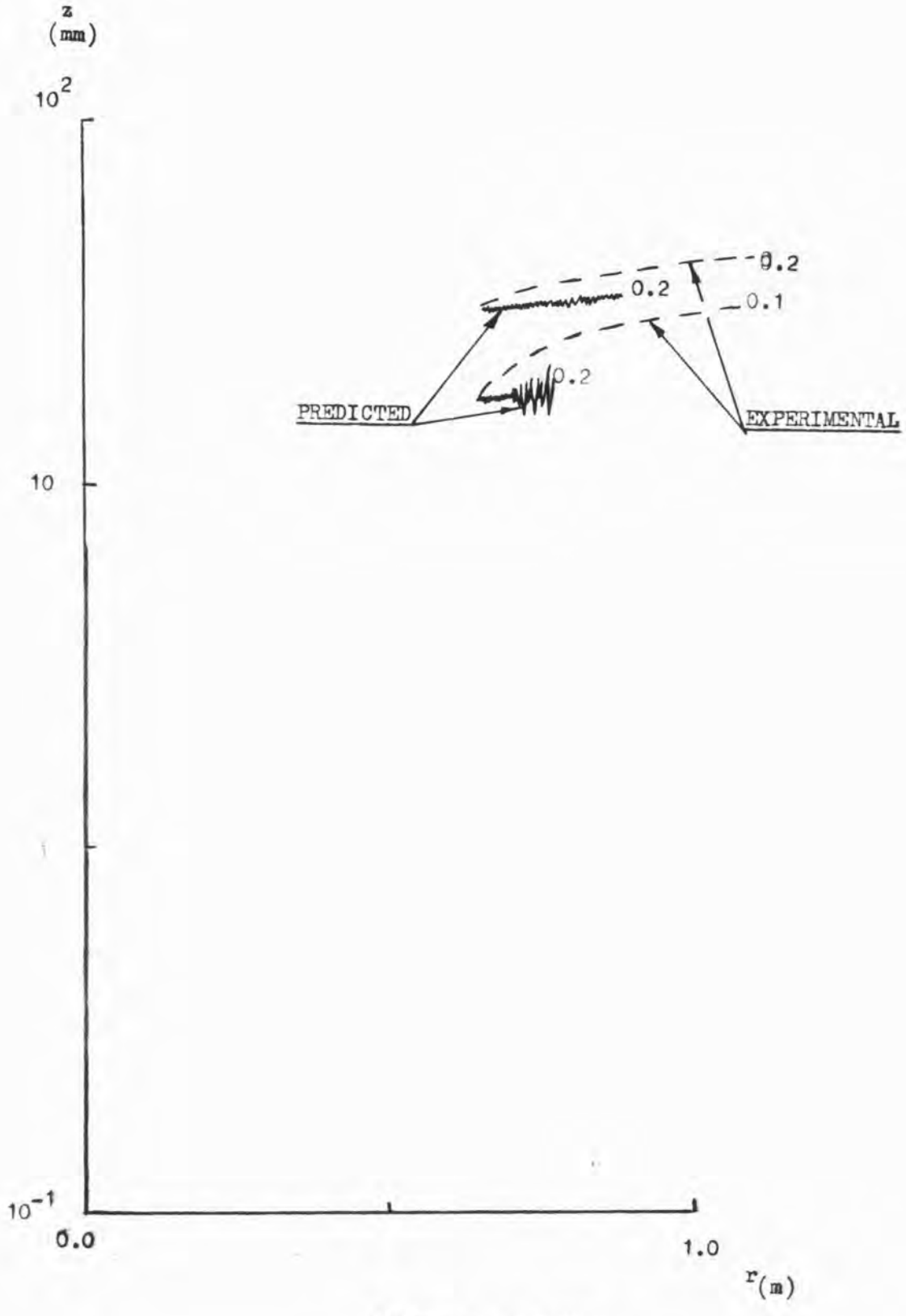

OXYGEN COMPARISONS

FIGURE 9.24

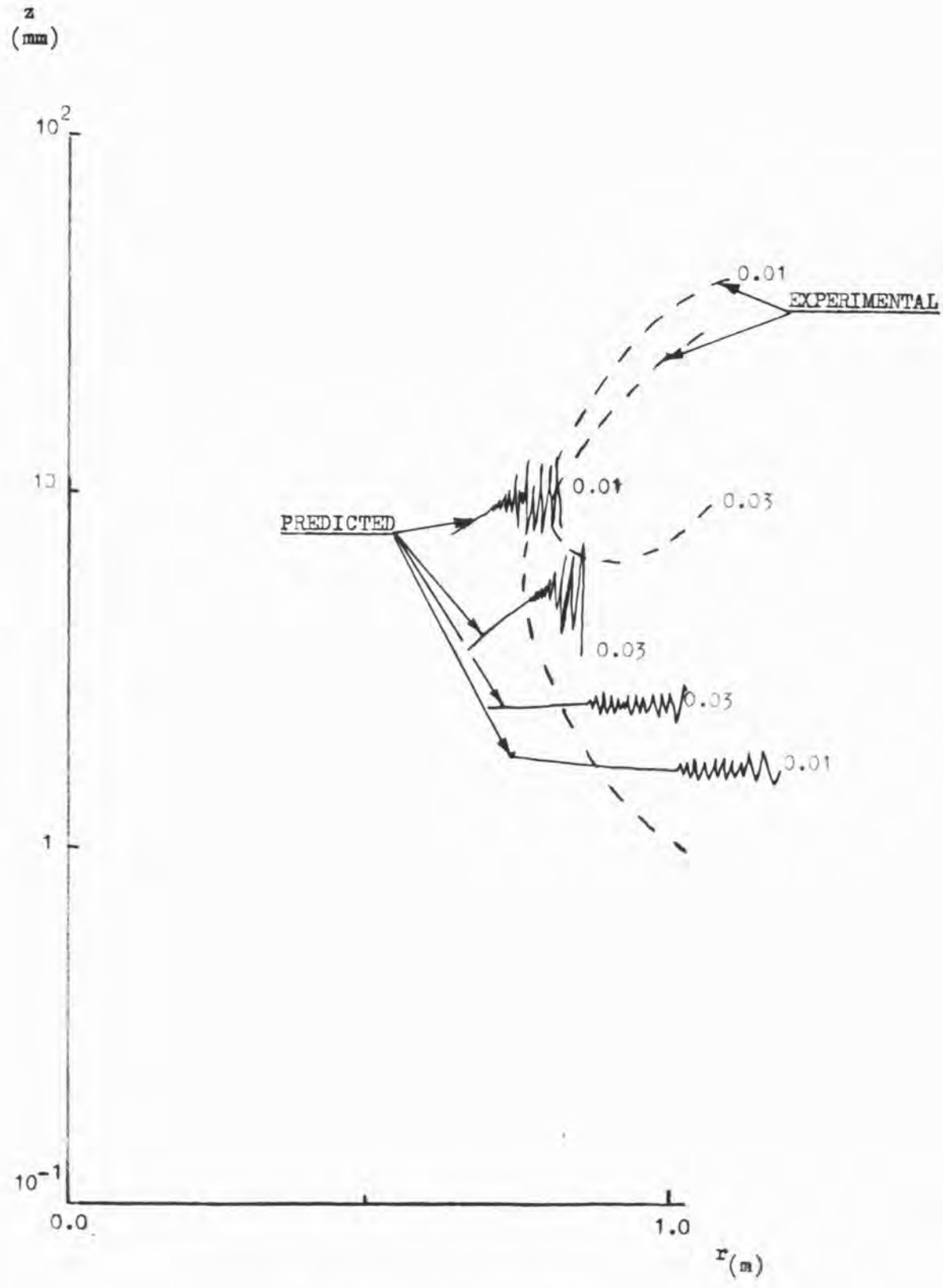

CARBON DIOXIDE COMPARISONS

FIGURE 9.25

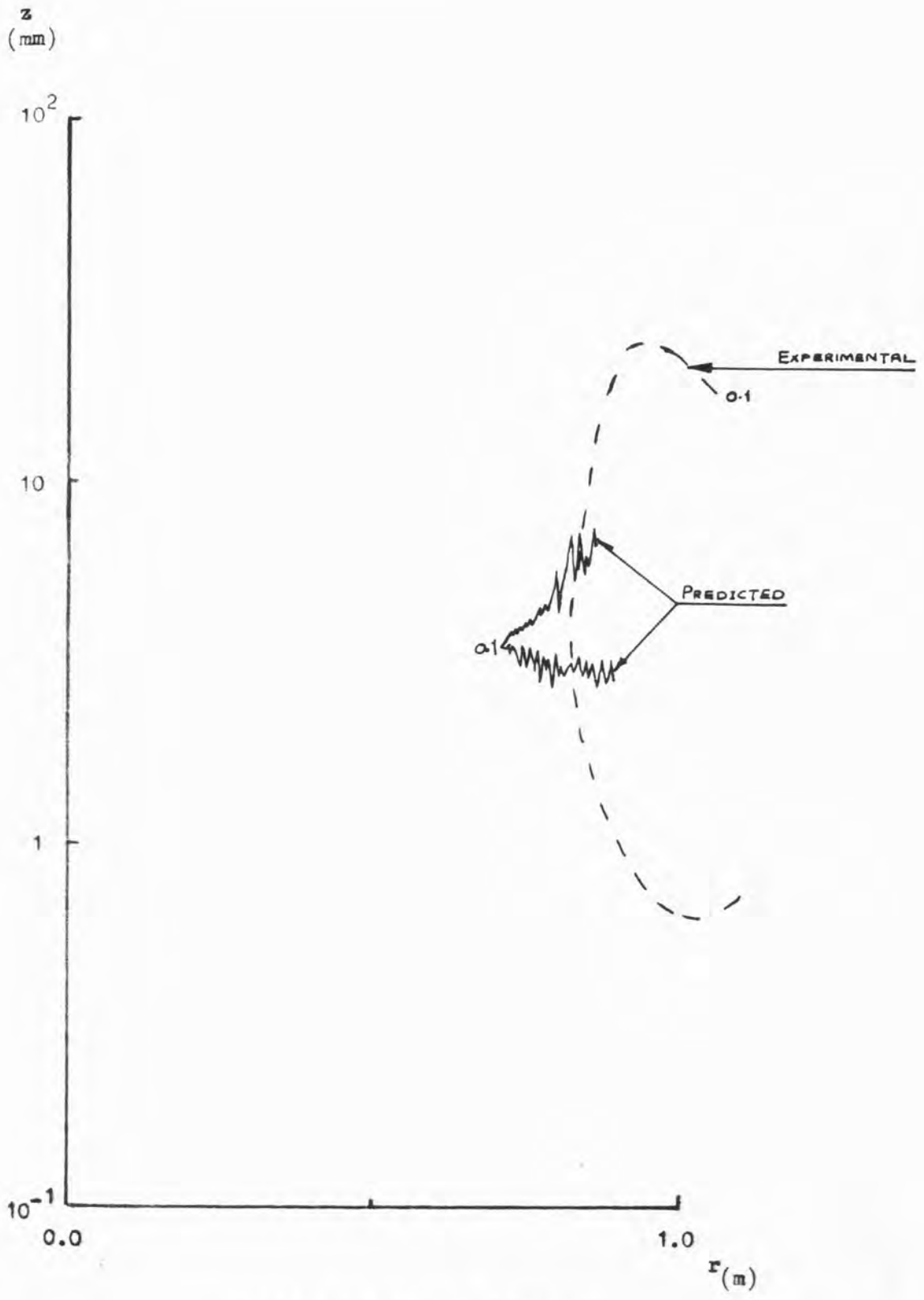

CARBON MONOXIDE COMPARISONS

FIGURE 9.26

The reason for this assumption being made is as follows. The procedures for estimating the turbulent and physical properties and the numerical error of the modelling technique have been thoroughly assessed when simulating radial wall jets - see the discussion presented in chapters six to eight. Whilst these effects caused errors in the predictions they did not cause instability . Since the flow situation being examined in this chapter is in most respects, the exception being combustion, similar to those simulated in chapters six to eight; it is felt that deficiences in the reaction model cause the reported oscillations.

Predictions of the gravimetric concentrations of Methane and then Carbon Monoxide are the first two to show signs of oscillating - see figures 9.23 and.26 . Detailed examination of these results indicated that unrealistic estimations of the reaction rates accounted for the oscillations in the predicted data. There are two major reasons for the unrealistic estimates of the reaction rates. The first is that the two-step global reaction model used in the simulations presented in this chapter can produce unrealistic results under certain combustion conditions. This is because the oxidation of the fuel directly to Carbon Monoxide and then Carbon Dioxide, if sufficient oxidant exists, is experimentally unrealistic - since it takes no account of the various intermediate hydro-carbon reactions which can considerably affect the combustion processes. Cohen[134], has found several hydro-carbon reactions which cannot be adequately simulated with global reaction models. This subject is covered in greater detail in chapter eleven. The second reason for the unrealistic estimates of the reaction rates is that the Arrhenius rate equations, used in the specified two-step global reaction model, and the latest heat of reaction term in the energy conservation equation take no account of unmixedness.

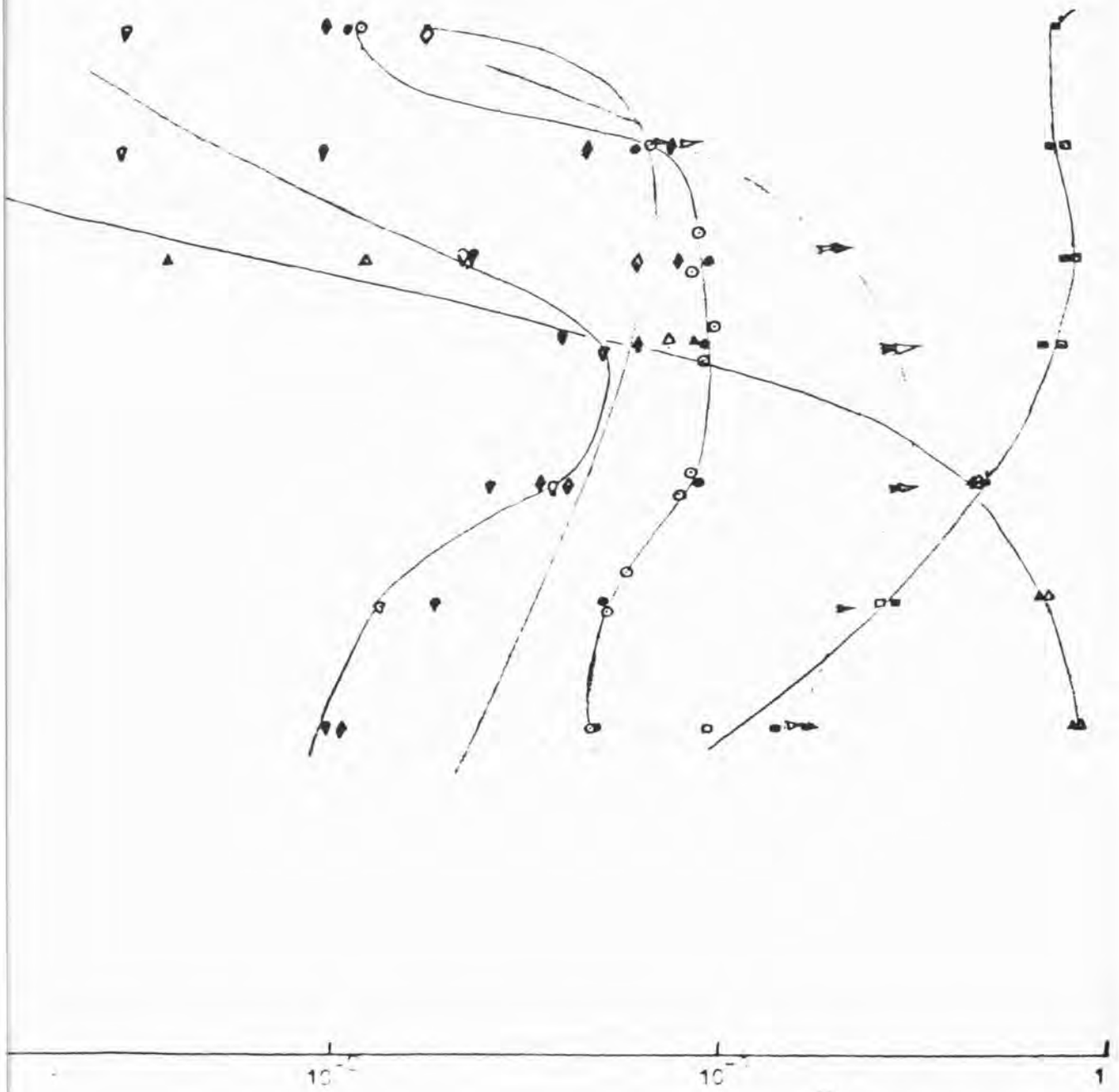

CROSS-STREAM FLOW PATTERN AT r = 0.080m

FIGURE 5.28

For reactions to occur in a real flow the fluctuations of the turbulent reacting species must be approximately in phase - or in other words the species must be at the same place at the same time. In the modelling technique and chemical reaction model used in this section only the time averaged properties, which are insensitive to phase, are known or predicted. Thus these procedures take no account of the unmixedness which will occur in real flows and inhibit the combustion process. Under these circumstances it is possible that the reaction models will produce unrealistic estimates of the reaction rate.

9.4 Conclusions

The recommended modelling techniques could not successfully simulate the time averaged velocity, concentrations and temperature fields within part of a chemically reacting radial wall jet. The techniques failure was primarily caused by deficiencies in the procedures for estimating the effects of turbulent chemical reaction between Methane, Carbon Monoxide, Oxygen and Carbon Dioxide.

Chapter 10

Discussions and Recommendations

The various specimen radial wall jet simulations carried out with the modelling technique incorporating a variable mesh network, and making use of an interactive scheme, are detailed in table 10.1. In this table are presented brief details of the flow situations simulated, the turbulent transfer processess involved and brief notes showing where details of the simulations can be found.

In the first three flow situations, i to iii in table 10.1, the predicted time averaged results were in general agreement with measured data, but deficiences did exist. The discrepancies in the results were acceptable for most engineering applications, being of the order ten percent. Improvements can still be made and in section 1 the most realistic and profitable changes are detailed.

The specified modelling technique could not accurately simulate a radial wall jet flow involving turbulent momentum, mass and heat transfer with chemical reaction. (In table 10.1 this flow is designated iv.) The implications of this finding is considered in section 2.

The various experimental studies of impinging flows presented in this work were primarily concerned with providing measured data for assessing the performance of the recommended modelling technique. However, these experimental studies also provided novel information about the time averaged flow patterns. In section 3 the presented studies are briefly reviewed, and recommendations for future work detailed and discussed.

Table 10.1

Examined Flows					
	Turbulent transfer processes involved	Detailed in	Temperature	Chemical reaction	Constituents
i	Momentum	Chapter 6	Same as submerging air	None	Air
ii	Momentum and mass	Chapter 7 Appendix 4	Same as submerging air	None	Nitrogen and Oxygen
iii	Momentum, mass and heat	Chapter 8 Appendix 5	Greater than submerging air	None	Argon, Nitrogen & Oxygen
iv	Momentum, mass and heat with chemical reaction	Chapter 9 Appendix 6	"	Reaction between Methane & Carbon Monoxide Oxygen	Methane, Oxygen Nitrogen, Carbon Monoxide and Carbon Dioxide

In section 4 a discussion is presented of the subject of future trends in flow modelling techniques.

10.1 Improvements

Discrepancies in the predicted results from the modelling techniques are caused by deficiences in either the mathematical method or turbulence information. In this section the practical improvements that can be made to these portions of the modelling technique, so that more accurate simulations of the simpler forms of radial wall jet flows can be obtained, are discussed.

Considerable effort has been made in this thesis to ensure that the recommended modelling technique solved the time averaged conservation equations with the least numerical error. This has been achieved by interactively manipulating the mesh network covering the flow so that assumptions between real and assumed cross-stream velocity profiles were within specified limits. Greater accuracy could be obtained with the presented technique by increasing the complexity of the mesh network manipulations. Alternatively, one of the many finite element methods could be used to solve the conservation equations in a more accurate manner. Examples of such techniques are those proposed by Campion-Renson and Crochet[53], and Taylor and Hood[54]. However, at this stage such efforts are unnecessary, because the turbulence information supplied to the technique seems the major contributor to the discrepancies in the predictions - as estimated by Prandtl[24], Schlichting[22] and Lauder and Spalding[28].

In the specimen simulations presented in chapters six to eight, detailed in points i to iii of table 10.1, the discrepancies between the predicted and experimental data were sufficiently small to make any major changes in the turbulence information unprofitable. Obviously, the phenomenological turbulence theories used in the simulations could be replaced with ones that are based upon better theoretical considerations. For example, in flows dominated by turbulent momentum transfer the kinetic energy equation, 3.3 in chapter 3, could be used instead of Cebeci's model to estimate the effective viscosity. Alternatively, the turbulence models used in this thesis could be tuned to meet specified accuracy requirements in the narrow range of specimen flow situations simulated. The second approach has not been followed, nor is it recommended, because of the intellectual sterility of empirically modifying the specified turbulence models in such limited flow situations. This subject is dealt with more fully in section 4; after further discussions on the findings of the work presented in this thesis.

10.2 Complex Flows

The modelling technique could not accurately simulate a radial wall jet containing two chemically reacting constituents, because the model for the combustion processes did not work. This finding has far wider implications than discussed in chapter nine, because all complex flow simulations involving turbulent momentum, mass and heat transfer - with two or more chemical or ionic reactions - are governed by the same conservation equations. Therefore, it is likely that the problem encountered in chapter nine in modelling the reactions will occur in all flows of a similar type.

There are three ways of obtaining stable and reasonably accurate predictions of the complex flows. The most obvious procedure, which has been used by Spalding -Patanker[7], is to persevere with the recommended modelling technique; but re-estimate the constants in:

a) Arrhenius's relationships for the reaction rates

and b) the models for the physical properties.

In the short term this appears a reasonable solution, because it offers some hope of predictions in actual flows for a small amount of effort. Another approach, successfully used by many authors, is not to model the flow under investigation but a simplified version of it. For example, when simulating chemically reacting Methane air flows Spalding- Patankar[7 & 46] and Whitelaw - Khalil[51] have simplified the reaction to:

fuel + oxidant = reactant;

and modified the conservation equations for heat and mass transfer accordingly. This approach has resulted in stable and reasonably consistant predictions. However, the discrepancy between the predicted and experimental results are uncertain, because the real flow has not been simulated. The final alternative is to completely re-formulate the modelling technique, so that it is more closely allied to the turbulent motion being simulated. A discussion on this subject is presented in section 4.

Budgetry considerations and accuracy requirements define which of the declared methods of obtaining stable predictions in complex flows is the most suitable. If approximate solutions are being sought, the first and second alternatives appear to be the most suitable. However, if accurate solutions, which can be enhanced when necessary, are required in complex flows the final alternative appears the best, because of it's inherent flexibility.

10.3 Experimentation

In each of the experimental studies detailed in this work the time averaged flow patterns were measured. However, these results do not give a full picture of the turbulent transport processes, because the relevant fluctuating flow properties were not measured.

The discussions on the performance of the recommended modelling technique in sections 1 and 2; showed that to obtain accurate predictions in complex flow situations more information about the turbulent and physical properties must be obtained. In the context of the presented experimental studies this means we require a fuller understanding of the relevant correlation of the fluctuating properties. This leads to the only recommendation of this section. This is that in future experimental work for validating modelling techniques, both the time averaged and transient transport processes be measured. For it is only in this way that the modelling technique being tested can be realistically updated and corrected.

Obviously, using this approach the modelling technique becomes a mathematical process for manipulating turbulence information; with the flow properties measured being dependent upon the types of conservation equations used. These equations, as well as the properties to be measured, are discussed in section 4.

10.4 Future Trends in Flow Modelling Techniques

In this work it has been shown that when simulating simple radial wall jets - involving turbulent momentum, mass and heat transfer - the prescribed modelling technique predicted the time averaged flow properties with sufficient accuracy for most engineering applications. However, in the one complex flow simulation - involving chemical reactions between Methane, Carbon Monoxide and Oxygen - accurate predictions were not obtained, because of deficiences in the chemical reaction model. To obtain realistic and accurate predictions in flows of this sort the modelling technique must be more closely allied to measured time averaged and fluctuating turbulent data.

Obviously this new modelling technique need not be all embracing nor last for perpetuity Instead, a technique for the next decade that can make use of all experimental work should be sought. The recommended procedure for formulating such a technique is detailed in figure 10.1. This procedure is based upon the solution of the exact transport equations of turbulence, and is heavily influenced by measured results. The choice of both the form and number of turbulent transport equations solved is of considerable importance. Bradshaw[3] , has discussed this subject for flows in which the momentum transfer rates are predominant. However, no guidelines as to which transport equations to use are available when heat and mass transfer affect the flow through turbulent conduction, convection and radiant transfer.

It is recommended that the starting point for the construction of a new modelling technique be a comprehensive study of which transport equations to use. The author favours the use of the Reynolds stress, and compatible equations for heat and mass transfer rates, because several techniques of this sort have been formulated and tested for turbulent flows involving momentum transfer. For example, Bradshaw[3] has solved Reynolds stress equation after substituting an algebraic length scale; and Harlow[55] has solved the same equation after using further transport relationships to account for the disapation rates.

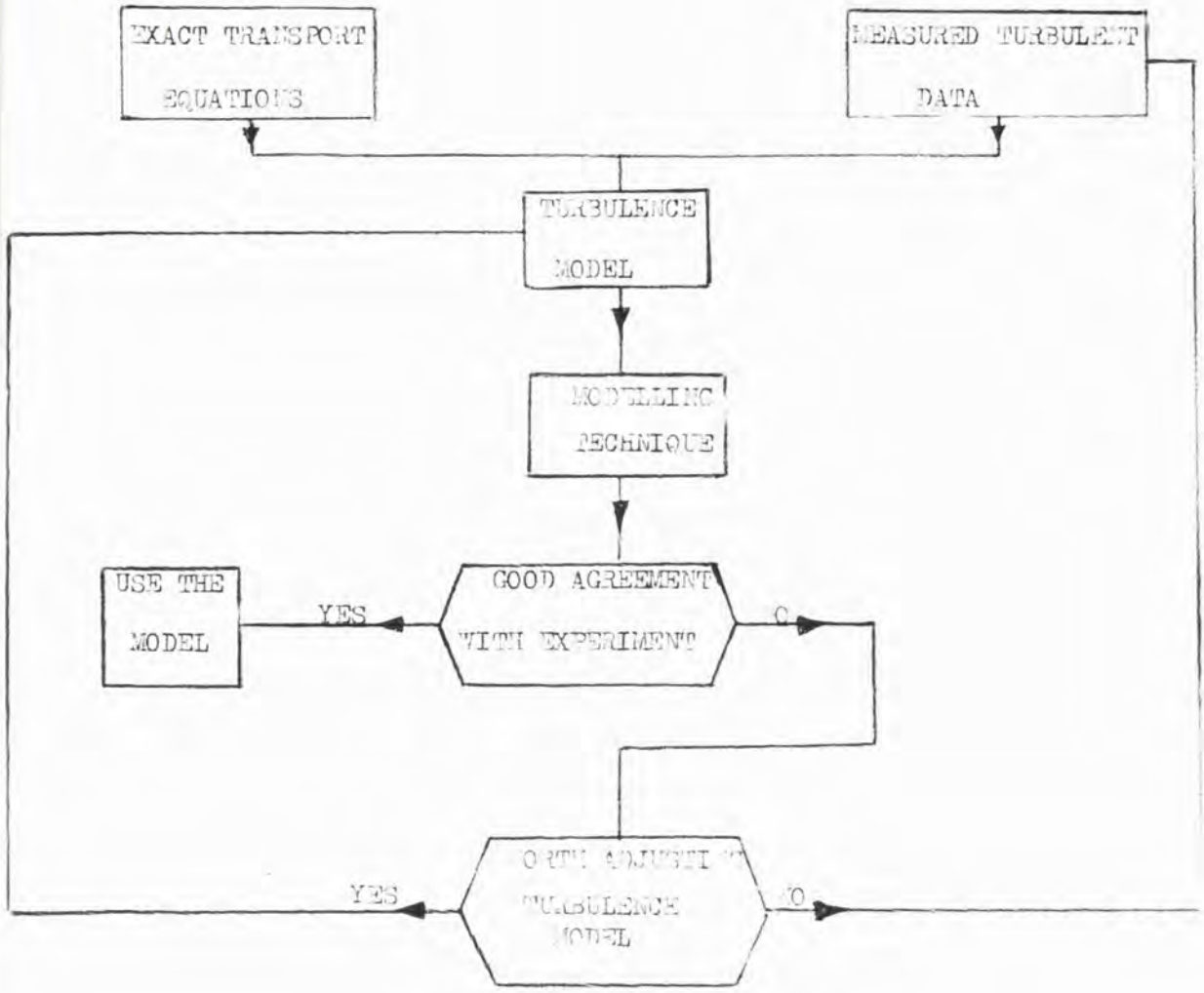

FLOW CHART FOR DEVELOPEMENT OF MODELLING TECHNIQUE

FIGURE 10.1

Chapter 11

Significant Advances

The subject of this thesis is the simulation of complex turbulent flows - particularly flames. In the years since the presented work was completed there have been significant advances. In this chapter these advances are discussed.

The simulation of complex turbulent flows remains one of the most challenging areas of research, because of the complexity of this type of turbulent motion. The simulation of furnace and combustion chamber flame flows has received considerable attention over the last decade. This is due to the relatively simple behaviour of such flows, as much as industries need to save fuel through more efficient design. Certain techniques for modelling these flows have achieved some measure of success. For example, the Imperial College Group under D.B.Spalding, have reported predictions with a modelling technique that qualitatively correspond with measured data - for further details see the results presented in references 59,60 and 61. Such techniques are useful design tools when they are used within previously tested limits, because then the accuracy of the predictions can be confidently assessed. However, as reported by Bilger in reference 62, outside these limits the probable accuracy of the prediction cannot be estimated and the techniques should be used with caution. (The main reason for this restriction is that the turbulence models embodied in the modelling techniques, and

used for estimating the turbulent viscosity, Schmidt and Prandtl numbers are only adequate when used to interpolate over tested ranges of conditions).

The advances in the prediction of flame flows, up to the early 1970s, has been detailed by Beér and Chigier,[63] in their book titled Combustion Aerodynamics ,and Swithenbank[64], in a report titled Combustion Fundamentals. From these works three points are important to this discussion. The first and second points place the recent advances in flame prediction in their historical context. Both Swithenbank and Beér make use of the classical aerodynamicists description of turbulence to explain turbulent motion in a flame. (Namely that the larger eddies in the flow are anisotropic and react with one another to produce a complete range of eddy sizes. The smallest eddies decrease in size by vortex stretching, with their energy being dissipated at the molecular level.) In this explanation the effect of different mixtures as well as density & temperature changes are not fully considered. The second point, concerns the quality of the turbulence models used in the early modelling techniques. The turbulent viscosity was normally predicted with Prandtl's mixing length hypothesis - Beér etal recommend this procedure in their book. The turbulent Prandtl and Schmidt numbers were almost always taken as constants, with their values being derived from the limited amount of available experimental evidence. Spalding and Pantankar[7,46] used

this procedure in their flow modelling technique of 1972. The third point, concerns the possibility that the combustion processes in a flow can generate turbulence. Such turbulence is often referred to as flame generated turbulence. Karlovitz,Denniston and Wells[65] were the first to examine the concept of flame generated turbulence. They proposed that flame generated turbulence accounted for the discrepancies between measured and predicted turbulent flame speeds. (The turbulent flame speed has been defined by Beer[63] as the velocity of steady propagation when referred to the unburnt state). For the theoretical part of their study Karlovitz etal made use of the wrinkled laminar flame model of Damkohler[66], but with augmentation which allowed for flame generated turbulence. Shcelkin[67] , using a similar model,but without the augmentation detailed above and different measured data,found no discernible discrepancy between measured and predicted flame speeds. He thus concluded that flame generated turbulence was negligible. In the early 1970's the existence of flame turbulence had been neither proved or disproved. It is interesting to note that this question has yet to be convincingly answered - as will be discussed when examining turbulence modelling.

To simulate a flow involving momentum, heat and mass transfer, the equations that represent the turbulent transfer of these properties have to be solved. In their most basic form these equations represent the instantaneous transfer of these properties. The momentum and energy equations are normally referred to the mixture and take the form:

$$\rho \frac{DU}{Dt} = -\nabla.P + F - \nabla.\left[\mu \nabla.U\right] \qquad (11.1$$

$$\rho \frac{Dh}{Dt} = \frac{DP}{Dt} + \frac{\partial Q}{\partial t} + \Phi_D + \nabla.\left[k \nabla.T\right] - \nabla.q_r \qquad (11.2$$

In the momentum equation F and P represent the body forces and pressure. In the energy equation Q, Φ_D, k and q_r represent the internal heat generation, mechanical dissipation, thermal conductivity and radiation heat flux. The mass transfer equations are applied to those reactants, products and inert gases, which the modeller estimates are important. The equation takes the form:

$$\rho \frac{Dc_i}{Dt} = \nabla \cdot \left[\rho D \nabla \cdot c_i \right] , \qquad (11.3$$

where c_i represent the concentration of species 'i' and D the coefficient of molecular diffusion.

These equations cannot be solved for the instantaneous properties, because the numerical manipulations required for a solution are beyond our capabilities. As an example of this point Schuman[68] and Gresho, Lee and Sani[69] have separately sought to compute some simple three-dimensional turbulence phenomena from the prescribed turbulent momentum equation. They have found the computing costs to be large and the results obtained poor, because of the disparities between the scale of typical eddies in the flow being simulated and the size of the domain that can be practically computed.

To overcome this problem these equations have been reduced in complexity by removing the time dependent terms. Two of the most popular ways of achieving this end are by replacing the transient properties U, h and c_i by their:

i) Mean time averaged and fluctuating components.

or ii) Favre averaged and transient components.

In its original form Favre[70] averaging means that the instantaneous velocity is weighed by the instantaneous density before time averaging. The momentum equations for a boundary flow that results from the two forms of averaging are presented below:

$$\bar{\rho}\tilde{U}\frac{\partial\tilde{U}}{\partial x} + \rho\tilde{V}\frac{\partial\tilde{U}}{\partial y} = \frac{\partial p}{\partial x} - \frac{\partial}{\partial y}\left(\widetilde{\bar{\rho}\overline{u''v''}}\right) \qquad (11.4$$

$$\bar{\rho}\bar{U}\frac{\partial\bar{U}}{\partial x} + \bar{\rho}\bar{V}\frac{\partial\bar{U}}{\partial y} = -\frac{\partial p}{\partial x} - \frac{\partial}{\partial y}\left(\bar{\rho}\overline{u'v'}\right)$$

The tildes designate Favre averaging and overbars mean time averaging. Each averaging procedure has it's own disadvantages and advantages. Mean time averaging is easy to apply and visualize; however, this approach does not allow density variations to be considered. Density variations have a direct effect on the turbulent fluxes; for example, the Reynolds stress $\overline{\rho u'v'}$ may be modified by the density having a large fluctuating component. Favre averaging takes into account density fluctuations, because the properties are weighed by the instantaneous and not averaged density. Flame generated turbulence, if it exists, can also be incorporated into this approach. Bilger[62] has discussed this issue and we shall return to it later. One disadvantage, which time will repair, is that modellers have little experience of using this approach.

Equations representing mass and energy transfer in a boundary flow can be derived by using time or Favre averaging. They take the form of:

$$\bar{\bar{\rho}}\bar{\bar{U}}\frac{\partial\bar{\bar{\phi}}}{\partial x} + \bar{\bar{\rho}}\,\bar{\bar{V}}\frac{\partial\bar{\bar{\phi}}}{\partial y} = \bar{\bar{J}} + \bar{\bar{s}}\,, \qquad (11.5$$

where the doublescore over properties means that they are either mean or Favre averaged. The general statistical property, ϕ, associated flux, J, and source terms, S, are defined in table one. In this table h_i^o and w_i represent the enthalpy of formation and rate of chemical reaction of species 'i'. The general equation 11.5 has been solved by computerized

Table One

General Property $(\bar{\bar{\phi}})$	Flux $(\bar{\bar{J}})$	Source $(\bar{\bar{s}})$
$\tilde{u}$	$\frac{\partial}{\partial y}\left(\overline{\bar{\rho}\ v''h''}\right)$	$-\frac{\partial p}{\partial x}$
$\hat{h}$	$\frac{\partial}{\partial y}\left(\overline{\rho\ v''h''}\right)$	$-\sum_{i=1}^{n} h_i^o\ c_i - q_R$
$\tilde{c}_i$	$\frac{\partial}{\partial y}\left(\overline{\rho\ u''c_i''}\right)$	$\bar{\rho}\left(\frac{\overline{\dot{w}_i}}{\rho}\right)$
$\bar{u}$	$\rho\ \overline{u'v'}$	$-\frac{\partial p}{\partial x}$
$\bar{h}$	$\overline{\rho\ v'h'}$	$\sum_{i=1}^{n} h_i^o c_i - q_R$
$\bar{c}_i$	$\overline{v'c_i'}$	$\dot{w}_i$

mathematical algorithms. The algorithms proposed up to mid 1970 have been discussed in chapter two; the more recent advances are summarized in section one.

The prescribed time and Favre averaged equations for the general property, ϕ, contain certain statistical terms involving correlations of the fluctuating components of the averaged properties. There is no direct way of knowing the magnitude of these terms. There has been an assumption, by many workers, that the fluctuating correlations obtained by using the Favre averaging model in the same way as the equivalent time averaged correlations. Although this is an excellent starting assumption it is not necessarily correct in all the flow situations. In a recent paper Bilger[62] has pointed out that the degenerate time averaged Reynolds stress, $\overline{\rho u'v'}$, is still only partially understood; but almost nothing is known of the equivalent Favre stress, because experimental devices capable of measuring it have only recently become available. For this reason we will limit our discussion to the fluctuating time averaged correlations. They are approximated, or modelled, in terms of the properties available in the flow modelling technique. Many authors, for example Spalding and Launder, have called these approximate procedures, turbulence models. In this thesis turbulence models by Cebeci[19,49] have been used to approximate the turbulent fluxes $\overline{\rho u'v'}$ and $\overline{\rho h'v'}$. In recent years turbulence models rated for use in a variety of complex flows, particularly flames, have been proposed. In section two the most successful of these models are detailed and discussed.

In the equation representing transport of a particular species (equation 11.5 with ϕ set to c_i) the source term contains w_i which represents the rate at which species 'i' is generated or destroyed by chemical reaction. No direct way exists of estimating this term, because time, one of the unknown properties, is required in the estimation. This term is normally modelled from known quantities with an Arrhenius type equation. The most significant advance in this field are presented in section three.

Radiation within the flow situation being simulated is allowed for in the averaged energy equation by the term q_R. This term can be extremely difficult to estimate, because the quantities that define radiation - the absorption and transmission properties of the boundaries encompassing the flow and the gases and suspended particles comprising the working fluid - are difficult to prescribe. The most suitable procedures for estimating the radiation are detailed and discussed in section four.

11.1 Modelling Techniques

There are a vast number of mathematical calculation procedures for solving the averaged differential equation for the general property 'Ø'. These calculation procedures are often called modelling techniques. A review of the older modelling technique has been presented in chapter two. As will be remembered from this chapter, most of the older modelling techniques used finite difference approximations to reduce the differential equation discussed above to a set of simultaneous algebraic equations. These were then solved by standard mathematical algorithms - for example a form of the Gauss elimination method[38] is often used. In recent years the basic concepts behind the use of finite difference approximations in published modelling techniques have been examined; the works of Roache[71], and more recently Leonard[72], being the most fundamental and thorough investigations. In sub-section a the finite difference based modelling techniques that are presently popular are detailed and discussed, and then the recent works that examine the errors associated with various finite difference approximations are summarized.

Finite element calculation procedures for simulating simple hydrodynamic and aerodynamic flow problems, have often been advanced over the last decade. The authors normally claim great accuracy as their chief reason for proposing such techniques. However, this claim remains unsubstantiated, because practical turbulent flows have not been thoroughly simulated with these techniques. Zienkiewicz[73], has argued that finite element methods will be increasingly used by

hydro & aerodynamicists because of their greater flexibility when simulating three dimensional flow situations. He cites as an example the science of structural mechanics, where modelling techniques based upon finite element methods, have almost totally replaced those that made use of finite difference approximations. A discussion of the various finite element methods used for simulating fluid flows is presented in sub-section b.

11.1a Finite Differences

There are a vast number of flow modelling techniques based upon the use of finite difference approximations. In part i those techniques which have proved most popular in industry are briefly discussed. As previously mentioned no discussion on finite difference based modelling technique would be complete without a review of the recent work dealing with the errors associated with the various finite difference approximations - this summary is presented in part ii.

i. Popular Modelling Techniques

The modelling techniques used in this thesis are based upon the technique proposed by Spalding and Patankar in references 7 and 46. These techniques solve the parobolic form of the time averaged equation for momentum conservation; which in von Mises co-ordinate system becomes:

(11.6

$$\frac{\partial U}{\partial x} = \frac{\partial}{\partial \psi} (\tau r) - \frac{1}{\rho U} \frac{dp}{dx}$$

In these techniques central differences are used to represent the convective and diffusive terms. This modelling technique

was originally heralded by some as a major advance.; however, this has not proved to be the case. The techniques major limitation is that it cannot simulate re-circulating flow situations, which means that it cannot be expanded to deal with general two dimensional flows contained by complex boundaries.

The modelling technique proposed by Gosman etal[74] , and since modified by many authors, has become one of the most popular techniques for simulating two-dimensional flows. All these techniques solve the elliptic form of the general differential equation, for a two dimensional flow, for the general property $\emptyset$. The version of this technique known as TEACH - see Gosman, Kahil and Whitelaw[75] - has been widely used in various scientific and industrial investigations. For example Whitelaw and Green[76] , Peck and Samuelson[77] and Wormeck and Pratt [78] have used this type of modelling technique to predict the turbulent flow patterns in furnaces and combustors.
In these predictions the finite difference approximations did not produce significant errors ; although it has often proved difficult to separate the errors from the finite difference approximations and the various turbulence models. In a study of isothermal flows in furnaces, with a two equation turbulence model, Whitelaw and Green[76] found discrepancies between predicted and measured results of the order of 25 percent in zones where re-circulation occurred , elsewhere the error was 5 percent. They further noted that to achieve this accuracy the positioning of grid nodes required a succession of calculations to identify very high pressure gradients and to ensure that they were resolved adequately within the limitation of the total number of grid nodes available.

Spalding and Patankar have proposed a series of modelling techniques for simulating three dimensional flow situations - as detailed in references 79, 80 and 81. These techniques only deal with a limited number of the many three dimensional flow situations that occur in engineering practice. The techniques simulate turbulent momentum, mass and heat transfer, in a manner similar to that used by Spalding and Patankar in their early works - see referencies 7 or 46.

The errors from these techniques are reasonable in certain specified flow situations. However, until these modelling techniques are tested in a far wider range of flow situations most engineers have reserved judgement as to their adequacy.

ii. Errors

Leonard[72] has discussed the errors associated with all the finite difference assumptions discussed above, and attempted to estimate the errors associated with the various terms in momentum conservation equation. He recommends third order differences for the advection terms:

$$\left[U\frac{\partial\phi}{\partial x}\right]_i = U_i\left[\frac{\phi_{i+1} - \phi_{i-1}}{2.\Delta x} - \frac{\phi_{i+1} - 3\phi_i + 3\phi_{i-1} - \phi_{i-1}}{6.\Delta x}\right] - \frac{1}{12}\phi^{IV}\Delta x^3 + HOT_1 \quad (11.7$$

or

$$\left[U\frac{\partial\phi}{\partial x}\right]_i = U_i\left[\frac{\phi_{i+1} - \phi_{i-1}}{2.\Delta x} - \frac{\phi_{i+2} - 3\phi_i + 3\phi_{i-1} - \phi_{i-1}}{6.\Delta x}\right] + \frac{1}{12}\phi^{IV}\Delta x^3 + HOT_2 \quad (11.8$$

and second order central differences for the remaining differential:

$$\left[\frac{\partial^2\phi}{\partial x_2}\right]_i = \left[\frac{\phi_{i+1} - 2\phi_i + \phi_{i-1}}{\Delta x^2}\right] + \frac{1}{12}.\phi^{IV}\Delta x^2 + HOT_3 \quad (11.9$$

The general property ϕ can represent either the main or cross-stream velocities, and HOT stands for the higher order term of the difference expansion.

Leonard has called these finite difference approximations consistent because they represent the exact polynomials of the same order - in this case three. These polynomials contain the velocity as the dependent variable and relative displacement as the independent variable. This recommendation is based upon the premise that consistent finite difference approximations of the polynomial of order "a", are more accurate than finite differences which are not consistent and have an order less than "a".

Other authors, for example Spalding - Patankar [7&46], Flugge-Lotz [22] and Cosman etal [74] have proposed and used modelling techniques which, in Leonards sense, do not use 'consistent' finite difference assumptions. Instead these authors have used differences with leading order error discretization terms of the same order. (The leading order discretization term is the term with the lowest order in the finite difference expansion after the removal of the finite difference relationship.) In the third and second order differences recommended by Leonard , the leading order discretization error terms are $\pm \frac{1}{12} \phi^{IV} (\Delta x)^3$ and $\frac{1}{12} \phi^{IV} (\Delta x)^2$ respectively. These leading order terms have errors of the order Δx^3 and Δx^2.

Neither of these approaches provide realistic estimates of the errors from the finite difference assumptions, when they are used in modelling techniques that simulate flows typically dealt with in engineering. Consistency only means that the finite difference assumptions in the flow modelling algorithm can exactly represent the same order polynomial in the general property $\emptyset$; if $\emptyset$ does not correspond to this, polynomial consistency provides no information. The alternative approach provides excellent information on the probable error from each finite difference approximation as the separation of the mesh lines approach zero. However as the purpose of the most modern modelling techniques is to have as large as possible separation of mesh lines, to reduce the amount of computational work required for a solution, this approach does not provide information of direct interest to the practising engineers.

The use of first order one sided finite differences to represent $\frac{\partial \emptyset}{\partial x}$ has always been extremely popular, because the modelling technique using this assumption seemed far more stable than those using the other types of first order differences - normally central differences. This phenomena was first noted by Courant, Issacson and Rees[82] - as detailed by Richlmyer[83]. Courant etal[84] have used one sided differences in a modelling technique which they used for simulating various supersonic flow situations.
In the momentum conservation equation, numbered 11.5, only the advection or convection terms, $U\frac{\partial U}{\partial x}$ and $V\frac{\partial U}{\partial y}$, contain first order differentials.

When using one-sided differences the term $(U\frac{\partial U}{\partial y})_i$ can be represented by:

$$\left[\frac{U\partial U}{\partial x}\right]_i = U_i\left\{\left[\frac{U_i - U_{i-1}}{\Delta x}\right] + \tfrac{1}{2}U_i''(\Delta x) + HOT\right\} \quad (11.12$$

or

$$\left[\frac{U\partial U}{\partial x}\right]_i = U_i\left\{\left[\frac{U_{i+1} - U_i}{\Delta x}\right] - +\tfrac{1}{2}U_i'' (\Delta x) + HOT\right\} \quad (11.14$$

Many authors have called the one-sided difference designated by equation-11.12 an upstream or upwind difference . When using central differences this term is represented by:

$$\left[\frac{U\partial U}{\partial x}\right] = U_i\left\{\left[\frac{U_{i+1} - U_{i-1}}{2\Delta x}\right] - \frac{1}{6}U_i'''(\Delta x)^2 + HOT\right\} \quad (11.15$$

Roache[71] , has presented a partial explanation why modelling techniques using one sided differences to represent the advection terms can be more stable than those making use of central differences. Leonard[72] , later provided a more complete explanation. This explanation is summarized here and comprises two parts. Firstly, the error term in both one-sided differences, represented by the leading order discretization error $\frac{U\bar{U}}{2}''(\Delta x)''$, is considerably greater than the error from the central difference-which is equivalent to $\frac{U_i U'''(\Delta x)^2}{6}$. In fact the leading order error term of the one-sided differences can be considered as a

diffusion term with an effective diffusion coefficient of $\pm \frac{U_i \Delta x}{2}$.

Secondly, on examining the error terms in equations 11.12 and 11.14 Leonard noted that this false diffusion term has a stabilizing effect in equation 11.12 when U is greater than zero, and in equation 11.14 when U is less than zero. This stabilization is the cause of the stability reported by Courant etal [84].

11.1b. Finite Element

Modelling techniques based upon finite element schemes can be applied to problems mathematically defined by either a set of differential equations or a mathematical principle. In both cases the modelling technique integrates the prescribed differential equation, or principle, over a specified domain.

Finite element methods have the ability to deal with domains that have complex shapes, because they can employ irregular mesh-networks and yet retain accuracy. Further, the generality of the mathematical procedures used to define finite element techniques enables them to deal with complex boundary conditions. This means that in many cases the finite element techniques can provide approximate solutions of the same order of accuracy as reputable finite difference techniques but use less computing power. It should be noted that regardless of the finite element technique used, accurate solutions of most viscous flow problems will require vast amounts of computer time and data storage.

The early finite element modelling techniques simulated the inviscid and slow viscous flow of fluids- examples of such techniques will be presented below. More recently techniques that are capable of solving the full two-dimensional turbulent Navier-Stokes equations have been proposed. The success obtained in this final area has been difficult to gauge, because the approximate nature of the turbulence models used in these techniques means that discrepancies in the predictions cannot be assigned solely to the numerical errors from the modelling technique. Examples of these techniques will be given later.

Most of the early finite element techniques dealt with subsonic flows, because the governing momentum equations are elliptic. The hyperbolic equations obtained with transonic and supersonic flows are far more difficult to solve. The differential equation governing isotropic, inviscid,steady,irrotational,compressible subsonic flow is:

$$\frac{1}{2}\left[\left(\frac{\partial \phi}{\partial x}\right)^2 + \left(\frac{\partial \phi}{\partial y}\right)^2 + \left(\frac{\partial \phi}{\partial z}\right)^2\right] + \frac{d}{d\rho}(\rho E) = 0 \quad , \qquad (11.16$$

where ϕ represents the velocity potential,

ρ the fluid density

and E the internal energy/unit mass.

The relationship between the internal energy and density is given by:

$$p = \rho^2 \frac{dE}{d\rho} \qquad (11.17$$

where p isthe pressure.

For a two-dimensional flow Gelder[85] produced one of the earliest finite element formulations in terms of the stream function, ψ.

Where from von Mises [86] :

$$U = \frac{1}{\rho}\frac{\partial \psi}{\partial y} \quad \text{and} \quad V = \frac{1}{\rho}\frac{\partial \psi}{\partial x} \qquad (11.18$$

Under these circumstances the continuity, combined momentum and energy equation of state, and associated functions become:

$$\nabla.\left[\frac{1}{\rho}.\nabla\psi\right] = 0 \qquad (11.19$$

$$\frac{\rho_o}{\rho} = \left\{1 + \left[\frac{k-1}{2c_o^2}\right].\frac{1}{\rho^2}.\nabla\psi.\nabla\psi\right\}^{\left(\frac{1}{k-1}\right)} \qquad (11.20$$

$$I(\psi) = \tfrac{1}{2}\int_{\Omega}\frac{1}{\rho}\nabla\psi.\nabla\psi\, d\Omega - \int_{S}\psi f\, dS \qquad (11.21$$

These equations form the basis of a convergent iterative scheme, with the associated function, 11.21, being used to derive element equations for the discretized solution domain. De Vries, Berard and Norrie[87] and Periaux[88] have separately produced similar finite element techniques using this type of procedure. Peraux used his model to simulate several flow situations which had a perfect gas as the working fluid. The two most interesting situations involved the flow of a gas through a two dimensional nozzle and around an aerofoil section. The results obtained were compared with exact theoretical, and some experimental, results and found to be extremely accurate.

More recently finite element techniques capable of solving the full Navier Stokes equations have been proposed. The earliest techniques solved the Navier-Stokes equations for an incompressible flow situation . These techniques are described below, because their simplicity allows the various solution techniques to be easily described. Thereafter the finite element solutions of the compressible Navier-Stokes equations in turbulent flow situations are discussed.

In a cartesian co-ordinate system the Navier-Stokes equation takes the form:

$$U\frac{\partial U}{\partial x} + V\frac{\partial U}{\partial y} = -\frac{1}{\rho}\frac{\partial P}{\partial x} + \frac{\mu}{\rho}\nabla^2 U \quad , \qquad (11.22$$

$$U\frac{\partial V}{\partial x} + V\frac{\partial V}{\partial y} = -\frac{1}{\rho}\frac{\partial P}{\partial y} + \frac{\mu}{\rho}\nabla^2 V \quad ; \qquad (11.23$$

with continuity represented by:

$$\frac{\partial U}{\partial x} + \frac{\partial V}{\partial y} = 0 \qquad (11.24$$

Three different finite element formulations have been used to solve this set of equations. These formulations take their names from the major properties used in defining the mesh network - and are commonly called stream function, stream and vorticity function and velocity and pressure formulations. At present there is insufficient data, concerning the accuracy of the finite element techniques using these formulations, to enable the best to be assessed.

The stream function formulation was first seriously considered by Olson [89]. The principle was obtained by combining the continuity and Navier-Stokes equation after applying von Mises stream function. The resultant principle takes the form:

$$\frac{\partial \psi}{\partial y} \nabla^2 \left(\frac{\partial \psi}{\partial x}\right) - \frac{\partial \psi}{\partial x} \nabla^2 \left(\frac{\partial \psi}{\partial y}\right) = \frac{\mu}{\rho} \nabla^4 \psi \qquad (11.25$$

No classical variational principle exists for this equation. Olson [89], recognized that if a pseudo variational principle could be found, it would provide a convenient procedure for deriving the element equations. Under certain circumstances such a pseudo-variational principle can be found. For example, consider a triangle element, of the type shown in figure 11.1, with boundary conditions along 1-2 such that:

$$\psi = \text{Constant or } \frac{\partial P}{\partial \xi} = 0 \qquad (11.26$$

and either:

$$\frac{\partial \psi}{\partial \eta} = 0 \text{ or } \mu \left(\frac{\partial U}{\partial \xi} + \frac{\partial V}{\partial \eta}\right) = 0 \qquad (11.27$$

(The symbols ξ & η represent the transformed co-ordinate system of the element-as shown in figure 11.1). The stream function satisfying equations 11-25 to .27 extremizes the function:

$$I(\psi) = \int_{\Omega} \left[\frac{1}{2}(\nabla^2\psi)^2 + \left(\frac{\partial \psi}{\partial \eta} \nabla^2 \psi\right) \frac{\partial \psi}{\partial \xi} - \left(\frac{\partial \psi}{\partial \xi} \nabla^2 \psi\right) \frac{\partial \psi}{\partial \eta}\right] d\xi\, d\eta \qquad (11.28$$

$$+ \int_{-b}^{a} \left[2\nu \frac{\partial^2 \psi}{\partial \xi^2} \frac{\partial \psi}{\partial \eta} - \left(\frac{\partial \psi}{\partial \xi} \frac{\partial^2 \psi}{\partial \xi^2} + \frac{\partial \psi}{\partial \eta} \frac{\partial^2 \psi}{\partial \eta^2}\right)\psi\right]_{\eta=1} \frac{\partial P}{\partial \xi} d\xi$$

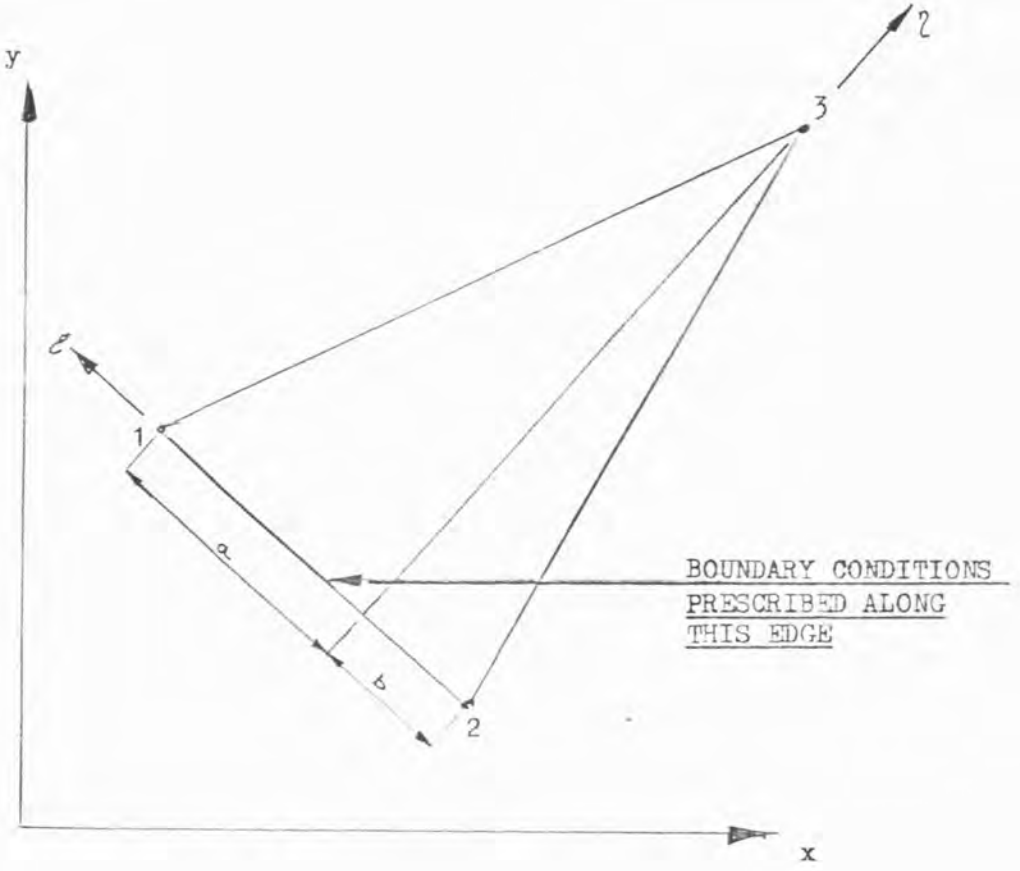

TRIANGULAR ELEMENT

FIGURE 11.1

which acts as the pseudo-variational principle. The summation of 'a' and 'b' equals the length of the boundary 1-2 in figure 11.7.The underscores designate the terms which are to be taken as invariants. Olson[89] has employed this technique with an eighteen degree of freedom triangular element with ψ, $\underline{\frac{\partial\psi}{\partial x}}$, $\underline{\frac{\partial\psi}{\partial y}}$, $\underline{\frac{\partial^2\psi}{\partial x^2}}$, $\underline{\frac{\partial^2\psi}{\partial x\partial y}}$ and $\underline{\frac{\partial^2\psi}{\partial y^2}}$ as nodal variables. The system equations obtained from this procedure were solved with the Newton-Rapheson iteration technique for non-linear matrices. Olson has checked the validity of this technique by solving several sample laminar flow situations - these included fully developed parallel, circulating square cavity and channel entrance flows. Olson summarizes his findings as follows; "the present method yields accuracies comparable to the finite difference method with an order of magnitude fewer equations. The computing process, derived from the described finite element method, consistently exhibits ultrafast convergence for all element grids. Furthermore, the actual finite element predictions of the various flow quantities also converge rapidly to correct results as the element grids are refined".

Instead of working with one fourth order partial differential equation, as Olson did; many works have chosen to use two coupled second order equations in the stream function, ψ, and vorticity, ω_v. Examples of such workers are Taylor and Hood[91], Baker[92 &94], Cheng[95] and Skiba etal[96]. The governing equations for the general transient case are:

$$\nabla^2 \psi = -\omega_v$$

$$\frac{\partial \omega_v}{\partial t} + \frac{\partial \psi}{\partial y}\frac{\partial \omega_v}{\partial x} - \frac{\partial \psi}{\partial x}\cdot\frac{\partial \omega_v}{\partial y} = \frac{\mu}{\rho}\nabla^2\omega_v \qquad (11.29$$

The pressure distribution can be calculated from the ω_v and ψ fields with:

$$\nabla^2 P = -2\rho\left[\frac{\partial U}{\partial y}\cdot\frac{\partial V}{\partial x} - \frac{\partial U}{\partial x}\cdot\frac{\partial V}{\partial y}\right] \qquad (11.30$$

Two types of finite element solution of equation 11.29 have been proposed. Taylor and Hood used the method of weighed residuals to obtain a solution; Baker[92 and 94], Cheng[95] and Skiba etal[96] made use of the pseudo-variational principle. (By pseudo-variational we mean that variational techniques are used but no classical variational principle is available). When weighed residuals have been used, a set of simultaneous equations which can be solved for the nodal values of ψ and ω_v are obtained. The pseudo-variational formulation

used by Cheng is extremely versatile and widely applicable. Cheng[95] has demonstrated the adequacy of this method by simulating several flow situations. The most interesting situation is the flow of a fluid through a two dimensional channel containing a venturi section. The results from laminar flow were satisfactory and the finite element technique was stable and convergent at high Reynolds numbers.

Taylor and Hood[91] and Yamuda, Ito, Yorkouchi, Lamani and Ohtsubo[97] have used the velocity and pressure formulation. The approach followed by both sets of authors relies upon the Galerkin method - for a detailed descripion of this method see reference 98. The Gelerkin method reduces the equation governing the fluids motion to:

$$- \int_{\Omega} N \left[U \frac{\partial U}{\partial x} + V \frac{\partial U}{\partial y} + \frac{1}{\rho} \frac{\partial P}{\partial x} - \frac{\mu}{\rho} \nabla^2 U \right] d\Omega = 0 \qquad (11.31$$

$$- \int_{\Omega} N \left[U \frac{\partial V}{\partial x} + U \frac{\partial U}{\partial y} + \frac{1}{\rho} \frac{\partial P}{\partial y} - \frac{\mu}{\rho} \nabla^2 V \right] d\Omega = 0 \qquad (11.32$$

$$\int_{\Omega} N \left[\frac{\partial U}{\partial x} + \frac{\partial V}{\partial y} \right] d\Omega = 0 \qquad (11.33$$

In these equations N designates the iteration number and Ω represents the domain area. In these equations a solution is obtained by integrating, by parts, all the terms not directly involving U and V. Taylor and Hood[91], have used this finite element formulation for simulating several flow situations, and found the results to be reasonably accurate.

They cite the following reasons for using this type of formulation:

i) The method can easily be extended to deal with three dimensional flow situations.

ii) Pressure, velocity, velocity gradient and stress boundary conditions can be directly incorporated into the finite element method.

iii) Free surface problems are tractable.

iv) Experience has shown that techniques using this formulation run faster than those previously described.

The three aforementioned finite element methods have been extensively modified to deal with free surfaces, compressibility effects and turbulence. For example, the pressure velocity formulation of Taylor and Hood[91] has been modified, on several separate occasions, to accommodate these changes. Chang and Finlayson[99] modified the technique to give it the capability of dealing with free surfaces and also added the visco elastic terms. The latest version of this technique, and the equivalent computer coding , is often known by the name "Fluid"; and has been fully detailed by Chang, Patten, Adams and Finlayson[100]. Chang etal[100] have examined results from this technique when it has been used to simulate several flow situations. The results obtained were sufficiently accurate for most engineering purposes. Baker and Soliman[101] have made use of the Galerkin weighed

residual method to produce a finite element solution of the Navier-Stokes equation. Baker[102] has used this technique to simulate several turbulent boundary layer flows. The turbulent viscosity was obtained with the aid of van Driest's turbulence model-with the experimental derived closure constants taking the values prescribed by van Driest. Baker reports that the results obtained were sufficiently close to published experimental data for most engineering applications. Further, the absolute error from the technique,with the finest discretization, was significantly larger than the error expected from the finite element method alone. The authors interpreted this as an indication of the accuracy limit of practically useful discretization. Beyond this limit other sources tended to obliterate the refined solution theoretically attainable from discretization refinement.

11.2 Turbulence Models

Turbulence models are used to estimate the terms containing fluctuating components of the density, velocities, concentrations and enthalpy in the averaged equation of motion 11.5.

The preponderance of work in this area has been concerned with estimating the term $\rho\overline{u'v'}$ and more recently $\rho\overline{h'v'}$. The first turbulence hypothesis was postulated by Boussinesq[103] and assumed that:

$$\rho\overline{u'v'} = \mu_t \frac{\partial U}{\partial y} \qquad (11.34$$

The quantity μ_t is called the turbulent viscosity. This quantity is analogous to the molecular viscosity, μ_l ; the former being dependent on the situation being examined, whereas the latter is a property of the fluid. Boussinesq's hypothesis cannot be used as part of a model for the turbulent viscosity, because no known or calculablequantities occur in it.

Prandtl[1,12], 1925, made the next major contribution by employing the algebraic relationship:

$$\mu_t = \rho l_m^2 \left| \frac{\partial U}{\partial y} \right| \qquad (11.35$$

This equation has become known as the mixing length hypothesis, with I_m defined as the mixing length. The mixing length must be prescribed algebraically with the aid of experimental evidence. For nearly two dimensional boundary layer air flows at room temperature, with insignificant pressure gradients, the mixing

length provides results that are only now being surpassed by more recent turbulence models. Prandtl's 1925 turbulence model, and others making use of similar hypotheses, have not been successful for other two dimensional, and nearly all three dimensional flows. For example, in plane wall jets various authors, particularly Pai and Whitelaw[104], have shown that turbulence models using the mixing length hypothesis unrealistically predict small or zero turbulent viscosity in regions where $\frac{\partial U}{\partial y}$ is near or equal to zero. This lack of success prompted many practical engineers to propose algebraic formulae for the turbulent viscosity. These involve velocity, U_e, and length y_e, scales of the mean motion, and a term referring to the position in the shear flow "$f(\frac{y}{\delta})$". Representing these relationships in a general manner:

$$u_t = f_1 \left[\rho, U_e, y_e, f(\frac{y}{\delta}) \right] \qquad (11.36$$

One such example is the following algebraic formulation used by Gosman etal[74]:

$$\mu_t = KD^{2/3} L^{-1/3} p^{2/3} (mU^2)^{1/3} \qquad (11.37$$

This formula was specifically designed to estimate turbulent viscosity in axi-symmetric furnaces. The term D and L represent the diameter and length of the right circular combustion chamber, mU^2 denotes the inlet kinetic energy

and K is an empirical coefficient - which from reference 28 is equal to 0.012. Turbulence models of this type normally have a narrow range of applicability, because their original purpose was to solve specific engineering problems. For example Peck etal[77], when simulating bulk mixed combustion of methane in a furnace with a modelling technique after Cosman etal[74], compared predictions when using the abovementioned algebraic turbulence equation and Jones and Launder's[105] two equations turbulence model. They found that the most accurate predictions were obtained when the algebraic equation was used. Spalding, one of the originators of this turbulence equation, has pointed out in his comments on this publication that this equation was not formulated or intended for general use.

In Prandtl's[24] second turbulence model the turbulent viscosity is determined by the solution of a differential equation in which the turbulent kinetic energy k is the independent property. Typically this equation takes the form:

$$\rho \frac{Dk}{Dt} = \frac{\partial}{\partial y}\left[\frac{\mu_t}{\sigma_k} \cdot \frac{\partial k}{\partial y}\right] + \mu_t \frac{\partial U}{\partial y} - \frac{C_D \rho k^{3/2}}{l} \quad , \quad (11.38$$

where C_D and σ_k are constants. The turbulent viscosity being determined with:

$$\mu_t = \rho l \sqrt{k} \quad . \quad (11.39$$

The length scale l has to be described algebraically, and value prescribed for the constants which factor the dissipative

and productive terms in the kinetic energy equation. Measurements of the mean-velocity distribution near a wall were originally used to decide length scale distribution. For example Wieghardt, in the appendix of Prandtl's 1925 paper, used Nikuradse's[31] data to prescribe the mixing length l. This type of model has a far wider range of applicability than those previously described, because it is founded on a greater degree of scientific information.

The elegance of this model prompted other investigators to refine and enhance Prandtl's work. Most notable are the models proposed by Nee and Kovasnay[27] and Bradshaw, Ferris and Atwell[106]. The model by Nee etal involves the solution of a differential equation in which the independent variable is the turbulent kinematic viscosity, represented by $\frac{\mu_t}{l}$. This approach is no more direct than that proposed by Prandtl, because the length scale of turbulent motion is still required before a solution can be sought. The model by Bradshaw etal does not use the concept of turbulent viscosity, but instead derives the turbulent energy equation by assuming that the kinematic shear stress is directly proportional to the turbulence energy. Models of this type, which involve one differential equation, have become known as one or single equation models of turbulence.

The one-equation turbulence models are nearly as limited in their range of applications as those based upon the mixing length hypothesis. The original Prandtl formulation is regarded by many as the best of the one equation models. Launder and Spalding[28] have detailed how the Nee-Kovasanay model is no more general and certainly not as widely tested as Prandtl's. Ng and Spalding[107], and Sivasegaram and Whitelaw[108] have shown that there is little to choose in the way of accuracy, between predictions obtained with Bradshaw etal's model[106] and Prandtl's original mixing length hypothesis.

Kolmogroff[25] was the first to propose a two-equation model for turbulence. Like Prandtl[24], whose paper was published a few years later, Kolmogroff proposed that the character of turbulence be presented by two properties. He chose the turbulent energy, k, and the characteristic frequency of the energy containing eddies, f, such that:

$$\mu_t = \frac{\rho k}{f} \qquad (11.40$$

However, unlike Prandtl, Kolmogroff proposed that both these properties be determined from differential transport equations. At the time of publication there were no electronic computational aids capable of dealing with the calculation procedures involved in solving these differential equations. This resulted in the model fading into obscurity, until the above mentioned dissatisfaction with the various mixing length and one-equations turbulence models, caused it to be re-examined.

Kolmogroff's two equation model appeared to circumvent many of the problems of the previously mentioned models, by prescribing the form of the length scale with a scientifically derived differential equation. However, the model was not satisfactory, because the form of frequency equation used was not adequate. Rotta[109] commented upon this failing, and attempted to circumvent it by using the length scale as the dependent variable in the second transport equation. However, this procedure has not proved popular, because the length scale does not diffuse at a rate proportional to $\frac{\partial l}{\partial y}$. Regarding this limitation both Rotta[110] and Spalding etal[111] have separately used the product of 'k' and 'l' as the dependent variable in the second transport equation. Other authors have used different terms for their independent variables in the transport equations. For example, Chou[112], Jones and Launder[113] used $\frac{k^{3/2}}{l}$ and ε_L, and Spalding[114] proposed $\frac{k}{l^2}$ and W_L. In this context ε_L represents the turbulence energy dissapation rate and W_L the square of the frequency of the energy containing eddies. Comparison of the predictions from these models have been attempted - see for example Spalding-Launder[28] and Ng and Spalding[107]. However, the uncertainty of the experimental evidence and wide range of situations examined makes it impossible to assess which model is the best. What has emerged from these studies is that the two equation models are far more universal than those previously discussed, and can be modified to give extremely accurate results in particular flow situations.

Multi-equation turbulence models have been proposed and used in specific flow situations. These models predict the various stresses of the flow and not the turbulent viscosity, μ_t, which is after all proportional to a particular stress. As their name implies these models involve the solution of more than two differential equations to predict the various stresses. For example, Hanjalić[115] proposed a model comprising a transport equation for sheer stresses by assumingthe normal stresses proportional to the turbulent energy. Harlow etal[116] used transport equations for the normal and shear stresses and an equation for the length scale. At present these models have not been fully developed and tested.

Two equation models of turbulence are presently the most popular of those discussed above. As detailed, they have proved adequate when simulating a wide range of aerodynamic, and some complex flows. However, the variety of flow situations over which these models have been rigorously tested is not sufficient to categorically state that they are always the best model to use.

None of the described turbulence models are capable of dealing with flame generated turbulence, because they are based upon time averaged equations. To deal with this phenomena the turbulent energy equation must be re-derived using Favre averaging, and the various constants and length scales required for closure estimated from new experimental evidence. Flame generated turbulence,

if it exists, will primarily alter the structure of a flow through terms in the Favre form of the turbulent kinetic energy equation:

$$\bar{\rho}\tilde{u}\frac{\partial}{\partial x}\left(\tfrac{1}{2}q^2\right)+\bar{\rho}\tilde{v}\frac{\partial}{\partial r}\left(\tfrac{1}{2}q^2\right)=-\widetilde{\bar{\rho}u''v''}\frac{\partial\tilde{u}}{\partial r}-\bar{\rho}.\widetilde{\frac{v''}{\rho}\frac{\partial p}{\partial r}} \qquad (11.41$$

$$-\frac{1}{r}\frac{\partial}{\partial r}\left\{\tfrac{1}{2}\,r\widetilde{\bar{\rho}v''(u''^2+v''^2+w''^2)}\right\}$$

A tilde over a property means that it has been subject to a Favre averaging. Bilger[62], suspects that turbulence can be generated by flows involving pressure fluctuations - for example flames. (The author also inclines to this view, however, until further experimental evidence on this subject is published the existence of flame generated turbulence cannot be proved.) Bilger's argument for the generation of flame turbulence by pressure fluctuations is as follows. The pressure-velocity correlation from the Favre form of the turbulent kinetic energy equation takes the form:

$$-u''_k\frac{\partial\bar{p}}{\partial x_k}-\frac{\partial}{\partial x_k}\left(\overline{pu''_k}\right)+\overline{p'\rho\frac{D\left(\frac{1}{\rho}\right)}{Dt}}-\rho_h g_k u''_k \qquad (11.42$$

when buoyancy effects have been included. In this expression p is relative to the hydrostatic pressure p_h - where $\frac{\partial p}{\partial x_k}=\rho_h g_k$.

The density ρ_h is a space and temporal mean of the density at x_k. The symbols u_k and g_k represent the fluctuating velocity and gravity components in the direction k. The third term is the only one containing pressure fluctuations. In uniform density flows this term will be zero, in non-uniform density flows the third term will contribute to the turbulent kinetic energy whenever it has a net correlation. Bilger suspects that turbulence can be generated through this term, by the interaction of pressure fluctuations on a volume increase which has directionality associated with it - such as in a flame.

The various models for the turbulent Prandtl number are far less sophisticated than those for turbulent viscosity. These models all introduce simplifying assumptions and make use of experimental evidence to obtain closure. Cebeci[19,49] provides an excellent review of the models available before the mid-seventies. Dreisler,[117] has produced a model based upon a variation of Prandtl's mixing length hypothesis, with experimental evidence allowed for in various correlation coefficients. The model provides adequate results in predicting heat transfer in flows where the Prandtl number is small - as detailed by Simpson, Whitten and Moffat[118]. Cebeci's[49] model for

the turbulent Prandtl number, which is used extensively in this thesis, is based upon considerations of Stokes flow. The algebraic expressions for the turbulent Prandtl number being obtained by modelling the viscous sub-layer as a Stokes type flow in the manner of Van Driest[2]. Cebeci[49], has shown that for engineering purposes, these expressions accurately predict the turbulent Prandtl number in a variety of boundary flows with measured high and low Prandtl numbers.

Authors making use of single or multi-equation models of turbulence have tended to use single equation models for the correlation $\rho \overline{v \cdot h'}$ of the form:

$$\bar{\rho}\,\overline{v'h'} = -\frac{\mu_{eff}}{\sigma}\left[\frac{\partial h}{\partial x} + \frac{\partial h}{\partial y}\right]$$

where σ is prescribed by reference to suitable experimental evidence.

Wormeck and Pratt[78], Spalding etal[7,46] and Cannon etal[162] have published results which show the adequacy of this type of model.

The turbulent Schmidt number, represented by the correlation $\overline{\rho'u'c'}$, is normally assumed to conform to a simple algebraic formula. This approach has been adopted because the experimental tools necessary to understand this correlation are not presently available. The algebraic formulas used by various modellers are obtained from experimental evidence concerning the variation of the turbulent Schmidt number in specific flow situations.

.3 Combustion Models

The final goal of those who propose and test combustion models is that they can be used by practical engineers to accurately predict the reaction rates of specified fuels and oxidants . By predictive, they mean that the models can be used in both an interpolative and extrapolative sense with respect to the experimental evidence on which they are based. Regardless of the apparent sophistication of some combustion models it is important to remember they are only approximate prediction techniques. The reason for this is that the models being presently constructed work on the basis that they reproduce observed phenomena, which are not all encompassing. Some of these approximate models produce adequate results in particular flow situations, and will be discussed below, but at present there is no single all encompassing combustion model.

In flames in which the fuel and oxidant are premixed before combustion,sometimes called premixed flames, the rate at which reaction proceeds is substantially controlled by the gross reaction rate - as substantiated by among many Beér etal [63]. In dealing with such flows the fuel-mass fraction is normally regarded as representative of the gross reaction rate. The resulting reaction rate in the conservation equation for the fuel was originally determined with an equation of the form specified by Arrhenius. Combustion models of this type are often called global reaction models.

Arrhenius's interpretation of a single step reaction takes the form:

$$k = A \exp\left(\frac{-E}{RT}\right) \qquad (11.43$$

Where k is the reaction rate, A a constant and E the activation energy-often defined as the excess energy of the molecules taking part in the reaction. More recently the reaction rate has been prescribed with models that attempt to account for turbulence through statistical modelling of certain scalars. (These models will be fully discussed later in this text.)

In flames where the fuel and oxidant are not mixed before ignition, the combustion process can be controlled by either the reaction rate, as above, or the rate at which diffusion between the fuel and oxidant occurs. In boundary flows in which the turbulence levels are low, and adverse pressure gradients do not occur, it has been found that diffusion, or mixing, is normally the limiting parameter - as detailed by Hinze[121]. In these types of flow many investigators have considered the reaction rate to be infinitely fast, since this allows for the assumption that the time taken for mixing is greater than that for reaction. Under these circumstances the parameters controlling the reaction are the same as those that define the mixing process. One such parameter, used by Spalding - Patankar[7,46] and Gosman etal[74], is the

mixture fraction.The relation between the reaction process and the mixture fraction has been examined through a variable - often called 'f' - which has been defined by:

$$f = r.\ Y_{fu} - Y_{ox} \quad , \qquad (11.44$$

where Y represents the mass fraction, r the stoichiometric mass ratio, and the sub-scripts fu and ox designate fuel and oxidant respectively. The conservation equation for 'f' has no source term and further the identity:

$$Y_f = \frac{f - f_{ox}}{f_{fu} - f_{ox}} \qquad (11.45$$

holds with Y_f equalling 1 in the fuel and zero in the oxidant phase. Three models have been used to describe the reaction process between fuel and oxidant - they are called the frozen, equilibrium and partial-equilibrium composition models.

In the frozen composition model it has been assumed that the infinitely fast reaction is restricted to an infinitely small reaction zone situated on a surface where Y_f has it's stoichiometic valve, Y_{fst}. Outside this zone the reaction is assumed quenched. Under these conditions:

$$Y_f = 0 \text{ for } Y_f < Y_{fst} \text{ and } Y_{ox} = 0 \text{ for } Y_f > Y_{fst};$$

the respective values of Y_{ox} and Y_{fu} are found from equations 11.44 and .45.

In the equilibrium composition model infinitely fast reactions, occurring in both the forward and reverse directions, are allowed throughout the flow field. This results in a local equilibrium composition which is governed by the local mixture fraction and enthalpy,h. Von Duyvenvoorden[122] has proposed a model of this type for methane combustion. In it two dimensional mapping of the relevant thermodynamics and chemical properties has been achieved with a double Chebyshev polynomial of the type:

$$Y_i \quad (h, Y_{f_u}) = \sum_{i=1}^{I} \sum_{j=1}^{J} a_{ij} \hat{T}_i(h^*) \hat{T}_j(Y_{f_u}^*), \qquad (11.46$$

where h^* and Y_f^* are normalized values of h and Y_{fu}, and $\hat{T}_k$ denotes a Chebyshev polynomial of degree k. Solution of this equation allows the equilibrium conditions to be calculated over the flow.

In the partial- equilibrium composition model it is assumed that in the fuel rich region the oxidant does not completely react. The non-reacting species concentrations and their temperature are calculated with the aid of the equilibrium composition model - with the prescribed constraint on the oxidant. This model takes account of the reported results of Van Duyvenvoorden[122] in a methane diffusion flame. In this flow the fuel was consumed in the flame front, but not all the oxidant, because of the short residence time of each parcel of gas in the flame. Beyond

the flame further reaction with the oxygen was suppressed and a frozen composition with finite oxygen concentration found. Balau[123] has pointed out that in hydrocarbon flames this assumption is reasonably correct. For after the fuel rich region, the oxygen can only react to give radials OH, H and O which immediately recombine to quench the reaction.

In the above mentioned combustion models the effects of the fluctuating scalars on the combustion rate has been neglected. Evidence showing that the effect of these scalars is negligible has not been forthcoming, and consequently in recent years attempts been made to include these turbulence effects into the combustion models.

The Arrhenius rate equation, 11.43, which has been used to estimate the reaction rate in premixed flames is not really appropriate when the flow is turbulent, because when this equation is decomposed into mean and fluctuating scalar properties large and unknown fluctuating correlations remain. Decomposition of the scalar properties in the Arrhenius equation results in the following relationship:

$$k = \nu_i W_j^{-1} \rho^{-2} \bar{Y}_i \bar{Y}_j A \exp\left[\frac{-E}{R\bar{T}}\right]$$

$$\left[1 + \frac{\overline{\rho'^2}}{\bar{\rho}^2} + \frac{\overline{Y_i' Y_j'}}{\bar{Y}_i \bar{Y}_j} + \frac{\overline{2\rho' Y_i'}}{\overline{\rho Y_j}} + \frac{E}{RT} \right. \tag{11.47}$$

$$\left. \left\{ \frac{\overline{Y_t' T'}}{\bar{Y}_i \bar{T}} + \frac{\overline{Y_j' T'}}{\bar{Y}_j \bar{T}} + \left[\frac{E}{2R\bar{T}} - 1 \right] \frac{\overline{\bar{T}^{12}}}{\bar{T}^2} \right\} - \right]$$

where the fluctuating correlation terms contained within the square bracket are unknown. Equations can be derived for the double correlations $\overline{Y_j' Y_j'}$ $\overline{Y_i' T'}$ etc., in terms of higher order correlations, but then the number of variables increase and the normal closure problem arises. Donaldson[124] and Donaldson & Varma[125] have published the theoretical background of this analysis.

Many combustion models have been proposed that attempt to take into account the fluctuating motion of turbulent flames. For example, Libby[167], Bray and Moss[120], Lockwood and Naguib[127] and Spalding[128], have all produced combustion models that are applicable to premixed flows involving two reactants and one product. These models can be sub-divided into two categories. In the first category the interaction of turbulence and the fluctuations of the important scalars are represented by balance equations for the kinetic energy of turbulence and for the mean fluctuations of the reaction progress. The reaction progress being defined as the normalized mass fraction of the product. Normalization being used to make the reaction progress equal to one when combustion is complete. Fluctuations in the rate of reaction are incorporated through the introduction of a probability distribution function of the progressing variable. The models proposed by O'Brian and Libby use this approach, with the probability distribution function

derived from a suitably set up balance equation. However, Bray and Moss chose to specify the probability distribution function in their combustion model empirically, because of the simplicity of the resulting model. In the second type of model the reaction rate is related to the flow pattern by some hypothetical reasoning and a series of assumptions. Spalding[119] has proposed and tested a model of this type. Briefly, the model comprises an expression for the time averaged reaction rate for a flow with two reactant and one product, and allows for a uniform or non-uniform air-fuel ratio. The expression is derived with the concept that the flow contains "parcels" of coherent gas, which are subjected to a stretching process, while reaction and small scale mixing take place. Jones and McGuirk[129] have used this model with the modelling technique proposed by Gosman et al[74], to simulate the flow field within a gas turbine combustion chamber. They found the model capable of accurately predicting the gross fuel-oxidant levels, but not sufficiently refined for assessing the pollutant, primarily Carbon Monoxide levels. The use of a finite-rate reaction model for representing the oxidation of Carbon-Monoxide to Carbon-Dioxide was recommended.

A model capable of dealing with finite chemical reaction rates has been proposed and partially validated by Varma, Sandri and Donaldson[130]. This model has the ability to deal with any type of fuel and oxidant reaction, and thus represents a considerable advance over the combustion models for premixed and unmixed flames. A series of Delta functions are used to model the probability distribution function, or pdf, of all the scalars in a turbulent reacting flow. Kewley[131] and Varma etal[130] have separately made some limited use of this model. Kewley found that, for most forms of pdf, reasonable predictions of the reaction rates can be obtained in simple flows. Jones, at the Agard Conference (numbered 275) on Combustion Modelling, suggested that predictions with this type of model could be far more influenced by the choice of pdf than Kewley's results indicated. This effect, Jones suggested, would be caused by the influence of temperature on the probability distribution functions.

The prediction of pollutant levels has received considerable attention because of the noxious effect of many pollutants. For example, the predictions Carbon Monoxide and Nitrous Oxide levels from Hydrocarbon fuels is of considerable importance to the combustion engineer.

One of the earliest models for predicting pollutant levels, and recently used by Dryer and Westbrook[132], is a modification of the global model. The fuels and pollutants are assumed to react at rates given by the Arrhenius equation. This model is best explained in an illustrative case. Consider the post-induction phase, with lean oxidation, of Methane at atmospheric pressure in an enclosed flow reactor. Assume that we are concerned with the amount of Carbon Monoxide produced. For this type of oxidation Dryer and Glassman[133] recommend a two-step global model. In the first step they allow the fuel to react to the pollutant, Carbon Monoxide:

$$CH_4 + \frac{3}{2} O_2 \longrightarrow CO + 2H_2O \qquad (11.48$$

and in the second step:

$$CO + \frac{1}{2} O_2 \longrightarrow CO_2 \qquad (11.49$$

The rates of these two reactions being derived from the following "Arrhenius" type"equations:

$$\frac{-d(CH_4)}{dt} = 10^{13.2} \exp\left(\frac{-48000}{RT}\right) \cdot (CH_4)^{0.7}(O_2)^{0.8} \text{ mole/cm}^3\text{s} \qquad (11.50$$

$$\frac{d(CO_2)}{dt} = 10^{14.75} \exp\left(\frac{-43000}{RT}\right) (CO)^{1.0}(H_2O)^{0.5}(O_2)^{0.25} \qquad (11.51$$

Cohen, Dryer and Glassman[134], have shown that with many hydro-carbon fuels unrealistic results can be obtained with global combustion models of the above type. This is because the reduction of the hydrocarbon fuel directly to Carbon Monoxide and Hydrogan based products is experimentally unrealistic taking no account of the reactions to hydro-carbon intermediaries. The rates at which these intermediate reactions

occur are often dependent upon the initial concentration of fuel and oxidant, and affect the amount of pollutant produced.

Edelman and Harsha[135], in a review of laminar and turbulent gas dynamics in combustion, have defined a slightly more complex form of the global combustion model which takes account of Cohen's etal's[134] objection. This is called the "quasi-global reaction model". In this model, the oxidation of a hydro-carbon fuel to Carbon Monoxide and Hydrogen is represented by several single step global reactions. The effects of further oxidation can, if required, be considered in detail-that is as a series of sequential or parallel, uni or bi-molecular reactions. Edelman, Turan, Harsha and Wong[138] have used this type of model to predict the property flow patterns in a jet stirred Longwell-Weiss reactor - as defined in reference 136. The reactions allowed for are:

i) pyrolysis C_nH_m ^{BN} + M $\longrightarrow$ $C_xH_{..}$ + M + BN (11.52

ii) partial oxidation $C_nH_m + O_2 \longrightarrow CO + H_2$ (11.53

$C_xH_y + O_2 \quad CO + H_2$

iii) soot formation $C_nH_m \longrightarrow C_{(s)} + H_2$ (11.54

$C_xH_y \longrightarrow C_{(s)} + H_2$ (11.55

& iv) soot oxidation $C_{(S)} + O_2 \longrightarrow CO + CO_2$ (11.56

The symbol BN represents bound nitrogen and M the third body. The subscripts n,m,x and y designate the type of hydro-carbon fuel and "s" shows that the carbon being considered is in the form of soot. The bound nitrogen can oxidize to nitrous oxide under certain conditions, and this reaction will be discussed later. Edelman etal[138] have described the reaction rates at which H_2, CO and BN were converted into H_2O, CO_2 and NO_x with Arrhenius type relationships. The constants in these relationships being defined from the published data of Edelman etal[135] and Lee, Thring and Beér[137]. Edelman etal[138] have reported some success with this type of model in a well stirred reactor. However, other authors, for example Dryer and Westbrook[132], have pointed out that this approach has not been fully tested.

The production of nitrous oxide, NO, has received considerable attention in recent years, primarily because of the increasing severity of pollution laws in the United States. This type of reaction is normally considered as an adjunct to the partial oxidation of the hydrocarbon fuel in the quasi-global model. It is normally assumed that the Nitro-oxide is formed by a high temperature reaction between N_2 and O_2. This type of reaction is sometimes referred to as "thermal nitrous oxide formation".

The rate of generation of NO is usually based upon the Zeldovitch[161] mechanism, with the reactant rate given by:

$$\dot{w}'_{NC}(Y_f) = 2k_z p \frac{Y_{N2}(Y_f)}{M_N} \cdot \frac{Y_0(Y_f)}{M_0} \cdot \exp\left(\frac{-E_z}{T(Y_f)}\right) \qquad (11.57$$

with $k_z = 10^{11.15}$ and $E_z = 3.75 \times 10^4$ from from Van Duyvenvoorden[122]. The symbols M_{N_2} and M_0 represent the molecular weight of nitrogen and oxygen. Paauw, Stroo and van Koppen[139] have used a Nitrous Oxide model of this type. They calculated the property patterns in natural gas diffusion flames, using the frozen, equilibrium and partial equilibrium composition models (detailed above) plus the above mentioned NO formation model. They found that the calculated values of NO were always less than measured values. When the equilibrium model was used to simulate the reactants of the combustion process, the estimates for Nitrous Oxide were particularly poor. This result Paauw etal attribute to the fact that either "super equilibrium oxygen" or "prompt nitrous oxide" played a substantial role in the reactions. (Paauw defines "super equilibrium oxygen"as oxygen in a fuel rich region that does not react. This phenomena occurs when the residence time of the oxidant in the flame front is so short that it does not have time to fully react).

11.4 Radiation

The basis of any model for predicting radiative heat exchange between gases is the radiant energy transfer equation:

$$(n.\Delta)I_{\omega'} = -(k'_{\omega' a}p + k'_{\omega' s}p)I_{\omega'} + k'_{\omega' a}pI_{b,\omega'} + k'_{\omega' s}p\int_0^{4\pi} I(\beta)\, d\beta \qquad (11.58)$$

This equation represents a balance of the monochromatic radiant energy transfer through a small volume of an emitting, absorbing and scattering medium. In this equation the second term represents the reduction in intensity caused by either absorption or scattering within the elemental volume. The third and fourth terms represent the increase in intensity due to emission from, and scattering into, the volume.

Obviously, the direct application of the radiant energy equation to a flow situation is impractical, for the following reasons. Firstly, an infinite amount of computing power would be required to solve equation 11.58, because in the form that it is cast the flow situation being simulated must be divided into an infinite number of elemental volumes. Secondly, the specific spectral coefficients, represented by 'k'', used in assessing emission, absorption and reflection cannot be precisely defined.

A practical radiation model must comprise two parts. In the first part, the radiative properties that define the absorption and emission characteristics of the species present, at the prevailing temperatures, are prescribed. In the second part the radiant energy exchange between the various areas of the flow situation being simulated are evaluated. (The data from the first part of the model is used as input into the second). In sub-section 'a' the procedures for prescribing the radiative properties are described. In sub-section 'b' the models for evaluating radiative energy exchange are defined and discussed.

11.4a Radiative Properties

The definition of the radiative characteristics of a particular flow situation is a necessary prelude to using any radiation model. These characteristics are used with certain of the scalar properties of the flow situation to describe the absorptivity, and emissivity of both the gases comprising the working fluid and the surface of the container that constrains the flow.

The dominant radiative processes in most engineering applications are absorption and emission. In fact most workers assume that scattering is negligible. Under these circumstances the absorptivity, α_g, and emissivity, ϵ_g, are related by:

$$\alpha_g + \epsilon_g = 1. \qquad (11.59$$

Thus the problem of defining the radiative characteristics reduces to defining the emissivity, ϵ_g.

Gases can emit and absorb radiation in two ways. In the first, radiation is emitted and absorbed over the complete spectrum - such gases are called grey. In the second, radiation is emitted and absorbed only in discrete bands of the spectrum - such gases are often referred to as "real." For a grey gas the emissivity, ϵ_g, is defined by:

$$\epsilon_g = 1 - \exp(-k'pL), \qquad (11.60$$

where k' represents the specific absorption coefficient, p the partial pressure of the gas and L the pathlength of the radiation.

The absorption coefficient, k', can be represented by the sum over the spectrum of the specific absorption coefficients, K'_ω, at the wavenumber ω'. This coefficient, about the line wavenumber ω, can be calculated for a broadened line with:

$$k'_\omega = \frac{s}{\pi}\left[\frac{b_c}{(\omega' - \omega'_o)^2 + b_c^2}\right] \qquad (11.61$$

- as detailed by Penner[141] and Tien[142].

In combustion, line broadening is caused by molecular collision - as reported by Bartelds[143]. However, other effects can cause this phenomena - for example Hottel and Sarafim[144] report that Dopler effects cause line broadening in low pressure flows-such as the exhaust plumes from rocket engines. In the presented equation for the absorptivity S is the integrated line intensity, and is equivalent to the area under the curve for the broadened line, and b_c is the collision half width of the line.

One of the simplest models for predicting emissivity of a real gas is the so called "one clear and two grey gas model". As its name implies this model represents the emissivity of a real gas by taking the sum of the weighted emissivities of one clear and two grey gases. In this context a clear gas is one which does not absorb or emit radiation, and a grey gas is one which both absorbs and emits radiation. Johnson[145], derives the emissivities as follows:

$$\epsilon_g = \sum_{n=1}^{3} \epsilon_{g,n} = \sum_{n=1}^{3} a_{g,n}(T_g)(1-\exp -k'_n px) \qquad (11.62$$

with $a_{g,n} = b_{1n} + b_{2n} T_g$

The weighing factor, a_{gn}, represents the quotient of the spectral black body intensity integrated over the wavenumber region where k equals k_n, and the spectral black body intensity integrated over the spectrum. The constants b_{1n} and b_{2n} and the spectrum aborption coefficient k'_n are derived from experimental data for the particular flow situation being considered. Hadvig[146], has published such data for the products of simple hydrocarbon and oxygen reactions. Johnson[145], has used this model and Hadvig's data to estimate the emissivities of the products caused by methane combustion. (The clear gas was defined by setting k = 0 — this meant that it corresponded to the weakly and non-absorbing part of the spectrum. The partial pressure, p,

was set to the sum of the partial pressures of the radiating gases - in this case carbon dioxide and water vapour). Both Johnson[145] and Bartelds[143] state that this model has deficiencies in large furnaces. Johnson qualifies his statement by remarking that for methane combustion, the model becomes increasingly inaccurate when the mean pathlength of the radiation is larger than 4m - the partial pressures of carbon dioxide and water vapour were assumed to be 0.3bar. (Johnson assessed accuracy by comparing his predicted results with Hadvig's measured data.)

A modern version of this model has achieved slightly more accurate predictions. In this model the emissivity of the real gas under consideration is represented by the sum of the weighed emissivities of four grey gases. Some authors, for example Bartelds,[143] call this the " four grey gas model".

There is mounting evidence that the above mentioned models cannot adequately represent the emissivity characteristics of the gases involved in a real combustion process. The main reason for this is that these models only refer to the combustion gases of one fuel. Thus accurate results are obtained where the reaction has one predominant fuel - Johnson[145] has verified this result in methane and natural gas flames; and Beér and Claus[147] in certain oil flames. However, when the reactions become complex, that is various fuel sources occur, the model becomes inappropriate. To overcome these problems "spectral radiative models" have been proposed. Typically these are formulated so that the spectral absorption coefficient is

a function of the temperature. We shall now describe the two most popular models. The first is based upon the previously mentioned "four grey gas model", but replaces the monochromatic absorption coefficients in each of the four selected regimes by an average value at a fixed temperature. Thus the emissivity can be represented by:

$$\varepsilon_g = \sum_{n=1}^{4} \left\{1 - \exp(-k'_n(T_g).pX)\right\} \quad a_{gn}(T_g) \qquad (11.63$$

where

$$a_{gn}(T_g) = \frac{\int_o^n I_{b,\omega}(T_g)\, d\omega}{\int_o^\omega I_{b,\omega}(T_g)\, d\omega} \qquad (11.64$$

Bartelds[143] has used this model for predicting the emissivities of the gases involved in the combustion of methane - among the products are water vapour and carbon dioxide. His division of the spectrum into four regions is detailed in table two and is somewhat arbitrary. The various values taken by a_{gn}, at various temperatures T_g, were evaluated with the tabulated black body radiative fractions published by Siegel and Howell[150]. The portion of this data used by Bartelds[143] is presented in table three. The predicted values of ε_g had an average deviation from Hadvig's[146] data of less than one percent, which indicates that Barteld's sub-division of the spectrum is appropriate.

Table Two

Division of Electromagnetic Spectrum in Water Vapour and Carbon Dioxide

	Bands of Increasing Strength (μm)
n = 1	0.0 - 2.6111
	2.7778 - 3.7778
	5.5556 - 5.7222
	6.9444 - 11.1111
	50.0000 - -
n = 2	2.6111 - 2.7778
	3.7778 - 3.9444
	4.7778 - 5.5556
	5.7222 - 6.9444
	11.1111 - 14.6667
	31.1111 - 50.0000
n = 3	3.9444 - 4.2222
	4.3889 - 4.7778
	14.6667 - 31.1111
n = 4	4.2222 - 4.3889

Table Three

Weighing Factors and Absorption Coefficients of Four Grey Gas Model for the Products of Methane Combustion

T=	1000K	1200K	1400K	1600K	1800K	2000K		1000-2000K
a_1	.540900	.607500	.672000	.733100	.789600	.840200	k_1	.106165
a_2	.304100	.261200	.219300	.178300	.139300	.101300	k_2	1:652800
a_3	.124900	.109900	.093870	.078300	.064960	.055120	k_3	21.212000
a_4	.029980	.021390	.014810	.009851	.006130	.003296	k_4	146.308000

An even more general spectral model has been proposed by Bartelds[143]. Its purpose is to calculate the emissivities of both gas mixtures and soot. This model only differs from that previously described in one point. This is that the spectral absorption coefficient is taken as the function of the composition, pressure and temperature. Thus the emissivity is now represented by:

$$\varepsilon_g = \sum_{n=1}^{m} a_{g,n}(T_g).\left\{1 - \left[\exp -k'_n(\text{composition},P,T_g).x\right]\right\} \qquad (11.65$$

Bartelds[143], has presented some sample results which indicate that this model is reasonably accurate in certain cases.

The problems associated with estimating the radiative properties of the surfaces of the furnace should not be underestimated. Electromagnetic theory can be used to assess these properties when the surfaces can be precisely defined. This means that the surfaces are optically smooth and both physically and chemically clean. However, in practical situations where the surfaces are normally rough and chemically contaminated, there is very little information available on the radiative properties. Perry[148] and Bartelds[143] have published some measured data on rough contaminated surfaces. Van Kuijk and Spanjer's[149] have detailed how surface temperatures, and the material from which the furnace is constructed, affect absorptivity. However, at present there is still insufficient data available to enable modellers to define the radiative properties of rough or contaminated surfaces with confidence.

Radiation Models

A perfect radiation model would predict radiation exchange within an enclosure by spectral summing up of the multiple reflections, absorptions and scatterings of an infinite number of monochromatic beams. It is not practical to formulate such a model for the following reasons. Firstly, spectral information defining the surface radiative characteristics of the enclosure containing the flow being examined is not precise enough to warrant the construction of such an all encompassing model. Secondly, there is insufficient information on the emission, absorption and scattering characteristics of radiation from soot, pulverized fuels and certain gases for accurate predictions in many practical engineering flow situations. Thirdly, at present computers are not sufficiently powerful to deal with the mathematical algorithms required to simulate an infinite number of monochromatic beams. With these physical and computational limitations in mind several approximate radiation models have been proposed. The most popular ones are called the "Monti-Carlo", Zone and Flux models.

The first model makes use of the Monti-Carlo principle and is potentially the most flexible and accurate. However, as pointed out by Stewart and Canon,[162] the vast amount of computational time required for a solution make this approach commercially impractical.

The second model sub-divides the flow situation into several zones. Each zone is assumed to have constant radiative properties,

and an equivalent radiative area defined from tables of the type published by Tien[151] . The exchange between a pair of zones is then calculated with the aid of the radiative energy equation. Hottel and Cohen[152], Steward and Guruz[153] and Johnson[145] have described, used and assessed the performance of this type of model in furnace flow situations. The model is unsuitable for embodying into flow modelling techniques for the following reasons.

The assumption of constant radiative properties in each zone produces unrealistic predictions unless a large number of zones are specified. When a large number of zones are specified the computational difficulties involved in dealing with the connections between the various zones and the fluid dynamics model becomes so immense that this approach is commercially impractical.

Flux models replace the exact integra-differential equations of radiative heat transfer, equation 11.58, by approximate differential ones. The advantage of this approach is that these differential equations can be solved by the standard finite difference or finite element techniques typically used in the mathematical algorithms that solve the momentum, heat and mass transfer equations.

The first flux models were devised for the solution of astro-physical problems - Schuster[154] published the first paper on this subject. These models simulate radiative transfer in one direction, however, as the radiative flux can go both forwards and backwards they are known as "two flux models". Various models

of this type have been proposed and tested. The mathematical form assumed by these models depends upon the method of averaging used to reduce the radiant integra-differential equation to a form that can be easily solved. The models thus obtained are normally named after the inventors of the averaging procedure used in their derivation. We shall briefly describe the models which have been successful in engineering applications. The Schuster and Schwarzchild model[163] assumes that the radiation intensity is constant within a hemisphere. A discontinuity in the intensity thus occurs at the plane between these hemispheres. Differential equations are derived within each hemisphere by integrating radiant energy equations over each hemisphere with the constant intensity assumption applied. Standard finite difference and element methods can be used to solve the resulting approximate radiation equation. The Milne[157], or Eddington[158], model is based upon the assumption that the radiation intensity is a function of cos $\emptyset$ - where $\emptyset$ is a solid angle at the source of the radiation. The Hamaker[164] model is derived from that used by Schwarzchild., but omits the mean obliquity factor for one-half. Siddall[155] has compared predictions from these models for an emitting grey gas between parallel plates. He demonstrated that the models proposed by Schuster-Schwarzchild [157] and Eddington[158] gave the best agreement with the exact solution of this problem.

Siddall points out that more accurate predictions

would be obtained if the radiant flux were allowed to travel in more directions.

Whilst two flux models were satisfactory for simulating astro - physical problems, they were found to be unsuitable for dealing with engineering situations where more than one predominant direction of radiation transfer occurred.

To overcome this problem "four and six flux models" were formulated. (The four flux model being able to simulate radiation transfer along two principal axis, and the six flux model along three axis). These models are derived by using the following procedures. The flow domain being examined is divided into several zones. In the four flux model these zones are triangular in shape, and in the six, and greater, flux models cones are used. (The apex of triangle or cone is situated at the source of radiation). In each zone the intensity of radiation is assumed constant. The integra-radiant energy equation is then integrated over each zone to produce a differential equation - which can then be solved by a finite difference or element method. Bartelds[143] has compared predictions from two and four flux models for methane combustion in an axi-symmetric cylindrical furnace. Not only did they find the four flux model to be the more accurate, but also the easiest to combine into aero and thermo-dynamic modelling technique he used.

Gosman and Lockwood[159] have employed a four flux model, which was derived in a similar manner to the method prescribed by Schuster[154] for two flux models, to predict radiative transfer from a gas flame

in a furnace. (This furnace had a square cross-section and has been detailed by Johnson and Beér[160]). Radiation fluxes were allowed for in the axial and radial direction. The turbulent viscosity was determined with a two equation turbulence model. The radiation model gave reasonable predictions of temperature near the chamber wall, but far less satisfactory predictions in the center of the furnace.

Flux models of radiant energy transfer will remain popular, because of the ease with which they combine with the modelling techniques that predict heat, mass and momentum transfer within a fluid. It is probable that new flux models will allow for more domains to be specified where the radiant energy equation is applied. This will produce more accurate predictions, because such multi flux models are better equipped to simulate reality. Just as important is the fact that these models will have the capability of dealing with strongly anisotropic radiation - as obtained in flames produced from pulverized fuels.

Appendix 1

Spalding — [illegible] tankar

The purpose of the modelling technique proposed by Spalding and tankar is to solve the equation representing momentum conservation in a boundary flow 1.1 for the mainstream velocity U. The solution takes the form of a series of algebraic expressions that can be interpreted, and solved for the velocity U by an electronic computer.

$$\frac{\partial}{\partial x} = \frac{\partial}{\Gamma_y} \quad \gamma) - \frac{1}{\rho} \frac{\partial p}{\partial x} \qquad 1.1$$

The co-ordinate system and mesh network covering the area of the flow simulated are detailed in section one. The mathematical method used to manipulate and transform equation 1 so that it can be solved for the velocity U is specified in section two.

1.1 Co-ordinate System

The modelling technique uses a co-ordinate system in:

a) in the streamwise direction the distance along the impervious surface x - as shown in figure 1.1

and b) in the cross-stream direction the non-dimensional stream function $\omega \left(= \frac{\psi - \psi_1}{\psi_2 - \psi_1} \right)$ - where

ψ representing a stream function, and the subscripts 1 and 2 refer to the impervious surface and free edge of the boundary flow.

The mesh network used to cover the flow is detailed in figure 1.1. The network comprises a series of cross-stream strips Δx wide, and several stream tubes - bounded at their edges by lines

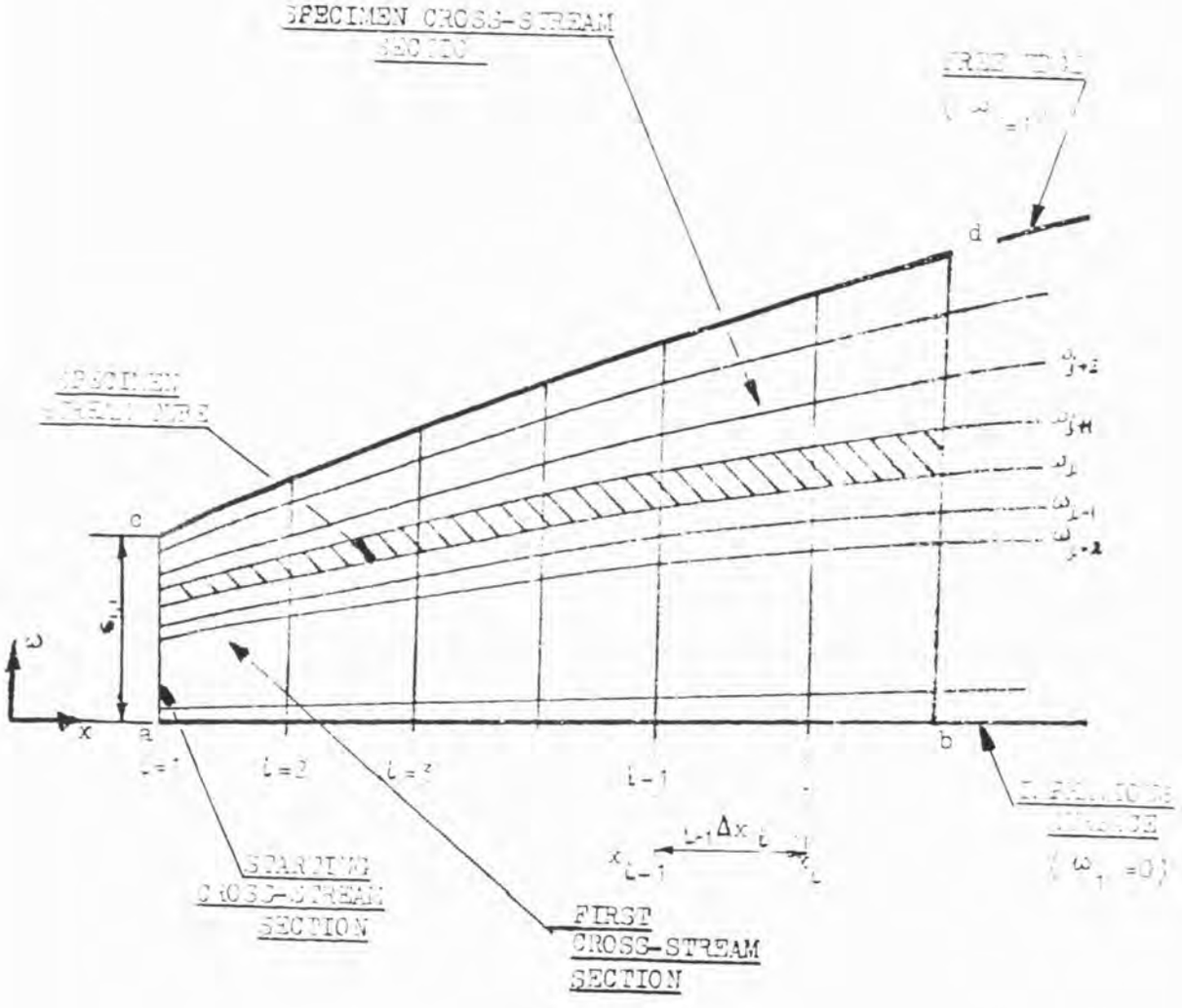

MESH NETWORK

FIGURE 1.1

along which the non-dimensional stream function ω is constant.

1.2 Mathematical Method

The mathematical method upon which the modelling technique is based, makes use of the co-ordinate system and mesh network described in secion 1. The method has been split into two parts. Firstly, an approximate and limited solution to equation 1.1 has been obtained within a trapezium flow element; this part of the method is detailed in sub-section a. Secondly, the procedure for extending this limited solution to provide predictions for the velocity within a boundary flow is detailed in sub-section b.

1.2a Approximate Solution

Trapezium shaped flow elements are located in the mesh network as shown in figure 1.2 Each element, say abce designated by 'A' in figure 1.2, is positioned within the network so that:

a) the parallel sides ac and be coincide with the boundaries of the cross-stream strip,

and b) the pairs of corners a,b and c,e are equi-distant between the non-dimensional mesh stream lines ω_{j+1}, ω_j and ω_j, ω_{j-1} respectively.

It has been assumed that the flow properties, including the velocity U, are known at the upstream section ac of the specimen element. The purpose of the approximate algebraic solution to equation 1.1, within the flow element, is to relate the velocities at the downstream section be to the properties at the upstream section ac. Spalding-Patankar have derived such algebraic

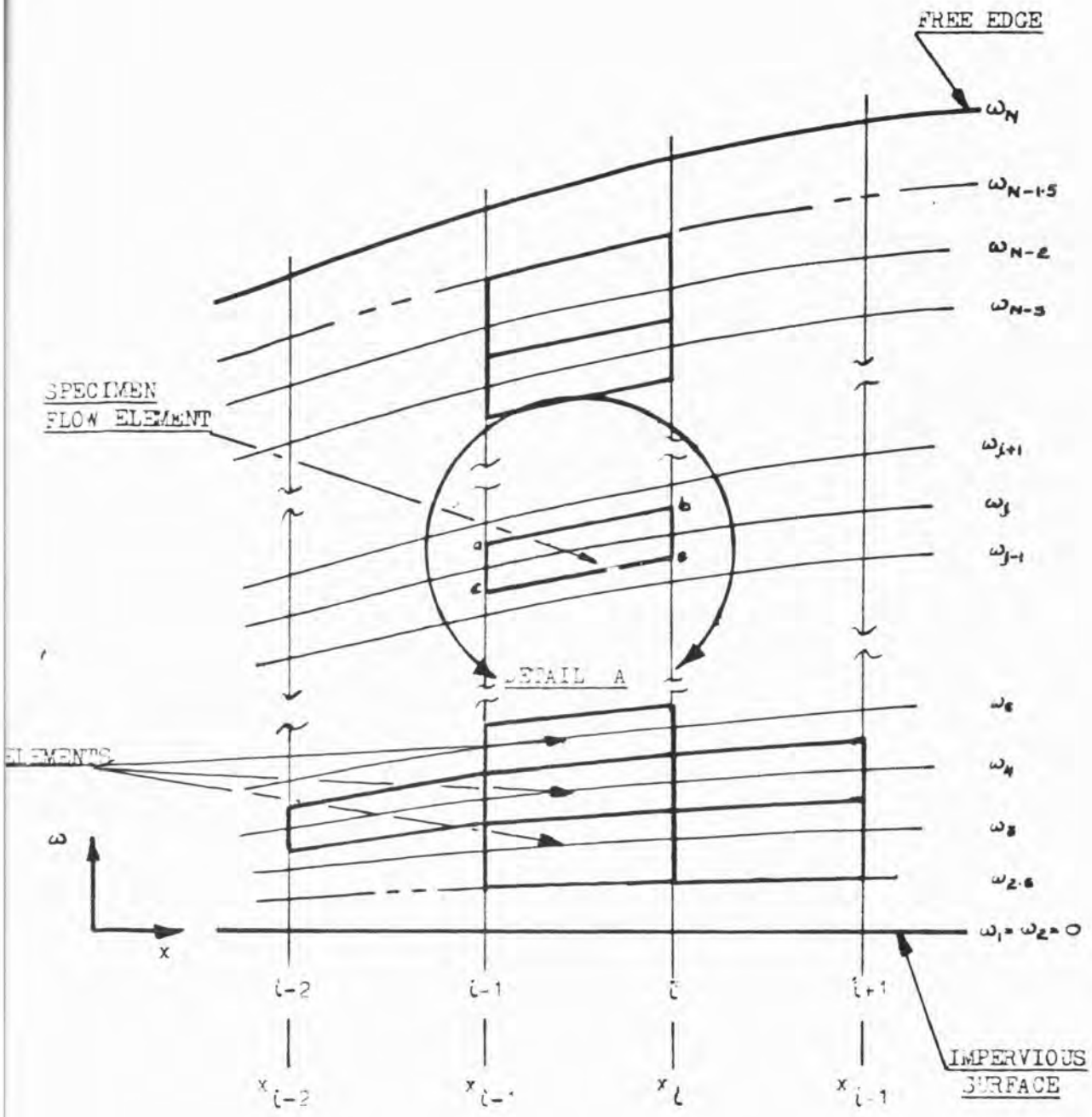

POSITIONING OF FLOW ELEMENTS

FIGURE 1.2

equations for specimen flow elements positioned within the wall, mainstream and free-edge regimes of the boundary flow shown in figure 1.5. The derivation of these equations are detailed below, after defining the areas occupied by the wall and free-edge regimes. The wall regime has been assumed to occupy that area of the flow where the effects of the impervious surface dominate the transfer processes . The free-edge regime occupies that portion of the flow near the free-edge, where the cross-stream velocity profile is the form of:-

$$U \propto (y)^2 \qquad (1.2$$

(i) Wall Regime

The wall regime is bounded in the streamwise direction by the impervious surface, at which ω_1 and $\omega_2 = 0$, and the non-dimensional stream function $\omega_{2.5}$ - which has been positioned so that:

$$\omega_{2.5} = \frac{\omega_3}{2} \qquad (1.3$$

A single trapezium shaped flow element covers the wall regime at each cross-stream strip - as illustrated in figure 1.4a. Spalding-Pantankar used the following relationship:

$$U_{2,i} = U_{3,i} \left(\frac{}{1 + \sqrt{\frac{s}{K}}} \right)_{i-1} \qquad (1.4$$

to represent the change in the mainstream velocity U across this regime . In this equation s represents $\frac{\tau_o}{\rho U^2}$,

with τ_o designating the shear stress at the surface.

The following assumptions have been used to derive this relationship from equation 1.1:

a) Couette flow occurs within the wall regime,

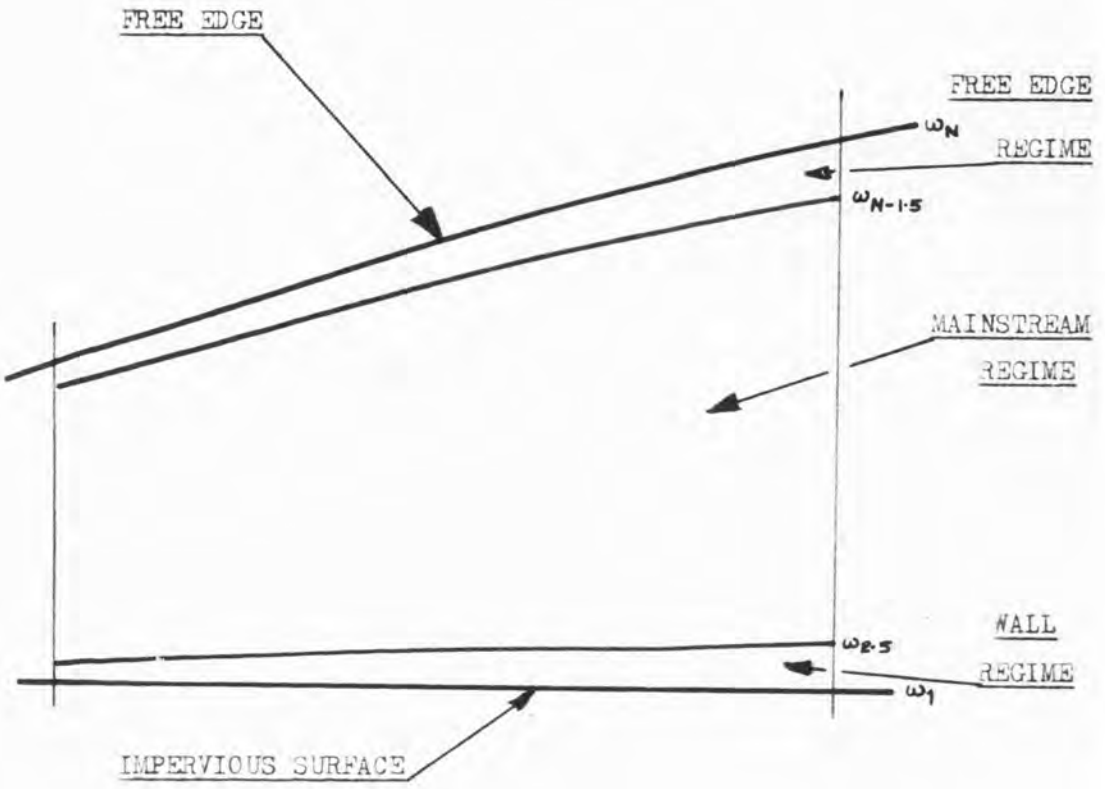

FLOW REGIMES

FIGURE 1.3

b) the velocity profile within the wall regime, and at any cross-stream section i, is of the form of:

$$U \propto \left(\omega \right)^{\left(\frac{\sqrt{s}}{K + \sqrt{s}} \right)_{i-1}} , \qquad (1.5$$

as detailed schematically in figure 4.b

and c) at $\omega_{2.5,j}$ $\quad \frac{dU}{d\omega} = \frac{U_{3,j} - U_{2,j}}{\omega_{3,j}} = \tan(\alpha_j)$

- the angle α_j is detailed in figure 4b.

The unknown parameters $\sqrt{\frac{s}{K}}$ in equations 1.4 and .5 were estimated by the numerical integration of Van Driest's[2] turbulent viscosity formulae:

$$\mu_t = \rho K^2 y \left\{ 1 - \exp\left[\frac{-y\sqrt{\tau\rho}}{u_t A_+} \right] \right\}^2 \frac{dU}{dy} \qquad (1.6$$

across a boundary flow, to give:

$$\left(\frac{\sqrt{s}}{K} \right)_{j-1} = \frac{1}{K^2 R_{2.5,j-1}} - \frac{0.1561}{(K^2 R_{2.5,j-1})^{0.45}} + \frac{0.08723}{(K^2 R_{2.5,j-1})^{0.3}} \qquad (1.7$$

$$+ \frac{0.03713}{(K^2 R_{2.5,j-1})^{0.18}}$$

where μ_t is the turbulent viscosity, ρ represents the density, K is a constant set to 0.4, and $R_{2.5,j-1} = \frac{\bar{u}_{2.5,j-1} \cdot y_{2.5}}{\mu_{eff,2.5}}$.

(ii) Mainstream Regime

The mainstream regime is bounded in the streamwise direction by the non-dimensional stream lines $\omega_{N-1.5}$ and $\omega_{2.5}$. The mesh stream line $\omega_{N-1.5}$ coincides with the lower edge of the free-edge regime, and $\omega_{2.5}$ has been defined in sub-section 'i'.

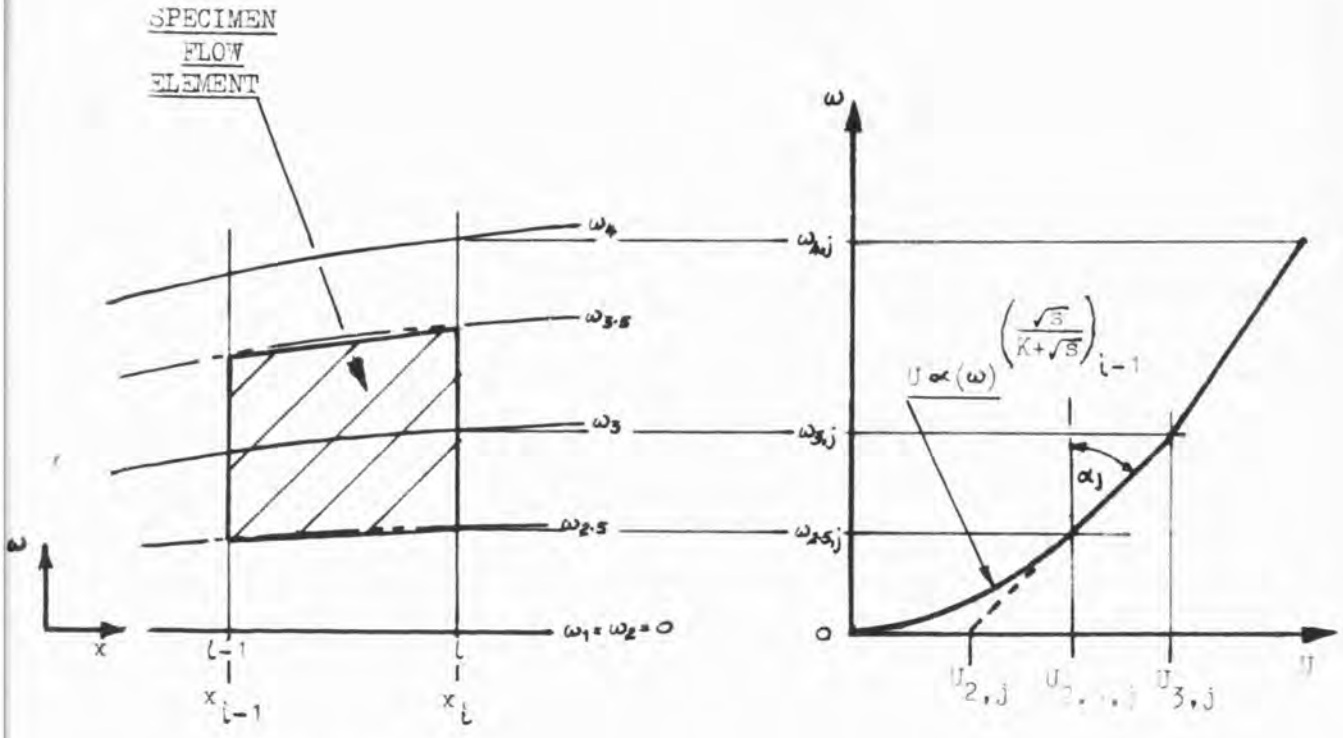

a. SPECIMEN ELEMENT

b. VELOCITY PROFILE AT x_{i-}

WALL REGIME

FIGURE 1.4

The mainstream region is covered with trapezium shaped elements in the manner previously described. An illustration of their position with respect to the mesh network is presented in figures 1.2 & 1.5. Spalding-Pantankar have derived the following algebraic equation:

$$U_{i,j} = A_{i,j} U_{i,j+1} + B_{i,j} U_{i,j-1} + C_{i,j} \qquad (1.5$$

to describe the variation of the mainstream velocity over any one of the trapezium elements in the mainstream regime. In this equation the coefficient $A_{i,j}$, $B_{i,j}$ and $C_{i,j}$ are dependent upon the flow parameters at the points u_{j+1}, u_j and u_{j-1} in figure 1.5, and take the values:

$$A_{i,j} = \left[\frac{E_5 - E_1 + S_1}{E_2 + E_5 + E_6 - S_2}\right]_{i,j} ,$$

$$B_{i,j} = \left[\frac{E_6 - E_3 + S_3}{E_2 + E_5 + E_6 - S_2}\right]_{i,j} ,$$

& $$C_{i,j} = \left[\frac{S_4 - E_4}{E_2 + E_5 + E_6 - S_2}\right]_{i,j} ;$$

with

$$E_1 = P_1 + Q + R_1$$

$$E_2 = P_2 + R_2$$

$$E_3 = P_3 - Q + R_1$$

$$E_4 = P_1 U_{i-1,j+1} - P_2 U_{i-1,j} - P_3 U_{i-1,j-1}$$

where

$$S_1 = \frac{P_1}{(\rho U^2)_{i-1,j+1}} \cdot \frac{dp}{dx} \left({}_{i-1}\Delta x_i\right)$$

$$S_2 = \frac{P_2}{(\rho U^2)_{i-1,j}} \left({}_{i-1}\Delta x_i\right) \frac{dp}{dx}$$

$$S_3 = \frac{P_3}{(\rho U^2)_{i-1,j-1}} \left({}_{i-1}\Delta x_i\right) \frac{dp}{dx}$$

$$S_4 = -2 \frac{dp}{dx} \left({}_{i-1}\Delta x_i\right) \left[\frac{P_1}{(\rho U)_{i-1,j+1}} + \frac{P_2}{(\rho U)_{i-1,j}} + \frac{P_3}{(\rho U)_{i-1,j+1}} \right]$$

$$P_1 = \frac{\omega_{i,j+1} - \omega_{i,j}}{4(x_i - x_{i-1})(\Delta\omega)}$$

$$P_2 = \frac{3}{4(x_i - x_{i-1})}$$

$$P_3 = \frac{\omega_{i,j} - \omega_{i,j-1}}{4(x_i - x_{i-1})(\Delta\omega)}$$

$$Q = \frac{a}{\Delta\omega}$$

$$R_1 = \frac{b}{4}\left[\frac{\omega_{i,j+1} + 3\omega_{i,j}}{\Delta\omega}\right]$$

$$R_2 = -\frac{b}{4}$$

$$R_3 = -\frac{b}{4}\left[\frac{\omega_{i,j-1} + 3\omega_{i,j}}{\Delta\omega}\right]$$

$$S\ \Delta\omega = \omega_{i,j+1} - \omega_{i,j-1}$$

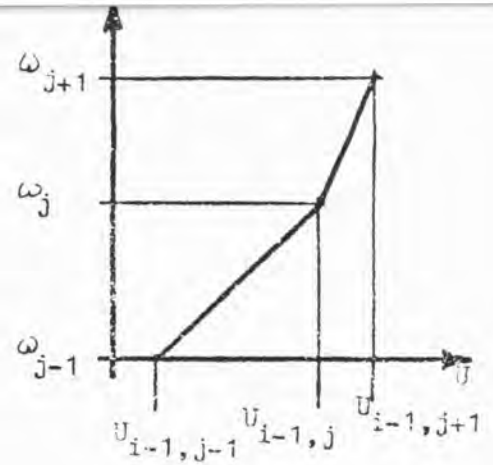

c. CROSS STREAM VELOCITY PROFILE AT THE UPSTREAM BOUNDARY

(x_{i-1})

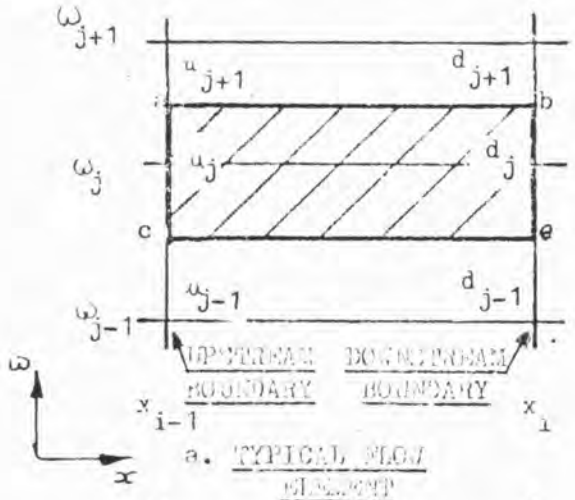

a. TYPICAL FLOW ELEMENT

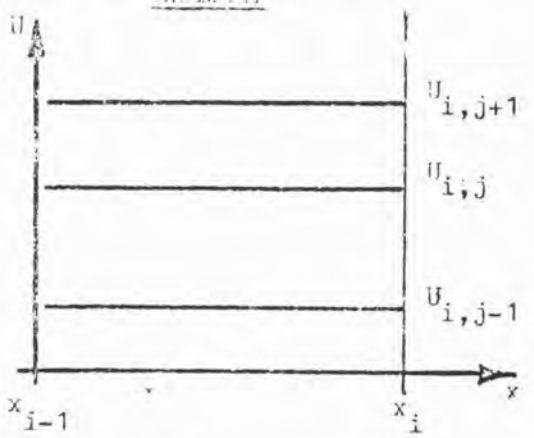

b. STREAM-WISE VELOCITY PROFILE BETWEEN x_{i-1} AND x_i

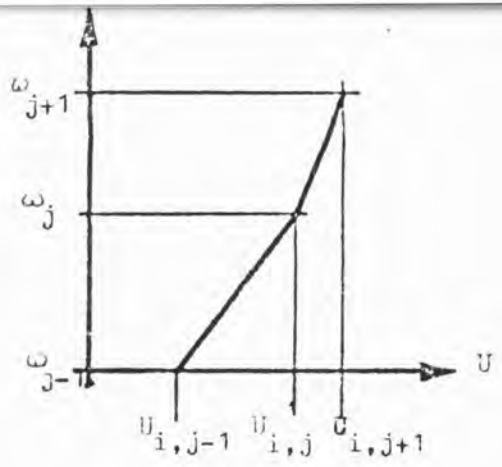

d. CROSS STREAM VELOCITY PROFILE AT THE DOWNSTREAM BOUNDARY

(x_i)

ASSUMED VELOCITY PROFILES AROUND A SPECIMEN FLOW ELEMENT

FIGURE 1

Equation 1.8 is derived from the equation of motion 1.1 by the following procedure. Firstly, the variation of the mainstream velocity along the boundaries of a specimen element, say abce in figure 1.2 , are described. (A closeup view of element abce, designated by detail A in figure 1.2 , is shown in figure 1.5.) Spalding-Pantankar achieved this by defining the variation in the velocity along the lines of the mesh network that surround the specimen element. That is along the mesh stream lines $u_{j+1}\ d_{j+1}$, $u_j\ u_j$ and $u_{j-1}\ d_{j-1}$, and in the cross-stream direction $u_{j-1}\ u_j$, $u_j\ u_{j+1}$, $d_{j-1}d_j$ and $d_j\ d_{j+1}$ - in figure 1.5 . Along the specified mesh stream lines the mainstream velocity U has been assumed constant and equal to its value at the downstream boundary $d_{j+1}\quad d_j\quad d_{j-1}$. The assumed velocity profiles are detailed schematically in figure 1.5b.Along the cross-stream lines $u_{j-1}\ u_j$, $u_j\ u_{j+1}$, $d_{j-1}\ d_j$ and $d_j\ d_{j+1}$ the velocity is assumed to vary linearly with the cross-stream ordinate ω . Schematic representation of these velocity profiles along the upstream and downstream sections of the element are detailed in figures 1.5c and d respectively. Secondly, it had been assumed that when the flow element abce is small:

$$\text{a)}\quad \frac{\partial U}{\partial \omega} = \frac{dU}{d\omega}$$

$$\text{b)}\quad \frac{\partial}{\partial \omega}\left(\mu_{eff}\frac{\partial U}{\partial \omega}\right) = \frac{d}{d\omega}\left(\mu_{eff}\frac{dU}{d\omega}\right) \qquad (1.9$$

$$\text{c)}\quad \frac{\partial U}{\partial x} = \frac{dU}{dx}$$

Spalding-Pantankar derived equation 1.8 by using the following procedure. Firstly, by substituting into equation 1.1 both the above expressions and the assumed velocity profiles. Secondly, by integrating the resultant expression over the flow element.

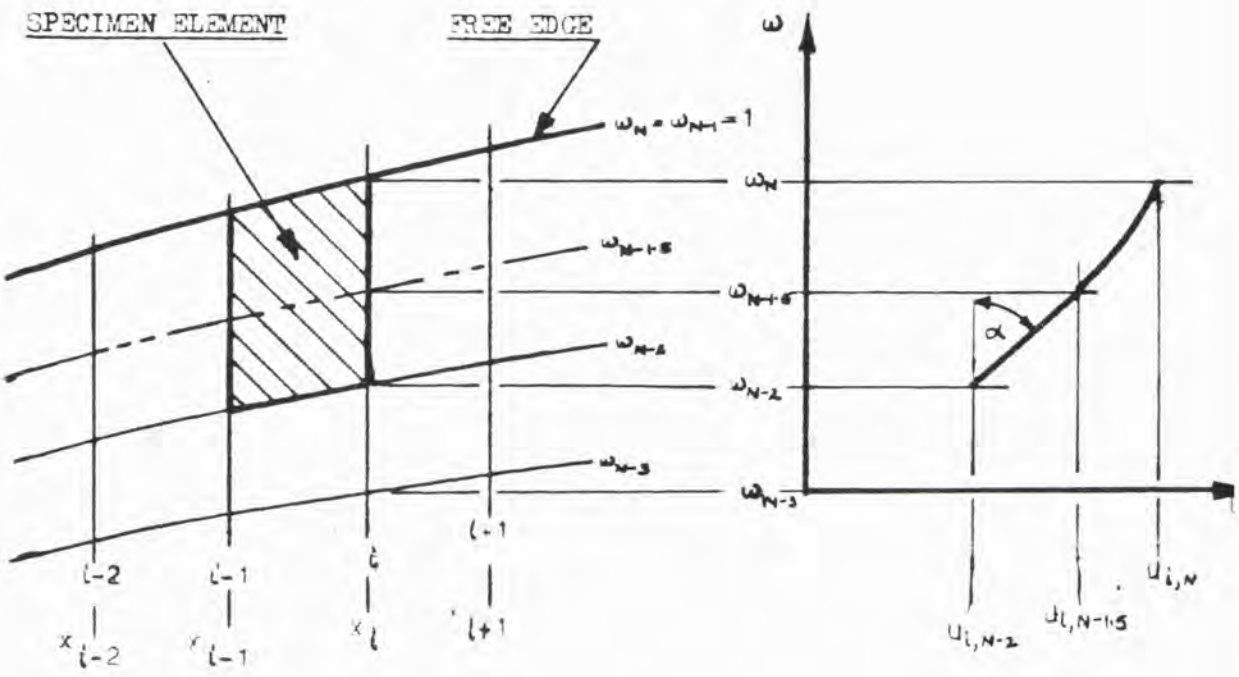

a. SPECIMEN ELEMENT

b. FLOW DISTRIBUTION AT CROSS-STREAM SECTION x_i

FREE EDGE REGIME

FIGURE 1.6

(iii) Free-Edge Regime

This regime lies between the non-dimensional stream lines of the mesh network ω_N and $\omega_{N-1.5}$ - as shown in figure 1.o. The free-edge of the flow coincides with the stream line ω_N.

A single flow element covers the free-edge regime at each cross-stream strip; an example of one such element in the cross stream strip where $x_{i-1} \leq x \leq x_i$ is presented in figure 1.6a. The equation:

$$U_{i,N-1} = U_{i,N}\, C + U_{i,N-2}\,(1-C), \qquad 1.10$$

with

$$C = \frac{U_{i-1,N-1} + U_{i-1,N} - 3\,U_{i-1,N-2}}{5\,U_{i-1,N-1} + 5U_{i-1,N} + 8U_{i-1,N-2}}$$

has been used by Spalding–Patankar to represent the change in velocity over the specified flow element. This relationship was derived from the equation of motion 1.1, after assuming that in the free-edge regime:

a) the cross-stream velocity profile is of the form

$$U - U_N \propto (y - y_N)^2 ,$$

b) the mainstream velocity does not vary in the streamwise direction

and c) at $\omega_{i,N-1.5}$ $\left(\frac{dU}{d\omega}\right) = \left(\frac{U_{N-2} - U_{N-1}}{\omega_{N-2} - \omega_N}\right)_L = \tan \alpha$

- the angle α is designated in figure 1.6b.

1.2b Overall Solution

The technique used to combine the three limited conservation equations, 1.4 ,1.9 and 1.10, to predict the mainstream velocity within a boundary flow is as follows. Firstly, the extent of the flow is mathematically specified. Secondly, the procedure for manipulating and then solving the limited equations is described.

The extent of the boundary flow has to be specified by detailing:

a) the variation of the mainstream velocity along the impervious surface, free-edge and starting cross-stream section of the flow - that is along ab, cd and ac respectively in figure 1.1.

and b) the height of the flow $\delta_{1,1}$ at the starting cross-stream section.

The technique used to assemble the limited equations for momentum conservation is as follows. Trapezium shaped flow elements are ordered into each cross-stream strip of the mesh network in the manner specified in section 1.2a. The algebraic relationships representing momentum conservation for flow elements in the wall, mainstream and free-edge regimes - equations 4,8 and 10 respectively - are applied to their respective elements within the first cross-stream strip shown in figure 1. This results in the following set of equations:

$$U_{2,2} = \frac{U_{3,2}}{\left[1 + \sqrt{\frac{S}{K}}\right]_1}$$

$$\sum_{j=4}^{N-2} \left(-U_{2,j} + A_{2,j}\, U_{2,j+1} + B_{2,j}\, U_{2,j-1} + C_{2,j} \right) = 0$$

$$U_{2,N-1} = U_{2,N} G + U_{2,N-2}(1-G) :$$

These equations can be solved for $U_{2,j}$ $J = 2, N - 1$ when the variation of the mainstream velocities along the starting cross-stream section, free-edge and impervious surface are substituted. The boundary substitution procedure, of limited conservation equations and boundary conditions, can be applied to the second cross-stream strip shown in figure 1.1, and the resultant set of equations solved for $U_{3,j}$ $j = 2$ to $N - 1$. This procedure can be continued cross-strip strip by strip until the complete flow is covered.

Appendix 2

Denny-Landis

The modelling technique proposed by Denny-Landis solves the equation representing momentum conservation in a boundary flow 2.1 for the mainstream velocity U:

$$\frac{\partial U}{\partial x} = \frac{\partial}{\partial \psi}(\mathcal{C}) - \frac{1}{\rho U}\frac{dp}{dx} \qquad (2,1$$

The co-ordinate system, and mesh network used by the modelling technique to cover the area of the flow simulated are detailed in section 1. The mathematical method used to manipulate and transform the equation of motion 2.1, until it can be solved for the streamwise velocity U, is specified in section 2.

2.1 Co-ordinate System

The modelling technique uses a co-ordinate system of:

a) in the streamwise direction the distance along the impervious surface x - as shown in figure 2.1,

and b) in the cross-stream direction the non-dimensional stream-function Ω equal to $\left[\frac{\psi - \psi_1}{\psi_N - \psi_1}\right]^{\frac{1}{FN}}$ -

where ψ represents the stream function, FN is an integer set to 2 or 1; and the subscripts 1 and N refer to the impervious surface and free-edge of the flow respectively.

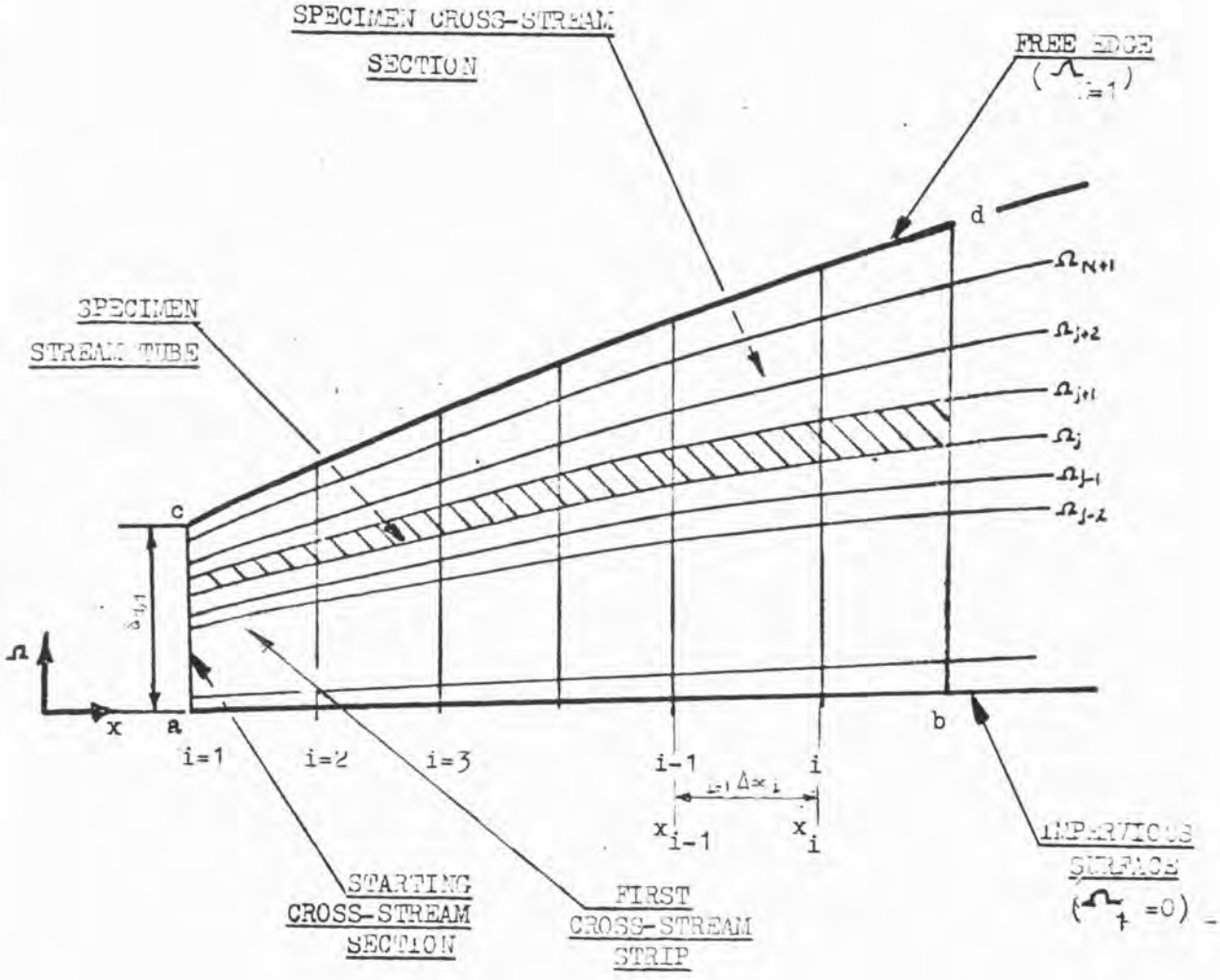

MESH NETWORK

FIGURE 2.1

A typical network is shown in figure 2.1. It comprises a series of cross-stream strips of width Δx, and several stream tubes - bounded at their edges by lines along which the non-dimensional mesh line Ω is constant.

2.2 Mathematical Method

The mathematical method used to manipulate and transform equation 2.1, so that it can be solved for the mainstream velocity U, falls within the marching integration class described in chapter 2. The method makes use of the co-ordinate system and mesh network described in section 1.

The derivation of the method has been split into two parts. Firstly, a technique to obtain an approximate and limited solution of equation 2.1 for the velocity U within a trapezium shaped element is presented. This part of the derivation is detailed in sub-section a. Secondly, the procedure for extending the limited solution of equation 2.1 to give predictions for the velocity within any boundary flow is detailed in sub-section b.

2.2a Approximate Solution

Trapezium shaped elements are positioned within the network so that:

a) their parallel sides, say ac and bd in figure 2-1 coincide with the boundaries of the cross-strip strip,

and b) the corners a, b and c, e are equi-distant between the non-dimensional mesh stream lines Ω_{j+1}, Ω_j and Ω_j Ω_{j-1} respectively.

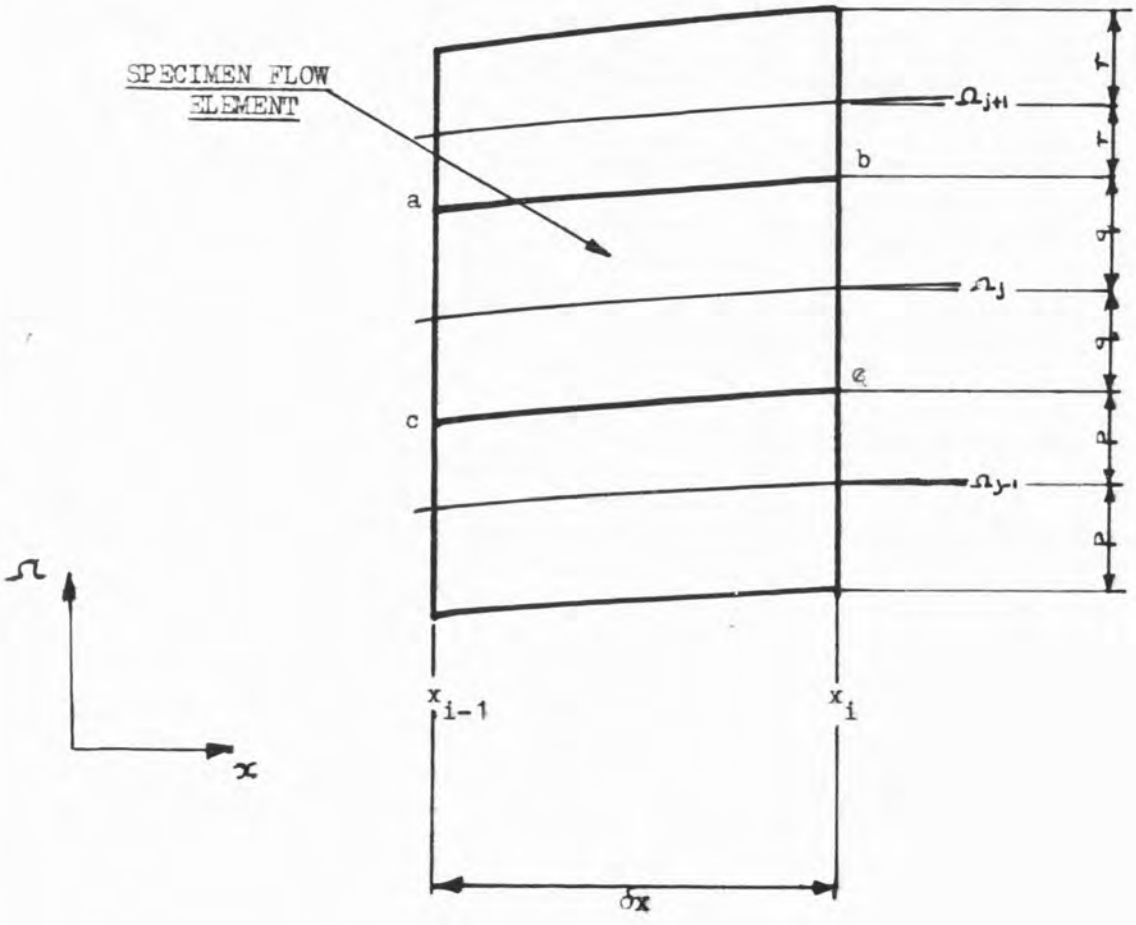

FLOW ELEMENTS

FIGURE 2.2

The purpose of the approximate algebraic solution to equation 2.1 within a specimen element, say abce in figure 2.2 is to relate the velocities at the down-stream section 'be' to known or assumed properties at the upstream section 'ac'. The algebraic solution takes the form:

$$U_{i,j} = A'_{i,j}\, U_{i,j-1} + B'_{i,j}\, U_{i,j+1} + C'_{i,j} \qquad (2.2$$

where:

$$A'_{i,j} = \left[\frac{S'_5 - S'_1 + s'_1}{S'_2 + S'_5 + S'_6 + s'_2}\right]_{i,j}$$

$$B'_{i,j} = \left[\frac{S'_6 - S'_3 + s'_3}{S'_2 + S'_5 + S'_6 - s'_2}\right]_{i,j}$$

and $$C'_{i,j} = \left[\frac{s'_4 - S'_4}{S'_2 + S'_5 + S'_6 - s'_2}\right]_{i,j}$$

with

$$S'_1 = P'_1 + Q + R'_1$$
$$S'_2 = P'_2 + R'_2$$
$$S'_3 = P'_3 - Q + R'_1$$
$$S'_4 = P'_1 U_{i-1,j+1} - P'_2 U_{i-1,j} - P'_3 U_{i-1,j-1}$$

$$s'_1 = \frac{P'_2}{(\rho U^2)_{i-1,j+1}} \frac{dp}{dx} \left({}_{i-1}\Delta x_i\right)$$

$$s'_2 = \frac{P'_2}{(\rho U^2)_{i-1,j}} \left({}_{i-1}\Delta x_i\right) \frac{dp}{dx}$$

$$s'_3 = \frac{P'_3}{(\rho U^2)_{i-1,j-1}} \left({}_{i-1}\Delta x_i\right) \frac{dp}{dx}$$

$$s'_4 = -2 \frac{dp}{dx} \left({}_{i-1}\Delta x_i\right) \left[\frac{P'_1}{(\rho U)_{i-1,j+1}} + \frac{P'_2}{(\rho U)_{i-1,j}} + \frac{P'_3}{(\rho U)_{i-1,j+1}}\right]$$

$$P_1' = \left(\frac{2.FN}{\Delta x.\Delta\Omega\left(\Omega_{i,j+1}-\Omega_{i,j}\right)}\right)\left[\left(\frac{\Omega_{i,j+\frac{1}{2}}^{FN+1}-\Omega_{i,j}^{FN+1}}{FN+1}\right)-\Omega_{i,j}\left(\frac{\Omega_{i,j+\frac{1}{2}}^{FN}-\Omega_{i,j}^{FN}}{FN}\right)\right]$$

$$P_2' = \left(\frac{2FN}{\Delta x.\Delta\Omega}\right)\left[\left(\frac{\Omega_{i,j+\frac{1}{2}}^{FN+1}-\Omega_{i,j}^{FN+1}}{(FN+1).\Delta\Omega}\right)+\left(\frac{\Omega_{i,j+\frac{1}{2}}^{FN}-\Omega_{i,j}^{FN}}{FN}\right)\left(\frac{\Omega_{i,j+1}}{\Omega_{i,j+1}-\Omega_{i,j}}\right)\right.$$
$$\left.+\left(\frac{\Omega_{i,j}^{FN+1}-\Omega_{i,j-\frac{1}{2}}^{FN+1}}{(FN+1)\left(\Omega_{i,j}-\Omega_{i,j-\frac{1}{2}}\right)}\right)-\left(\frac{\Omega_{i,j}^{FN}-\Omega_{i,j-\frac{1}{2}}^{FN}}{FN}\right)\left(\frac{\Omega_{i,j-1}}{\Omega_{i,j}-\Omega_{i,j-1}}\right)\right]$$

$$P_3' = \left(\frac{2.FN}{\Delta x.\Delta\Omega.\left(\Omega_{i,j}-\Omega_{i,j-1}\right)}\right)\left[\Omega_{i,j}\left(\frac{\Omega_{i,j}^{FN}-\Omega_{i,j-\frac{1}{2}}^{FN}}{FN}\right)-\left(\frac{\Omega_{i,j}^{FN+1}-\Omega_{i,j-\frac{1}{2}}^{FN+1}}{FN+1}\right)\right]$$

$$R_1' = \left(\frac{2b}{\Delta\Omega}\right)\left(\frac{\Omega_{i,j+\frac{1}{2}}^{FN+1}-\Omega_{i,j}^{FN+1}}{(FN+1)\left(\Omega_{i,j+\frac{1}{2}}-\Omega_{i,j}\right)}\right)$$

$$R_2' = \left(\frac{2b}{\Delta\Omega}\right)\left[-\left(\frac{\Omega_{i,j+\frac{1}{2}}^{FN+1}-\Omega_{i,j}^{FN+1}}{(FN+1)\left(\Omega_{i,j+\frac{1}{2}}-\Omega_{i,j}\right)}\right)+\left(\frac{\Omega_{i,j}^{FN+1}-\Omega_{i,j-\frac{1}{2}}^{FN+1}}{(FN+1)\left(\Omega_{i,j}-\Omega_{i,j-\frac{1}{2}}\right)}\right)\right]$$

$$R_3' = -\left(\frac{2b}{\Delta\Omega}\right)\left[\frac{\Omega_{i,j}^{FN+1}-\Omega_{i,j-\frac{1}{2}}^{FN+1}}{(FN+1)\left(\Omega_{i,j}-\Omega_{i,j-\frac{1}{2}}\right)}\right]$$

$$\Delta\Omega = \Omega_{i,j+1}-\Omega_{i,j}$$

$$\Delta x = x_i - x_{i-1}.$$

The coefficients $A_{i,j}'$, $B_{i,j}'$ & $C_{i,j}'$ in equation 22 are dependent upon the properties of the upstream section. The mathematical method used to obtain this approximate solution is as follows. Firstly, the variation for the mainstream velocities

along the boundaries of the specimen flow element are prescribed. Denny-Landis achieved this by detailing the variation of the velocity along the lines of the mesh network encompassing the specimen element. That is along the mesh stream lines $u_{j+1}\ d_{j+1}$, $u_j\ u_j$, and $u_{j-1}\ d_{j-1}$ in the streamwise direction, and $u_{j-1}\ u_j$, $u_j\ u_{j+1}$, $d_{j-1}\ d_j$ and $d_j\ d_{j+1}$ in the cross-stream direction - as shown in figure 2.3a. Along the portions of the mesh stream lines represented by $u_{j+1}\ d_{j+1}$, $u_j\ d_j$ and $u_{j-1}\ d_{j-1}$ the mainstream velocity is assumed constant, and equal to it's value at the downstream boundary. The assumed velocity profiles are detailed schematically in figure 2.3b. Along the cross-stream lines $u_{j-1}\ u_j$, $u_j\ u_{j+1}$, $d_{j-1}\ d_j$ and $d_j\ d_{j+1}$ the mainstream velocity is assumed to vary linearly with the cross-stream ordinate Ω. Schematic representations of the velocity profiles along the upstream and downstream sections of the specimen element are detailed in figures 2.3c and d respectively. Secondly, it had been postulated that when the flow element abc is small:

$$\text{a)}\quad \frac{\partial U}{\partial \Omega} \simeq \frac{dU}{d\Omega} \qquad (2.3$$

$$\text{and}\quad \text{b)}\quad \frac{\partial U}{\partial x} \simeq \frac{dU}{dx}$$

Denny-Landis derived equation 2.2, by substituting both the equalities specified in 2.3 and the assumed velocity profiles at the boundaries of the element into equation 2.1, and integrating the result over the flow element.

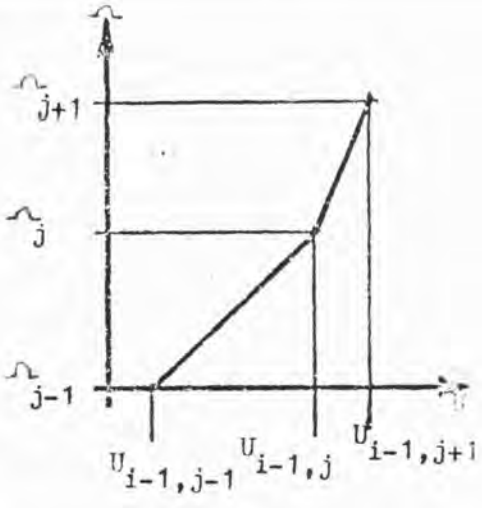

c. CROSS STREAM VELOCITY PROFILE AT THE UPSTREAM BOUNDARY

(x_{i-1})

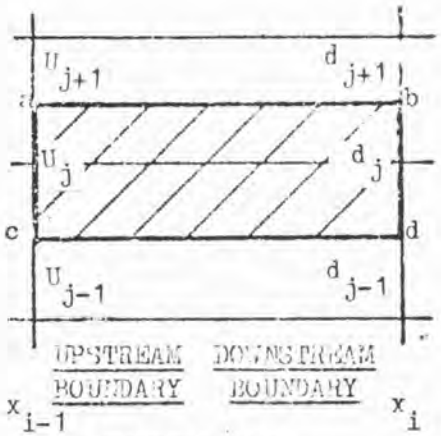

a. TYPICAL FLOW ELEMENT

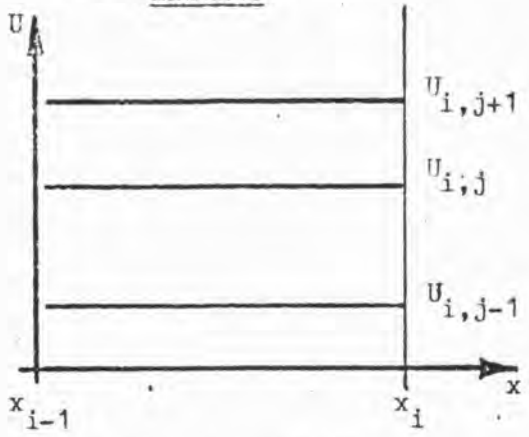

b. STREAM-WISE VELOCITY PROFILE BETWEEN x_{i-1} AND x_i

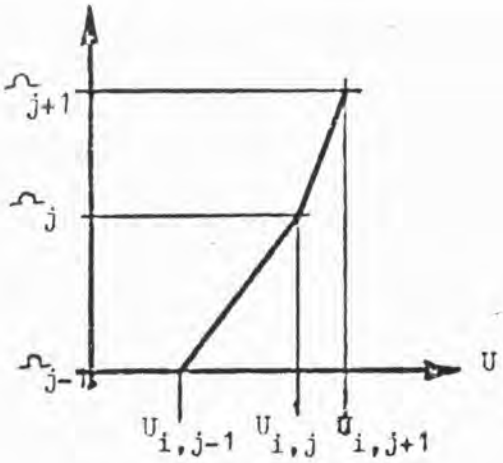

d. CROSS STREAM VELOCITY PROFILE AT THE DOWNSTREAM BOUNDARY

(x_i)

ASSUMED VELOCITY PROFILES AROUND A SPECIMEN FLOW ELEMENT

2.2b Overall Solution

The technique used to extend the limited solution of the momentum equation 2.2, to give an overall solution of conservation equation over the boundary flow, comprises two inter-related parts. Firstly, the extent of the flow situation to be simulated has to be mathematically defined. Secondly, the procedure for extending the limited solution for momentum conservation over the flow has to be developed.

The extent of the boundary flow is defined by specifying:

a) the variation of the mainstream velocity along the impervious surface, free-edge and starting cross-stream section of the flow - that is along ab, cd and ac respectively in figure 2.1,

and b) the height of the flow δ_{11} at the starting cross-stream section.

The procedure for extending the approximate solution, represented by equation 2.2, over all the specified flow is as follows. Equation 2.2 is applied to each flow element within the first cross-stream strip of the boundary flow in figure 2.1. Resulting in a set of equations of the form:

$$\sum_{j=2}^{N-1} \left(-U_{2,j} + A'_{2,j}\, U_{2,j-1} + B'_{2,j}\, U_{2,j+1} + C'_{2,j} \right) = 0$$

which are solved for $U_{2,j}$, j = 2 to N-1. The approximate solution is then applied to the elements in the second cross-stream strip; and the resulting set of equations:

$$\sum_{j=2}^{N-1} \left(U_{3,j} + A'_{3,j}\, U_{3,j-1} + B'_{3,j}\, U_{3,j+1} + C'_{3,j} \right) = 0$$

solved for $U_{3,j}$, j = 2 to N-1. This procedure is continued, cross-stream strip by strip, until the complete boundary flow has been covered.

Appendix 3

Recommended Modelling Technique

The development of an accurate, widely-applicable and economical method of solving the conservation equations for a boundary flow has been the central theme of this thesis. A computer programme is a necessary link between the formal description of the mathematical method in chapter four and the practically useful predictions in terms of numbers. The computer programme that was used for making these predictions is detailed in this appendix.

The programme is written in Fortran IV and was run on an Elliot 4130 computer. The program is so designed that the partial differential equation for velocity U will always be solved; in addition, any desired number of conservation equations, of the type 6.2 and 6.3, can be solved for other dependent variables. The programme handles all the dependent variables and other auxiliary quantities in a destructive way; i.e the values in the computers store at any time refer to only one value of x, and these are destroyed and replaced by the values for the next down-stream station as the calculation proceeds. This reduces the necessary storage space required by the computer program.

The subroutines in the present programme can be divided into four groups. Those of the first group are valid for flow problems of all types. In the second group of subroutines are entered statements about the type of flow: laminar, turbulent, etc. (In section 3 , where the listing of the whole programme is given, we shall present, for the second group, subroutines for a turbulent flow using the physical properties as defined in chapter 8. Preparation of corresponding subroutines for laminar flow or for turbulent flow with a different hypothesis can present few difficulties.) The third group of subroutines provides information

relating to a particular flow situation-here are entered the initial boundary conditions, the fluid properties, and other data for the problem. Of such subroutines only examples are given. In section 2; however, a precise description will be given of what functions they must perform, so that the user should have no difficulty in either tailoring the sample subroutines to his own needs or writing new ones. In the last group of subroutines the procedures used to control the interactive scheme are briefly discussed. However, we shall concentrate more on detailing the ideas behind the subroutines than detailing the Fortran text used, because most of the language used was only suitable for the Elliot 4130 computer which is now obsolete.

3.1 Conventions and Symbols

Before going into the finer details of the various subroutines a general familiarity with the programme can be developed by studying the different conventions and symbols used therein. The following sub-sections have been written with this in mind. Fortran symbols are printed in Roman type.

3.1a Subscripts for the grid lines.

The numbering of the mesh stream lines is slightly different to that used in chapters 4 to 9; with the subscripts 1 and NPS used to represent the impervious surface and free-edge.

3.1b Dependent Variables

The array U(I) is used for velocities at grid points. The dependent variables of the other conservation equations are stored in the form F(J,I). Where J denotes the serial number of the dependent variable, and I denotes the serial number of the mesh stream lines. J can vary from 1 to NPH, where NPH - the number of equation - is given by:

$$NPH = NEQ - 1, \qquad (3.1$$

where NEQ is the number of partial differential equations to be solved, one of which is always for momentum conservation.

3.1c Specifications of the type of boundary

KIN and KEX are the two numbers specifying which type streamwise boundaries the flow has. Each of these numbers can take the value 1, 2 or 3, according to whether the boundary is a surface, free-edge or a line of symmetry. KASE is a quantity derived from KIN and KEX; KASE equals 1 when at least one of the boundaries is a surface, otherwise KASE equals 2. INDI(J) and INDE(J) refer to the $\bar{\Phi}$ boundary condition at the streamwise boundaries of the flow. J stands for the serial number of the Φ equation involved. INDI(J) and INDE(J) take the values 1 or 2 according to whether the value of Φ or the corresponding flux is specified.

3.1d Effects of Radius

KRAD is the number which supplies the information regarding the inclusion or otherwise of the radia effects. When KRAD equals zero, it is an instruction to neglect the variation of radius across the boundary flow ; otherwise the radius effects are properly accounted for. This device is mainly used for the exact treatment of plane flows without making the radius infinitely large. It should be noted that KRAD = 0 suppresses the variation of radius merely across the flow ; the variation of radius in the stream direction, if it exists, is always taken into account.

3.1e List of FORTRAN symbols

Other symbols do not need much explanation. Given below is the list of all important FORTRAN symbols used in the programme and wherever possible their algebraic equivalents. Where the symbols has a close connection with a particular subroutine, the name of that subroutine is also given.

FORTRAN symbol	*Meaning*	*Related subroutine*
A (J, I)	A	COEFF
AJE (J)	$J_{ux,\ast\ast}$	WALL
AJI (J)	$J_{ux,\ast'}$	WALL
AJFS	Φ_S or J_{ux}	FBC
AK	K	
AL	l	VEFF
ALMG	λ	VEFF, ENTRN
AM	$\bar{m}_S^-$	MASS
AME	m^-	
AMI	m^+	
AMU	μ (reference value)	VISCO
AU (I)	A''	COEFF, SLIP
B (J, I)	B^+	
BU (I)	B'	COEFF
C (J, I)	C^0	
CS		SOURCE
CSALFA	$\cos\alpha$	RAD, READY
CU (I)	C	COEFF
DEN	ρ (reference value)	DENSTY
DPDX	dp/dx	PRE
DX	$(x_D - x_U)$	MAIN, COEFF
EMU	μ_{eff}	VEFF, COEFF
F (J, I)	Φ	
FR	fraction in the definition of y_{ϕ_1}	LENGTH
G1(I), G2(I), G3(I)	g_1, g_2, g_3	COEFF
GAMA (J)	γ	WALL
IND	equals 1 or 2 according to whether Φ_S or J_{ux} is specified	FBC
INDE (J)	IND for the E boundary	
INDI (J)	IND for the I boundary	
INTG	number of integrations performed	MAIN

FORTRAN symbol	*Meaning*	*Related subroutine*
KASE	equals 1 or 2 according to whether or not a wall boundary exists	
KEX	specifies the type of the E boundary	
KIN	specifies the type of the I boundary	
KRAD	when equals zero, suppresses the cross-stream radius effects	READY
N	N	BEGIN
NEQ	number of partial differential equations to be solved	
NP1	$N+1$	
NP2	$N-2$	
NP3	$N+3$	
NPH	number of Φ equations	
OM (I)		
P1, P2, P3	P_1, P_2, P_3	COEFF
PEI	$(\psi_E - \psi_I)_U$	
PR, PR (J)	σ	COEFF
PREF (J)	σ_{ref}, σ_t	COEFF
RHO (I)	ρ	DENSTY
R (I)	r	
R1	$r_{\ell 1}$	RAD
TAUE	$\tau_{\ell N}$	OUT
TAUI	$\tau_{I 2}$	OUT
U (I)	u	
UMAX	maximum value of u	LENGTH
UMIN	minimum value of u	LENGTH
X	x	FBC, RAD
XD	x_D	MAIN
XL	value of x at which computation is to be terminated	MAIN
XP	value of x previous to x_U	MAIN
XU	x_U	MAIN
Y (I)	y	READY
YEM	y for a point near the E boundary	LENGTH
YIP	y for a point near the I boundary	LENGTH
YL	y_I	VEFF, LENGTH

3.2 Description of the subroutines

Figure 3.1 shows the flow diagram of the computer programme. It indicates the sequence of operations, the inter-connexions of various parts of the programme and their functions in brief. This will serve as the common map that links the individual subroutines which are described in this section. (Listing of all the subroutines are given in section 3. The more important FORTRAN symbols used below have been defined in section 1). In this section brief descriptions of these subroutines will be presented.

3.2a Subroutines of general validity

MAIN

Strictly speaking, the main programme cannot be called a 'subroutine' according to FORTRAN terminology; however, this point is of little significance for the present purposes. The main programme starts the computation and controls the sequence of operations. The choice of forward step is made here. The listing given in section 3 implies the use of equation 4.5 in chapter 4, i.e. of a step size which depends upon the entrainment rate. The listing also contains a stopping condition which terminates the integration when x exeeds a predetermined value XL.

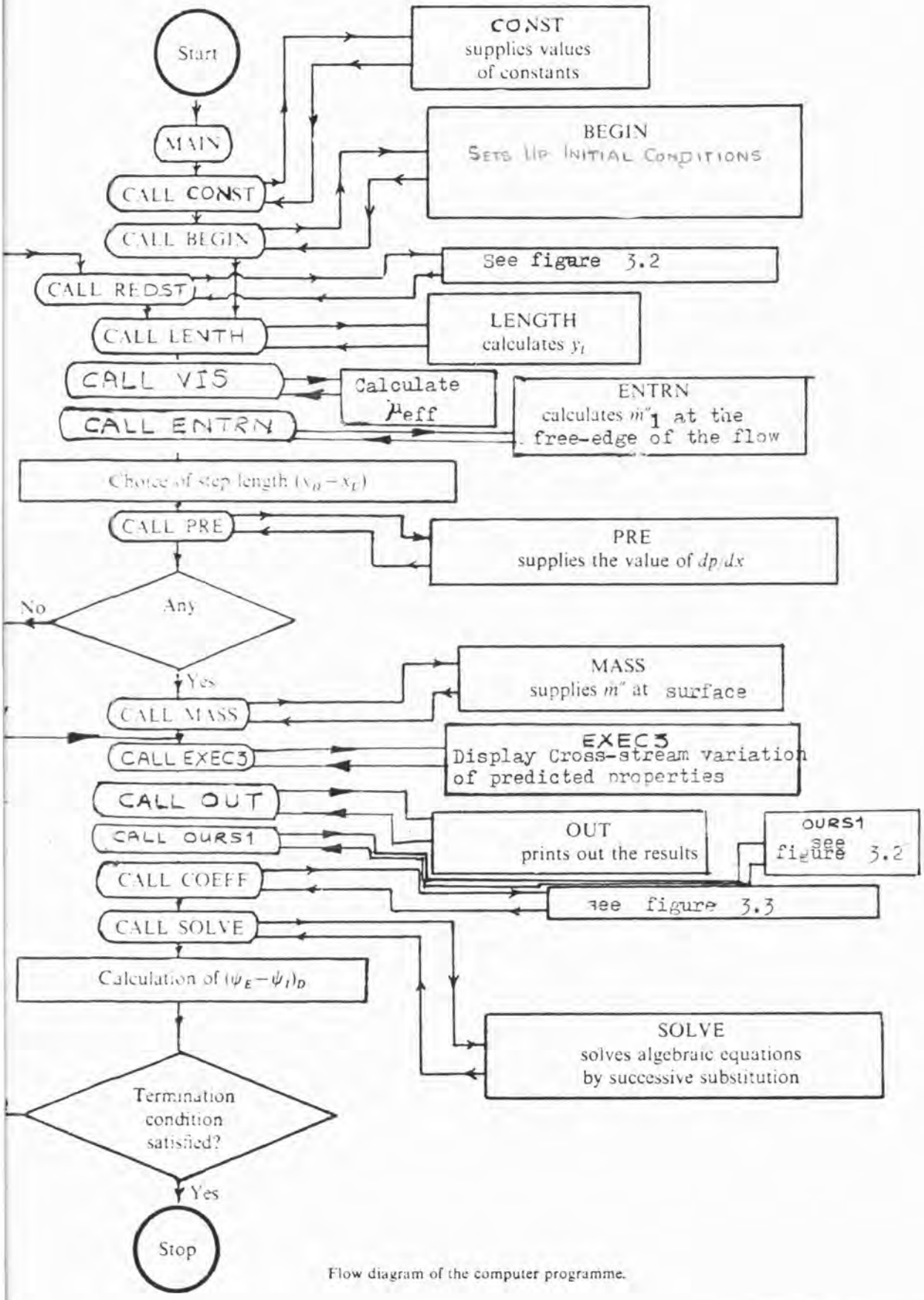

Flow diagram of the computer programme.

FIGURE 3.1

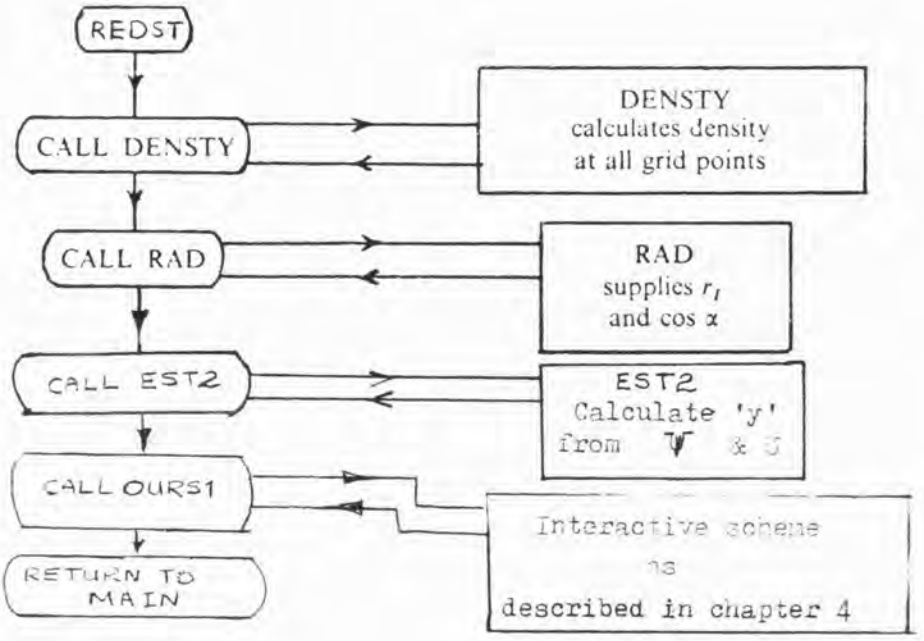

FIGURE 3.2

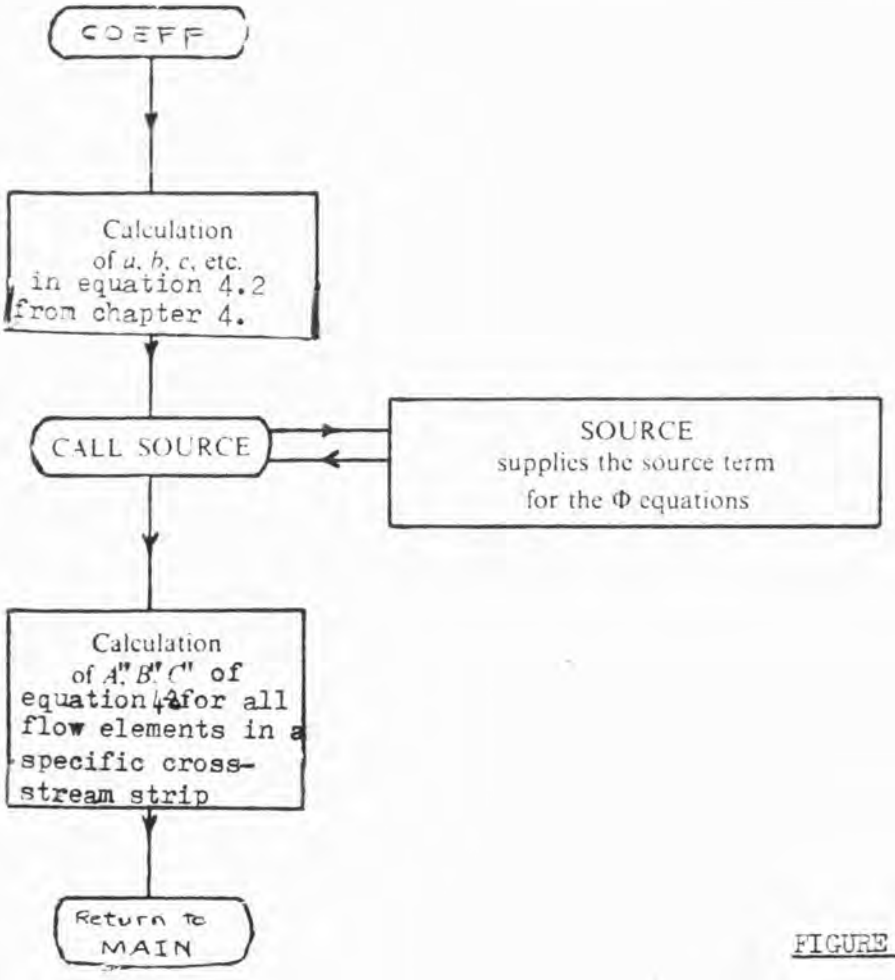

FIGURE 3.3

COEFF

The subroutine COEFF can be described as the heart of the programme. Its purpose is to provide the coefficients A",B"and C" of equation 4.8 for all conservation equations at all intermediate grid points. During this assembling process, various registers are used as temporary storage space.

SOLVE

The subroutine SOLVE performs the mathematical operation of solving simultaneous equations of the type 4.9 . The calling statement is:

CALL SOLVE (A,B,C,F,NP3) ,

where A,B,C are the arrays for the given coefficients, F is the array for the values of Φ , and NP3 is the size of the array F which includes the known values at the boundaries.

REDST

After each streamwise step we know the values of U and other Φ's for known values of ψ. The subroutine through ESTP2 then undertakes the calculation of the corresponding normal distance y, and radius r, for every grid point. REDST needs the value of density ρ at all grid points and the specification of r_1 and α ; these obtained from subroutines DENSITY and RAD.

3.2b Subroutines where the physical hypotheses enter

VEFF

The subroutine VEFF is intended to supply the effective viscosity μ_{eff} according to the hypthesis used. The calling statement is:

CALL VEFF (I,I + 1, EMU)

which indicates that the required μ_{eff} value, EMU, is to be

evaluated midway between the mesh stream lines designated I and I+1.

ENTRN

The evaluation of the entrainment rates $\dot{m}''_{FE}$ at free-edge is done in subroutine ENTRN according to specified formulae. For boundary layer equation 4.6 was used to estimate entrainment, and for radial wall jet equation 6.6.

3.2c Subroutines which specify a particular problem

When the conservation equations are written in the form 4.8 , the actual expression for the source term R is the main feature that distinguishes one equation from the other. To supply the source terms for all $\bar{\Phi}$ equations is the purpose of the subroutine SOURCE. The calling statement is:

CALL SOURCE (J,I,CS,DS) ,

where J is the serial number of the $\bar{\Phi}$ equation; I refers to the mesh streamline at which source term is required, and CS and DS are the output of this subroutine.

In section three, two examples of this subroutine are presented. One of them puts the source term equal to zero; this is appropriate when Φ stands for m_j with R_j zero. The other example gives the source term when Φ stands for h.

CONST

The values of different constants, including some fluid properties mixing length constants etc., are given in the user subroutine CONST. There are various ways of supplying these numbers. It is good practise to give all the necessary constants in this subroutine alone and to use the corresponding symbols in other subroutines. Those constants which are functions of others are also computed here.

DENSTY

The purpose of the DENSTY subroutine is to evaluate the density at all the grid points as a function of the dependent variables. Actual expressions will vary according to the type of the problem and the nature of the fluid. The symbol DEN, the value of which may be given in the subroutine CONST, can be conveniently used as a reference velue of density. The example given in section 3 makes the density inversely proportional to the absolute temperature; there F (1,I) is supposed to stand for the absolute temperature and DEN for the density at the free-edge of the flow.

VISCO

The function subprogramme VISCO(I) is employed to obtain the molecular viscosity at any grid point I. In turbulent flow situations, the use of this function is mainly near a wall. For laminar flows, more extensive use can be made. The example in section 3 gives the laminar viscosity as a function of the absolute temperature F (1,I), when AMU represents the viscosity at the free-edge of the flow.

RAD

The subroutine RAD supplies the geometrical information regarding the problem. The task of this subroutine is to give the values of r_1 and $\cos\alpha$ for a given value of x. The calling statement is:

CALL RAD (X,R1,CSALFA)

For plane flows, the user is advised to set R1 to a constant such as 1. It is not necessary to make R1 very large and it must not be put to zero in this case. The value of R1 for plane flows has no physical significance; it is a dummy value.

Two examples of this subroutine will be given in section 3. The first one is applicable to plane flows; the second one is for a radial wall jet.

PRE 1 and PRE 2

The specification of the pressure gradient is through the subroutine PRE 1 or PRE 2. The calling statement is:

CALL PRE I (XU,XD,DPDX) ,

with I either 1 or 2. The value of pressure gradient DPDX is the output, while XU and XD are the two given values of x between which the pressure-gradient value is required. In subroutine PRE 1, DPDX is set to zero, and in PRE 2, DPDX is calculated with Bernoullis equation.

MASS

When a surface exists as a boundary of the flow the mass transfer through it should be supplied, this is done in the subroutine MASS. The calling statemnt is:

CALL MASS (XU , XD, AM) ,

where XU and XD are two given values of x. The subroutine supplies the mass transfer rate AM between XU and XD. The example in section 3 is a simple version of this subroutine used for an impervious surface.

FBC

At a surface the velocity U (relative to the surface) is always zero; however, we need to know the boundary conditions for other dependent variables. These are supplied by the subroutine

FBC. The calling statement is:

CALL FBC (X,J,IND,AJFS)

Here X and J are the given quantities which stand the distance x and the serial number of the $\bar{\Phi}$ equation under consideration. IND and AJFS are the outputs. IND will be 1 or 2 according to whether the value of $\bar{\Phi}$ or the corresponding flux is specified. The register AJFS will then contain that specified value. Two examples are given in section 3: the first one specifies $F(1,I)$ as a linear function of x; while the other gives a uniform flux at the wall.

When no surface exists, the subroutines MASS and FBC are not called.

BEGIN

The initial profiles and other auxiliary quantities are specified in subroutine BEGIN. Although the user can arrange to specify the initial profiles in any way he desires.

In this subroutine, it is necessary to specify: the values of KRAD, NEQ, KIN, KEX, N; the initial value of x; the initial u~y profiles and the corresponding profiles of other dependent variables. The user should note that this subroutine is a convenient place to read in all the data for the problem including the boundary conditions, property values etc. These quantities are transferred to their respective subroutines via COMMON statements.

OUT

The instructions for printing out the results are contained in the OUT subroutine. The rest of the programme makes no demand on this subroutine, except that of freedom of interferance, and therefore the user has complete liberty to make arrangements here to print out any information he desires. The integar variable INTG, which counts the number of integrations, can be profitably used to obtain the print-out after a desired number of integrations. In the example in section 3, the value of x and the corresponding velocity and temperature profiles are arranged to be printed out after every 5 integrations or at specified values of x.

EST2

At each streamwise step EST2 calculates the normal distance y for every grid point.

3.2d Subroutines Pertaining to the Interactive Scheme

It would be wasteful to go into the finer details of the subroutines pertaining to the interactive scheme, because they were specifically tailored for the peripherals and software packages available on an Elliot 4130. In this sub-section we will briefly describe the two major interactive subroutines. OURS1 and EXEC3.

OURS1

This subroutine is used to manipulate the mesh network of the modelling technique, as described in chapter four. In the text OURS1 was only used at the starting cross-stream section, however, in the computer program it can be used at any cross-stream section.

EXEC3

This subroutine displays on the calligraphic screen the predicted results in the form of $\bar{f}$ $\bar{\theta}$ or y.

3.3 Fortran Program

```
      INTEGER DISP(6000)
      CALL RESET (DISP,6000,100)
       CALL   MP1
      STOP
        END
      SEGMENT

      SUBROUTINE    BEGIN
      COMMON /GEN/PEL,AMI,AME,DPDX,PREF(2),PR(2),P(2),DEN,AMU,XU,XD ,XP,
     1XL,DX,INFO,CSALFA,MMG
     1/I/N,NP1,NP2,NP3,NEQ,NPH,KEX,KIN,KAGE,KRAD
     1/B/BETA,GAMA(2),TAUI,TAUE,AJI(2),AJE(2),INDI(2),INDE(2)
     1/V/U(43),E(2,43),R(43),RHO(43),OM(43),Y(43)
     1 /NRR/ COF(10,42)
     1/RZN/ APP(43)
     1  /EQUPE OMO(43)
     1/LO/PI1,RI1,TI1,LT1,TU1
     1/L10/L11
       PROBLEM    SPEC..
      READY  QQQQQQQ
       RI1=1  FOR  A  PLANE   FLOW.
       RI1=2  FOR  A  WALL  JET.
      RI1=3  FOR A  AxISYMMETRIC  MIXING  LAYER  &  JET.
       QQQQQQ
      TI1=1  A  STEP   WALL   TEMP.,  IS  GIVEN
      TI1=2  UNIFORM  FLUX  IS  GIVEN
```

```
      KRAD=20

      NEQ=5

  READ (7,5589) (KIN,KEX,LT1,TU1)
  WRITE (2,5675) (KIN,KEX,LT1,TU1)
  N=40
  RI1=1.0
  ------------------------------------------------------------
    INDI(1)=1
    INDI(2)=1
    INDE(1)=1
    INDE(2)=1
  KASE=2
  IF (KIN.EQ.1.OR.KEX.EQ.1)      KASE=1
  NPH=NEQ-1
  NP1=N+1
  NP2=N+2
  NP3=N+3
  INITIAL   VEL.,   VALUES.
   TRY   TO   PUT   IN   PRRV.
  IF  (LT1.NE.1)   GO   TO  250

   US=U(NP3)
  U(1)=0.0
```

```
      Y(1)=0.0

      ZMU=AMU/DEN
      FN=1.0/7.0
      IF (TU1.EQ. 1.0) DELT=0.37*XU*((ZMU/(US*XU))**0.2)
      IF (LT1.EQ. 1) DELT=5.83*(SQRT(ZMU*XU/US))

      WRITE (2,721) (XU,ZMU,US,DELT)
1     FORMAT (6HCHECK2,4E10.3)

      NPZ=NP5

      Y(1)=0.0
      DO 200 I11=2,NP3
      Z=Y(I11)/Y(NP3)
      IF (TU1.EQ. 1.0) U(I1)=US*((Z)**FN)
      IF (LT1.EQ. 1) U(I11)=S*Z
      IF (LT1.EQ. 1) U(I11)=US*(1.5*Z-0.5*(Z**3.0))
0 CONTINUE
0 CONTINUE
  CALC., OF SLIP VEL., &DISTANCES.
  BETA=0.143
  GO TO (71,72,73), KIN
1   CONTINUE
  GO TO 74
2 U11=U(1)*U(1)
```

```
      U13=U(1)*U(3)
      U33=U(3)*U(3)
      SQ=84.0*U11-12.*U13+9.0*U33
       U(2)=(16.0*U11-4.0*U13+U33)/(2.0*(U(1)+U(3))+SQRT(SQ))
      Y(2)=Y(3)*(U(2)+U(3)-2.0*U(1))*0.5/(U(2)+U(3)+U(1))
      GO   TO   74
3     IF  (KRAD.NE.0)     GO  TO 89
      U(2)=(4.0*U(1)-U(3))/3.0
      Y(2)=0.0
      GO  TO  74
9     U(2)=U(1)
      Y(2)=Y(3)/3.0
4       GO   TO     ( 75,76,77),    KEX
5       CONTINUE
       GO  TO  78
6       CONTINUE
      GO   TO   78
7     U(NP2)=(4.0*U(NP3)-U(NP1))/3.0
      Y(NP2)=Y(NP2)
8     CONTINUE
      IF   (NEQ.EQ.1)   GO  TO  45
      DO   83   J=1,NPH
      PUT   IN   HERE   THE    OTHER   INITIAL   PRFLS.,<
      IF (L11.NE.1) GO TO 251
       FCP=0.24
       FCP=FCP*778.161
       F(1,1)=65.0*FCP
       F(1,NP3)=60.0*FCP+U(NP3)*U(NP3)/2.0
       F(2,1)=0.0
       F(2,NP3)=0.0
         DO 252   I11=1,NP3
        IF (J.NE. 1) GO TO 23
          Z=Y(I11)/Y(NP3)
```

```
      F(J,I11)=FCP*F(J,I11)+U(I11)*U(I11)/2.0
        GO TO 24
23      F(J,I11)=0.
24    CONTINUE
52  CONTINUE
51  CONTINUE
      L11 IS ACOUNTING TERM TO ENABLE THE PROFILES TO BE SKIPPED AFTER
     1RUN.
      GAMA(J)=0.143
      GO   TO    (81,82,83),KIN
81      CONTINUE
        GO    TO     84
82      G=(U(2)+U(3)-8.0*U(1))/(5.0*(U(2)+U(3))+8.0*U(1))
        GF=(1.0-PREF(J))/(1.0+PREF(J))
      GF=(G+GF)/(1.0+G*GF)
      F(J,2)=F(J,3)*GF+(1.0-GF)*F(J,1)
        GO    TO     84
83    F(J,2)=F(J,1)
      IF   (KRAD.EQ.0)F(J,2)=(4.0*F(J,1)-F(J,3))/3.0
84      GO   TO    (85,86,87),KEX
85      CONTINUE
      GO   TO    88
86  G=(U(NP2)+U(NP1)-8.0*U(NP3))/(5.0*(U(NP2+U(NP1))+8.0*U(NP3))
      GF=(1.0-PREF(J))/(1.0+PREF(J))
      GF=(G+GF)/(1.0+G*GF)
      F(J,NP2)=F(J,NP1)*GF+(1.0-GF)*F(J,NP3)
       GO   TO   88
87  F(J,NP2)=(4.0*F(J,NP3)-F(J,NP1))/3.0
88  CONTINUE
5   CONTINUE
      L11=L11+1
      CALL    DENS
```

```
      IF (RI1.EQ. 1.) CALL RAD1 (XU,R(1),CSALFA)
      IF (RI1.EQ. 2.) CALL RAD2 (XU,R(1),CSALFA)
      IF (CSALFA.EQ.0.OR.KRAD.EQ.0)    GO    TO    27
      DO    28    I=2,NP3
      R(I)=R(1)+Y(I)*CSALFA
   28 CONTINUE
      GO  TO    29
   27 DO    30   I=2,NP3
      R(I)=R(1)
   30 CONTINUE
   29    CONTINUE
      CALC; OF THE OMEGA VALUES
         OM(1)=0.0
         DO  49   I=2,NP3
      OM(I)=OM(I-1)+0.5*(RHO(I)*U(I)*R(I)+RHO(I-1)*U(I-1)*R(I-1))*(Y(I)-
     1Y(I-1))
   49 CONTINUE
         WRITE (2,1112)  (OM(I),I=1,NP3)
      PEI=OM(NP3)
      WRITE (2,778) (PEI)
   778   FORMAT (E10.3)
         DO 59 I=1,NP3
      OM(I)=OM(I)/PEI
   59 CONTINUE
         WRITE (2,1112)  (OM(I),I=1,NP3)
   112   FORMAT (10E10.3)
      IF (NEQ.EQ.1)   RETURN
      DO   69   J=1,NPH
      IF (KEX.EQ.1)  INDE(J)=1
      IF (KIN.EQ.1)  INDI(J)=1
   69 CONTINUE
         OM(1)=0.0
```

```
      CALL OURS1(1,1)
      RETURN
    1 FORMAT (10E10.3)
    2 FORMAT (3I5,F10.0)
    3 FORMAT (5HINPUT,3I10,E10.3)
      END
      SUBROUTINE    CONST
      COMMON /GEN/PEI,AMI,AME,DPDX,PREF(2),PR(2),P(2),DEN,AMU,XU,XD ,XP,
     1XL,DX,INTG,CSALFA,MMG
     1/LO/PI1,RI1,FI1,ET1,TU1
     1/L10/L11
      COMMON/L/AK,ALMG
     1/L1/YL,UMAX,UMIN,FR,YIP,YEM
      AK=0.435
      ALMG=0.09
      FR=0.01
      PREF(1)=0.7
      PREF(2)=0.7
      PR(1)=0.7
      PRRAT=PR(1)/PREF(1)
      PR(2)=0.7
      P(1)=3.68*(PRRAT-1.0)*PRRAT**(-0.25)
      P(2)=P(1)
      DEN=0.075
      AMU=0.00001196
      RETURN
      END

      SUBROUTINE REDST
      DIMENSION COR (2,43), B(10),B1(10) ,STOR(43)
      INTEGER ACTION
      COMMON /GEN/PEI,AMI,AME,DPDX,PREF(2),PR(2),P(2),DEN,AMU,XU,XD ,XP,
```

```
      T/L/OM/INTG/CSALFA/MMG
      T/I/N,NP1,NP2,NP3,NEG,NPH,KEX,KIN,KASE,KRAD
      T/B/BETA,GAMA(2),TAUI,TAUE,AJI(2),AJE(2),INDI(2),INDE(2)
      T/V/U(43),F(2,43),R(43),RHO(43),OM(43),Y(43)
     1 /NRRE COF(10,42)
      T/RZN/ APP(43)
     1  /GURE GMO(43)
      T/LO/PI1,RI1,TI1,LI1,TU1
      T/L10/L11
        WRITE (2,505)((Y(I),U(I),F(1,I),F(2,I),RHO(I),R(I),APP(I),OM(I))
     1,I=1,NP3)

        CALL DEN
        US=U(NP3)
      CALL SPLN (OM,APP,NP3)
        CALE EST2
        IF (RI1.EQ. 1.) CALL RAD1 (XU,R(1),CSALFA)
        IF (RI1.EQ. 2) CALL RAD2 (XU,R(1),CSALFA)
        WRITE (2,505)((Y(I),U(I),F(1,I),F(2,I),RHO(I),R(I),APP(I),OM(I))
     1,I=1,NP3)
    5   FORMAT (8E11.3)
        IF (ICYC.GT.1) RETURN
        CALL EXEC3(1,11,OM,U,NP3)
        CALL DELETE (600)
        CALL DELETE (601)
        CALL DELETE (602)
        RETURN
        FORMAT (4F10.0)
      FORMAT (I5)
      RETURN
      END
        SEGMENT
        SUBROUTINE   MASS   (XU,XD,AM)
        AM=3.0
        RETURN
        END
```

```
      SUBROUTINE COEFF
      COMMON /GEN/PEI,AMI,AME,DPDX,PREF(2),PR(2),P(2),DEN,AMU,XU,XD ,XP,
     1ZL,DX,INTG,CSALFA,MMG
     1/I/N,NP1,NP2,NP3,NEQ,NPH,KEX,KIN,KASE,KRAD
     1/B/BETA,GAMA(2),TAUI,TAUE,AJI(2),AJE(2),INDI(2),INDE(2)
     1/V/U(43),E(2,43),R(43),RHO(43),OM(43),Y(43)
     1/C/SC(43),AU(43),BU(43),CU(43),A(2,43),B(2,43),C(2,43)
     1 /NRP/ COF(10,42)
     1/LO/PI1,RI1,TI1,LT1,TU1
     1 /RZ/APP(43)
     1 /NEW15/  MP(43)
      COMMON/L/AK,ALMG
      DIMENSION G1(43),G2(43),G3(43),D(2,43),S1(43),S2(43),S3(43)
      CALC  OF   SMALL    C.>.
       IPRINT=1
       DO 98 I=1,NP2
      RHP=0.5*(RHO(I)+RHO(I+1))
      RAP=0.5*(R(I)+R(I+1))
      UAP=0.5*(U(U1))
      VAP=0.5*(EMUP(I)+EMUP(I+1))
      SC(I)=RHP*UAP*RAP*RAP*VAP/(PEI*PEI)
```

```
      WD=OM(I)
      WDDP=(OM(I+1)+OM(I))/2.0
      A1=0.0
      DO 6891  J=2,MMG
      A1=A1+(J-1)*COF(J,I)*((WDDP-WD)**(J-2))
 1    CONTINUE
        SC(I)=SC(I)/A1
      IF (IPRINT.NE. 1) RTE (2,6555)  (HOLD,SC(I))
 5    FORMAT  (5H TOUT,2E11.4)
 9    CONTINUE
*************************************************************************
PRINT=5, TO OBTAIN THE NEW SC , NOTE IT DOES-NOT WORK.
      .R.     5. JUNE.
      IF (IPRINT.NE. 5) GO TO 6666
*************************************************************************
       DO  99 I=1,NP2
      CALL VEFF  (I,I+1,EMU)
   CUU=.25*EMU/(PEI*PEI))*((RHO(I+1)+RHO(I)*(UI+1)+U(I))*(((R(I
  1 +1)+R(I))/2.0)**2.0)-4.0*RHO(I)*U(I)*R(I)*R(I))
      WD=OM(I)
      WDDP=(OM(I+1)+OM(I))/2.0
      WDM=OM(I-1)
      WDDM=(OM(I)+OM(I-1))/2.0
      A1=0.0
      DO  6821     J=2,MMG
      A1=A1+(J-1)*CF(J,I*((WDDP-WD)*(J-))
 1     CONTINUE
      SC(I)=CUUP/AI
 2     CONTINUE
 5     CONTIUE
  THE   CONVECTION   TERM.
      THE FORMULAE DX=XD-XU WAS REMOVED  BECAUSE IT SEEMED NOT TO FUNCT
      SA=R(1)*AMI/PEI
       SB=(R(NP3)*AME-R(1)*AMI)/PEI
```

```
**********************************************************************
HE ORIGNAL SPDING PANTANKER CEFFICITS,USED TO TEST THE NEW E.

      IF (IPRINT .EQ. 1) GO TO 858
    OMD=OM(I+1)-OM(I-1)
    P2=0.25/DX
    P3=P2/OMD
    P1=(OM(I+1)-OM(I))*P3
    P3=(OM(I)-OM(I-1))*P3
    P2=3.0*P2
    Q=SA/OMD
     R2=-SB*0.25
     R3=R2/OMD
     R1=(OM(I+1)+3.0*OM(I))*R3
    R1=-R1
    R3=(OM(I-1)+3.0*OM(I))*R3
      IF (IPRINT.NE. 1) WRITE (2,223) (P1,P2,P3,Q,Q,R1,R2,R3)
23   FORMAT    (4E11.4,11H      0.0    ,4E11.4)
  **********************************************************************
58     CONTINUE
**********************************************************************

    OMD=OM(I+1)-OM(I-1)
      WDP1=0.5*(OM(I+1)+OM(I))
      WDM1=0.5*(OM(I)+OM(I-1))
      OMD=OM(I+1)-OM(I-1)
      WP=OM(I+1)-OM(I)
      WDP=0.5*WP
      WM=OM(I)-OM(I-1)
      WDM=0.5*WM
********** ********** ********** ********** ********** ****
      IF (IPRINT.EQ. 1) GO TO 825
```

```
      APP1=APP1*APP1/8.
      APP2=(3./8.)*((OM(I)-OM(I-1))**2.0)
      APQ1=(OM(I+1)-OM(I))/2.0
      APQ2=(OM(I)-OM(I-1))/2.0
      WRITE (2,827)   (APP1,APP2,APQ1,APQ2)
*************************************************************************
5     CONTINUE
      APP1=0.
      APP2=0.
      APQ1=0.
      APQ2=0.
      APZ1=0.
      APZ2=0.
      DO 10 L=2,MMG
      APP1=APP1+(L-1)*COF(L,I  )*((WDP)**L)/L
      APP2=APP2+((L-1)  )*COF(L,I-1)*(WM**L-WDM**L)  /L
      APQ1=APQ1+COF(L,I  )*(WDP**(L-1))
      APQ2=APQ2+COF(L,I-1)*(WM**(L-1)-WDM**(L-1))
0     CONTINUE
      IF (IPRINT.NE. 1) WRITE (2,827) (APP1,APP2,APQ1,APQ2)
7     FORMAT (4E11.4)
************ ***************** ******************* ***********.*** ****
      DO 39 L=1,MMG
      APZ1=APZ1+COF(L,I  )*(WDP**L)/L
      APZ2=APZ2+(1./L)*COF(L,I-1)*(WM**L-WDM**L)
9     CONTINUE
      P1=2.0*APP1/(DX*OMD*WP)
      P2=(2.0/(DX*OMD))*(APQ1-APP1/WP+APP2/WM)
      P3=(2.0/(DX*OMD))*(APQ2-APP2/WM)
      Z1=SA/OMD
      Z2=0.
      Z3=-Z1
```

```
      R3=R1*(APZ2/WM)
      R3=-R3
      R1=R1*(APZ1/WP)
      IF (IPRINT.NE. 1) WRITE (2,821)  (P1,P2,P3,Z1,Z2,Z3,R1,R2,R3)
821   FORMAT  (9E11.4)
      G1(I)=P1+Z1+R1
      G2(I)=P2+Z2+R2
      G3(I)=P3+R3+Z3
      CU(I)=-P1*U(I+1)-P2*U(I)-P3*U(I-1)
      AU(I)=2.0/DM(I)
      BU(I)=SC(I-1)*AU(I)/(DM(I)-DM(I-1))
      AU(I)=SC(I)*AU(I)/(DM(I+1)-DM(I))
      IF (NEQ.EQ.1)   GO   TO  33
      DO   34   J=1,NPH
      C(J,I)=-P1*F(J,I+1)-P2*F(J,I)-P3*F(J,I-1)
      CALL    SORS  (J,I,CS,D(J,I))
      C(J,I)=-C(J,I)+CS-F(J,I)*D(J,I)
      A(J,I)=AU(I)/PREF(J)
      B(J,I)=BU(I)/PREF(J)
34    CONTINUE
      SOURCE   TERM   FOR  THE   VEL.,   EQUN...
33    CONTINUE
      S1(I)=DPDX*DX
      IF(S1(I).NE.0.0) GO TO 412
      S1(I)=0.0
      S2(I)=0.0
      S3(I)=0.0
      CU(I)=-CU(I)
      GO TO 417
412   CONTINUE
      S2(I)=P2*S1(I)/(RHO(I)*U(I))
```

```
      S3(I)=S2(I)
      IF (I.GE. 3)  S3(I)=P3*S1(I)/(RHO(I-1)*U(I-1))
      S1(I)=P1*S1(I)/(RHO(I+1)*U(I+1))
      CU(I)=-CU(I)-2.0*(S1(I)+S2(I)+S3(I))
      S1(I)=S1(I)/U(I+1)
      S2(I)=S2(I)/U(I)
       IF (I.EQ.2)   S3(I)=S2(I)
      IF (I.EQ. 3)  S3(I)=S3(I)/U(I-1)
2       CONTINUE
21 CONTINUE
      COEFF.,   IN   THE   FINAL   FORM.
         DO 91 I=2,NP2
      RL=1.0/(G2(I)+AU(I)+BU(I)-S2(I))
      AU(I)=(AU(I)+S1(I)-G1(I))*RL
      BU(I)=(BU(I)+S3(I)-G3(I))*RL
      CU(I)=CU(I)*RL
91 CONTINUE
      IF  (NEQ.EQ.1)   GO   TO   76
      DO   92   J=1,NPH
       DO 92 I=2,NP2
       RL=1.0/(G2(I)+A(J,I)+B(J,I)-G(J,I))
      A(J,I)=(A(J,I)-G1(I))*RL
      B(J,I)=(B(J,I)-G3(I))*RL
      C(J,I)=C(J,I)*RL
92 CONTINUE
76    CONTINUE
      RETURN
      END

      SUBROUTINE    LENTH
      COMMON /GEN/PEI,AMI,AME,DPDX,PREF(2),PR(2),P(2),DEN,AMU,XU,XD ,XP,
     1XL,DX,INTG,CSALFA,MMG
     1/V/U(43),E(2,43),R(43),RHO(43),OM(43),Y(43)
```

```
      1/I/N,NP1,NP2,NP3,NEQ,NPH,KEX,KIN,KASE,KRAD
      1/L1/YL,UMAX,UMIN,FR,YIP,YEM
      1/LG/PI1,EI1,TI1,LT1,TU1
        IF (LT1.EQ. 1) RETURN
      SEARCH   FOR  THE   MAX.,& MIN  VEL.,.
C     UMAX=U(1)
      UMIN=U(1)
      DO   41  J=3,NP3
      IF  (J.EQ.NP2)   GO  TO  41
      IF  (U(J).GT.UMAX)     UMAX=U(J)
       IF  (U(J).LT.UMIN)     UMIN=U(J)
41  CONTINUE
       DIF=ABS((UMAX-UMIN)*FR)
      SEARCH     NEAR    THE     I    BOUNDARY
      IF (KIN.NE.2)   GO  TO  43
      U21=ABS(0.5*(U(2)+U(3))-U(1))
      IF  (U21.LT.DIF)   GO   TO 47
      YIP=SQRT(DIF/U21)*(Y(2)+Y(3))*0.5
      GO  TO  44
47  J=2
48  J=J+1
      UJ1=U(J)-U(1)
       IF (ABS(UJ1).GE.DIF)   GO     TO       49
          IF (J.LE. NP3)  GO TO 111
          WRITE (2,112)
2         FORMAT  (2HL1)
          STOP
111       CONTINUE
      GO  TO   48
49  A1=1.0
      IF (UJ1.LT.0.0)     A1=-1.0
      YIP=Y(J-1)+(Y(J)-Y(J-1))*(U(1)+A1*DIF-U(J-1))/(U(J)-U(J-1))
      GO  TO  44
```

```
3   YIP=0.0
4 IF (KEX.NE.2)   GO  TO  45
  U21=ABS(0.5*(U(NP1)+U(NP2))-U(NP3))
  IF  (U21.LT.DIF)   GO  TO  50
  YEM=SQRT(DIF/U21)*(0.5*(Y(NP1)+Y(NP2))  -Y(NP3))+Y(NP3)
  GO  TO  46
0 J=NP2
1 J=J-1
  UJ1=U(J)-U(NP3)
  IF(ABS(UJ1).GE.DIF)   GO  TO  52
     IF (J.GE. 1)  GO TO 117
     WRITE (2,118)
     FORMAT (2HL2)
    STOP
7     CONTINUE
  GO  TO  51
2 A1=1.0
  IF (UJ1.LT.0.0)   A1=-1.0
  YEM=Y(J+1)+(Y(J)-Y(J+1))*(U(NP3)+A1*DIF-(U(J+1)))/(U(J)-U(J+1))
  GO  TO  46
5 YEM=Y(NP3)
6 YL=YEM-YIP
  RETURN
  END


  SUBROUTINE    ENTRN
  COMMON /GEN/PEI,AMI,AME,DPDX,PREF(2),PR(2),P(2),DEN,AMU,XU,XD ,XP,
 1XL,DX,INTG,CSALFA,MMG
 1 /NRR/ COF(10,42)
 1/LO/PI1,RI1,TI1,LT1,TU1
  COMMON/L/AK,ALMG
 1/V/U(43),F(2,43),R(43),RHO(43),OM(43),Y(43)
 1/B/BETA,GAMA(2),TAUI,TAUE,AJI(2),AJE(2),INDI(2),IND=(2)
```

```
      1/I/N,NP1,NP2,NP3,NEQ,NPH,KEX,KIN,KASE,KRAD
     1/LT/YL,UMAX,UMIN,FR,YIP,YEM
      USES   THE    MIXING   LENGTH.
       IF (LT1.EQ. 1) CALL ENTNL
       IF (LT1.EQ. 1) RETURN
      GO   TO   ( 71,72,73),KIN
    1 GO   TO   74
    2    IF (LT1.EQ. 1) AF=(VISCO(2)+VISCO(3))/2.0
         IF (TU1.EQ. 1) CALL  VEFF (2,3,AF)
         AMI=AF*(R(2)+R(3))/(R(1)*(Y(3)-Y(2)))
**** ***** ******* ********* ******** ********** ********* *********
      AMI=2.0**RHO(2)*((ALMG*YL)/(Y(2)+Y(3)))**2*ABS(U(2)+U(3)-2.E*U(1))
**** ***** ******* ********* ******** ********** ********* *********
      GO   TO    74
    3 AMI=0.0
    4 GO   TO   ( 81,82,83),KEX
    1 RETURN
    2 CONTINUE
         IF (LT1.EQ. 1) AF=(VISCO(NP2)+VISCO(NP3))/2.0
         IF (TU1.EQ. 1.0) CALL VEFF (NP2,NP3,AF)
         AME=-AF*(R(NP2)+R(NP3))/(R(NP3)*(Y(NP3)-Y(NP2)))
**** ***** ******* ********* ******** ********** ********* *********
      AME=-3.0*RHO(NP3)*((ALMG*YL)/(2.0*Y(NP3)-Y(NP2)-Y(NP1)))**2.0*ABS(
     1 U(NP1)+U(NP2)-2.0*U(NP3))
**** ***** ******* ********* ******** ********** ********* *********
      RETURN
    3 AME=0.0
      RETURN
      END

       SUBROUTINE PRET (XU,XD,DPDX)
      COMMON/PR/UGU,UGD
     1/V/U(43),F(2,43),R(43),RHO(43),OM(43),Y(43)
```

```
1/I/N,NP1,NP2,NP3,NEQ,NPH,KEX,KIN,KASE,KRAD
1/LO/PI1,RI1,TI1,LT1,TU1
1 /NEWS/ ITRB,ICYC
  IF (INTG.EQ. 3  .AND.   ICYC.EQ. 0) GO TO 500
 DPDX=(UGU+UGD)*(UGU-UGD)*0.5*RHO(NP3)/(XD-XU)
  RETURN
    DPDX=0.0
  RETURN
  END

 SUBROUTINE   PRE2  (XU,XD,DPDX)
 COMMON/PR/UGU,UGD
1/V/U(43),F(2,43),R(43),RHO(43),OM(43),Y(43)
1/I/N,NP1,NP2,NP3,NEQ,NPH,KEX,KIN,KASE,KRAD
1/LO/PI1,RI1,TI1,LT1,TU1
 DPDX=0.0
 RETURN
  END

   SUBROUTINE OUT (IP,STEP,PQQ,IPRNT)
     DIMENSION T(43)
 COMMON /GEN/PEI,AMI,AME,DPDX,PREF(2),PR(2),P(2),DEN,AMU,XU,XD ,XP,
1XL,DX,INTG,CSALFA,MMG
1/V/U(43),F(2,43),R(43),RHO(43),OM(43),Y(43)
1/C/SC(43),AU(43),BU(43),CU(43),A(2,43),B(2,43),C(2,43)
1 /NRK/ COF(10,42)
1/LO/PI1,RI1,TI1,LT1,TU1
1/PR/UGU,UGD
 COMMON/L/AK,ALMG
1/L1/YL,UMAX,UMIN,FR,YIP,YEM
1/I/N,NP1,NP2,NP3,NEQ,NPH,KEX,KIN,KASE,KRAD
1/B/BETA,GAMA(2),TAUI,TAUE,AJI(2),AJE(2),INDI(2),INDE(2)
1 /RZW/ APP(43)
```

```
1 /NEW5/  ITRS,ICYC

  UI=0.5*(U(2)+U(3))
   CALL PROP (SP,S,UI,IPRNT)


   IF (INTG.EQ. 1) GO TO 775
   IF (INTG.LE. IP) GO TO  2121
   IF (IPRNT.NE. 1) RETURN
   WRITE (2,10)  IPRNT
0    FORMAT (I5)
*     ***    ***    ***    ***     ***    ***    ***    ***    ***    ***
    IP=INTG+1
 MAKES A PRINT OUT OF THE 5 CYCLES AFTER THE ACTUAL SECTION.
EC   OUT

*     ***    ***    ***    ***     ***    ***    ***    ***    ***    ***
5   CONTINUE
     GO TO 855
     IF (ICYC.EQ.1 .AND. INTG.EQ. 1) GO TO 2121
   IF (ITRS.NE. 10) RETURN
   IF (ICYC.EQ. 2) GO TO 2121
1        CONTINUE
3   CONTINUE
  WRITE (2,52) (XU)
2  FORMAT   (8HSECTION=,F10.7)
   IF (ITRB .EQ. 1) RETURN
   WRITE(2,49)   (OM(I),I=1,NP3)
) FORMAT  (25H1 THE VALUES OF OMEGA ARE/(1F10.4))


   FCP=0.24*778.161
```

```
      DO 771   I=1,NP3
      T(I)=(F(1,I)-U(I)*U(I)/2.0)/FCP
771   CONTINUE
C
C
      WRITE (2,70)
70  FORMAT (1H1,4H....,1HY,9H.........,1HU,9H.........,1HF,4H....)
      WRITE (2,51) ((Y(I),U(I),T(I),F(1,I),F(2,I)),I=1,NP3)
51    FORMAT (5E10.3)
C
C
      UTOR = SQRT (TAUI/RHO(NP3))
      DO 815 II=2,NP3
      W=U(II)/U(NP3)
      Q=Y(II)/Y(NP3)
      S=(U(NP3)-U(II))/UTOR
      H=R(NP3)*AME-R(1)*AMI
      H=-(1.0/RHO(II))*(QM(II)*H+R(1)*AMI)
      H=H/R(II)
      WRITE (2,819)      (W,Q,H,S)
819   FORMAT (4E10.3)
815   CONTINUE
      WRITE (2,1732)   (EMUP(II),II=1,NP3)
1732  FORMAT (5HEMUp=,10E10.3)
      RETURN
      END
C
C
      SUBROUTINE   PROP ( SP,S,UI,IPRNT)
      DIMENSION ST(2)
      COMMON /GEN/PEI,AMI,AME,DPDX,PREF(2),PR(2),P(2),DEN,AMU,XU,XD ,XP,
     1XL,DX,INIG,CSALFA,MMG
```

```
1/V/U(43),F(2,43),R(43),RHO(43),OM(43),Y(43)
1/I/N,NP1,NP2,NP3,NEW,NPH,KEX,KIN,KASE,KRAD
1/S/BETA,GAMA(2),TAUI,TAUE,AJI(2),AJE(2),INDI(2),INDE(2)
1 /NRR/ COF(10,42)
1/LO/PII,RII,TII,LTI,TUI
1/WL/STO,AKS,ET,FT,AMT
1 /RZN/ APP(43)
1 /NEW1S/   EMUP(43)
 COMMON/L/AK,ALMG
   REX=U(NP3)*XU*RHO(NP3)/VISCO(NP3)
    CALL       PROP1(SP,S,UI)
   SQ=(TAUI*2.0)/(RHO(NP3)*U(NP3)*U(NP3))
     ZNEW=SQ*SQRT(REX)
   GO TO 11
   DO 10 J=1,2
   ST(J)=(1.0/(F(1,1)-F(1,NP3)+U(NP3)*U(NP3)/2.0))*(AJI(J)/(RHO(NP3)
1 *U(NP3)))
10   CONTINUE
   CONTINUE
   ST(1)=0.0
   ST(2)=0.0
   IF (IPRNT.NE. 1) RETURN
   WRITE (2,20)
20 FORMAT (15HWALL PROPERTIES)
   WRITE (2,30) (REX,SQ,ST(1),ST(2),XU)
30 FORMAT (4HREX=,E10.3,4HCDF=,E10.3,4HSTI=,E10.3,4HSTM=,E10.3,2HX=,
1E10.3)
   RETURN
   END

   SUBROUTINE PROP1(SP,S,UI)
   DIMENSION ST(2)
 COMMON /GEN/PEI,AMI,AME,DPDX,PREF(2),PR(2),P(2),DEN,AMU,XU,XD ,XP,
```

```
     1/L/DM,INTG,CSALFA,MMG
     1/V/U(43),P(2,43),R(43),RHO(43),OM(43),Y(43)
     1/I/EN,NP1,NP2,NP3,NEQ,NPH,KEX,KIN,KASE,KRAD
     1/B/BETA,GAMA(2),TAUI,TAUE,AJI(2),AJE(2),INDI(2),INDE(2)
     1 /NRR/ COF(10,42)
     1/LO/PI1,RE1,TI1,LT1,TU1
     1/WL/STO,AKS,RT,FT,AMT
     1 /RZN/ APP(43)
     1 /NEW15/    EMUP(43)
      COMMON/L/AK,ALMG
       RAP=0.5*(R(1)+R(2))
       RHA=0.5*(RHO(1)+RHO(2))
       UA=0.5*(U(1)*U(2))
         OM1=0.
          OM2=0.
         DO 79 J=1,MMG
9       OM2=OM2+COF(J,1)*(OM(2)**(J-1))
       SQ=(U(2)-U(1))/(OM2-OM1)
         SQ=SQ*((RAP*RHA*UA)/PSI)
        TAUI=EMUP(1)*SQ
       RETURN
       END


       SUBROUTINE   SOLVE  (A,B,C,F,NP3)
     RANGE OF THE SOLUTION IS  I=2,NP2.
     DIMENSION A(NP3),B(NP3),C(NP3),F(NP3)
     NP2=NP3-1
     B(2)=B(2)*F(1)+C(2)
      DO   48   I=3,NP2
     T=1.0/(1.0-B(I)*A(I-1)    )
     A(I)=A(I)*T
     B(I)=(B(I)*B(I-1)+C(I))*T
     CONTINUE
```

```
      J=NP2-I+2
      F(J)=A(J)*F(J+1)+B(J)
50  CONTINUE
      RETURN
       END

      SUBROUTINE   DENS
      COMMON /GEN/PEI,AMI,AME,DPDX,PREF(2),PR(2),P(2),DEN,AMU,XU,XD ,XP,
     1XL,DX,INTG,CSALFA,MMG
     1/V/U(43),F(2,43),R(43),RHO(43),OM(43),Y(43)
     1/I/N,NP1,NP2,NP3,NEQ,NPH,KEX,KIN,KASE,KRAD
      DO   45   I=1,NP3
      RHO(I)=DEN*F(1,NP3)/F(1,1)
45  CONTINUE
      RETURN
      END

      SUBROUTINE   RAD1  (X,R1,CSALFA)
      CSALFA=1.D
      R1=1.D
      RETURN
      END

      SUBROUTINE   RAD2  (X,R1,CSALFA)
      CSALFA=0.D
      R1=X
      THE   COMMON   A   /V/U(43)   IS  OUT.
       RETURN
      END

      FUNCTION   VISCO(I)
      COMMON /GEN/PEI,AMI,AME,DPDX,PREF(2),PR(2),P(2),DEN,AMU,XU,XD ,XP,
```

```
1XL,DX,INTG,CSALFA,MMG
1/V/U(43),F(2,43),R(43),RHO(43),OM(43),Y(43)
1/I/N,NP1,NP2,NP3,NEQ,NPH,KEX,KIN,KASE,KRAD
 VISCO=AMU*(F(1,I)/F(1,NP3))**0.76
 RETURN
  END

     SUBROUTINE SPLN (X,Y,M)
     DIMENSION X(M ),Y(M )
     DIMENSION  AL(43),AM(43),AR(43),RHS(43)
  COMMON /NRR/ COF(10,42)
E FIRST EQUATION.
       M1=M-1
     H1=X(2)-X(1)
     H2=X(3)-X(2)
     AL(2)=0.0
     AM(2)=3.0*H1+2.0*H2
      AR(2)=H2
     RHS(2)=6.0*((Y(3)-Y(2))/H2-(Y(2)-Y(1))/H1)
E LAST EQUATION.
     H2=X(M-1)-X(M-2)
     H1=X(M)-X(M-1)
     AL(M-1)=H2
     AM(M-1 )=(2.0*H2-3.0*H1)
     RHS(M-1)=6.0*((Y(M)-Y(M-1))/H1-(Y(M-1)-Y(M-2))/H2)
```

```
      AR(M-1)=0.0
       M2=M-2
      DO 10 I=3,M2
      H1=X(I)-X(I-1)
      H2=X(I+1)-X(I)
      AL(I  )=H1
      AM(I  )=2.0*(H1+H2)
      AR(I  )=H2
10    RHS(I  )=6.0*((Y(I+1)-Y(I))/H2-(Y(I)-Y(I-1))/H1)
C NEW SOLUTION FOR THE SPLINE THEORY.      .R.    9 JUNE.
         K=2
      CALL  SOLV (AL,AM,AR,RHS,M1,K,45)
      RHS(M)=RHS(M1)
       RHS(1)=RHS(2)
      DO 20 J=1,10
      DO 20 I=1,M1
10    COF(J,I)=0.0
       DO110 I=1,M1
      COF(1,I)=Y(I)
       COF(2,I)=(Y(I+1)-Y(I))/(X(I+1)-X(I))-(X(I+1)-X(I))*(2.0*RHS(I)+R
     1HS(I+1))/6.0
      COF(3,I)=RHS(I)/2.0
      COF(4,I)=(RHS(I+1)-RHS(I))/(6.0*(X(I+1)-X(I)))
       CONTINUE
      CALL CHK (X,Y,M)
       RETURN
       END

      SUBROUTINE SOLV (B,D,A,C,N,K,L)
      DIMENSION B(L),D(L),A(L),C(L)
C THE END VALUE FOR THE ARRAY.
C THE STARTING VALUS FOR THE ARRAY.
      L=K+1
```

```
      R=S(I)/D(I-1)
      D(I)=D(I)-R*A(I-1)
10    C(I)= C(I)-R*C(I-1)
CK SUBSTITUTION.
      C(N)=C(N)/D(N)
      DO 20 I=L,N
      J=N+K-I
20    C(J)=(C(J)-A(J)*C(J+1))/D(J)
      RETURN
      END

      SUBROUTINE CHK (X,Y,M)
      RETURN
      END

      SUBROUTINE   SORS  (J,I,CS,DS)
      PUT IN THE OTHER SOURCE AT A LATER DATE.
     CS=0.0
     DS=0.0
     RETURN
      END

     SUBROUTINE    FBC1    (X,J,IND,AJFS)
     IND=2
     AJFS=50.0
     RETURN
      END

     SUBROUTINE    FBC 2 (X,J,IND,AJFS)
     IND=1
        AJFS=65.0*0.24*778.191
     RETURN
```

```
      END

      SUBROUTINE VEFF (I,IP1,EMU)
      COMMON /GEN/PEI,AMI,AME,DPDX,PREF(2),PR(2),P(2),DEN,AMU,XU,XD ,XP,
     1XL,DX,INTG,CSALFA,MMG
     1/II/N,NP1,NP2,NP3,NEQ,NPH,KEX,KIN,KASE,KRAD
     1/B/BETA,GAMA(2),TAUI,TAUE,AJI(2),AJE(2),INDI(2),INDE(2)
     1/V/U(43),F(2,43),R(43),RHO(43),OM(43),Y(43)
     1/C/SC(43),AU(43),BU(43),CU(43),A(2,43),B(2,43),C(2,43)
     1 /NRR/ COF(10,42)
     1/RZN/ APP(43)
     1  /GUP/ OMO(43)
     1/LO/PI1,RI1,TI1,LT1,TU1
     1/L10/L11
     1/PR/UGU,UGD
     1 /NRW/ AML,AMZ
     1 /NEWS/  ITRE,ICYC
     1   /NEW7/   AOM(43),AF(2,43),ZU(43)
     1 /NEW8/ UHOLD(43)
     1 /NEW15/   EMUP(43)
      COMMON/L/AK,ALMG
      EMU=EMUP(I)
      RETURN
      END

      SUBROUTINE VIS
        DIMENSION  SU(3,43),YEDGE(6)
      COMMON /GEN/PEI,AMI,AME,DPDX,PREF(2),PR(2),P(2),DEN,AMU,XU,XD ,XP,
     1XL,DX,INTG,CSALFA,MMG
     1/II/N,NP1,NP2,NP3,NEQ,NPH,KEX,KIN,KASE,KRAD
     1/B/BETA,GAMA(2),TAUI,TAUE,AJI(2),AJE(2),INDI(2),INDE(2)
     1/V/U(43),F(2,43),R(43),RHO(43),OM(43),Y(43)
     1/C/SC(43),AU(43),BU(43),CU(43),A(2,43),B(2,43),C(2,43)
```

```
      1/ANRW/ COF(43,42)
      1/RZNE/ APP(43)
      1  /GUP/ OMO(43)
      1/LC/PI1,RI1,TI1,LI1,TU1
      1/LC1O/LI1
      1/ZR/UGU,UGD
      1 /NRW/ AML,AMZ
      1 /NEWS/  ITRE,ICYC
      1   /NEWZ/   AOM(43),AF(2,43),ZU(43)
      1 /NEW8/ UHOLD(43)
      1 /NEW15/   EMUP(43
      1/L1/YL,UMAX,UMIN,ER,YIP,YEM
       COMMON/L/AK,ALMG
        ITEST=1
        ITEST=0
         UFAC=3.01
        DUDYMN=ER*(ABS(U(1)-U(NP3)))/Y(NP3)
        DO 10 I=2,NP1
        S U(1,I)=(U(I+1)-U(I))/(Y(I+1)-Y(I))
        S U(2,I)=0.0
   10   IF (ABS(S U(1,I)) .GT. DUDYMN)  S U(2,I)=1.0
        IF (KIN.EQ. 1) S U(2,2)=1.0
        IF ( KEX.EQ. 1)  S U(2, NP1)=1.0
        S U(2,1)=0.0
        IF (ITEST.EQ. 0) GO TO 1007
          TEST=1.0
        WRITE (2,101)   (TEST,DUDYMN,ER,AK,ALMG,)
        WRITE (2,101)   (SU(1,I),I=2,NP1)
        WRITE (2,101)   (SU(2,I),I=2,NP1)
    7   CONTINUE
        K=1
        DO 13 L=1,6
    3     YEDGE(L)=Y(NP3)
```

```
DO 11 I=2,NP1
IF (S U(2,I).EQ. U(2,I-1)) GO TO 11
 YEDGE(K)=Y(I)
K=K+1
IF (K.GT. 6) GO TO 14
 CONTINUE
 EL12=(YEDGE(2)-YEDGE(1))*ALMG
EL34=(YEDGE(4)-YEDGE(3))*ALMG
EL56=(YEDGE(6)-YEDGE(5))*ALMG
IF (ITEST.EQ. 0) GO TO 1002
  TEST=2.0
WRITE (2,101)  (TEST,EL12,EL34,EL56,(YEDGE(I),I=1,6))
CONTINUE
DO 12 I=2,NP1
S U(3,I)=0.0
IF (Y(I) .GE. YEDGE(1))    S U(3,I)=EL12
IF (Y(I) .GE. YEDGE(2))  S U (3,I=0.0
IF (Y(I) .GE. YEDGE(3)) S U(3,I)=EL34
IF (Y(I) .GE. YEDGE(4))  S U(5,I)=0.0
IF (Y(I) .GE. YEDGE(5))  S U(3,I)=EL56
IF (S U(1,I) .EQ. 0.0) GO TO 15
ELMAX=0.2*U(I)/ABS(S U(1,I))
IF (S U(3,I) .GT. ELMAX)  S U(3,I)=ELMAX
 CONTINUE
PAK=AK*0.5*(Y(I)+Y(I+1))
IF (KIN.EQ. 1  .AND.  S U(3,I) .GT. PA) S U(3,I)=PAK
PAK=AK*(Y(NP3)-0.5*(Y(I)+Y(I+1)))
IF (KEX.EQ. 2   .AND.  S U(3,I). GT. PAK)  S U(3,I)=PAK
 CONTINUE
IF (ITEST.EQ. 0) GO T 009
  TEST=3.0
WRITE (2,101)  TEST
WRITE (2,101)   (SU(3,I),I=2,NP1)
```

```
ENT  LAMINAR
     DO 23 I=2,NP1
23   EMUP(I)=0.5*(VISCO(I)+VISCO(I+1))
ENT  TURBOLENT.
     DO 25 I=2,NP1
     DUDYL=  ABS(S U(1,I)*S U(3,I))
     UDMIN=UFAC*0.5*(U(I)+U(I+1))
     IF (DUDYL .LT.  UDMIN)  DUDYL=UDMIN
     RHM=0.5*(RHO(I)+RHO(I+1))
     EMUT=RHM*S U(3,I)*DUDYL
     IF (KIN.EQ. 2   .AND.  I.LT. 5) GO TO 21
     IF (KEX.EQ. 2  .AND.  I.GT.  N-2) GO T O  21
     IF  (EMUT.GT.  EMUP(I)*50.0)   GO TO 21
     IF (EMUT. GT.  EMUP(I)*10.0) GO TO 22
     EMUP(I)=EMUP(I)+EMUT*EMUT*0.0008/EMUP(I)
     GO TO 20
22    EMUP(I)=1.23*EMUT-10.5*EMUP(I)
     GO TO 20
21    EMUP(I)=EMUP(I)+EMUT
20   CONTIN UE
                    **************************
FILLING IN THE REST OF THE EMUP ARRAY.
.R.     24  OCT.
     EMUP(1)=EMUP(2)
     EMUP(NP1)=EMUP(N)
     EMUP(NP2)=EMUP(N  )
     EMUP(NP3)=EMUP(N  )
                    **************************
     IF (ITEST.EQ. 0) GO TO 1010
       TEST=4.0
     WRITE(2,101)   TEST
     WRITE (2,101)   (EMUP(I),I=1,Np3)
```

```
0    CONTINUE
1    FORMAT  (10E11.2)
     RETURN
     END

     SUBROUTINE OURS (IPIC)
     COMMON /GEN/PEI,AMI,AME,DPDX,PREF(2),PR(2),P(2),DEN,AMU,XU,XD ,XP,
    1XL,DX,INTG,CSALFA,MMG
    1/I/N,NP1,NP2,NP3,NEQ,NPH,KEX,KIN,KASE,KRAD
    1/S/BETA,GAMA(2),TAUI,TAUE,AJI(2),AJE(2),INDI(2),INDE(2)
    1/V/U(43),F(2,43),R(43),RHO(43),OM(43),Y(43)
    1 /NRR/ COF(10,42)
    1/RZN/ APP(43)
    1  /GUP/ OMO(43)
    1/LO/PI1,RI1,TI1,LT1,TU1
    1/L10/L11
      COMMON /ZZZ/ MX,MY,ILEN,CORD(2,43)
         IPRINT=0
                    MMG=10
         DO 10 I=1,42
         DO 10 J=1,10
0    COF(J,I)=0.
     IF (ITG.NE. 1)GO TO 1423
        DO  1451  I=1,NP3
        APP(I)=OM(I)
1    CONTINUE
3    CONTINUE
     IF (IPIC.NE. INTG) RETURN
     CALL EXEC2(IPIC)
   CALL SPLN (OM,APP,NP3)
        RETURN
     END
     SEGMENT
```

```
      SUBROUTINE EXEC2(IPIC)
       INTEGER DISP (6000)
      INTEGER          BUFF(200),X,Y
      INTEGER ACTION
     COMMON /GEN/PEI,AMI,AME,DPDX,PREF(2),PR(2),P(2),DEN,AMU,XU,XD ,XP,
    1XL,DX,INTG,CSALFA,MMG
    1/V/U(43),F(2,43),R(43),RHO(43),OM(43),Y(43)
    1/I/N,NP1,NP2,NP3,NEQ,NPH,KEX,KIN,KASE,KRAD
      COMMON /ZZ/ MX,MY,ILEN,CORD2,43)        IRET2
       CONTINE
      ILEN=500
      MX=150
     MY=150
      KK=ACTION(1,FOUND)
      IF (KK.EQ. 8) RETURN
      CALL DATA
       CALL AXIS (2)
     CALL GRP (4,CORD)
      IF (ACTION(1,FOUND).EQ. 5) GO TO 500
     CALL DEFIN
      J=ACTION(1,FOUND)
    IF (J.EQ. 1) CALL PLOT
      IRET=ACTION(1,FOUND)
      IPIC =ACTION (1,FOUND)
      IF (IPIC.EQ. 1) IPIC=INTG+1
      IF (IPIC.GT. 1) IPIC=IPIC*10
      IF (IPIC.EQ. 8) IPIC=IPIC*1000
      CALL DELETE (5)
      CALL DELETE (300)
      CALL DELETE(312 )
      CALL DELETE(313)
      CALL DELETE(314)
      CALL DELETE (321)
```

```
      CALL DELETE (322)
       CONTINUE
      CALL DELETE(2)
      CALL DELETE(3)
      CALL DELETE(4)
      IF(IRET.EQ. 1) GO TO 35
      DO 10 I=1,NP3
      OM(I)=CORD(1,I)
       CONTINUE
      OM(1)=0.0
      RETURN
      END
       SUBROUTINE DATA
     COMMON /GEN/PEI,AMI,AME,DPDX,PREF(2),PR(2),P(2),DEN,AMU,XU,XD ,XP,
    1XL,DX,INTG,CSALFA,MMG
    1/V/U(43),F(2,43),R(43),RHO(43),OM(43),Y(43)
    1/I/N,NP1,NP2,NP3,NEQ,NPH,KEX,KIN,KASE,KRAD
      COMMON /ZZ/ MX,MY,ILEN,CORD(2,43)
     NQ=2
     MM=1
      WRITE (2,41) ((U(I),OM(I)),I=1,NP3)
      FILLS UP ARRAY CORD ON EACH CYCLE.
      AMAX=U(1)
      DO 70 I=2,NP3
     IF (U(I).GT. AMAX) AMAX=U(I)
      CONTINUE
      DO 10 I=1,NP3
      CORD(1,I)=OM(I)
      GO TO (20,30,40),MM
      CORD(2,I)=U(I)/AMAX
      GOTO 10
      CORD(2,I)=F(1,I)
      GOTO 10
```

```
      CORD(2,I)=F(2,I)
      CONTINUE
      WRITE (2,50) ((CORD(I,J),J=1,NP3),I=1,2)
   50 FORMAT (4HAAAA,12E10.3)
   51 FORMAT (12E10.3)
      RETURN
      END
      SUBROUTINE DEFIN
      LOGICAL SWITCH
       INTEGER ACTION,IBUF(6000)
      DIMENSION  AX(6),AY(6),INTX(6),INTY(6)
      DIMENSION ACHK(2,43),IRANJ(6),SUM(10),AMAX(3),NOM(3),ARR(10, 3),
     1  AORD(4,43),IDEC(6)
      DIMENSION B(10)
      DIMENSION ISI(3)
     COMMON /GEN/PEI,AMI,AME,DPDX,PREF(2),PR(2),P(2),DEN,AMU,XU,XD ,XP,
     1XL,DX,INTG,CSALFA,MMG
     1/I/N,NP1,NP2,NP3,NEQ,NPH,KEX,KIN,KASE,KRAD
      COMMON /ZZ/ MX,MY,ILEN,CORD(2,43)
      DO 11 K=1,3
        ISI(K)=1
      CALL NEWBUF(IBUF,100)
     WRITE (12,499)
     FORMAT (120X,'K1 FOR U=FUNC(OM)'/120X,'K2 FOR OM=FUNC(U)')
      CALL INSERT (20,0)
      IAXIS=ACTION(1,FOUND)
      CALL DELETE(20)
      IC1=1
      IC2=2
      IF (IAXIS.EQ. 1) GO TO 51
      IC1=2
      IC2=1
      CONTINUE
```

```
      CALL NEWBUF (IBUF,100)
      WRITE (12,500)
  500 FORMAT (120X,' AREAS (MAX=3) TO BE CHANGED,K1 TO COME OUT'/120X,
     1  '          & POSITION')
      CALL INSERT (20,0)
      CALL SETRAK (.TRUE.)
      DO 10 I=1,6
      J=ACTION (1,FOUND)
      IF (J.EQ. 1) CALL TRAK (INTX(I),INTY(I))
   10 CONTINUE
      CALL SETBAK (.FALSE.)
      DO 60 I=1,6
      A=INTX(I)-MX
      BB=ILEN
      C=INTY(I)-MY
      IF (A.GT. 0.0  .AND. C.GT. 0.0) GO TO 20
      A=0.0
        C=0.0
      INTX(I)=150
      INTY(I)=150
   20 CONTINUE
      AX(I)=A/BB
      AY(I)=C/BB
      WRITE (2,501) (AX(I),I=1,6)
  501  FORMAT (' THE X CORDINAES OF THE  AREAS',6E10.3)
      WRITE (2,503)  (AY(I),I=1,6)
  503 FORMAT (' THE Y CORDINATES OF THE NEW AREAS',6E10.3)
      CALL NEWBUF (IBUF,100)
      DO 40 I=1,6
      CALL POINT (INTX(I),INTY(I),1)
      CALL VECTOR (0,MY-INTY(I),1)
   40 CONTINUE
      CALL INSERT (5,0)
```

```
      CALL     DELETE (20)
      CALL NEWBUF (IBUF,50)
      WRITE (12,502)
  502   FORMAT (120X,' K1 IF YOU WANT TO TRY AGAIN')
      CALL INSERT (20,0)
      J=ACTION(1,FOUND)
      IF (J.NE. 1) GO TO 50
      CALL DELETE (20)
      CALL DELETE (5)
      GO TO 30
   50 CONTINUE
      CALL DELETE (20)
      MPOW=9
      MCOL=MPOW+1
      CALL ALTER1(MPOW,MCOL,CORD,B,IC1,IC2)
ECKING THAT THE POLYNOMIAL IS A REASONABLE REPRESENTARTION OF THE CU
      DO 70 I=1,NP3
      ACHK(IC2,I)=0.0
      ACHK(IC1,I)=CORD(IC1,I)
      DO 71 K=1,MCOL
      ACHK(IC2,I)=ACHK(IC2,I)+B(K)*(ACHK(IC1,I)**(K-1))
   71 CONTINUE
      CALL GRP (300,ACHK)
      CALL NEWBUF (IBUF,50)
      WRITE (12,514)
  514   FORMAT (120X,'  KEY 1 IF OK')
        CALL INSERT (301,0)
    J=ACTION (1,FOUND)
      IF (J.NE. 1) CALL DELETE (300)
      CALL DELETE (301)
      IF (J.NE. 1) GO TO 72
TTING UP THE RANGES FOR THE M/C.
      DO 81 I=1,6
```

```
      DO 80 J=1,NP3
      IF (CORD(1,J).LT. AY(I))       GO TO 80
      IRANJ(I)=J
       GO TO 82
      CONTINUE
        CONTINUE
      CONTINUE
C ESTIMATE THE DOMINANT COEFFICIENT IN EACH RANGE.
      DO 90 I=1,5,2
           DO 301  K=1,MCOL
        SUM(K)=0.0
      II=1
      IF (I.EQ. 3) II=2
       IF (I.EQ. 5) II=3
      I1=IRANJ(I)
      I2=IRANJ(I+1)
      DO 61 J=I1,I2
      DO 91 K=2,MCOL
       SUM(K)=SUM(K)+CORD(IC1,J)**(K-1)
       CONTINUE
      SUM(1)=B(1)
      DO 96 K=2,MCOL
      AC=IRANJ(I+1)-IRANJ(I)
      SUM(K)=SUM(K)/AC
      SUM(K)=SUM(K)*B(K)
      CONTINUE
C ARCH.
      AMAX(II)=SUM(1)
      NOM(II)=1
      DO 92 K=2,MCOL
      IF (SUM(K).LE. AMAX(II)) GO TO 92
      AMAX(II)=SUM(K)
      NOM(II)=K
```

```
    CONTINUE
    CONTINUE
     WRITE  (2,516)((NOM(J),AMAX(J)),J=1,3)
     FORMAT  (I5,E10.3)
LLING ARR   WITH  B.
    DO 100 I=1,3
    DO 100J=1,MCOL
    ARR(J,I)=B(J)
TTING AORD(4,I)=CORD(2,I)
TTING UP IDEC.
    DO 102 I=1,3
     IDEC(I)=100
    CALL DELETE (300)
TOMATIC ADJUSTEMENT OF THE CURVES + DISPLAY & DECISION.
    CALL NEWBUF (IBUF,50)
    WRITE (12,541)
     FORMAT ('PLOTTING THE NEW CURVES')
    CALL INSERT (306,0)
    DO 110 I=1,3
    IF (IDEC(I).EQ. I) GO TO 117
    L=I
    IF (I.EQ. 2) L=3
    IF (I.EQ. 3) L=5
CREASING THE MAXIMUM COEFFICIENTT.
    IP=IRANJ(L)
    IP1=IRANJ(L+1)
    DO 111 J=IP,IP1
    ACHK(IC2,J)=0.0
    ACHK(IC1,I)=CORD(IC1,I)
    DO 111 K=1,MCOL
    ACHK(IC2,J)=ACHK(IC2,J)+ARR(K,I)*(ACHK(IC1,J)**(K-1))
     CONTINUE
    CONTINUE
```

```
      IF (I.NE. 3) GO TO 9521
      CALL GRP(303,ACHK)
       CONTINUE
      CONTINUE
CISION ABOUT WHICH GRAPH TO MODIFY.
      CALL NEWBUF (IBUF,70)
      WRITE (12,521)
      FORMAT (120X,'FOR QUIK K8')
      CALL INSERT (311,0)
      DO 131 J=1,500
      IF (SWITCH(8)) CALL QUIK(IDEC,J)
      CONTINUE
      CALL DELETE (311)
      CALL NEWBUF (IBUF,70)
       WRITE (12,523)
      FORMAT (120X,'FOR SIGN K1')
      CALL INSERT (311,0)
      DO 132 J=1,500
      IF (SWITCH(1)) CALL SIGN(ISI)
       CONTINUE
      CALL DELETE (311)
      ID=0
      DO 113 I=1,3
      IF (IDEC(I).EQ. I) GO TO 113
      ID=ID+1
      CONTINUE
       IF (ID.EQ. 0) GO TO 143
      CALL DELETE (303)
      DO 145 I=1,3
      IF (IDEC(I).EQ. I) GO TO 145
      K=NOM(I)
      ARR(K,I)=ARR(K,I)+(ARR(K,I)/10000.)*ISI(I)
      CONTINUE
```

```
      GO TO 114
ECISION ABOUT WHICH GRAPH TO MODIFY.
3     CALL DELETE (306)
      DO 141 L=1,6
1     IDEC(L)=100
      CALL NEWBUF (IBUF,50)
      WRITE (12,525)
5     FORMAT (120X,'SMOOTH')
      CALL INSERT (300,0)
      DO 147 ISPA=1,43
      CALL          SMOTH (INTX,INTY,ACHK,IRANJ,ISPA,IDEC)
      CALL GRP (571,ACHK)
      ISTP=ACTION (1,FOUND)
      IF (ISTP.EQ. 8) CALL QUIK(IDEC,6)
      INO=0
      DO 149 L=1,6
      IF (IDEC(L).EQ. L) INO=INO+1
      CONTINUE
      CALL DELETE (571)
      IF (INO.EQ. 6) GO TO 531
7     CONTINUE
      CALL DELETE (300)
      CALL NEWBUF (IBUF,50)
      WRITE (12,518)
8     FORMAT (120X,' KEY 1 FOR THE ORIGINAL GRAPH')
      CALL INSERT (300,0)
      J=ACTION (1,FOUND)
      IF (J.EQ. 1) GO TO 120
      CALL DELETE (4)
      CALL RENAME (303,4)
      DO 139 I=1,NP3
      CORD(IC1,I)=ACHK(IC1,I)
      CORD(IC2,I)=ACHK(IC2,I)
```

```
T A BEST CURVE THROUGH CORD (I,J).
     WRITE (2,5739) (CORD(2,II),II=1,NP3)
    FORMAT (8E10.3)
    CALL ALTER1(MPOW,MCOL,CORD,B,IC1,IC2)
T A BEST CURVE THROUGH CORD (I,J).
    DO 121 I=1,NP3
    CORD(IC2,I)=0.0
    DO 121 K=1,MCOL
    CORD(IC2,I)=B(K)*(CORD(IC1,I)**(K-1))+CORD(IC2,I)
    CALL DELETE (4)
    CORD(1,NP3)=1.0
    CORD(2,NP3)=1.0
    CALL GRP (4,CORD)
    CALL MAGI1(313)
    CALL MAGI2(312,CORD)
    CALL MAGI2(321,ACHK)
    CALL MAGI2(322,ACHK)
    RETURN
      CALL DELETE (303)
    CORD(1,NP3)=1.0
    CORD(2,NP3)=1.0
  CALL DELETE (4)
    CALL GRP (4,CORD)
    CALL MAGI1(313)
    CALL MAGI2(312,CORD)
    CALL MAGI2(321,ACHK)
    CALL MAGI2(322,ACHK)
    RETURN
      FORMAT ('***CHECK***',10E10.3)
    END
    SUBROUTINE GRA (NO,A,B,IR)
    DIMENSION A(4,43),B(2,43)
    INTEGER DISP (5000)
```

```
      INTEGER IBUF (1000)
      COMMON /GEN/PEI,AMI,AME,DPDX,PREF(2),PR(2),P(2),DEN,AMU,XU,XD ,XP,
     1XL,DX,INTG,CSALFA,MMG
      COMMON /ZZ/ MX,MY,ILEN,CORD(2,43)
      INTEGER ACTION
      CALL NEWBUF (IBUF,1000)
     CALL POINT (MX,MY,1)
      FOR THE NON DIMENSIONALISED PLOTS.
        DO 10 J=2,NP3
      AY=(B(1,J)-B(1,J-1))*ILEN
      AU=(A(IR,J)-A(IR,J-1))*ILEN
      LY=AY
       LU=AU
       CALL VECTOR (LU,LY,1)
       CONTINUE
      CALL INSERT (NO,0)
      RETURN
      END
     SUBROUTINE QUIK (IDEC,IPT)
      DIMENSION IDEC(6)
      INTEGER IBUF(500),ACTION
      LOGICAL   SWITCH
      DO 112 I=1,IPT
      CALL NEWBUF(IBUF,70)
      WRITE (12,521)
      FORMAT (165X,'KEY I TO KEEP GRAPH I')
      CALL INSERT (305,0)
      IF (IDEC(I).EQ. I) GO TO 10
        CONTINUE
      IDEC(I)=ACTION (1,FOUND)
       IF (IDEC(I).EQ. 8) GO TO 512
     GO TO 20
      CALL NEWBUF (IBUF,100)
```

```
      WRITE (12,522)
2     FORMAT (170X,'MISS   MISS')
      CALL INSERT (353,0)
      JJ=ACTION (1,FOUND)
      IF (JJ.NE. 7) GO TO 40
       CALL DELETE (353)
       CONTINUE
      CALL DELETE (305)
2      CONTINUE
      RETURN
      END
      SUBROUTINE  SMOTH (INTX,INTY,ACHK,IRANJ,ISPA,IDEC)
      DIMENSION INTY( 6),INTX( 6),IRANJ(6),ACHK(2,43)  ,IDEC(6)
      DIMENSION ISTOR (7)
      INTEGER ACTION
     COMMON /GEN/PEI,AMI,AME,DPDX,PREF(2),PR(2),P(2),DEN,AMU,XU,XD ,XP,
    1XL,DX,INTG,CSALFA,MMG
    1/I/N,NP1,NP2,NP3,NEQ,NPH,KEX,KIN,KASE,KRAD
      COMMON /ZZ/ MX,MY,ILEN,CORD(2,43)
      ACHK(1,1)=0.0
      ACHK(2,1)=0.0
      IF (ISPA.GT. 1) GO TO 52
      IF (ACTION(1,FOUND).NE. 1) GO TO 52
      CALL SETRAK(.TRUE.)
      JJJ=ACTION (1,FOUND)
      IF (JJJ.EQ. 1) CALL TRAK (IX,IY)
      IPLO=1
      ZZ=FLOAT(IY-MY)/FLOAT(ILEN)
      WRITE (2,21) (IY,MY,ILEN,ZZ)
      FORMAT (3I5,E10.3)
      DO 7 K=1,NP3
      IF (ACHK(1,K).GE. ZZ) GO TO 8
      WRITE (2,25) (ZZ,ACHK(1,K))
```

```
     FORMAT (2E 10.3)
    CONTINUE
    IPHI=K
     I11=IPLO
    I22=IPHI
    IF (IPHI.EQ. NP3) STOP
     CALL SETRAK(.FALSE.)
    GRAD=(ACHK(1,IPHI)-ACHK(1,IPLO))/(ACHK(2,IPHI)-ACHK(2,IPLO))
    CON=ACHK(1,IPLO)-GRAD*ACHK(2,IPLO)
    DO 51 I=IPLO,IPHI
    ACHK(1,I)=GRAD*ACHK(2,I)+CON
      ISTOR(1)=1
    DO 9 J=2,6
    IF (IDEC(J).EQ. J) GO TO 9
  IF (J.EQ. 1) GO TO 6
    IF (INTY(J).EQ. INTY(J-1)) GO TO 9
  IPHI=IRANJ(J)+ISPA
    IPLO=IRANJ(J)-ISPA
    IF (IPLO.LT. 1) IPLO=2
    IF (IPHI.GT. NP3) IPHI=NP3
    IF (IPLO.EQ. IPHI .AND. IPLO.EQ. 1) IPHI=2
  ISTOR(J)=IPLO
    IF (J.GT. 1  .AND.  IPLO.LE. ISTOR(J-1)) GO TO 9
OOSHING SMOOTHING  SMOOOTHING.
    ZZ=ACHK(2,IPHI)-ACHK(2,IPLO)
    IF (ZZ.GT. 0.0) GO TO 30
     CONTINUE
     FORMAT (I5)
    WRITE (2,40)      (J,IPHI,IPLO,ACHK(2,IPHI),ACHK(2,IPLO))
    FORMAT (3I10,2E10.3)
    GRAD=(ACHK(1,IPHI)-ACHK(1,IPLO))/(ACHK(2,IPHI)-ACHK(2,IPLO))
    CON=ACHK(1,IPLO)-GRAD*ACHK(2,IPLO)
    DO 20 I=IPLO,IPHI
```

```
      ACHK(I,1)=GRAD*ACHK(2,I)+CON
      CONTINUE
      RETURN
      END
      SUBROUTINE SIGN(ISI)
      DIMENSION ISI(3)
      INTEGER IBUF(500),ACTION
      LOGICAL SWITCH
      INTEGER  ACTION
       DO 20 I=1,3
      IF (I.GE. 2) CALL DELETE (511)
      CALL NEWBUF (IBUF,100)
      WRITE (12,10)
   10 FORMAT (125X,'2 -VE.3 +VE.4 X5 . 5X10  . 6 /5  . 7  /10  .')
      CALL INSERT (511,0)
      CONTINUE
    J=ACTION(1,FOUND)
      GO TO (50,51,52,53,54,55,56,57),J
      GO TO 11
      ISI(I)=-1
      GO TO 20
      ISI(I)=1
      GO TO 20
    ISI(I)=ISI(I)*5
      GO TO 20
      ISI(I)=ISI(I)*10
      GO TO 20
    ISI(I)=ISI(I)/5
      GO TO 20
    ISI(I)=ISI(I)/10
      GO TO 20
      CONTINUE
      CONTINUE
```

```
      CALL DELETE (511)
      RETURN
      END
      SUBROUTINE MAGI2 (NOP,ACHK)
      DIMENSION ACHK(2,43),ORD(2,43)
     COMMON /GEN/PEI,AMI,AME,DPDX,PREF(2),PR(2),P(2),DEN,AMU,XU,XD ,XP,
    1XL,DX,INTG,CSALFA,MMG
    1/V/U(43),F(2,43),R(43),RHO(43),OM(43),Y(43)
    1/I/N,NP1,NP2,NP3,NEQ,NPH,KEX,KIN,KASE,KRAD
      COMMON /ZZ/ MX,MY,ILEN,CORD(2,43)
      ILEN=IILEN
      IMX=MX
      IMY=MY
      INP3=NP3
      IILEN=ILEN
      ISPAN=5
         MX=700
       MY=700
      ILEN=250
      IF (NOP.EQ. 321) GO TO 30
      IF (NOP.EQ. 322) GO TO 50
       JLIM=-10
      DO 12 I=1,NP3
      IF (ACHK(1,I) .GE. 0.0) GO TO 12
      JLIM=I
     CONTINUE
      IF (JLIM.LT. 0.0) GO TO 13
      I=JLIM+5
      IF (I.GT. NP3) I=NP3
      GO TO11
      DO 10 I=1,NP3
      XX=ACHK(1,I)*ILEN
      ITEP=XX
```

```
      IF (ITEP.GT. ISPAN) GO TO 11
      CONTINUE
      DO 20 K=1,I
      DO 20 J=1,2
   20 ORD(J,K)=ACHK(J,K)/ACHK(J,I)
      NP3=I
      GOTO 40
   11  CONTINUE
       AN=ACHK(2,10)/500.
      DO 31 K=1,10
      DO 31 J=1,2
   31 ORD(J,K)=ACHK(J,K)*AN
      INP3=NP3
      NP3=10
      GO TO 40
      DO 51 I=1,NP3
      ORD(1,I)=CORD(1,I)
      ORD(2,I)=ACHK(1,I)
      WRITE (2,71) ((ORD(J,I),I=1,NP3),J=1,2)
   71  FORMAT (8E10.3)
      CALL GRP (NOP,ORD)
      MX=IMX
      MY=IMY
      NP3=INP3
      ILEN=IILEN
      RETURN
      END
      SUBROUTINE MAGI1 (NOP)
      COMMON /ZZ/ MX,MY,ILEN,CORD(2,43)
      IMX=MX
      IMY=MY
      INP3=NP3
      IILEN=ILEN
```

```
      ILEN=IILEN
      MY=700
         MX=700
      ILEN=250
      CALL AXIS (313)
      NP3=INP3
      MX=IMX
      MY=IMY
      ILEN=IILEN
       RETURN
      END

     SUBROUTINE EXEC3 (IPIC1,INTG,IPIC,OM,U,NP3)
       DIMENSION OM(43),U(43) ,ACHK(2,43),IBUF(500)
      COMMON /ZZ/ MX,MY,ILEN,CORD(2,43)
      INTEGER ACTION
      LOGICAL SWITCH
      IPP=10
      MX=400
     MY=400
      ILEN=250
      CALL NEWBUF(IBUF,50)
      WRITE (12,501)
      FORMAT (120X,'K 8 TO GO IN OUT OF POSITION')
      CALL INSERT (605,0)
      O 11 J=1,500
   IF (SWITCH(8))    IPIC1=NTG
      IF (SWITCH(8)) IPP=1
    CONTINUE
      CALL DELETE(605)
    IF (IPIC1.NE. INTG) RETURN
      IPIC1=IPIC1+2
      IF (IPP.NE.1) GO TO 60
```

```
   IF (ACTION(1,FOUND).EQ. 1) IPICINTG
  CNTINUE
  IF (TG.LE.1  TO     CAL DELETE (600
   CALL DELETE (602)
   CALL DELETE (601)
    AMAX=U(1)
   DO 30 I=2,NP3
   IF (U(I).GE. AMAX) AMAX=U(I)
   CONTINUE
   DO 31 I=1,NP3
   ACHK(1,I)=OM(I)
   ACHK(2,I)=U(I)/AMAX
   CAL AXIS (600)
   CALL GRP(6 2,ACHK)
  RETURN
   END
   SUBROUTINE AXIS (NOF)
   NTE P(5 00),ACTIOnFF(5
ICAL   SWITCH
  COMONEN/PEI,AMI,AME,DPDX,PREF(2),PR(2),P(2),DEN,AMU,XU,XD ,XF,
TL,DX,INTG,CSALFA,MMG
1/II/N,NP1,NP2,NP3,NEQ,NPH,KEX,KIN,KASE,KRAD
   COMMON /ZZ/ MX,MY,ILEN,CORD(2,43)
  CAEF (100)    J=MX+ILE
 CALL POIT (J,MY1)
   CALL  VECTOR (-ILEN,0,1)
   WRITE (12,501)
   FORMAT ('0')
  CALL POINT (MX,MY,1)
   CALL  VECTOR (0,ILEN,1)
   CALL INSERT (NOF,0)
   NOF=NOF+1
   CALL LABEL (NOF)
  RETURN
```

```
  END
   SUBROUTINE GRP (NO,AORD)
   DIMENSION AORD(2,43)
   INTEGER DISP(6000),IBUF(5000)
   INTEGER ACTION
  COMMON /GEN/PEI,AMI,AME,DPDX,PREF(2),PR(2),P(2),DEN,AMU,XU,XD ,XP,
 1XL,DX,INTG,CSALFA,MMG
 1/I/N,NP1,NP2,NP3,NEQ,NPH,KEX,KIN,KASE,KRAD
   COMMON /ZZ/ MX,MY,ILEN,CORD(2,43)
   CALL NEWBUF (IBUF,5000)
  CALL POINT (MX,MY,1)
   FOR THE NON DIMENSIONALISED PLOTS.
     DO 10 J=2,NP3
   AY=(AORD(1,J)-AORD(1,J-1))*ILEN
   AU=(AORD(2,J)-AORD(2,J-1))*ILEN
   LY=AY
    LU=AU
    CALL VECTOR (LU,LY,1)
    CONTINUE
   CALL INSERT (NO,0)
   RETURN
   END
    SUBROUTINE LABEL (NOF)
   INTEGER DISP(5000),BUFF(100),X
  COMMON /GEN/PEI,AMI,AME,DPDX,PREF(2),PR(2),P(2),DEN,AMU,XU,XD ,XP,
 1XL,DX,INTG,CSALFA,MMG
 1/I/N,NP1,NP2,NP3,NEQ,NPH,KEX,KIN,KASE,KRAD
   COMMON /ZZ/ MX,MY,ILEN,CORD(2,43)
 IS ASSUMED THAT X=Y.
   CALL NEWBUF (BUFF,100)
 NO=1  X AXIS.
 NO=2  Y AXIS.
   IDV=ILEN/5
```

```
      NOM=ILEN+1
       DO 10 NO=1,2
      DO 10 I=1,NOM,IDV
       IF (NO.EQ. 2) GO TO 20
    II=ILEN+MX+1-I
      CALL POINT (II,MX,1)
      CALL VECTOR (0,20,1)
      GO TO 10
      II=MX+I-1
      CALL POINT (MX,II,1)
      CALL VECTOR (20,0,1)
       CONTINUE
      CALL INSERT (NOF,0)
      RETURN
       END
      SEGMENT


     SUBROUTINE OURS1(ISET,IPIC)
     COMMON /GEN/PEI,AMI,AME,DPDX,PREF(2),PR(2),P(2),DEN,AMU,XU,XD ,XP,
    1AL,DX,INTG,CSALFA,MMG
    1/I/N,NP1,NP2,NP3,NEQ,NPH,KEX,KIN,KASE,KRAD
    1/B/BETA,GAMA(2),TAUI,TAUE,AJI(2),AJE(2),INDI(2),INDE(2)
    1/V/U(43),F(2,43),R(43),RHO(43),OM(43),Y(43)
    1/C/SC(43),AU(43),BU(43),CU(43),A(2,43),B(2,43),C(2,43)
    1 /NRR/ COF(10,42)
    1/RZN/ APP(43)
    1  /GUP/ OMO(43)
    1/LO/PI1,RI1,TI1,LT1,TU1
    1/L10/L11
    1/PR/UGU,UGD
    1 /NRW/ AML,AMZ
    1 /NEW5/  ITRB,ICYC
    1   /NEW7/   AOM(43),AF(2,43),?U(43)
```

```
      COMMON /ZZ/ MX,MY,ILEN,CORD(2,43)
      COMMON/L/AK,ALMG
C     COMMON AS IN THE  MAIN PROGRAM.
      IF (ICYC.GE. ISET) ITRB=10
      CALL OURS(IPIC)
      IF (ITRB.EQ. 10) GO TO 20
      DO 10 I=1,NP3
       IF (ICYC.GT. 1) GO TO 20
      ZU(I)=U(I)
      AOM(I)=OM(I)
       AF(1,I)=F(1,I)
       AF(2,I)=F(2,I)
      F(1,I)=AF(1,I)
              AF(2,I)=F(1,I)
      RETURN
        IF (ITRB.EQ. 10) RETURN
      DO 30 I=1,NP3
      U(I)=ZU(I)
      F(1,I)=AF(1,I)
       F(2,I)=AF(2,I)
        RETURN
      END


       SUBROUTINE  MP1
      COMMON /GEN/PEI,AMI,AME,DPDX,PREF(2),PR(2),P(2),DEN,AMU,XU,XD ,XP,
     1XL,DX,INTG,CSALFA,MMG
     1/I/N,NP1,NP2,NP3,NEQ,NPH,KEX,KIN,KASE,KRAD
     1/B/BETA,GAMA(2),TAUI,TAUE,AJI(2),AJE(2),INDI(2),INDE(2)
     1/V/U(43),F(2,43),R(43),RHO(43),OM(43),Y(43)
     1/C/SC(43),AU(43),BU(43),CU(43),A(2,43),B(2,43),C(2,43)
     1 /NRR/ COF(10,42)
     1/RZN/ APP(43)
     1  /GUP/ OMO(43)
```

```
1/LO/PI1,RI1,TI1,LT1,TU1
1/L10/L11
1/L1/YL,UMAX,UMIN,FR,YIP,YEM
1/PR/UGU,UGD
1 /NRW/ AML,AMZ
1 /NEW5/  ITRB,ICYC
1   /NEW7/   AOM(43),AF(2,43),ZU(43)
1 /NEW8/ UHOLD(43)
1 /NEW15/   EMUP(43)
  COMMON /ZZ/ MX,MY,ILEN,CORD(2,43)
 COMMON/L/AK,ALMG
  ICYC=1
   ITRB=1
  DATA ITRB,IPIC,ISET/10,1,1/
  READ(7,9111) (XU,XL,PQQ,STEP)
  FORMAT (4F10.0)
    XU=XU/12.
  XL=XL/12.
  PQQ=PQQ/12.
  STEP=STEP/12.
  IPIC1=1
  IPIC=1
 INTG=1
  IPRNT=1
 L11=1
*    ***   ***   ***   ***    ***   ***   ***   ***   ***   ***
   IP=1
MAKES A PRINT OUT OF THE 5 CYCLES AFTER THE ACTUAL SECTION.


*    ***   ***   ***   ***    ***   ***   ***   ***   ***   ***
 CALL  CONST
```

```
      FRA=0.5
      AMI=0.0
        AME=0.00000001
      CALL REDST
       CALL   LENTH
      CALL  VIS
C*************** ** ******** ************************ **,** ** ** **
       UGU=U(NP3)
       UGD=U(NP3)
      FOR ANY OTHER TYPE OF FLOW USE BERNOULLI.
C*********************************,**********************************Q*****


6     ICYC=ICYC+1
      IPRNT=IPRNT+1
      UGU=UGD
      UGD=U(NP3)

     IF (ICYC.EQ. 1) INTG=INTG+1
        INUE
2     CONTINUE
       IF (ICYC.GT. 1) GO TO 612

      IF (INTG.NE. 1) GO TO 612
**    ***   ***   ***   ***   ***   ***   ***   ****   ***   ***
       DX=0.05*Y(NP3)
**    ***   ***   ***   ***   ***   ***   ***   ****   ***   ***
       XD=XU+DX

2     CONTINUE
```

```
      DX=FRA*PEI/(R(1)*AMI-R(NP3)*AME)
      IF (DX.LT. 0.0)  DX=ABS(DX)
***   ***   ***   ***   ***   ***   ***   ***   ****   ***   ***
    IF (DX.GT. 0.05*Y(NP3))   DX=0.05*Y(NP3)
***   ***   ***   ***   ***   ***   ***   ***   ****   ***   ***


    XD=XU+DX
     IF (XD.LT. PQQ) GO TO 752
    XD=0.0
    IF (PQQ-XU) 127,127,128
7     PQQ=PQQ+STEP
    WRITE (2,9631) (XU,PQQ,STEP)
1     FORMAT (3E10.3)
     GO TO 152
8       DX=PQQ-XU
    READ (7,9112) STEP
    FORMAT (F10.0)
    WRITE ( 2,9113) PQQ,STEP
     FORMAT (2E10.3)
    STEP=STEP/12.0
    IPIC=INTG
      PQQ=PQQ+STEP
   XD=XU+DX
   CALL   ENTRN
  CONTINUE
   CALL  PRE1 (XU,XD,DPDX)
  IF  (KASE.EQ.2)   GO  TO  26
  IF  (KIN.EQ.1)  CALL  MASS  (XU,XD,AMI)
  IF  (KEX.EQ.1)  CALL   MASS  (XU,XD,AME)
```

```
      CALL        EXEC3 (IPIC1,INTG,IPIC,OM,U,NP3)
      CALL OUT (IP,STEP,PQQ,IPRNT)
      IF (IPIC.EQ. INTG) CALL OURS1(IT,IPIC)
      CALL   COEFF
      SETTING   UP   VEL.,  AT  A  FREE   BOUNDARY.
***   ***   ***   ***   ***   ***   ***   ***   ***   ****   ***
***   ***   ***   ***   ***   ***   ***   ***   ***   ****   ***
      IF (KIN.EQ.2)  U(1)=SQRT(U(1)*U(1)-2.0*(XD-XU)*DPDX/RHO(1))
      CALL   SOLVE   (AU,BU,CU,U,NP3)
      SETTING  UP  VEL.,  AT   A   LINE  OF   SYM.,.
      IF  (KIN.NE.2)     GO   TO   71
      U(1)=U(2)
       IF  (KRAD.EQ.0)  U(1)=0.75*U(2)+0.25*U(3)
71    IF   (KEX.EQ.3)  U(NP3)=0.75*(NP2)+0.25*U(NP1)
72    CONTINUE
      IF   (NEQ.EQ.1)   GO  TO  30
      DO   45   J=1,NPH
        DO    46   I=2,NP2
       AU(I)=A(J,I)
      BU(I)=B(J,I)
      CU(I)=C(J,I)
46    CONTINUE
      DO  47   I=1,NP3
      SC(I)=F(J,I)
47    CONTINUE
      CALL    SOLVE    (AU,BU,CU,SC,NP3)
      DO   48   I=1,NP3
      F(J,I)=SC(I)
48    CONTINUE
      IF   (KASE.EQ.2)   GO   TO   81
      SETTING   UP   WALL  VALUES   OF   F.
```

```
      IF(KIN.EQ.1.AND.INDI(J).EQ.2)  F(J,I)=((1.0+BETA+GAMA(J))*F(J,2)-(
     11.0+BETA-GAMA(J))*F(J,3))*0.5/GAMA(J)
      IF (KEX.EQ.1.AND.INDE(J).EQ.2) F(J,NP3)=((1.0+BETA+GAMA(J))*F(J,NP
     12)-(1.0+BETA-GAMA(J))*F(J,NP1))*0.5/GAMA(J)
      SETTING   UP   SYM.,   LINE   VALUES   OF   F.
   1 IF   (KIN.NE.3)   GO   TO     82
      F(J,1)=F(J,2)
      IF   (KRAD.EQ.0)     F(J,1)=0.75*F(J,2)+0.25*F(J,3)
   2 IF (KEX.EQ.3)  F(J,NP3)=0.75*F(J,NP2)+0.25*F(J,NP1)
   5 CONTINUE
     1    CONTINUE
       IF (ITR3.EQ. 1 ) GO TO 16
      XP=XU
      XU=XD
      PEI=PEI+DX*(R(1)*AMI-R(NP3)*AME)
      THE   TERMINATION   CONDITION.
       UGU=UGD
      IF   (XU.LT.XL)   GO   TO   15
       RETURN
      END

       SUBROUTINE ALTER1(MPOW,MCOL,CORD,B,IC1,IC2)
      DIMENSION A(10,10),B(10),CORD(2,43)
      COMMON /GEN/PEI,AMI,AME,DPDX,PREF(2),PR(2),P(2),DEN,AMU,XU,XD ,XP,
     1*L,DX,INTG,CSALFA,MMG
     1/I/N,NP1,NP2,NP3,NEQ,NPH,KEX,KIN,KASE,KRAD
    LSQ   LSQ   LSQ   LXQ   LSQ   LSQLL
      IF (MPOW.GT. 9) STOP
      A(1,1)=NP3
      DO 10 I=1,MCOL
      DO 10 J=1,MCOL
      IF (I.EQ. 1.AND. J.EQ. 1) GO TO 10
      A(J,I)=0.0
```

```
      NO=I+J-2
      DO 20 L=1,NP3
      A(J,I)=A(J,I)+CORD(IC1,L)**NO
   20 CONTINUE
      WRITE (2,40) ((A(J,I),J=1,MCOL),I=1,MCOL)
MPOW IS THE POLYNOMIALS POWER.
MCOL IS THE NUMBER OF COLUMNS.
  = THE LEAST SQUARE POWER.
      DO 32 I=1,MCOL
      B(I)=0.0
      DO 30 L=1,NP3
      NO=I-1
      IF (NO.EQ. ) GO TO 31
      B(I)=B(I)+(CORD(IC1,L)**NO)*CORD(IC2,L)
      GO TO 30
   31 B(I)=B(I)+CORD(IC2,L)
   30 CONTINUE
   32 CONTINUE
      WRITE (2,40) (B(I),I=1,MCOL)
       CALL MA02A (A,B,MCOL,MCOL)
      WRITE (2,40) (B(I),I=1,MCOL)
   40  FORMAT (10E10.3)
      RETURN
      FORMAT (10E10.3)
            END


      SUBROUTINE EST2
     COMMON /GEN/PEI,AMI,AME,DPDX,PREF(2),PR(2),P(2),DEN,AMU,XU,XD ,XP,
    1XL,DX,INTG,CSALFA,MMG
    1/V/U(43),F(2,43),R(43),RHO(43),OM(43),Y(43)
    1/I/N,NP1,NP2,NP3,NEQ,NPH,KEX,KIN,KASE,KRAD
    1/B/BETA,GAMA(2),TAUI,TAUE,AJI(2),AJE(2),INDI(2),INDE(2)
    1 /NRR/ COF(10,42)
```

```
1/LO/PI1,RI1,TI1,LT1,TU1
1 /NRW/ AML,AMZ
   Y(2)=((2.0*AMZ)/(RHO(2)*U(2)*R(2)+RHO(1)*U(1)*R(1)))+Y(1)
   AVAZ=2.0*PEI /(R(1)+SQRT(R(1)*R(1)+2.0*Y(2)*PEI*CSALFA))
   Y(2)=Y(2)/AVAZ
   DO 101  I=3,NP3
**********************************************************************
     IF (I.LE. NP2) AAA=COF(1,I)
     IF (I.EQ. NP3)  AAA=1.0
CHANGE IN THE PROCEDURE OF EST2.

**********************************************************************
   BBB=COF(1,I-1)
   Y(I)=Y(I-1)+0.5*(AAA-BBB)*(1.0/(RHO(I)*U(I))+1.0/(RHO(I-1)*U(I-1)
1))
1     CONTINUE
  IF (CSALFA.EQ.1.0.OR.KRAD.EQ.0)   GO  TO  51
  DO  52  I=2,NP3
  Y(I)=2.0*Y(I)*PEI/(R(1)+SQRT(R(1)*R(1)+2.0*Y(I)*PEI*CSALFA)  )
2 CONTINUE
  GO  TO  56
1 DO  54   I=2,NP3
  Y(I)=PEI*Y(I)/R(1)
  CONTINUE
     CONTINUE
  CALC.  OF  THE  RADI.
  DO  57   I=2,NP3
  IF (KRAD.EQ.0)   R(I)=R(1)
  IF (KRAD.NE.0)  R(I)=R(1)+Y(I)*CSALFA
  CONTINUE
    RETURN
   END
```

Appendix 4

Radial Wall Jet Study

An appreciation of the time averaged rates of change of momentum and mass transfer within a turbulent radial wall jet has been obtained, by mapping the time averaged radial velocity and species concentration fields within this flow.

The radial wall jet was produced by normally impinging a Nitrogen jet onto a horizontal flat surface. The free edge of the flow was exposed to the atmosphere. The equipment used in this experiment is described in section 1; and the techniques and associated devices employed to measure the velocity and species concentrations are detailed in sections 2 and 3 respectively. The experimental procedure is presented in section 4, and the results obtained are discussed and detailed in sections 5 and 6 respectively.

4.1 Equipment

The equipment used in this experiment is shown in figure 1a. The surface over which the radial wall jet passed is shown in more detail in figure 1b, and was made from sheets of steel and vulcanite measuring 0.04 x 0.75 x 0.75m. The upper vulcanite surface was ground flat to within $\pm$ 0.0001m, and had a reference line drawn on it. This line was parallel to one of the surfaces sides, and passed through an imaginary point at the intersection between the axi-symmetric center line of the nozzle ab and vulcanite surface.

The construction and sizing of both the nozzle and pipe that connected to a pressurized Nitrogen gas supply are shown in figure 4.2.

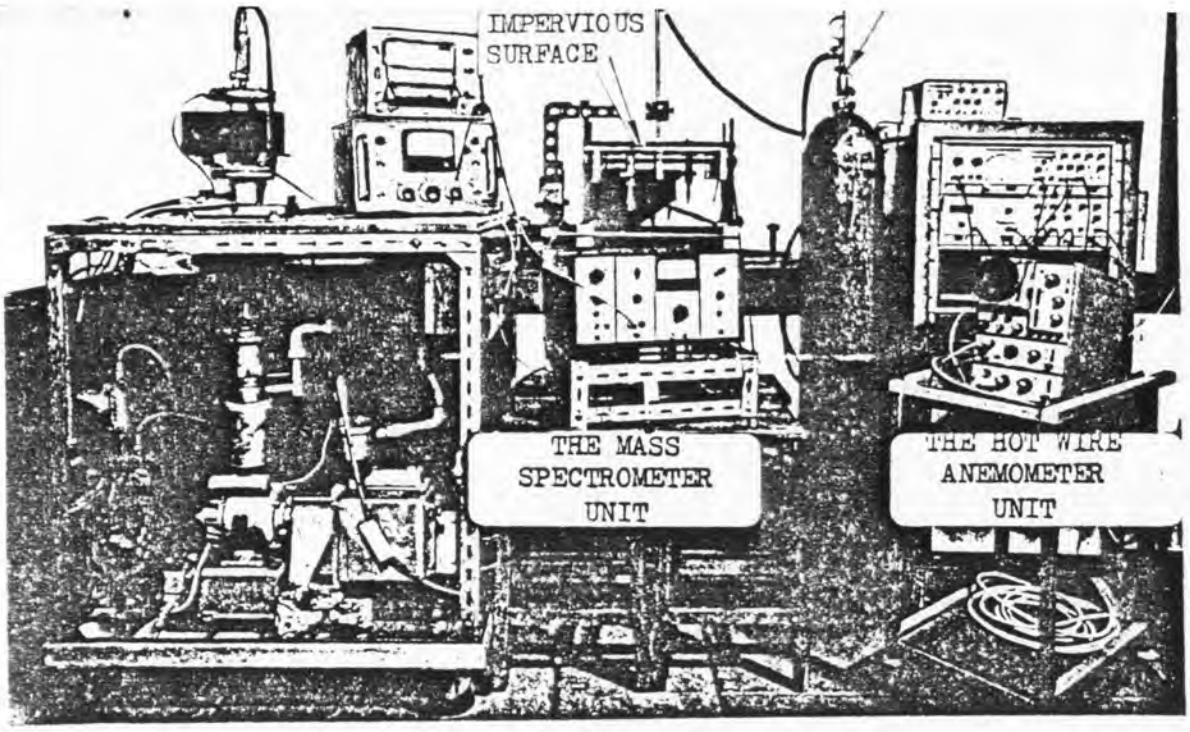

a. EQUIPMENT

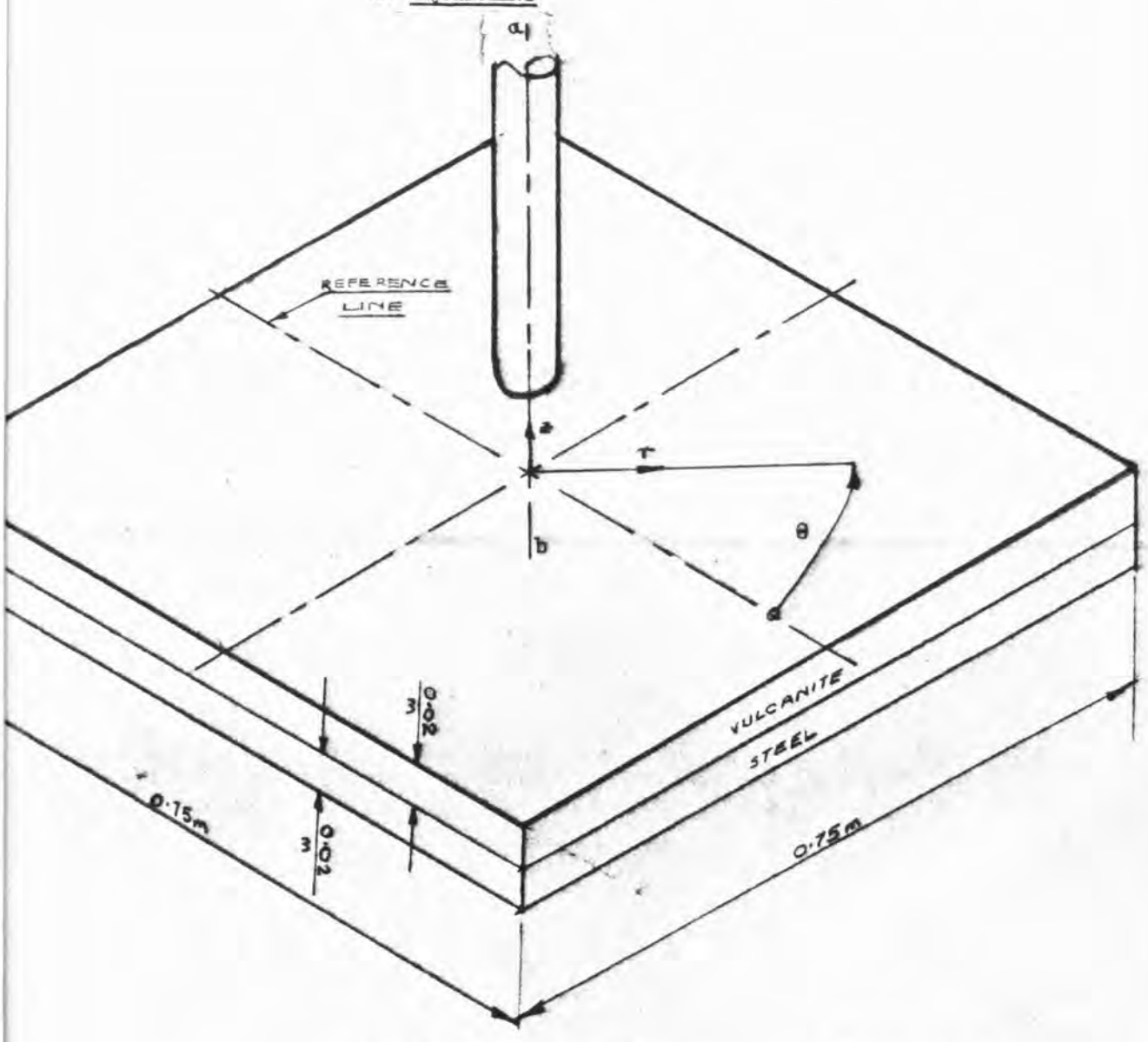

b. VULCANITE SURFACE

FIGURE 4.1

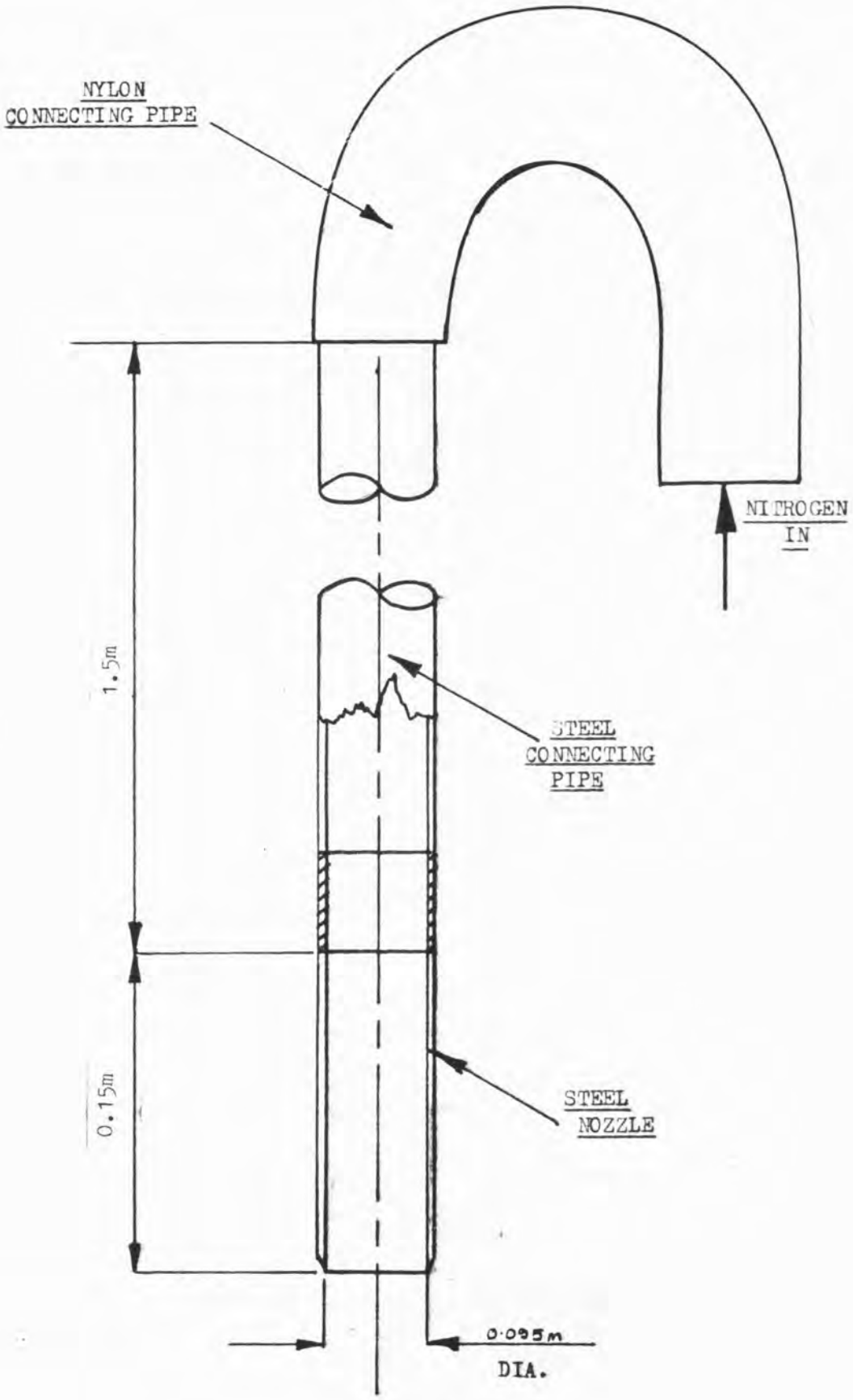

NOZZLE

FIGURE 4.2

The most important dimensions shown in this figure are:

a) the internal diameter of the nozzle at 0.0095m

and b) the 1.5m straight pipe that connects to the Nitrogen supply ; this length of pipe ensured a fully developed flow into the nozzle.

The time averaged species concentration of Nitrogen and Oxygen were measured with a Mass Spectrometer, an MS10 manufactured by A.E.I. The working principles of this device, and the sampling technique used to measure concentrations are described in section 2.

Hot wire anemometry was used to measure the radial velocity. The hot Wire Anemometer Unit used in this experiment is shown in figure 1a, it was manufactured by Disa and designated type D5501. The unit was used with a Disa hot wire probe (type D101). Further information on these devices is presented in section 3.

A measurement pillar was used to move and position the measuring probes deployed during this experiment. An exploded view of the pillar is presented in figure 4.3. The pillar was made of steel, and had a lengthwise slot cut in it. This slot was machined to just hold the mounting block that held any of the measuring probes. The base of the pillar was ground flat at right angles to the slot. The mounting block was brass and held the probe with their center line ab in a plane parallel to the base of the pillar. A micrometer was used to move the mounting block along the slot.

4.2 Mass Spectrometer

The purpose of this device is to output:

a) data which enables a sampled gas to be identified

and b) a current signal in amps which is related to both the partial pressures and molecular weights of the constituents in a sample.

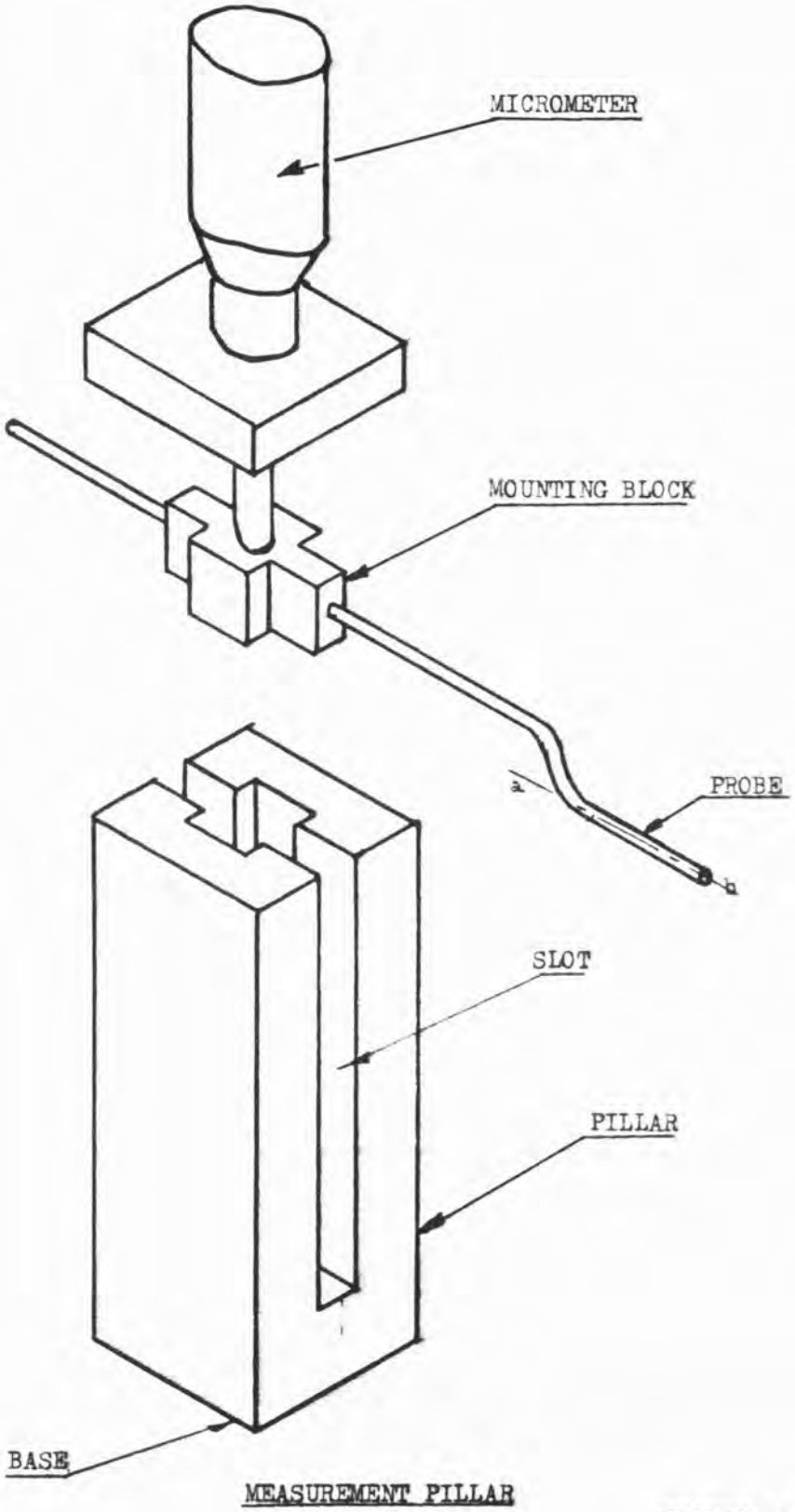

MEASUREMENT PILLAR

FIGURE 4.3

Before further discussing this output, and the way in which it can be used, the construction of the measuring probe and then the operational principles of the mass spectrometer are detailed.

The probe used with the mass spectrometer was made from stainless steel, and is detailed schematically in figure 4.4. The flow distortion produced when sampling was reduced to a minimum by setting the internal diameter of the probe to 0.0015m. With this size of probe the velocity at which sampled gas was extracted from the radial wall jet was of the same order of magnitude as velocities within the studied flow.

A schematic layout of a typical mass spectrometer is presented in figure 4.5. The operational principles will be explained by following the path taken by the sampled gas through this device. The gas sample is sucked into the mass spectrometer through the measuring probe. The venturi meter fixed the volumetric flow rate at which the sample was introduced to a value specified by the manufacturer. The sample then passes through a velocity filter. This is cylindrical in shape, and is maintained at a pressure far less than atmospheric. Focusing slits S_1 and S_2 are situated at either end of the filter, and co-terminus electric and magnetic fields are produced between them. These fields exert opposing forces upon the ions produced and passing through the filter, so that those successfully passing through the outlet focusing slit S_2 possess a unique velocity given by:

$$v = \frac{\sigma E'}{H'} \qquad (4.1$$

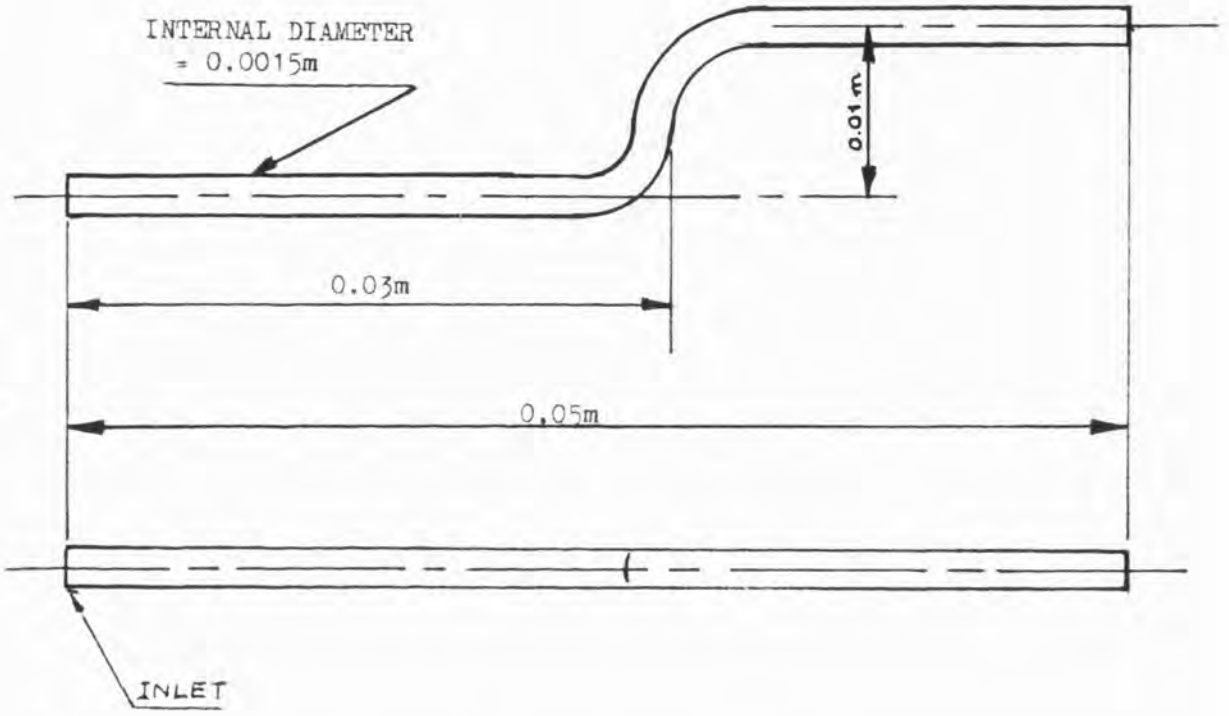

MASS SPECTROMETER PROBE

FIGURE 4.4

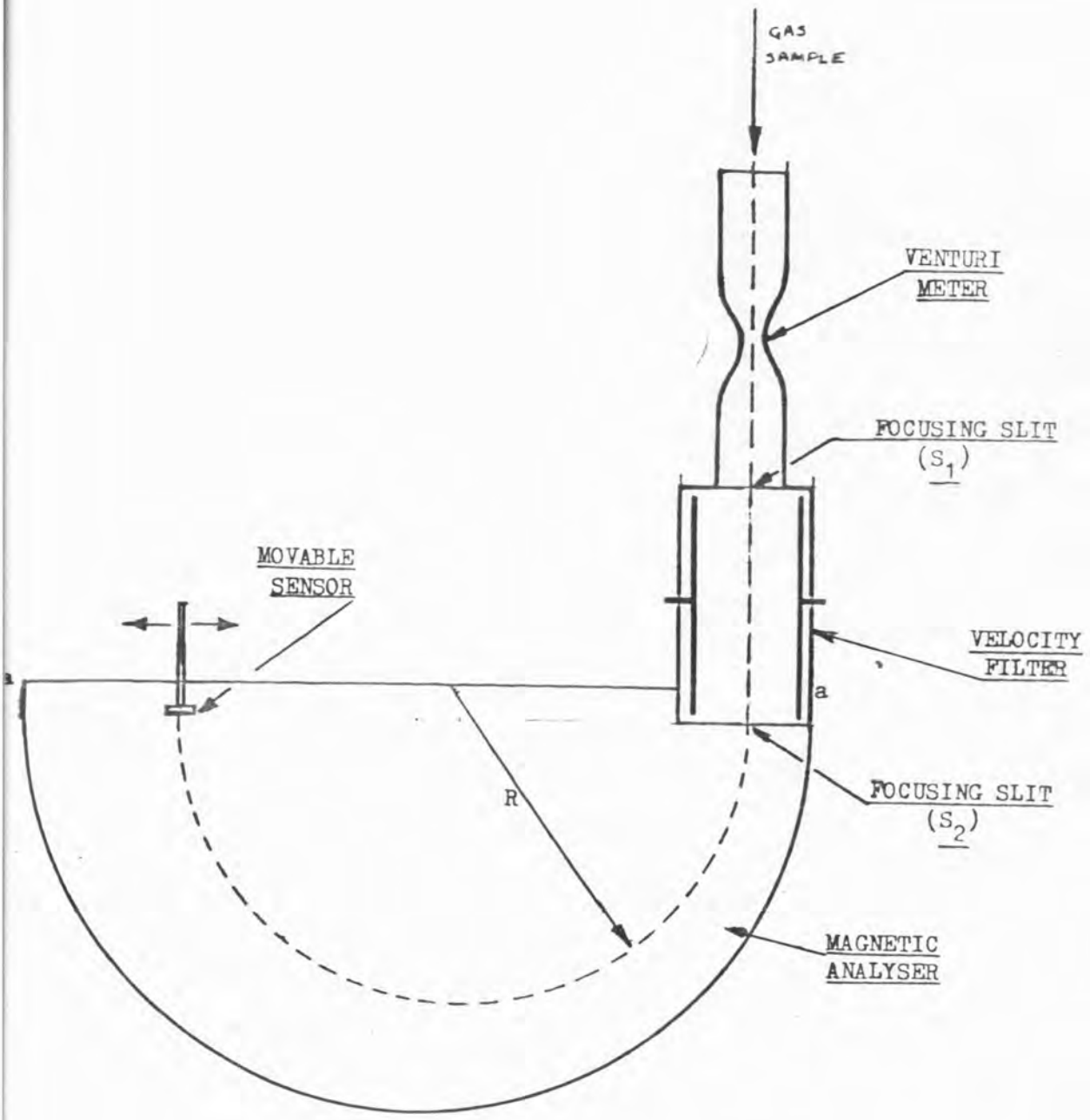

MASS SPECTROMETER

FIGURE 4.5

In this equation c' represents the speed of light, and E' and H' specify the strength of the electric and magnetic fields respectively. The ions then pass into the magnetic analyser, also with a uniform magnetic field strength H', and are deflected along tracks with radii of curvature R given by a balance between magnetic and centrepedial forces acting upon each ion:

$$R = \frac{U}{e} \quad \frac{c'^2 E'}{(H')^2} \qquad (4.2$$

A moveable sensor located at the exit of the analyser can be moved to any point along the diameter aa in figure 4.5. This sensor is automatically positioned at various radii R, corresponding to integar molecular weights between one and a hundred, and at each position the number of ions impinging upon the sensor recorded and outputted as a current signal. It is this signal which is used to identify and determine the concentrations of the species in a sample.

The following procedure has been used to transform output signals from the mass spectrometer into the gravimetric concentrations of Nitrogen and Oxygen. Firstly, the partial pressures of Nitrogen p_{N_2} and Oxygen p_{O_2} are estimated from the ouput signals at molecular weights of 18, 28 and 32 - represented by I_{18}, I_{28} and I_{32} respectively - with equations 4.3 and 4. These equations have been supplied by the manufacturer of the mass spectrometer. The gravimetric concentration of Nitrogen m_{N_2} and Oxygen m_{O_2} are then obtained from the calculated partial pressures by using Gibbs and Daltons Law.

$$P_{O_2} = \left[\frac{I_{32} - 0.118(I_{18})}{2.6}\right] \times 10^{-5} \text{ torr} \quad (4.3$$

$$P_{N_2} = \frac{I_{28}}{3.6} \times 10^{-5} \text{ torr} \quad (4.4$$

4.3 Anemometer Unit

The Disa Anemometer unit (type D5501) measured the voltage across a D101 hot wire probe maintained at a constant temperature. The mode of operation of this type of unit is detailed in the Disa handbook[56]. Briefly it is as follows:

a) the hot wire probe is placed in the studied flow, with the wire at right angles to the flow direction - as shown in figure 4.6,

b) the voltage across the probe was integrated over 10 seconds and then measured

and c) the velocity over the probe was read from measured calibration charts for both anemometer unit and probe.

In this experiment the calibration chart for the anemometer unit and probe details the relationship between the velocity over the wire against the voltage supplied by the anemometer unit, for various concentrations of Nitrogen and Oxygen. The prescribed concentrations used are detailed in table 4.1. A specimen calibration chart is presented in figure 4.7; the experimental data from which it was derived is detailed in section 6.

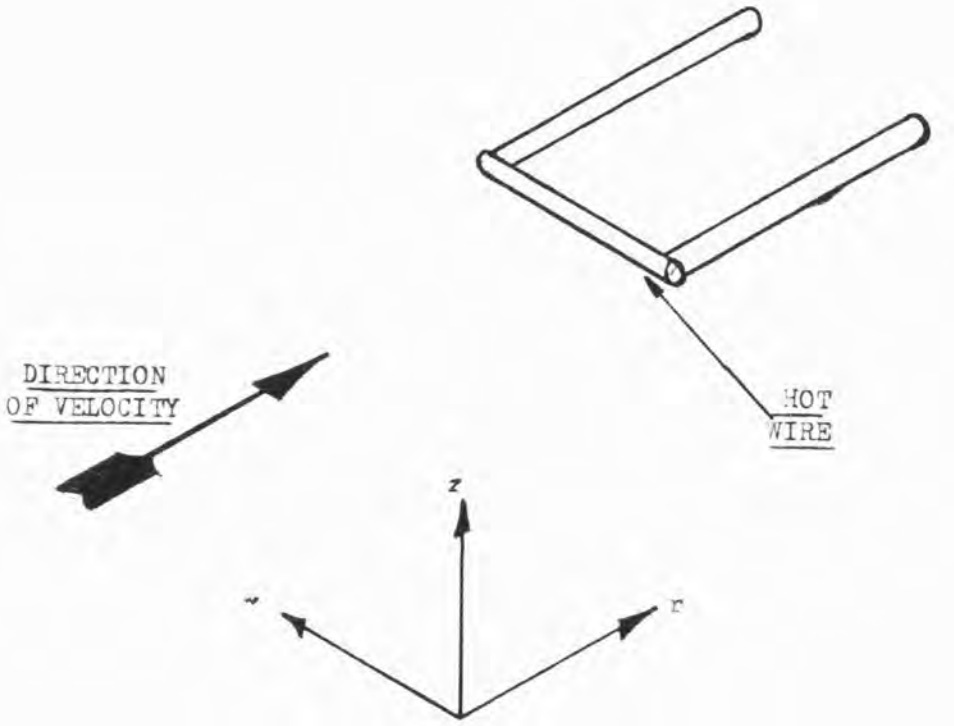

HOT WIRE

FIGURE 4.6

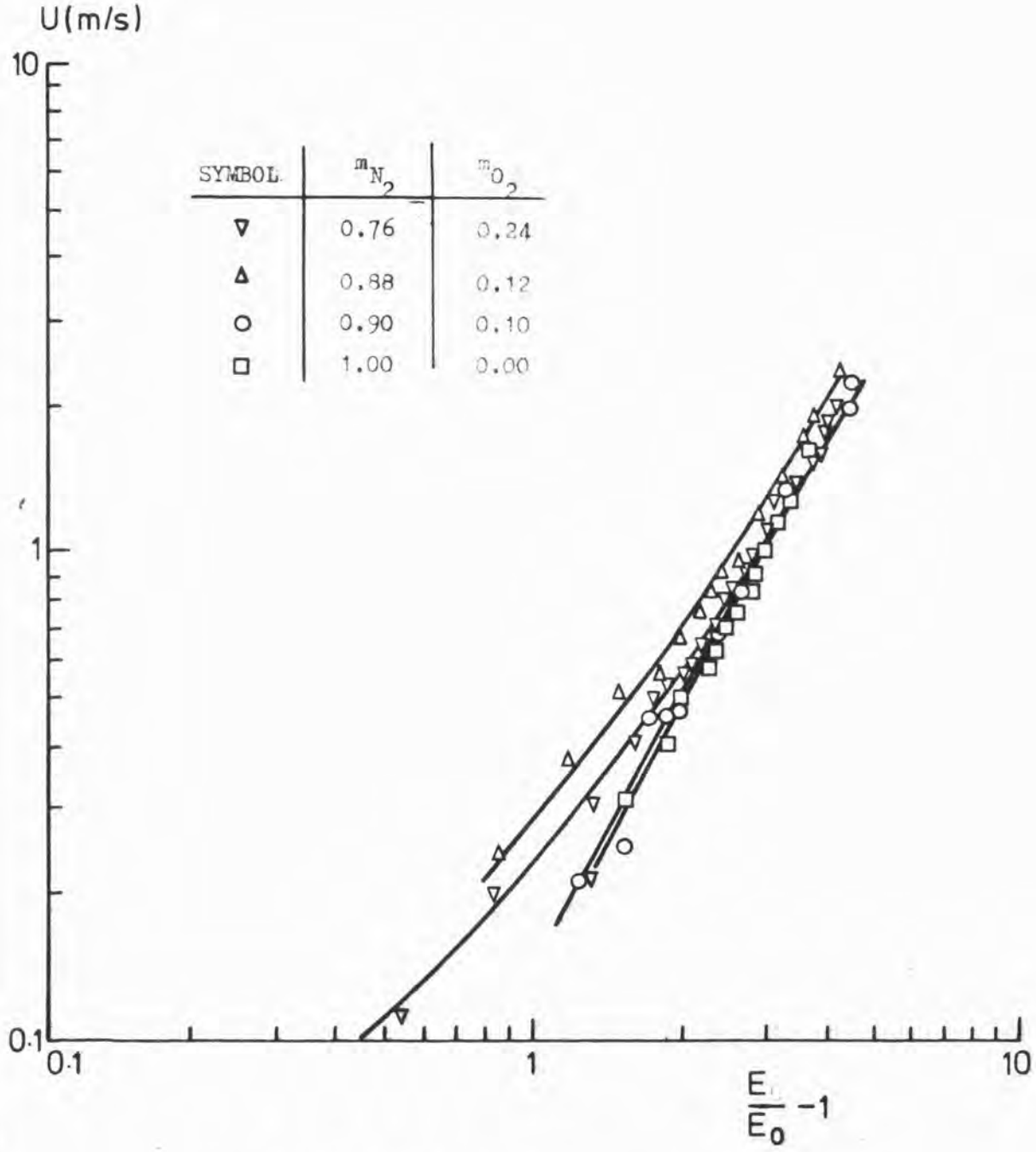

THE CALIBRATION CURVES

FIGURE 4.7

Table 4.1

Concentration Levels

Gas	Concentration Levels			
Nitrogen	0.76	0.88	0.90	1.0
Oxygen	0.23	0.12	0.10	0.0

The equipment used to calibrate the hot wire probe and anemometer unit is shown in figure 4.8. The major component is the straight length of duct 2.0 metres long and 0.075m internal diameter. At one end of this duct a system of subsidiary ducts carried measured volumetric flowrates of Nitrogen and Oxygen. These subsidiary ducts were 0.02 and 0.04m internal diamter; with the inner duct having an outside diameter of 0.022m. A three dimensional movement mechanism, comprising three micrometers, was positioned at the other end of the straight duct. The mass spectrometer, pitot static tube and hot wire probes were mounted in this mechanism with their axis, designated aa, bb & cc in figure 4.8, parallel to the center line of the straight duct. The mass spectrometer probe has been described in section 2, and the samples taken were processed in the specified manner.

The pitot static tube used had an internal diameter of 0.002m, and conformed to British Standard 1042 part 2A. The dynamic pressure this probe sensed was measured with an electric manometer. The hot wire probe and associated anemometer unit were as specified above.

The experimental procedure used to obtain data for the calibration chart is best explained by detailing how one point was measured - for thereafter repetition of this procedure provides all the necessary data. Firstly, the volumetric flowrates of Nitrogen and Oxygen into the straight duct were set, so that at a reference point on the ducts center line and 0.01m from it's exit the concentration of Nitrogen and Oxygen were at one of the levels

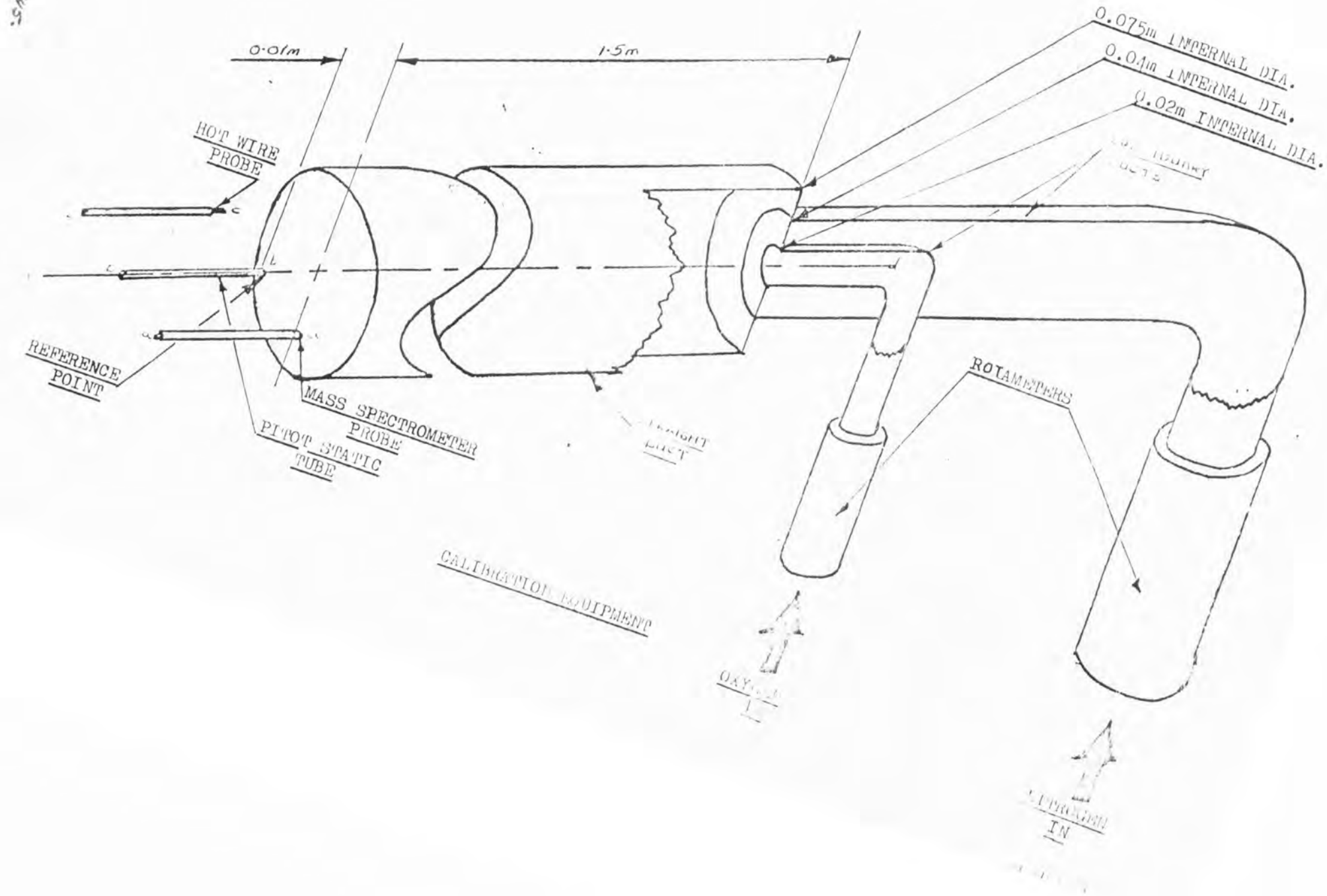
0·01m
1·5m
0.075m INTERNAL DIA.
0.04m INTERNAL DIA.
0.02m INTERNAL DIA.
HOT WIRE PROBE
REFERENCE POINT
MASS SPECTROMETER PROBE
PITOT STATIC TUBE
CALIBRATION EQUIPMENT
ROTAMETERS
OXYGEN IN
NITROGEN IN

specified in table 4.1. The concentration was measured with the mass spectrometer probe at the reference point and the center lines of the probe and duct, aa and dd in figure 4.8, coincident. The gravimetric concentrations were derived from the output readings from the mass spectrometer at molecular weights of 18,28 and 32, represented by I_{18}, I_{28} and I_{32}, with equations 4.3 and .4. Secondly, the described pitot static tube was positioned at the reference point, again with the axi-symmetric center lines of the probe and straight duct coincident. The velocity U was derived from the measured dynamic head P_D using:

$$U = \sqrt{\frac{2P_D}{\rho_{mix}}} \qquad (4.7$$

In this equation ρ_{mix} represents the density of the mixture, which was obtained from the equation of a perfect gas:

$$\rho_{mix} = \frac{P}{RT}\left[(M_m)_{N_2} + (M_m)_{O_2}\right] \qquad (4.7$$

Finally, the hot wire probe was positioned at the reference point, with the hot wire located in a plane at right angles to the axi-symmetric axis of the calibration duct, dd in figure 4.8 and the voltage reading from the anemometer unit E recorded. The measured concentrations m_{N_2} and m_{O_2}, velocity U and voltage E are the co-ordinates of one point upon the calibration chart.

4.4 Experimental Procedure

The procedures for setting up, and then mapping the radial velocity and species concentration fields in the radial wall jet are detailed in sub-section a and b respectively.

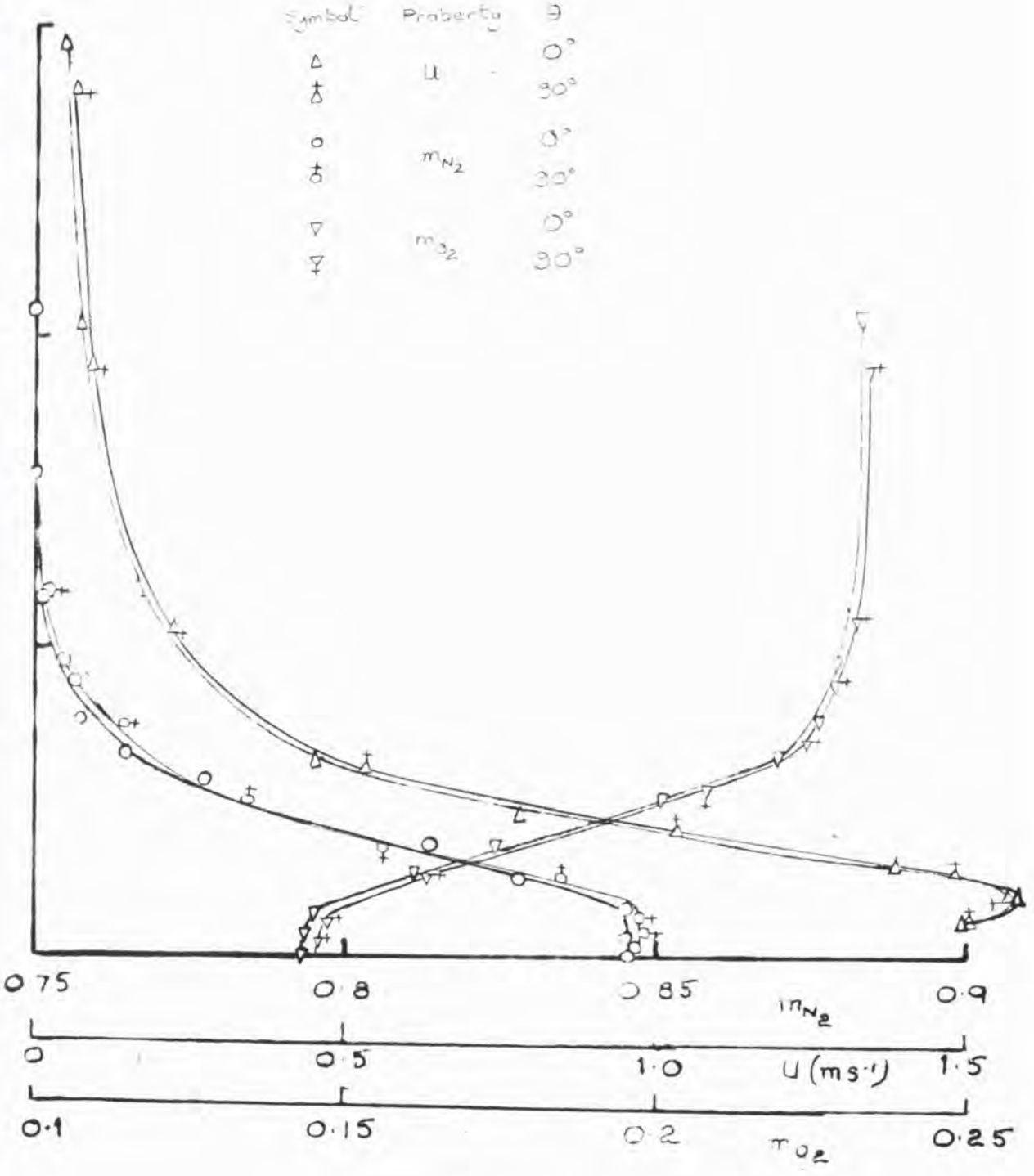

CROSS-STREAM FLOW PATTERNS AT r = 1.5m

FIGURE 4.3

4.4a Setting Up

Throughout the experiment the volumetric flowrate of Nitrogen to the nozzle was maintained at 49.0 litres/min.

The impinging flow, which included the radial wall jet, was considered symmetrical about the center line ab of the nozzle in figure 4.1 when the following conditions were met. Firstly, that impervious surface was horizontal and the nozzle center line ab vertical. Secondly, differences of less than five percent were obtained in the measured flow properties at points located in different portions of the flow - that is at different angles θ in figure 4.1 - but at the same vertical height z and radius of 0.05m. Two specimen plots are presented in figure 4.9 which show that the studied flow meets this condition. The plots detail the variation of the measured properties at two cross-stream sections at a radius of 0.05m, these sections were separated by an angle of ninety degrees. In these results the specified maximum percentage discrepancies are less than five percent.

4.4b Mapping

This part of the experiment has been split into two parts - namely the mapping of the time averaged species concentration and then radial velocity flow patterns.

In part one the mass spectrometer probe was held in the measurement pillar with it's center line, ab in figure 4.3, positioned in the same radial plane as the reference line on the vulcanite surface. The measuring head of the probe was postioned at radii 0.047, 0.05, 0.075, 0.10, 0.125,

0.15, 0.175 and 0.20m; and at each section the mixture was sampled at several different heights. The results from the mass spectrometer take the form of current readings at molecular weights of 18, 28, 32 and 44 and are detailed in section 6b.

In the second part of the experiment the hot wire probe was positioned with the measurement pillar. Again the measurement head of the probe was positioned at the radii previously specified; and at various heights the voltage across the plane measured. The experimental data thus obtained is presented in section 6c. The radial velocity at each of the points under investigation was looked up from the calibration chart using the measured voltage and species concentration at that point.

Plots of the measured radial velocity and Nitrogen and Oxygen concentrations at radii of 0.05, 0.075, 0.100, 0.125, 0.15, 0.175 and 0.20m are presented in figures 7.2 to 7.8 in chapter 7. The symbols used in these figures are detailed in 7.1.

4.5 Discussion

The degradation of the Nitrogen content in the jet was caused by both air entrainment at the free-edge and turbulent transfer processes within the jet. However, because the Nitrogen and Oxygen concentration in the jet were similar to those in the submerging fluid, the rates of change in these properties were slow.

4.6 Data

a. Calibration Data for the Hot Wire Anemometer

Pressure from Pitot Static Tube H x 10^{-4} (m of water)	E (volts)
i) $m_{N_2} = 0.76$, $m_{O_2} = 0.24$ and $E_0^+ = 0.6$v	
0.03	0.930
0.05	1.100
0.08	1.400
0.10	1.566
0.15	1.652
0.175	1.733
0.190	1.811
0.21	1.886
0.25	1.943
0.30	2.020
0.39	2.108
0.43	2.158
0.52	2.231
0.60	2.287
0.73	2.410
0.92	2.510
1.05	2.598
1.15	2.727
1.40	2.873
1.55	3.936
1.80	3.000
2.10	3.069
2.40	3.168

+ E_0 represents the base voltage of the anemometer.

continued

	Pressure from Pitot Static Tube $H \times 10^{-4}$ (m of water)	E (volts)
ii) $m_{N_2} = 0.88$, $m_{O_2} = 0.12$ and $E_0 = 0.56v$		
	0.075	1.015
	0.010	1.217
	0.180	1.446
	0.210	1.590
	0.300	1.703
	0.400	1.790
	0.480	1.872
	0.550	1.935
	0.620	2.055
	0.980	2.210
	1.350	2.380
	2.050	2.580
	3.900	2.960
iii) $m_{N_2} = 0.911$, $m_{O_2} = 0.09$ and $E_0 = 0.54v$		
	0.025	1.260
	0.125	1.504
	0.135	1.605
	0.225	1.697
	0.270	1.854
	0.475	2.000
	1.075	2.262
	2.245	2.678
	2.915	2.900

continued

Pressure from Pitot Static Tube H x 10^{-4} (m of water)	E (volts)

iv) $m_{N_2} = 1.0$, $m_{O_2} = 0.0$ and $E_0 = 0.5$

0.028	1.120
0.080	1.440
0.150	1.436
0.200	1.640
0.220	1.676
0.290	1.738
0.320	1.800
0.480	1.914
0.600	1.970
0.780	2.066
1.050	2.158
1.380	2.258
1.620	2.308
2.000	2.354
2.500	2.445
2.800	2.492
3.100	2.545

b. Concentration Data

Height of the probe above the impervious surface (z) x 10^{-4}m	Readings from the Mass Spectrometer at molecular weights of: 18	28	32	44
i) r = 0.05m				
0.64	1.20	118.08	9.25	0.56
1.64	0.95	107.83	8.50	0.53
2.64	0.87	94.08	8.40	0.48
3.64	0.90	92.33	9.08	0.53
4.64	0.95	86.83	9.50	0.53
5.64	1.00	82.83	10.25	0.53
6.64	1.09	80.58	10.68	0.61
7.64	1.13	78.83	10.85	0.63
9.64	1.17	77.33	10.80	0.63
11.64	1.20	76.08	10.78	0.63
15.64	1.20	75.58	10.68	0.65
20.64	1.20	76.83	10.98	0.71
ii) r = 0.075m				
0.64	1.03	86.14	8.72	0.53
1.64	1.00	82.53	8.53	0.47
2.64	0.95	79.67	8.46	0.47
3.64	0.98	80.56	8.75	0.41
4.64	0.96	79.70	8.79	0.41
5.64	0.96	78.84	9.12	0.41
8.14	1.03	73.53	9.57	0.40
10.64	1.08	76.24	9.91	0.40
13.14	1.12	74.38	10.19	0.40
15.64	1.14	73.27	10.28	0.44
18.14	1.17	72.41	10.04	0.46
20.64	1.20	71.80	10.13	0.51

continued

Height of the probe above the impervious surface (z) x 10^{-4}m	Readings from the Mass Spectrometer at molecular weights of: 18	28	32	44
iii) r = 0.10m				
0.64	1.44	109.08	8.4	0.85
1.64	1.25	99.82	8.7	0.81
2.64	1.10	93.05	8.9	0.69
3.64	0.99	86.54	9.7	0.69
5.64	0.99	83.72	9.4	0.71
8.14	1.01	82.25	9.5	0.71
10.64	1.04	80.99	9.7	0.74
13.14	1.14	80.98	9.9	0.82
15.64	1.17	80.97	9.9	0.83
18.14	1.22	79.95	10.2	0.86
20.64	1.28	79.84	10.5	0.97
iv) r = 0.125m				
0.64	0.78	89.06	9.51	0.38
1.64	0.73	85.36	9.19	0.40
2.64	0.67	84.67	9.54	0.49
3.64	0.68	84.48	9.52	0.55
5.64	0.71	83.79	9.50	0.48
8.14	0.77	82.34	9.49	0.50
10.64	0.78	81.90	9.67	0.59
13.14	0.82	80.95	10.15	0.62
15.64	0.88	80.26	10.23	0.64
18.14	0.92	79.57	10.46	0.66
20.64	0.96	78.87	10.47	0.73
v) r = 0.15m				
0.64	0.91	81.89	9.60	0.57
1.64	0.91	79.41	9.37	0.59
2.64	0.90	78.67	9.32	0.61
3.64	0.89	81.94	9.65	0.64

continued

Height of the probe above the impervious surface (z) x 10^{-4}m	Readings from the Mass Spectrometer at molecular weights of: 18	28	32	44
vii) r = 0.175m				
0.64	1.64	125.39	14.56	0.81
1.64	1.48	111.33	12.95	0.77
2.64	1.16	98.52	11.52	0.68
3.64	1.06	89.47	10.58	0.57
4.64	0.96	83.16	9.84	0.46
5.64	0.79	77.10	9.00	0.44
8.14	0.58	64.29	7.88	0.38
10.64	0.59	63.23	7.79	0.37
13.14	0.75	69.17	8.67	0.33
15.64	0.79	69.12	8.73	0.36
18.14	0.82	68.56	8.58	0.38
20.64	0.81	66.00	8.49	0.36
viii) r = 0.2m				
0.64	1.0	85.40	10.55	0.74
1.64	0.85	80.39	9.89	0.73
2.64	0.79	76.07	9.33	0.71
3.64	0.77	78.51	9.87	0.66
4.64	0.83	79.44	9.91	0.57
5.64	0.87	78.88	10.04	0.55
8.13	0.86	78.31	9.98	0.51
10.64	0.86	78.25	9.94	0.49
15.64	0.82	77.48	9.88	0.47
20.64	0.83	76.62	10.05	0.44

Velocity

Height of the probe above the impervious surface (z) x 10^{-4}m	Voltage from the Anemometer Unit (E) volts
i) r = 0.05m	
1.512	2.26
2.012	2.37
2.512	2.24
3.012	2.04
3.512	1.93
4.012	1.76
4.512	1.70
5.012	1.65
5.512	1.54
6.512	1.21
7.512	1.14
8.512	1.12
9.512	1.05
10.512	1.01
11.512	0.95
12.512	0.93
13.512	0.87
14.512	0.84
15.512	0.83

continued

Height of the probe above the impervious surface (z) x 10^{-4}m	Voltage from the Anemometer Unit (E) volts
ii) r = 0.075m	
1.512	2.032
2.012	2.136
2.512	2.185
3.012	2.220
3.512	2.157
4.012	2.112
4.512	2.047
5.012	1.975
5.512	1.892
6.012	1.820
6.512	1.758
7.512	1.588
8.512	1.382
9.512	1.217
10.512	1.100
11.512	1.000
12.512	0.915
13.512	0.876
14.512	0.854
16.512	0.800

continued

Height of the probe above the impervious surface (z) $\times 10^{-4}$m	Voltage from the Anemometer Unit (E) volts
iii) r = 0.100m	
1.512	1.610
2.012	1.680
2.512	1.710
3.012	1.732
3.512	1.723
4.012	1.710
4.512	1.690
5.012	1.670
5.512	1.612
6.012	1.590
6.512	1.520
7.512	1.440
8.512	1.330
9.512	1.230
10.512	1.140
11.512	1.030
12.512	0.950
13.512	0.900
14.512	0.820
16.512	0.720
19.012	0.660

continued

Height of the probe above the impervious surface (z) $\times 10^{-4}$m	Voltage from the Anemometer Unit (E) volts
iv) r = 0.125m	
1.512	1.370
2.012	1.460
2.512	1.562
3.012	1.584
3.512	1.605
4.012	1.615
4.512	1.603
5.012	1.598
5.512	1.586
6.012	1.563
6.512	1.515
7.512	1.480
8.512	1.410
9.512	1.340
10.512	1.250
11.512	1.160
12.512	1.105
13.512	1.005
14.512	0.920
15.512	0.930
16.512	0.780

continued

Height of the probe above the impervious surface (z) x 10^{-4}m	Voltage from the Anemometer Unit (E) volts
v)r = 0.150m	
1.512	1.190
2.012	1.245
2.512	1.345
3.012	1.395
3.512	1.434
4.012	1.450
4.512	1.455
5.012	1.454
5.512	1.440
6.012	1.420
6.512	1.414
7.512	1.380
8.512	1.340
9.512	1.285
10.512	1.200
11.512	1.145
12.512	1.118
13.512	1.048
14.512	0.990
15.512	0.920
16.512	0.865
17.512	0.830
19.012	0.755

continued

vi) r = 0.175m

Height of the probe above the impervious surface (z) x 10^{-4}m	Voltage from the Anemometer Unit (E) volts
1.512	0.920
2.012	0.970
2.512	1.000
3.012	1.130
3.512	1.160
4.512	1.180
5.012	1.200
5.512	1.250
6.012	1.270
7.012	1.270
8.012	1.240
9.012	1.180
10.012	1.140
11.012	1.100
12.012	1.050
13.012	0.990
14.012	0.950
15.012	0.940
16.012	0.930
17.012	0.880
18.012	0.850

continued

	Height of the probe above the impervious surface (z) $\times 10^{-4}$m	Voltage from the Anemometer Unit (E) volts
vii) r = 0.200m		
	1.512	0.780
	2.012	0.870
	2.512	0.985
	3.012	1.055
	3.512	1.075
	4.012	1.110
	4.512	1.120
	5.012	1.130
	5.512	1.160
	6.012	1.180
	6.512	1.170
	7.012	1.158
	6.512	1.170
	8.012	1.198
	8.512	1.190
	9.012	1.188
	10.012	1.098
	11.512	1.085
	14.012	1.000
	16.512	0.930
	19.012	0.838
	21.512	0.782

Appendix 5

Turbulent Impinging Argon, Nitrogen and Oxygen Flow

The intent of the experimental work presented is to map the variation of the time averaged radial velocity, species concentration and temperature within an impingement flow. These results are used in chapter eight to assess the adequacy of a flow modelling technique.

The flow was produced by the normal impingement of a hot argon jet on to a horizontal flat impervious surface - as shown in figure 5.1 The free edge of the flow was exposed to the atmosphere. The pieces of equipment used to both produce the flow and measure the specified flow properties are described in section 1. The experimental procedures followed to set up the flow, and then to measure the specified flow properties, are discussed in section 2. The results obtained are discussed in section 3, and the associated experimental data is detailed in section 4.

5.1 Equipment

The studied flow was produced by the normal impingement of a hot argon jet on to a horizontal impervious surface. The Argon jet was generated with an industrial plasma torch that is described in sub-section a; and the surface is detailed in sub-section b. The equipment, including suitable probes, used to measure the time averaged radial and vertical velocities, species concentration and temperatures are presented in sub-sections c, d and e respectively.

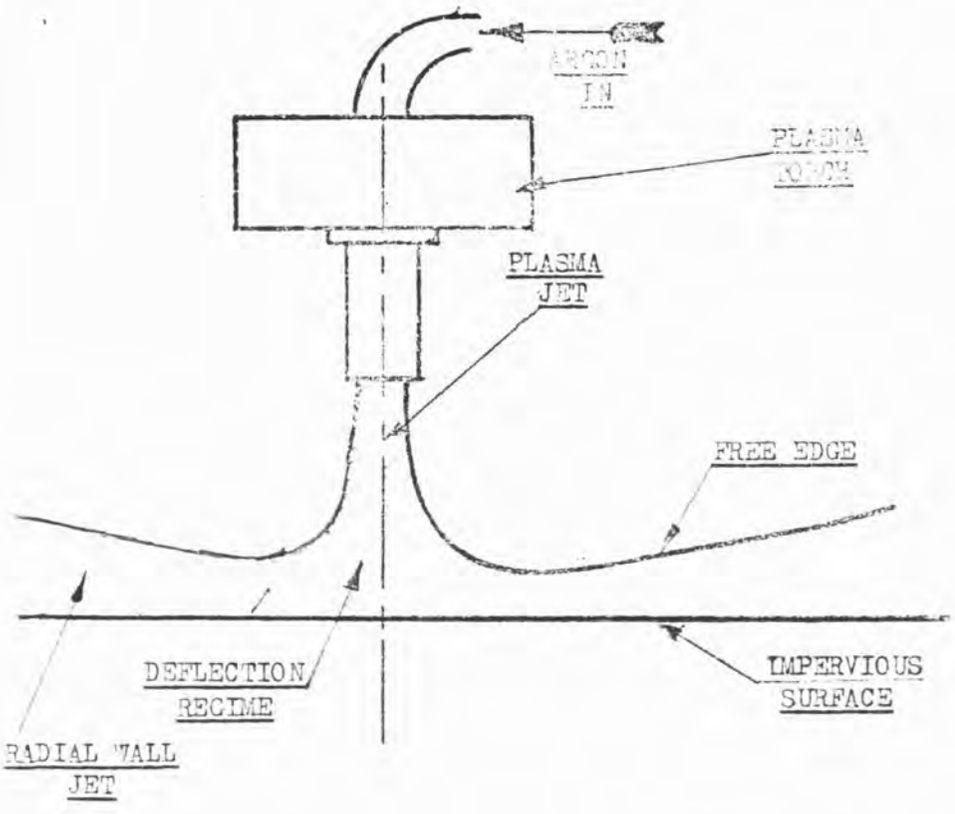

EXPERIMENTAL LAYOUT

FIGURE 5.1

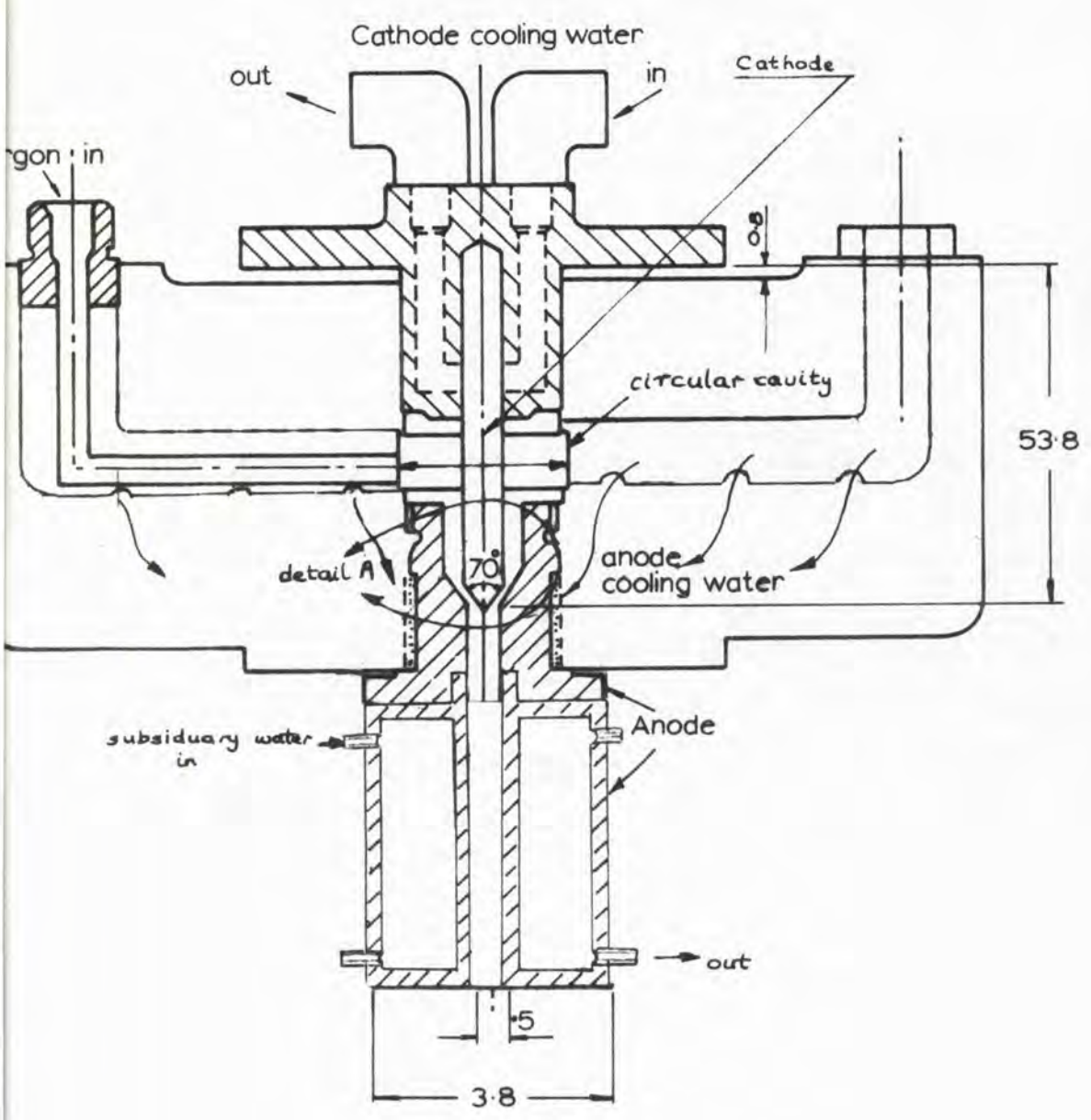

a ELEVATION ON AA

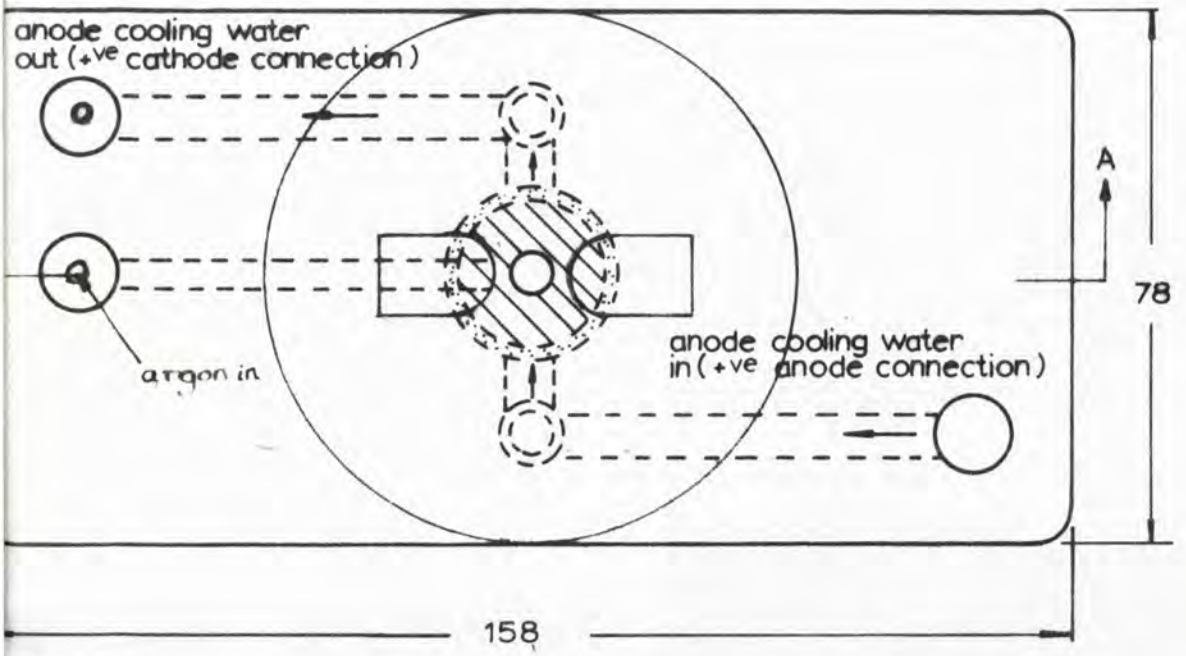

b. PLAN

all dimensions mm

INDUSTRIAL PLASMA TORCH

FIGURE 5.2

5.1a Plasma Torch

Two schematic views of the plasma torch are detailed in figure 5.2. The side elevation, figure 5.2a, shows a sectional view on the plane aa, and details the torches internal construction. The plan view, figure 5.2b, shows the position of the imput and output ports for the Argon gas and cooling water.

A plasma is generated by this torch in the following manner. Argon gas enters the torch under pressure - typically at a pressure of two to three atmospheres. This gas is fed into the nozzle through a circular cavity 0.02m dia. x 0.0075m deep. The nozzle is made by the gap between the anode and cathode, as shown in detail 'A' of figure 5-2a. The anode is made from brass, and connects to the positive terminal of the electrical supply; the cathode is a carbon rod and connects to the negative terminal. On passing through the nozzle the gas is heated by electrical discharge between the anode and cathode. The temperature of the plasma at the exit from the torch is approximately 7.5×10^3K. The anode and cathode are both cooled by conduction and convection to water heat sinks.

The electrical voltage and current supplied the plasma torch and gas and water flow rates were maintained at measured values throughout the experiment. Argon gas was supplied to the torch from several pressurized gasbottles connected in parallel, and it's volumetric flowrate was measured before entry into the torch.

5.1b Impervious Surface

Details of the impervious surface are given in figure 5.3. In figure 5.3a a side elevation on the plane BB shows the internal construction of the surface and supporting structure. A plan view of the surface, as viewed from AA, is given in figure 5.3b. The surface has a diameter of 0.45m, and had been ground flat to a tolerance of $\pm$ 0.0005m. Both it and the supporting structure were made from steel.

The impervious surface and supporting structure form a water tight right circular cylinder 0.40m outside diameter and 0.15m deep. Water was pumped into this cylinder through a vertical nozzle of 0.02m diameter, located at the center of the cylinders bottom surface aa, and was extracted through the four ports of 0.01m diameter shown in figure 5.3a.

5.1c Velocity

The time averaged velocity in a prescribed direction ($\tilde{N}$) was determined from the measured dynamic pressure of the flow in that direction (P_D) with the relationship :

$$U_{\tilde{N}} = \sqrt{\frac{2(P_D)}{\rho(1+\varepsilon_p)}}$$

where $\varepsilon_p = -\frac{M^2}{4} + HOT$

M represents the Mach number, ρ the local density and HOT designates the higher order terms of the expansion for ε_p. The solution for $U_{\tilde{N}}$ was obtained by predicting $U_{\tilde{N}}$ with $\varepsilon_p = 0$, calculating M and then re-estimating $U_{\tilde{N}}$. The final two steps of this procedure were continued until three sequential predictions of U_N differed by less than 0.1 percent.

The instantaneous dynamic pressure over a small area of flow was sensed with a Pitot Static Tube of 0.002m diameter that conformed to British Standard 1042 part 2A. An electronic manometer was used to measure the dynamic pressure P_D after integrating the signal from the probe over a five second time interval.

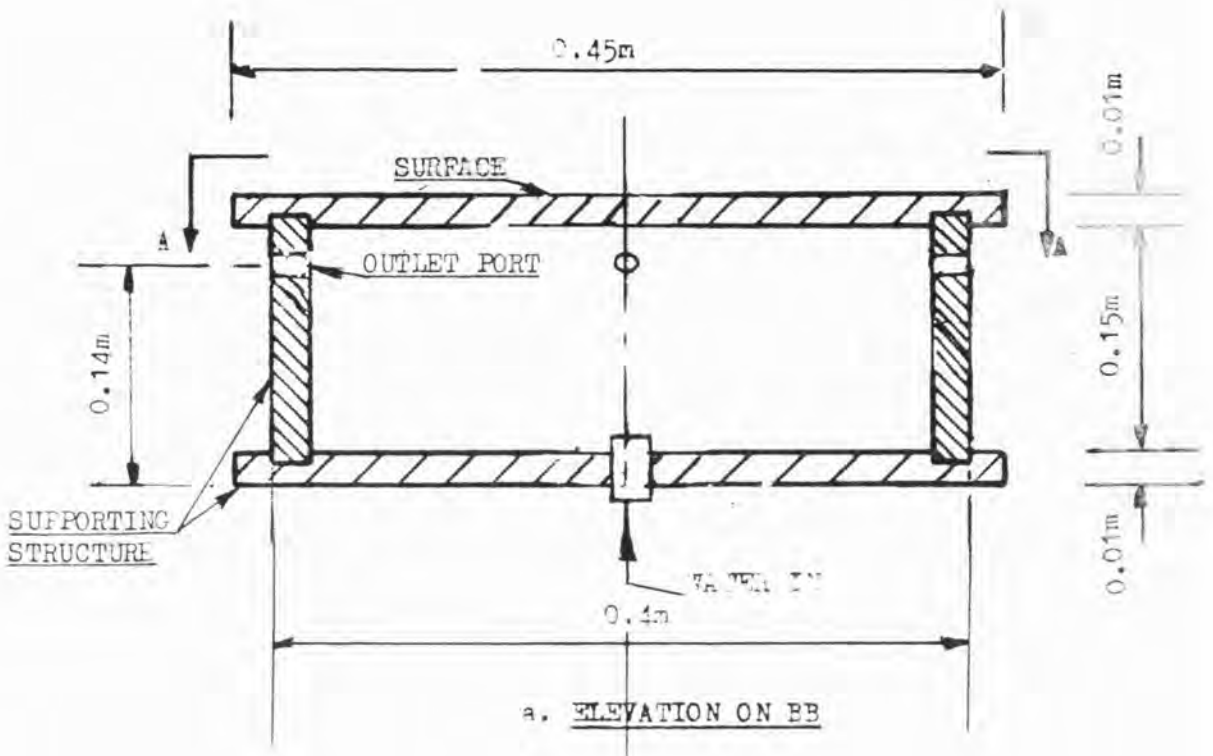

a. ELEVATION ON BB

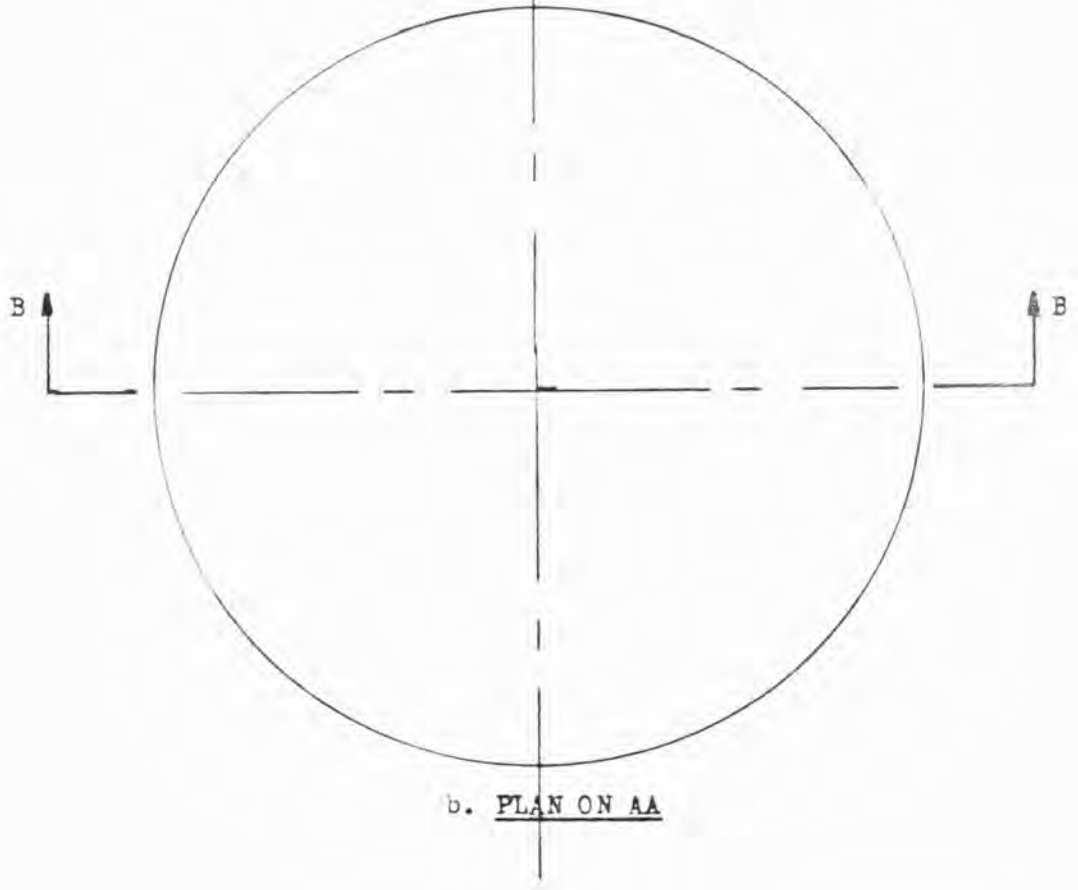

b. PLAN ON AA

SURFACE

FIGURE 5.3

5.1d Concentration

The gravimetric concentrationsof Argon, Nitrogen and Oxygen were measured with the aid of a mass spectrometer and probe previously described in appendix 4. However, in this experiment the empirical relationships, supplied by the mass spectrometer manufacturer, to estimate partial pressures of the constituents in torrs were:

$$p_{Ar} = \frac{I_{40}}{5.6} \times 10^{-6},$$

$$p_{N_2} = \frac{I_{28}}{3.6} \times 10^{-6}, \qquad (5.2$$

and $$p_{O_2} = \left[\frac{I_{32} - 0.116\, I_{14}}{0.56}\right] \times 10^{-6}$$

In these relationships I_{40}, I_{28}, I_{32} and I_{14} represent the output current reading from the mass spectrometer at molecular weights of 40, 28, 32 and 14 respectively. The gravimetric concentration of the constituents in the sample are derived from the partial pressure with Dibos and Dalions Law.

5.1e Temperature

Two thermocouples have been used to measure the temperature. The thermocouples differ in their recommended range of temperature measurement, and the materials from which they are made. The first thermocouple was made from wires of Nickel Chromium and Nickel Aluminium and had an operating range from - 40 to 1100°C. The second sensor was made from wires of Tungsten and Tungsten Rhenium and had an operating range of 1000 to 1750°C . The thermocouples were made from wires 6.35×10^{-4}m in diameter and are detailed in figure 5.4. These sensors were sized using the criteria proposed by Moffat,[57] and manufactured according to British Standards 1041.

The voltage generated by the electron motive force (e.m.f.) at the junction of the Nickel Chromium and Nickel Aluminium wires was integrated over a five second interval, and then converted into the time averaged temperature of the junction with a Comak Temperature Box. This device had an automatic cold junction. The estimated error in temperature measurement is $\pm$ 1.0°C. The e.m.f. generated by the tungsten and tungsten rhenium thermocouple was integrated over a five second time interval, measured with a potentiometer, and the temperature of the junction looked up from the British Standards 1061.

5.2 Experimental Procedure

The experiment has been split into two parts. Firstly, the symmetry of the impinging flow about the center line aa in figure 5.5a was assessed - the procedure followed is detailed in sub-section a. Secondly, the time averaged velocity, species concentration and temperature were measured at various points within the flow; the procedure followed is specified in sub-section b.

In both parts of this experiment the following parameters were set and maintained at the values specified below:

a) voltage difference between the anode and cathode of the plasma torch = 30 volts

b) current supplied to the cathode = 332 amps

c) Argon flow rate to the torch = $7.1 \times 10^{-4} m^3 s^{-1}$

d) flowrate of cathode cooling water = $33.3 ccs^{-1}$

e) flowrate of anode cooling water = $40.5 ccs^{-1}$

f) flowrate of subsidiary anode cooling water = $40.5 ccs^{-1}$

g) flowrate of cooling water for the impervious surface = $150 ccs^{-1}$

and h) vertical distance between the exit from the nozzle and the impervious surface. = 0.04m

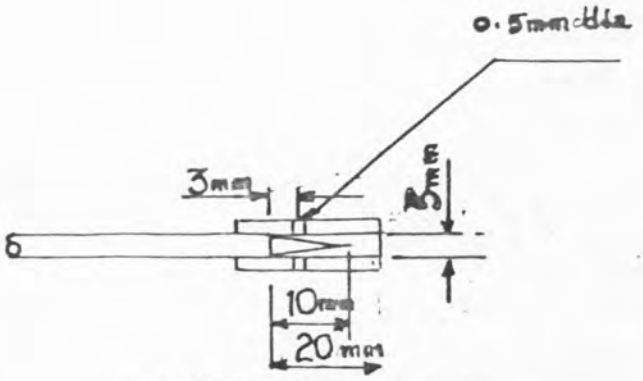

SHIELDED THERMOCOUPLE

FIGURE 5.4

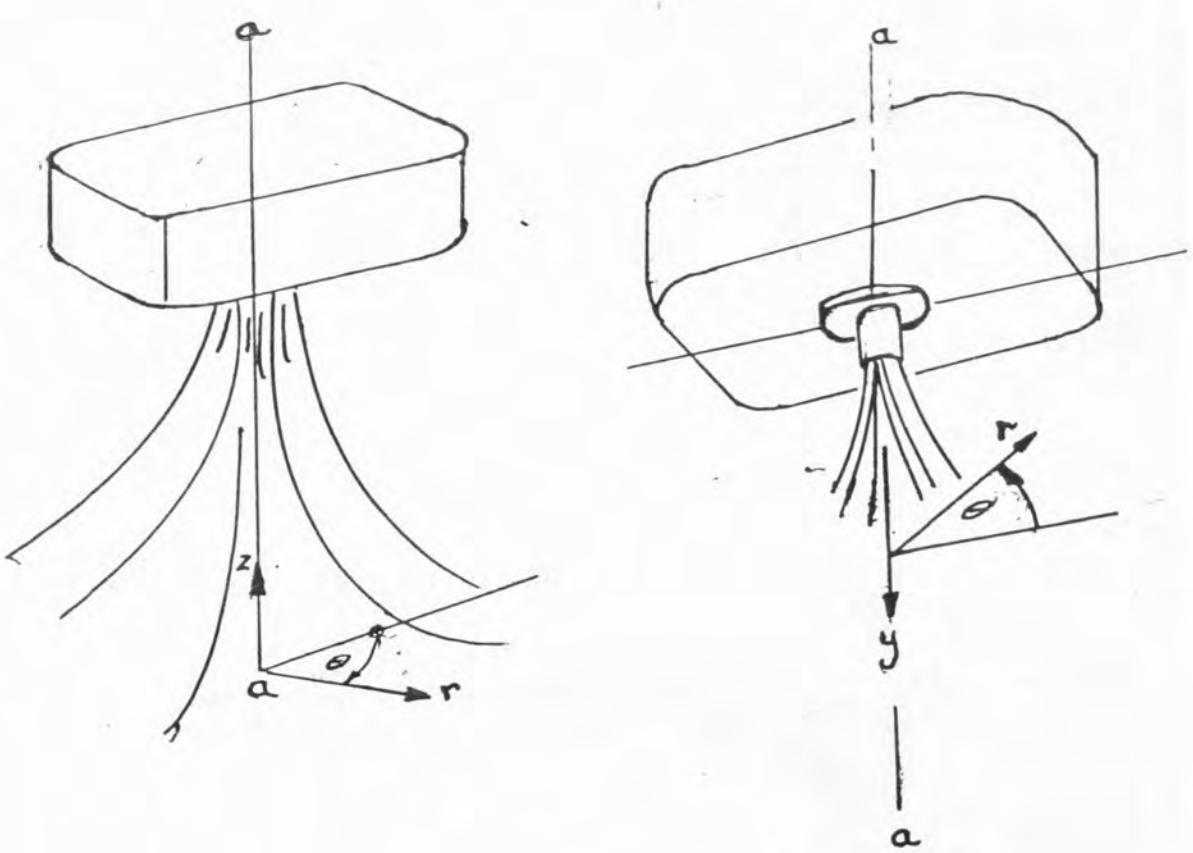

a IMPINGING JET

b FREE PLASMA JET

FIGURE 5.5

5.2a Symmetry

Two tests were conducted to ensure that the studied impinging flow was symmetrical about the vertical center line aa in figure 5.5. The first concerned the symmetry of the free jet, the second, the symmetry of the impinging flow.

In the first test the flow was assumed symmetrical about aa in figure 5.5b, when the time averaged profiles for velocity, species concentration and temperature at the same distance from the nozzle but on various radial planes, as specified by θ in figure 5.5a and b, differed by less than ten percent at the same radii r. The specified flow properties were measured along radii separated by an angle θ of 60° and 0.025, 0.045 and 0.05m from the nozzles exit. The experimental data is detailed in section 4, and the associated results are presented in figure 5.6 to .8. The symbols used to represent the measured properties are given in table 5.1. The maximum percentage discrepancies in the specimen results on the same horizontal sections are specified in table 5.2 and are less than ten percent. The procedure used to measure the flow properties were as follows. In turn pitot static, mass spectrometer and thermocouple sensors were positioned at various points along the radii, and their outputs recorded in the manner detailed in section 1.

In the second test, symmetry was assumed when the measured properties at the same radius, of 0.05m, and height, but in different portions of the flow, differed by no more than ten percent. The symmetry of the impinging flow about the center line aa in figure 5.5a was assessed by measuring, and then comparing, the flow

Table 5.1

Sympol	θ^+	Property
▷	0°	V
▷+	60°	
◁	0	
◁+	60°	
▽	0°	m_{Ar}
▽+	60°	
△	0°	m_{N_2}
△+	60°	
□	0°	m_{O_2}
□+	60°	
○	0°	
○+	60°	

† For a definition of θ see figure

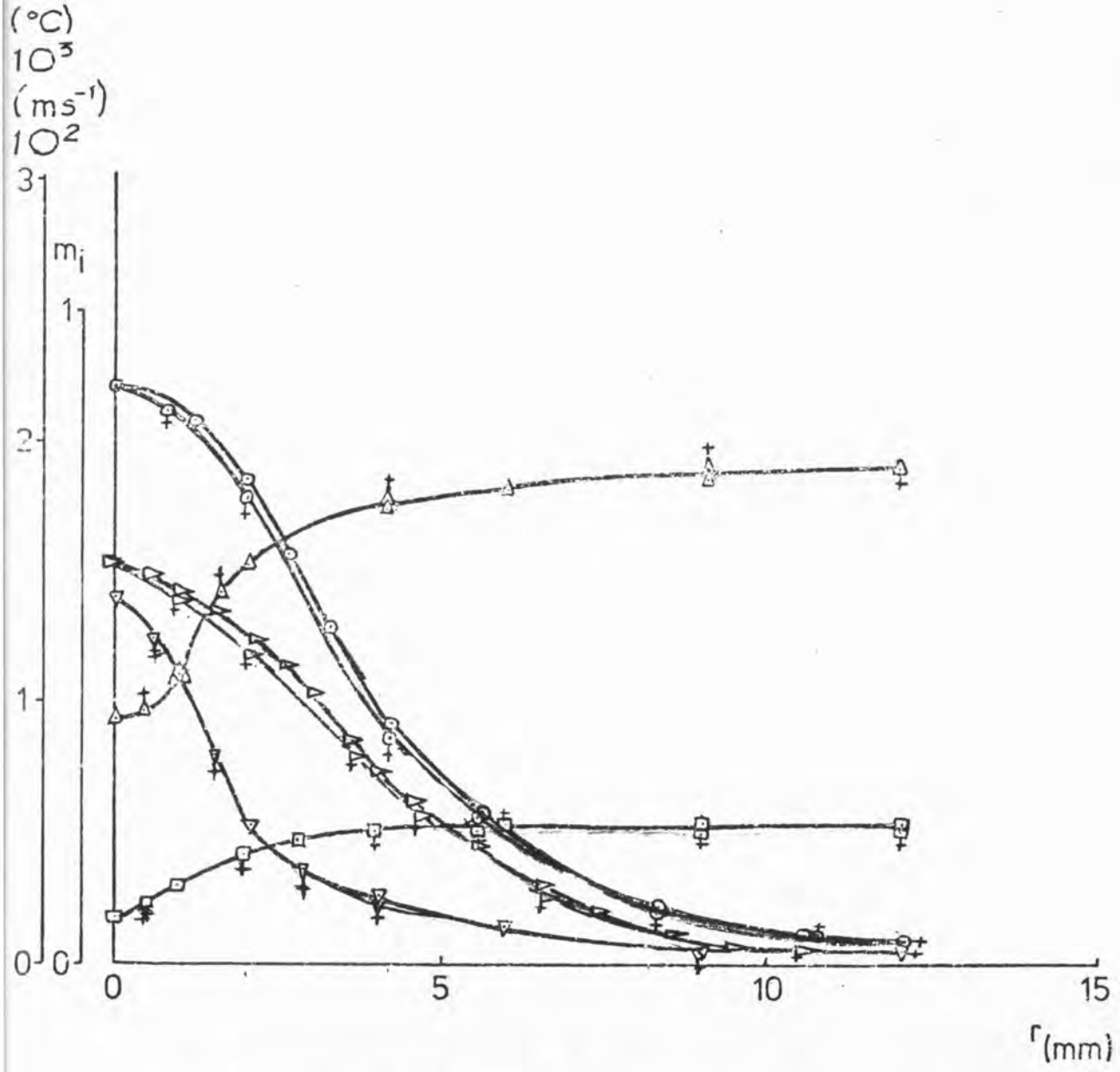

THE FLOW PATTERN 0.025m FROM NOZZLE EXIT

FIGURE 5.6

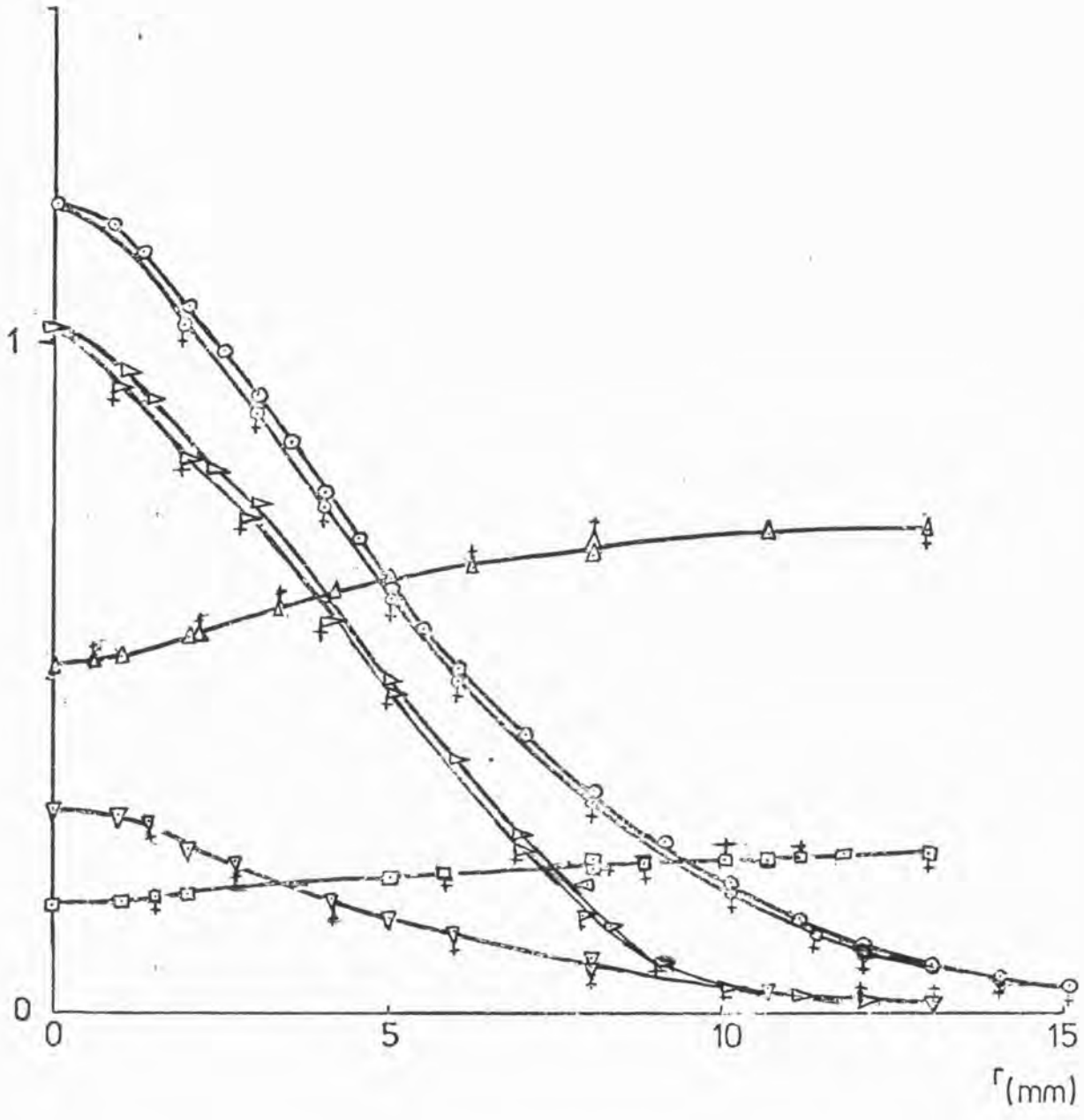

THE FLOW PATTERN 0.04m FROM THE NOZZLE EXIT

FIGURE 5.7

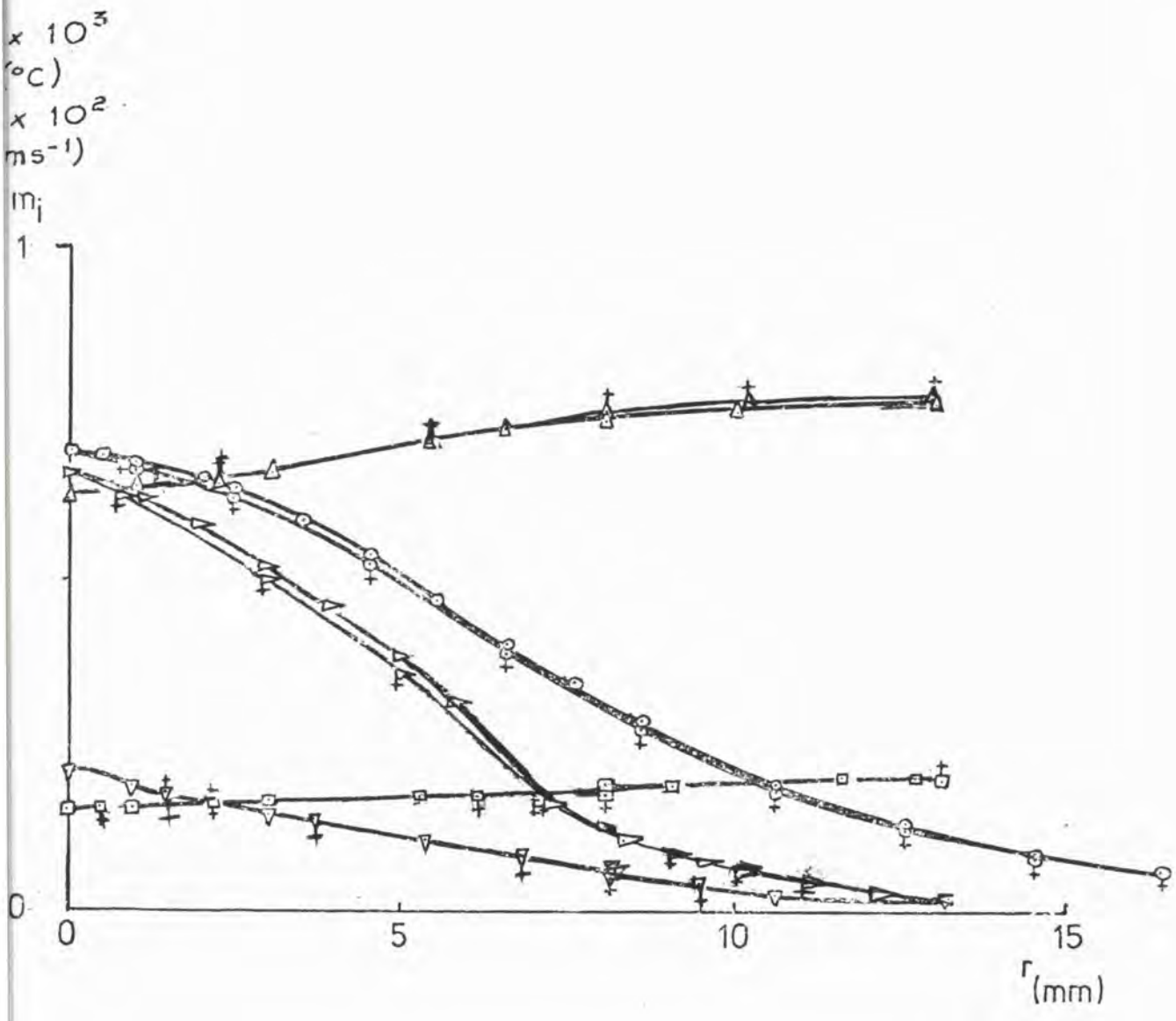

THE FLOW PATTERN 0.05m FROM THE NOZZLE EXIT.

FIGURE 5.8

Table 5.2

Discrepancies

Distance from nozzles exit (m)	Maximum percentage discrepancies at the same radii between the following properties:				
	V (ms^{-1})	T ($^{\circ}C$)	m_{A_r}	m_{N_2}	m_{O_2}
0.025	9.4	8.1	7.4	3.1	8.0
0.04	7.5	9.2	8.4	2.7	8.5
0.05	5.4	7.2	5.1	4.1	6.1

Table 5.3

Discrepancies

Maximum percentage discrepancies at r = 0.05m between the following properties:				
U (ms^{-1})	T ($^{\circ}C$)	m_{A_r}	m_{N_2}	m_{O_2}
9.3	8.4	5.1	6.7	8.1

properties at a radius of 0.05m in planes separated by an angle of 60°. The flow properties were measured on these planes with pitot static, mass spectrometer and temperature probes. The measuring pillar, described in appendix 4, was used to hold and position the probes at the specified section. Specimen results are presented in figure 5.9; the associated experimental data is detailed in section 4. The maximum percentage discrepancies between specimen results at the same vertical height z but at different radial sections are presented in table 5.3; these discrepancies are less than ten percent.

5.2b Mapping

The vertical and radial velocities, species concentration and temperature were measured at various points at radii of 0.0 to 0.13m with the probes and devices prescribed in section one. Throughout the experiment the probes were held and positioned with the measurement pillar described in appendix 4. Plots of these properties are presented in figures 8.3 to .20 in chapter eight. The experimental data from which they are derived is detailed in section 5.4.

The radial and vertical components of the velocity were derived from measured dynamic pressures with equation 5.1. When measuring the dynamic components of pressure, the center line aa of the probe shown in figure 5.10 was located in the horizontal and vertical planes.

The species concentration of the mixture was derived from the specified output signals from the mass spectrometer. Throughout this experiment the center line of the probe, aa in figure 5.10, was held in the horizontal plane.

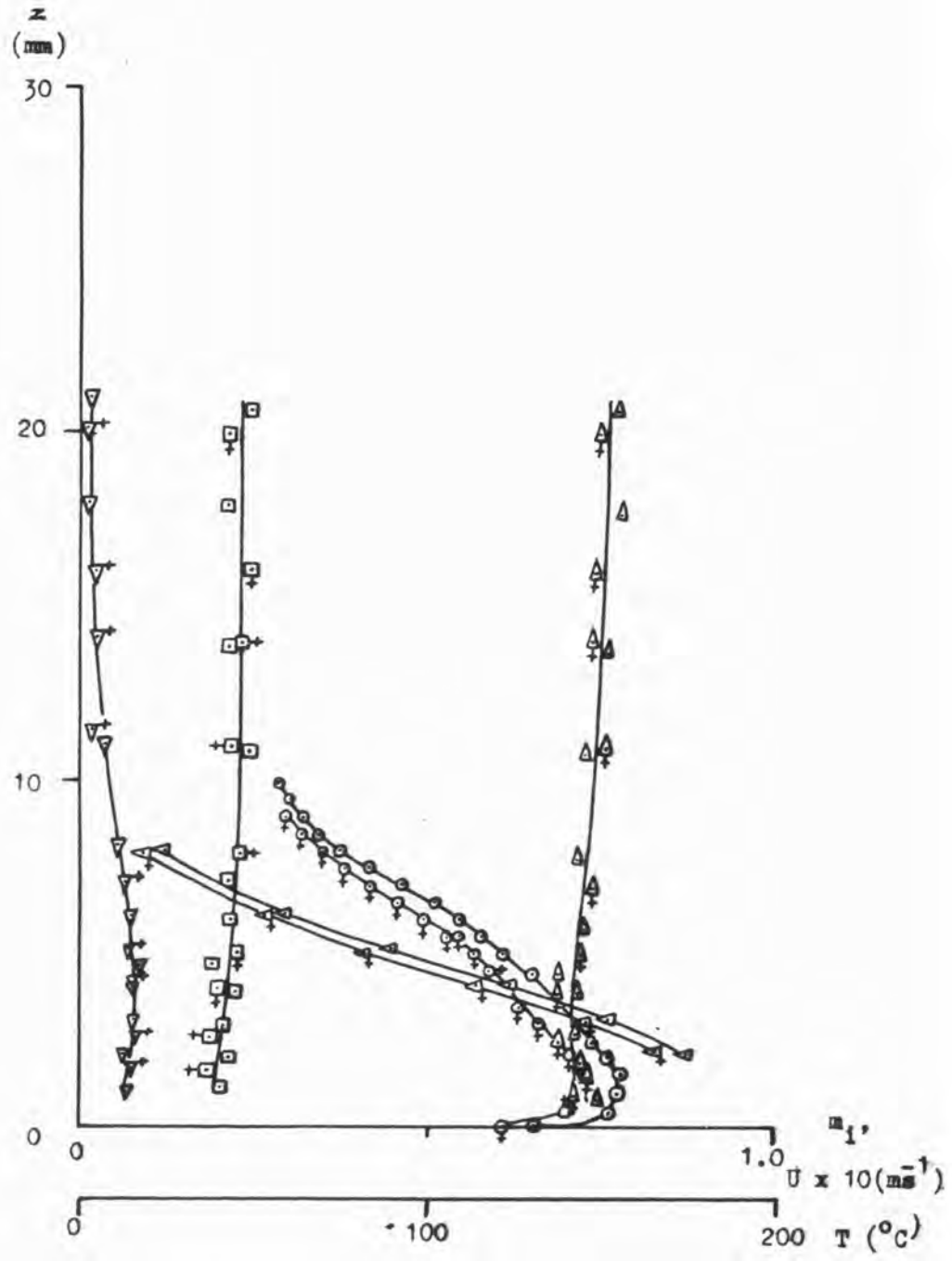

TWO CROSS-STREAM FLOW PATTERNS AT r = 0.05m ,

FIGURE 5.9

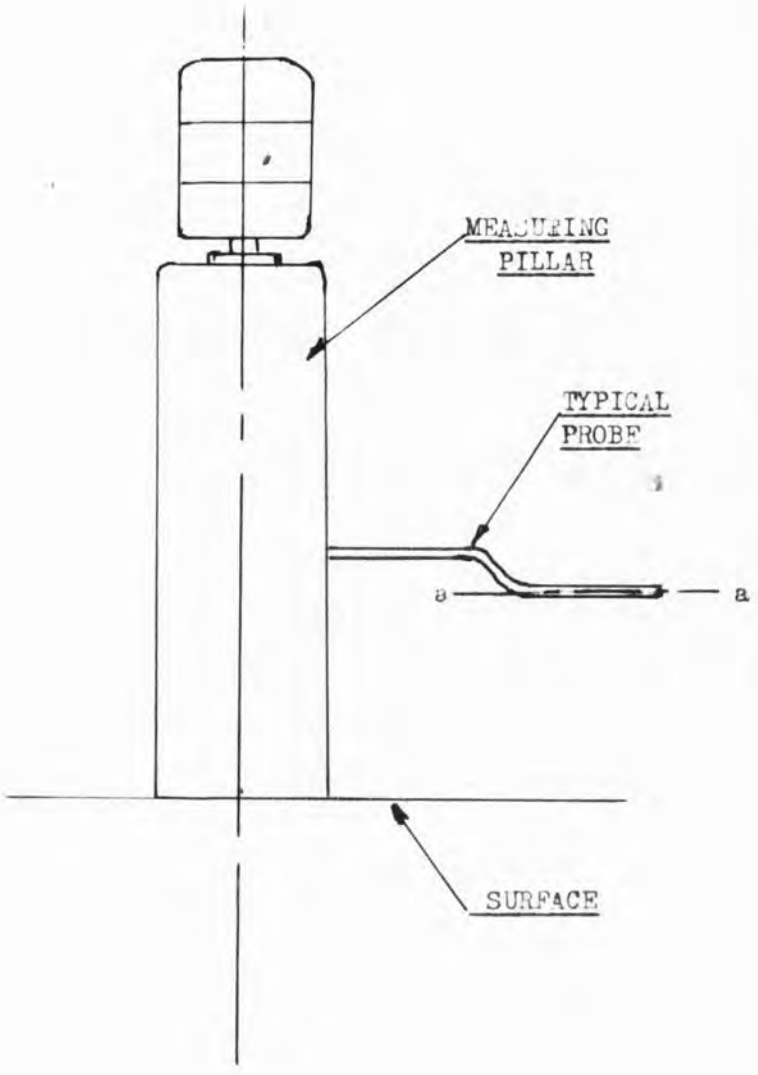

PROBE POSITIONING

FIGURE 5.10

The temperature of the fluid was measured using the appropriate thermocouple and associated measuring device.

5.3 Discussion

Impingement flows have historically been sub-divided into the jet, deflection and wall regimes illustrated in figure 5.1. The first regime contains that part of the jet unaffected by impingement. In this experiment this regime contained an argon plasma at a temperature of approximately 7500 K; and was not studied. The deflection regime contains that portion of the flow directly beneath and affected by the jet; the results obtained in this regime are discussed in sub-section a. The radial wall jet extends over the remainder of the flow and the results are considered in sub-section b.

5.3a Deflection

The deflection regime is contained within a right circular cylinder of approximately 0.03m diameter and 0.025m in height. Measured results, at radii 0, 0.0025, 0.005, 0.0075, 0.01 and 0.15m are presented in figures 8.3 to .8 in chapter 8. These results are re-presented in figures 5.11 to .13; and show the radial variation of the measured properties at horizontal sections 0.015, 0.005 and 0.0025m above the impervious surface. The symbols used to represent the flow properties are detailed in table 5.4. The results have been re-presented, because in this form they give a more understandable picture of the flow pattern. These results show the jet both slowing and cooling down as the impervious surface was approached. The re-structuring of the flow pattern, shown in the presented results, was caused by both

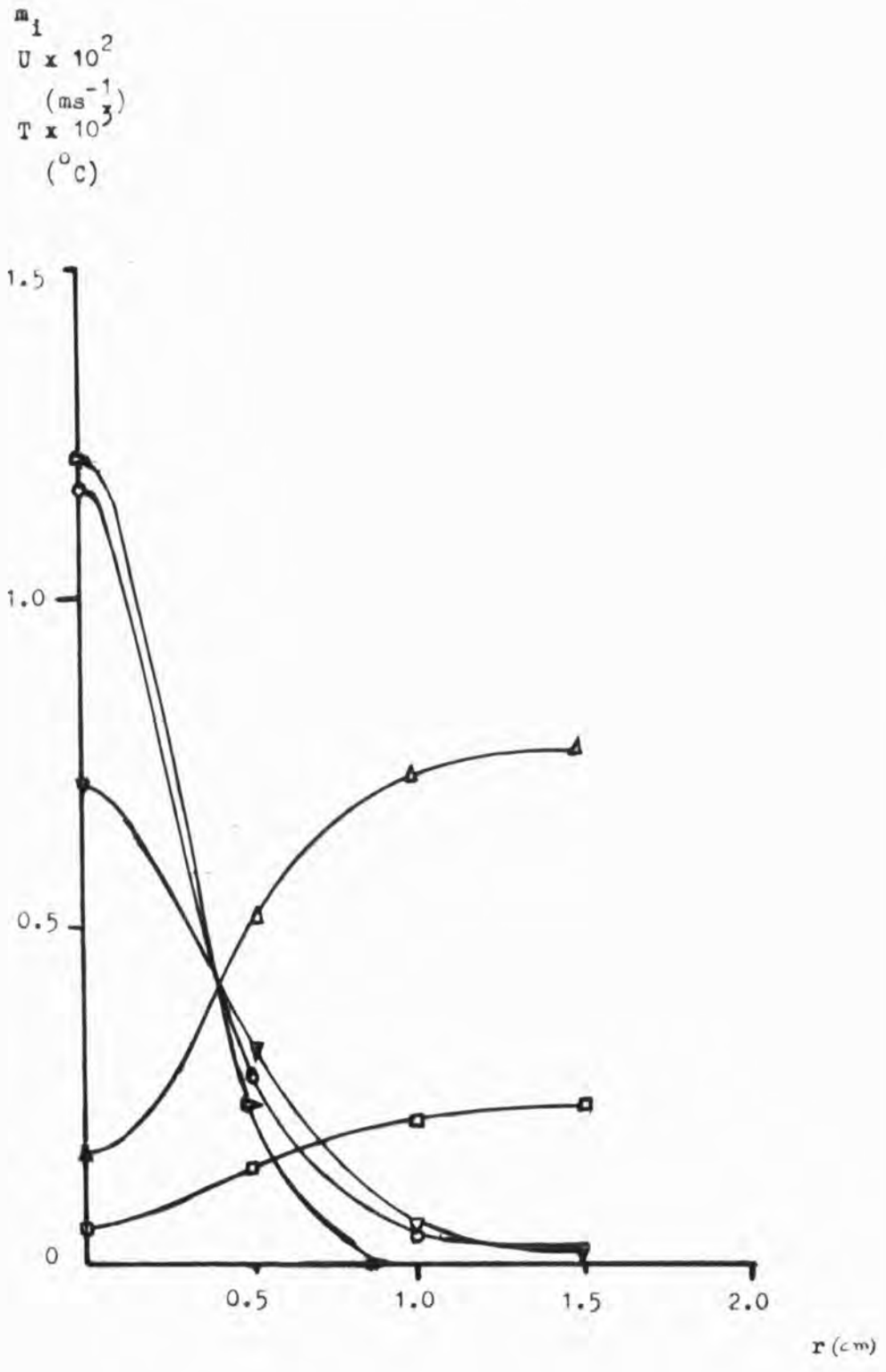

FIGURE 5.11

FLOW PATTERN AT y = 0.01 cm

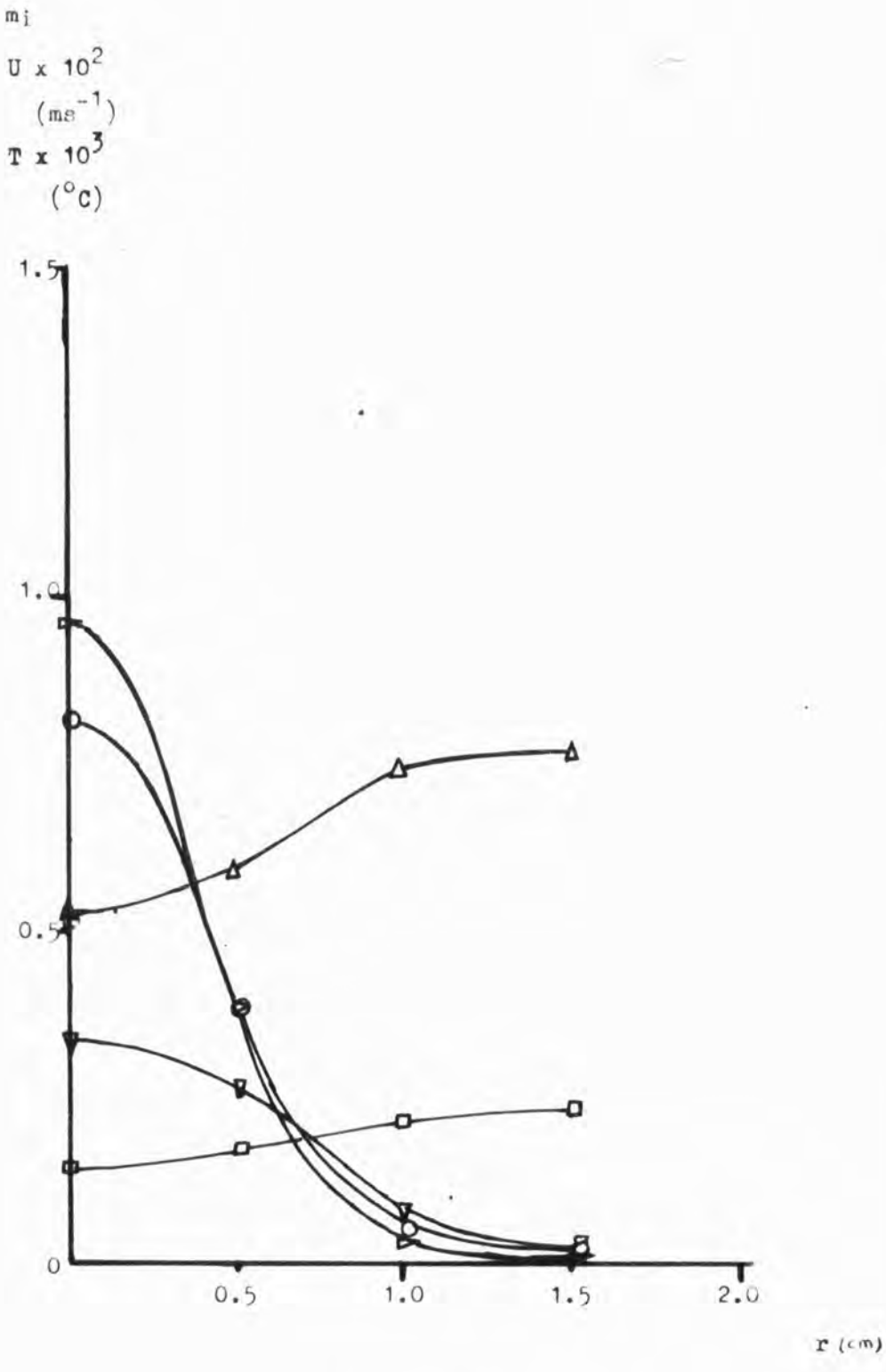

FLOW PATTERN AT y = 0.005m

FIGURE 5.12

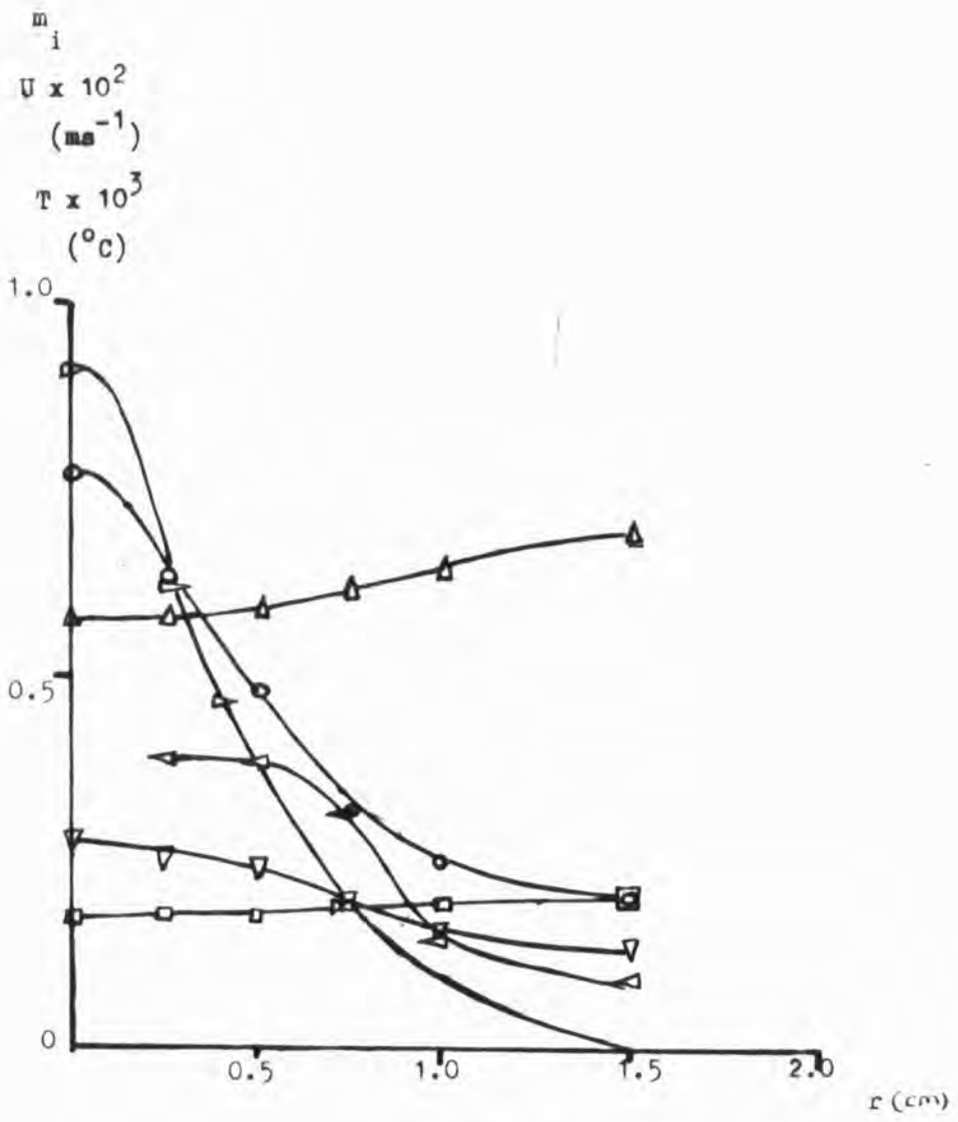

FLOW PATTERN AT y = 0.0025m

FIGURE 5.13

Table 5.1

Symbol	Property	
▷	V	(Vertical velocity)
◁	U	(Horizontal velocity)
○	T	(Temperature)
▽	m_{A_r}	(Gravimetric concentration) of Argon
□	m_{O_2}	(Gravimetric concentration) of Oxygen
△	m_{N_2}	(Gravimetric concentration) of Nitrogen

turbulent transfer within the jet, and entrainment of air - with traces of re-cycled argon - at the regime edge. The final set of results at 0.0025m above the surface, shown in figure 5.13, shows two interesting facts. Firstly, the beginnings of the radial wall jet can be seen in the measured radial velocity profile detected at this section. Secondly, the concentration of argon at the downstream edge of the regime, at r = 0.015m, is considerably greater than that observed at the other studied sections. This occurred, because this portion of the cross-stream edge butted against the beginning of the radial wall jet regime.

5.3b Radial Wall Jet

The radial wall jet extends from a radius of approximately 0.02 to 0.13m; the measured results in this regime, at radial steps of 0.01m, are presented in figures 8.9 to .20 in chapter 8. Plots showing the variation in the streamwise direction of the maximum velocity U_{max} and temperature T_{max} and the heights at which the mainstream velocity equals U_{max} and $\frac{U_{max}}{2}$ are given in figure 5.14. These plots are derived from the measured results; with no results for r < 0.06m presented, because of the scarcity of measured data close to the surface. Experimentally verified predictions of Porsch et al for a radial wall jet in which momentum transfer rates predominate are of the form of:

$$\frac{\mu_{max}\, b}{\sqrt{K_N}} \propto \frac{r}{b}^{-1.1} \qquad (5.3$$

$$\frac{\delta_1}{b} \qquad \frac{r}{b}^{0.9} \qquad (5.4$$

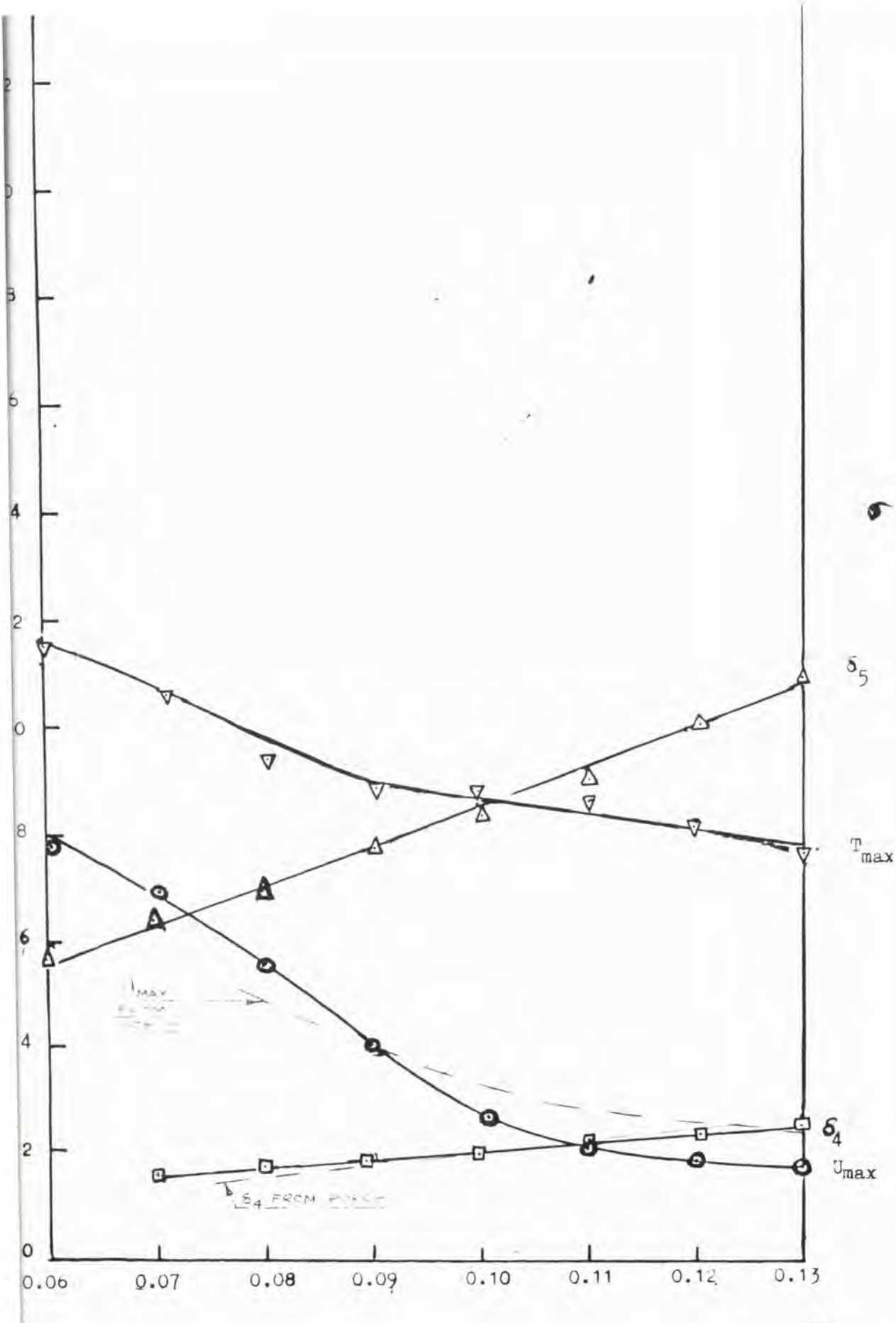

VARIATION OF PROPERTIES IN THE RADIAL DIRECTION

FIGURE 5.14

In these relationships K_j represents the jet momentum flux of the nozzle, and b the distance between the surface and nozzle. Plots of these relationships are shown with dotted lines in figure 5.14; with the constants of proportionality being determined at r = 0.09m. (The symbols used in this figure are detailed in table 5.5.)

Table 5.5

Symbol	Meaning
⊙	U_{max}
▽	T_{max}
△	δ_5
⊡	δ_4

This crude model gives reasonably accurate predictions of the prescribed gross parameters of the jet - indicating that the heat and mass transfer rates do not greatly affect the flow structure.

5.4 Experimental Data

a. Dynamic Pressures

(i) Radial Component

z (mm)	Radial Dynamic Pressure (mm of water)
a) r = 0.0025m	
0.635	78.00
1.135	56.00
1.635	39.50
2.135	23.10
26.35	12.20
3.135	
3.260	
b) r = 0.005m	
0.635	95.00
0.760	86.00
0.885	78.00
1.135	64.50
1.635	45.00
2.135	31.25
2.635	21.46
3.135	15.00
3.635	9.40
4.135	5.33
4.635	2.03
4.885	0.00
c) r = 0.0075m	
0.635	70.77
0.885	45.00
1.135	35.00
1.635	31.75
2.135	22.10
2.635	14.73
3.135	9.65
3.635	6.10
4.135	3.30
4.635	2.03
5.135	0.05
5.635	0.00

z (mm)	Radial Dynamic Pressure (mm of water)

d) r = 0.01m

0.635	45.00
1.135	41.00
1.635	17.60
2.135	9.70
2.635	5.20
3.135	2.80
3.635	1.60
4.135	0.85

e) r = 0.015m

0.635	73.66
1.135	40.64
1.635	15.75
2.135	7.37
2.635	2.79
3.135	0.15
3.635	0.00

f) r = 0.02m

.635	30.48
.885	26.16
1.135	23.37
1.385	18.54
1.635	14.75
1.885	9.65
2.135	7.11
2.385	4.83
2.635	3.05
3.135	0.76
5.635	0.00

z (mm)	Radial Dynamic Pressure (mm of water)

g) r = 0.03m

0.635	17.53
0.865	16.76
1.135	15.49
1.385	13.46
1.635	11.94
1.885	9.40
2.135	8.38
2.385	6.60
2.635	5.33
2.885	4.06
3.135	2.79
3.385	2.03
3.635	1.27
3.885	0.76
4.135	0.51
4.385	0.25
4.635	0.00

h) r = 0.04m

0.635	7.62
0.885	7.62
1.135	7.87
1.385	7.37
1.635	7.11
1.885	6.35
2.135	5.84
2.385	5.33
2.635	4.83
2.885	4.06
3.135	3.30
3.385	2.79
3.635	2.29
3.885	1.79
4.135	1.52
4.385	1.02
4.635	0.76
4.885	0.51
5.135	0.25
5.385	0.25
5.635	0.01
5.885	0.00

z (mm)	Radial Dynamic Pressure (mm of water)

i) $r = 0.05m$ & $\theta = 0^{\circ}$

1.25	3.10
1.75	3.05
2.25	2.90
2.75	2.60
3.25	2.10
3.75	1.65
4.25	1.40
4.75	1.00
5.25	0.60
5.75	0.45
6.25	0.39
6.75	0.11

i) $r = 0.05m$ & $\theta = 60^{\circ}$

1.25	3.30
1.75	3.40
2.25	3.20
2.75	2.80
3.25	2.40
3.75	2.05
4.25	1.55
4.75	1.18
5.25	0.80
5.75	0.50
6.25	0.40
6.75	0.10

z (mm)	Radial Dynamic Pressure (mm of water)

j) r = 0.06m

0.635	2.87
0.885	2.90
1.135	3.02
1.385	3.05
1.635	3.05
1.885	2.90
2.135	2.79
2.385	2.62
2.635	2.49
2.885	2.36
3.135	2.11
3.385	2.03
3.635	1.88
4.135	1.65
4.635	1.37
5.135	1.09
5.635	0.79
6.135	0.61
6.635	0.46
7.135	0.30
7.635	0.18
8.135	0.00

k) r = 0.07m

.635	2.01
.885	2.13
1.135	2.16
1.385	2.16
1.635	2.13
1.885	2.13
2.135	2.13
2.385	2.08
2.635	2.03
3.135	1.88
3.635	1.70
4.135	1.45
4.635	1.27
5.135	1.09
5.635	0.91
6.135	0.71
6.635	0.61
7.135	0.46
7.635	0.36
8.135	0.33
8.635	0.25
9.135	0.013
9.635	0.005
10.135	0.000

z (mm)	Radial Dynamic Pressure (mm of water)
1)r = 0.08m	
0.635	1.60
0.885	1.70
1.135	1.80
1.385	1.85
1.635	1.85
1.885	1.83
2.135	1.80
2.385	1.78
2.635	1.73
2.885	1.65
3.135	1.57
3.385	1.50
3.635	1.40
3.885	1.35
4.135	1.27
4.385	1.17
4.635	1.09
5.135	1.02
5.635	0.86
6.135	0.75
6.635	0.58
7.135	0.48
7.635	0.41
8.135	0.33
8.635	0.25
9.135	0.15
9.635	0.10
10.135	0.050
10.635	0.020
11.135	0.010
11.635	0.0
12.635	

z (mm)	Radial Dynamic Pressure (mm of water)
m)r = 0.09m	
0.635	1.75
1.885	1.78
1.135	1.83
1.385	1.88
1.635	1.91
1.885	1.91
2.135	1.91
2.385	1.91
2.635	1.85
2.885	1.83
3.135	1.78
3.385	1.70
3.635	1.65
3.885	1.57
4.135	1.52
4.385	1.47
4.635	1.37
4.885	1.19
5.200	1.02
5.650	0.59
6.150	0.48
6.650	0.33
7.150	0.25
7.650	0.20
8.150	0.15
8.650	0.10
9.150	0.04
10.150	0.02
11.150	0.00

z (mm)	Radial Dynamic Pressure (mm of water)
n) r = 0.10m	
0.635	1.35
0.885	1.55
1.135	1.70
1.385	1.75
1.635	1.70
1.885	1.65
2.135	1.65
2.385	1.65
2.635	1.60
2.885	1.55
3.135	1.55
3.385	1.55
3.635	1.50
3.885	1.49
4.135	1.40
4.385	1.30
4.635	1.25
5.135	1.15
5.635	1.05
6.135	0.95
6.635	0.80
7.135	0.70
7.635	0.60
8.135	0.55
8.635	0.48
9.635	0.30
10.635	0.20
11.635	0.10
12.645	0.00

z (mm)	Radial Dynamic Pressure (mm of water)
0)r = 0.11m	
0.635	0.85
0.885	0.95
1.135	1.00
1.385	1.05
1.635	1.13
1.885	1.18
2.135	1.13
2.385	1.13
2.635	1.13
2.885	1.05
3.135	1.03
3.385	1.00
3.635	0.95
4.135	0.95
4.635	0.93
5.135	0.90
5.635	0.85
6.135	0.80
6.635	0.75
7.135	0.65
7.635	0.55
8.135	0.50
8.635	0.40
9.135	0.35
9.635	0.30
10.135	0.25
10.635	0.20
11.635	0.10
12.635	0.05
13.635	0.00

z (mm)	Radial Dynamic Pressure (mm of water)
p)r = 0.12m	
0.635	0.85
0.885	0.95
1.135	1.00
1.385	1.05
1.635	1.10
1.885	1.10
2.135	1.15
2.385	1.12
2.635	1.10
2.885	1.05
3.135	1.02
3.385	1.00
3.635	0.95
4.153	0.90
4.635	0.87
5.135	0.85
5.635	0.75
6.135	0.70
6.635	0.65
7.635	0.65
8.635	0.45
9.635	0.30
10.635	0.25
11.635	0.20
12.635	0.15
13.635	0.10
14.635	0.05
15.635	0.00

z (mm)	Radial Dynamic Pressure (mm of water)
q) r = 0.13m	
0.635	0.54
0.885	0.61
1.135	0.69
1.385	0.71
1.635	0.72
1.885	0.76
2.135	0.79
2.385	0.76
2.635	0.75
2.885	0.75
3.135	0.74
3.385	0.71
3.635	0.68
4.135	0.675
4.635	0.67
5.135	0.66
5.635	0.61
6.135	0.59
6.635	0.54
7.135	0.52
7.635	0.44
8.635	0.33
9.635	0.27
10.635	0.22
11.635	0.17
12.635	0.12
13.635	0.07
14.635	0.05
15.635	0.02
16.635	0.00

(ii) Vertical Component

z (mm)	Vertical Dynamic Pressure (mm of water)
a) r = 0.0m	
2.1	143.0
2.5	144.0
3.0	147.0
3.5	149.0
4.0	152.5
5.0	158.0
6.0	164.0
7.0	172.0
8.0	178.0
9.0	186.0
10.0	193.0
11.0	200.0
12.0	207.0
13.0	212.0
14.0	208.0
b) r = 0.025m	
2.5	79.0
3.0	76.0
3.5	74.0
4.0	73.5
5.0	71.5
6.0	70.0
7.0	68.0
8.0	65.0
9.0	63.0
10.0	62.5
12.0	61.5
15.0	59.5
18.0	58.0
21.0	56.0
24.0	54.0
27.0	53.0

z (mm)	Vertical Dynamic Pressure (mm of water)
c) r = 0.005m	
2.5	54.0
3.0	53.0
3.5	51.0
4.0	49.0
4.5	47.0
5.0	45.0
6.0	33.0
7.0	29.0
8.0	27.5
9.0	26.0
10.0	24.0
12.5	23.0
15.0	21.0
17.5	18.0
20.0	14.5
22.5	11.0
25.0	8.5
27.5	4.5
30.0	2.0
32.5	0.9
35.0	0.2
d) r = 0.0075m	
2.5	14.0
3.0	9.5
3.5	9.0
4.0	8.0
4.5	6.5
5.0	6.0
5.5	5.5
6.0	4.9
7.5	4.5
8.5	3.6
10.0	2.5
14.0	2.0
16.0	0.85
18.0	0.35
20.0	0.00

z (mm)	Vertical Dynamic Pressure (mm of water)
e) r = 0.01m	
2.5	3.8
3.0	4.3
3.5	4.1
4.0	3.6
4.5	3.1
5.0	2.4
5.5	2.3
6.0	1.8
7.0	1.3
8.0	0.0
9.0	0.5
10.0	0.3
11.0	0.2
12.0	0.0

b. Concentrations

	z (mm)	Readings from the Mass Spectrometer at Molecular Weights of: 18	28	32	40
b) r = 0.0025	0.635	1.87	75.0	10.0	31.0
	1.635	1.70	71.3	9.675	26.5
	2.635	1.65	71.0	9.65	24.5
	3.635	1.60	70.0	9.45	23.2
	4.83	1.54	62.5	8.35	33.60
	5.83	1.40	59.3	8.10	31.90
	8.83	1.36	55.4	7.550	33.0
	10.83	1.34	53.2	7.250	34.30
	12.83	1.32	51.0	6.975	36.30
	14.83	1.33	50.7	6.750	39.60
	16.83	1.30	48.2	6.600	41.60
	18.83	1.30	44.8	6.050	43.60
	20.83	1.30	42.7	5.750	47.00
c) r = 0.0050m	0.635	1.77	84.2	11.475	31.2
	1.635	1.77	78.0	10.775	23.6
	2.635	1.56	72.6	10.150	21.725
	3.635	1.56	71.6	10.0	19.1
	4.635	1.60	74.8	10.65	18.25
	5.83	1.60	65.0	9.05	25.3
	6.83	1.61	65.0	8.93	25.2
	8.83	1.62	64.9	8.95	25.2
	10.83	1.62	64.6	8.93	25.0
	12.83	1.63	65.0	9.00	27.2
	14.83	1.40	78.20	10.95	33.6
	17.33	1.40	72.2	10.18	32.7
	19.83	1.40	66.2	9.44	32.6
	22.33	1.30	63.4	8.93	32.6
	24.83	1.30	60.7	8.50	33.0
	27.33	1.25	59.6	8.43	33.6
	29.83	1.25	57.8	8.18	34.8
d) r = 0.0075m	0.635	1.55	60.6	8.5	24.4
	1.635	1.60	63.0	8.95	18.8
	2.635	1.58	65.9	9.3	15.75
	3.635	1.57	67.6	9.8	13.075
	4.635	1.62	69.3	9.9	11.2
	6.83	1.50	74.70	10.43	17.88
	8.83	1.80	84.0	12.05	19.88
	10.83	1.72	79.5	11.75	18.18
	12.83	1.65	76.8	11.25	17.25
	14.83	1.65	75.6	11.03	16.08
	17.33	1.65	76.0	11.28	15.05
	19.83	1.67	76.8	11.30	13.90
	22.33	1.70	78.5	11.60	12.60
	24.83	1.75	80.6	11.83	10.90
	29.83	1.80	85.0	12.70	5.60

	z	Readings from the Mass Spectrometer at Molecular Weights of:			
	(mm)	18	28	32	40
e)r = 0.010m	0.635	1.70	63.5	9.05	22.05
	1.635	1.60	64.1	9.1	17.75
	2.635	1.60	67.2	9.675	13.375
	3.635	1.65	70.0	10.25	10.0
	4.635	1.65	72.2	10.55	7.45
	6.635	1.72	76.4	11.2	4.3
	6.83	1.86	92.00	14.15	10.05
	8.83	1.82	89.25	13.75	8.25
	10.83	1.82	87.00	13.50	6.85
	12.83	1.80	86.00	13.33	6.23
	14.83	1.82	85.00	13.52	5.32
	17.33	1.84	84.75	13.25	4.56
	19.83	1.82	85.00	13.25	3.92
	22.33	1.84	86.25	13.48	3.10
	24.83	1.85	86.25	13.48	2.10
	29.83	1.85	86.30	13.60	1.82
f)r = 0.015m	0.635	1.64	69.0	9.675	18.9
	1.635	1.65	69.7	10.125	15.25
	2.635	1.68	72.7	10.49	11.1
	3.635	1.65	74.2	10.80	5.825
	4.635	1.7	77.0	11.20	3.1
	6.635	1.72	76.2	11.25	1.85
	8.83	2.05	88.75	14.20	1.90
	10.83	2.00	88.0	13.85	1.78
	14.83	2.00	87.5	13.75	1.74
	19.83	2.00	89.5	14.10	1.74
	29.83	2.00	87.5	13.75	1.74
g)r = 0.020m	1.8	1.80	75.0	10.0	13.450
	2.8	1.82	74.6	10.1	11.40
	3.8	1.80	78.2	10.725	6.20
	6.8	1.80	81.2	11.15	5.175
	11.8	1.75	80.8	11.175	3.375
	16.8	1.75	78.8	10.125	1.25
h)r = 0.030m	1.8	1.22	35.5	4.55	4.700
	2.8	1.20	33.7	4.40	4.150
	3.8	1.20	33.0	4.39	3.800
	4.8	1.20	32.7	4.45	3.200
	5.8	1.20	33.0	4.34	2.35
	6.8	1.20	33.0	4.38	0.800
	8.3	1.20	32.8	4.36	0.720
	11.3	1.17	32.7	4.35	0.700
	16.8	1.20	32.4	4.20	0.70
	26.8	1.20	31.0	4.00	0.60
i)r = 0.40m	1.8	2.6	61.50	9.550	6.6
	2.8	2.60	58.25	9.200	6.0
	3.8	2.48	57.50	8.85	5.650
	4.8	2.47	56.20	8.60	5.000
	5.8	2.42	57.50	8.84	4.570
	6.8	2.40	58.20	8.950	3.650
	7.8	2.38	58.40	9.00	2.530
	9.8	2.37	58.50	9.075	1.650
	11.8	2.37	58.80	9.00	1.21
	14.3	2.36	58.30	8.876	1.210
	16.8	2.30	57.30	8.850	1.00
	21.8	2.35	58.00	9.000	1.00
	26.8	2.30	54.00	8.250	0.90

z

Readings from the Mass Spectrometer

at Molecular Weights of:

	(mm)	18	28	32	40
j) r = 0.050m	1.8	2.44	77.5	11.375	6.72
	2.8	2.42	72.5	10.77	6.40
	3.8	2.30	67.5	10.00	5.93
	4.8	2.25	64.25	9.60	5.25
	5.8	2.25	63.00	9.25	4.55
	6.8	2.18	62.50	9.175	4.20
	7.8	2.17	60.00	9.005	3.50
	8.8	2.15	59.25	8.875	2.82
	9.8	2.13	59.25	8.850	2.30
	10.8	2.20	63.25	9.100	2.05
	11.8	2.20	61.25	9.100	1.60
	14.3	2.15	61.00	9.125	1.40
	16.8	2.15	59.25	8.900	1.22
	21.8	2.15	60.00	8.775	1.20
k) r = 0.60m	1.8	2.15	65.00	10.000	4.92
	2.8	1.96	62.50	9.400	4.77
	3.8	1.97	60.50	9.100	4.55
	4.8	2.00	62.00	9.250	4.41
	5.8	2.00	60.00	9.050	4.00
	7.8	1.95	59.50	8.925	3.50
	9.8	2.00	61.25	9.125	2.82
	11.8	2.00	63.00	9.300	2.10
	13.8	2.00	63.75	9.375	1.66
	16.8	2.05	63.75	9.375	1.42
	21.8	2.10	63.75	9.375	1.30
	26.8	2.10	63.75	9.375	1.25
l) r = 0.070m	1.8	2.35	76.40	11.575	5.46
	2.8	2.13	70.20	10.700	5.04
	3.8	2.07	66.00	10.125	4.68
	4.8	1.96	63.00	9.67	4.33
	5.8	1.85	61.20	9.300	3.97
	6.8	1.83	59.00	9.025	3.78
	7.8	1.82	61.20	9.450	3.57
	8.8	1.80	60.00	9.150	3.22
	9.8	1.83	59.30	9.075	3.05
	11.8	1.85	59.80	9.200	3.30
	14.3	1.85	60.00	9.200	1.70
	16.8	1.90	60.00	9.250	1.45
	21.80	1.92	60.00	9.250	1.30
	26.80	1.94	61.00	9.30	1.30

	z	Readings from the Mass Spectrometer at Molecular Weights of:			
	(mm)	18	28	32	40
m) r = 0.080m	1.8	2.00	64.20	9.800	4.1
	2.8	1.97	61.20	9.425	3.95
	3.8	1.95	61.15	9.350	3.92
	4.8	1.92	60.00	9.200	3.72
	5.8	1.90	59.00	9.050	3.50
	6.8	1.90	59.00	9.000	3.42
	7.8	1.90	58.40	8.950	3.30
	9.8	1.90	59.00	9.075	3.00
	11.8	1.90	56.80	8.750	2.38
	14.3	1.90	57.60	8.850	1.85
	16.8	1.90	56.20	8.750	1.52
	21.8	1.90	57.00	8.875	1.25
	26.8	1.90	57.20	9.000	1.48
n) r = 0.090m	1.8	2.02	63.00	9.97	3.88
	2.8	2.28	66.00	10.250	3.98
	3.8	2.10	64.90	10.000	3.78
	4.8	2.03	62.40	9.625	3.65
	5.8	2.05	61.40	9.500	3.45
	6.8	2.00	60.50	9.5000	3.40
	7.8	1.95	60.50	9.550	3.16
	9.8	2.00	60.80	9.550	3.00
	11.8	1.95	60.30	9.550	2.75
	14.3	2.00	60.00	9.450	2.30
	16.8	1.97	60.00	9.500	1.86
	21.8	1.97	60.70	9.550	1.50
	26.8	1.95	61.00	9.550	1.40
o) r = 0.100m	1.8	3.32	88.50	13.425	4.72
	2.8	3.22	83.00	12.700	4.60
	3.8	3.08	79.00	11.825	4.40
	4.8	3.08	75.80	11.500	4.08
	5.8	2.92	73.80	11.200	3.93
	6.8	2.90	71.50	10.900	3.78
	7.8	2.90	71.00	10.750	3.62
	8.8	2.84	70.20	10.600	3.45
	9.8	2.84	69.80	10.300	3.15
	11.8	2.80	68.50	10.130	3.10
	11.8	2.80	68.80	10.100	3.05
	13.3	2.75	68.40	10.250	2.70
	16.8	2.70	66.40	10.000	2.47
	19.3	2.70	66.40	10.000	2.00
	21.8	2.70	66.20	10.000	1.80
	26.8	2.70	66.30	10.000	1.65

	z	Readings from the Mass Spectrometer at Molecular Weights of:			
	(mm)	18	28	32	40
p) r = 0.110m	1.8	2.88	71.50	10.825	4.05
	2.8	2.80	68.50	10.500	3.84
	3.8	2.76	67.80	10.375	3.70
	4.8	2.73	67.20	10.250	3.60
	5.8	2.70	66.50	10.005	3.55
	6.8	2.75	66.80	10.100	3.50
	7.8	2.70	67.70	10.300	3.55
	8.8	2.75	69.90	10.625	3.50
	9.8	2.76	69.9	10.750	3.45
	11.8	2.88	88.70	13.650	3.74
	14.3	2.84	84.70	12.800	3.30
	16.8	2.80	82.50	12.625	2.60
	19.3	2.77	81.20	12.550	2.50
	21.8	2.85	82.80	12.600	2.20
	26.8	2.82	83.70	12.600	2.08
q) r = 0.120m	1.8	2.95	87.60	13.375	4.50
	2.8	2.90	83.60	12.850	4.40
	3.8	2.90	82.40	12.750	4.15
	4.8	2.84	81.60	12.550	4.10
	5.8	2.84	81.00	12.500	4.04
	6.8	2.83	81.00	12.375	3.95
	8.8	2.80	81.30	12.550	3.78
	11.8	2.82	82.00	12.575	3.60
	14.3	2.85	82.00	12.600	3.27
	19.3	2.90	82.70	12.825	2.72
	21.8	2.92	83.70	12.875	2.50
	26.8	2.92	83.60	12.800	2.35
r) r = 0.130	1.80	3.12	90.75	14.075	4.70
	2.80	2.94	87.60	13.450	4.30
	3.80	2.90	84.20	13.050	4.22
	4.80	2.88	82.70	12.680	4.80
	6.80	2.83	82.20	12.700	3.90
	9.30	2.83	82.30	12.700	3.82
	11.80	2.83	82.20	12.750	3.70
	16.80	2.85	82.20	12.600	3.10
	21.80	2.90	83.00	12.750	2.81
	26.80	2.90	83.50	12.875	2.18
	23.317	3.30	108.50	16.750	2.70
	28.31	3.27	99.50	15.425	2.40
	33.317	3.07	93.25	14.500	2.20
	38.31	2.95	90.50	14.075	2.18
	48.317	2.90	87.50	13.175	2.10

c. Temperatures

z (mm)	Temperature (°C)
a) r = 0.0m	
0.00	660.0
0.12	720.0
0.25	750.0
0.38	755.0
0.50	752.0
0.75	755.0
1.00	757.0
1.50	750.0
2.00	750.0
2.50	750.0
3.00	760.0
3.50	765.0
4.00	772.0
4.50	780.0
5.00	790.0
5.50	800.0
6.00	815.0
6.50	825.0
7.00	840.0
7.50	853.0
8.00	865.0
9.00	900.0
10.00	930.0
11.00	970.0
12.00	1010.0
12.50	1025.0
13.00	1045.0
13.50	1070.0
14.00	1090.0

z (mm)	Temperature (°C)
b) r = 0.0025m	
0.00	655.0
0.13	690.0
0.25	610.0
0.38	710.0
0.50	700.0
0.75	690.0
1.00	680.0
1.50	657.0
2.00	635.0
2.50	615.0
3.00	605.0
3.50	595.0
4.00	587.0
4.50	583.0
5.00	578.0
5.50	578.0
6.00	574.0
6.50	570.0
7.00	570.0
8.00	580.0
9.00	580.0
10.00	585.0
12.00	590.0
14.00	603.0
16.00	610.0
18.00	615.0
20.00	615.0
22.00	600.0
24.00	590.0
26.00	570.0

z (mm)	Temperature (°C)
c)r=0.005m	
0.00	610.0
0.13	657.0
0.25	655.0
0.38	650.0
0.50	610.0
0.75	610.0
1.00	587.0
1.50	543.0
2.00	500.0
2.50	470.0
3.00	435.0
3.50	415.0
4.00	390.0
4.50	377.0
5.00	365.0
5.50	352.0
6.00	345.0
7.00	325.0
8.00	320.0
9.00	310.0
10.00	305.0
12.00	290.0
14.00	275.0
16.00	250.0
18.00	230.0
20.00	225.0
25.00	170.0

z (mm)	Temperature (°C)
d) r=0.0075m	
0.00	420.0
0.13	545.0
0.25	520.0
0.38	505.0
0.50	495.0
0.75	470.0
1.00	445.0
1.50	387.0
2.00	337.0
2.50	293.0
3.00	255.0
3.50	225.0
4.00	200.0
4.50	182.0
5.00	168.0
5.50	153.0
6.00	142.0
6.50	135.0
7.00	128.0
8.00	120.0
9.00	97.0
10.00	77.5
12.00	67.0
14.00	54.0
16.00	48.0
18.00	44.0
20.00	35.0
25.00	25.0

z (mm)	Temperature (^{o}C)
e)r=0.01m	
0.00	407.0
0.13	455.0
0.25	460.0
0.50	445.0
0.75	427.0
1.00	400.0
1.50	350.0
2.00	300.0
2.50	255.0
4.00	217.0
4.50	180.0
5.00	150.0
5.50	125.0
6.00	110.0
6.50	95.0
8.00	82.5
9.00	75.0
10.00	57.0
12.00	52.0
14.00	47.0
16.00	42.0
18.00	99.0
20.00	36.0
25.00	34.0
f)r=0.015m	
0.00	345.0
0.50	360.0
1.00	327.0
1.50	285.0
2.00	240.0
2.50	197.0
3.00	150.0
3.50	110.0
4.00	80.0
4.00	60.0
5.00	47.0
6.00	38.0
7.00	34.0
8.00	32.0
9.00	31.0
10.00	32.0
15.00	32.0
20.00	32.0
25.00	32.0

z (mm)	Temperature (°C)
g)r=0.02m	
0.00	345.0
0.50	410.0
0.25	410.0
1.00	390.0
1.50	350.0
2.00	293.0
2.50	240.0
3.00	195.0
3.50	152.0
4.00	115.0
4.50	80.0
5.00	65.0
5.50	53.0
6.00	45.0
6.50	41.0
7.00	39.5
7.50	38.0
8.00	38.0
10.00	38.0
15.00	38.0
20.00	38.0
25.00	38.0
h)r=0.03m	
0.00	160.0
0.50	195.0
0.25	192.0
0.18	182.0
0.068	175.0
0.75	196.0
1.00	195.0
1.50	186.0
2.00	177.0
2.50	165.0
3.00	152.0
3.50	134.0
4.00	115.0
4.50	98.0
5.00	78.0
5.50	67.0
6.00	56.0
6.50	50.0
7.00	44.0
7.50	40.0
8.00	37.5
9.00	36.0
10.00	34.0
12.00	33.0
20.00	33.0
25.00	33.00

z (mm)	Temperature (°C)
i) r=0.04m	
0.00	160.0
0.50	190.0
0.25	185.0
0.38	187.0
0.75	193.0
1.00	190.0
1.50	187.0
2.00	183.0
2.50	175.0
3.00	170.0
3.50	157.0
4.00	150.0
4.50	135.0
5.00	122.0
5.50	112.0
6.00	97.0
6.50	85.0
7.00	74.0
7.50	65.0
8.00	57.0
8.60	55.0
9.00	50.0
10.00	45.0
12.00	42.0
15.00	40.0
20.00	39.0

z (mm)	Temperature (°C)

j) r=0.05m & θ=0°

0.00	120.0
0.50	140.0
1.00	142.0
1.50	142.0
2.00	140.0
2.50	137.0
3.00	132.0
3.50	127.0
4.00	125.0
4.50	117.0
5.00	114.0
5.50	110.0
6.00	100.0
6.50	90.0
7.00	83.0
7.50	77.0
8.00	72.0
8.50	65.0
9.00	60.0
9.50	59.0
10.00	52.0
11.00	51.0
12.00	44.0
13.00	42.5
15.00	40.0
17.00	39.0
25.00	39.0

j) r=0.05m & θ=60°

0.00	130.0
0.50	152.0
1.00	152.0
1.50	155.0
2.00	150.0
2.50	147.0
3.00	145.0
3.50	141.0
4.00	137.0
4.50	130.0
5.00	121.0
5.50	115.0
6.00	110.0
6.50	102.0
7.00	92.0
7.50	84.0
8.00	76.0
8.50	72.0
9.00	65.0
9.50	62.0
10.00	57.0
11.00	52.0
12.00	45.0
13.00	42.0
15.00	39.0
17.00	39.0
25.00	39.0

z (mm)	Temperature (°C)
k)r=0.06m	
0.00	98.0
0.50	112.0
1.00	115.0
1.50	112.0
2.00	111.0
2.50	111.0
3.00	110.0
3.50	109.0
4.00	105.0
4.50	102.0
5.00	97.0
5.50	92.0
6.00	89.0
7.00	83.0
8.00	77.0
9.00	66.0
10.00	60.0
11.00	54.0
12.00	49.0
13.00	43.5
14.00	42.0
15.00	40.0
20.00	38.5
25.00	37.0
l)r=0.07m	
0.00	80.0
0.50	105.0
0.25	100.0
1.00	105.0
0.75	108.0
1.50	105.0
2.00	105.0
2.50	105.0
3.00	105.0
3.50	102.0
4.00	98.0
4.50	96.0
5.00	92.0
6.00	91.0
7.00	85.0
8.00	79.0
9.00	77.0
10.00	67.0
12.00	56.0
14.00	47.0
16.00	42.0
18.00	38.0
20.00	37.0
22.00	35.0
24.00	35.0

z (mm)	Temperature (°C)
m) r=0.08m	
0.00	85.0
0.50	92.0
1.00	93.5
1.50	92.0
2.00	92.0
2.50	91.0
3.00	91.0
3.50	90.7
4.00	89.5
4.50	88.0
5.00	86.0
6.00	83.0
7.00	80.5
8.00	76.0
9.00	71.5
10.00	67.5
11.00	66.0
13.00	57.0
15.00	53.0
20.00	41.0
22.50	38.0
n) r=0.09m	
0.00	70.0
0.50	86.0
1.00	91.0
1.50	89.0
2.00	88.0
2.50	87.0
3.00	87.0
4.00	86.5
5.00	84.0
6.00	84.0
7.00	80.0
8.00	77.0
9.00	71.0
10.00	68.0
12.00	63.0
14.00	53.0
16.00	46.0
18.00	42.0
20.00	38.0
25.00	37.0

z (mm)	Temperature (°C)
o)r=0.10m	
0.00	87.0
0.50	86.0
1.00	86.5
1.50	86.0
2.00	85.5
2.50	86.0
3.00	85.0
3.50	84.0
4.00	83.0
4.50	82.0
5.00	82.0
6.00	81.0
7.00	79.0
8.00	76.0
9.00	75.0
10.00	72.0
12.00	67.0
14.00	61.0
15.00	55.0
18.00	49.0
20.00	46.0
22.00	43.0
p)r=0.11	
0.00	85.0
0.50	86.0
1.00	86.0
1.50	85.0
2.00	85.0
2.50	84.0
3.00	83.0
3.50	82.5
4.00	81.5
5.00	81.5
6.00	82.0
7.00	80.0
8.00	78.0
9.00	76.0
10.00	75.0
11.00	72.0
12.00	68.0
13.00	65.0
15.00	62.0
17.00	57.0
19.00	51.0
21.00	48.0
23.00	44.0

z (mm)	Temperature (°C)
q) r=0.12m	
0.00	78.0
0.50	80.0
1.00	81.0
1.50	79.0
2.00	78.0
2.50	77.0
3.00	77.0
4.00	77.0
5.00	77.0
6.00	76.0
7.00	75.0
8.00	74.0
9.00	72.0
10.00	69.0
11.00	66.0
12.00	64.0
15.00	57.0
20.00	47.0
22.50	44.0
r) r=0.13m	
0.00	58.5
0.50	63.5
1.00	65.0
1.50	66.5
2.00	66.0
2.50	66.0
3.00	65.5
3.50	65.5
4.00	65.0
5.00	64.7
6.00	63.5
7.00	63.0
8.00	61.0
9.00	60.0
10.00	59.0
12.00	56.5
14.00	54.0
16.00	50.0
18.00	46.0
20.00	42.0
22.00	39.0
23.00	38.0

Appendix 6

Turbulent Chemically Reacting Impinging Flow

The objective of the experimental work detailed in this appendix, was to map the variation of the time averaged velocity , species concentration and temperature within a specified impingement flow. The results obtained are used to firstly estimate the variation of the time averaged transfer processes; and secondly to validate a theoretical model of this flow elsewhere in the thesis.

The equipment used to produce and contain the impingement flow is detailed in section 1. The devices employed to measure the time averaged velocity, species concentration and temperature are detailed in section 2. The experimental procedures results and data are presented in sections three to five.

6.1 Equipment

The studied flow was produced by impinging an air jet normally onto a porous surface, through which Natural Gas passed at a uniform rate. The experiment layout is detailed in figure 6.1. Natural Gas was found to contain Methane, Nitrogen and Oxygen in the following gravimetric composition 0.81 , 0.15 and 0.03. In certain portions of the flow there was an incomplete chemical reaction between Methane CH_4, Oxygen O_2 and Carbon monoxide CO that produced Carbon Dioxide CO_2 and Water Vapour H_2O - as shown in equation 6.1.

$$a\ Ch_4 + b\ O_2 + c\ CO + d\ CO_2 + e\ H_2O + f\ N_2 \qquad (6.1)$$

$$g\ CH_4 + h\ O_2 + i\ CO + j\ CO_2 + k\ H_2O + j\ N_2.$$

In this equation a to k represent the various weights of species involved in the reaction. It has been assumed that Nitrogen, N_2 , did not take part in the reaction.

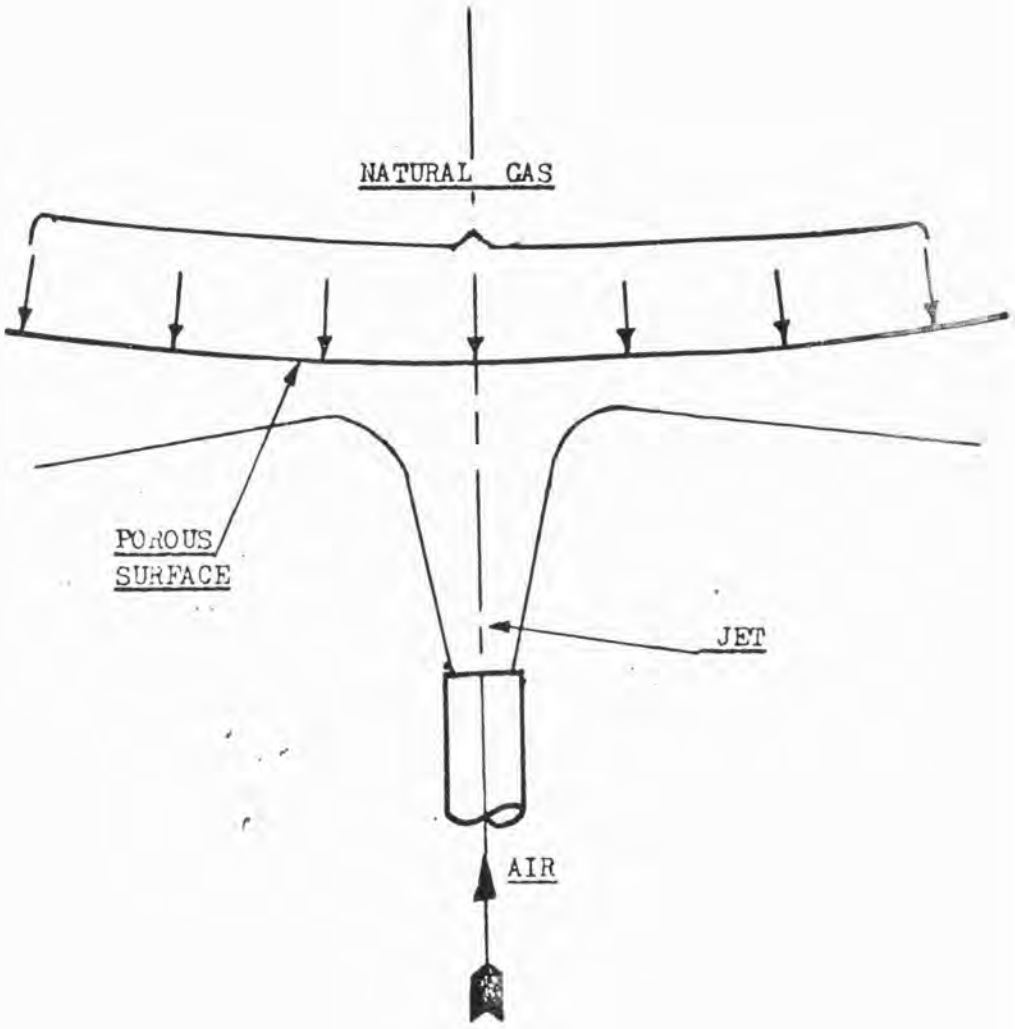

IMPINGEMENT FLOW

FIGURE 6.1

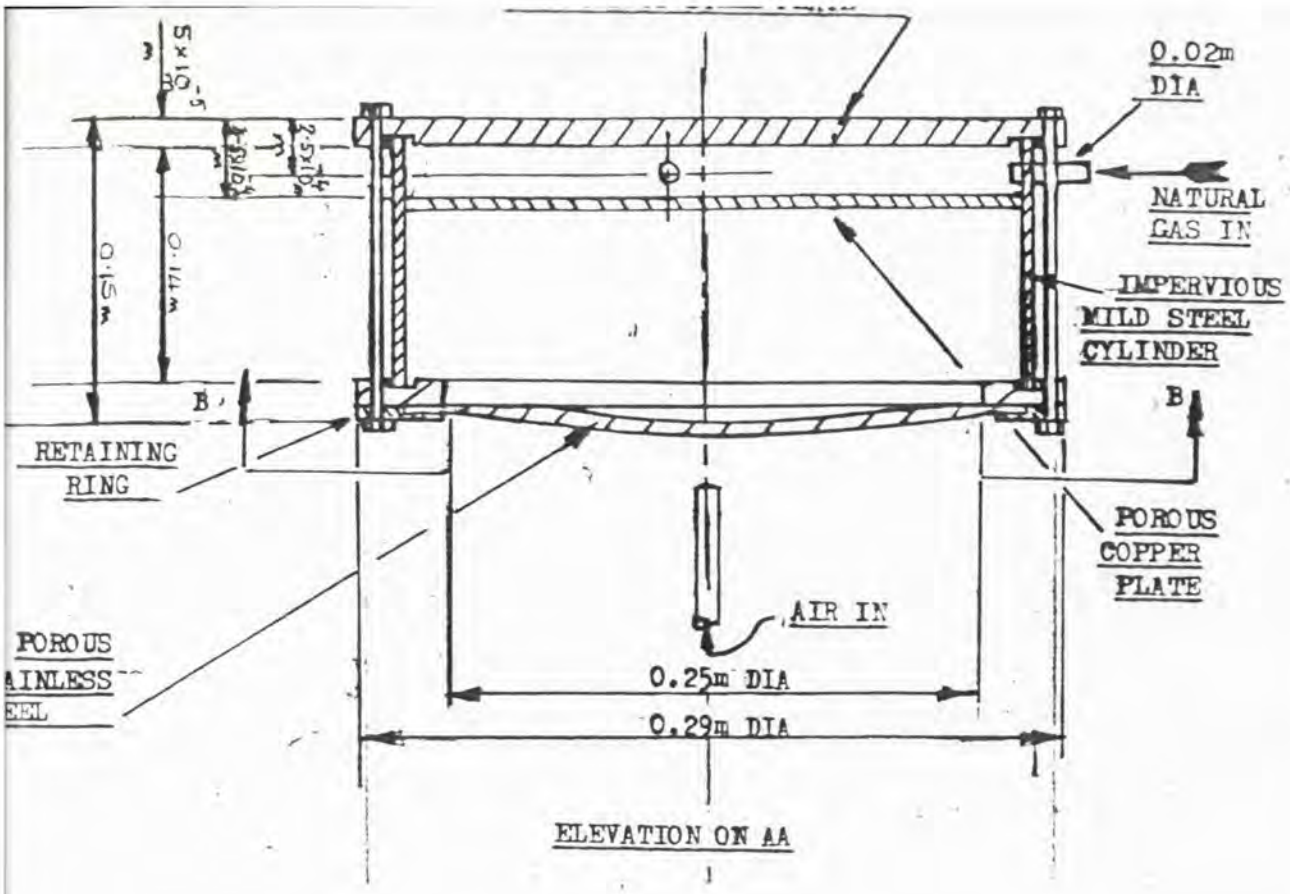

ELEVATION ON AA

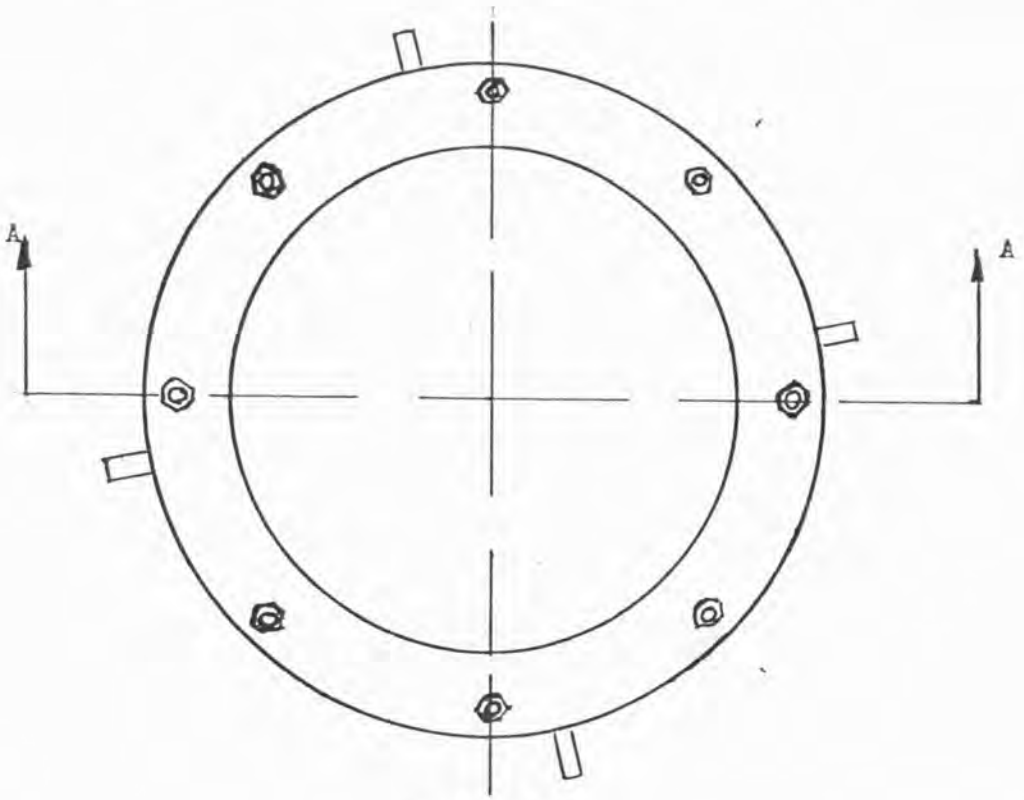

PLAN ON BB

NOZZLE AND BURNER

FIGURE 6.2

The porous surface was part of a cylindrical burner detailed in figure 2. The construction of the burner and nozzle are detailed in sub-section a. The burner and nozzle were contained within an enclosure, which is shown schematically in figure 3, and described in sub-section b. The purpose of the enclosure was to isolate the impinging flow from disturbances in the atmosphere contained by the laboratory.

6.1a Burner and Nozzle

Two views of the burner and nozzle are presented. In figure 6.2a a sectional side elevation along a plane AA is shown, and in figure 6.2b a plan of the burner is given.

The burner had a diameter of 0.29m and depth of 0.15m. The porous stainless steel surface had an effective diameter of 0.25m, was 0.0025 thick and had a radius of curvature of 1.75m. The top and sides of the burner were made from impervious steel sheet, and the porous surface was positioned with a retaining ring. These components were held together by eight retaining bolts, and all joints were sealed by asbestos mixed with high temperature adhesive. A second porous plate, this one made from sintered copper pieces and 0.0025m thick, was located 0.045m below the top surface of the burner - as shown in figure 6.2a. The joint between this plate and the burner was again sealed with asbestos and adhesive. Natural Gas entered the cavity formed by the copper plate through four inlet ports, each of 0.02m diameter, and situated 0.025m below the top surface of the burner. The purpose of the copper porous plate was to modify the Natural Gas flow in the cavity, so that the flow out of the stainless

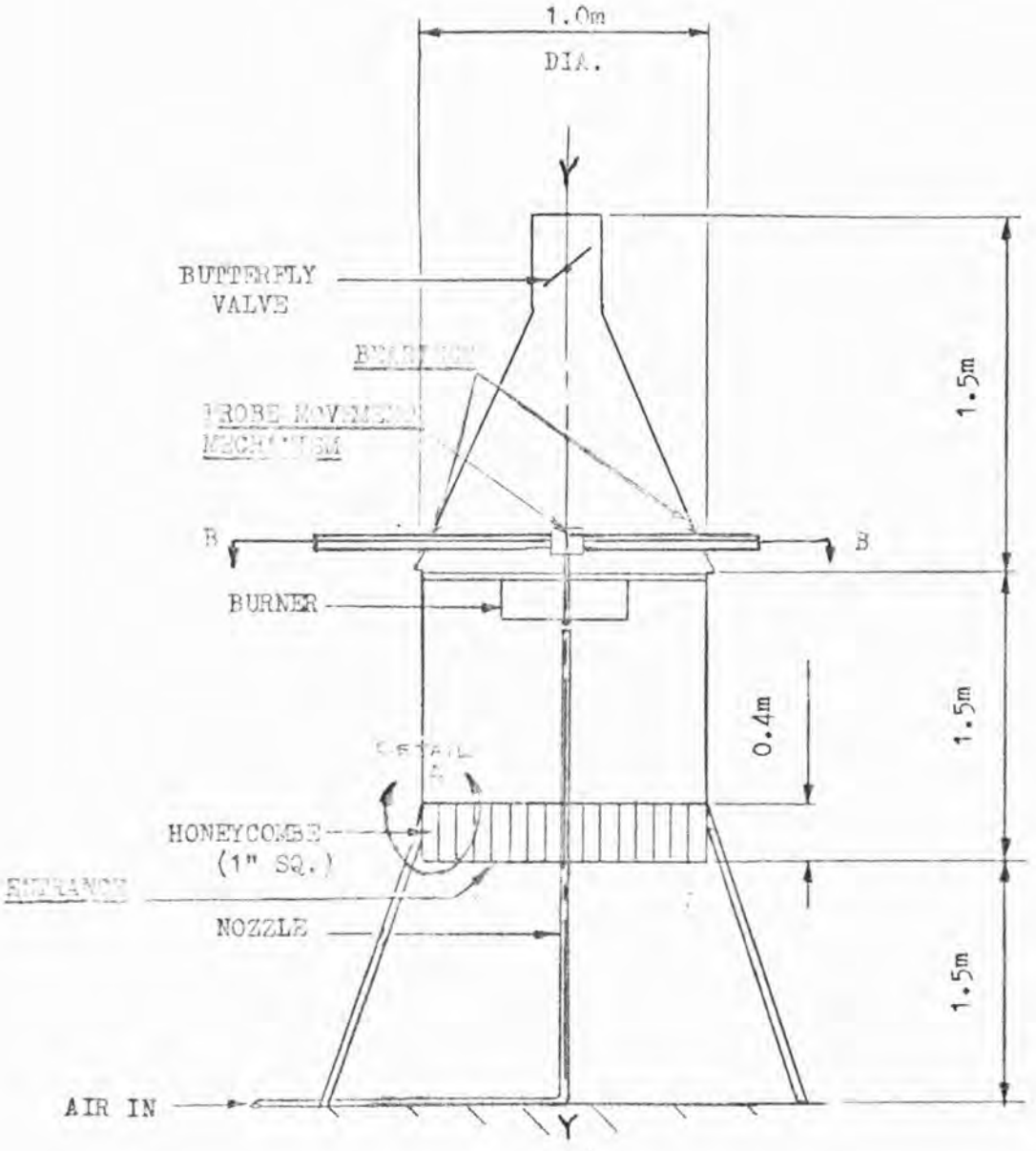

ELEVATION ON AA

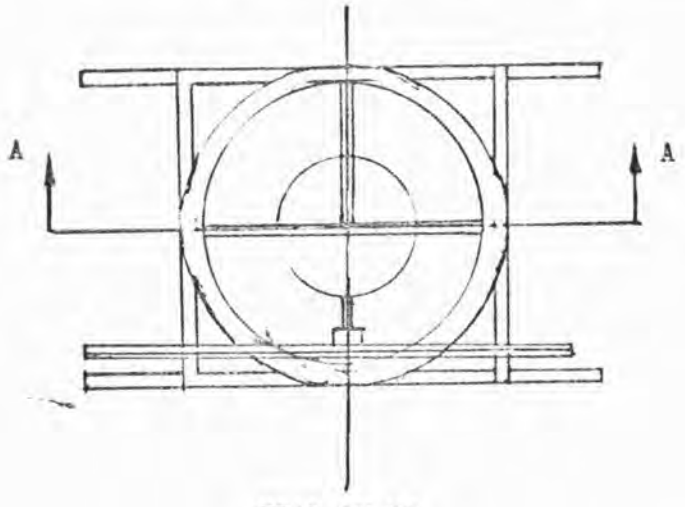

PLAN ON BB

ENCLOSURE

FIGURE 5.3

steel surface was uniform. The shape of this plate was obtained by trial, with the uniformity of the vertical velocity of methane on a plane 0.005m below the porous stainless steel surface taken as the criteria for success. To obtain the sample vertical velocity profile methane was pumped into the burner at $5.65 \times 10^{-3} m^3 s^{-1}$ and the vertical velocity profile measured with a suitably positioned pitot static tube.

The nozzle for the air jet is shown in figure 6.2. It had an internal diameter of 0.004m m. The pipe connecting the nozzle to the natural gas supply had the same internal diameter as the nozzle and a straight length of 2.0m.

6.1b Enclosure

A side elevation and plan view of the enclosure are presented in figure 2a and b respectively. The side elevation details the internal construction of the enclosure along the plane AA in the plan view. The top of the burner was located in a horizontal plane 1.5m above the entrance to the enclosure. The nozzle had it's exit 0.04m below the porous stainless steel surface of the burner; with the vertical center lines of the nozzle, burner and enclosure coincident.

Air flowed through the enclosure when the natural gas and oxygen were ignited, because of buoyancy effects from the hot products of the chemical reaction. The volumetric flowrate of this flow was regulated by a butterfly valve at the exit of the enclosure. Air, from the atmosphere was drawn in at the bottom of the enclosure through a section of honeycombed wax paper. This section was 0.4m deep by 1.5m in diameter, and was made from 0.025m square wax paper as detailed in figure 5. The purpose of this section was to straighten and remove any

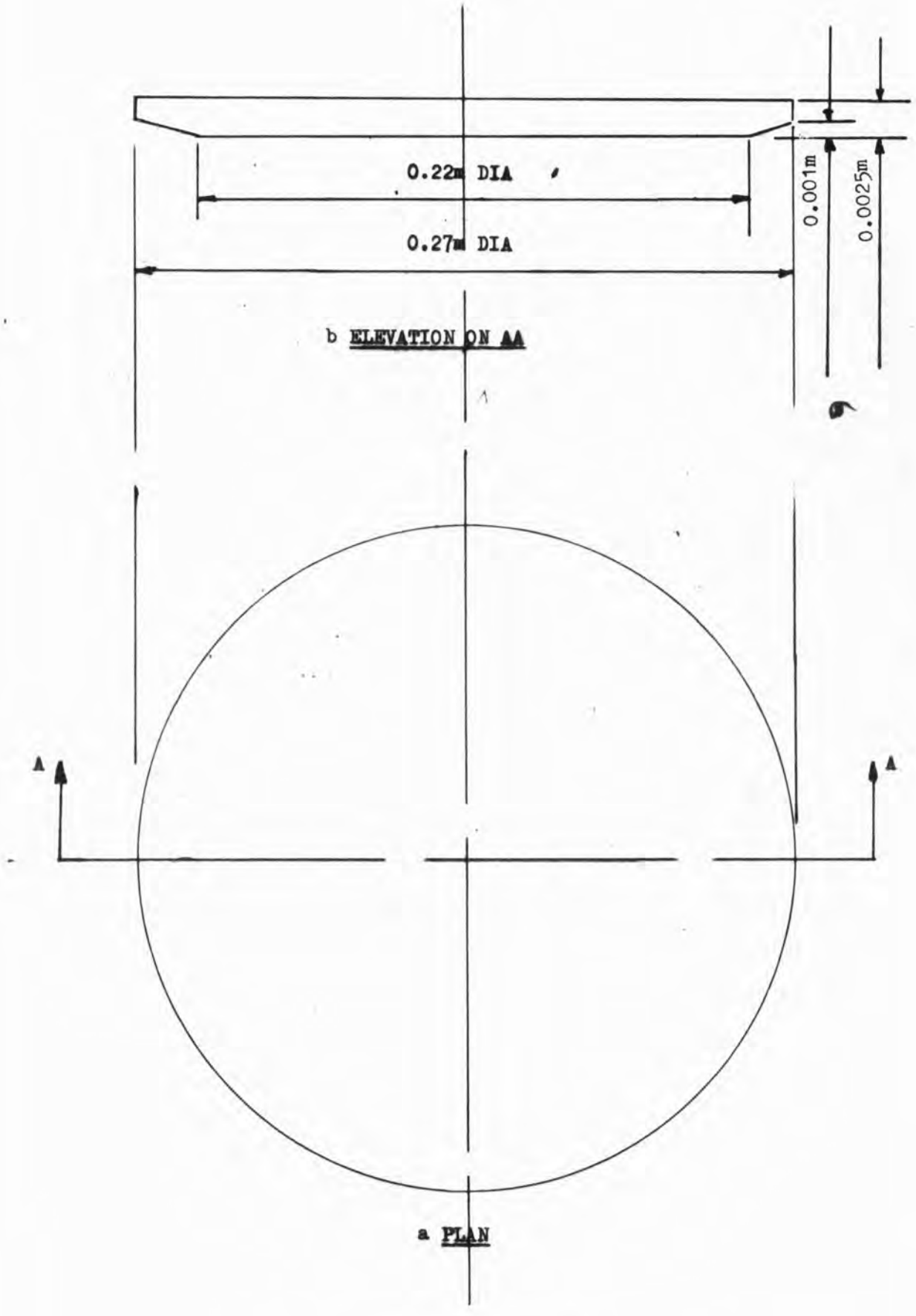

COPPER POROUS SURFACE

FIGURE 6.4

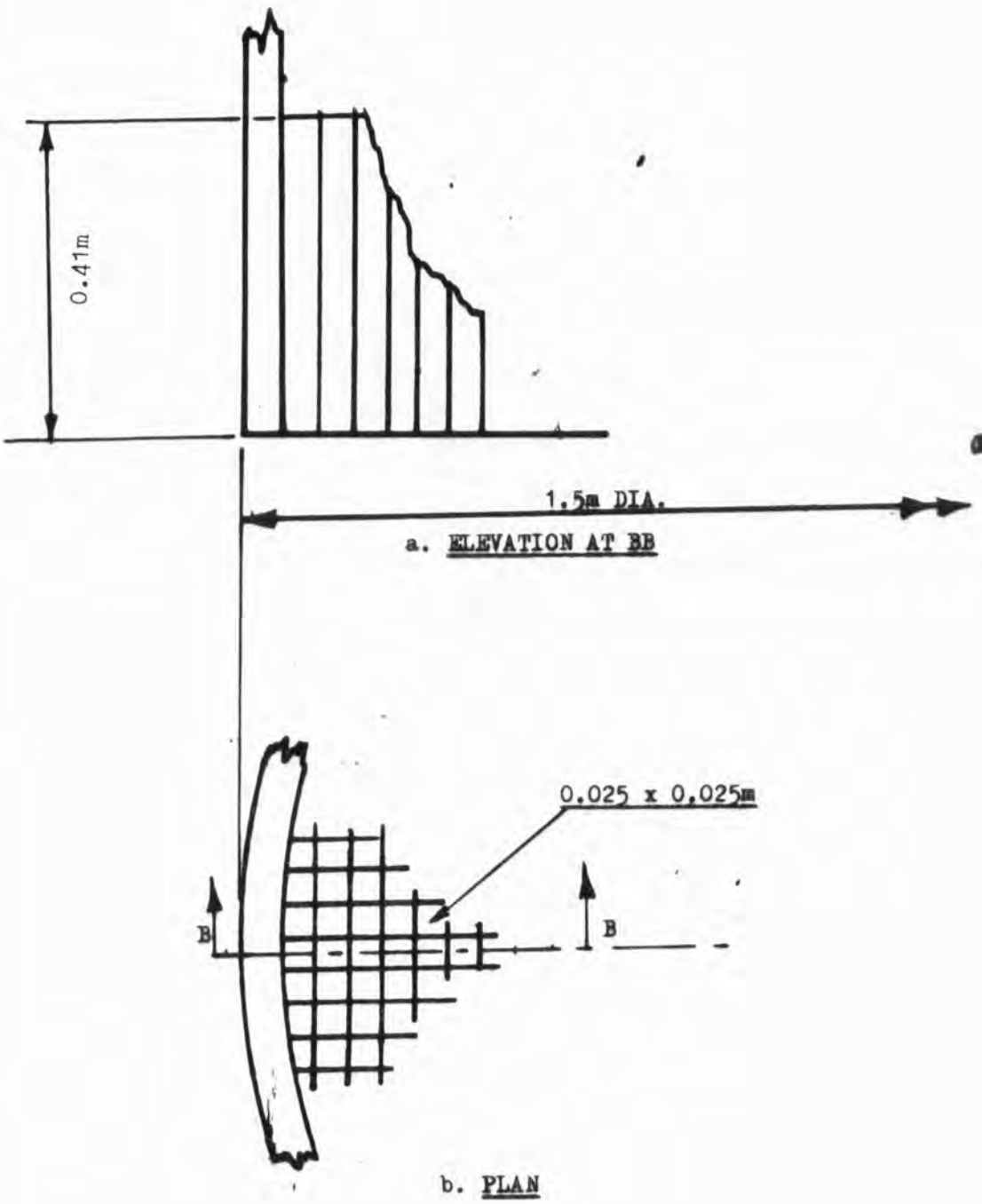

a. ELEVATION AT BB

b. PLAN

FEATURE 'A' OF
FIGURE 23

FIGURE 6.5

bulk rotation of the entrant air. Tests conducted to assess the symmetry about the center line YY in figure 6.3 of the flow in the enclosure form part of the experimental procedure, and are described in section 3.

6.2 Measuring Devices

The probes and equipment used in measuring the time averaged velocity, species concentrations and temperature within the specified flow are described in sub-sections a, b and c respectively. The mechanism used to manipulate and position the probes is detailed in sub-section d.

6.2a Velocity

The radial and vertical components of the time averaged velocity were measured with the pitot static tube and electronic manometer described in appendix 4 .

6.2b Species Concentrations

The time averaged partial pressures, and hence concentrations, were measured with the mass spectrometer described in appendix 4. The following empirical relationships, supplied by the manufacturer, were used to convert the output current from the spectrometer I into the partial pressures of the constituent gases in each sample:

$$P_{CH_4} = \frac{1.1655 \ (I_{15})}{39} \times 10^{-6}$$

$$P_{H_2O} = \frac{I_{18}}{35} \times 10^{-6}$$

$$p_{N_2} = \frac{I_{14} - 0.2331\,(I_{15})}{42} \times 10^{-6}$$

$$p_{CO} = \frac{(I_{28} - 42p_{N_2}\,10^{-6} - 0.114\,(I_{44})) \times 10^{-6}}{38}$$

$$p_{O_2} = \frac{(I_{32} - 5.3305\,p_{H_2O} \times 10^{-6}) \times 10^{-6}}{19}$$

$$p_{CO_2} = \frac{(I_{44}) \times 10^{-6}}{41}$$

In these relationships p represents partial pressure and the associated sub-script define the gas being considered. The numerical sub-scripts associated with I represent the molecular weight at which the signal was recorded. The gravimetric concentration of the constituents are derived from the calculated partial pressures with Gibbs and Daltons Law.

The probe used to collect the gas sample for the mass spectrometer is shown in figure 6.6. The sampling tube was of stainless steel, and had internal and external diameters of 0.002 and 0.0025m respectively. A stainless steel wire filter was situated in the sampling tube for the purpose of removing soot particles from the sample. A water jacket, with the dimensions specified in figure 6.7 surrounded the sampling tube. Water maintained at an inlet temperature of 16°C and volumetric flowrate $1.105 \times 10^{-5} cm^3/sec$ was circulated through the jacket; this sufficiently cooled the sampled gas to stop chemical reaction within approximately 0.005m of it entering the sampling tube.

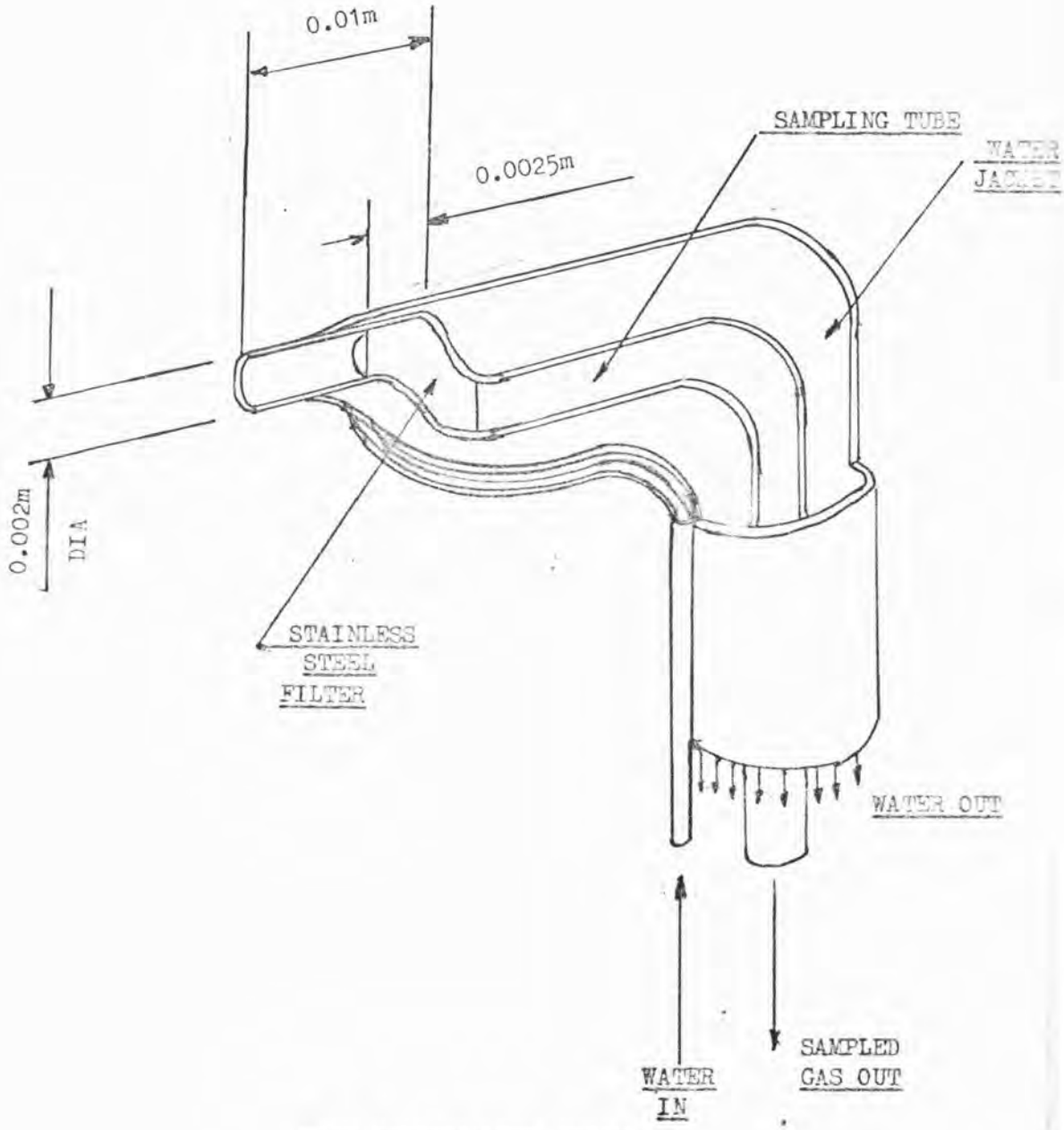

MASS SPECTROMETER PROBE

FIGURE 6.6

The ability of the sampling probe to stop chemical reaction within the prescribed distance of 0.005m was verified in the following manner. A twice full size scale model of the probe, but with a glass sampling tube was built, and is schematically detailed in figure67. An inspection notch in the water jacket enabled the first 0.0075m of the sampling tube to be visually inspected. The products from various chemically reacting Natural Gas free jets were sampled with the model probe. The nozzle used to produce the free jet was 0.05m diameter, and the volumetric flow rate of Natural Gas supplied varied between 1.964×10^{-2} and $9.819 \times 10^{-2} m^3 s^{-1}$. In each test the model probe was positioned at the edge of the chemically reacting jet 0.10m below the nozzle - as shown in figure68. The mixture was sampled at twice the volumetric flow rate of the mass-spectrometer probe, and the temperature and flowrate of cooling water were set and maintained at $15^{\circ}C$ and $1.105 \times 10^{-5} cm^3 s^{-1}$ respectively. Visual inspection of the glass sampling tube in each test showed that chemical reaction within the sample had stopped 0.005m after entering the probe.

6.2c Temperature

The temperature of the mixture was measured with a shielded thermo-couple that conformed to the dimensions shown in figure69. The thermo-couple was made from 25μm diameter Nickel Chromium and Nickel Aluminium wires costed in silicon. These wires have been electronically welded, whilst submerged in an argon atmosphere, in the shape of a hairpin. This configuration and size of thermocouple has been recommended by Smith and Cardon[58] - in an experimental investigation concerning temperature measurement with thermo-couples in a Methane diffusion flame. The thermo-couple wires were shielded from indirect

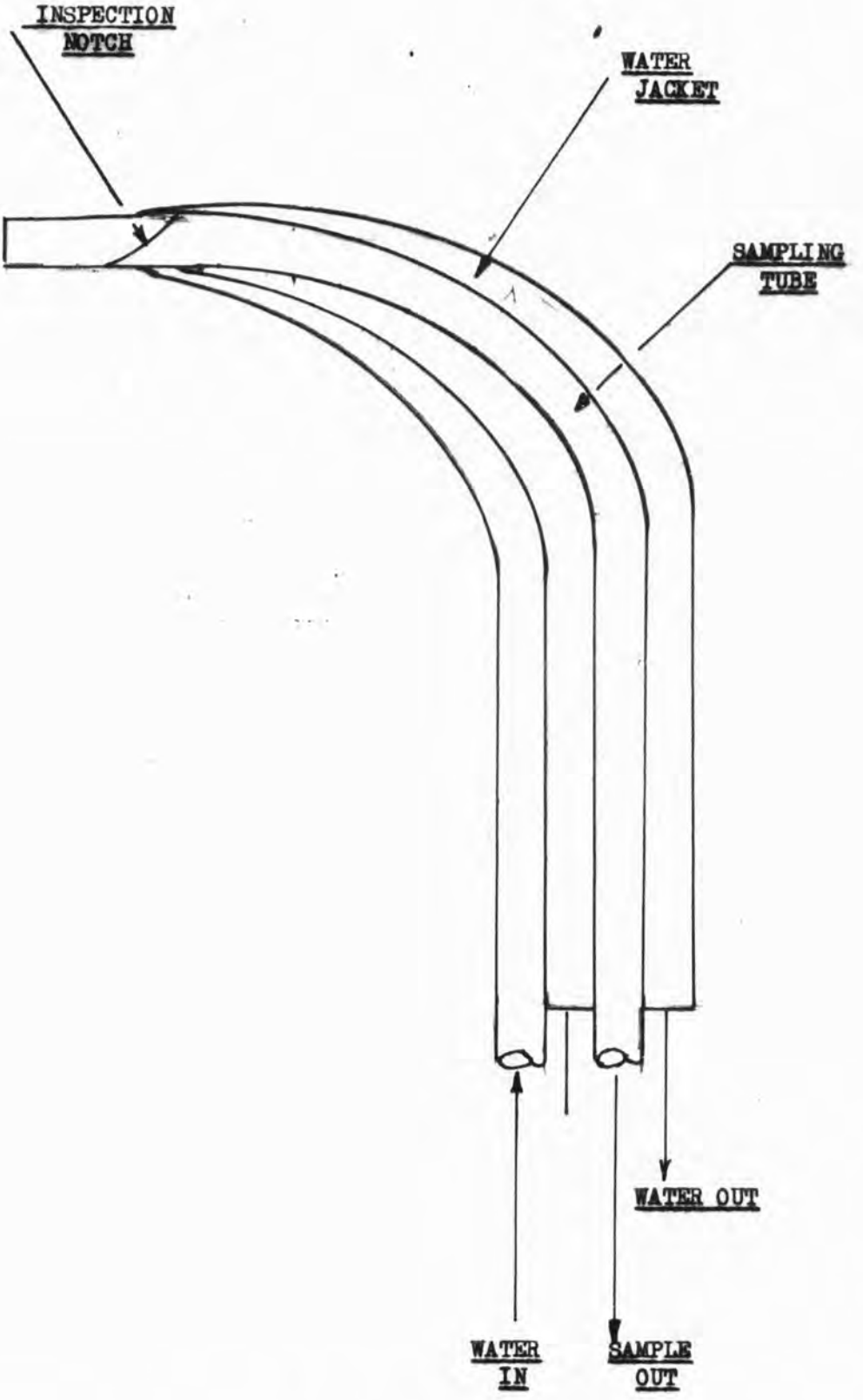

SCALE MODEL

FIGURE 6.7

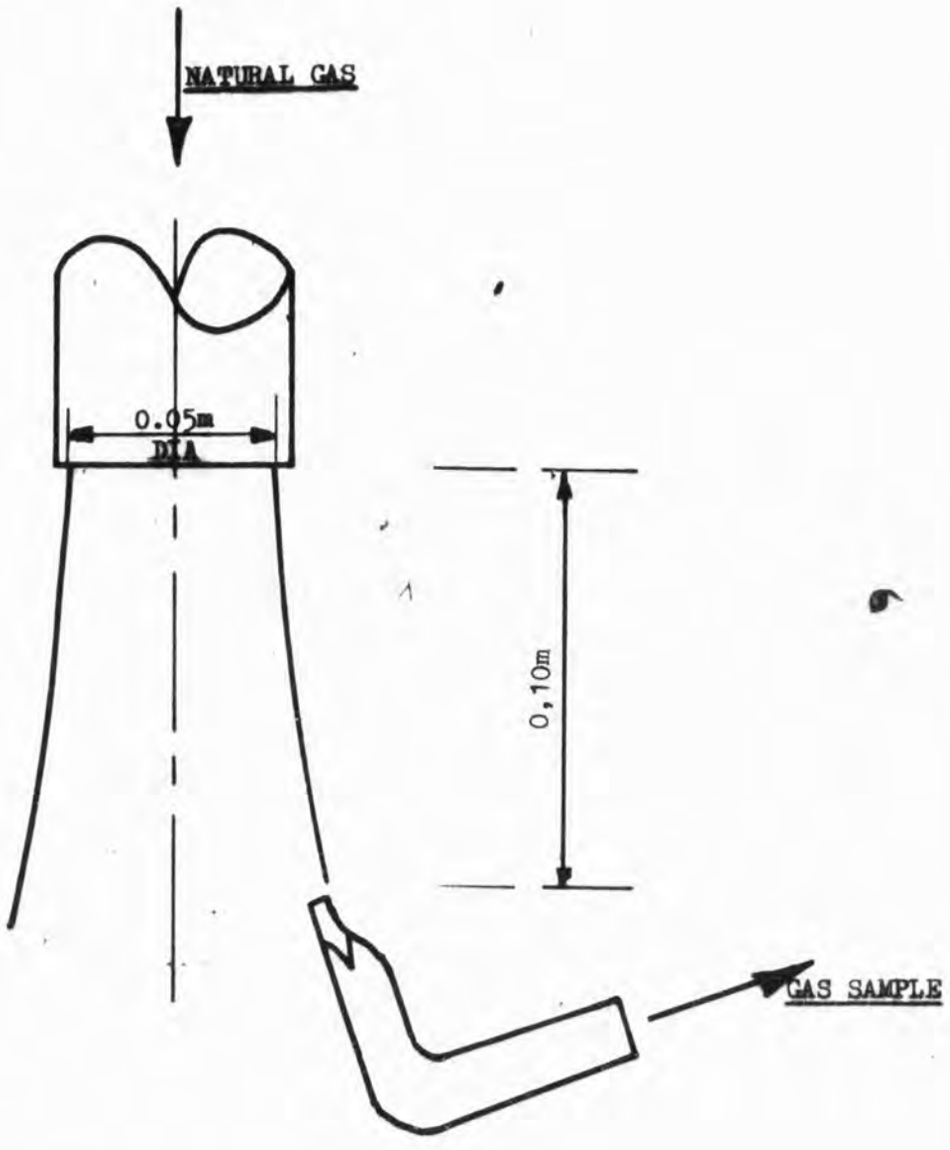

PROBE TESTING

FIGURE 6.8

radiation by being contained within an open ended cylinder. The dimensions of this cylinder have been derived from criteria postulated by Moffat[57]. The cylinder had an internal diameter of 0.03 m by 0.01 m long; and had four 0.005 m diameter holes drilled at the base.

6.2 d Probe Movement Mechanism

The intent of this sub-section is to detail the operation and construction of the mechanism used to position and manipulate the measuring probes. The mechanism is shown schematically in figure 6.10. The purpose of this mechanism is to position each probe at a specified radius r in the flow, with it's sensing head at a prescribed angle θ and height z from the porous surface - as shown in figure 6.11.

The mechanism was located in the enclosure with it's center line AA, as specified in figure 6.10, located at the intersection of:

a) the horizontal plane 0.3m above the burners porous surface

and b) a vertical plane 0.8m from, and parallel to the center line as shown in the plan view of the enclosure in figure 6.3.

The square cross sectioned support beam of the mechanism ran through suitably shaped journal bearings, which were supported by the enclosure. The probe was positioned at a particular radius by sliding the movement mechanism and support beam between the bearings.

The movement mechanism was used to position the probe at a

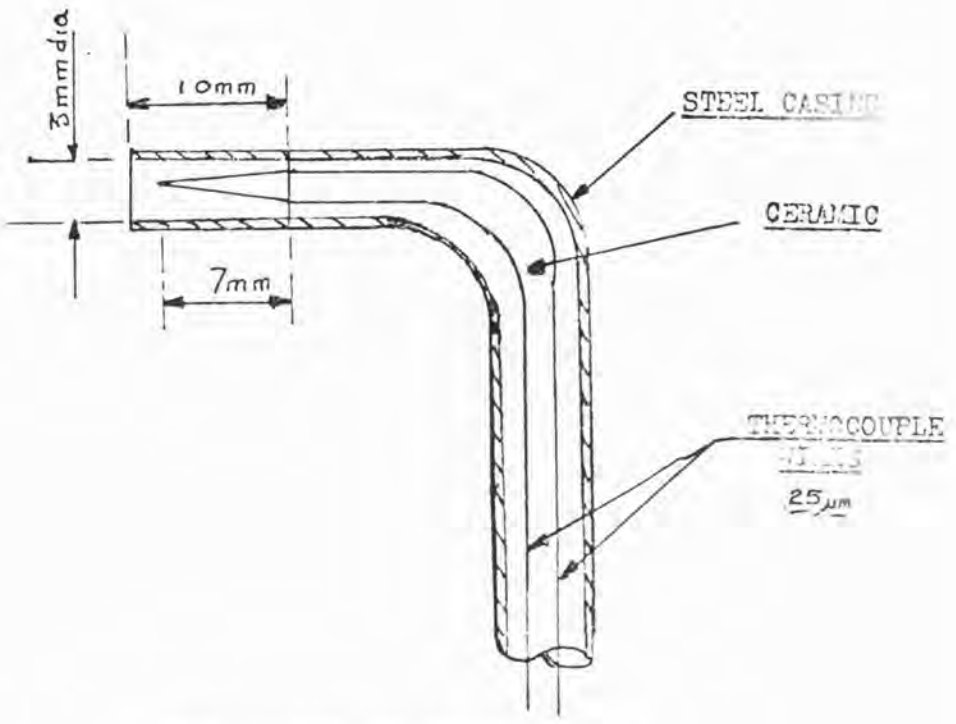

a. VIEW ON SECTION THROUGH SENSOR

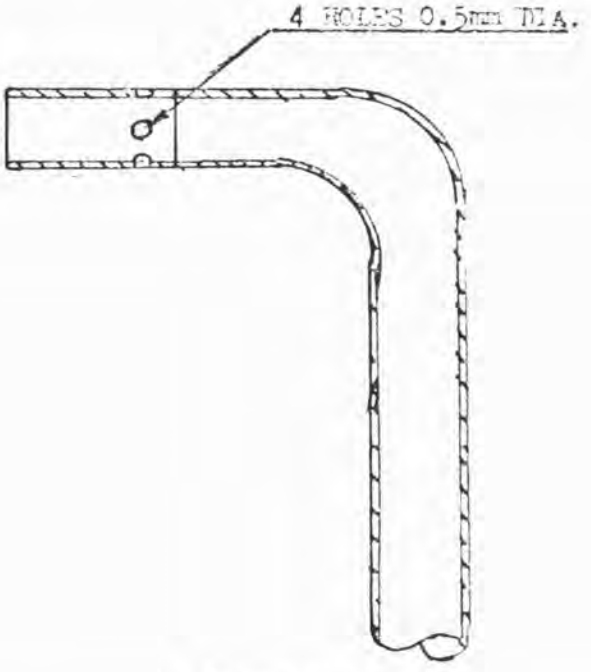

b. ELEVATION

TEMPERATURE SENSOR

FIGURE 6.9

specified angle and height with respect to the porous surface. The construction of the mechanism is first described, and then the technique used to position the probe detailed.

The major component of the mechanism is a five to one reduction gear box. It's input shaft extended through the support beam, and at it's end was connected to a pointer and handle positioned against a scale which was marked out in degrees. The output shaft of the gearbox connected to a faceplate and pinion. The faceplate formed a tight fitting journal bearing with the shaft. The pinion was keyed on to the shaft as shown in figure 6.12. The pinion was connected to a rack with 80 teeth/inch. The rack was positioned in the vertical plane, and the probes were mounted on it. A clutch was used to lock the faceplate in a fixed position. The clutch is shown in figure 6.10; and in more detail in figure 6.13. The clutch is a steel block, with the faceplate positioned in a specified slot. A copper push rod can lock the faceplate against one side of the slot-as shown in figure 6.13b. The position of the push rod was controlled from outside the enclosure by rotating an eccentric on the end of a control shaft.

The following procedure was used to position each probe with this mechanism. Firstly, each probes center line, aa in figure 6.11, was positioned parallel to the tangent of the porous stainless steel surface at the radius r being studied. This angle is designated θ in figure 6.11, the procedure for setting the probes center line aa at an angle θ to the horizontal was as follows. With the clutch released the input shaft was rotated through five times the angle θ. The faceplate was then locked in position by engaging the clutch.

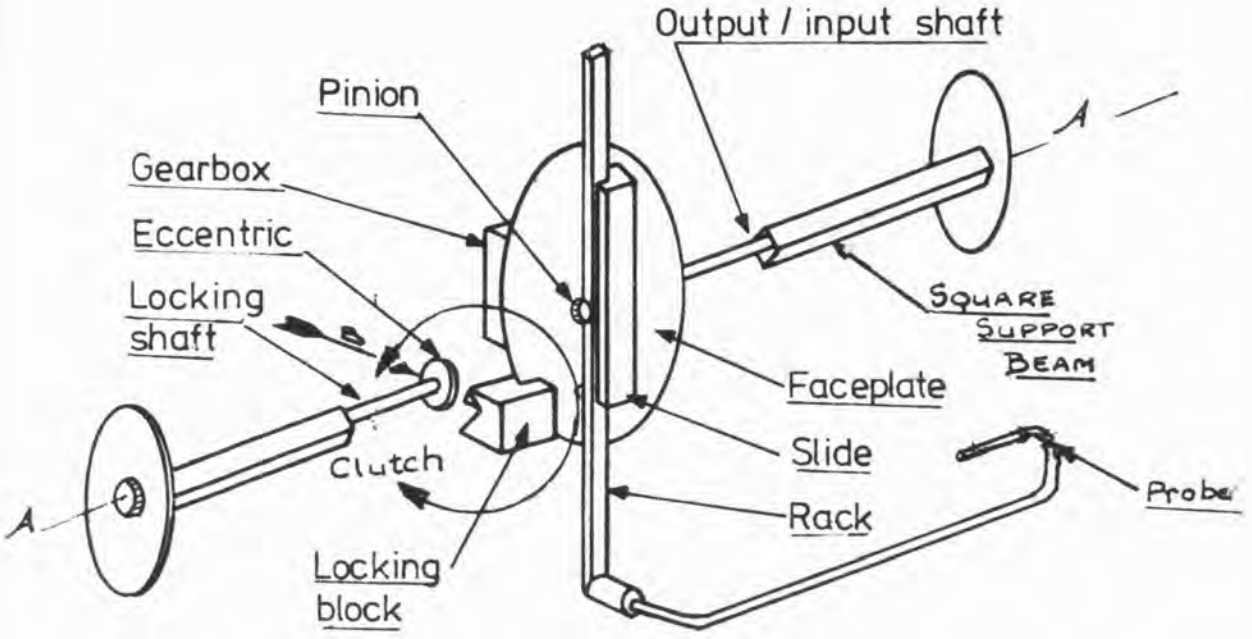

PROBE MOVEMENT MECHANISM

FIGURE 6.10

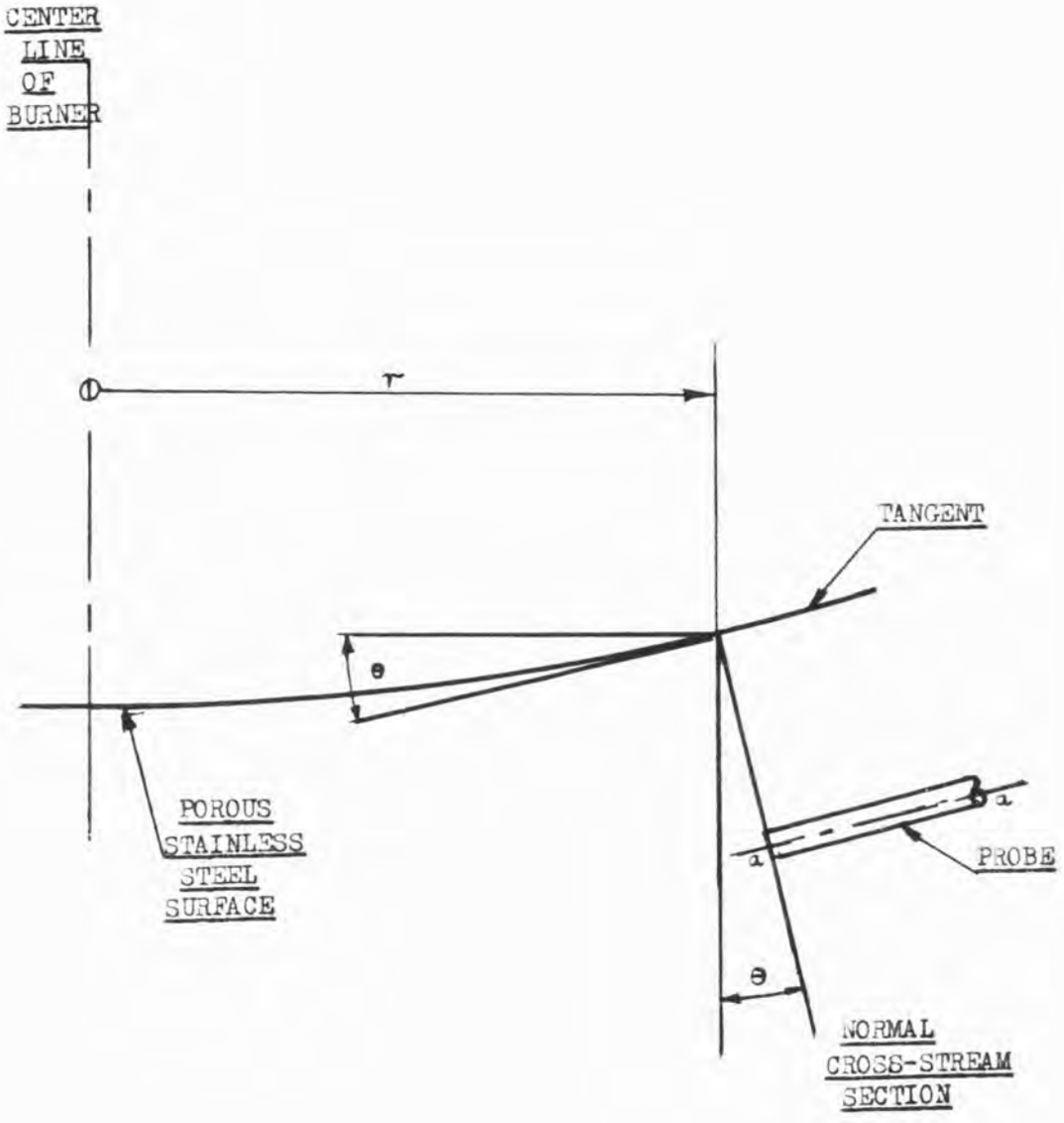

PROBE POSITIONING

FIGURE 6.11

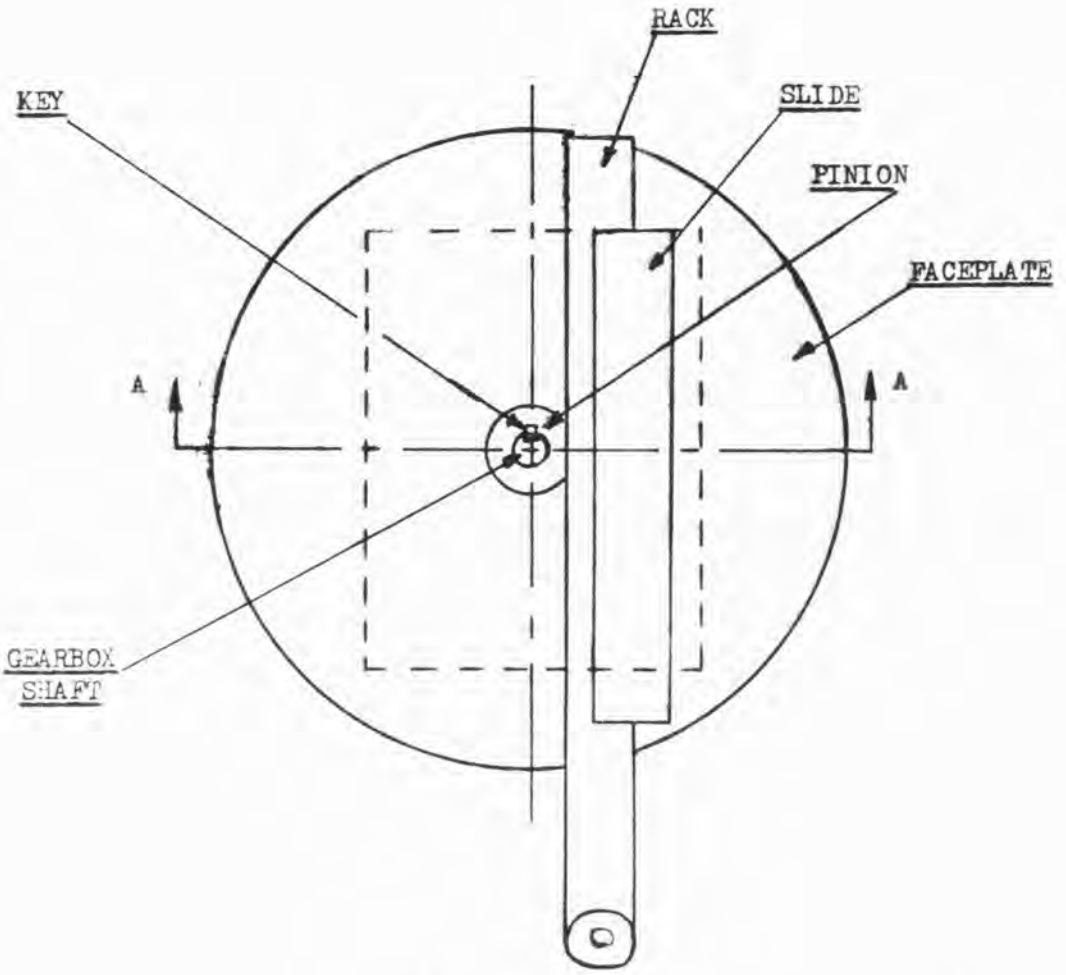

a. ELEVATION

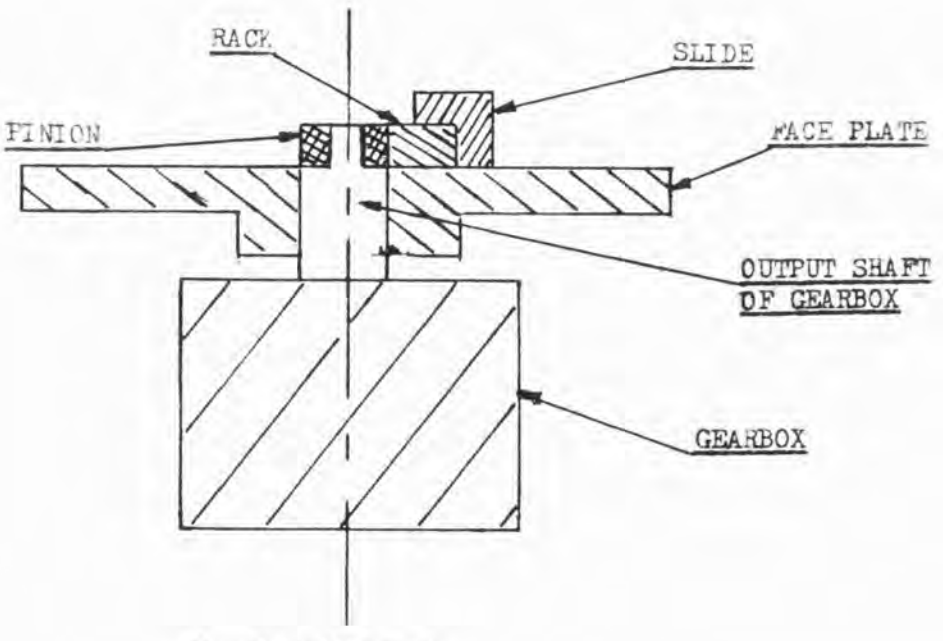

b. PLAN VIEW AT
SECTION AA

GEARBOX ARRANGEMENT

FIGURE 6.12

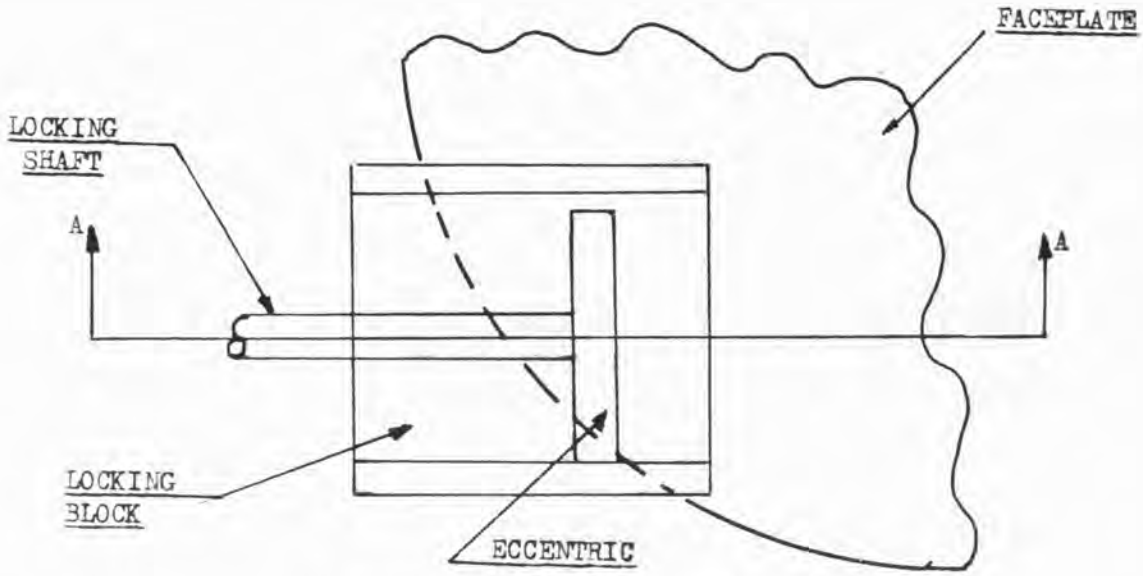

a ELEVATION FROM DIRECTION B IN FIGURE 6.10

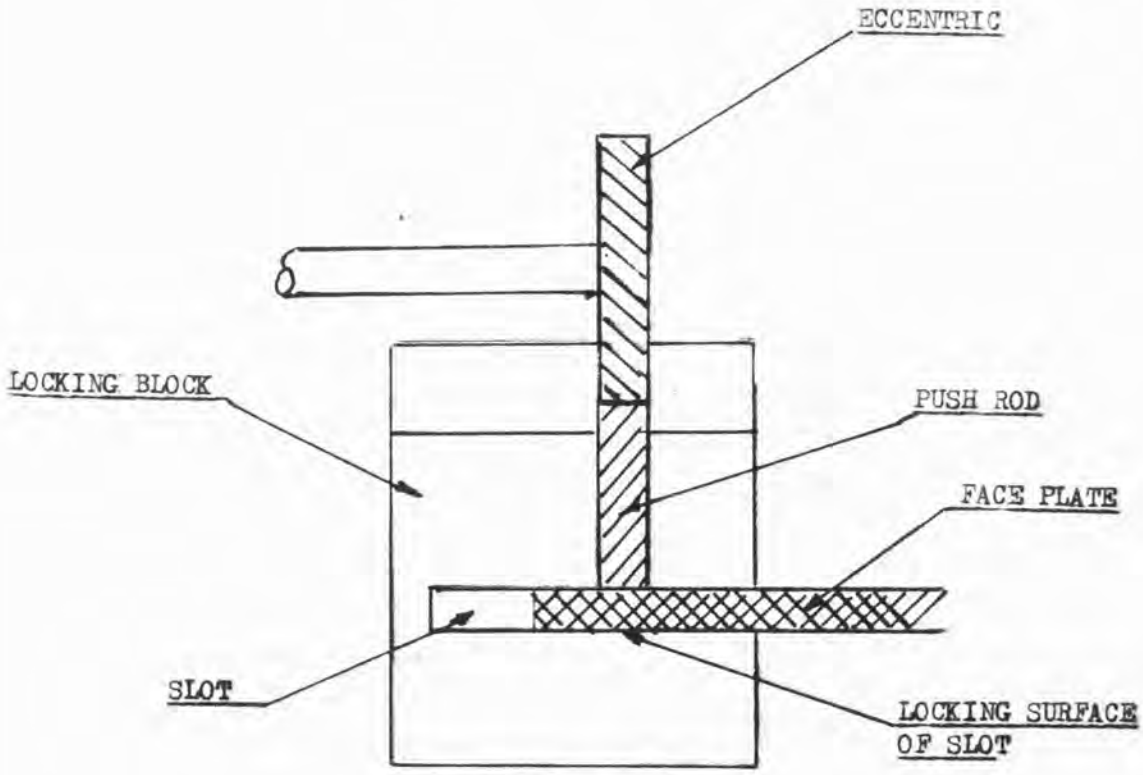

b PLAN ON AA

CLUTCH

FIGURE 6.13

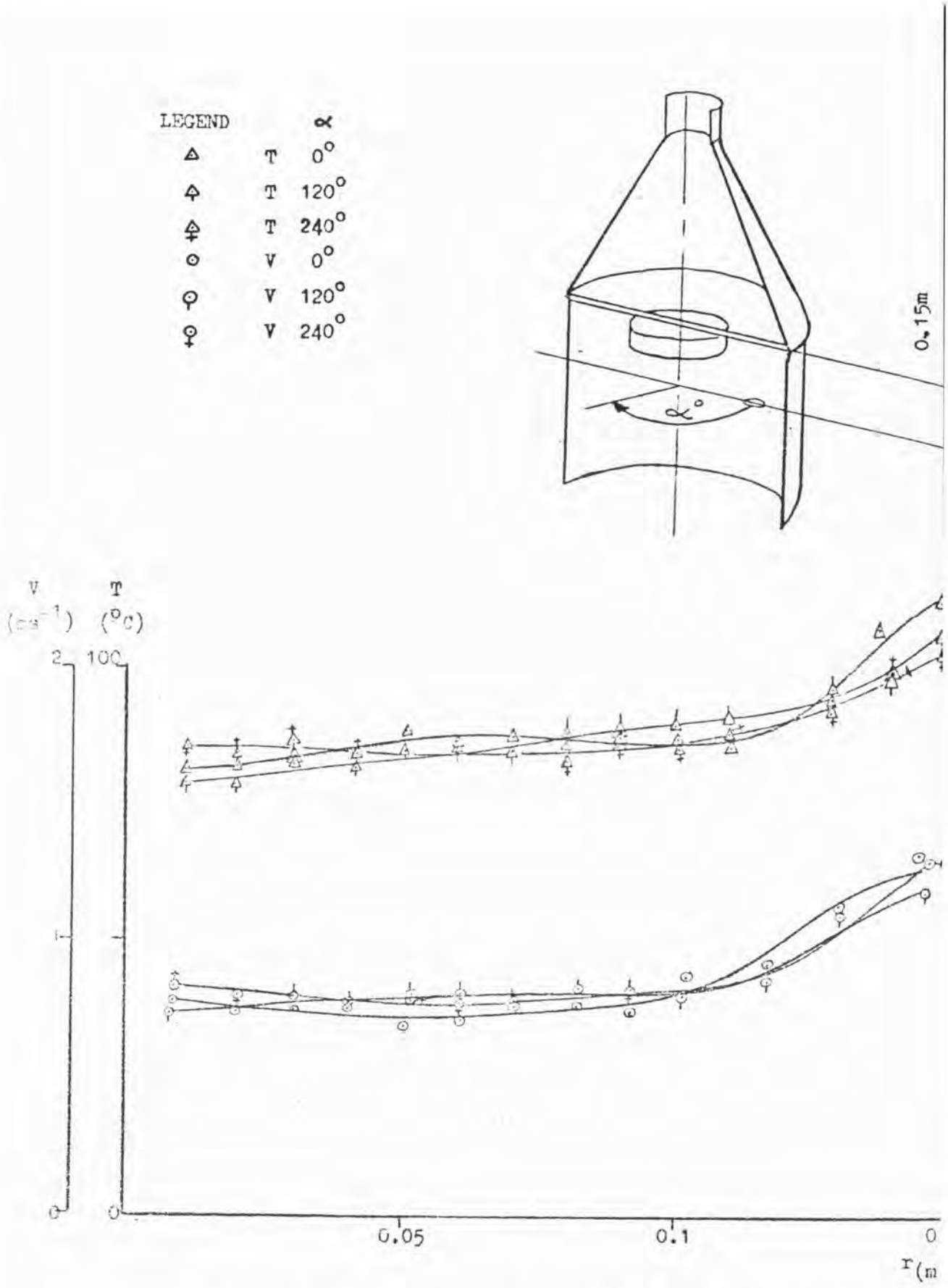

VELOCITY AND TEMPERATURE PROFILES IN THE ENCLOSURE

0.15m BELOW THE BURNER.

FIGURE 6.14

Further rotation of the gearboxes input shaft resulted in the pinion turning, and hence movement of the rack and probe normal to the porous surface.

6.3 Procedure

Throughout this experiment the volumetric rates of natural gas and air to the burner and nozzle were maintained at 3.65×10^{-2} and $8.1 \times 10^{-2} m^3 s^{-1}$. The natural gas comprised of Methane, Oxygen and Nitrogen in the following gravimetric concentrations 0.31 0.03 and 0.15. The velocity, temperature and concentration were measured with the aid of the sensors and devices described in section 2.

The experiment was split into two parts. Firstly, the technique used to assess whether the chemically reacting and enclosure flows were symmetrical about center line YY of the enclosure and burner in figure 6.3, is detailed in sub-section 3a. Secondly, the procedure used to map time averaged velocity , species concentration and temperature along various lines normal to the porous surface, but in the same radial plane, is presented in sub-section b.

6.3a Symmetry

All symmetry tests were conducted with the volumetric flowrates of natural gas and air set and maintained at the values described, and the impinging flow ignited.

The following procedure was used to check that the flow through the enclosure was symmetrical about the vertical center line YY in figure 6.3 The temperature and vertical velocity were measured along three radi, separated by angles of 120° and situated in a horizontal plane 0.15m below the lowest point of the burners porous surface. The flow was considered symmetrical when the same properties at the same radii differed by less than ten percent. Specimen

results are presented in figure 6.14 the associated data is detailed in section 5 .

The symmetry of the impinging flow about the vertical axis YY of the rig was assessed in the following manner. The radial velocity, species concentration and temperature were measured at several points along two cross-stream sections at a radius of 0.04m and separated by 120°. A set of successful results are presented in figure 6.15 , the associated experimental data is presented in section 5. . The flow was considered symmetrical about the specified center line when the same properties at the same height and radius showed a discrepancy of less than ten percent. If in either test the examined flow did not meet the specified tolerancies for symmetry, the position and orientation of the burner, nozzle and rig were checked and where necessary reset, and the tests repeated.

6.3b Mapping

The velocity, temperature and species concentrations were measured at various cross-stream sections in the flow, with the aid of sensors and devices detailed in section 6.1. The cross-stream sections have been specified by the radial measurement at which they intersect the porous surface - as shown in figure 6.11. Experimental results for radii of 0.0 to 0.11m are presented in figures 9.2 to 9.11 in chapter 9, the associated data is detailed in section 5. The symbols used in these figures are detailed in table 9.1 in chapter 9.

The accuracy of the presented experimental data was checked by repeating the experiment. The discrepancy between the two sets of data was greatest at a radius of 0.08m. The measured data at this section is detailed in section 6.4 and is plotted in figure 28 in chapter nine. The symbols used in this plot are detailed in table 9.1, with the filled in symbols representing one set of readings and the open symbols the other set.

6.4 Discussion

The experimental results have been replotted to show the variation of each measured property over the flow. Plots showing

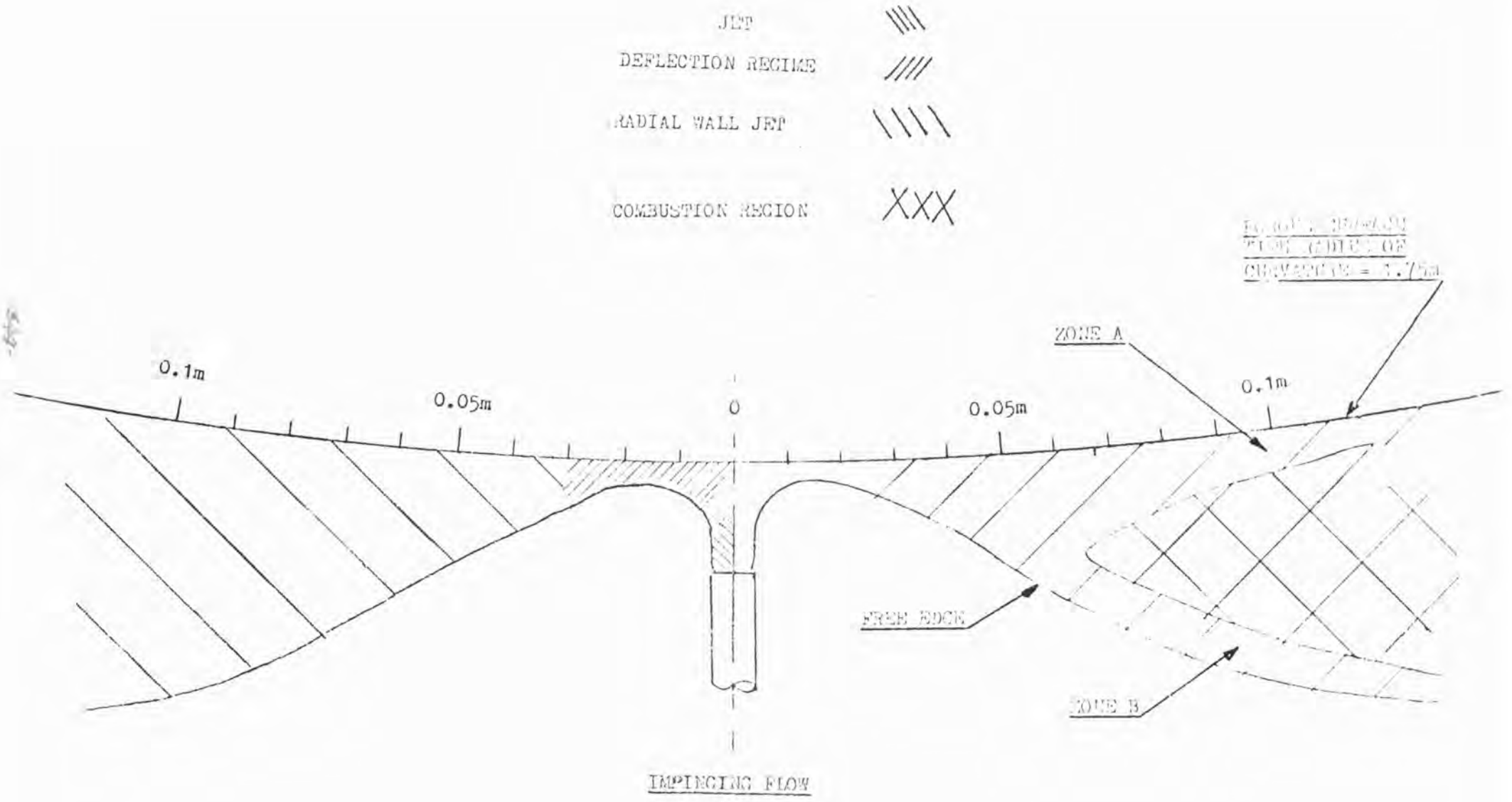
JET
DEFLECTION REGIME
RADIAL WALL JET
COMBUSTION REGION
0.1m
0.05m
0
0.05m
0.1m
ZONE A
FRESH EDGE
ZONE B
IMPINGING FLOW

FIGURE 6.1

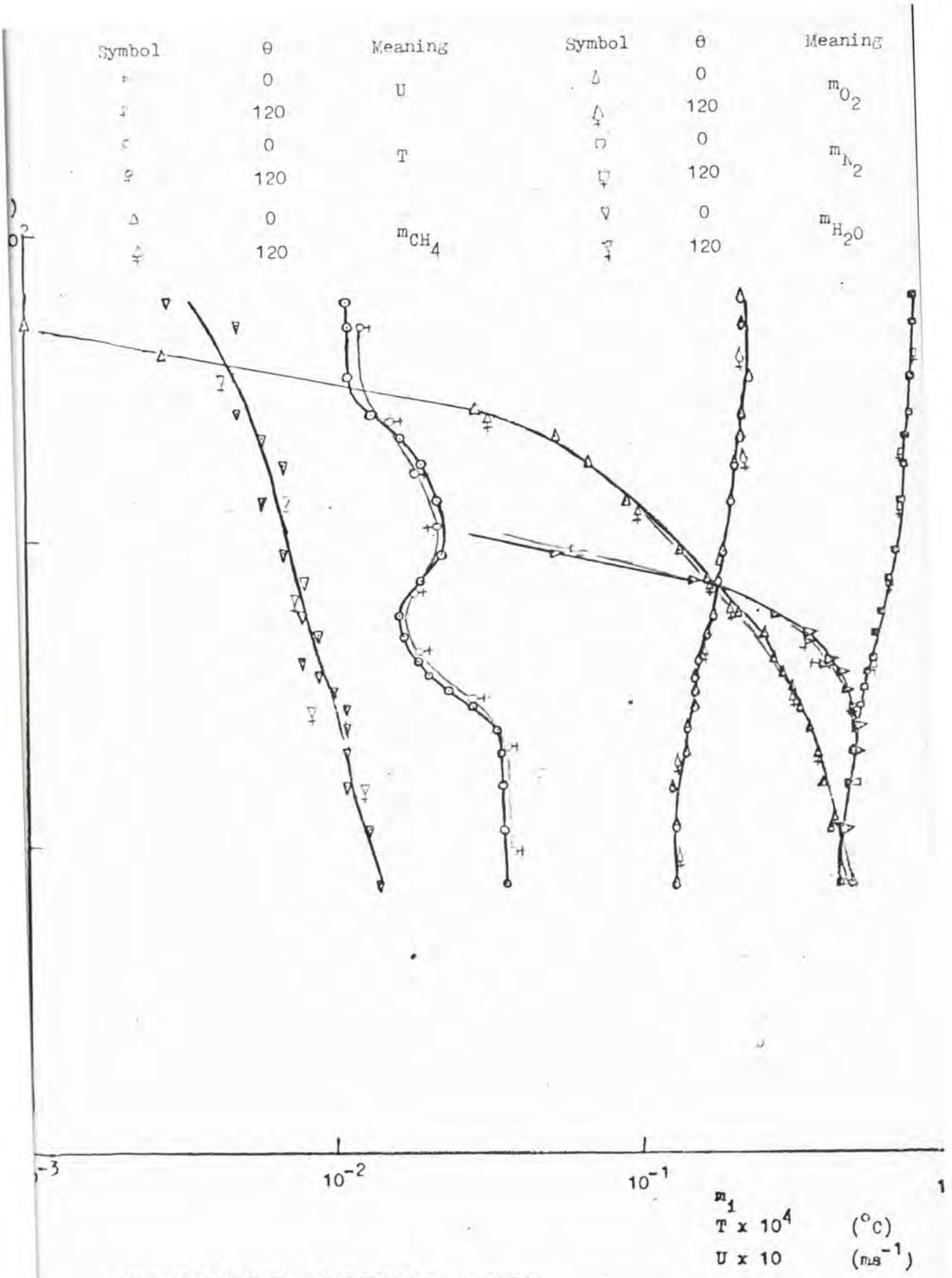

COMPARISON OF FLOW PATTERN AT r = 0.04m

FIGURE 6.16

the variation of the temperature, radial velocity and species concentration of Methane, Oxygen, Carbon-Dioxide, Carbon-Monoxide and Water Vapour in figures 9.12 to .19 respectively in chapter 9. In figures 9.13 to .19 the spatial variation of temperature is also included, being designated by dotted lines, to provide a basis on which to found the discussion of these results. The symbols used to designate the flow properties are the same as those used in chapter 9. The impinging flow consists of the jet, deflection and radial wall jet regimes shown in figure 6.15.

The jet regime occupied the area of flow where $0.0 < r \leq 0.03$m and $0.015 < z \leq 0.04$m. Measured variations of the specified time averaged properties are presented in figures 9.2 to .6 . The time averaged flow pattern in the jet being re-structured by turbulent transfer processes and radiant heat transfer. Turbulent momentum transfer at the free edge caused entrainment of the submerging air; which resulted in both the spreading and reduction in percentage methane content in the jet. The central core of the jet, that is where $0.0 < r \leq 0.001$m, was largely unaffected by entrainment, although turbulent transfer did reduce the radial variations in the measured properties. Illustrations of these changes are shown by the results at radii 0.0 and 0.005m shown in figures 9.2 and .3 respectively. Radiant energy transfer from the chemically reacting part of the flow heated the jet and submerging air to an almost constant temperature of $100^{o}C$ - as shown by the results in figure 9.2 and 6.14 respectively.

The deflection regime occupies the volume where $0.00 \leq r \leq 0.03$m and $0.00 \leq z \leq 0.02$m; a sectional view of this regime on a radius through the flow is shown in figure 6.15. Measured cross-stream profiles in this regime for r = 0.0 to 0.002m are presented in figures 9.2 to .6. The central core of the jet regime dominated that portion of the deflection regime directly beneath it, and consequently the temperature and species concentration in both regimes are similar - as shown by the measured variations in these properties at radii of 0.005 and 0.010m in figures 9.3 and .4. The portion of the jet deflected by impact with the porous surface, could not be detected with the measuring devices. Over the remainder of this regime the measured flow properties varied in the following manner. Local temperatures, at the same distance from the impervious surface, increased in the downstream direction, because of radiant energy transfer from the chemically reacting portion of the flow. An illustation of this variation is presented in the temperature field plotted in figure 9.12. The portion of the jet deflected in the radial direction, increased in both in width and speed - as shown by the results at radii of 0.01, 0.015 and 0.02m in figures 9.4 to .6 ; and more particularly the map of the mainstream velocity presented in figure 9.13 . The percentage methane content increased in the downstream direction, because of it's introduction through the porous surface. An illustration of this variation is shown in figure 9.14 which details the spatial distribution of Methane.

The radial wall jet regime contains the deflected portion of the impinging jet, and is exposed at it's free edge to the flow through the enclosure. The regime has been sub-divided into the Combustion and Mixing regions shown in figure 6.15 . The transfer processes in these regions are discussed below, with precedence being given to the Combustion Region, because the radiant energy transfer from it dominated all other transfer processes within this flow.

The chemical reaction between the fuels, Methane and Carbon Monoxide, and oxidant Oxygen are confined by the Combustion Region. Over most of this region these reactions are complex, being dependent upon instantaneous transfer processes, and result in the production of Carbon Dioxide, Carbon Monoxide and Water Vapour - as shown by the results presented in figures 9.17 to .19. However, two zones - or areas of the flow -have been identified where the reactions simplify. In the first zone Carbon Dioxide is predominately generated, that is where $m_{CO_2} > 0.06$ - as can be verified by referring to figure 9.17. There are small amounts of unused Methane and Oxygen in this zone, but only traces of Carbon Monoxide as shown in figures 9.14,.15 and .18 respectively. The temperature of the mixture reached a maximum in the vicinity of this zone, as shown in figure 9.12, because of the energy released gains from the chemical reactions and radiant heat transfer. In the other zone where $m_{CO} > 0.15$, in figure 9.18, the chemical reaction results in Carbon Monoxide being predominately generated. There are large amounts of unused Methane and small

quantities of Oxygen, Carbon Dioxide and Water Vapour present in this zone, as shown by the maps in figures 9.14,.15,.17 and .19 respectively.

The area occupied by the Mixing Region is shown in figure 6.15. The gases in this region are heated by radiant energy transfer from the Combustion Region to the reaction temperature of Methane and Oxygen. In the area upstream of the Combustion Region, where $0.03 \leqslant r \leqslant 0.65$m; the Methane, Oxygen and Nitrogen entering from the impingement regime are supplemented by Natural Gas at the porous surface and air at the free edge and mixed by turbulent transfer The resulting structure of the Methane, Oxygen and Nitrogen concentration fields are presented in figures 9.14,.15 and.16. The area beneath the Combustion Region, zone A in figure 6.15, is rich in Methane, because Natural Gas has been supplied through the porous surfaces. The amount of Methane can be seen in the result presented in figure 9.14 . The area above the Combustion region, zone B in Figure 6.15 contains air entrained from the enclosure flow and the diffused portion of products and fuels from the chemical reaction.

6.5 Experimental Results.

	z (m) x 10^{-3}	T (^{o}C)	P_D (mm water) radial	P_D (mm water) vertical	The Mass Spectrometer output at Molecular Weights of: 14	15	18	20	28	32	44
a) r = 0.0m	4.074	108.71	0.0	251.712	9.939	0.010	0.711	0.050	46.430	6.500	0.209
	6.568	123.100	0.0	185.138	9.543	0.010	0.692	0.000	45.530	6.200	0.118
	10.725	110.500	0.0	155.876	9.272	0.000	0.653	0.000	44.230	5.675	0.127
	15.710	70.321	0.0	136.883	9.126	0.000	0.694	0.000	42.930	5.925	0.136
	19.71	50.450	0.0	115.192	9.030	0.000	0.785	0.000	41.230	5.675	0.145

b) r=.005m

z (m) x 10^{-3}	T (°C) x 10^{3}	P_D (mm water) radial	P_D (mm water) vertical	The Mass Spectrometer output at Molecular Weights of: 14	15	18	20	28	32	44
0.750	0.127	0.65	0.0	16.019	3.360	1.13	0.0	41.58	4.800	0.0
2.037	0.126	0.5	0.0	16.082	3.140	1.05	0.0	41.45	4.795	0.0
3.307	0.123	0.35	0.0	15.796	2.560	0.90	0.0	41.12	4.550	0.0
4.608	0.121	0.3	0.0	15.959	2.830	0.84	0.0	40.39	4.580	0.0
5.971	0.120	0.2	0.0	15.843	3.120	0.75	0.0	39.560	4.390	0.0
7.275	0.1193	0.17	0.0	15.286	3.120	0.80	0.0	37.430	4.130	0.0
8.585	0.119	0.13	0.0	15.125	2.800	0.84	0.0	37.000	4.070	0.0
9.889	0.117	0.12	0.0	15.486	2.850	0.867	0.0	36.241	3.892	0.0
11.103	0.1145	0.05	0.0	15.021	1.930	0.823	0.0	36.282	4.003	0.0
12.506	0.113	0.03	0.0	14.557	1.550	0.780	0.0	35.623	3.834	0.0
15.110	0.110	0.015	0.0	14.267	0.970	0.727	0.0	35.364	3.976	0.0
17.728	0.107	0.01	0.0	13.928	0.570	0.743	0.0	34.706	3.907	0.0
22.949	0.1045	0.02	0.0	13.913	0.300	0.710	0.0	35.407	3.928	0.0
28.157	0.105	0.015	0.0	14.074	0.200	0.737	0.0	35.008	3.839	0.0
36.609	0.105	0.0	0.0	13.884	0.000	0.683	0.0	34.829	3.950	0.0

	z (m) x 10^{-3}	T (^{o}C) x 10^{3}	P_D (mm water) radial	vertical	The Mass Spectrometer output at Molecular Weights of: 14	15	18	20	28	32	44
c) r = 0.010m	0.150	0.132	0.42	0.0	16.32	4.450	1.210	0.0	38.530	4.220	0.0
	1.166	0.133	0.55	0.0	15.800	4.220	1.029	0.0	40.011	4.464	0.0
	1.583	0.130	0.52	0.0	15.318	3.900	0.937	0.0	38.393	4.309	0.0
	1.997	0.125	0.35	0.0	14.840	3.580	0.980	0.0	37.274	4.133	0.0
	2.412	0.120	0.14	0.0	14.788	3.860	1.100	0.0	36.356	4.037	0.0
	2.827	0.115	0.14	0.0	13.335	4.040	1.02	0.0	36.437	4.041	0.0
	2.244	0.1095	0.10	0.0	13.533	4.200	0.98	0.0	36.619	4.066	0.0
	3.659	0.1055	0.09	0.0	14.870	4.120	1.01	0.0	36.100	3.970	0.0
	4.074	0.105	0.08	0.0	16.126	4.650	1.150	0.0	41.520	4.650	0.0
	4.492	0.099	0.043	0.0	15.562	4.110	1.064	0.0	40.227	4.456	0.0
	5.736	0.0976	0.03	0.0	15.023	3.020	0.939	0.0	39.033	4.331	0.0
	7.401	0.0975	0.03	0.0	14.673	0.950	0.993	0.0	39.140	4.307	0.0
	9.063	0.0995	0.03	0.0	14.609	0.450	1.028	0.0	39.047	4.392	0.0
	10.725	0.1005	0.02	0.0	14.245	0.400	0.992	0.0	38.053	4.278	0.0
	14.084	0.102	0.01	0.0	14.256	0.400	1.117	0.0	38.760	4.383	0.0
	19.037	0.11	0.00	0.0	14.267	0.300	1.031	0.0	38.667	4.301	0.0
	24.023	0.1135	0.00	0.0	14.500	0.200	1.186	0.0	41.473	4.764	0.0
	29.012	0.1175	0.00	0.0	14.999	0.000	1.210	0.0	41.680	4.760	0.0

	z (m) x 10^{-3}	T (^{o}C) x 10^{3}	P_D (mm water) radial	vertical	The Mass Spectrometer output at Molecular Weights of: 14	15	18	20	28	32	44
d) r = 0.015m	0.750	0.136	0.600	0.0	19.272	16.250	1.32	0.0	54.72	6.35	0.0
	1.583	0.1265	0.680	0.0	18.129	15.800	1.26	0.0	51.09	6.07	0.0
	1.997	0.123	0.700	0.0	17.560	16.375	1.16	0.0	49.37	5.79	0.0
	2.472	0.1185	0.40C	0.0	16.867	15.100	1.18	0.0	47.44	5.54	0.0
	2.827	0.1145	0.110	0.0	16.724	15.000	1.11	0.0	46.12	5.4	0.0
	3.244	0.11	0.080	0.0	16.331	14.900	1.14	0.0	45.98	5.38	0.0
	4.074	0.1055	0.03	0.0	16.537	14.650	1.18	0.0	46.16	5.29	0.0
	4.906	0.104	0.025	0.0	17.219	14.775	1.35	0.0	49.04	5.7	0.0
	6.568	0.1065	0.025	0.0	16.826	12.400	1.36	0.0	48.21	5.5	0.0
	8.230	0.107	0.015	0.0	16.783	10.525	1.39	0.0	48.38	5.45	0.0
	11.557	0.108	0.05	0.0	16.739	6.275	1.41	0.0	48.46	5.41	0.0
	15.710	0.111	0.0	0.0	16.521	3.025	1.45	0.0	48.23	5.5	0.0
	20.7	0.112	0.0	0.0	16.203	0.900	1.45	0.0	47.61	5.5	0.0
	27.35	0.12	0.0	0.0	16.135	0.000	1.56	0.0	46.68	5.95	0.0
	34.0	0.12	0.0	0.0	16.041	0.000	1.50	0.0	46.75	5.55	0.0
	40.648	0.126	0.0	0.0	16.198	0.000	1.57	0.0	46.83	5.5	0.0
	56.425	0.128	0.0	0.0	166430	0.000	1.48	0.0	48.10	5.59	0.0

	z (m) x 10^{-3}	T (^{o}C) x 10^{3}	P_D (mm water) radial	P_D (mm water) vertical	The Mass Spectrometer output at Molecular Weights of: 14	15	18	20	28	32	44
e) r = 0.020m	0.750	0.155	3.1	0.0	15.547	14.275	1.125	0.0	39.821	4.375	0.0
	1.166	0.154	3.0	0.0	14.905	13.650	1.109	0.0	39.012	4.219	0.0
	1.583	0.153	2.93	0.0	14.612	13.150	1.114	0.0	38.103	4.094	0.0
	1.997	0.1425	2.8	0.0	14.219	15.275	1.068	0.0	36.794	4.048	0.0
	2.412	0.1265	1.9	0.0	14.126	13.900	1.153	0.0	35.785	4.013	0.0
	2.827	0.122	1.15	0.0	13.834	12.600	1.127	0.0	33.075	3.937	0.0
	3.244	0.120	0.70	0.0	13.416	14.900	1.012	0.0	30.566	3.252	0.0
	3.659	0.119	0.25	0.0	13.2	14.100	1.036	0.0	30.157	3.286	0.0
	4.074	0.118	0.06	0.0	13.105	6.150	1.101	0.0	30.748	3.211	0.0
	4.492	0.117	0.03	0.0	12.988	6.230	1.135	0.0	30.239	3.105	0.0
	5.422	0.116	0.01	0.0	12.795	6.410	1.090	0.0	29.930	3.060	0.0
	7.401	0.113	0.0	0.0	13.102	6.500	1.215	0.0	30.821	3.195	0.0
	10.725	0.114	0.0	0.0	12.635	6.525	1.109	0.0	30.612	2.759	0.0
	14.048	0.115	0.0	0.0	14.867	5.450	1.184	0.0	35.403	3.184	0.0
	17.375	0.117	0.0	0.0	14.299	2.650	1.268	0.0	36.194	3.468	0.0
	22.361	0.1185	0.0	0.0	13.656	3.420	1.243	0.0	33.685	2.783	0.0
	27.350	0.1185	0.0	0.0	13.164	1.000	1.347	0.0	34.575	3.077	0.0
	34.0	0.116	0.0	0.0	12.546	0.200	1.512	0.0	32.666	3.512	0.0
	39.907	0.119	0.0	0.0	13.628	0.000	1.516	0.0	35.657	3.916	0.0
	50.153	0.122	0.0	0.0	13.900	0.000	1.591	0.0	35.448	3.841	

	z (m) x 10^{-3}	T (°C) x 10^{3}	P_D (mm water) radial	vertical	The Mass Spectrometer output at Molecular Weights of: 14	15	18	20	28	32	44
f) r = 0.040m	0.750	0.360	0.800	0.0	21.091	47.800	1.488	0.0	35.949	4.457	0.0
	1.66	0.354	0.850	0.0	20.812	45.100	1.302	0.0	35.673	4.354	0.0
	1.587	0.352	0.950	0.0	20.341	40.000	1.210	0.0	36.096	4.341	0.0
	2.00	0.347	1.050	0.0	20.124	38.600	1.112	0.0	36.620	4.398	0.0
	2.412	0.340	1.100	0.0	19.668	36.200	1.090	0.0	36.844	4.335	0.0
	2.827	0.282	1.180	0.0	19.411	33.950	1.068	0.0	37.768	4.602	0.0
	3.244	0.235	1.200	0.0	18.780	30.980	0.976	0.0	38.191	4.489	0.0
	3.659	0.201	1.300	0.0	17.212	28.130	0.854	0.0	37.315	4.406	0.0
	4.058	0.187	1.100	0.0	16.721	26.000	0.752	0.0	39.039	4.443	0.0
	4.906	0.168	0.800	0.0	15.981	22.930	0.730	0.0	37.263	4.430	0.0
	5.736	0.164	0.550	0.0	15.154	17.400	0.648	0.0	36.586	4.267	0.0
	7.401	0.194	0.150	0.0	14.721	12.700	0.646	0.0	37.710	4.354	0.0
	9.063	0.224	0.005	0.0	14.316	10.600	0.504	0.0	37.734	4.301	0.0
	13.219	0.217	0.000	0.0	14.001	7.170	0.482	0.0	38.858	4.468	0.0
	17.375	0.194	0.000	0.0	13.978	5.259	0.460	0.0	38.981	4.475	0.0
	21.532	0.165	0.000	0.0	14.096	4.100	0.448	0.0	39.605	4.682	0.0
	25.685	0.134	0.000	0.0	14.215	2.178	0.376	0.0	39.729	4.589	0.0
	34.000	0.112	0.000	0.0	14.110	0.250	0.314	0.0	24.053	2.826	0.0
	50.623	0.114	0.000	0.0	14.052	0.100	0.352	0.0	40.576	4.553	0.0
	67.248	0.113	0.000	0.0	14.020	0.000	0.230	0.0	39.600	4.420	0.0

	(m) x 10^{-3}	T ($^{\circ}$C) x 10^{3}	P_D (mm water) radial	vertical	The Mass Spectrometer output at Molecular Weights of: 14	15	18	20	28	32	44
g) r = 0.065m	0.750	0.372	0.03	0.0	27.540	75.700	1.355	0.10	33.068	3.365	0.0
	1.166	0.374	0.033	0.0	24.570	68.300	1.090	0.10	32.135	3.260	0.0
	1.583	0.372	0.03	0.0	23.910	58.100	1.074	0.10	32.303	3.474	0.0
	1.997	0.357	0.029	0.0	20.450	46.100	1.039	0.10	33.970	3.549	0.0
	2.412	0.343	0.03	0.0	19.230	37.500	0.974	0.10	35.338	3.874	0.0
	2.827	0.335	0.03	0.0	18.720	32.500	0.909	0.10	36.306	3.899	0.0
	3.244	0.33	0.03	0.0	18.330	29.100	0.954	0.10	37.373	3.984	0.0
	3.655	0.364	0.03	0.0	17.740	25.800	0.968	0.10	37.641	4.018	0.0
	4.074	0.36	0.025	0.0	17.580	23.900	1.033	0.10	37.908	4.073	0.0
	4.905	0.33	0.023	0.0	18.160	21.150	0.948	0.10	38.476	4.158	0.0
	5.736	0.36	0.021	0.0	17.530	18.700	0.973	0.10	38.644	3.983	0.0
	7.410	0.396	0.016	0.0	16.540	14.030	1.108	0.10	35.711	4.018	0.0

g) r = 0.65m
Con

z (m) x 10^{-3}	T (°C) x 10^{3}	P_D (mm water) radial	vertical	The Mass Spectrometer output at Molecular Weight of: 14	15	18	20	28	32	44
8.978	0.46	0.010	0.0	15.970	10.950	1.042	0.10	39.779	4.972	0.0
13.219	0.690	0.008	0.0	15.310	9.400	0.917	0.10	39.046	3.217	0.0
17.391	0.810	0.005	0.0	14.670	2.870	0.912	0.10	39.914	2.202	0.0
21.532	0.840	0.0025	0.0	14.480	1.320	0.827	0.10	40.282	1.967	0.0
25.685	0.725	0.001	0.0	19.420	0.750	1.062	0.10	43.349	2.782	0.0
29.841	0.565	0.0	0.0	14.860	0.500	1.106	0.10	43.117	4.036	0.0
34.000	0.340	0.0	0.0	14.720	0.270	1.191	0.10	42.484	4.751	0.0
38.154	0.360	0.0	0.0	14.650	0.260	1.186	0.10	42.320	4.426	0.0
42.31	0.390	0.0	0.0	14.760	0.250	1.160	0.0	42.020	4.391	0.0
50.623	0.370	0.0	0.0	14.580	0.200	1.176	0.0	41.487	4.386	0.0
67.248	0.128	0.0	0.0	14.310	0.110	1.170	0.0	40.755	4.880	0.0
83.37	0.115	0.0	0.0	14.320	0.100	1.235	0.0	40.522	4.880	0.0

	z (m) x 10^{-3}	T (^{o}C) x 10^{3}	P_D (mm water) radial	vertical	The Mass Spectrometer output at Molecular Weights of: 14	15	18	20	28	32	44
h) r = 0.080m at an angle of 0^{o}	0.750	0.472	0.008	0.0	14.530	55.650	0.577	0.0	5.690	0.000	0.0
	1.165	0.485	0.090	0.0	13.040	43.850	0.364	0.0	7.205	0.000	0.0
	1.583	0.530	0.130	0.0	10.920	32.950	0.411	0.0	8.320	0.000	0.0
	3.244	0.820	0.220	0.0	7.890	14.180	0.119	0.0	10.680	0.000	0.400
	3.659	0.881	0.230	0.0	7.740	12.600	0.226	0.0	11.095	0.000	0.450
	4.074	0.912	0.240	0.0	7.420	10.300	0.173	0.0	11.010	0.000	0.600
	4.492	0.902	0.190	0.0	11.630	16.800	0.680	0.0	17.075	0.000	0.820
	4.906	0.924	0.200	0.0	9.680	14.430	0.660	0.0	17.375	00000	1.000
	5.736	0.965	0.210	0.0	8.180	10.250	0.530	0.0	15.575	0.000	0.900
	6.568	0.980	0.220	0.0	7.200	0.000	0.380	0.0	14.075	0.000	0.600
	7.407	0.965	0.230	000	4.630	5.100	2.610	0.0	9.775	0.000	0.700
	9.063	1.005	0.220	0.0	3.300	3.900	1.980	0.0	7.075	0.000	0.650
	10.725	0.965	0.200	0.0	2.330	7.030	1.720	0.0	5.075	0.000	0.650
	12.387	0.884	0.180	0.0	2.380	5.230	0.480	0.0	5.175	0.000	0.600
	14.048	0.790	0.120	0.0	0.000	7.350	3.970	0.0	3.775	0.000	0.400

	z (m) x 10^{-3}	T (°C) x 10^{3}	P_D (mm water) radial	vertical	The Mass Spectrometer output at Molecular Weights of: 14	15	18	20	28	32	44
h) r = 0.080m Con. at an angle of 0°	17.375	1.010	0.080	0.0	7.893	0.150	0.585	0.0	21.029	0.210	0.854
	20.700	0.934	0.050	0.0	7.925	0.050	0.585	0.0	21.221	0.620	0.646
	24.023	0.830	0.045	0.0	8.287	0.000	0.714	0.0	21.762	0.903	0.638
	27.350	0.680	0.020	0.0	8.584	0.000	0.833	0.0	22.354	1.400	0.600
	30.674	0.470	0.020	0.0	9.246	0.000	0.972	0.0	24.345	2.290	0.223
	34.000	0.278	0.015	0.0	10.629	0.000	1.112	0.0	27.737	3.210	0.115
	37.325	0.190	0.010	0.0	13.311	0.000	1.661	0.0	36.428	4.660	0.108
	43.972	0.140	0.005	0.0	14.393	0.000	1.890	0.0	39.429	5.270	0.100
	50.623	0.134	0.000	0.0	16.900	0.000	1.820	0.0	40.000	7.030	0.067
	58.936	0.126	0.000	0.0	15.900	0.090	1.880	0.0	40.100	7.060	0.033
h) r = 0.080m Con. at an agle of 270°	0.750	485	0.010	0.0	15.250	54.100	0.410	0.0	7.060	0.000	0.290
	1.583	535	0.135	0.0	11.392	31.700	0.396	0.0	10.484	0.000	0.407
	3.244	891	0.200	0.0	8.210	15.210	0.100	0.0	12.101	0.000	0.350
	7.407	967	0.220	0.0	4.300	1.716	0.701	0.0	11.036	0.000	0.750
	12.387	938	0.190	0.0	2.380	0.000	0.500	0.0	8.579	0.000	0.550
	24.023	670	0.060	0.0	7.204	0.000	0.640	0.0	19.883	1.610	0.202
	50.623	120	0.00	0.0	19.400	0.000	0.700	0.0	48.605	6.480	0.000

	z (m) x 10^{-3}	T (^{o}C) x 10^{3}	P_D radial	P_D vertical	The Mass Spectrometer output at Molecular Weights of: 14	15	18	20	28	32	44
i) r = 0.095m	0.750	0.530	0.04	0.0	15.650	66.930	1.158	0.10	48.303	0.000	1.400
	1.165	0.570	0.04	0.0	19.030	60.600	0.495	0.00	48.075	0.100	1.100
	1.583	0.581	0.055	0.0	15.500	41.800	0.743	0.00	38.248	0.200	1.300
	2.000	0.600	0.080	0.0	12.600	29.600	0.940	0.00	34.270	0.210	1.850
	2.412	0.666	0.080	0.0	11.300	20.380	0.690	0.00	36.613	0.100	1.500
	2.827	0.880	0.085	0.0	10.430	24.200	0.590	0.00	28.627	0.000	1.400
	3.244	0.920	0.090	0.0	8.900	18.600	0.530	0.00	27.540	0.000	1.200
	3.650	0.955	0.130	0.0	7.050	11.400	0.510	0.00	27.653	0.000	1.000
	4.074	1.000	0.150	0.0	6.820	10.500	0.700	0.00	28.567	0.000	1.000
	4.492	0.970	0.170	0.0	5.790	6.700	0.560	0.00	28.780	0.000	1.000
	4.906	0.995	0.200	0.0	5.900	5.720	0.610	0.00	30.693	0.000	1.000
	5.736	1.047	0.210	0.0	6.000	4.300	0.750	0.00	32.007	0.000	1.200
	6.568	1.057	0.220	0.0	6.0000	2.000	0.630	0.00	31.720	0.000	1.200
	7.400	1.075	0.300	0.0	8.420	1.950	0.396	0.00	44.195	0.000	1.600
	8.280	1.086	0.200	0.0	7.900	1.940	0.311	0.00	41.580	0.020	1.600
	9.063	1.092	0.100	0.0	6.650	1.270	0.357	0.00	34.665	0.010	1.500
	9.892	1.098	0.098	0.0	5.680	1.000	2.693	0.00	30.650	0.010	1.200
	10.725	1.100	0.092	0.0	5.500	0.520	2.879	0.00	29.535	0.030	1.100
	11.557	1.099	0.081	0.0	5.020	0.500	3.084	0.00	27.620	0.000	1.100
	11.923	1.098	0.750	0.0	4.980	0.400	2.900	0.00	26.605	0.000	1.150
	12.387	1.097	0.700	0.0	4.890	0.210	2.706	0.00	26.190	0.000	1.200

r = 0.095m.
on.

z (m) x 10^{-3}	T (^{o}C) x 10^{3}	P_D (mm water) radial	vertical	The Mass Spectrometer output at Molecular Weights of: 14	15	18	20	28	32	44
14.048	1.087	0.650	0.0	4.720	0.150	2.418	0.00	25.375	0.050	1.100
14.881	1.080	0.155	0.0	4.700	0.100	2.427	0.00	25.360	0.000	1.100
16.543	1.046	0.500	0.0	4.910	0.000	2.273	0.00	26.345	0.000	1.150
18.204	0.915	0.450	0.0	4.910	0.050	1.899	0.000	26.130	0.200	1.100
19.857	0.870	0.350	0.0	4.800	0.000	1.644	0.00	25.415	0.420	1.000
21.532	0.831	0.300	0.0	4.700	0.000	1.400	0.00	23.500	0.520	0.950
23.194	0.903	0.300	0.0	5.340	0.000	2.588	0.00	28.790	1.000	1.000
24.856	0.850	0.250	0.0	5.210	0.000	2.676	0.00	27.960	1.100	0.900
26.517	0.775	0.200	0.0	5.240	0.000	2.625	0.00	27.730	1.450	0.800
29.841	0.652	0.100	0.0	5.280	0.000	2.653	0.00	28.100	2.050	0.650
34.000	0.435	0.100	0.0	5.720	0.000	2.661	0.00	30.470	3.200	0.400
38.154	0.265	0.050	0.0	6.150	0.000	2.629	0.00	32.640	4.070	0.300
42.310	0.165	0.040	0.0	7.860	0.000	2.037	0.00	42.610	6.030	0.300
46.467	0.145	0.025	0.0	7.580	0.000	1.500	0.00	40.280	5.810	0.300
50.623	0.137	0.000	0.0	7.650	0.000	1.164	0.00	40.550	5.330	0.300
54.779	0.134	0.000	0.0	7.170	0.000	0.912	0.00	37.520	5.510	0.250

	z (m) x 10^{-3}	T (°C) x 10^{3}	P_D (mm water) radial	vertical	The Mass Spectrometer output at Molecular Weights of: 14	15	18	20	28	32	44
j) r = 0.110m	0.750	0.573	0.030	0.0	11.000	41.100	0.654	0.0	17.566	0.000	0.800
	1.167	0.603	0.045	0.0	10.880	36.900	0.489	0.0	18.011	0.000	0.750
	1.583	0.750	0.100	0.0	9.256	28.900	0.503	0.0	17.242	0.000	0.700
	2.000	0.807	0.200	0.0	8.200	24.700	1.157	0.0	17.123	0.000	0.800
	2.412	0.830	0.320	0.0	7.169	20.700	0.501	0.0	15.604	0.000	0.750
	2.827	0.855	0.450	0.0	6.388	16.400	0.506	0.0	15.559	0.100	0.600
	3.244	0.895	0.250	0.01	7.980	15.100	0.653	0.0	35.291	0.243	1.027
	4.074	0.932	0.380	0.0	8.891	13.650	0.366	0.0	36.182	0.096	0.995
	4.908	0.962	0.300	0.0	8.387	10.650	0.400	0.0	38.273	0.380	1.082
	5.736	0.986	2.700	0.0	10.433	10.300	0.533	0.0	50.464	0.043	.709
	7.401	0.912	2.200	0.0	11.003	9.050	0.116	0.0	37.755	0.000	1.436
	9.063	0.983	2.000	0.0	8.974	9.900	0.229	0.0	40.945	0.000	1.364
	10.725	0.913	1.800	0.0	9,945	7.840	0.122	0.0	34.936	0.000	1.391

	z (n) x 10^{-3}	T (^{o}C) x 10^{3}	P_D (mm water) radial	vertical	The Mass Spectrometer output at Molecular Weights of: 14	15	18	20	28	32	44
j) r = 0.110m Con.	12.387	0.981	1.700	0.0	8.615	4.000	0.135	0.0	38.127	0.000	1.418
	13.219	1.033	0.130	0.0	7.381	4.700	1.629	0.0	37.918	0.000	1.345
	14.048	1.064	0.110	0.0	7.357	2.540	2.082	0.0	40.909	0.000	1.573
	15.710	1.080	0.070	0.0	7.692	1.100	2.095	0.0	42.800	0.000	1.900
	17.373	1.075	0.060	0.0	8.068	0.820	1.978	0.0	44.091	0.000	1.927
	21.532	1.025	0.040	0.0	8.473	0.610	1.931	0.0	45.282	0.000	2.205
	25.685	0.884	0.035	0.0	8.269	0.520	1.945	0.0	44.173	1.421	2.032
	29.841	0.750	0.020	0.0	8.215	0.500	2.068	0.0	43.764	2.805	1.709
	34.000	0.663	0.010	0.0	8.180	0.500	1.971	0.0	43.855	3.898	1.386
	38.154	0.383	0.005	0.0	7.986	0.450	2.034	0.0	44.075	4.841	1.014
	42.310	0.245	0.000	0.0	8.222	0.450	2.817	0.0	43.936	5.809	0.891
	46.467	0.155	0.000	0.0	7.977	0.510	2.610	0.0	42.727	6.087	0.718
	50.623	0.140	0.000	0.0	8.093	0.600	2.694	0.0	42.818	6.170	0.745
	54.779	0.133	0.000	0.0	8.069	0.600	2.417	0.0	42.809	6.064	0.723

Appendix 7

Error Analysis of the Interactive Technique

The partial differential equation representing main-stream momentum transfer is:

$$\frac{\partial U}{\partial x} = \frac{\partial}{\partial \psi}(\tau) - \frac{1}{\rho U}\frac{dp}{dx} \qquad (1$$

Alternatively the equation can be cast in the form:

$$\frac{\partial U}{\partial x} + (a + b\omega)\frac{\partial U}{\partial \omega} = \frac{\partial}{\partial \omega}\left(c\,\frac{\partial U}{\partial \omega}\right) - \frac{1}{\rho U}\frac{dp}{dx} \qquad (2$$

with

$$a = \frac{r_I' m_I''}{(\psi_E - \psi_I)\sum_{i=2}^{\infty}(i-1)a_1\Delta\omega^{i-2}}$$

$$b = \frac{r_E' m_E'' - r_I' m_I''}{(\psi_E - \psi_I)^2\sum_{i=2}^{\infty}(i-1)a_i\Delta\omega^{i-2}}$$

$$c = \frac{\rho U r^2 \mu_{eff}}{(\psi_E - \psi_I)^2\left[\sum_{i=2}^{\infty}(i-1)a_i\Delta\omega^{i-2}\right]^2}$$

As detailed in chapter four section three, which deals with the derivation of the new interactive modelling technique, this equation is reduced to an algebraic equation applicable within a finite element of fluid. This step is accomplished by substituting finite difference approximations for the partial differentials in this equation. The purpose of this operation is to estimate how approximate

the finite differences used in the derivation of the interactive technique are, and upon what other parameters they are dependent.

The finite difference assumption used in the interactive technique have been detailed in chapter four, and the results obtained are presented in table overleaf. The coefficients P_j and R_j, for j = 1 to 3; & c_i, for i = 1 and 2, are defined in terms of known parameters in table 2. The velocity profiles assumed for the finite difference assumptions are shown schematically in figure 4 - chapter 4 with ϕ , the general property, taking the value U.

The error analysis described below makes use of two basic assumptions. Firstly, that the fluid elements, into which the flow being simulated is divided, all have the same dimensions. A sketch of the fluid elements and mesh network are presented in figure one, the elements are all Δh high and Δx wide. This means that the mesh network has a uniform grading - the spacing between sequential mesh stream, $\Delta\omega$, is constant-as shown in figure one. Secondly, it has been assumed that the relationships between the velocity at adjacent nodal points of the mesh network can be represented by the following Taylors series:

$$U(x + q) = U(x) + q.U'(x) + \frac{q^2}{2}.U''(x) + \frac{q^3}{6}.U'''(x) \quad - \; -$$

and $$U(x - q) = U(x) - q.U'(x) + \frac{q^2}{2}.U''(x) - \frac{q^3}{6}.U'''(x) \quad - \; - -$$

where q can represent $\Delta\omega$ or Δx in figure one.

The error terms associated with the finite difference assumptions shown in table 1 were obtained by substituting for $U_{d,j+1}$ and $U_{d,j-1}$ the differential given by Taylors theorem. (The subscripts d and j are defined in figure 4 chapter four). The results obtained are detailed in table 3.

Table 1

Finite Difference Assumptions

Finite Difference	Finite Difference Assumptions
$\frac{\Delta U}{\Delta x}$	$P_1 U_{d_{j+1}} + P_2 U_{d_j} + P_3 U_{d_{j-1}}$
$a \frac{\Delta U}{\Delta \omega}$	$a \left[\frac{U_{d_{j+1}} - U_{d_{j-1}}}{\omega_{d_{j+1}} - \omega_{d_j}} \right]$
$b\omega \frac{\Delta U}{\Delta \omega}$	$R_1 U_{d,j+1} + R_2 U_{d,j} + R_3 U_{d,j-1}$
$\frac{\Delta}{\Delta \omega} \left[c \frac{\Delta U}{\Delta \omega} \right]$	$\frac{1}{\omega_{D-} - \omega_D} \left[C_+ \left[\frac{U_{d,j+1} - U_{d,j}}{\omega_{d,j+1} - \omega_{d,j}} \right] - C_- \left[\frac{U_{d,j} - U_{d,j-1}}{\omega_{d,j} - \omega_{d,j-1}} \right] \right]$

Coefficients	Definitions
P_1	$\left[\frac{2}{(x_{d,j}-x_{u,j})(\omega_{d,j+1}-\omega_{d,j-1})(\omega_{d,j+1}-\omega_{d,j})}\right]\left\{\sum_{i=2}^{\infty}\left(\frac{i-1}{i}\right)a_i\left(\frac{\omega_{d,j+1}-\omega_{d,j}}{2}\right)^i\right\}^i$
P_2	$\left[\frac{2}{(x_{d,j}-x_{u,j})(\omega_{d,j+1}-\omega_{d,j})}\right]\left\{\sum_{i=2}^{\infty}a_i\left(\frac{\omega_{d,j+1}-\omega_{d,j}}{2}\right)^{i-1}-\left(\frac{1}{\omega_{d,j-1}-\omega_{d,j}}\right)\sum_{i=2}^{\infty}\left(\frac{i-1}{i}\right)a_i\left(\frac{\omega_{d,j+1}-\omega_{d,j}}{2}\right)^i\right.$ $\left.+\left(\frac{1}{\omega_{d,j}-\omega_{d,j-1}}\right)\left[\sum_{i=2}^{\infty}\left(\frac{i-1}{i}\right)a_i\left(\omega_{d,j}-\omega_{d,j-1}\right)^i-\sum_{i=2}^{\infty}\left(\frac{i-1}{i}\right)a_i\left(\frac{\omega_{d,j}-\omega_{d,j-1}}{2}\right)^i\right]\right\}$
P_3	$\frac{2}{(x_{d,j}-x_{d,j-1})(\omega_{d,j+1}-\omega_{d,j-1})}\left[\sum_{i=2}^{\infty}a^i(\omega_{d,j}-\omega_{d,j-1})^{i-1}-\sum_{i=2}^{\infty}a_i\left(\frac{\omega_{d,j}-\omega_{d,j+1}}{2}\right)^{i-1}\right.$ $\left.-\left(\frac{1}{\omega_{d,j}-\omega_{d,j-1}}\right)\left\{\sum_{i=2}^{\infty}\left(\frac{i-1}{i}\right)a_i\left(\omega_{d,j}-\omega_{d,j-1}\right)^i-\sum_{i=2}^{\infty}\left(\frac{i-1}{i}\right)a_i\left(\omega_{d,j}-\omega_{d,j-1}\right)^i\right\}\right]$

Table 2 cont

Definitions

Coefficients	Definitions
R_1	$\left[\frac{2.b}{\left(\omega_{d,j+1}-\omega_{d,j-1}\right)\left(\omega_{d,j+1}-\omega_{d,j}\right)}\right]\left[\sum_{i=1}^{\infty}\frac{a_i}{i}\left(\frac{\omega_{d,j+1}-\omega_{d,j}}{2}\right)^i\right]$
R_2	$-\left[\frac{2.b}{\omega_{d,j+1}-\omega_{d,j-1}}\right]\left[\left(\frac{1}{\omega_{d,j+1}-\omega_{d,j}}\right)\sum_{i=1}^{\infty}\frac{a_i}{i}\left(\frac{\omega_{d,j+1}-\omega_{d,j}}{2}\right)^i-\left(\frac{1}{\omega_{d,j}-\omega_{d,j-1}}\right)\right.$ $\left.\left[\sum_{i=1}^{\infty}\frac{a_i}{i}\left(\omega_{d,j}-\omega_{d,j-1}\right)^i-\sum_{i=1}^{\infty}\frac{a_i}{i}\left(\frac{\omega_{d,j}-\omega_{d,j-1}}{2}\right)^i\right]\right]$
R_3	$-\left[\frac{2.b}{\left(\omega_{d,j+1}-\omega_{d,j-1}\right)\left(\omega_{d,j}-\omega_{d,j-1}\right)}\right]\left[\sum_{i=1}^{\infty}\frac{a_i}{i}\left(\omega_{d,j}-\omega_{d,j-1}\right)^i-\sum_{i=1}^{\infty}\frac{a_i}{i}\left(\frac{\omega_{d,j}-\omega_{d,j-1}}{2}\right)^i\right]$

Coefficients	Definition
c_+	$\dfrac{\rho U r^2 \mu_{eff}}{(\psi_E - \psi_I)^2 \sum_{i=2}^{\infty} (i-1)\, a_i \left(\dfrac{\omega_{d,j+1} - \omega_{d,j}}{2}\right)^{i-2}}$
c_-	$\left[\dfrac{\rho U r^2 \mu_{eff}}{(\psi_E - \psi_I)^2}\right] \left[\dfrac{1}{\sum_{i=1}^{\infty} (i-1) a_i \left(\dfrac{\omega_{d,j} - \omega_{d,j-1}}{2}\right)^{i-2}} - \dfrac{1}{\sum_{i=1}^{\infty} (i-1) a_i (\omega_{d,j} - \omega_{d,j-1})}\right]$

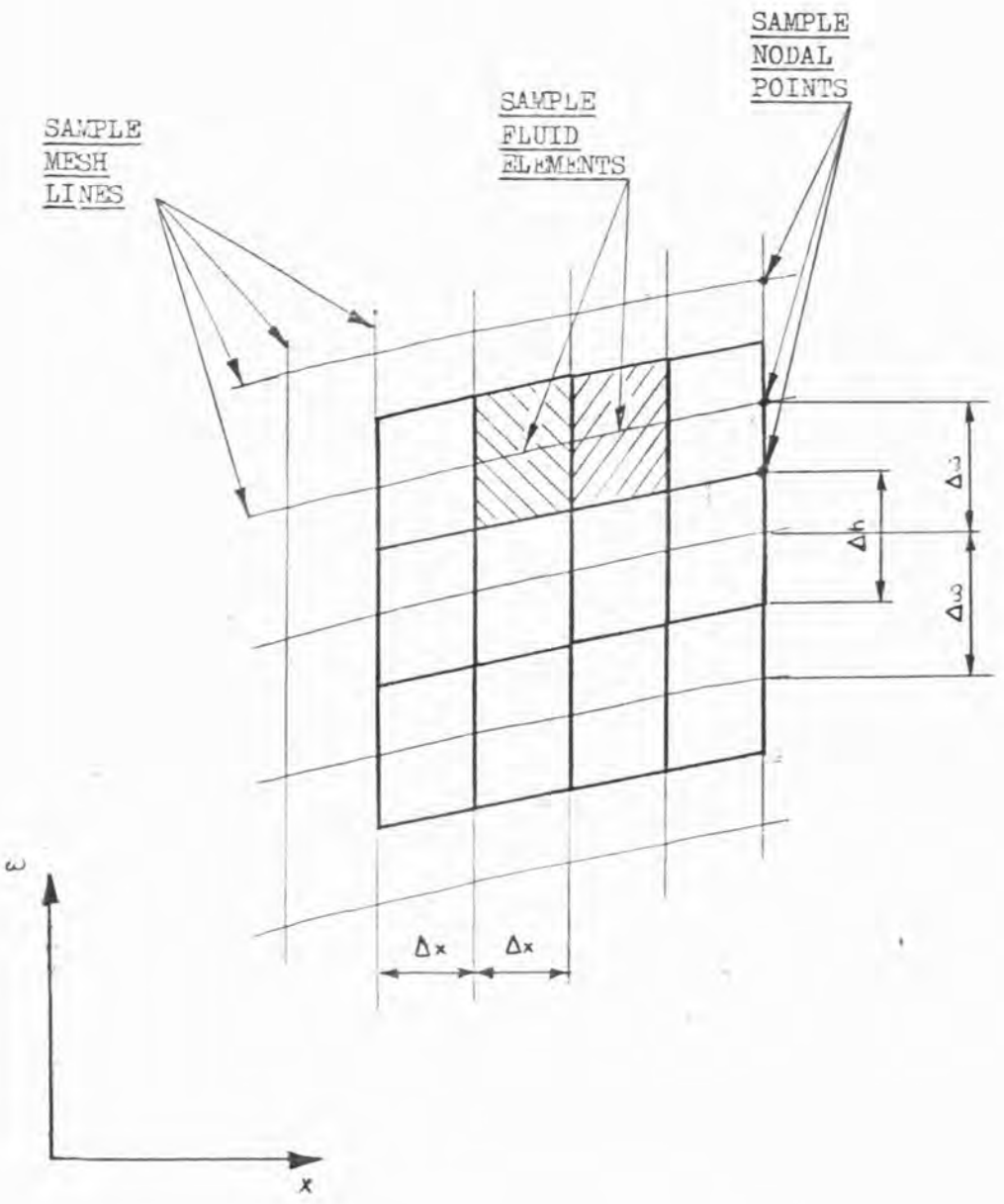

PORTION OF MESH NETWORK

FIGURE ONE

Partial Differential	Error
$aU'(\omega)$	$a\frac{\Delta\omega^2}{6}U'''(\omega) + a\frac{\Delta\omega^3}{24}U^{iv}(\omega) + HOT_1$
$U'.(cU'(\omega))$	$u'(\omega)(c_+ - \underline{c}) + \frac{\Delta\omega}{6}U'''(\underset{+}{c} - \underset{-}{c}) + \frac{\Delta\omega^2}{24}U^{iv}(\omega)(\underset{+}{c} + \underset{-}{c}) + HOT_2$
$U'(x)$	$U''(x)\,\Delta x\Delta\omega(P_1 - P_3) + U'''(x)\frac{\Delta x\,\Delta\omega^2}{2}(P_1 + P_3) + HOT_3$
$b\ U'(\omega)$	$U''(\omega)\frac{\Delta\omega^2}{2}(R_1 + R_3) + U'''(\omega)\frac{\Delta\omega^3}{6}(R_1 - R_3) + HOT_4$

Acknowledgements

The author respectfully acknowledges the support and advice of his supervisor, the late, Dr. R.N. Maxwell. Professor C.D.S. MacLellan, who monitored the writing of this thesis, constructive and helpful criticisms are also gratefully acknowledged.

References

In this section each reference is detailed in the following way;-

1. For a publication - Authors Name, Journal, Volume, Page, Year.

2. For a book - Authors Name, Title, Publisher, Year.

3. For a Thesis - Authors Name, Title, University, Degree, Year.

1 PRANDTL,L.,Über die ausgebidete Turbulenz,Z.A.M.M., Vol.5,page 136-,1925.

2 VAN DRIEST,E.R., On turbulent flow near a wall , Heat Trans. & Fluid Mech., University of California,1955.

3 BRADSHAW,P.,The understanding and prediction of turbulent flows,Aeronautical Journal,Vol11,page 423,1972. Also,On turbulent flow near a wall,J.Aeronaut, Vol 23,page 1007-,1956.

4 BEER,G.M.& CHIGIER,N., Combustion Aerodynamics , Applied Science Publishers, 1972.

5 SMITH,M.G., Plasma Physics , The Institute of Physics, 1973.

6 KESTIN,J.,MAEDER,P.F.,& SOGIN,H.H,Z.,The influence of turbulence on the transfer of heat to cylinders near the stagnation point,Agnew.Math.Phys., Vol12,page 115,1961.

7 SPALDING,D.B.& PATANKAR,S.V., Heat & Mass Transfer in Boundary Layers , Intertext,1970.

8 DENNY,V.E.& LANDIS,R.B., Animproved transformation of the Spalding-Patankar type for the numerical solution of two dimensional boundary layers, International Journal of Heat & Mass Transfer, Vol.14,page 1389,1972.

9 GRUSCHWITZ,E. ,Die turbulente Reibungsschicht in ebener Strömung bei Druckabfall und Druckansteig,Ing.-Arch., Vol. 2, pages 321-46,1931.

10 CARTER,H.C., The developement of turbulent boundary layers,Aeronautical Research Council, page 2133,1944.

11 VON DOENHOFF,A.E.& TETERVIN,N.,Determination of general relations for the behaviour of turbulent boundary layers. N.A.C.A. Rep.772,1943.

12 PRANDTL,L.,Collected Works,Vol.II,page 620,1932.

13 FALKNER,V.M,Aircraft Engineering, Vol.15,page 65,1943.

14 SQUIRE,H.B.& YOUNG,A.D.,Aeconautical Research Council R.M.1938,1838.

15 PASTSCH,J.,Zur thecretischen Berechnung des Profilwiderstandes.Jb.dt. Luftfahrtforschung I,Vol 61,1938.

16 TRUCKENBRODT,E.,Ein Quadraturverfahren zur Berechnung der laminaren und turbulenten Reubungsschic bei ebener und rotations symmetrischur Stromung,Ing.,Arch.,Vol.20,page 211,1952.

17 HEAD,M.R.,Entrainment in the turbulent boundary layer, ARCR and M .3152,1960

18 HARTREE,D.R.& WOMERSLEY,J.R.,A method for the numerical or mechanical solution of certain types of partial differential equation,Proc.Roy,Soc. London,Vol.161 series A,Page 353-,1937.

19 CEBECI,T.,Behaviour of Turbulent Flow near a Porous Wall with Pressure Gradient,Vol.8, page 2152-,1970.

20 SMITH,A.M.O.,JAFFE,N.A.& LIND,R.C.,Study of a general method of solution of the incompressible turbulent boundary layer equation,Fluid Mechanics & Flight Dynamics Branch, RRRE-4,1965.

21 MELLOR,G.L.,Turbulent boundary layers with arbitrary pressure gradients & divergent or convergent cross flows,Dept.Aerospace Mech.Sci.Gas Dynamics Lab.Rep.-,1966.

22 SCHLICHTING,H.,Boundary Layer Theory (Sixth Edition), McGraw-Hill,1968.

23 HIRSCHFELDER,J.O.,CURTIS,C.F.& BIRD,R.B., Molecular Theory of Gases & Liquids. John Wiley & Son NewYork,1965.

24 PRANDTL,L.,Über einneues Formel system für die ausgebildete turbulenz. Nachrichten der Akad.Wiss.,Gottingen,Mathphys page 6- Van den Loeck & Ruprecht, Gothingen.

25 KOLMOGROFF, A.N., Equations of turbulent motion of an incompressible fluid, Izv. Akad. Nauk SSSR Ser. Phys., Vol VI, No.162, page 56-, 1942.

26 GLUSHKO, G.S., Turbulent boundary layer on plane plates incompressible fluid, Izv. Akd., Nauk. Mech., Vol 4, page13-, 1965.

27 [illegible], V.V. & YOVAGIAY, L.G.G., Simple Phenomenological Theory of Turbulent Shear Flow, Journal of Physics(USSR), VolIX, No.3, page 235-, 1965

28 LAUNDER, B.E. & SPALDING, D.B., Mathematical models of Turbulence, Academic Press, 1972.

29 CLAUSER, F.H., Turbulent boundary layers in adverse pressure gradients, Journal of Aerospace Science, Vol.21.2, page 91-, 1954.

30 SCHOENHERR, K.E, Resistance of flat surfaces moving through a fluid, Trans. Soc. Nav. Arch & Mar Eng., Vol.40, page 279, 1932.

31 IKURADSE, I., Untersuchungen über die Strömunger des Warsers in konvergenten und divergenten Kanölen, Forschungsarbeiten of the V.D.I, No.289, 1929.

32 SCHWARZ, W.H & COSART, W.P., The two dimensional turbulent wall jet, Journal of Fluid Mechanics, Vol.10, page 481-, 1961.

33 GERALD, C.F, Applied Numerical Analysis, Addison & Wesley, 1970.

34 RIGAL, A. & ALEIX, M., Journal of Numerical Methods in Engineering, 1974.

35 COLES, D., The law of the wake in the turbulent boundary layer, Journal of Fluid Mechanics, Vol.I, page 191, 1956.

36 PORCH, M., TSUEI, Y.G. & GERMAK, J.E., Investigation of a Turbulent Radial Wall Jet, Journal of Applied Mechanics, Vol.8, page 457, 1967.

37 SOUTH,N.E. & KELLY,J.P., Ford Motor Co., NC Development Unit,Product Engineering Office,1965.

38 FROBERG,C.E., Numerical Analysis, Addison-Wesley Publishing Co.,1970.

39 SEBAN,R.A. & BACK,L.H.,Effectiveness & heat transfer for a turbulent boundary layer with tangential injection & variable free stream velocity, American Soc.of Mechanical engineers ,Vol.10, page 45-,1962

40 NARASIMHA,R.,YEGNA NARAYAN,K.& PARTHASARATHY,S.P., Aeronautical Journal,Vol.13,page355-,1973.

41 TOWNSEND,A.A.,Journal of Fluid Mechanics,Vol.11, page 97-,1961.

42 BAKKE,P.,The Radial Wall Jet,Journal of Fluid Mechanics, Vol.II,page 467-,1957.

43 BRADSHAW,P.,The understanding and prediction of turbulent flow,Aeronautical Journal,July, page 213,1972.

44 GLAUERT,M.B.,The Wall Jet,Journal of Fluid Mechanics, Vol.1,page 625-,1955.

45 ROGERS,G.F.C.& MAYHEW,Y.R., Thermodynamic & Transport Properties of Fluids,Blackwell.,1967.

46 SPALDING,D.B. & PATANKAR,S.V.,A finite difference procedure for solving the equation of the two dimensional boundary layer,International journal of Heat & Mass Transfer, Vol.1, page 1389-,1967.

47 ROBERTSON,J.M.,Journal of Applied Mechanics,Vol.18, page 95-,1955.

48 OLD,M, PhD. Thesis, University of Leicester.

49 CEBECI, T., Turbulent Prandtl Number near a wall, Journal of Heat Transfer, Vol.12, page 227, 1973.

50 AFGAN, N.H. & BEER, J.M., Heat Transfer in Flames, Halstead Press, 1974.

51 WHITELAW, J.H. & KHALIL, E.E., The calculation of local flow in two dimensional furnaces, Report from Imperial College of Science & Technology, HTS/74/38, Nov.1974.

52 KONDAT'EV, V.N., Chemical Kinetics of Gas Reactions, Pergamon Press, 1964.

53 CAMPION-RENSON, A. & CROCHET, M.J., On the Stream Function Vorticity Finite Element Solutions of Navier-Stokes Equations, Int.Jnl., for Numerical Methods in Engineering, Vol.12, page 1809-18, 1978.

54 TAYLOR, C. & HOOD, P. A., Numerical Solution of the Navier-Stokes Equations using the Finite Element Technique, Computers Fluids, No.1, 1973.

55 HARLOW, F.H., Transport of anisotropic or low intensity turbulence, Los Alamos Science Lab., University of California, LA-3947, 1968.

56 DISA HANDBOOK, Disa, 1968.

57 MOFFAT, R.J., Gas Temperature Measurements, Vol.III, Reinhold Pub.Co., 1962.

58 SMITH, S.R. & GARDON, A.S., Journal Physical Chemistry, Vol.60, page 759, 1956

59 SPALDING, D.B., Numerical Computation of Practical Combustion Chamber Flows. A.G.A.R.D No.164, An Analytical & Numerical Method for Investigation of Flow Fields with Chemical Reaction, Section 1, Part 1, 1974.

60 SPALDING, D.B., Mathematical Models of Turbulent Flames - a Preview, Comb, Sci.&.Tech. Vol.13, page 3-, 1976.

61 SWITHENBANK,J., TURAN,A., FELTON,P.G.& SPALDING,D.B., Fundemental Modelling of Mixing, Evaporation & Kinetics in Gas Turbine Combustors A.G.A.R.D No 275,on Combustion Modelling,page 4,1979.

62 BILGER,R.W., Turbulent Jet Diffusion Flames. Prag.Eng. Camb.Sci, Vol.1,page 87,1976.

63 BEER,J.M.& CHIGIER,N.A.,Combustion Aerodynamics, Applied Science,1974.

64 SWITHENBANK,J, Combustion Fundementals, Prandtl Lecture, Von Karmen Institute,1972.

65 KARLOVITZ,B., DENNISTON,D.W & WELLS,F.E, J.Chem.Phys, Vol.19,page 541-,1951.

66 DAMKÖHLER,G., English Translation,N.A.C.A Tech. Memo. 1112 1947.

67 SHCELKIN,K.I.,English Translation, N.A.C.A Tech.Memo.1110, 1947.

68 SCHUMAN,A.,Sixteenth International Conference on Combustion(International) University of Swansea.

69 GRESHO,P.,LEE,R.L & SANI,R.L, On the Time Dependent Solution of the Incompressible Navier-Stokes Equations in two and three Dimensions, Recent Advances in Numerical Methods in Fluids, Peneridge Press,1980.

70 FAVRE,A., Problems of Hydrodynamics & Continium Mechanics, Soc.of Ind.&App.Mech.,page 23-,1969.

71 ROACHE,P.J., Computational Fluid Mechanics, B.L.L.D 77/18429,1976.

72 LEONARD,B.P., A Survey of Finite Difference ----- Equation, City Univ. of New York.

73 ZIENKIEWICZ,O.C., The Finite Element Method, Mc Graw Hill, 1977.

74 GOSMAN,A.D. PUN ,W.M., RUNCHAL,A.K SPALDING,D.B. & WOLFSHTEIN,M. Heat & Mass Transfer in Recirculating Flows, Academic Press,1969.

75 GOSMAN,A.D., KHALIL,E.E. & WHITELAW,J.H The Calculation of two Dimensional Turbulent Recirculating Flows, Turbulent Shear Flows, Springer Verlay,1979.

76 WHITELAW,J.H.& GREEN,A., Measurement & Calculations of the Isothermal Flow in Axisymmetric Models of Combustor Geometries, J.Mech.Eng.Sci., Vol.2,No.3, page 119-,1980.

77 PECK,R.E.& SAMUELSON,G.S., Eddy Viscosity Modelling in the prediction of Turbulent Backmixed Combustion Performance.

78 WORMECK, J.& PRATT,D.T.,Computer Modelling in a Longwell Jet Stirred Reactor, J.Chem.Eng., page 1583-, 1977.

79 PATANKAR,S.V.& SPALDING,D.B., A Calculation Procedure for Heat,Mass and Momentum Transfer in three Dimensional Parabolic Flows, Int.J.Heat & Mass Tr.Vol.15,page 1787-,1972.

80 SPALDING,D.B.& PATANKAR,S.V.,Simultaneous Predictions of Flow Patterns & Radiation for three Dimensional Flames, Heat Transfer in Flames, Halstead Press,1974.

81 SPALDING,S.B.& PATANKAR,S.V., Simultaneous Predictions of Flow Patterns & Radiation from Three Dimensional Flames, Scripta Technica,1980.

82 COURANT,R.ISAACSON,E.&REES,M., On the Solution of non-Linear Hyperbolic Differential Equations with Finite Differences, Com.Pure & Appl. Math., Vol V, 245-,1952.

83 RICHTYMER,R.D., A Survey of Difference Methods for Non-Steady Fluid Dynamics,N.C.A.R,Tech.Note,

84 COURANT,R.,FRIEDRICHS,K & LEWY,H,On the Partial Difference Equations of Mathematical Physics,Inter-Science Pub.Inc.,Newyork,1967.

85 GELDER,D., Solution of Compressible Flow Equations, Int.J.Numer.Methods Eng.,Vol.3,1971.

86 VON MISES,R.,Bemerkungen Zur Hydrodynamic, Z.A.M.M, Vol 7, page 425-,1972.

87 DE VRIES,G.,BERARD,G.P. & NORRIE,D.H.,Applications of the Finite Element Technique to Compressible Flow Problems,Univ.Calgary,Mech.Eng.Rept. 18,1974.

88 PERIAUX,J.,Three Dimensional Analysis of Compressible Potential Flows with Finite Element Methods, Int.Symp.of Finite Element Methods,1974.

89 OLSON,M.D.,A Variational Finite Element Method for Two-Dimensional Steady Viscous Flows,Joint McHill,University-Eng.Institute of Canada Conference,1972.

90 IKENOUCHI,U.& KIMUA,N.,International Symposium on Finite Elements held at University of Swansea,1974.

91 TAYLOR,C.& HOOD,P., A Numerical Solution of the Navier-Stokes Equations using the Finite Element Technique,Computers Fluids, Vol.1,1973.

92 BAKER,A.J.,Finite Element Theory for Viscous Fluid Dynamics, Bell Aero,Co.Res.Rept.9500-920189, 1970.

93 BAKER,A,J.,A Numerical Solution Technique for Two-Dimensional Problems in Fluid Dynamics Formulated with the use of Discrete-Element, Bell Aerospace Systems Co.Report,TN/TCTN1005, 1970.

94 BAKER,A.J., Finite Element Solution Algorithm for Viscous Incompressible Fluid Dynamics,Int.J.Numer. Methods Eng., Vol.6,1973.

95 CHENG,R.T.,Numerical Solution of the Navier-Stokes Equations by the Finite Element Method,J.Phys.Fluids Vol 15,1972.

96 SKIBA,E.,UNNY,T.E.& WEAVER,D.S., A Finite Element Solution for a Class of Two-Dimensional Viscous Flow Dynamics Problems,Symposium held at University of Waterloo,1971.

97 YAMADA,K.,YOKOUCHI,Y.,LAMANO,T.& OHTSUBA,T., Finite Element Analysis of Steady Fluid & Metal Flow, International Symposium on Finite Elements held at University of Swansea,1971.

98 HUEBNER,H., Finite Element Methods for Engineers, Addison-Wesley,1978.

99 CHANG,P.W. & FINLAYSON.B.A., Math.Comp.Sim., Vol20, page 83-,1978.

100 CHANG,PING-WU,PATTEN,T.W.,ADAMS,F.T.& FINLAYSON,B.A., Galerkin & Collation Finite Element Methods for Newtonian & Viscoelastic Fluids, Recent Advances in Numerical Methods in Fluids,Pineridge Press,page 119-,1980.

101 BAKER,A.J.& SOLIMAN,M.O., Accuracy,Convergence & Utility of Finite Element Generated Solution Algorithm for Initial Value Problems, J.Comp Phys,1980.

102 BAKER,A,J.,Laminar & Turbulent Boundary Flows, Recent Advances in Numerical Methods in Fluids, Pineridge Press,page 287-,1980.

103 BOUSSINESQ,J.,Theorie De L'ecoulement Tourbillant, Mem.Prés.Acad.Sci.XXIVI,Vol46, 1877.

104 PAI,B.R.& WHITELAW,J.H., The Prediction of Wall Temperature in the presence of Film Cooling, Imp.Col.Rep. EHT/TN/A/22,1970.

105 JONES,W.P. & LAUNDER,B.E.,The Prediction of Laminarisation with a Two Equation Model of Turbulence,Int.J.Heat 7 Mass Transfer, Vol. 15,page 301-,1972.

106 BRADSHAW,P.,FERRIS,D.H.&ATWELL,N.P., Calculation of Boundary Layer Development Using the Turbulent Energy Equation, J.Fluid Mech. Vol 28,page 593-,1967.

107 NG,K.H.& SPALDING,D.B.,A Comparison of three Methods of Predicting the Hydrodynamic Behaviour of Two Dimensional Turbulent Boundary Layers,Phy.of Fluids Vol 15,1972.

108 SIVASEGARAM,S.& WHITELAW,J.H., The Prediction of Turbulent Supersonic Two Dimensional Boundary Layer Flows,Aero.Qrt.,Vol.22, page 274,1971.

109 ROTTA,J.,Statistishe Theorie Nighthomogener Turbulenz, Zeitsch.Fur Physik, Vol 129, page 457-, 1951.

110 ROTTA, J., Recent Attempts to Develop a Generally Applicable Calculation Method for Turbulent Shear Flows, AGARD. 1971.

111 SPALDING, D.B. & RODI, W., A Two Parameter Model of Turbulence & it's application to Free Jets, Wärme und Stoffubertraguug, Vol3, page 85-, 1970.

112 CHOU, P.Y., On the Velocity Correlation & the Solution of the Equations of Turbulent Fluctuations, Quarterly Jnl. of Applied Mathematics, Vol.3, page38-, 1945.

113 JONES, W.P. & LAUNDER, B.E., The Prediction of Laminisation with a Two-Equation Model of Turbulence, Int. N.Heat & Mass Tra. Vol 15, page 301-, 1972.

114 SPALDING, D.B., The Prediction of Two-Dimensional Steady Turbulent Flows, Imp.Col.Heat Tr. Sec^{n}. Rep. EF/TN/A/16.

115 HANJALIĆ, K., Two-Dimensional Asymmetric Flow in Ducts, PhD. Thesis, University of London.

116 HARLOW, F.H. & NAKAYAMA, P.I., Transport of Turbulence, Univ.Cal.Rep., Rep.LA-3854.

117 DREISLER, R.G., Turbulent Heat Transfer & Temperature Fluctuations in a Field with Uniform Velocity & Temperature Gradients, Int.J. of Heat & Mass Tran., Vol 6, page 257-, 1963.

118 SIMPSON, R.L., WHITTEN, D.G. & MOFFAT, R.J., An Experimental Study of the Turbulent Prandtl Number of Air with Injection & Suction. Int.J. Heat & Mass Tran., Vol 13, page125-, 1970.

119 SPALDING, D.B. KHALIL, E.E. & WHITELAW, J.H., The Calculation of Local Flow Properties in Two Dimensional Furnaces, Int.J.Heat & Mass. Tran., Vol 18, page 775-, 1979.

120 BRAY, K.N.C. & MOSS, J.B., A Unified Statistical Model of the Premixed Turbulent Flame. Deta Astronautica, Vol.4, page 291-, 1977.

121 HINZE, J.O., Turbulence, McGraw Hill, 1972.

122 VAN DUYVENVOORDEN, C., Beradering van fysische an chemische groothesden uit rookgassen van Graningen aardgas/lucht mengsels door Chebyshev dubbel polynomen, Laharotorium voor Energievoorziening Delft, Rep. VS7703, 1977.

123 BALAU, J.R., Radical Overshoots & Dissociation in Methane & Air Flames, J.Chem.Phys, Vol.162, page 3605-, 1975.

124 DONALDSON, C.du.P., Turbulent Mixing in Non-reactive & Reactive Flows, Plenum Press, New York, page 131-, 1975.

125 DONALDSON, C.du.P. & VARMA, A.K., Remarks on the construction of a second order closure description of turbulent reacting flows, Combustion Science & Technology, Vol.13 Nos.1-6, page 55-, 1976.

126 BORGHI, R., Methods Analytique de Prevision des taux de Reaction Chimique on Presence D'une Turbulence non Homogene, A,G,A,R,D Nos 164 On Analytical & Numerical Methods for the Investigations of Flow Fields with a Chemical Reaction, Section 2, Part 4, 1974.

127 LOCKWOOD, F.C. & NAGUIB, A.S., The predictions of the Properties of Free, Round jet, Turbulent Diffusion Flames, Combustion & Flame, Vol.24, page 105-, 1975.

128 SPALDING, D.B., A General Theory of Turbulent Combustion, the LaGrangian Aspects, AIA Paper No.77, page 141-, 1975.

129 JONES, W.P. & Mc GUIRK, J.J., Mathematical Modelling of Gas Turbine Combustion Chambers, A.G.A.R.D. on Combustion Modelling, page 4-, 1974.

130 VARMA, A.K. SANDRI, G. & DONALDSON, C du P., Modelling of Scaler pdf's in Turbulent Flows, Project ARAP-1-PU, 1978.

131 KEWLEY, D.J., Developement of a Second Order Closure Model for Turbulent Reacting Flows, 6th Australasian Hyd. & Flu.Mech.Conf., Dec 5-9 1977, Adelaide Australia.

132 DRYER, F.L. & WESTBROOK, C.K., A Comprehensive Mechanism for Methane of Oxidation, Camb.Sci.& Tech., Vol.20, page 125-, 1979.

133 DRYER, F.L. & GLASSMAN, I., Combustion Chemistry of Chain Hydrocarbons, Prog. in Astronautics & Aeronautics, Vol.62, 1977.

134 COHEN,R.S.,DRYER,F.L.& GLASSMAN,L., The Combustion of Hydro-Carbons in an Adiabatic Flow Reactor, Joint Fall Meeting of Central & Weston States Sections of the Combustion Institute, San Antonio,Texas,April 1975.

135 EDELMAN,R.B.& HARSHA,P., Current States of Laminar & Turbulent Gas Dynamics in Combustors, Spring meeting of the Central States Section of the Combustion Institute,Law Research Centre,Cleveland,Ohio,March 1977.

136 LONGWELL,J.P.& WEISS,M.A.,Ind.Eng.Chem.,Vol.47,page 1634-, 1955.

137 LEE,K.B.,THRING,M.W & BEER,J.M., On the rate of Combustion of soot in a Laminar Flame,Vol.6,page 137-, 1962.

138 EDELMAN,R.B.,TURAN,A.HARSHA,P.T.,WONG,E.& BLAZOWKI,W.S., Fundamental Characterization of Alternative Fuel Effects in Continuous Combustion Systems, A.G.A.R.D No.275 on Combustion Modelling, Vol.13,1979.

139 PAAUW,T.A.,STROO A.J.& VAN KOPPEN,C.W.J., An Effective Probalistic Simulation of the Turbulent Flow & Combustion in Axi-Symmetric Furnaces,A.G.A.R.D No.275 on Combusttion Modelling,Vol.21,1971.

140 LOWES,T.M.& HEAP,M.P.,Emission /AttenuationCoefficients of Luminous Radiation,I.F.R.F.,Proceedings of 2nd Member Conference,Ijmuiden,1971.

141 PENNER,S.S.,Quantative Molecular Spectroscopy & Gasemissivities, Addison-Wesley,1959

142 TIEN,C.L.,Thermal Radiation Properties of Gases, Advances in Heat Transfer (Editors J.P. Hartrett & I.F.Irvine),Vol.5,page 253-,1968.

143 BARTELDS,H.,Development & Verification of Radiation Models,A.G.A.R.D, No.275 on Combustion Modelling,Vol.11,1979.

144 HOTTEL,H.C.& SAROFIM,A.F., Radiative Transfer, McGraw & Hill,1967.

145 JOHNSON,T.R.,Application of the Zone Method of Analysis to the Calculation of Heat Transfer, PhD.Thesis,Sheffield Univ.1971.

146 HADVIG,S., Gas Emissivity & Absorptivity, J.Inst.Fuel, Vol.43,page 129-,1970.

147 BEER,J.M.& CLAUS,J., The Traversing Method of Radiation measurement in Luminous Flames, J.Inst.Fuel ,Vol.35,page437-443,1962.

148 PERRY,J.H.,Chemical Engineers Handbook, McGraw & Hill, 1963.

149 VAN KUIJK,R.M.& SPANJERSTH.Th.H.,De overdracht van de in een ouurhaurd van een stoomketel ontwikkelde warmte een het door de verdampe rpijpen stomendi koclwater,Nederlanase vereniging voor Vlamonderzook,I.F.R.F,1973.

150 SIEGEL,R.& HOWELL,J.R.,Thermal Radiation Heat Transfer, Vols.I-III,N.A.S.A.,1971.

151 TIEN,C.L.,Thermal Radiation Properties of Gases in Heat Transfer (ed.Hartnett,J.P & Irvine,T.F), Vol.5,page 253-,Academic Press,1968.

152 HOTTEL,H.C.& COHEN,E.S.,Radiant Heat Exchange in a Gas Filled Enclosure:allowances for non-uniformity of gas temperature,A.I.Ch.E., Vol.4,pages 3-14,1958.

153 STEWARD,F.R.& GURUZ,H.K.,Mathematical Simulation of a Industrial Boiler by the Zone Method, Heat Tr. in Flames,Halstead Press, Chapter Three,1974.

154 SCHUSTER,A., Astrophys,J, Vol 21, pages 1-22,1905.

155 SIDDALL,R.G., Flux Methods for the Analysis of Radiant Heat Transfer, Inst. of Fuel & B.F.R.C., 4th Flame & Ind.Symp.,1972.

156 SCHWARZCHILD,K.,Sitzber.Preuss,Akad,Wiss., Physik-Math., Klasse, page 1183,1941.

157 MILNE,E.A.,Hnadbuch Der Astophsik., Vol.3,1930.

158 EDDINGTON,A.S.,The Internal Constitution of Stars, Dover Press,1954.

159 GOSMAN,A.D.& LOCKWOOD,F.C.,Paper Presented at Fourteenth Symp.(International) on Combustion, Penn.State University,1972.

160 JOHNSON,T.R.& BEÉR,J.M.,Further Development of the Zone Method, Fourteenth Symp.(International) on Combustion,Penn State University,1972.

161 ZELDOVICH,B.Ya.,Avta Physiochim (USSR),Vol.21,page 577, 1946.

162 STEWART,F.R. & CANON,P.,Tha Calculation of Radiative Heat Flux in a Cylindrical Enclosure using the Monte Carlo Method,Int.Jul Heat & Mass Transfer,Vol.14,page 245,1974.

163 SCHWARZCHILD.,K,Nachr.Akad,Wiss., Math.Physik - Klasse 1, 1960.

164 NASH,P.K.,Kingston Poly., London,Private Communication.

165 HAMAKER,H.G.,Phillips Research Reports Nos. 2,55,103, 112 and 420,1974.

166 Proceeding of General Discussions on Heat Transfer, Inst.Mech.Eng.,1951.

167 LIBBY,P.A.,Studies Related to Turbulent Flows Involving Fast Chemical Reaction. AGARD No. 164

AUTHORS	REF.NO.	AUTHORS	REF.NO.
AFGAN & BEER	50	COURANT,ISAACSON & REES	82
BAKER	93	DAMKÖHLER	66
BAKER	92	DENNY & LANDIS	8
BAKER	94	DISA	56
BAKER	102	VON DOENHOFF & TETERVIN	11
BAKER & SOLIMAN	101	DONALDSON	124
BAKKE	42	DONALDSON & VARMA	125
BALAU	123	DREISLER	117
BARTELDS	143	VAN DRIEST	2
BEER & CHIGIER	4	DRYER & GLASSMAN	133
BEER & CHIGIER	63	DRYER & WESTBROOK	132
BEER & CLAUS	147	VAN DUYVENDOORDEN	122
BILGER	62	EDDINGTON	158
BORGHI	126	EDELMAN & HARSHA	135
BOUSSINESQ	103	EDELMAN & TURAN	138
BRADSHAW	3	FALKNER	13
BRADSHAW	43	FAVRE	70
BRADSHAW,FERRIS & ATWELL	106	FRÖBERG	38
BRAY & MOSS	120	GARNER	10
CAMPION,RENSON & CROCHETT	53	GELDER	85
CEBECI	19	GERALD	33
CEBECI	49	GLAUERT	44
CHANG & FINLAYSON	99	GLUSHKO	26
CHANG,PING-WU,PATTEN & ADAMS	100	GOSMAN & KAHIL	75
CHENG	95	GOSMAN & LOCKWOOD	159
CHOU	112	GOSMAN & PUN	74
CLAUSER	29	GRESHO,LEE & SANI	69
COHEN,DRYER & GLASSMAN	134	GRUSCHWITZ	9
COLES	35	HADVIG	146
COURANT,FREDERICHS & LEWY	84	HAINES	5

AUTHOR	REF.NO	AUTHOR	REF.NO.
HANJALIC	115	MELLOR	21
HARLOW	55	MILNE	157
HARLOW & NAKAYAMA	116	VON MISES	86
HARTREE & WORMERSLEY	18	MOFFAT	57
HAMAKER	165	NARASIMHA & YEGNA NARAYON	40
HEAD	17	NASH	164
HINZE	121	NEE & KOVASNAY	27
HIRSCHFELDER, CURTIS & BIRD	23	NG & SPALDING	107
HOTTEL & COHEN	152	NIKURADSE	31
HOTTEL & SAROFIM	144	OLD	48
HUEBNER	98	OLSON	89
IKENOUCHI & KIMUA	90	PAAUW, STROO & VAN KOPPEN	139
JOHNSON	145	PAI & WHITELAW	104
JOHNSON & BEER	160	PANTANKAR & SPALDING	79
JONES & LAUNDER	113	PECK & SAMUALSON	77
JONES & LAUNDER	105	PENNER	141
JONES & MC.GUIRK	129	PERIAUX	88
KARLOVITZ, DENNISTON & WELLS	65	PERRY	148
KESTIN & MAEDER	6	PORCH, TSUEI & GERMAK	36
KEWLEY	131	PRANDTL	1
KOLMOGROFF	25	PRANDTL	12
KONDAT'EV	52	PRANDTL	24
VAN KUIJK & SPANJERS	149	PRETSCH	15
LAUNDER & SPALDING	28	RICHTYMER	83
LEE & THRING	137	RIGAL & ALEIX	34
LEONARD	72	ROACHE	71
LOCKWOOD & NAGUIB	127	ROBERTSON	47
LONGWELL & WEISS	136	ROGERS & MAYHEW	45
LOWES & HEAP	140		

AUTHOR	REF. NO.	AUTHOR	REF. NO
ROTTA	110	SPALDING & PATANKAR	46
ROTTA	109	SPALDING & PATANKAR	7
SHCELKIN	67	SPALDING & PATANKAR	80
SCHLICHTING	22	SPALDING & PATANKAR	81
SCHOENHERR	30	SPALDING & RODI	111
SCHUMAN	68	STEWARD & GÜRÜS	153
SCHUSTER	154	STEWART & CANON	162
SCHWARZCHILD	163	SQUIRE & YOUNG	14
SCHWARZCHILD	156	SWITHENBANK	64
SCHWARZ & COSART	32	SWITHENBANK, TURAN, FELTON & SPALDING	61
SEBAN & BECK	39	TAYLOR & HOOD	54
SIDDALL	155	TAYLOR & HOOD	91
SIEGEL & HOOD	150	TIEN	142
SIMPSON, WHITTEN & MOFFAT	118	TIEN	153
SIVASEGARAM & WHITELAW	108	TOWNSEND	41
SKIBA, UNNY & WEAVER	96	TRUCKENBRODT	16
SMITH & GARDON	58	DE VRIES, BERARD & NORRIE	87
SMITH & JAFFE	20	VERMA, SANDRI & DONALDSON	130
SOUTH & KELLY	37	WHITELAW & KHALAL	51
SPALDING	60	WHITELAW & GREEN	76
SPALDING	59	WORMECK	78
SPALDING	128	YAMADA, YOKOUCHI, LAMANO & OHTSUBA	97
SPALDING	114	ZIENKIEWICZ	73
SPALDING & KHALIL	119	ZELDOVITCH	161

Nomenclature

Symbol	Meaning
A	coefficient in Spalding-Patankars modelling technique
A_1	constant in equation 8.6
A_+	constant in van Driest's turbulence model
A'	coefficient in the modelling technique proposed by Denny-Landis
b	distance between surface and exit nozzle
B	coefficient in Spalding-Patankar
B'	coefficient in the modelling technique
c	coefficient in the modelling technique proposed by Denny-Landis
c'	speed of light
C_D	constant in turbulent energy equation
C_f	total skin friction
C'	coefficient in the modelling technique proposed by Denny-Landis
d_1	nozzle width
d_1	portion of friction work transformed into heat
D	diameter
E	voltage
E_k	activation energy in Arrhenius type equation
E_0	base voltage
E'	electric field strength
f	functional relationship
Fr	constant in equation 3.8 and 6.8
F_k	frequancy factor in Arrhenius equation
FN	constant in Λ relationship (set to 1 or 2)
G	terms in generalized conservation equation 4.7

Symbol	Meaning
h	enthalpy
H	terms in generalized conservation equation 4.7
H_{12}	shape factor $= \left(\frac{\delta_1}{\delta_2}\right)$
H'	magnetic field strength
I	output signal in amps. from mass spectrometer
J_h	turbulent species flux
J_k	turbulent enthralpy flux
k	turbulent kenetic energy
k_m	constants in Cebeci's turbulence model designated 8.6
k_n	constants in Cebeci's turbulence model designated 8.6
K	constant in van Driests turbulence model
l	length scale distribution in turbulent energy equation 3.3
l_m	Prandtl's mixing length
L	velocity gradient limit
m	gravimetric concentrations
m_k	gravimetric concentration of species k
m_+	dimensionless mass flow rate through surface
$\dot{m}''_{fe}$	entrainment rate at free-edge
$\mathcal{M}$	molecular weight
p	time averaged static pressure
p_+	dimensionless pressure
$(Pr_t)_0$	Prandtl number at surface
Pr	Prandtl number
p_D	time averaged dynamic pressure

Symbol	Meaning
r	radial distance from stagnation point
R	radius of curvature
$\mathcal{R}$	universal gas constant
$\dot{w}_k$	reaction rate of species k
Re_x	Reynolds number $\left(=\left(\frac{U_\infty x}{\nu}\right)\right.$
Sc	Schmidt number
t_1	energy of turbulent motion
T	time averaged temperature
u'	fluctuating mainstream velocity
U	time averaged mainstream velocity
C_f	skin friction coefficient $\left(= \frac{\tau_0}{\frac{1}{2}\rho U^2}\right)$
U_∞	free-stream velocity
v'	fluctuating cross-stream velocity
V	time averaged cross-stream velocity
$\dot{V}$	volumetric flowrate
y	distance in cross-stream direction from prescribed datum
y_+	dimensionless distance
μ	viscosity
ρ	time averaged density
ρ'	fluctuation density
τ	shear stress
τ_0	shear stress at surface
Φ	general predicted property

Symbol	Meaning
ψ	stream function
Ψ	non-dimensional stream function $\left[= f\left(\frac{\psi - \psi_1}{\psi_N - \psi_1}\right)\right]$
ω	non-dimensional stream function $\left[= \frac{\psi - \psi_1}{\psi_N - \psi_1}\right]$
Ω	non-dimensional stream function $\left[= \left(\frac{\psi - \psi_1}{\psi_N - \psi_1}\right)^{1/FN}\right]$
θ	angle in degrees
Δr	small increment of r
Δx	small increment of x
δ	width of two dimensional nozzle
δ_1	displacement thickness
δ_2	momentum thickness
δ_3	energy thickness
δ_4	height, in plane or radial wall jet, where $U = U_{max}/2$
δ_5	height, in plane or radial wall jet, where $U = \frac{U_{max}}{2}$ and $\delta_5 > \delta_4$
$\delta_{1,1}$	height of flow at starting cross-stream section
α	angle in degrees
α_k	constant in turbulent energy equation 3.3
ν	kinematic viscosity shape factor
γ	normal distance between a prescribed line and curve

Subscripts

Symbols	Meanings
AV	average
Ar	Argon
CH_4	Methane
CO_2	Carbon Dioxide
CO	Carbon Monoxide
eff	effective component
l	molecular component
max	maximum
mix	mixture
n	nozzle
N^1	surface free-edge
N_2	Nitrogen
O_2	Oxygen
t	turbulent component

Abstract

Momentum, Heat and Mass Transfer Rates in Boundary Flows

R. Waters

A modelling technique for simulating the time averaged properties in boundary flows has been formulated. The technique solves the time averaged equations representing conservation of momentum, mass and heat transfer with an approximate mathematical method; and makes use of an interactive scheme, involving manipulation of the mesh into which the flow is divided, to reduce errors from the mathematical method.

This technique has been used to simulate the time averaged momentum, mass and heat transfer rates in a series of radial wall jet flows. It has been shown that the technique can predict momentum, mass and heat transfer rates in flow situations similar to those commonly found in industry. However, accurate simulation of the turbulent transfer processes in a chemically reacting Methane, Carbon Monoxide and Oxygen flow was found to be impossible, because of deficiences in the reaction model. From these results it was deduced that to accurately simulate the transfer processes in complex flows, involving chemical or ionic reactions, a more sophisticated modelling technique should be constructed. It is recommended that this technique be based upon the exact turbulent transport equations.